

**Investigation of the Thermo-Hygro-Chemico-Mechanical performance of
the Bentonite Barrier at the High-Level Radioactive Waste Canister
Interface**

Student: Christopher William Davies

**Supervisor(s): Dr Colin T Davie (CEG), Professor Stephanie Glendinning (CEG) and
Dr Alasdair Charles (CEAM)**

Doctor of Philosophy

School of Civil Engineering and Geosciences

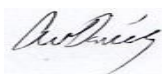
September 2017

Declaration

“I hereby certify that this work is my own, except otherwise acknowledged and no other copy had been submitted for academic accreditation at any institution prior to this submission.”

Christopher William Davies

Signed:



C. Davies recognises the funding received from the **EPSRC** (Grant EP/I036427/1) as well as patronage from the **Radioactive Waste Management Limited (RWM)** (<http://www.nda.gov.uk/rwm>), a wholly-owned subsidiary of the Nuclear Decommissioning Authority. RWM is committed to the open publication of such work in peer reviewed literature, and welcomes e-feedback to rwmdfeedback@nda.gov.uk.

Acknowledgement

This project was conducted as part of a research consortium known as SAFE Barriers, consisting of several academic and industrial institutions. I appreciate the support from the NDA and the BGS during the research project which enabled the progression and direction of this work.

Many thanks to my supervisors Dr Colin T Davie and Dr Alasdair Charles for their academic support and encouragement throughout my research. Also, I would like to express my appreciation to Mr Stuart Patterson, Mr Fred Beadle, Mrs Maggie White and Dr Anker Neumann for their extremely useful support and mentoring during my experimental work. I feel I have greatly expanded my knowledge base and skill set in the laboratory due to their invaluable assistance.

I would like to extend my utmost appreciation to my family and close friends who have supported me in all aspects of my life during this undertaking. You all have provided the much-needed encouragement for me to keep calm and carry on.

Abstract

This research focuses specifically on the geotechnical and physicochemical evolution of the highly-compacted Bentonite at the radioactive waste canister interface, with respect to the multi-barrier system for deep geological disposal of radioactive waste. The research investigated the geomechanical (i.e. Swelling pressure, self-healing, permeability and rheology) and mineralogical (i.e. Fe enrichment/ integration into the aluminosilicate structure and alteration to the accessory minerals) evolution of the Bentonite barrier under key life phases of the near-field regarding thermo-hygro-mechanical-chemico factors. Such life phases were derived from leading concepts and were simplified into three fundamental stages replicating key stages of the near-field. The first phase was “early-life” replication where high temperatures/ drying conditions were exposed to the interface. The second phase replicated the “mid-life” conditions, subjecting the interface to resaturation using high saline ground water with high temperatures but lower than the initial thermal exposure. The final phase replicated the “late-life” conditions which subject the interface to background thermal loading, representative of background temperatures of a crystalline host rock, with a completely saturated/ hydrostatic saline pore-water environment. Post analysis examined the impact on the geomechanical and physicochemical properties with respect to how these relate to the desired functionality of the passive barrier system. Previous work has seldom addressed this interface system from a coupled engineering and physicochemical perspective. A comprehensive investigation looking at how the near-field environment inhibits the desired engineering function and the related physicochemical state will enable insight into building a UK specific safety case.

This research employed an experimental approach exploring the boundary conditions that the interface would experience as inferred from leading international radioactive waste repository concepts. Experimental methods included batch testing, interface replication and geotechnical constant volume tests. Batch tests looked at a mix of variable boundary conditions relevant to the near-field interface environment and isolated specific conditions to measure the intrinsic alterations to the desired engineering function. Interface replication tests subject MX-80 Bentonite, compacted to in-situ emplacement conditions, and carbon steel to an interface environment under three separate “life-phases” (as stated earlier) to assess what phase had the most significant impact on the geomechanical and physicochemical state of the barrier. Finally, the constant volume experiments subject oedometer samples to “mid-life”

conditions as well as isolated “mid-life” variables respectively. Post exposure measurements looked at the impact of the various “mid-life” boundary conditions and their associated impact on the swelling pressure, swelling kinetics, permeability and rheology. “Mid-life” conditions were chosen to carry forward into the oedometric tests as this phase was considered to subject the Bentonite to the highest thermal loading under the most complex chemical environment.

This work has highlighted key near-field factors that alter the interface barrier function after relatively short-term exposure. Such as thermal loading and exposure to high salinity, both induce alterations to the swelling pressure, swelling kinetics and rheological properties. It was observed that high temperature-saline exposure caused loss in the dielectric constant and reduction in the Diffuse Double Layer (DDL), as well as the dissolution/ precipitation of silica which inhibited the swelling and plasticity of the MX-80. Exposure to corrosion products derived from S275 carbon steel appear not to significantly affect the physical properties of the Bentonite compared to thermal and saline factors after short-term experimental contact. However, corrosion integrated into the Bentonite matrix after thermal loading in the presence of Deionised (DI) water displayed a slight increase in the kinetic behaviour. This was concluded to be due to the high volumetric capacity of the hydrated corrosion products within the clay matrix. Furthermore, interface tests indicate some alteration to Ferro-saponite type smectites, indicating some Fe integration into the octahedral layer resulting in a trioctahedral smectite. The outer zone furthest away from the canister was characteristic to Mg-type saponite. Nonetheless, XRD displayed that the clay component remained high charge smectite with no alteration to the d-spacing after swelling. Green rust and Goethite was observed at the interface and mid zones respectively, the ferrous mineral appeared to be meta-stable when exposed to ambient conditions. Physicochemical analysis indicated the presence of ferrous hydroxides complexed to the edge sites of the clay. High diffusion rates and dissolution rates of iron corrosion and secondary minerals respectively were greater in “mid-life” and “late-life” conditions. This indicates that thermal loading, as well as a high saline hydraulic gradient, aided the corrosion process and displacement of interlayer cations away from the corrosion rich zone. This resulted in the development of a high pH environment which ultimately increased dissolution rates of the secondary minerals. The dissolution of silica minerals induced precipitation of siliceous by-products upon cooling which essentially “fused” clay particles together, ultimately inhibiting the macro swelling properties and ductility. Results show that the macro-scale geomechanical properties of the

Bentonite do not deviate below the design limits set out by leading concepts, but do come close to the minimum limits for swelling pressure (1 – 2MPa). Concern is however highlighted for combined thermo-saline-chemical exposure, which appears to cause significant loss in the ductility of the MX-80. This may be disadvantageous to the stress distribution around the canister which is necessary to ensure that the canister is not breached due to potential rock displacements etc. Neither comparative data, nor design limits were set out for barrier stiffness, therefore the study suggests that high thermal exposure and duration is kept to an absolute minimum. The research has further highlighted the need to investigate the impact of a completely reduced iron-rich environment on the engineering function of the Bentonite barrier, as completely reduced conditions were difficult to obtain within the time-scale of this study. Other research suggests that a Fe^{2+} rich environment would accelerate clay alteration as well as alterations to layer charge and lattice stresses potentially inducing 2:1 to 1:1 alteration, all of which potentially lead to complete loss in the swelling behaviour of the clay.

Table of contents

1.	Introduction	1-37
1.1.	Project aim and objectives	2-3
1.2.	Research questions	3
1.3.	Scope	4-5
1.4.	Thesis Structure	5-6
1.5.	Current leading HLW/SF disposal concepts	6-16
1.5.1.	SKB Concept	8-10
1.5.2.	NAGRA Concept	10-12
1.5.3.	POSIVA Concept	12-13
1.5.4.	ANDRA Concept	13-15
1.5.5.	BMWi Concept	15-16
1.5.6.	Concluding statement	16
1.6.	The need to develop a long-term strategy within the UK	16-37
1.6.1.	Existing SURF/HLW, ILW and LLW volumetric waste forms and the current interim storage situation	22-24
1.6.2.	The UK's deep geological facility concept and commonly considered host rock lithology's	25-35
1.6.3.	The UK's engineered multi-barrier concept	36-37
2.	Literature review	38-111
2.1.	Near-field considerations and its impact on the Bentonite within the multi-barrier disposal system	38
2.1.1.	Near-field THCM evolution	38-42
2.1.2.	Near-field environment for a crystalline host rock concept	42-44
2.1.3.	Buffer design parameters	44-46
2.1.4.	Geomechanical and geochemical parameters of the EBS system	46-54
2.1.5.	Steel corrosion development at the clay/ canister interface	54-55
2.1.6.	Thermal evolution impact within the near-field	56-62
2.1.7.	Near-field pH and its associated impact	62-63
2.1.8.	Natural analogues	63-64
2.1.9.	Overview of the microbial considerations of the near-field	64-65
2.1.10.	Concluding statement	65-66
2.2.	Thermo-Hydro-Mechanico-Chemico studies on MX-80 Bentonite	67- 111
2.2.1.	Montmorillonite mineralogy and heterogeneity	67-70
2.2.2.	THCM studies and their effects on the geomechanical/ physicochemical properties on the MX-80	70-109
2.2.3.	Concluding statement	109-111
3.	Experimental and post analysis testing methodologies	112-164
3.1.	Pilot batch test methodology	113-120
3.2.	Carbon steel/ Bentonite interface experimental study	120-125

3.3.	Constant volume experimental structure and post analysis test methodology	125-127
3.4.	Thermal loading and duration experiments	127-128
3.5.	Thermal loading, duration and high saline pore water experiments	128-130
3.6.	Bentonite compaction methodology	130-140
3.7.	Geotechnical post testing methodologies	140-149
3.8.	Physicochemical post testing methodologies	149-162
3.9.	Concluding statement	162
4.	Material characterisation	163-195
4.1.	Geomechanical classification and comparison between two MX-80 sources	163-178
4.2.	Geotechnical comparison- Concluding statement	178-179
4.3.	Physicochemical classification of the two MX-80 sources	179-194
4.4.	Concluding statement	195
5.	Batch test results	196-247
5.1.	Batch test series results	198-240
5.1.1.	Batch #1- Saline/MX-80 studies	198-203
5.1.2.	Batch #2- Saline/ compacted MX-80 studies	203-206
5.1.3.	Batch #3- Thermo-Saline/ compacted MX-80 studies	206-208
5.1.4.	Batch #4- Steel-Saline/ MX-80 studies	208-216
5.1.5.	Batch #5- Thermo-Duration/ MX-80 studies	216-221
5.1.6.	Batch #6- Saline-Thermo-Duration/ MX-80 studies	221-222
5.1.7.	Batch #7- Steel-Thermo-Duration-saline/ MX-80 studies	223-235
5.1.8.	Batch #8 &9- 1-year steel-saline/ MX-80 studies and 2-year steel/ MX-80 studies	235-240
5.2.	Discussion	240-246
5.3.	Conclusion	246-247
6.	Experimental interface results	248-298
6.1.	Interface post-mortem inspection	249-255
6.1.1.	Phase #1: Initial conditions	249-250
6.1.2.	Phase #2: Mid-life conditions	250-251
6.1.3.	Phase #3: Late-life conditions	251-252
6.1.4.	Interface corrosion integration comparison	252
6.1.5.	Oxidation study on the green Bentonite taken from the interface	253-255
6.2.	Post THC exposure geotechnical testing	255-260
6.2.1.	Plastic limit measurements	255-256
6.2.2.	Plasticity index measurements	256-257
6.2.3.	Swell index measurements	257-258
6.3.	Post THC exposure physicochemical analysis	258-293
6.3.1.	CEC measurements	258-259
6.3.2.	XRD analysis	259-278

6.3.3.	SEM analysis	278-285
6.3.4.	UV spectrophotometric analysis	285-286
6.3.5.	ICP elemental analysis	286-291
6.3.6.	Mossbauer analysis	291-293
6.4.	Conclusion	293-298
7.	Constant volume test results	299-311
7.1.	Swelling pressure results	300-304
7.2.	Swelling kinetics results	304-306
7.3.	Permeability	306-308
7.4.	Rheology	308-309
7.5.	Conclusion	309-311
8.	Conclusions and recommendations for further research	312-320
8.1.	Batch tests findings summary	313-314
8.2.	Interface findings summary	315-318
8.3.	Constant volume geomechanical batch tests findings summary	318-319
8.4.	Recommended areas of further research	319-320
9.	Bibliography	321-346
10.	Appendix	347+

Table of figures

Figure 1: Target site location for the SKB disposal concept in Forsmark	8
Figure 2: The KBS-3 multi-barrier concept	8
Figure 3: Diagrammatic representation of the HLW deposition hole	10
Figure 4: Repository layout schematic for the deposition of the HLW/SF	11
Figure 5: Photo of the Mont Terri rock laboratory, open tunnel wall of the Opalinus clay	11
Figure 6: The Horizontal disposal gallery with the multi-barrier configuration	12
Figure 7: The Posiva repository based on the KBS-3V design	13
Figure 8: Callovo-Oxfordian formation of the Parisian basin underlying Meuse/ Haute-Marne	14
Figure 9: HLW/ SF Canister configuration	15
Figure 10: Bentonite emplacement schematic	15
Figure 11: German HLW/SF disposal concept	16
Figure 12: MWRS framework for site selection and community involvement	19
Figure 13: Air-cooled interim storage systems for vitrified HLW at Sellafield	24
Figure 14: The GDF concept for HLW long-term storage	26
Figure 15: 12Km^3 simplified model of of a host rock displaying 2 nd and 3 rd order discontinuities	27
Figure 16: A realistic discontinuity map for a 16Km^3 of a crystalline host rock in south-eastern Sweden	27
Figure 17: Thermal conductivity and permeability of host rocks	33
Figure 18: Young's modulus of granite as a function of increasing temperature	35
Figure 19: The multi-barrier concept as well as the safe barriers operational structure	37
Figure 20: Inferred interface evolution form the NAGRA concept	39
Figure 21: Diagrammatic representation of the impact of salt on the osmotic pressure gradient	48
Figure 22: Swelling pressure and Hydraulic conductivity with respect to dry density with various salt concentrations	49
Figure 23: Pore water pressure in elevated temperature clay media	50
Figure 24: Simplified depiction of the importance of the barrier ductility	51
Figure 25: Comparison between Na and Ca homo-ionic bentonites	52
Figure 26: Thermal-temporal evolution from canister heat dissipation	57
Figure 27: Temperature profile for the Swiss concept	57

Figure 28: Predicted thermal profile for the Posiva concept	58
Figure 29: Thermal contour profile of the Posiva repository concept	59
Figure 30: Comparison of the MX-80 exposed to hydrothermal treatment and ambient temperatures	60
Figure 31: Conversion rates of smectite to illite according to Pytte/ Reynolds model using an activation energy of 27Kcal/mol	61
Figure 32: pH temporal distribution profile of the near-field	62
Figure 33: Corresponding photos of the samples supplementing the data in Table 14	63
Figure 34: Unit cell configuration of the Montmorillonite mineral and reference points for basal spacing measurements	67
Figure 35: Concept of turbostratic configuration	70
Figure 36: Layered structure of montmorillonite	71
Figure 37: Liquid limit reduction of two smectite clays with increasing salt concentration	71
Figure 38: XRD patterns from the THC Bentonite NaOH reaction	72
Figure 39: XRD patterns after THC Bentonite reaction with KCl and KOH after 150°C for 2 months	73
Figure 40: Na-smectite reacted with KCO_3 displays run product and starting material XRD patterns	74
Figure 41: TEM image of zeolite development in Na-smectite after THC exposure to 150°C in a KCO_3 solution	74
Figure 42: TEM image of zeolite development in MX80 after 300°C exposure	75
Figure 43: TEM image of Calcium silicate hydrate development in Na,Ca-smectite after 150°C THC exposure	76
Figure 44: Plagioclase dissolution after 300°C, SEM image	77
Figure 45: TEM image of Calcite, Quartz or cristobalite and Fe-Oxyhydroxides within the Bentonite matrix after 80°C and 150°C	78
Figure 46: TEM image of Neofomed palygorskite-type minerals after 80°C (6 months) and 150°C (3 months)	78
Figure 47: XRD spectra of MX-80 exposed to three thermal loading and duration increments	79
Figure 48: Proctor compaction curves displaying dry density of MX-80 with different salt solutions	80
Figure 49: Free swell measurements of MX-80 with different salts and concentrations	81
Figure 50: Liquid limit Vs. salt concentration	81
Figure 51: Permeability measurements from consolidation tests with increasing salt CaCl and NaCl	81
Figure 52: Hydraulic conductivity of compacted MX-80 with increasing concentration of Na cations	82

Figure 53: Liquid limit on MX-80 Vs. monovalent cation concentration	82
Figure 54: Random mount XRD of Bentonite before and after thermal exposure	83
Figure 55: Change in permeability with increasing suction	84
Figure 56: Hydraulic conductivity with respect to the suction and state of saturation of the MX-80	84
Figure 57: Unsaturated hydraulic conductivity measured under confined conditions and different temperatures as a function of the suction	85
Figure 58: Influence of permeant composition on the materials permeability with density	85
Figure 59: The permeability of THC exposed MX-80 with a comparison to the control	86
Figure 60: Volumetric strain of confined Bentonite under thermal loading	87
Figure 61: BET measurements of the MX-80 with distance from the heated interface	88
Figure 62: CEC and exchangeable cation concentration measurements with distance from the heated interface	88
Figure 63: Bulk powder XRD patterns for the MX-80/ Fe THC samples	89
Figure 64: BET measurements on MX-80 with respect to thermal duration	90
Figure 65: XRD patterns for THC exposed samples (MX-80, 300°C) with a comparison to the starting MX-80	91
Figure 66: MX-80 water absorption capacity in an NaCl solution	92
Figure 67: Oriented XRD patterns from the NaCl saturated tests at 25°C after a reaction time of 2, 10, 50, 122, 214, 307, 402 and 508 days	93
Figure 68: Gypsum formation on the surface of the montmorillonite crystals and aggregated gypsum within the intra-layer voids	94
Figure 69: Siliceous by-products precipitated on Bentonite particles taken from the natural analogue in Kinnekulle	95
Figure 70: Rheology data displaying the reduction in strain with increasing thermal exposure	95
Figure 71: Silica particles formed on Montmorillonite particles	96
Figure 72: Illustration of the cementation of particles which causes increased hydraulic conductivity as well as reduced stiffness and swelling pressure	97
Figure 73: Random powder XRD on samples taken at different distances from the heater	98
Figure 74: Cation concentration with respect to distance from the heated surface	98

Figure 75: CEC measurements over the Bentonite block with respect to distance from heater	99
Figure 76: Free swell of MX-80 with temperature	100
Figure 77: PI Vs. thermal loading	101
Figure 78: d001 reflections with respect to RH (%) with different chemically exposed sample	103
Figure 79: XRD pattern on post Fe/MX-80 exposure after heating at 250°C in NaCl solution for 92 days	106
Figure 80: Structural Fe oxidation patterns for post THC Bentonite	107
Figure 81: TEM image of the Fe altered smectite, displaying 2:1 to 1:1 modification	108
Figure 82: Sorption sites for Fe(II) cations as well as structural iron reduction via electron pathways	109
Figure 83: Batch test #1 MX-80 in contact with increasing saline solution no volumetric constraints	116
Figure 84: Batch test #2 compact with no volumetric constraints	116
Figure 85: Batch test #3 C-steel plate in contact with uncompact Bentonite	116
Figure 86: Batch test #4 compacted and heated to 100°C within a constant volume cell	117
Figure 87: Batch test #5 Synthetic groundwater batch test set up for 150°C	117
Figure 88: Batch test #6 C-steel plate in contact with uncompact Bentonite at 20°C for 1 year	117
Figure 89: Groundwater elemental analysis taken from the east gate borehole	119
Figure 90: Pre-compacted Bentonite block supplied by claytechAB	122
Figure 91: Steel-Bentonite interface experimental configuration for THC exposure	122
Figure 92: 3D concept of the interface cell	123
Figure 93: Fully annotated schematic of the interface concept	123
Figure 94: Bentonite physical phase state representative of early to long-term conditions	123
Figure 95: Nitrogen purged glove box for interface sub-sampling and post testing sample allocation	124
Figure 96: Constant volume batch sample dimensions	126
Figure 97: Constant volume batch thermo exposure cell	126
Figure 98: Compaction pilot test mould and instron apparatus	133
Figure 99: Dry density Vs. compaction pressure of two types of Bentonite at 8% moisture	134
Figure 100: Test #1 of pilot compaction tests (55MPa)	135
Figure 101: Test #2 of the pilot compaction tests (55MPa)	135

Figure 102: Test #3 of the pilot compaction tests (9MPa)	137
Figure 103: Test #4 of the pilot compaction tests (100MPa)	137
Figure 104: Measured rebound of sample diameter over 9 days after peak pressure of 100MPa	138
Figure 105: Measured rebound of sample height over 9 days after peak pressure of 100MPa	138
Figure 106: ELE manual oedometer apparatus	143
Figure 107: GDS AOES apparatus	144
Figure 108: ELE oedometer calibration curves	144
Figure 109: Direct shearScan2 with modifications	146
Figure 110: Fabricated pulley with loading assembly	146
Figure 111: Load cell measuring applied force and displacement transducer measuring sample creep	147
Figure 112: Consolidation curve on a root time axis displaying T_{90}	147
Figure 113: UV-Vis spectrophotometer	151
Figure 114: Mossbauer spectra for a saprolitic soil containing Fe oxides within the clay matrix and within the structure	153
Figure 115: Spectra before and after “washing” of the interlayer oxides	153
Figure 116: Ionised argon plasma jet and temperature profile at nebuliser outlet	155
Figure 117: A simplification of a mineral structure with a consistent spacing displaying the incidence X-Ray and associated angle	157
Figure 118: Oriented sample preparation for XRD analysis- clay suspension on watch glass	161
Figure 119: Oriented air dried sample on glass slides	161
Figure 120: PSD for MX-80 Bentonite	164
Figure 121: PSD analysis comparison of both MX-80 consignments	165
Figure 122: Control swell index results for batches #1 and #2 along with a comparison to the Ca-type Bentonite	169
Figure 123: Control swelling pressures for the RS® MX-80	170
Figure 124: Oedometric swelling pressure tests conducted on samples under reference properties	171
Figure 125: Swelling pressure Vs. Dry density results with controls	172
Figure 126: Swelling kinetics measurements for the control samples on the RS MX-80	172
Figure 127: Swell stage graphs for control USS samples under 4MPa normal stress	174
Figure 128: Area correction illustration for circular shear box	174
Figure 129: Compiled stress Vs. strain graphs for the control specimens	175
Figure 130: Control rheology results	176
Figure 131: Consolidation graph for control sample #2	177

Figure 132: Available zones for cation sorption and surface area comparison between smectite and kaolinite	
Figure 133: Oriented XRD spectra for the RS MX-80 control	180
Figure 134: Oriented XRD spectra for the RS MX-80 control, focusing more closely on the high angle peaks	182
Figure 135: Bulk XRD spectra run on both RS MX-80 and SKB MX-80	185
Figure 136: Oriented air-dried and glycolated control runs for both RS and SKB materials	187
Figure 137: Air dried oriented high angle peaks for both control materials	188
Figure 138: 002/003 intensity ratios for both control materials	189
Figure 139: Mossbauer comparison of the two starting bentonites at -133°C and -269°C	190
Figure 140: Several temperature Mossbauer profiles of the RS MX-80 Bentonite at 20°C, -133°C and -269°C	191
Figure 141: Elemental composition of the starting materials, digested samples	193
Figure 142: SEM-EDX analysis on the starting materials	194
Figure 143: Saline/ MX-80 batch tests 1-month duration	199
Figure 144: Swell index results for the MX-80/ salt exposure and the Ca-Bentonite in NaCl solution	200
Figure 145: Diagrammatic representation of the swelling hypothesis given by Lee et al (2012)	201
Figure 146: MX-80 PI and activity Vs. Saline solution concentration for the individual electrolyte batch tests	202
Figure 147: Compacted MX-80 with S275 particles	
Figure 148: Batch samples after 1 month of saturation with increasing saline solution (NaCl)	203 204
Figure 149: Swell index results for batch #2	
Figure 150: Plastic limit results for batch #2	205
Figure 151: From Batch test #3 (steel/MX-80 and distilled water)	205
Figure 152: Batch #3 swell index measurements post THC exposure	206
Figure 153: Batch #3 plastic limit measurements post THC exposure	207
Figure 154: CEC measurements on interface and outer sub-samples from batch test #3	208 208
Figure 155: From Batch test #4 C-Steel plate in contact with uncompact Bentonite (DI Water)	209
Figure 156: Effects on anisotropic compaction on the structure of Bentonite	209
Figure 157: Steel/ clay batch test sub-sample locations for post-tests, batch #4	210
Figure 158: Batch test #4 corrosion diffusion extent	211

Figure 159: Batch #4 swell index measurements	211
Figure 160: Swell index comparison of batch #2 and batch #4	212
Figure 161: Swell index comparison of batch tests #2, #3 and #4	213
Figure 162: Plastic limit results for batch test #4	214
Figure 163: Plastic limit comparison between batch tests #2 and #4	214
Figure 164: CEC measurements on batch series #4	215
Figure 165: Batch #4 and batch #3 comparison	216
Figure 166: Average swell index measurements with increasing thermal exposure for 24 hrs	217
Figure 167: Average plasticity index with increasing thermal exposure for 24hrs	218
Figure 168: Average swell index after thermal loading and duration	219
Figure 169: Average plasticity index after thermal loading and duration	219
Figure 170: CEC measurements for thermal loading tests	220
Figure 171: CEC measurements for thermal duration tests	
Figure 172: Plasticity index Vs. temperature exposure for 56 days with difference salt solutions	222
Figure 173: Swell index measurements for batch series #7	223
Figure 174: Plasticity index for batch series #7	224
Figure 175: Low angle XRD for batch MX-80+ DI water and carbon steel at 20°C	225
Figure 176: Low angle XRD pattern for batch MX-80 + DI water only at 150°C	225
Figure 177: Low angle XRD pattern for batch MX-80 + synthetic groundwater only at 20 °C	225
Figure 178: Low angle XRD pattern for batch MX-80 + synthetic groundwater only at 150 °C	226
Figure 179: Low angle XRD pattern for batch MX-80 + synthetic groundwater and C-Steel at 20 °C	226
Figure 180: Low angle XRD pattern for batch MX80+synthetic groundwater and C-steel at 150°C	226
Figure 181: 002/003 intensity ratio for the DI water + C-steel at 20 °C	227
Figure 182: 002/003 intensity ratio for the DI water +C-steel at 150 °C	228
Figure 183: 002/003 intensity ratio for the groundwater + clay only at 20 °C	228
Figure 184: 002/003 intensity ratio for the groundwater + clay only at 150 °C	229
Figure 185: 002/003 intensity ratio for the groundwater + clay + C-steel at 20 °C	229
Figure 186: 002/003 intensity ratio for groundwater + clay + C-steel at 150 °C	231
Figure 187: High angle peak pattern for the DI water +C-steel at 20 °C	232

Figure 188: High angle peak pattern for the DI water + C-Steel at 150 °C	232
Figure 189: High angle peak pattern for the groundwater + clay only at 20 °C	232
Figure 190: High angle peak pattern for the groundwater + clay only at 150 °C	233
Figure 191: High angle peak pattern for the groundwater + clay + C-steel at 20 °C	233
Figure 192: High angle peak pattern for the groundwater + clay+ C-steel at 150 °C	234
Figure 193: High angle peak pattern for the groundwater + clay+ C-steel at 150 °C of precipitate	235
Figure 194: Swell index results for the 1-year ambient batch test series	236
Figure 195: 1-year batch test series corrosion colour development	237
Figure 196: Plasticity index results for the 1-year batch test series	238
Figure 197: Swell index results for the 2-year batch test with only DI-water	239
Figure 198: Plasticity index results of the 2-year batch samples with DI-water	240
Figure 199: Swell index comparison of DIW samples with respect to temperature and duration	241
Figure 200: Plastic limit comparison of DIW samples with respect to temperature and duration	242
Figure 201: Plasticity index Vs. exposure duration under ambient conditions	243
Figure 202: Reference buffer geometry for the SKB concept	244
Figure 203: Swell index results for the MX-80/ salt exposure and the Ca-Bentonite in NaCl	246
Figure 204: Interface post-mortem diagram for phase #1	250
Figure 205: Interface post-mortem diagram for phase #2	251
Figure 206: Interface post-mortem diagram for phase #3	252
Figure 207: Time-lapse pictures for the dry ambient oxidation tests	253
Figure 208: Time-lapse pictures of the hydrated oxidation tests	254
Figure 209: Average plastic limit profile for each environmental phase for interface samples	255
Figure 210: Outer zone plasticity index measurements for all phases with a comparison to the control parameter	256
Figure 211: Average swell index profile for the interface sub-sampled zones	257
Figure 212: CEC measurements for the interface sub-samples	259
Figure 213: Clay swelling component XRD patterns for interface sub-samples	260-261
Figure 214: Clay swelling component XRD patterns for mid sub-samples	262

Figure 215: Clay swelling component XRD patterns for outer sub-samples	263-264
Figure 216: Clay range XRD profile for interface phase 1 sub-samples	265-266
Figure 217: Clay range XRD profile for interface phase 2 sub-samples	266-267
Figure 218: Clay range XRD for interface phase 3 sub-samples	267-268
Figure 219: 02/003 peak intensity XRD patterns for phase 1 interface sub-samples	270
Figure 220: 002/003 peak intensity XRD patterns for phase 2 interface sub-samples	271
Figure 221: 02/003 peak intensity XRD patterns for phase 3 interface sub-samples	272
Figure 222: Higher angle peak profile for phase 1 interface sub-samples	274-275
Figure 223: Higher angle peak profile for phase 2 interface sub-samples	276-277
Figure 224: Higher angle peak profile for phase 3 interface sub-samples	277-78
Figure 225: Coupon surface EDX elemental measurements compiled for all phases	279
Figure 226: Magnetite on the surface of the interface phase 1 coupon	280
Figure 227: Magnetite on the surface of the interface phase 2 coupon	281
Figure 228: Magnetite on the surface of the interface phase 3 coupon	281
Figure 229: SEM image of the coupon surface taken from phase 2 interface showing Bentonite and oxides	282
Figure 230: Phase 1 interface coupon displaying stress corrosion cracks and phase 3 comparison	283
Figure 231: EDX analysis on interface phase 1 sub-samples	284
Figure 232: EDX analysis of phase 2 interface sub-samples	284
Figure 233: EDX analysis on phase 3 interface sub-samples	285
Figure 234: Fe(iii) concentration profile	285
Figure 235: Fe(ii) concentration profile	286
Figure 236: Compiled ICP results measuring Aluminium concentration for each interface sub-sample and phase respectively	287
Figure 237: Compiled ICP results measuring Calcium concentration for each interface sub-sample and phase respectively	288
Figure 238: Compiled ICP measuring Iron concentration for each interface sub-sample and phase respectively	288
Figure 239: Compiled ICP results measuring potassium concentration for each interface sub-sample and phase respectively	289
Figure 240: Compiled ICP results measuring Magnesium for each interface sub-sample and phase respectively	290

Figure 241: Compiled ICP results measuring Sodium concentration for each interface sub-sample and phase respectively	290
Figure 242: Compiled ICP results measuring Silicon concentration for each interface sub-sample and phase respectively	291
Figure 243: Hyperfine field parameter identification of Fe species	293
Figure 244: Characteristic swelling pressure profiles	300
Figure 245: Comparison between free access of DI water and a high saline solution	304
Figure 246: Characteristic swelling kinetics measurements for each constant volume test with average control comparison	305
Figure 247: Characteristic rheology results under 20% shear stress for 48hrs	308

Table of Tables

Table 1: Commonly considered types of Bentonite for the main European concepts	7
Table 2: Average mineralogical composition from 7 sub-samples of Wyoming MX-80	7
Table 3: Average mineralogical composition from 5 sub-samples of Ibeco-RWC	7
Table 4: Summary of initial screening criteria	20
Table 5: DECC and NDA 2013 waste inventory, waste quantities as of April 2013	22
Table 6: Future waste output prediction	23
Table 7: Physical properties of evaporates as a host rock	28
Table 8: Generic examples of various rock types and properties	29
Table 9: Comparison matrix of the three fundamental rock types with respect to the key properties associated to the stability of the host rock in a repository application	30
Table 10: Significant processes related to the systems approach	36
Table 11: Attributes for the buffer around the waste canister for the three leading design concepts	44-45
Table 12: Preliminary limiting values for the MX-80 barrier	46
Table 13: Comparison of the candidate bentonites	52
Table 14: pH and redox potential measurements	62
Table 15: Mineralogical composition of two batches of MX-80 Bentonite	68
Table 16: Average d-spacing's of MX-80 post hydrothermal treatment (80°C) for 3, 6 and 9 months	77
Table 17: CEC measurements post THC exposure	89
Table 18: Average values of CEC properties post THC exposure	90
Table 19: Methodology and key research questions matrix	113
Table 20: Pilot batch test details	114-115
Table 21: Pilot batch test post analysis details	118
Table 22: Calculated salt concentrations for a crystalline rock mass at 995m BGL	119
Table 23: Experimental matrix for interface replication tests	120
Table 24: Elemental composition of the S275 grade steel	124
Table 25: Post THC exposure testing allocation for the interface samples	125
Table 26: Constant volume batch experimental boundary conditions	126
Table 27: Post THC exposure testing allocation for the constant volume batch samples	127
Table 28: Powdered batch test matrix	128
Table 29: Post exposure geotechnical tests	128

Table 30: Batch test #1: thermal loading and electrolyte exposure at Eastgate concentrations	129
Table 31: Batch test #2: Bentonite/ salt concentration profiling	129
Table 32: Powder batch test #2: thermal loading and duration studies using synthetic groundwater and individual electrolytes	130
Table 33: Powder batch test #2: Thermal duration studies using synthetic groundwater in compacted Bentonite samples	130
Table 34: MX-80 block storage/ emplacement parameters and inferred long-term parameters	131
Table 35: Dry densities at 27% moisture and corresponding air voids	132
Table 36: Fe^{2+} and Fe_{Tot} sample allocation	150
Table 37: Chosen elements for concentration profiling of the interface experimental samples	156
Table 38: D-spacing database for common soil minerals, published by the international centre for diffraction data	158
Table 39: Thermal limits and associated d-spacing's for clay minerals used in XRD analyses	160
Table 40: Summary of experimental investigations	162
Table 41: Sedimentation results on powdered MX-80, batch #1	165
Table 42: Sedimentation results on powdered MX-80, batch #2	165
Table 43: Typical bulk composition of batch #1 MX-80	166
Table 44: Mineralogical composition of ClayTechAB, average from 6 samples, batch #2	166
Table 45: Average Atterberg limit values for the powdered MX-80, batch #1	167
Table 46: Average Atterberg limit values for the powdered MX-80, batch #2	167
Table 47: Generic activity values for standard clay minerals and common clays	168
Table 48: Control swelling pressure and kinetics values	173
Table 49: Ultimate shear strength comparison with and without applied area correction	175
Table 50: Rheology measurements on control samples	176
Table 51: Estimated permeability values for the control samples at the target dry density	177
Table 52: Example of calculated parameters for control permeability, sample 2	177-178
Table 53: Average measured control parameters for the starting materials	178
Table 54: CEC values measured for both batches	179
Table 55: CEC values of the three main clay mineral groups	179
Table 56: Hydration states of 2:1 silicate, d-spacing's	182
Table 57: The positions of useful reflections for estimating percent Illite/ EG-smectite	183

Table 58: Thermal limits and associated d-spacing's for clay minerals	184
Table 59: X-ray diffraction peaks for bulk analysis sample spectra, d-spacing values	186
Table 60: Mossbauer hyperfine parameters at 4K and 293K	191
Table 61: Fe species abundance in control materials	192
Table 62: Batch test regime	196-198
Table 63: General CEC values for the most common clay minerals	215
Table 64: Calculated salt concentrations for a crystalline rock mass at 995m BGL	221-222
Table 65: Compiled 002/003 peak intensity ratios for each batch	231
Table 66: Plasticity index results comparison of duration Vs. C-steel/Bentonite interface exposure at 20°C, also includes one 150°C result for comparison	242
Table 67: Inferred key life phases for interface replication experiments	248
Table 68: Visible corrosion integration comparison	252
Table 69: Interface sub-sample 002/003 intensity ratio	273
Table 70: List of measured elements conducted via ICP analysis	287
Table 71: Mossbauer hyperfine parameters at 4K for phase 2 interface sub-samples	292
Table 72: Constant volume batch test matrix	299
Table 73: Simplified barrier design limitations for three leading concepts	300
Table 74: Compiled swelling pressure results	301
Table 75: Initial swelling pressure mobilisation gradients for the respective average batch test profiles	303
Table 76: Compiled average accumulated axial strain and average strain rates for respective constant volume Batch tests as well as average control measurements	305
Table 77: Compiled average permeability measurements	306
Table 78: Compiled shear strain after 48 hours of axial rebound	309

Abbreviations

% wt: Percent weight

ACV: Aggregate Crushing Value

AOS: Automated Oedometer System

BET: Brunauer–Emmett–Teller

BGS: British Geological Society

CEAM: Chemical engineering and Advanced Materials

CEC: Cation exchange capacity

CEG: Civil Engineering and Geosciences

CoRWM: Committee on Radioactive Waste Management

CS: Carbon Steel

CTRL: Control

Cv: Consolidation Coefficient

DDL: Diffuse Double Layer

DI: Deionised

e: Void ratio

EBS: Engineered Barrier System

EG: Ethylene Glycol

FTIR: Fourier transform infrared spectroscopy

GDF: Geological Disposal Facility

GPa: Gigapascals

Gs: Particle specific gravity

HDPE: High-density polyethylene

HLW: High-Level-Waste

HRL: Hard Rock Laboratory

HT: Heat treated

I/S: Illite/ Smectite

IAEA: International Atomic Energy Agency

ICP: Inductively Coupled Plasma Optical Emission Spectroscopy

ILW: Intermediate-Level-Waste

kN: Kilonewton

KPa: Kilopascals

Ll: Liquid Limit

LLW: Low Level Waste

M: Molar

MPa: Megapascals

Mv: Coefficient of compressibility

NDA: Nuclear Decommissioning Authority

OECD-NEA: Organisation for Economic Co-operation and Development- Nuclear Energy Agency

PI: Plasticity Index

PL: Plastic limit

PSD: Particle size distribution

PTFE: Polytetrafluoroethylene

R&D: Research and development

RWM: Radioactive Waste Management

SAFE Barriers : Systems Approach For Engineered Barriers

SEM: Scanning Electron Microscope

SF: Spent Fuel

SI: Swell Index

SKB: Svensk Kärnbränslehantering AB

Sr: Degree of saturation

SynGW: Synthetic Groundwater

TEM: Transmission Electron Microscope

THC: Thermo-Hygro-Chemico

THMC: Thermo-Hygro-Mechanico-Chemico

T-O-T: Tetrahedral-Octahedral-Tetrahedral

URL: Underground Rock Laboratory

UV: Ultra-violet

XRD: X-Ray Diffraction

1. Introduction

This experimental project was conducted with the intent of exploring the performance of the **High-Level Nuclear Waste (HLW)** clay buffer material, located at the canister interface, when emplaced under deep geological conditions. Investigations conducted are concerned with the physicochemical and geotechnical property alterations throughout the canisters proposed “working life” of the barrier i.e. after insitu canister emplacement. The experimental protocol used inferred near-field environmental phases obtained from leading international research (Landolt et al, 2009 & Holton et al, 2012). The project approach to this investigation was experimental, with the principle objective of exposing the carbon steel/ compacted Bentonite interface to predicted near-field variables, using generic parameters closely related to probable UK conditions (e.g. mid to high salinity groundwater). Nonetheless due to the progress of siting a **Geological Disposal Facility (GDF)** within the UK at the time of this investigation, generic near- field conditions were derived from literature and industrial collaboration.

Correlating the geotechnical properties to the potential physicochemical alterations under the probable near-field conditions has seldom been conducted. By doing so, this investigation should consequently enable a methodical characterisation of interface longevity using the materials set out under the **Radioactive Waste Management (RWM)** guidance and supported by national and international synergies. Such guidance included the choice of preferred canister material and type of Bentonite used for the engineered barrier. Potential alterations to geotechnical properties such as Atterberg limits (i.e. clay consistency), swelling pressure, the hydraulic conductivity, density and stiffness are measured after laboratory exposure to variable **Thermo-Hygro-Chemico-Mechanical (THCM)** conditions in interface and other accompanying experiments. These are correlated to the mineralogical changes that are associated to corrosion precipitation, general chemical environment (i.e. pH and REDOX conditions), groundwater composition and variable temperature exposure. It is expected that initial high temperatures/ dry conditions (representative of early-life conditions) and low temperatures/ rewetting, with increased ground water salinity upon barrier saturation (representative of late-life conditions) are currently accepted premises for near-field environments at depths associated with the GDF concept (500-1000m BGL). The time scales involved from emplacement are considerable, predicted to be $\approx 1 \times 10^5$ years to complete cooling and $\approx 1 \times 10^2$ years for complete resaturation (Assuming the canister interface temperature has dropped below 100°C) (Hicks, 2010; Wilson et al, 2010; Wilson et al, 2006a,

b; Calson et al, 2005). These time scales obviously inhibit true experimental replication, therefore higher temperatures were also investigated and thereby possibly meeting potential activation energies for mineral transformation that would normally require significant time-scales. Increasing the thermal input into the system will increase the kinetic energy and therefore increasing the rates of reactions, this has been well theorised particularly by Maxwell and Boltzmann since the mid-1800s. Interaction of the Bentonite-steel interface when exposed to variable time-dependent environmental factors need to be investigated in terms of probable non-linear reaction kinetics as well as obtaining an understanding of the activation energies required for mineralogical conversion. Such alterations have been speculated in literature to be conversion from Smectites containing relatively low structural Fe to somewhat Fe-Rich clay minerals. Hence the development of associated 2:1 (and possibly 1:1, depending on activation energies involved) Fe-bearing clay minerals i.e. Nontronite, Saponite and Chlorites etc. (Wilson et al, 2010; Wilson et al, 2006a, b; Calson et al, 2005; Milodowski, 2009a,b; Ishidera et al, 2008; Schlegel et al, 2008; Wersin et al, 2007; Perronnet et al, 2008; Guillaume, 2003). However the reaction mechanisms are still seldom proven and firm experiential evidence is limited and diverse. Namely, the extent of alteration to sorbtion/ exchange capacity and degree of structural integration/ redox reactions of Fe^{3+}/Fe^{2+} on/ within the structure of smectites under near-field conditions. Such an investigation is necessary to enable a basis for future design principles and contingency management for the GDF HLW barrier system.

1.1. Project aims and objectives:

Project aim:

To assess and characterise the physicochemical and geotechnical integrity changes of the clay/steel interface within the Engineered Barrier System (**EBS**), to gain an extrapolative understanding of the effects of THCM evolution under crystalline host rock conditions.

Objectives:

1. To determine what the most probable environmental phases are throughout the EBS lifespan, focusing on UK specific hydrochemistry and the speculated major THCM phase definitions.
2. To implement a suitable testing methodology for THCM laboratory investigation of the clay/ steel interface. Examine relevant THCM cell design configurations and

material specification with respect to EBS interface replication considering the requirement for testing cell passivity to the corrosive conditions at the interface.

3. To determine the Bentonite colloidal reaction kinetics with respect to the corrosion products, thermo-mechanical behavior of the waste canister and the specific hydrochemistry over the EBS interface lifespan.
 - 3a. To evaluate the significant geotechnical property changes to the Bentonite buffer material at the interface, namely changes to swelling pressure, hydraulic conductivity, and rheology will be quantified.
 - 3b. To evaluate the mineralogical changes to the Bentonite after long-term THCM exposure in connection with objective 3a.
 - 3c. To assess the extent of the corrosion concentration profile over the sample specimen after THCM exposure.
4. To interpret the physicochemical factors with respect to the longevity of EBS clay/ steel interface over the predicted THCM phase evolution.

1.2. Research questions:

To successfully achieve the identified objectives of the suggested project, a set of essential key research questions have been compiled and will be addressed throughout the development of study:

1. How will the near-field conditions affect the engineering behavior of the buffer material; e.g. under higher temperatures and high saline groundwater re-saturation and carbon steel interaction?
2. What are the significant reaction kinetics and physicochemical alterations of the buffer material incurred at the interface under the anticipated environmental conditions; considering ground water salinity, corrosion products and Bentonite composition interactions? And what are the key mechanisms for these to occur?
3. To what extent does corrosion development occur within the Bentonite when exposed to temperatures up to a “worst case” scenario of 100°C, how does this modify the buffers geotechnical parameters and is the corrosion concentration magnitude and direction a function of the direction of groundwater flow?
4. To what spatial extent is the potential for interface Bentonite alteration i.e. inter-particle cementation and Illitisation, due to the presence of corrosion, high saline ground water compositions and high temperature?
5. What are the associated radial profile changes to the aforesaid in Q4 after subjection of THCM evolution phases?

1.3. Scope:

Both the intrinsic geotechnical and chemical alterations at the Bentonite-Canister interface is investigated post Thermo-Chemico exposure. Interface life conditions were inferred and experimentally replicated which subject the Bentonite to corrosion by-products, thermodynamic, hydrogeological and probable geological factors that are expected during the EBS lifespan. Mineralogical/ chemical alterations within the Bentonite have been infrequently correlated to the geotechnical characteristics as well as the overall engineering performance of the Bentonite barrier. To achieve a systematic and comprehensive understanding of the highly-coupled system, a suit of geotechnical tests is conducted alongside chemical analysis. The geotechnical parameters relevant to the barriers engineering performance is swelling pressure, hydraulic conductivity, dry density, liquid limit, stiffness, interface shear strength and soil shear strength respectively. These geotechnical parameters were measured via Atterberg limit and swell index equipment, Oedometric and adapted shear box tests (In compliance with BS1377 and ASTM D5890). Mineralogical and chemical alterations due to corrosion precipitation and high thermal exposure is investigated using SEM, XRD, Mossbauer, UV-spectrophotometry and ICP analysis.

The experiments were based upon inferred environmental conditions developed through research conducted by NAGRA (the waste management organisation in Switzerland) as well as the intrinsic interface composition was supported/ expressed by the Nuclear Decommissioning Authority (NDA) i.e. canister material type, saline composition/ concentrations and peak temperatures etc. This was to meet the research interests and requirements for the NDA. However, some additional experimental boundary conditions were explored to gain additional insight into the potential for these to accelerate the alteration kinetics, namely saline solution composition and higher temperatures were employed. It is expected that a crystalline host rock disposal environment will initially yield high temperatures with long-term conditions experiencing lower temperatures in conjunction with resaturation by “brackish” ground water (Bradbury et al, 2014; Delage et al, 2010; Landolt et al, 2009, Manning et al, 2007).

The experimental conditions were limited to the time constraints of the project, it is understood that the potential alterations of the Bentonite at the interface is time dependant and therefore the extent, nature and magnitude of the Bentonite modification may be inhibited. Thus, it is assumed that the implementation of higher temperatures enable insight into potential long-term chemical and engineering deviations that would naturally occur at

lower temperatures over longer time-scales. The experimental conditions such as temperature and saline solution composition are considered generic, this is due to the need for a permanent site within the UK. Therefore, the explored experimental conditions are limited as physicochemical conditions will differ spatially and temporally with respect to the geology for a specific site. Experimental testing protocol implemented several assumptions with respect to the near-field and engineering composition of the barrier based on previous research and industrial synergies (NDA, 2016; Bradbury et al, 2014; Landolt et al, 2009). It should also be noted that it is difficult to replicate true insitu conditions as it is impossible to accurately experimentally replicate conditions that would prevail after tens of thousands of years. Ultimately, the observations reported within this project are an insight into the potential alterations, possible mineralogical precursors/ pseudomorphs that may occur and the engineering considerations required to ensure containment. Conditions and measurements are therefore subject to a degree of inevitable systematic uncertainty.

1.4. Thesis Structure:

This section sets out the structure of the thesis and defines approach of the research. The following sections which conclude chapter 1 explores the current leading European HLW/ Spent Fuel (SF) disposal concepts and more importantly the progress and current geological and engineering considerations within the UK. Chapter 2 sets-out previously conducted research which explores the near-field conditions with respect to the impact on the Bentonite under EBS conditions. Furthermore, additional areas are discussed such as various near-field evolution premises based on various national concepts, engineering design considerations of the engineered Bentonite barrier and the corrosion/ mineralogical considerations. Natural analogue studies and microbial considerations are also summarised to support the long-term alterations that are presented by the findings of previous experimental and modelling research. This chapter is to aid the reader in the understanding of the scope of limits of current and up to date research as well as highlighting the research gap which supports the purpose of this work. Chapter 3 sets out the experimental methodologies and overall approach implemented to achieve the research objectives for the project. Following this, chapter 4 comprehensively classifies the materials used for the experimental testing in terms of the engineering and physicochemical behavior and composition which also enabled control measurements to be defined before exploring the post thermo-chemically exposed samples. Chapters 5 to 7 detail the experimental results obtained from the experimental methods. Section 8 discusses and summarises the experimental findings and links the

findings to one-another as well as previously conducted research with the fundamental aim to gain an extrapolative understanding of the barriers insitu longevity. Lastly, section 9 concludes the findings of the experiments as well as setting out areas of potential future work that became apparent during and after the experimental regimen.

1.5. Current leading HLW/SF disposal concepts:

There are several model concepts that form the basis of the UK's concept design on nuclear waste disposal, most of which implement the multi-barrier concept. This chapter details the main concepts and design premises for their respective multi-barrier approach. This review is not exhaustive and is compiled to give the reader an understanding of each system and the "local" reasons for their selection i.e. geological, hydrogeological and physicochemical constraints. The key concepts covered are Sweden, Switzerland, Finland, France and Germany. These European concepts are advanced in the research and development of their disposal strategies. Therefore, the UK has founded its concept on many years of research conducted by these organisations. The explored concepts are just a few of those involved in the OECD-NEA program (Organisation for Economic Co-operation and Development- Nuclear Energy Agency). These are implemented to encourage international synergy with respect to advanced nuclear infrastructures. The program consists of 31 European, North America and Asia-pacific regions (NEA, 2016). The use of Bentonite as a buffer is widely accepted for many of the concepts and extensive research is being conducted to classify and test the limits of this versatile naturally occurring material (Karnland, 1998; Carlson, 2004; Gaudin et al, 2009; Milodowski et al, 2009a, b; Wilson et al, 2010; Johannesson, 2010; Kiviranta and Kumpulainen, 2011; Muurinen, 2011; Rizzi et al, 2011; Savage and Arthur, 2012; Savage, 2014)

There are four main bentonites considered for use, predominantly within the European concepts. It is firmly established that sodium rich Bentonite is considered to be the most suited type that meets the barrier requirements (NDA, 2014). Wilson et al (2010) details three Bentonite types, Kunipa-F, MX-80 and Montigel with an additional type Ibeco-RWC, stated in the technical note by the NDA (2014) on the review of the development of the Bentonite barrier for the KBS-3 project. Sodium rich Bentonite displays higher swelling potential and lower intrinsic hydraulic conductivity (Lee et al, 2012; Cho et al, 1999). Johannesson (2010) states that the use of Calcium-rich Bentonite i.e. the Ibeco-RWC is suited for the back-filling application of the main deposition tunnel for the KBS-3 concept, with the compacted MX-80

as the buffer surrounding the canister. Table 1, displays the unit formulas for each of the specified bentonites.

Table 1: Commonly considered types of Bentonite for the main European concepts (Wilson, 2010; NDA, 2014)

Type	Unit formula	Reference
Kunipa-F	$(Na_{0.48}Ca_{0.03}K_{0.01}Mg_{0.002})(Al_{1.54}Mg_{0.33}Fe^{3+}_{0.09}Fe^{2+}_{0.02})(Si_{3.87}Al_{0.13})$	Wilson et al (2004)
MX-80	$(Na_{0.3})(Al_{1.55}Mg_{0.24}Fe^{3+}_{0.2}Fe^{2+}_{0.01})(Si_{3.96}Al_{0.04})$	Madsen (1998)
Montigel	$Ca, Mg_{0.28}(Al_{1.36}Mg_{0.35}Fe^{3+}_{0.31}Fe^{2+}_{0.01})(Si_4)$	Madsen (1998)
Ibeco-RWC	$Ca_{0.18}Na_{0.19}K_{0.02}Mg_{0.11}(Al_{2.87}Ti_{0.08}Fe^{3+}_{0.43}Mg_{0.59})(Si_{7.87}Al_{0.19})$	Karland (2010)

It should also be noted that the favorability to use Mx-80 Bentonite is due to the relatively low content of soluble minerals as detailed by Karland (2010). Table 2 & 3 displays the mineralogical compositions, obtained via semi-quantitative XRD of both MX-80 and Ibeco-RWC. The Tables show that the soluble secondary minerals such as Calcite exist in higher concentrations in the Ibeco-RWC, thus leaving the Bentonite vulnerable to density, permeability and mineral alterations. Furthermore, the higher presence of secondary minerals within the Ibeco-RWC Bentonite indicates a less homogeneity than that of the MX-80. This can have repercussions on the physicochemical characteristics of the Bentonite when within the localized environment around the HLW/SF canister (as detailed in section 2.3- Near-field considerations and its impact on the Bentonite within the multi-barrier system).

Table 2: Average mineralogical composition from 7 sub-samples of Wyoming MX-80 (Karland, 2010 & Karland et al, 2006)

Mineral	Average wt.%
Montmorillonite	81.4
Illite	0.76
Calcite	0.11
Cristobalite	0.9
Gypsum	0.93
Muscovite	3.41
Plagioclase	3.53
Pyrite	0.63
Quartz	3.54
Tridymite	3.77

Table 3: Average mineralogical composition from 5 sub-samples of Ibeco-RWC (Karland, 2010 & Karland et al, 2006)

Mineral	Average wt.%
Montmorillonite	81.42
Illite	4.62
Calcite	5.28
Dolomite	1.28
Goethite	1.5
Muscovite	1.38
Pyrite	1.1

1.5.1. Swedish Nuclear waste disposal concept (SKB: KBS-3):

The SKB waste management body was established in the 1970's and comprises of a consortium of Swedish nuclear energy companies. A site has been selected and plans were submitted in 2011 to build the GDF at Forsmark (see Figure 1). The host rock is a large Granitic crystalline formation located 500m below ground level (**bgl**) (SKB, 2016).

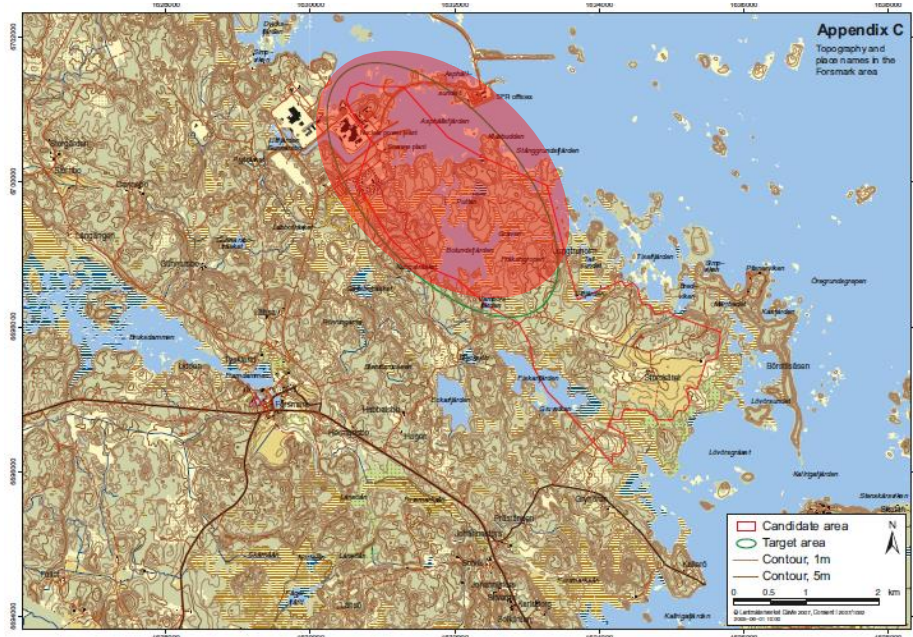


Figure 1: Target site location for the SKB disposal concept in Forsmark (Red shaded zone) (After Borjesson, 2011)

The chosen multi-barrier for the KBS-3 concept relies on three protective barriers, 1) The copper clad canister with a modular iron insert, 2) Highly compact Bentonite rings and 3) the crystalline bedrock. Figure 2 displays a diagrammatic representation of the KBS-3 concept given by SKB (2016).

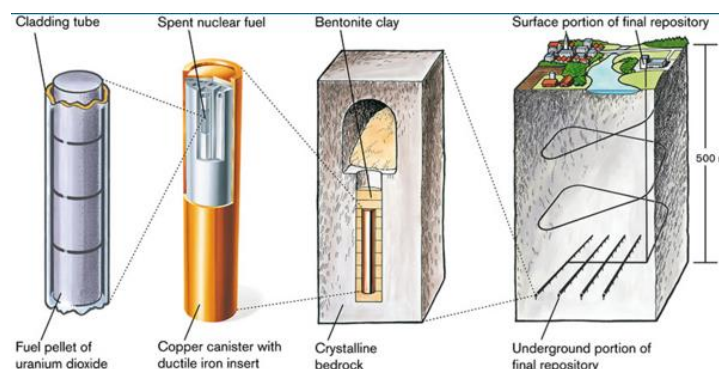


Figure 2: The KBS-3 multi-barrier concept (SKB, 2016)

The system consists of several horizontal deposition tunnels at the repository level, vertical boreholes that will accommodate the copper clad canisters and the buffer over pack.

The horizontal tunnels will be backfilled and compacted using Bentonite pellets to ensure a complete seal surrounding the excavated zone. Copper gladding was chosen based on several long-term experiments in the Äsprö Hard Rock Laboratory (HRL) or within independent small scale laboratories (Rosborg, 2013; Ollila, 2013). The Äsprö HRL has been operational since 1995, located in the Oskarshamn municipality and has contributed to the advancement in the design and construction of the GDF (SKB, 2016).

The SKB concept indicates that their research supports the multi-barrier system for use in the long-term disposal of HLW/SF. Ollila (2013) concluded that from their long-term copper coupon batch experiments that no visible changes were observed. The coupons were sealed within flasks containing deoxygenated DI water (Mili-Q) in a N_2 rich atmosphere, under a time scale of 3.5 years at a temperature of 25°C. Thus, indicating that copper under anoxic conditions is somewhat stable giving off very limited Hydrogen and little compromise to the thickness, the results coincided with Hultquist et al (2009). The aforesaid experiments leave many questions open for speculation of the realism on the environment the copper was exposed to. Rosborg (2013) investigated and analysed copper electrodes from the prototype repository at the Äsprö HRL. The copper was embedded within the Bentonite for 8 years at background temperatures, approximately 35°C. Rosborg (2013) discovered that mildly oxidising conditions still existed with minor pitting and the presence of Cu corrosion products. Kristensson & Börgesson (2015) published a canister retrieval report for the multi-barrier configuration, and gives more in-depth details schematic of the multi-barrier configuration, given in Figure 3.

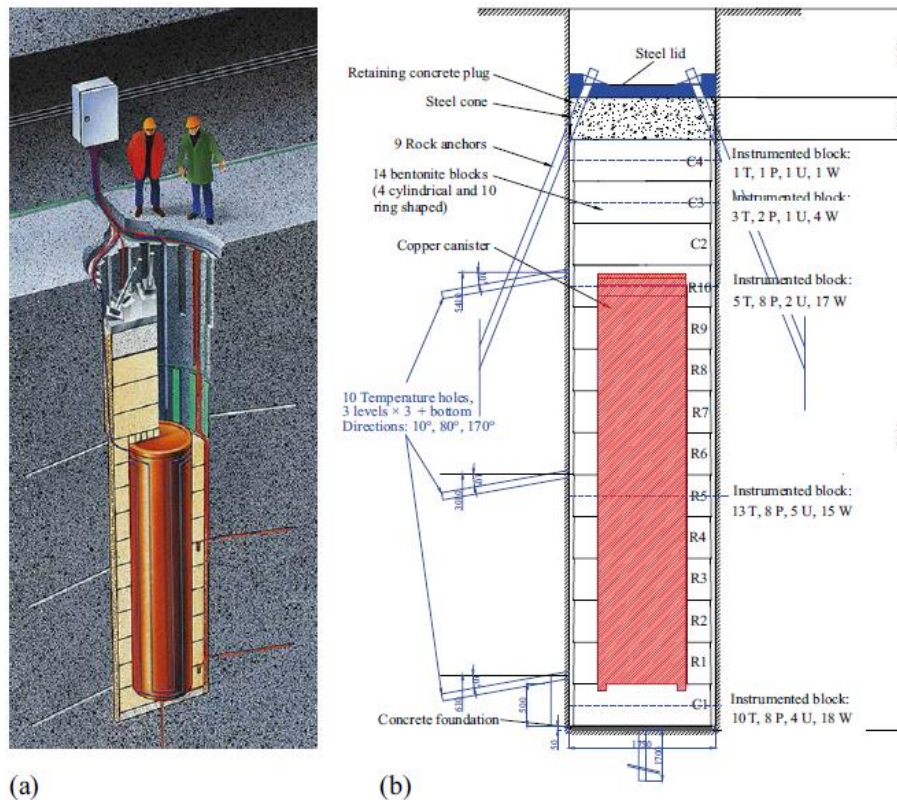


Figure 3: a) Diagrammatic representation of the HLW deposition hole; b) Deposition barrier dimensions Kristensson & Børgesson (2015)

1.5.2. Swiss Nuclear disposal concept (NAGRA):

The Nagra concept is the Swiss national cooperative that is directly responsible for the safe management and disposal of the country's nuclear waste (Patel et al, 2012). "Entsorgungsnachweis" was the project put forward to the Swiss government in 2002, which proposed the burial of HLW/SF and long-lived intermediate wastes within a GDF in Northern Switzerland (Landolt et al, 2009). The most suited host rock lithology chosen for this concept is the Argillaceous Opalinus clay deposit (Figure 4 and 5), which is approximately 110 meters thick (Nagra, 2016) and some 500 to 1 Km bgl (Bradbury et al, 2014; Wilson et al, 2010; Landolt et al, 2009). There has been extensive research into the canister materials and multi-barrier configuration, mostly conducted at the Mont Terri Rock laboratory. This has enabled a good understanding of the chemical interactions and properties of the host rock and barrier components (Nagra, 2016; Landolt, 2009; Johnson and King; 2003). The Swiss government aims to implement emplacement by the year 2050 with a finalised canister design by the year 2025, as well as design optimisation and prototype production taking place in between (Patel et al, 2012).

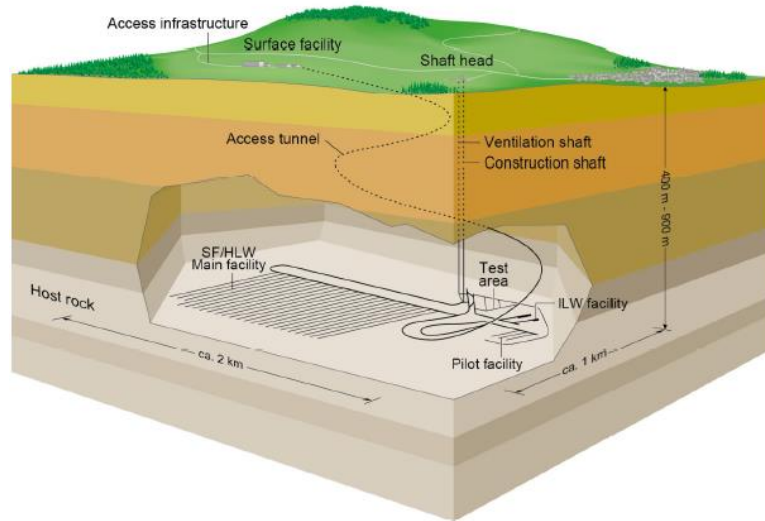


Figure 4: Repository layout schematic for the deposition of the HLW/SF (Bradbury et al, 2014)



Figure 5: Photo from the Mont Terri Rock Laboratory, open tunnel wall of the Opalinus clay; Picture courtesy of Dieter Enz (Nagra, 2016)

The current proposal for the long-term disposal of HLW/ SF is within horizontal emplacement tunnels within the midpoint of the Opalinus clay deposit, at a depth of ~ 600m bgl (Bradbury et al, 2014). Patel et al (2012) gives the dimensions and composition of the HLW/ SF canisters. The length and diameter of each canister is 5.35m and 1m respectively, with a Carbon steel composition that holds a minimum containment period of 1000 years and a maximum of 10000 years (Bradbury et al, 2014). Patel et al's (2012) report thoroughly examined all factors that influence the material choice i.e. Weldability, corrosion, structural performance, stress history and residual stress etc. Thus, Carbon steel was chosen as the suitable containing material. Their decision concluded that the nominal wall thickness of the canister would be approx. 150mm and would suffice the requirements.

The multi-barrier design is somewhat different to that of the SKB concept, as can be seen from Figure 6, the canisters will be seated on compacted blocks of Bentonite with a

compacted Bentonite backfill surrounding the canisters. Eventually the steel supporting arches will corrode, loose integrity and the secondary creep of the host rock will provide additional sealing of the environment. Compared to the SKB concept, the argillaceous rock environment also provides a good hydraulic and geochemical barrier and therefore the need for a highly compact Bentonite barrier is not as imperative. The combined hydraulic and geochemical resistance of both the host rock and the MX-80 will provide a suitable sealed environment, whereas the SKB concept depends on the Bentonite buffer to provide the hydraulic, geochemical and self-sealing environment. This also means that the corrosion and containment period of the canister is not as vital as the SKB concept, as there will be approximately 40m of argillaceous rock on either side of the canister. Therefore, some alteration is allowed within a limited zone at the canister interface i.e. a sacrificial layer. Bradbury et al (2014) states that the diffusion process is extremely slow and that the Bentonite will need approximately 100,000 to 200,000 years for any noticeable conversion to occur. They highlight that following onerous modelling conditions high proportions of Bentonite is still available after 10^6 years, indicating that iron corrosion phases such as magnetite or siderite are stable and decrease the available Fe^{2+} in the system.

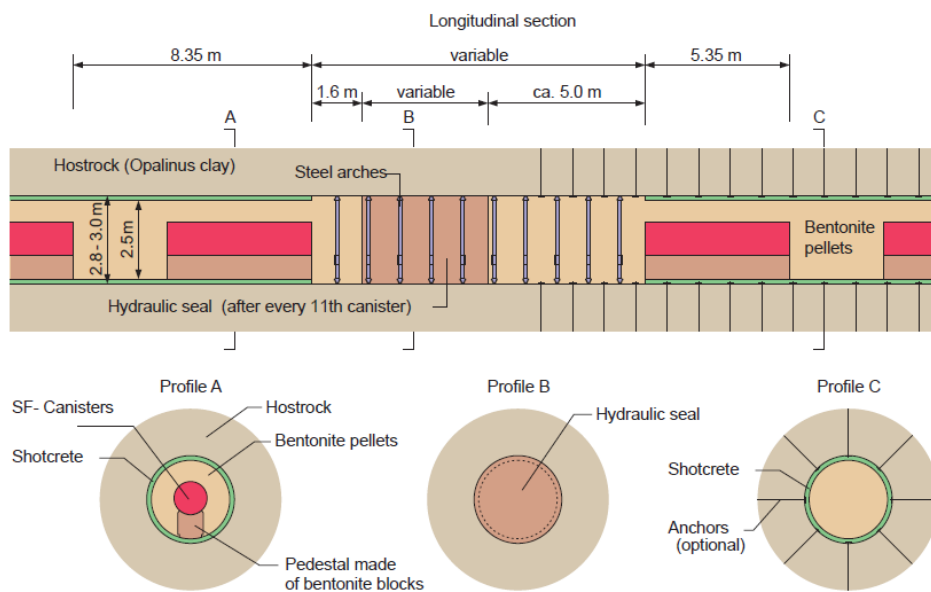


Figure 6: The horizontal disposal gallery with the multi-barrier configuration (Bradbury et al, 2014)

1.5.3. Finnish Nuclear Disposal Concept (Posiva):

The disposal concept under consideration in Finland is very similar to that of the SKB concept, Figure 7. Hellä et al (2014) states that the disposal scenario will be developed according to the KBS-3 concept. The final repository is to be constructed at the Olkiluoto site located within the Eurajoki municipality (Hellä et al, 2014). The bedrock/ host rock is located

400m bgl and is of crystalline nature (Idiart et al, 2013). According to Hellä et al (2014) canisters will be vertically arranged within boreholes located in the floors of deposition tunnels with the canisters comprising of a copper-iron composite design. The decision is based on four decades of research, the Posiva program was initiated in the 1970's and site specific characterisation initiated in the 1980's (Posiva, 2016). Work is still being conducted at the Olkiluoto site as well as continuous borehole monitoring for geomechanical and geochemical data collection.

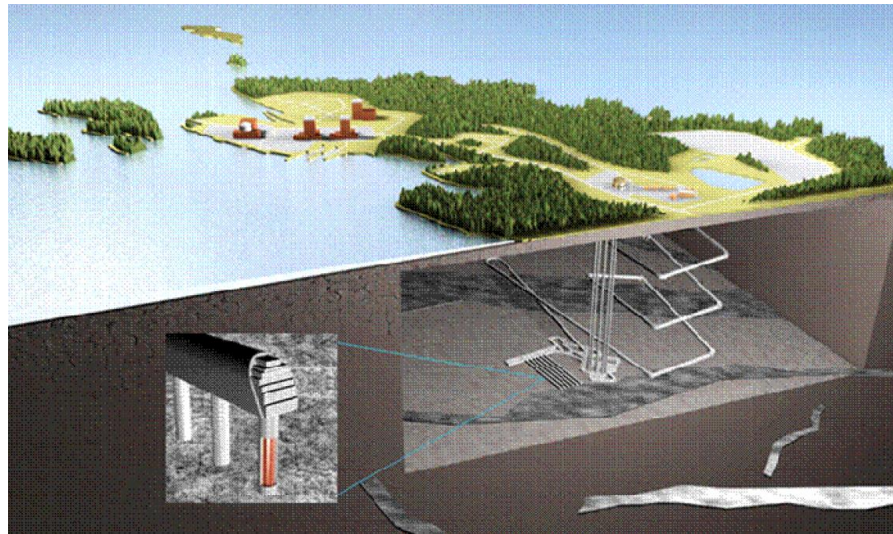


Figure 7: The Posiva repository based on the KBS-3V design (Hellä et al, 2014)

1.5.4. French Nuclear waste disposal concept (Andra):

Andra's nuclear waste management research has been conducted quite extensively for over 20 years. Much work has been conducted within the national Underground Rock Laboratory (URL) considering two host media, specifically Argillaceous and Crystalline formations (Andra, 2016; The Andra Dossier, 2005). The clay medium has been the most researched within France, the main URL is based at Meuse/ Haute-Marne created in 1999 (The Andra Dossier, 2005). The French concept has extensively used the Äsprö HRL for its research into crystalline host rock repositories (Andra Dossier, 2005). It appears that the Argillaceous formation is a probable candidate for the HLW repository. Set out within the 2005 Dossier, it is stated that the Andra concept has compiled sufficient evidence to consider that the Callovo-Oxfordian formation exhibits favourable properties for a HLW repository. Therefore, this is the likely location for the HLW/ SF repository within the host rock sequence known as the Callovo-Oxfordian formation (Figure 8).

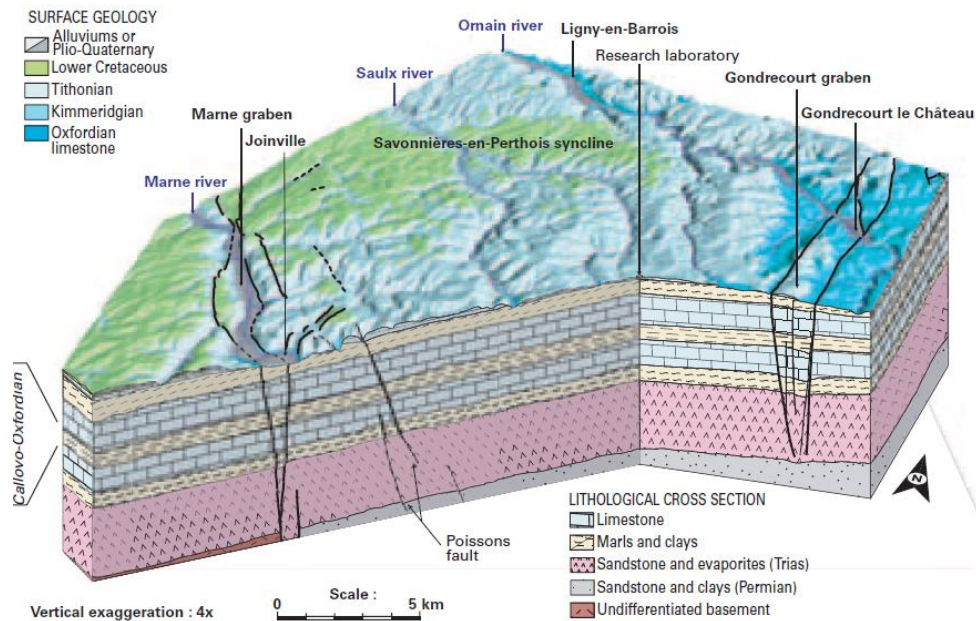


Figure 8: Callovo-Oxfordian formation of the Parisian basin underlying Meuse/ Haute-Marne (Andra Dossier, 2005)

The concept envisions the waste encapsulated within unalloyed steel canisters (Carbon steel) emplaced within a horizontal deposition tunnel within the clay (Wilson et al, 2010) (Figure 9). According to the 2005 Andra Dossier the concept proposes that the canister must contain the HLW/ SF matrix for at least 10000 years. Each horizontal deposition tunnel is lined with a perforated steel outer liner with blocks of Bentonite filling the annulus between the canister and the outer liner (Wilson et al, 2010), Figure 10. The concept is somewhat similar to that of the NAGRA disposal scheme. These both heavily depend on the physicochemical and geomechanical properties of the argillaceous rock and the intermediate barrier respectively. In this case the Bentonite is not the only line of defense to inhibit contaminates leaching into the biosphere.

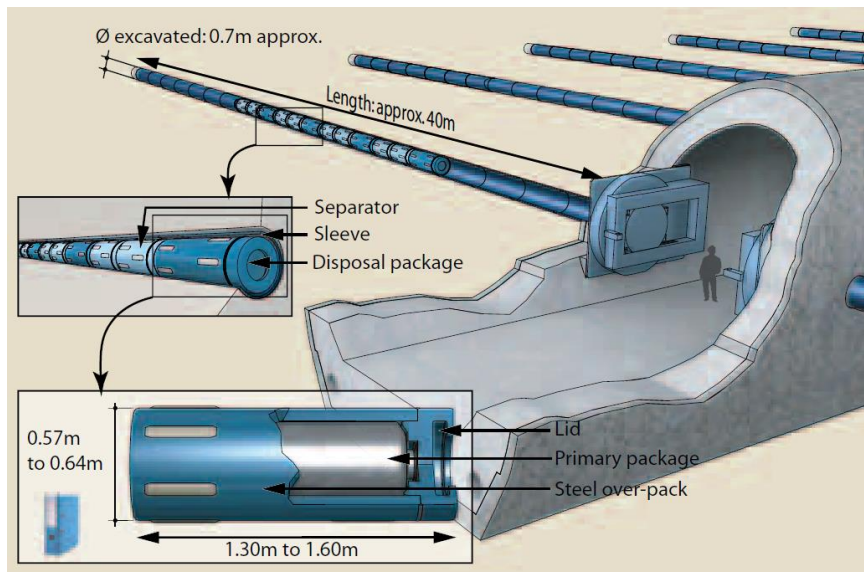


Figure 9: HLW/ SF canister disposal configuration (Andra Dossier, 2005)

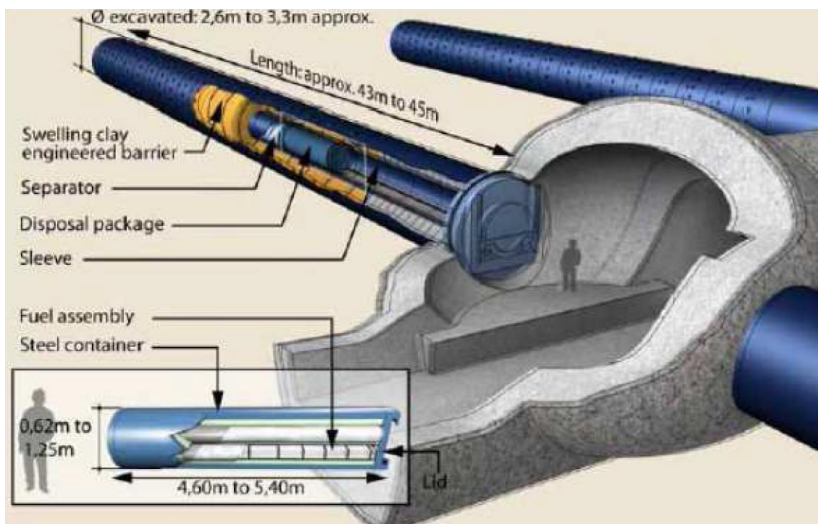


Figure 10: Bentonite emplacement schematic (Andra Dossier, 2005)

1.5.5. German Nuclear Disposal Concept (BMW):

The Federal Ministry for Economic Affairs and Energy (FMAE/ BMW) is responsible for the research and applications outlook on the long-term disposal of all levels of nuclear waste. Several locations have been considered for the disposal of the various waste categories. Plans were finalised in 2007 for the low heat generating and medium level wastes for the disposal within the former Konrad Iron-ore mine near Salzgitter (BMW, 2016). No absolute disposal concept has been developed to date for the German HLW/SF wastes, but extensive research has been conducted by the BMW and the Federal Institute for Geosciences and Natural Resources (BGR), primarily looking at the disposal within an evaporitic host rock. The research has been carried out since 1979 in the Gorleben salt dome located in lower Saxony (BMW, 2008), however the German government still requires a final appraisal after the final exploration and research has been carried out. Figure 11 displays

the preliminary concept for the HLW/SF disposal concept within a salt host rock formation (BMW, 2008).

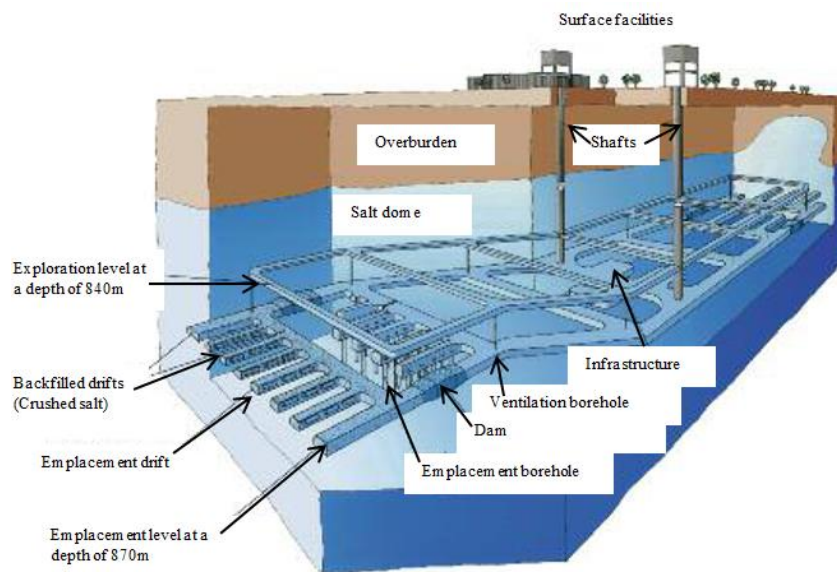


Figure 11: German HLW/SF (high heat generating waste) disposal concept; courtesy of the BMW (2008)

1.5.6. Concluding statement:

The explored national disposal concepts are at the forefront in the advancement of their long-term nuclear waste disposal schemes, and furthermore play an active role in the OECD/NEA international research synergy. Fundamentally, each nation must utilise their respective underlying geology in a favorable design, and if multiple host rock types are present, specific site/ legislative conditions must be met in order to conclude on a final host rock. The Swedish KBS-3 concept on the disposal of the HLW/SF within crystalline formations as well as the joint research with other concepts such as ANDRA, considering the use of Argillaceous rock, appear to have the most comprehensive background with respect to the long-term disposal of Radioactive wastes. Therefore, it is understandable that other nations, including the United Kingdom, have implemented their research programs based on the KBS-3 multi-barrier concept. However, it is still necessary for the respective concepts to conduct their own site specific research based on the underlying hydro-chemical/ geological factors, as well as the socio-political and economic considerations to generate more specified and in-depth safety cases.

1.6. The need to develop a long-term strategy within the UK:

The UK is active in nuclear research and development and has been since the mid 1940's, originally focusing on Atomic weapons research (MRWS, 2011). With the proficiency in nuclear scientific/ technological knowledge developing exponentially over the

past several decades, so has the nuclear waste legacy. There has been much controversy regarding nuclear fission reactors and their role in energy generation, as well as the ever-increasing developments in both academic, medical and defence technologies that use such highly active materials on day-to-day basis. All of which actively produce waste forms that are difficult to handle (NDA waste inventory, 2007). Focusing on energy production, the current environmental circumstances concerning carbon emissions indicate that nuclear power is, at present, one favoured energy source primarily due to its high energy to low carbon output ratio. Despite advanced reprocessing practices put in place to recycle the key elements, such as Uranium and Plutonium etc., output of highly active waste is nonetheless inevitable. Waste output of all levels has been managed and stored since the initiation of the first nuclear reactors largely by BNFL (British Nuclear Fuels Ltd.) & UKAEA (United Kingdom Atomic Energy Association) (NDA, 2013). Interim surface-level storage systems have been improved and adapted for dry-cooling and containment management in the past three decades. This has enabled enhanced longevity of the containment vessels and supporting systems in comparison to the conventional “wet” storage ponds. However, “wet-storage” methods have not been fully replaced and are still in use from older waste management applications (DECC, 2012 & IAEA 2006) i.e. for containment of SURF (Spent Unprocessed Radioactive Fuel) waste that predated the introduction of modern reprocessing methods (Roxburgh, 1987). SURF is known to have a much higher total thermal enthalpy, therefore requiring enhanced cooling methods. Nonetheless the research and development regarding UK based long-term geological disposal has been somewhat unhurried and problematic (NDA, 2013). One significant example is the rejection of a proposed underground rock laboratory in 1997, that supported the premise to further enhance scientific understanding through potential barrier and rock characterisation research within the Cumbria. Subsequently, it was refused by the government in conjunction with concerns brought forward by Cumbrian council’s and NGO’s regarding complaints of Nirex’s intent to “quietly” initiate waste emplacement without public consideration (NDA, 2010). Consequently, but not exclusively, the aforesaid dispute was followed by the degeneration of the Nirex programme. Nevertheless, the necessity for a long-term solution was/ is still present and ever-growing. In 2001 after the House of Lords review in 1999, the **MRWS (Managing Radioactive Waste Safely)** programme was initiated (NDA, 2010). This programme was developed to address the long-standing issue of the nuclear waste management and disposal of existing and future waste forms. The principal aim of the programme is to provide such solutions with professional and robust scientific advocacy (NDA, 2010 & MRWS, 2011).

One of the most predominant objectives highlighted within the 2008 white paper report published by the MRWS (Titled: A framework for implementing geological disposal) was the prerequisite to up-hold public confidence via a transparent framework and call for public involvement i.e. by maintaining impartiality and discretion throughout the process. The MRWS annual report (MRWS, 2011) also states the premises of its strategy in four key points, 1) An implementing organisation in the NDA, 2) robust and autonomous directive by the statutory regulators, 3) independent scrutiny and 4) advice from the Committee on Radioactive Waste Management (CoRWM) and partnership with local communities. The independent committee was established by the government and it includes professional individuals, both from academic and industrial disciplines with a high-level of scientific and technical knowledge to scrutinise, instruct and assist in the progression of MRWS programme. It was based on public and stakeholder engagement through the work of CoRWM between 2004 and 2006 that enabled the MRWS programme to produce the 2008 white paper report, by investigating and explicitly discussing the viability of various management/disposal options (NDA, 2010).

The MRWS white paper report openly expressed an invite to potential host communities with incentives of employment prospects that ensured that if a deep geological repository was to be constructed, it would benefit the economy of the localised area as well as the wider socio-economic framework (MRWS, 2008). However, and more importantly, the new strategy provides communities the right to withdraw at any stage of the selection process (namely from the desk based screening and site investigatory stages respectively), excluding the commencement of the construction implementation stage. The categorical stages are well-defined within the MWRS white paper report, but an overview of the framework is displayed below in Figure 12 and has maintained the preferred process to date (DECC, 2016).

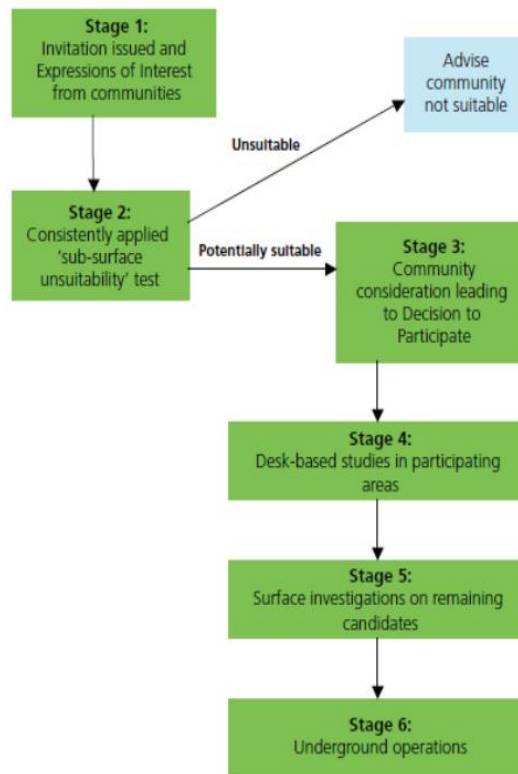


Figure 12: MRWS framework for site selection and community involvement (DECC, 2012)

In 2009 three Cumbrian council authorities (Allerdale & Copeland borough councils as well as the Cumbria county council) initiated talks on the site selection and disposal concept that involved various organisations such as the NDA, the British Geological Survey (BGS) and the west Cumbria MRWS partnership etc. Following this, the government invested over £1M/ year for investigatory and community education/ involvement activities to progress the site selection process. Such activities involved unsuitability screening studies, meetings/ workshops as well as other legal and expert advice. For example, the screening studies involved the publicly funded body, the BGS, who was tasked to conduct the unsuitability screening of west Cumbria using only geological exclusion criteria and existing knowledge i.e. a non-intrusive investigation (Powell et al, 2010). The principle aim of the screening was to rule out areas that fit the unsuitability criteria with evident geological reasoning and not highlight or indicate areas of definite site suitability. The site-specific suitability screening was intended for late stages involving localised sub-surface investigations. Exclusion criterion were derived by members of the geological and royal engineering societies, the criteria is generic and solely focuses on the geological aspects of an area under consideration. The site-specific information such as localised geological features, heavy engineering considerations and sociological/ infrastructure planning are involved later in the site selection process. The generic exclusion criteria are displayed in Table 4 as given in the BGS screening

report (Powell et al, 2010). This summary displays the key geological settings that question the feasibility of a GDF and are predominantly concentrated around points relating to potential natural resources and hydrological features. For instance, an area that may be exploited for its mineralogical importance in the future is considered an “intrusion risk” and additionally any biospheric groundwater features i.e. aquifers that may be contaminated by the potential release of long-life radionuclide’s, hence restricting any future potential groundwater abstraction zones.

Table 4: Summary of initial screening criteria (BGS- Powell et al (2010))

Resources	To be applied to the exclusion criteria	Reasons/ explanations and qualifying comments
Coal	Yes	Intrusion risk to depth, only when resource at >100m
Oil and gas	Yes	Intrusion risk to depth, for known oil and gas fields
Oil shales	Yes	Intrusion risk to depth
Metal ores	Some ores	Intrusion risk only where mined at depths >100m
Disposal of wastes/ gas storage	Yes	Only where already committed or approved at >100m depth
Aquifer	Yes	Where all or part of the geological disposal facility host rock is located within the aquifer
Shallow permeable formations	Yes	Where all or part of the geological disposal facility host rock would be provided by permeable formations that might reasonably be exploited in the future
Specific complex hydrogeological environments	Yes	Deep karstic formations and known source rocks for thermal springs

Most recently, in 2012 the Cumbrian borough and county councils rejected the advancement of the siting of a potential GDF by pulling out of the transition from the third to the fourth stages the MRWS framework. This ended their four-year involvement in the MRWS programme (NDA, 2013). This decision was conveyed in a letter to the secretary of state for Energy and Climate Change on the 7th of February 2012 which stated “*Resolution: Not to participate in stage four thereby excluding the Allerdale and Copeland areas of Cumbria from further consideration in the MRWS process, and to encourage the Government to make the necessary investment to improve surface storage facilities at Sellafield*”. The choice to withdraw was based on grounds of safety, the conclusion was that acceptable safety must be absolute with no uncertainty. However, from an engineering perspective, complete radionuclide retardation and absolute containment cannot be guaranteed, taking into consideration the time-scales required for long-life radionuclides to decay to safe activity levels (Roxburgh, 1987 & Gera, 1981). Moreover, no man-made/ engineered system or structure has ever been designed and constructed with an intended lifespan to withstand any

sort of natural and potentially aggressive environment $>1 \times 10^4$ years. Every engineered system encompasses inevitable uncertainty and risk, this can only be reduced and accounted for through comprehensive R&D. What appears to be overlooked, is that the GDF method of isolation reduces the risk of human intrusion and increases the distance/ passive barrier between the waste source and the biosphere. These engineered and natural barriers improve radionuclide concentration attenuation by enabling a slow/ diffusive release. This method of disposal allows for a degree of radionuclide decay before reaching the biosphere, particularly for the short-life radionuclides. Indicating that a multi-barrier system isolated from direct biosphere contact would result in a slow release and more importantly a dilute dispersion release process (Roxburgh, 1987). Therefore, passive systems discharging waste by-products post containment failure, in the region of 1×10^3 to 1×10^4 years after emplacement, may yield more acceptable concentrations over geological time-scales. In comparison to surface storage facilities which require regular maintenance and heightened security protocol for the duration of its use, this may be more at risk of adverse events which may result in a bulk release of radioactive material into the biosphere. Furthermore, Roxburgh (1987) also highlights the requirement of a permanent passive solution and states that the time-scales involved for the waste to decay to safe levels is significantly longer than the periods free from war. It is also important to consider the implications including cost and the social and economic stability etc. which are related to the active measures needed to ensure safety and the security of surface management of storage/ cooling systems. There is perhaps more uncertainty involved in the long-term safekeeping of active wastes in surface storage systems than there is if a thorough safety case and an intelligent design was implemented in a multi-barrier deep geological disposal scheme.

The Cumbrian partnership resolution for rejection to progress has delayed the development of a more permanent solution, site-specific research and sub-surface investigations. Laboratory and full-scale analogue replications using site specific parameters would/ will enable a better understanding of how the system will act over such time scales (i.e. $1 \times 10^3 \rightarrow 1 \times 10^5$ years) after emplacement of the waste containers. In turn, this would enable a better safety case to be developed and a reduction in the inevitable design life uncertainty. This uncertainty is a common aspect in scientific and engineering related predictions, particularly when extrapolating near- field systematic characteristics into the very distant future with several variable environmental factors. Ultimately, there is a large gap within UK R&D with respect to the development of a UK deep geological repository and

research into the safety of the Engineered Barrier Systems (EBS) concept for a UK-specific safety case. This is also expressed in terms of a “readiness & knowledge gap” in a 2009 report by the NDA, in which they express the need to use international knowledge to enable progression. This becomes increasingly evident when comparing the advances of other countries such as the most prominent Swedish concept (KBS3V/H) (Thurner et al, 2007) as well as the Swiss (NAGRA), French (ANDRA), Finnish (Posiva) and the German programmes etc. Therefore, at present the UK MRWS and the associated institutions will use the current KBS design concept and recent research findings to further assess, develop and advance the safety-case for implementing such a concept in the UK, using nonspecific geological conditions that are predominant at depths between 500m and 1000m bgl.

1.6.1. Existing SURF/ HLW, ILW and LLW volumetric waste forms, and the current interim storage situation:

Waste inventory reports are published every three years, the most recent was published in 2013, and presents data from several live waste streams regarding the volumetric quantities of Very Low Level Waste (VLLW), Low Level Waste (LLW), Intermediate Level Waste (ILW) and High Level Waste (HLW). The requirements of the reports are to quantify the total volume of all waste levels and predict future waste output volumes. The aforesaid wastes are considered to require for secure storage and are categorised in terms of their radioactivity and nature of radioisotopes present i.e. limits are defined in terms of the waste source and activity in Becquerels (Bq- a measure of nuclear transformation/ unit time $\approx 1\text{Bq} = 2.7 \times 10^{-11}$ Curie). The VLLW (Very Low Level Waste) and LLW are not considered as they are believed not to inflict significant harm to biological matter and does not require repository disposal (DECC, 2005). the ILW and HLW volumes are displayed in Table 5 as taken from the 2013 NDA waste inventory report (2013). The report was prepared by Pöyry energy ltd and AMEC plc.

Table 5: DECC & NDA 2013 waste inventory; waste quantities as of April 2013

Waste type	At 1/4/2013	Volume (m ³)	Mass (Tonnes)	No of packages
HLW	Total	1770	3400	
	Not yet conditioned	931	1200	0
	Already conditioned	844	2200	5626
ILW	Total	95600	120000	
	Not yet conditioned	67500	66000	1197
	Already conditioned	28100	53000	54129

To date, according to the 2013 waste inventory, there are currently 5626 HLW containers ready for long-term storage. With additional volumes undergoing the conditioning process,

the estimated future volumes are displayed in Table 6 below, which details an additional 695m³ of HLW. There are also an additional 931m³ of HLW awaiting recycling, vitrification and storage.

Table 6: Future waste output prediction

	HLW	ILW	LLW	Total
Volume (m³)	695	190000	1300000	4330000
Mass (Tonnes)	560	190000	1700000	4700000

The preferred method of interim storage of a particular category of nuclear waste is a function of its radioactivity and thermal output. At present HLW that is considered to be HAW (High Activity Waste) is stored at Sellafield in its pre-and post-vitrified state, depending on the emplacement period. Early spent fuel assemblages were directly emplaced within the cooling/ containment system, whereas the process of recycling became more predominant in recent years and therefore allowing the waste to be much lower in volume as well as reduced total enthalpy.

As explained in the NDA waste management summary (NDA, 2013), vitrification is the process which solidifies the waste in a borosilicate glass matrix, the waste either originating directly from historic liquid waste or the remnants from modern reprocessing techniques. Sellafield is one of the earliest sites in the UK for R&D in nuclear applications and since then it has become the main hub for spent fuel reprocessing, Mixed Oxide (MOX) fuel fabrication and interim storage. Subsequently the proposed plan for HLW after vitrification is a minimum 50-year interim storage period, historic unprocessed wastes are currently held within water-cooled ponds whereas modern engineered air-cooled systems hold new-build wastes (Figure 13). Interim storage is predominantly aimed to ensure sufficient heat decay has taken place prior to permanent storage (NDA, 2010). Nonetheless considering the UK has been actively producing active wastes since the 1940's, outdated/ historic storage facilities which contain historic untreated wastes will eventually need to be retrofitted for safety purposes (NDA, 2013). Hence this indicates that interim storage systems are completely active management systems and indicates the need for a solution toward a passive system, this would be a superior long-term resolution to the management of HAW (Roxbrugh, 1987).



Figure 13: Air-cooled interim storage systems for vitrified HLW at Sellafield (NDA, 2010)

High and Intermediate level wastes are defined as being unsuitable and unsafe for permanent surface disposal, this is primarily due to the dangers of radionuclide transportation to the biosphere and the unstable nature of the socio-political affairs of the current world (CoRWM, 2012). But an intelligent and well-designed management system that involves a symbiotic relationship between interim storage and permanent storage would result in an effective disposal strategy. Therefore, the need for surface storage is indeed necessary, but must be ruled out as a permanent solution (Roxbrough, 1987). CoRWM also emphasises within their 2006 report that interim storage is necessary to the long-term management strategy, but systems must be in place to reduce the risk of delay or failure to implement and GDF programme (CoRWM 2006). The report further highlights several key points that support CoRWM's recommendations one of which is ensuring stringent security measures of surface storage sites, particularly against the threat of terrorism or other extremist activities. Providing isolation from direct contact with possible human interference and reducing the probability of the radionuclides finding an easy pathway to the biosphere is of the uppermost importance. On the contrary to the uncertainty regarding deep geological disposal, the aforementioned statement demonstrates that the significance of an adverse event (natural or man-made) involving the surface facility, would have major biological, socioeconomic and political consequences. An event similar in terms of magnitude to the recent Fukushima incident (2013), and in addition to other nuclear related historic incidents, would possibly result in a greater bias with respect to the view on nuclear energy.

1.6.2. The UK's deep geological facility concept and commonly considered host rock lithology's:

The perception of a facility constructed deep within the crustal rock some 500m- 1000m below ground level to accommodate HAW is a publicly controversial issue. However, this concept is now widely acknowledged in both academic and industrial related fields as a viable solution to the permanent disposal of nuclear waste in many countries. Several currently active examples are SKB, NAGRA, ANDRA and NIRAS/ONDRAF etc. The aforesaid examples are some of the main European disposal concepts all of which are actively leading in full-scale research and implementation. As highlighted by Roxburgh (1987), the general criteria that a GDF should meet is set out by the International Atomic Energy Association (IAEA) and full details are expressed in the IAEA (1983) report on GDF guidance. In brief, the principle notion behind this guidance is that geological uncertainty must be reduced through systematic investigation of geological structures, limitations of the positioning of the waste and the wider hydrogeological characteristics of the rock mass respectively. A deep repository according to the Nuclear Energy Agency (NEA) should have a minimum confinement/ isolation period of at-least one hundred thousand years, this is supported by other literature (Bradbury et al, 2014; Savage, 2014; Pusch et al, 2013; Börjesson, 2011). This conclusion is based on the premise that the radiotoxicity of the waste from a repository after the aforesaid period would be very similar to that of uranium tailings. This ore extraction by-product is not isolated from the biosphere and is generally exposed to the surface environment on site. It is however subject to current regulatory guidance and alterations to safe activity limits.

The principle purpose of the GDF and more importantly the EBS is to isolate the radioactive waste and cease radionuclide transport from the near-field zone to the biosphere, it is therefore vital that a suitable repository and all elements of long-term characteristics of an EBS are investigated before finalising planning and implementation. Figure 14 displays a conceptual design of the proposed GDF concept (NDA, 2010) with a simplified arrangement and orientation of the EBS and HLW canister respectively (Landolt, 2009). The EBS design is a multi-barrier passive system, depending primarily on a systems approach, composing of the waste container of a selected steel type, the buffer material (Bentonite) and the host rock. The theory behind the implementation of the Bentonite is to provide a low permeability/ self-healing barrier, thus preventing early radionuclide discharge due to the relatively speedy corrosion of the canister due to the ingress of potentially aggressive groundwater.

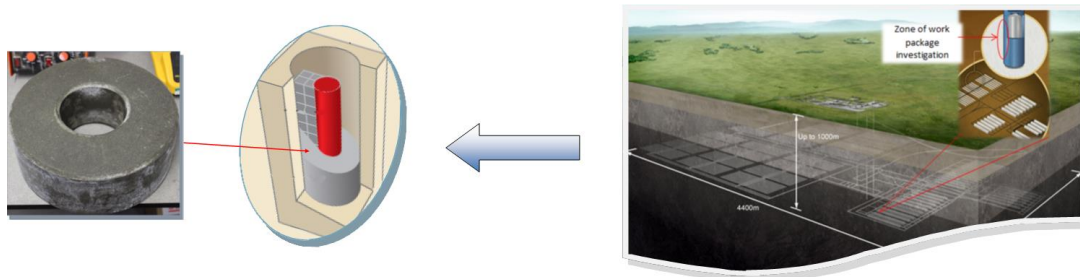


Figure 14: The GDF concept for HLW long-term storage (NDA, 2010 & Landolt, 2009)

The NDA RWM have based their GDF concept on the KBS-3V disposal programme in Sweden (SKB), which encapsulates the waste within a metallic over-pack and is positioned within vertical boreholes encompassed by excavated host rock vaults (Hicks, 2010). Surrounding the metallic canister is a highly-compacted Bentonite barrier. This particular clay is distinguished by its physicochemical characteristics and is widely used in ground engineering applications i.e. drilling muds and landfill liners etc., predominantly it is its hydration enthalpy, free swelling ability and its sorption capacity that make it a favourable candidate material.

There are three main types of host rock that are being comprehensively investigated by the host nation's disposal programmes and various research institutions. More specifically, Pusch et al (2013) highlights the key components in choice of host rock types. Pusch et al (2013) states that discontinuities must be defined when investigating the thermo-hygro-mechanico bulk performance of a potential host rock site and that major discontinuities should not directly intersect the deposition holes. Therefore, the host rock boundary conditions can be condensed into three major engineering premises, 1) Structural and intrinsic configurations and their favourability to the positioning of the repository (i.e. structural discontinuities and intrinsic physical phase relationships etc.), 2) Rock mass hydrological characteristics (Ground water infiltration rate which is determined by rock discontinuities and porosity etc.) and 3) The mineralogical characteristics of the rock and how it may influence the hydrochemistry and ultimately the EBS.

As Pusch et al (2013) stated, the choice and positioning within a rock mass needs to be based on the direction and order of the discontinuity. That is, through core, insitu testing and geophysical inference, fracture ordering as well as hydrological data can be mapped ultimately enabling efficient and effective positioning (see Figures 15 and 16 discontinuity maps from a Swedish granite batholith (Push et al (2013, 2008 & 2007))).

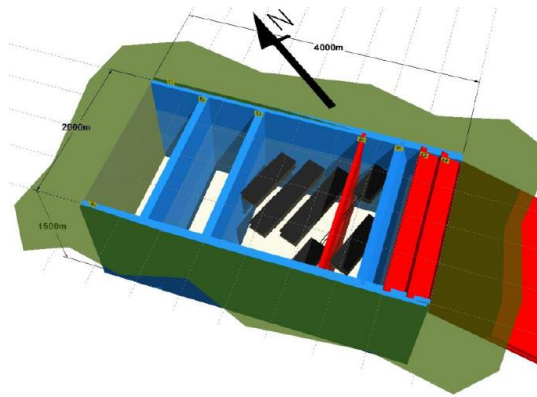


Figure 15: 12Km³ simplified model of a host rock the blue indicating 2nd order discontinuities (≈100m width) with red 3rd order discontinuities (≈30m width), the black areas indicating suitable repository positioning (Pusch, 2008)

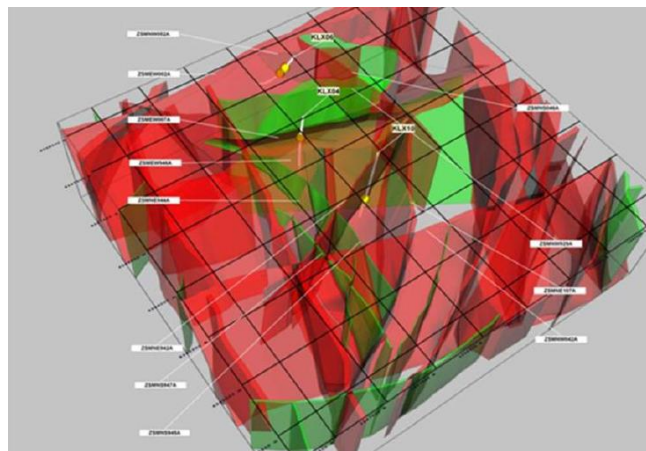


Figure 16: A realistic discontinuity map for a 16Km³ of crystalline rock in south-eastern Sweden derived from intrusive (Boreholes indicated by the yellow spheres) and geophysical investigation. Red and green structures are 2nd order discontinuities (Pusch et al, 2007).

The following points concisely outline the host rock type and both their preferential and potentially adverse geological, engineering and chemical characteristics for use as a GDF host rock:

- **Evaporite deposits (Salt rock):**

Roxburgh (1987) states that evaporite deposits have been considered favourable as a GDF setting due to their very low intrinsic moisture content and self-closing nature (due to their creep characteristics). Evaporite deposits are globally extensive and have been proven to extend more than 1.3Km in the USA as well as areas of Europe (Stuart, 1954). There are, at present, two leading nations that are investigating this option as a viable medium for a disposal facility host rock; Germany and the USA. Evaporites are probably the most heterogeneous of the potential host rock lithology's. Roxburgh (1987) highlights that there are approximately 120 minerals associated with marine and non-marine deposits but due to the stability, many of these minerals have altered within older deposits. Only approximately 40 common mineral types are present in older sequences. It is common in practice to

categorise these deposits by their dominant anion species i.e. Carbonates, Sulphates, Chlorides and Borates (Roxburgh, 1987).

Bell (1983) presents some physical properties of four different Evaporate types, as displayed in Table 7. The properties vary significantly and furthermore it can be observed that the stiffness of rock salt is much lower than the rest. Moreover, it has been reported that under a confining stress and/or thermal loading, when mechanically loaded to the elastic limit, the rock somewhat behaves in a more ductile manner. This indicates that GDF's may prove uneconomic at depths greater than 700-800m (Schwarzkopf et al, 2008; Roxburgh, 1987; Nicolas & Poirier, 1976).

Table 7: Physical properties of evaporates as a host rock (After Bell, 1983)

	Gypsum	Anhydrite	Rock Salt	Potash
Relative density	2.36	2.93	2.2	2.05
Dry density (Mg/m³)	2.19	2.82	2.09	1.98
Porosity (%)	4.6	2.9	4.8	5.1
Unconfined compressive strength (MPa)	2.1	3.7	0.3	0.6
Schleroscope hardness	27	38	12	9
Schmidt hardness	25	40	8	11
Youngs modulus (GPa)	24.8	63.9	3.8	7.9
Permeability (x10⁻¹⁰ m/s)	6.2	0.3	-	-

Hypothetically, this ductile nature when under stress relaxation at depth and thermal loading from the HLW may provide a natural self-sealing mechanism. However, one problem that may arise is the period between final emplacement and void closure: groundwater-salt interaction, in this case, it is greatly unfavourable. Fluid inclusions within macro-voids in an Evaporite formation will most probably be of a brine consistency and if the fluid is inflowing from overlying or underlying stratum then the probability of dissolution greatly increases. If dissolution was to occur then the resulting circumstances could perhaps be large displacements of the waste canisters, highly corrosive groundwater and ultimately radionuclide migration. James and Lupton (1978) investigated the solubility of gypsum with respect to the foundations of hydraulic structures; they determined that if the groundwater infiltration velocities exceed $\times 10^{-3}$ m/s then dissolution of gypsum is likely to occur. The intrinsic moisture content of Evaporite rocks is considered to be very low, although some moisture is present it is considered to be static and isolated in micro-voids of brackish consistency. It has been speculated that this moisture was present since the deposits were

initially formed and is therefore non-meteoritic according to Roxburgh (1987). Hydration of such rock types may also display volumetric alterations: Roxburgh (1987) states that upon hydration anhydrite beds can display a 30-58% volume increase and this swelling effect will undoubtedly exert elevated stresses on the canisters (as much as 69MPa swelling pressure has been reported by Bell (1983)). Bell (1983) also explains that hydration of anhydrite to gypsum with free access to water occurs relatively quickly, and has been reported in some cases to exhibit an explosive nature. Thermal conductivity also plays a major role in the choice of host rock in that the thermal enthalpy of the waste must be allowed to conduct into the surrounding environment to ensure that temperatures are kept at design boundaries. Roxburgh (1987) gives some values of thermal conductivity of various rock types (displayed in Table 8). This Table gives an indication that rock salt has a relatively high ability to transfer heat in comparison to the other rock types.

Table 8: Generic examples of various rock types and properties (Roxburgh, 1987)

Material	Thermal conductivity (W/m/K)
Earth's Crust (Average)	1.67
Soil (Dry)	0.14
Clay (Dry)	0.84-1.26
Clay (Wet)	1.26-1.67
Shale	1.67-3.34
Gneiss	2.09-2.51
Granite	1.67-3.34
Basalt	2.18
Chalk	0.84
Limestone	2.09-3.34
Marble	2.97
Marl	2.09-2.93
Rock salt	3.34-6.28
Gypsum	1.3
Sand (Dry)	0.33-0.38
Sand (10% Moisture)	1.26-2.51
Sandstone (Dry)	0.84-1.26
Sandstone (Wet)	2.09-2.93
Coal	0.13-0.3
Water	0.59

With all the aforesaid aspects considered, the use of salt formations as a GDF can be feasible with good engineering judgement and analysis, as this has been demonstrated by deep mining of halite operations worldwide. Also, engineering operations must ensure that the facility is constructed in areas with minimal chance of considerable groundwater ingress during and after the operation period.

The German Federal Ministry for Economic Affairs and Energy published a report in 2008, detailing their stance on their disposal concepts for all levels of radioactive wastes. Their concept for the disposal of heat generating wastes appear to be within a salt dome host rock. The report provides a comparative Table that compares the properties of the three commonly considered host rocks, Table 9. As can be seen, salt is a rather favourable material except for the dissolution characteristics and very low sorption potential. Hence if free water was to enter the salt deposit, it would rapidly go into solution and the mechanism would be a complete dissolution.

Table 9: Comparison matrix of the three fundamental rock types with respect to the key properties associated to the stability of the host rock in a repository application (BMW, 2008)

Property	Rock salt	Clay/ argillaceous rock	Crystalline rock (e. g. granite)
Thermal conductivity	High	Low	Medium
Permeability	Practically impermeable	Very low to low	Very low (unfractured) to permeable (fractured)
Strength	Medium	Low to medium	High
Deformation behavior	Visco-plastic (creep)	Plastic to brittle	Brittle
Stability of cavities	Self-supporting	Artificial reinforcement required	High (unfractured) to low (highly fractured)
In-situ stress	Isotropic	Anisotropic	Anisotropic
Dissolution behavior	High	Very low	Very low
Sorption behavior	Very low	Very high	Medium to high
Heat resistance	High	Low	High

Favorable property
 Average
 Unfavorable property

- **Argillaceous rock:**

Argillaceous rocks are those comprising predominantly of material that is in the order of magnitude of clay and silt grain sizes i.e. below $62\mu m$ and associated mineralogy respectively. The name is associated to a wide-ranging classification of sedimentary deposits. Roxburgh (1987) gives common secondary mineral constituents derived from information published in a study guide on shale mineralogy by Potter et al (1984). Some of the minerals can significantly alter the groundwater chemistry and can be potentially aggressive when in contact with steel and concrete components, and thus considerably reducing strength and increasing the corrosion rate. On the contrary, intact and non-fractured argillaceous rocks are considered to have an extremely low permeability and therefore ground water movement is slow and primarily diffusion controlled. One example of the aggressive compounds present are sulphides: these are commonly present in shale, such as pyrite (FeS_2), and are symptomatic of reducing conditions in deep sedimentary rocks. However, upon exposure to

water and atmospheric oxygen, oxidation of the mineral forms ferrous sulphate ($FeSO_4$) in addition to sulphur dioxide (SO_2) and readily decomposes to hydroxide in air. Furthermore, the presence of water subsequently produces sulphuric acid, the aforesaid reaction pathway forms localised aggressive groundwater that may speed up corrosion rates of the metallic canisters or even inhibit the favoured geotechnical longevity aspects of the barrier. In a multi-barrier concept conversion of the Bentonite barrier may occur in groundwater containing an abundant source of higher valence cations or acidic groundwater, which may aid illitisation and kaolinisation. This subsequently changes the favourable properties of the Bentonite barrier (See section 2.2- thermo-hydro-mechanico-chemico studies on MX80 Bentonite).

The term argillaceous rock can be applied to materials such as clays, shale, mudstones, marls and siltstones (Roxburgh, 1987; McLean and Gribble, 1992; Bently, 1995). As emphasised by Delage et al (2009) who states that clays exhibit low permeabilities and a large potential to retain radionuclides, both of which act favourably for the effectiveness of the EBS. In addition to these advantages, argillaceous rocks are also known to behave in a ductile manner when under pressure. Understandably, the modulus of elasticity of argillaceous rocks change with age i.e. consolidation time and degree of overburden stresses applied etc. Roxburgh (1987) also expresses the geomechanical advantages with respect to HLW repositories of younger clay deposits in that they display very low permeability, high plasticity and depending on the mineralogical composition, relatively high Cation Exchange Capacities (CEC) in comparison to other rock types. However, the disadvantage associated with highly plastic properties is that, from an engineering perspective, these rocks may prove difficult to construct at depth due to the increasing overburden stress. On the contrary, the comparably stronger and much older shale deposits are much more structurally stable, they are much more likely to include fractures that may enable easier groundwater ingress and radionuclide egress. As previously stated, argillaceous rocks are generally known to have a relatively high CEC in comparison to other rock types. This is however dependant on the clay group type i.e. from the three-fundamental clay mineral types Kaolinite is the most stable as well as having the lowest CEC, whereas the smectite group has a high sorption capability for certain radionuclides, with Illite being the intermediate. For example, Hicks et al (2008) expresses that Bentonite clay has a high CEC, with values ranging between 80-120 mEq per 100g of clay material. This can be particularly significant for radionuclide transportability, as noted by Sena et al (2008) who states that wastes with a high potential for by-product cations such as Cs^+ can be exchanged with interlayer ions such as Na^+ of the Bentonite. Clays display

a varied CEC and specific surface area but it is these two factors in clays, if they are sufficiently high, that contribute to cation sorption. Another associated environmental factor that determines the clays ability to slow radionuclide transportation is highlighted by Roxburgh (1987) who states thermal transfer for clays are relatively low and that the sorption capability of clay minerals indicate a reduction with increasing temperatures. This therefore indicates that repository settings within Argillaceous media must exhibit lower bound peak temperatures ($\leq 100^{\circ}\text{C}$).

Permeabilities related to such rock types, can be highly variable depending on the abundance of coarser particle sizes, porosity (which is directly related to the depth the stratum and hence the magnitude of overburden) and especially in deeper deposits, more stiff materials tend to be more fractured and can fracture once excavation operations start, due to stress relief.

- **Igneous rock:**

Crystalline rocks have been considered by many of the leading disposal programmes. More specifically in Sweden as part of the SKB concept which is currently studying the use of granitic host rock in their prototype repository research (Börjesson, 2010; Pusch, 2006; Birgersson et al, 2008 etc.). Roxburgh (1987) highlights the extensive spatial nature of such rock types and states that these rock types are favourable due to the widespread global distribution and their frequency to occur as massive sequences. The fundamental composition of granites is predominantly quartz, feldspars and sometimes micas. The high silica content of this material indicates that granites should be efficient at transferring heat. The range of thermal conductivities measured for granites is somewhat similar to argillaceous rocks, however argillaceous deposits are considerably weaker than granite masses and are more likely to be prone to thermal stress fracturing due to expansion and contraction. Figure 17 displays the thermal conductivities for some commonly considered host rock types, it can be seen that rock salt displays the most favourable thermal transfer properties.

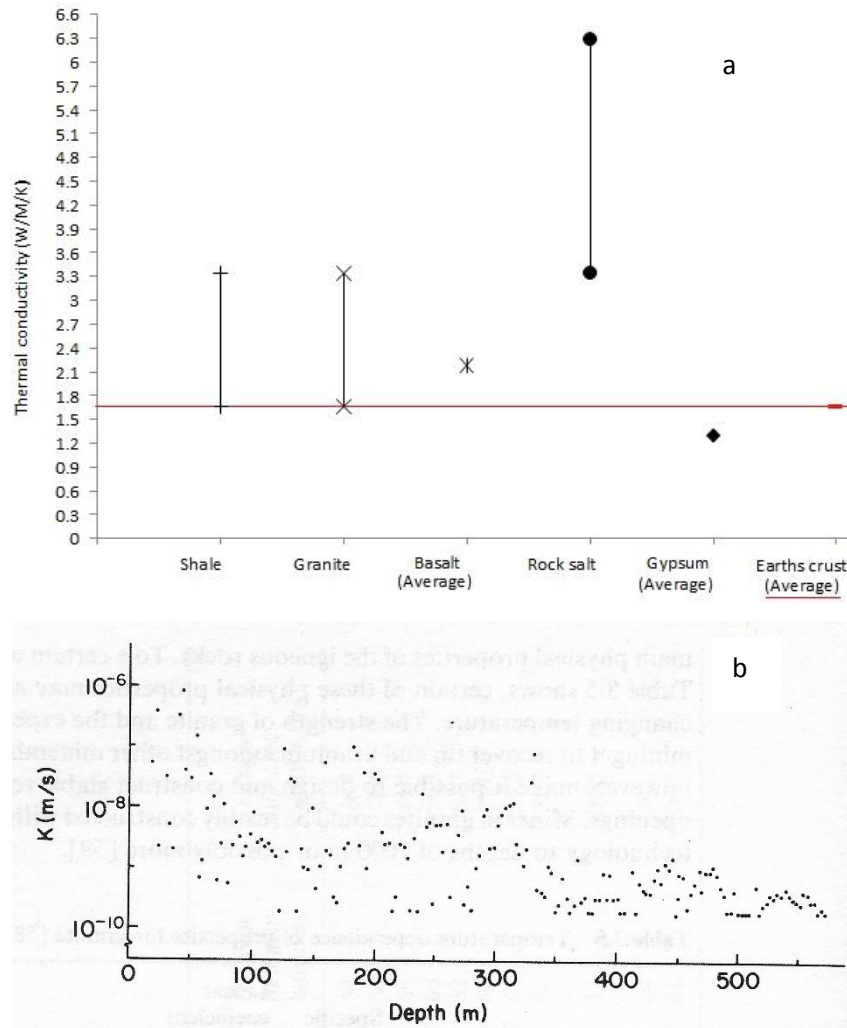


Figure 17: Thermal conductivity ranges for various rock types (a), data taken from Matthews (1982) and hydraulic conductivities from a crystalline borehole in Sweden (b) (After Brotzen, 1982)

When considering granite as an intact mass, it is virtually impermeable. However, on a larger scale the rock mass is likely to contain some fractures, their widths depending on the overburden stress present. Roxburgh (1987) states that various in-situ tests of igneous stratum have demonstrated considerable decrease in permeability with depth, as illustrated by Figure 17 related to the granite/gneiss complex in Sweden (Brotzen, 1981). This decrease of measured permeability is generally accepted due to the closure of voids with an increase in the magnitude of the overburden stress. Other factors that may affect the larger scale flow rate of groundwater through a granitic mass is the degree of infill in the larger fractures. This infill may also potentially aid in the sorption of certain radionuclides. On the contrary, fracture infill may indicate interaction with shallower stratum and subsequently may indicate a direct route for contaminants. Hence, adequate investigation must be employed to ensure no symbiosis of the respective stratum with the water acting as the contaminant vector.

However, the infill may be from deeper stratum and in this case, it would be considered favourable.

Research into the diffusion of radionuclides in the micro-fissures associated to the major fractures in the granites is considered to be of significant importance. Roxburgh (1987) presents examples of research that suggests that diffusion into these micro-fissures may well result in decay of significant radionuclides. By maintaining diffusion dominant processes the system would retain the radionuclides (Namely, Am^{241} , Np^{237} , Th^{229} and Ra^{226}) long enough for them to decay to low levels within a granitic barrier that is 350m thick, with only the long-life radionuclides (Cs^{135} , I^{129} and U^{238}) remaining (Roxburgh, 1987). Another favourable factor with respect to the use of such material as a host rock is the stability due to its intrinsic strength (neglecting the structural features that effect stability on a macro level, i.e. fractures). Widespread mining activities have been carried out in such rock for the extraction of various metals and have enabled the engineering discipline to be accustomed to the heavy engineering aspects of granite tunnelling i.e. Excavation and reinforcement methods. An interesting and unusual characteristic of granite that has been investigated, is its ability to display creep characteristics when at depth and/ or under elevated temperatures (Blacic, 1981). Blacic (1981) discovered that plastic deformation is likely to occur in these near-field zones that may prove problematic in the design. Figure 18 displays data produced by Blacic (1981): the tabulated data in the research reports many parameters as a function of temperature, however only the modulus of elasticity as a function of temperature has been plotted. Ideal peak temperatures within the immediate HLW environment are expected to reach approximately 100°C according to the NDA, UK concept but other concepts predict slightly higher temperatures i.e. the NAGRA concept predicts ~150°C (Landolt et al, 2009). Therefore, referring to Figure 18, there is approximately an 10GPa drop in the elastic modulus when heated at 150°C. This reduction is not absolute for all cases but it does demonstrate that there was an observed reduction as temperature increased, hence indicating a stiffness alteration to the material. However, if temperatures are maintained at 100°C, as specified by the current concept research in the UK (Holton et al, 2012), then localised creep is negligible and stiffness change is insignificant. Nonetheless a combination of elevated temperatures due to the decay of the waste and increase confining pressure may well result in increased creep characteristics and this should not be discounted during repository design and development of a safety case.

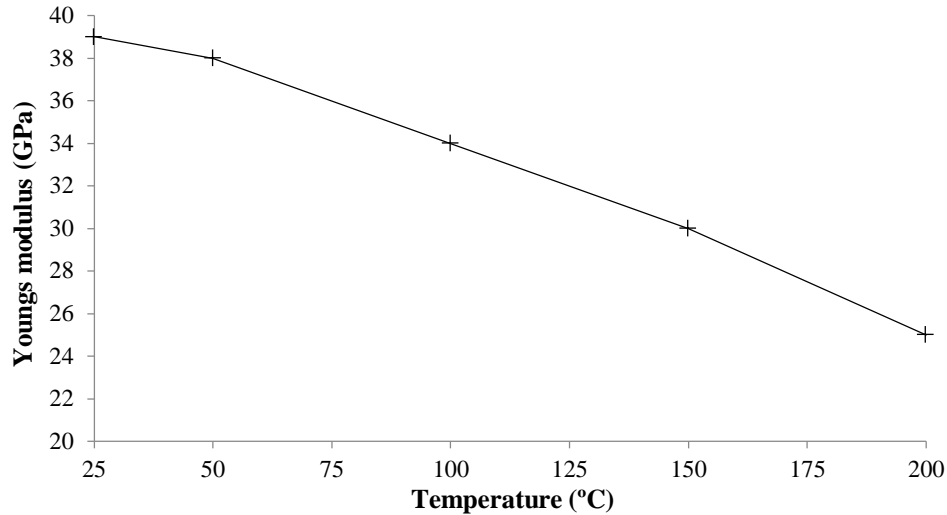


Figure 18: Young's modulus of granite as a function of increasing temperature Blacic (1981)

Overall granites and other rocks associated with the igneous group are largely considered within most of the ground engineering profession as strong rock. This gives the favourable characteristic of being somewhat self-supporting in excavation processes, hence reducing the need for additional engineered supports. The mineralogical composition of all igneous deposits varies considerably with location and origin. Roxburgh (1987) further explains this unfavourable aspect by stating that hydrous minerals within the rock matrix may yield higher mineral conversion rates, even at lower temperatures. This limitation of near-field temperature is a valid argument not to be taken carelessly in the consideration of a hard rock repository, temperatures greater than 200°C are known to cause alteration of hydrous minerals to form more stable anhydrous minerals. This form of dehydration also causes physical alterations, particularly exemplified in basalts, such as an increase in bulk density. Explicitly, the material becomes much more brittle due to porosity collapse as demonstrated in the investigation of tectonic subduction processes given by Hyndman and Peacock (2003).

Furthermore, crystalline rock masses are seldom free from fractures thus making the groundwater flow magnitudes and directions difficult to estimate from surface based and surface intrusive investigations. Thermal effects due to the presence of the HLW may also alter the hydrogeological aspects, since heating may cause dilation of localised fractures as well as convective groundwater cells developing around the canister array/ EBS. On the contrary, much of the findings in this section that has considered the movement of radionuclides via fractured medium have speculated that clay gouge can have a positive effect on the retention through its sorption characteristics.

1.6.3. The UK's engineered multi-barrier concept:

The composite multi-barrier approach is a means of providing several failsafe's in one system, by utilising the advantageous characteristics of the respective materials employed in the design. The primary aim of the multi-barrier is the prevention of radionuclide transport to the biosphere. The NEA (1984) published data detailing a summary of the processes that are significant in the systems approach, as displayed in Table 10. The first three processes detailed in the Table apply to all host rock media, and are based on the fundamental role for a geological repository. Within the most widely considered GDF configuration there are five distinct barriers employed to carrier out such a function:

1. The host rock
2. High alkali grouts that fill any fractures surrounding the waste deposition hole;
3. The highly-compacted Bentonite barrier (With $\geq 70\%$ montmorillonite content) Börjesson (2011)
4. The metallic over-pack (This may comprise of one or a composite design for structural stability and corrosion resistance purposes), metallic canisters such as carbon steel, copper, Nickel/ Titanium alloys and Stainless steel are all currently under consideration
5. The vitrified waste in a stable matrix (the matrix may comprise of borosilicate glass, cements, calcines etc.); currently the UK's method is HLW stabilisation in a borosilicate glass matrix

Table 10: Significant processes related to the systems approach (Roxburgh, 1987)

• Chemical Dissolution or precipitation of a solid phase
• Diffusion into or out of adjacent flow paths under concentration gradients
• Diffusion into the solid matrix of the host rock
• Diffusion into fluid not involved in the bulk flow of the groundwater
• Ion exchange with naturally occurring species
• Direction sorbtion on solid surfaces
• Chemical substitution reactions in which radio nuclides replace stable isotopes of a different element in a stable phase
• Ultrafiltration of large-effective-diameter radioactive solutes or radioelement-bearing colloids by the host medium

The principal factors for the near-field of the EBS are heat, structural containment corrosion, leaching, mineralogical changes, potential engineering property changes, principle

stress variations as well as changes to groundwater conditions over time. It is essential that all factors are deliberated to understand the performance of disposal systems i.e. the thermo-mechanical and associated physicochemical effects on the barrier systems. Engineered clay barriers are considered in most current literature to be most suited to the application of ILW & HLW containment when within the repository host rock due to these physicochemical properties (see previous section on argillaceous rock). The diffusion rate is also a very important aspect of the overall integrity of the containment system, due to the considerably low hydraulic conductivity.

The multi-barrier containment system considered for the UK concept includes a highly compact Bentonite barrier surrounding the waste form, as displayed in Figure 19. It is well known that Bentonite displays a high swelling characteristic which is primarily a function of its Montmorillonite content. Evidently the better the swelling capacity of the clay, the more effective the barrier will be in decelerating radionuclide transportation. This also indicates that the optimum density during compaction is fully achieved to enhance the EBS effectiveness. Decay heat caused by the fission products of β^- decay is a primary by-product of expended reactor fuel, during storage initial temperatures are likely to reach approximately 100°C at the containment Vessel-Bentonite interface, higher temperatures may be present in other concepts according to Delage et al (2009), Madsen (1997) and Landolt et al (2009). It is anticipated that the heat is likely to initially drive-off ground water at elevated temperatures (Wilson et al ,2010). Ultimately, the vertical barrier concept consists of a host rock to provide the outermost structural stability and containment, the intermediate zone will contain highly compact Bentonite to provide self-sealing and radionuclide containment and finally the inner zone will be the metallic waste container.

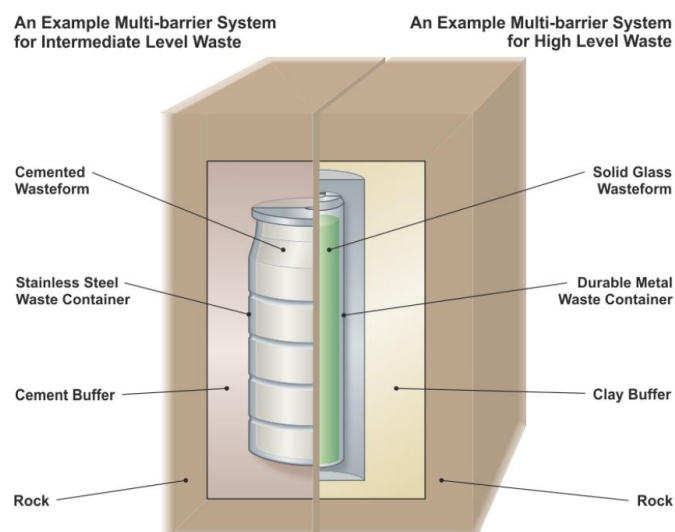


Figure 19: The multi-barrier concept for ILW and HLW/SF (DECC, 2014)

2. Literature review

2.1. Near-field considerations and its impact on the Bentonite within the multi-barrier disposal system

Section 2.1 covers the localised “Near-field” environmental factors that are associated with the multi-barrier concept. More specifically, the factors likely to be present in the Bentonite within the immediate zone around canister interface are explored. It is important to understand the fully coupled system with respect to the thermo-chemical-mechanical factors and their interaction with the containment system.

Bentonite has a wide range of ground engineering applications from drilling fluids to landfill liners i.e. clay barriers etc. These uses have been implemented and developed over several decades within the ground engineering industry. This clay mineral displays unique properties such as its high swelling ability, high plasticity, extraordinary cation exchange capacity/ sorption potential and its thixotropic characteristic due to its specific surface area and colloidal configuration (Delage et al, 2010). Bentonite is a naturally occurring material originating from the weathering process of volcanic tuff. The mineral that provides Bentonite with such unique properties is the Montmorillonite present in the bulk clay matrix. This gives the clay its ability to uptake a large volume of water while displaying some shear resistance and ductile behavior. Börjesson (2010) states the most significant functions of the buffer are the hydraulic conductivity, swelling pressure, stiffness and strength. These parameters are all a function of the Montmorillonite mineral content and dry density.

2.1.1. Near-field THCM evolution:

Delage et al (2009) indicates that clays exhibit a very low permeability as well as the ability to retain radionuclides due to physicochemical adsorption related to the negative layer charge of the clay mineral. The diffusion rate is a very important aspect of the overall integrity of the containment system, due to the considerably low hydraulic conductivity. It is well known that Bentonite displays a high swelling characteristic which is a function of its montmorillonite content. Evidently, the higher the swelling capacity of the clay, the more effective the barrier will be in decelerating radionuclide transportation. Thus, the optimum density during compaction needs to be fully achieved to enhance the EBS effectiveness, with little deviation over the barriers life-span. Decay heat caused by the fission products of β^- decay is a primary by-product of expended reactor fuel. During storage, initial temperatures are likely to reach approximately 100 – 150°C at the containment Vessel-Bentonite

interface, depending on the GDF concept (Delage et al, 2009; Madsen, 1997; Landolt et al, 2009; Leupin et al, 2014). It is anticipated that the heat is likely to initially drive-off ground water (Wilson et al, 2010). The speculated near-field transitional phases were expressed within the NAGRA reports (Landolt et al, 2009 and Leupin et al, 2014). A summary of the phase conditions at the canister surface are presented below and displayed in Figure 20 (Leupin et al, 2014; Landolt et al, 2009).

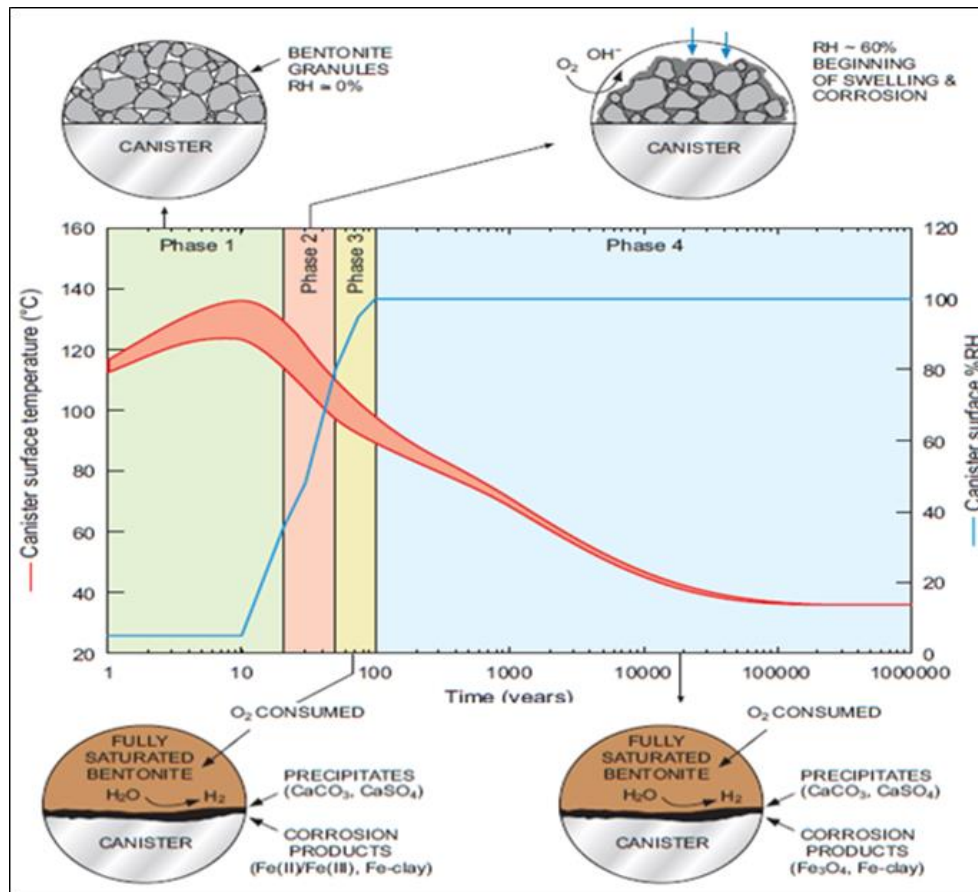


Figure 20: Inferred interface evolution for the NAGRA concept (after Landolt et al, 2009)

- **Phase 1- Aerobic dry:**

Post construction phase and emplacement of canisters within the deposition holes. Atmospheric pressures present with the peak temperatures at the interface reaching 100-150°C after ≈5-10 years after emplacement (depending on concept design premise). Continuation of phase 1 for ≈20-30 years with slow ground water migration and subsequent rewetting. Oxygen within the system is thought to be consumed due to the oxidation of the canister and aided by the elevated temperatures. Uniform concentrations of oxidation products are hypothetically assumed at the interface for simplicity, this however may not be the case and discrete corrosion cells may develop causing heterogeneous diffusion. It is also speculated that higher temperatures will liberate Sulphur from Sulphur containing minerals i.e. FeS₂ ->

S-> HS, H₂S, SO₂ which are corrosion aggressors and will speed up the oxidation process (Orden, 1989). Oxygen depletion will accelerate with increasing temperatures with respect to nature of thermodynamics.

- **Phase 2- Aerobic unsaturated:**

During and immediately after the peak thermal conditions, a dry environment will have formed surrounding the canister. This dry environment will have lost volume due to the water egress from the clay voids. However, progressive cooling with simultaneous ground water migration into the barrier toward the canister will slowly re-saturate the clay. The volume should return to normal and provide a fully sealed environment (assuming constant volume conditions, no adverse bulk alterations have taken place and no significant mineral alteration has occurred). The relative humidity will increase resulting in aqueous corrosion at the interface; the oxygen initially present will be fully consumed. The temperatures during this phase are thought to decrease with time from $\approx 100-90^{\circ}\text{C}$. Continuation of phase 2 is predicted for $\approx 20-30$ years, during which gradual saturation will cause heterogeneous swelling from the outer periphery of the buffer and progressing inwards. This is possibility due to salts re-dissolving and becoming precipitated within discrete zones during drying. The inflow of this high salinity water will result in an aqueous corrosion aggressor and change osmotic gradients for inter-lamellae swelling as well as cation exchange. High pore-water pressure will be present within the buffer due to the elevated thermal exposure and low porosity of the Bentonite.

- **Phase 3- Anaerobic unsaturated:**

This phase is predicted to be the transition between aerobic and anaerobic conditions. It is inferred that all oxidation products are fully formed and reduction is proceeding. This phase is thought to continue for ≈ 50 years. Landolt et al (2009) predict that the initiation of the reducing environment will initiate after 100 years, post emplacement. Canister surface temperatures during this phase is thought to be between $90-60^{\circ}\text{C}$, pore-water pressure in the Bentonite and swelling will also equilibrate over this period. This phase is thought to end in full saturation of the clay barrier and, more specifically, the clay within the interface zone. Leupin et al (2014) also discuss the pore-water pressure development within the near field and states that the pore-water pressures in the outer zones of the barrier will initially increase to several MPa after 100 years, resulting from the thermal dilation of pore-water within the inter and intra layers respectively. This will result in higher pressures around the canister due to a compounded effect of swelling, thermal expansion and the over burden pressure.

Thermal dilation of clay layers during heating has also been observed (Tang et al, 2008) (as discussed later in section 2.2). This thermal dilation may result in an increased permeability and ionic transit rates.

- **Phase 4- Anoxic:**

Complete saturation has been achieved and all oxidised products have been reduced with the only oxidant in the EBS system being H_2O . Landolt et al (2009) and Leupin et al (2014) highlight that hydrogen gas will form due to deprotonation of the water. Also, the effects of hydrolysis may yield hydrogen peroxide due to the decomposition of water near the radioactive waste. Secondary minerals initially dissolved may re-precipitate such as carbonates or hydroxides and may react with the surrounding Bentonite. During the mid-stage of phase 4, after approximately after 1000 years, Landolt et al (2009) highlights that hydrogen generation is reduced and that the pore-water pressure drops by several MPa resulting in a consolidation effect of the Bentonite. With respect to the corrosion product formation, it is speculated that during this time the mobility of the corrosion products will increase due to the elevated pH environment. Leupin et al (2014) state that mobile Fe cations will likely migrate through the Bentonite which will form Fe-rich clay minerals. The presence of calcite as an accessory mineral is predicted to remain stable even in the long-term (Idiart et al, 2013). This is also probably due to the high pH environment of the near-field. Simulations conducted by Idiart et al (2013) predict the extent of exchange of Na and Ca respectively, their data indicated that there was a 5% drop in sodium concentration and a 4% increase in calcium concentration after a 10000-year simulation. As can be seen from geochemical simulations conducted by Idiart et al (2013), sodium remains dominant in the exchanger, independent of the presence of Fe, and they state that their results indicated a geochemically stable buffer over the simulated time period. Nonetheless the modeling conducted by Idiart et al (2013) was limited and did not explore complex electrolyte composition and concentration.

It is also speculated by Landolt et al (2009) that hydrostatic head equilibrium will be achieved some 300-500 years after complete saturation, the local ground water chemistry will evolve with equilibration of the Bentonite pore water until steady state has been fully achieved. Landolt et al (2009) also suggest that the pressures exerted at the interface, also factoring in buffer swelling pressure, will be isotropic and approximately equal to 5-10 MPa. Furthermore, the lithostatic pressures at GDF level will range from 10-25 MPa; this range is given for periods of overburden fluctuations, i.e. potential glaciation etc. Background heat

generation will eventually lead to temperatures of 40- 35°c after 10⁴ years, depending on the host rock.

Senal et al (2010) and Leupin et al (2014) both state the alteration mechanisms that may be present in the interface after 10000 years, these are: 1) a dynamic REDOX environment with respect to the integrated Fe, 2) Cationic substitution, 3) Layer charge reduction due to replacement by higher valence cations within the clay structure and 4) Cation exchange within the interlayer of lyotropic substitution.

- **Canister breaching phase:**

Landolt et al (2009) state that the failure of the canister will be ultimately achieved in approximately 10000 years after emplacement. In the argillaceous host rock concept. The ambient temperatures are expected to be approximately 35-50°C. Hydrogen production will continue through the backfill into the host rock as well as the continuous diffusion of Fe^{2+} into the Bentonite. Leupin et al (2014) detail the hydro-chemical conditions prevailing post canister breach, and highlight that the pore water will contact the waste matrix and radionuclides will diffuse through the saturated buffer and into the host rock. Depending on the chemical forms and half-lives of the radionuclides, the transport distances into the rock will vary. Safety analysis calculations show that negatively charged non-sorption long-lived radionuclides (such as I^{129} , Cl^{39} , Se^{79}) might migrate into the biosphere after several hundred thousand years. It is thought that if diffusion processes are still the dominant transport mechanism, then release rates will not exceed background levels on the surface.

2.1.2. Near-field environment for a crystalline host rock concept:

Leupin et al (2014) provide details on the near-field evolution and boundary conditions for a concept set within a crystalline host rock, most relevant to the current premise for a GDF concept within the UK. It can be said that the corrosion/ physicochemical conditions, stated above for the argillaceous host rock concept will be identical with the only difference being the thermal limits and potentially the hydraulic dynamics of the host rock. Börjesson (2010) and Leupin et al (2014) highlight the importance of limiting the peak temperatures at the canister/ buffer interface, most concepts have selected 100°C to avoid mineral transformation. The thermal limitation is set because the only aspect of the multi-barrier system in a crystalline rock that acts as the attenuation barrier for radionuclides is the Bentonite buffer. In contrast to the argillaceous host rock that also has advantageous physicochemical and geomechanical properties in addition to the Bentonite buffer. Therefore,

the upper thermal limit must be lower in a crystalline host rock concept to prevent excessive alteration to the clay component of the barrier system. Geomechanical limits set to uphold the barriers functionality have been set out for the SKB concept, Leupin et al (2014) states that the barriers swelling capacity must be maintained over the entire lifespan of the EBS and that the minimal swelling pressure to ensure sufficient sealing criteria is 1MPa. Leupin et al (2014) also indicates that a peak pressure has been set out for the SKB concept, a combined hydraulic, over-burden and swelling pressure must not exceed 15MPa on the canister. Near-field chemical evolution for the SKB barrier concept was modelled by Senal et al (2010), they found that Ca-sulphides that are originally present in the MX-80 Bentonite mineralogy at the beginning of the thermal period, will precipitate anhydrites in the Bentonite pores due to the increase of temperature close to the outer boundary of the buffer. The aforesaid process is supported by Idiart et al (2013), their geochemical models indicate that after 10000 years, anhydrite is dissolved and calcium within the exchange sites increase considerably, however sodium is still dominant. Senal et al (2010) and Idiart et al (2013) also discuss the kinetics of silica dissolution by indicating that Silica, an abundant element within the system, is preferentially dissolved near the inner surface. and thermodynamic models predict that the Na is replaced by Ca due to the replacing power. Additionally, the dissolution of amorphous SiO_2 into solution in the saturated high temperature Bentonite may induce some cementing/stiffening effect on the barrier. This process was highlighted by Senal et al (2010) and Leupin et al (2014) who both indicate that interparticle cementation lead to intrinsic changes in rheology and swelling properties. Idiart et al (2013) investigated the geochemical evolution of the near-field for the SKB concept and discovered that dissolution of amorphous silica is greater in the heated interface than in the colder areas. They found that the concentrations for the interface and the outer cooler zone of the barrier was 5.2-7% and 3.4-4.2% respectively. This indicates that after cooling the re-precipitation of amorphous silica and/ or siliceous compounds could cause a cementing between particles. Leupin et al (2014) describes the adverse effects of cementation upon the barrier, stating that there are two main concerns about the effects of cementation on the Bentonite buffer. The influences of cementation on the Bentonite are 1) increase in hydraulic conductivity and 2) is an increase in shear strength i.e. stiffening.

The design limitations set out for the SKB project are detailed by Börjesson (2010), these limitations were determined after several years of R&D. Börjesson (2010) details the following geomechanical limits of the barrier to uphold safety-relevant functions, they state

that the hydraulic conductivities should be no greater than $\times 10^{-12}$ m/s and the swelling pressure should exceed 1MPa to prevent advective flow. Börjesson (2010) also states the limits for microbial development by limiting the saturated buffer density; this should be no less than $1.95Mg/m^3$ with a minimum swelling pressure of 2MPa. These limitations are thought to suffice the elimination of microbes. The transportation of colloids can be greatly reduced if the saturated density is maintained at or greater than $1.65Mg/m^3$. Canister displacement is kept to a minimum if the swelling pressure is greater than 200KPa (Börjesson, 2010). Additionally, due to the presence of brackish waters, Börjesson (2010) states that the barrier must function long-into the future, in the environment expected in the repository. After swelling the buffer should uphold the minimum swelling pressure of 2MPa and the hydraulic conductivity should not exceed $\times 10^{-12}$ m/s independently of dominating cation and for chloride concentrations up to 1 Molar.

2.1.3. Buffer design parameters:

Post emplacement conditions will give rise to complex interactions with the canister and the clay barrier (Leupin et al, 2014). The corrosion and deformation of the tunnel will occur but these factors are governed by the temporal dimension, complete deformation i.e. settlement of the host rock is thought to be fully achieved after approximately 1000 years (Leupin et al, 2014). The duration of deformation is thought to be a function of the stress-field, the mechanical properties of the host rock and the swelling pressure of the Bentonite. Leupin et al (2014) describes the need to keep the buffer parameters to limiting values, thus ensuring that the internal stress field is kept low and that the excavated zone and the canister are kept intact. They further state that if the swelling pressure around the canister is too high the initiation of fracture augmentation could occur within the host rock. Such an increase in fracture size may lead to higher inflow rates and erosion potential. It is therefore clear that there is a delicate balancing between maintaining the barriers design premise and the clay buffer causing an undesirable impact on the system. Below in Table 11 is a compiled list of the limiting near-field parameters set out for the various European concepts. Supported by Leupin et al (2014) they state that it is highly important to avoid transformation of the montmorillonite to non-expandable minerals, thus requiring target performance parameters and temperature to be defined.

Table 11: Attributes for the buffer around the waste canister for the three leading design concepts (after, Leupin, 2014 and Borjesson, 2010)

<u>Safety-relevant attributes</u>	<u>Favors/ contributes to</u>	<u>Nagra parameters</u>	<u>SKB parameters</u>	<u>Posiva parameters</u>
Low hydraulic	Attenuation safety	$K < \times 10^{-11}$ m/s for	$K < \times 10^{-12}$ m/s.	$K < \times 10^{-11}$ to \times

conductivity	functions of buffer, by ensuring diffusive transport. Limits advection.	buffer around canister	Swelling pressure must exceed 1MPa.	10^{-12} m/s
Chemical retention of radionuclides	Attenuation safety functions of buffer, by retarding transportation from the buffer.	No quantitative criterion, strong sorption is favored	Bulk density should exceed $1.65Mg/m^3$	No quantitative criterion, strong sorption is favored
Sufficient density	Attenuation safety functions of buffer, by preventing colloid transport. Attenuation safety function damp shear movement.	Bulk density $>1.65Mg/m^3$	(Dry density = $1.56Mg/m^3$)	Bulk density = $2.05Mg/m^3$
Sufficient swelling pressure	Attenuation safety function of rock, by mechanical stabilisation hence avoiding significant extension of EDZ.	$0.2MPa < P_s <$ minimum principal stress	$1MPa \leq$ Swelling pressure $\leq 15MPa$	$5MPa \leq$ Swelling pressure $\leq 15MPa$
Mechanical support	Safety function of canister, by ensuring it is surrounded by a protective layer (Stress buffering). Safety function to prevent canister sinking by a protective layer of buffer (Stress buffering).	Buffer must be sufficiently viscous to avoid canister sinking	Swelling pressure $> 0.2MPa$	Swelling pressure $> 0.2MPa$
Sufficient gas transport capacity	Attenuation safety function of buffer, by ensuring gas migrates without compromising hydraulic barrier.	No quantitative criterion; less than the minimum principal stress	No quantitative criterion	No quantitative criterion
Minimise microbial corrosion	Safety functions of canister, by ensuring conditions favorable to slow corrosion.	No quantitative criterion but higher densities are preferred to limit microbial activity	Bulk density should exceed $1.95Mg/m^3$. Minimum swelling pressure of 2MPa.	No quantitative criterion but higher densities are preferred to limit microbial activity
Resistance to mineral transformation	Longevity of other safety relevant attributes of buffer	No quantitative criterion	Thermal limit of $100^\circ C$	No quantitative criterion but limit the pyrite content within the Bentonite
SuiTable heat conduction (Tc)	1) Safety function of canister, by ensuring favorable maximum temperature conditions 2) Safety functions of buffer and rock, by ensuring favorable maximum temperature conditions	$0.4 < T_c < 2$ $W/m^3/K$ (for specific thermal heat load of 1500W)	Thermal limit of $100^\circ C$	Thermal limit of $100^\circ C$

As can be observed from Table 11, the limiting conditions vary slightly between concepts, this is due to the site-specific conditions. However, some concepts have not yet settled on a permanent site and therefore generic parameters are stated i.e. using those boundary conditions that are closely related to the most likely concept. SKB has the most developed and relevant concept of disposal research data resulting in many concepts working with the SKB concept to develop their safety cases (including the UK). Furthermore, more specific geomechanical limiting parameters were set out by Börjesson (2009) and Ahonen et al (2008) for Na-Bentonite, these are displayed in Table 12.

Table 12: Preliminary limiting values for the MX80 barrier (after Ahonen et al, 2008; Borjesson, 2009)

Parameter	Limiting value
Moisture content (%)	≤13
Swelling index (mL/2g)	≥20
Smectite content (%wt.)	≥75
Liquid limit (%)	≥250
CEC (mEq/100g)	≥70
Hydraulic conductivity (m/s)	≤ $\times 10^{-12}$
Swelling pressure (MPa)	≥1 and ≤10
Thermal conductivity (W/m/K)	≥1
Organic carbon (%wt.)	<1
Sulphide (%wt.)	≤0.5
Total sulphur (%wt.)	≤1

2.1.4. Geomechanical and geochemical parameters of the EBS system:

Over the past several decades' Bentonite has been developed to be a vital component within the radioactive waste disposal research and development programs for many countries. The fundamental application of the Bentonite is its implementation in an engineered barrier system that encases the vitrified waste in addition to the metallic over-pack within a borehole allocated in a deep geological disposal facility. Once the pre-compacted Bentonite is emplaced around the canisters and the facility moves into its post closure stage. Re-saturation of the facility is expected to occur and therefore the purpose of the barrier is to provide a low permeability, low oxygen environment at/ near the canister interface (Delage et al 2010; Wilson et al, 2010; Leupin et al, 2014). The design premise is to prevent accelerated corrosion, slow actinide release rates, slow microbial development and to provide a ductile buffer zone to compensate for any host rock displacement. It is anticipated that unavoidable canister breaching due to gradual material degradation will occur after considerable time scales, several reports state time scales in the order of $\times 10^5$ years (Landolt et al, 2009; Holton et al, 2012; Idiart et al, 2013; Leupin et al, 2014). Nonetheless it is at this point that the secondary purpose of the Bentonite barrier is partially fulfilled. Over time the gradual decay of certain radionuclide species (dependent on the actinides present within the waste

matrix) will occur but the longer life radionuclides may still be present. Fundamentally it is the purpose of the barrier during this stage to adsorb or slow down transportation sufficiently to allow decay of radioisotopes before reaching the biosphere (Roxburgh, 1987; Sena et al, 2008). The high swelling pressure that occurs upon hydration of the barrier, otherwise known as its “self-healing” capacity, is expected to be maintained to uphold a low transportation rate and canister positioning. The self-healing ability is a function of the dry density and therefore density should be high enough to cease advection and thus molecular transportation is diffusion controlled (Villar and Lloret, 2008). Wilson et al (2010) and Börjesson (2010) provide the barrier density maxima and minima for the SKB concept, the dry density limits are specified to be $\leq 1.56 Mg/m^3$ but $\geq 2.05 Mg/m^3$. Rationalisation of the limitations, according to the SKB concept, is that a maximum density of $2.05 Mg/M^3$ should not be exceeded due to the shear modulus being too high and thus sufficient ductility in the case of host rock movement is not met. Furthermore, a minimum dry density of $1.56 Mg/m^3$ should be maintained for adequate preservation of low hydraulic conductivities ($\leq \times 10^{-10} m/s$) and high swelling pressures ($\geq 0.1 MPa$) (SKB, 2006a; Börjesson, 2010; Leupin et al 2014). It is essential to ensure that the dry density is achieved and maintained, any deviation will result in a change in the hydraulic conductivity and swelling pressure (Cuevas et al, 2002; Ahn and Jo, 2009; Hicks et al, 2009; Wilson et al, 2010; Börjesson et al, 2010). The relationship between the hydraulic conductivity and swelling pressure with respect to the bentonites dry density is demonstrated in Figure 22, this also demonstrates the impact of salt on these properties. It is observed that as the salt concentration increases there is a reduction in swelling pressure. This is due to the osmotic pressure that contributes to the magnitude of inter-lamellae swelling and the concentration of electrolyte in the DDL, demonstrated in Figure 21.

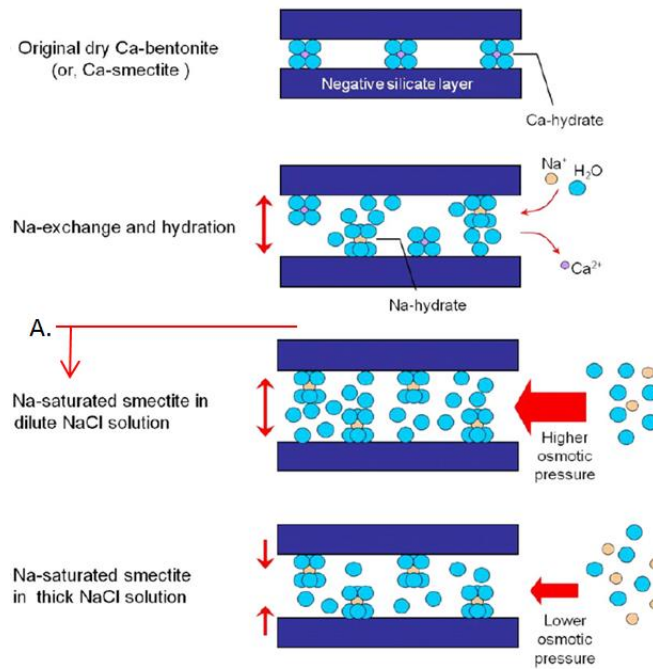


Figure 21: Diagrammatic representation of the impact of salt on the osmotic pressure gradient (After Lee et al, 2012)

It appears that the increase in salt concentration only slightly raises the hydraulic conductivity at each density. The corresponding dry densities of the aforesaid saturated densities are $1.54 Mg/m^3$ and $1.61 Mg/m^3$ assuming moisture content of 27% were calculated using equation 1, from BS1377 Pt [5]. A dry density of $1.54 Mg/m^3$ has been chosen for the reference density for the research, this is also supported by the prefabricated rings that were supplied by SKB via their sub-contractor ClayTech AB, with a saturated moisture content corresponding to approximately 27% ($S_r \approx 97\%$).

$$\rho_{dry} = \frac{(100 \times \rho)}{(100 + \omega)} \quad \text{Eq. (1)}$$

where:

ρ_{dry} : Dry density (Mg/m^3)

ρ : Saturated density (Mg/m^3)

ω : Moisture content (%)

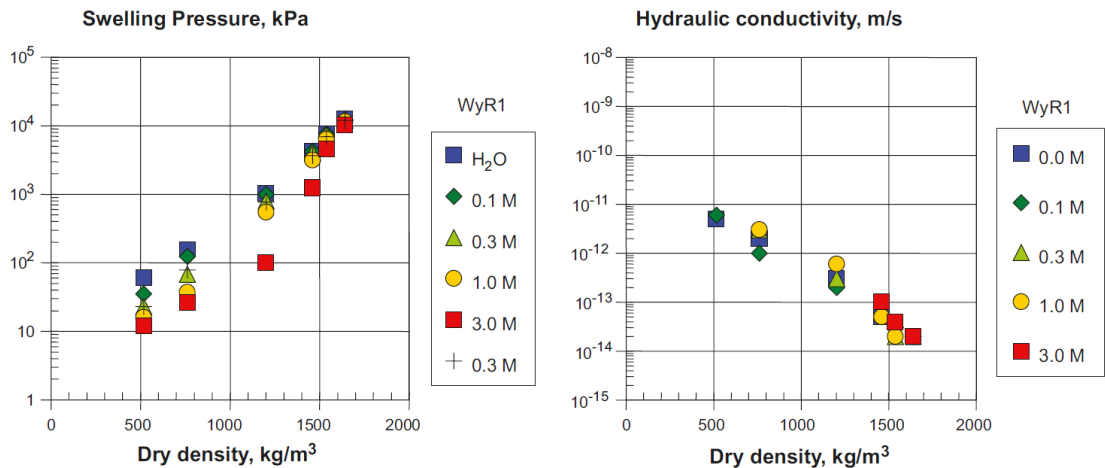


Figure 22: Swelling pressure and dry density with respect to dry density with various salt concentrations (after Borjesson, 2010)

The location of the host rock is essential to the hydraulic behavior of the engineered barrier system. The host rock needs to provide the outermost barrier before the biosphere is reached. Therefore, it needs to be of low permeability and low porosity (Delage et al, 2010). The concept most relevant to the current UK disposal concept is that of the KBS-3V design, consisting of the repository within a crystalline host rock. Push et al (2014; 2008; 1995) describe the nature of crystalline host rocks and discusses the hydrogeological characteristics. An important issue related to the structural geology of the crystalline host rocks is the major “water-bearing” structural elements governed by the 1st and 2nd order discontinuities. These discontinuities should not interconnect with the deposition hole that contains the major waste containing elements. During the early phase of the near-field the high temperatures are thought to induce pore-water pressurisation in the clay media, Delage et al (2010) states that in clays that are rapidly heated the thermal transfer is faster than the water flow, causing dilation. This temperature increase is coupled with a fast pore water pressure increase as is displayed in Figure 23. Pore-water pressurisation will be present within the Bentonite buffer. Therefore, increasing the confining stresses around the canister.

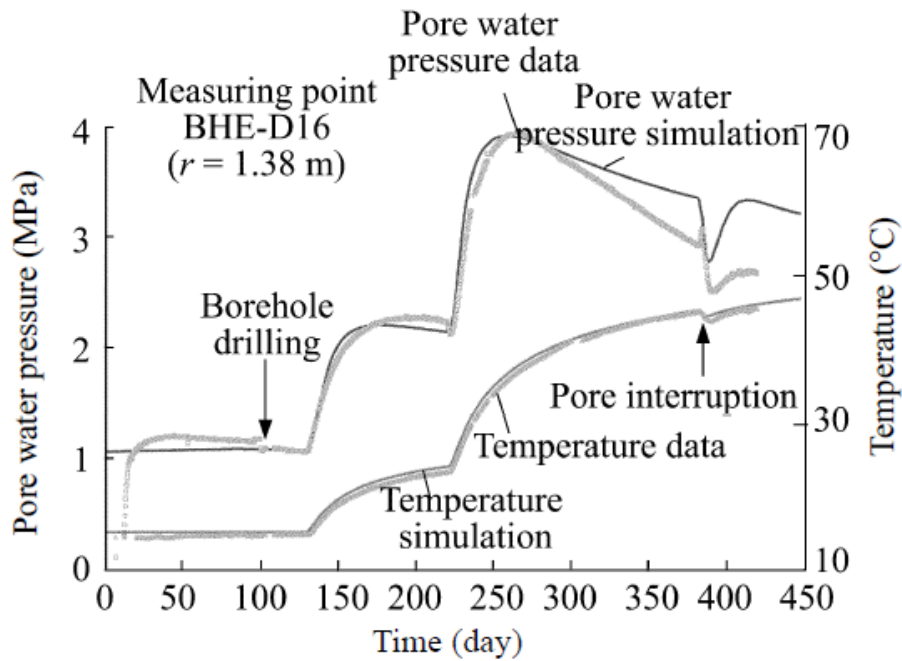


Figure 23: Pore water pressure in elevated temperature clay media (Kull et al, 2007)

Kull et al (2007) measured the pore-water pressure profile within a test borehole located in a crystalline host rock i.e. simulating the SKB concept. It is observed that as the temperature increases there is a noticeable increase in the Bentonite pore water pressure. This is due to an increase in the thermal dilation coefficient. This thermal induced pressurisation causes dilation within the pore spacing as well as an increase of the kinematic viscosity of the water. It is found that these are associated with a noticeable increase in the hydraulic conductivity (Cho et al, 1999; Kull et al, 2007; Tang et al, 2008; Ye et al, 2012).

With respect to the ductility of the barrier, one main design function is the ability to act as a stress buffer during the repository life. Leupin et al (2014) details the safety function for the buffer to protect the canister from rock movements and they state that the plasticity of the Bentonite alleviates shear stress transfer into the canister. However, the degree of compaction and hence the dry density should be limited, this is due to the development of less ductile, more brittle behavior the Bentonite will exhibit. Nonetheless the density needs to be sufficiently high to prevent canister displacement. If in the event of a host rock mass displacement, the stress should not be directly transferred into the canister via the barrier. Consequently, the barrier must remain ductile enough to adsorb the energy and deform meanwhile maintaining sufficiently high shear resistance / modulus to prevent excessive canister displacement. Figure 24 below, given in a combined report on a critical review of Bentonite in repository applications jointly published by independent research companies

Quintessa, Sweco and TerraSalus ltd (Wilson et al, 2010), depicts why ductility within the buffer must be maintained for canister integrity.

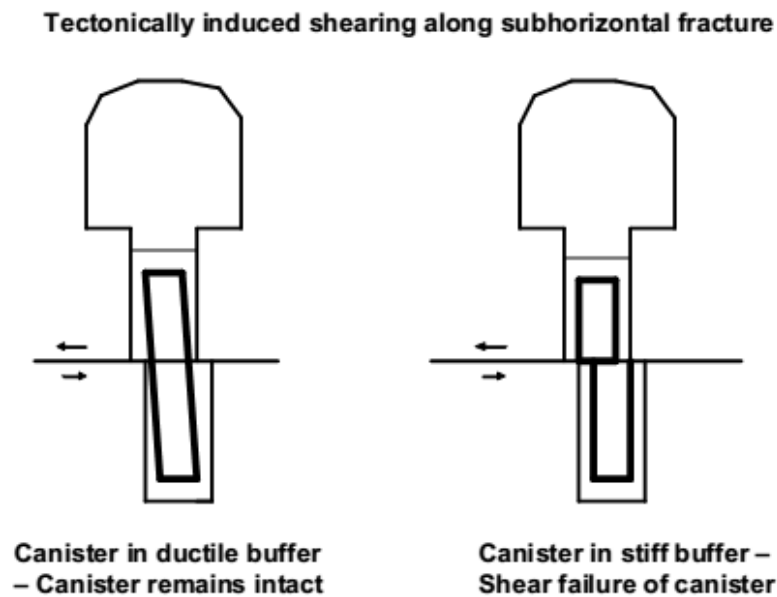


Figure 24: Simplified depiction of the importance on the barrier ductility (Wilson et al, 2010)

Pusch et al (2014) further states that if large fracture zones are present, particularly in brittle rock like a crystalline medium, the system may be subject to large displacements in the event of a tectonic or seismic movement. This further highlights the need for the barrier to minimize the impact on the canister by being ductile enough to allow stress dissipation. Pusch et al (2014) found that hydrothermal exposure of the Bentonite for one year, gave witness to creep measurements that highlighted significant stiffening.

There are two main types of Bentonite used in the HLW/SF engineered barrier system. These are sodium (Na^+) and calcium (Ca^{2+}) bentonites respectively and are considered homoionic in nature. Extensive research has been conducted into the performance of the two types, the Na-Bentonite displays superior swelling capability when compared to Ca-Bentonite as shown in Figure 25. The sodium MX-80 displays a swelling capacity over three times that of the calcium Bentonite. Delage et al (2010) provides geomechanical data and comparison between the commonly considered bentonites, Table 13.

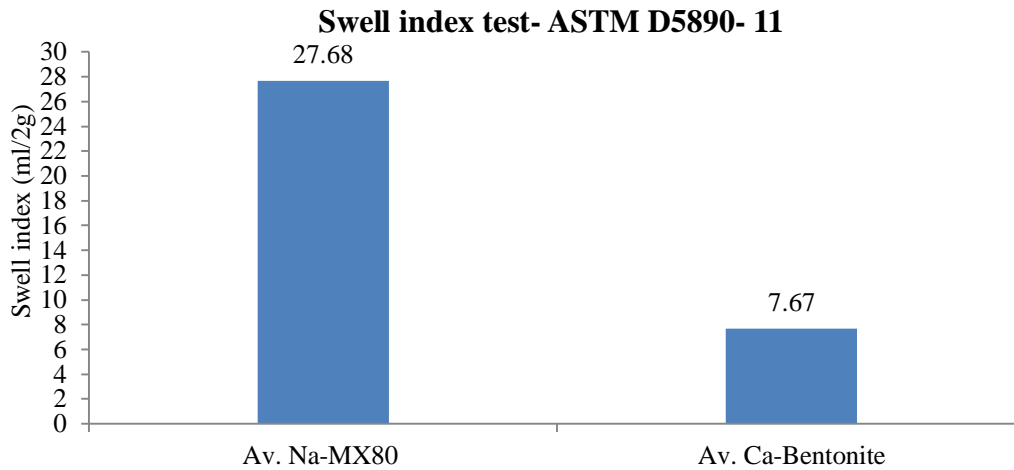


Figure 25: Comparison between Na and Ca homoionised bentonites, displaying the average swell index values from several sources and insitu test results (RS MX-80 only). Sources for Ca-Bentonite values from Lee et al (2012) & Koch (2008)

Table 13: Comparison of the candidate bentonites (after Delage et al, 2010)

<u>Bentonite type</u>	<u>Mineralogy</u>	<u>Liquid limit (%)</u>	<u>Plastic limit (%)</u>	<u>Plasticity Index (%)</u>	<u>Specific gravity (Mg/m^3)</u>	<u>Activity</u>	<u>Specific Surface Area (M^2/g)</u>	<u>CEC (mEq/100g)</u>
FoCa	Kaolinite/ Ca-smectite	112	50	62	2.67	0.78	300	54
Kunigel	64% Na-smectite	474	27	447	2.79	6.9	687	73.2
MX-80	85% Na/ 15% Ca smectite	520	62	458	2.65	5.4	700	68

From Table 13 it can be observed that the greater the content of Na-Bentonite the greater the swelling potential related to the PI and specific surface area. This swelling potential gives the clay its ability to expand and “plug” openings/ voids to produce a sealed containment zone within the host rock Madsen (1998). Also, it is seen that the CEC is higher for a Na homogenized Bentonite, this can have both a positive and a negative effect on the barriers functionality. The high CEC will result in the barriers ability to attenuate the release of the radionuclides into the biosphere in the long term. On the contrary, if the groundwater or minerals containing higher valence cations leach into the Bentonite during the high temperature/ re-saturation phase, then the barrier will readily exchange for the higher valence cation, thus reducing its chemico-mechanical effectiveness.

Hydraulic conductivity measurements for Ca and Na bentonites do not excessively deviate from one another at the same dry density. The hydraulic conductivity is known to change with density and various environmental factors (see above). Batchelor (1983), Cho et al (1999) and Hicks (2009) demonstrate this and conclude that any change in permeability is primarily due to the increase in kinematic viscosity with increasing temperature. Hicks (2009), Delage et al (2010) and Leupin et al (2014) presented average hydraulic conductivity

values for Ca and Na bentonites; these are $\times 10^{-14}$ m/s and $\times 10^{-11}$ m/s at 20°C and $1.56\text{Mg}/\text{m}^3 \pm 0.5\text{Mg}/\text{m}^3$ respectively. These hydraulic conductivity magnitudes are considered satisfactory to limit advection and maintain diffusion transportation. Na-Bentonite displays an inherently larger swelling capacity which can be correlated to a lower saturated hydraulic conductivity. Thus, it is more likely that lower hydraulic conductivities are upheld with the higher swelling Na-type Bentonite. Therefore, in terms of the barrier upholding its intended design function, many of the European disposal concepts have settled on using Na-Bentonite such as ANDRA, SKB, NAGRA and Posiva etc. Nonetheless there are some disposal concepts that are investigating the use of Ca-Bentonite, namely East Asian countries.

The coupled mechanical and physicochemical properties govern the slow groundwater movements (Delage et al, 2010). Emplacement of the Bentonite around the canister forms an excellent protection area (the buffer zone) with respect to the mechanical, hydraulic and chemical factors that are preset in the near-field Madsen (1998). Horseman and Volckaert (1996) conclude that the effect of local chemical and physical factors may change the magnitude of the inter-particle forces and deviation from Darcian flow laws may occur. This is due to the complex coupling of the thermo-chemico-hydro-mechanical responses of the near-field bulk water chemistry, temperature and loading response. This complex flow in highly compact media is governed by diffusive transport and when coupled with the high CEC ability of the clay, it provides a slowing and retardation of the actinides present within the canister that may eventually leach into the clay component of the barrier. Leupin et al (2014) states that it is imperative that the barrier slows the transport of dissolved solutes by maintaining diffusion dominated transport of corrosion products and actinides etc. The high swell potential, related to the high degree of compaction, clay surface area and structural charge, of the Bentonite ensures that there is no convective water flow in the system Madsen (1998). Leupin et al (2014) highlights the initial conditions during the resaturation stage and states that strong hydraulic gradients may present the potential of erosion of the outer zone of the Bentonite barrier if emplaced in highly fractured host rocks. Within the clay barrier classical groundwater flow driven by a hydraulic gradient (i.e. high pressure to low pressure) may not be the only flow driving force in the system. Horseman and Volckaert (1996) state that the groundwater flux within the Bentonite is driven, in part, by the non-hydraulic potential gradients, i.e. thermal gradients and osmotic pressure may also govern flow. These flow mechanisms are likely to occur once the groundwater enters the Bentonite pore network. However, the potential for erosion, if high inflow rates at the host rock/ Bentonite interface

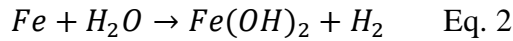
are present, is likely. Therefore, high inflow should be kept to a minimum. Overall Leupin et al (2014) defines the repository function as a means of confinement and attenuation, the multi-barrier concept aims to provide these mechanisms by use of man-made and natural geological obstruction in spite of the predicted aggressive near-field evolution. Thus, the coupled thermo-hygro-mechanico-chemical components of the system should be chosen and managed specifically to maintain the barriers desired functionality.

2.1.5. Steel corrosion development at the clay/ canister interface:

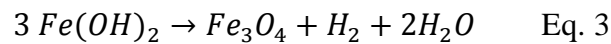
Corrosion of the canister is inevitable and the integration of the corrosion products is likely over the geological time scales envisaged for the GDF. Ishidera et al (2008) highlights that the groundwater and the by-products of secondary minerals will accelerate the corrosion of canister due to the presence of salts and the resultant corrosion by-products will migrate into the compacted Bentonite via diffusive transport. They state that the corrosion integration may alter the Bentonite to Fe-rich minerals and that such alteration could result in the whole or partial loss in the bentonites ability to swell and self-heal. This geomechanical degradation is thought to be due to the loss of layer charge due to isomorphic substitution and occupation of vacant octahedral/ tetrahedral sites. Nirex reported during a viability report of a phased geological concept in the UK during 2005 that the development of a high pH environment at the interface will slow down the rate of corrosion (Nirex, 2005). As the corrosion process proceeds, the pH of the solution will increase thus slowing the reaction kinetics in agreement with Morgan and Lahav (2007). The Nirex report states that upon the closure of the deposition tunnels, it is assumed that the tunnels are sealed. The oxygen will, eventually, be consumed through the corrosion of the steel in the system as well as the corrosion of other minor Fe-rich minerals. Eventually, anaerobic/ reducing conditions will develop due to the consumption of all free oxygen in the system. The Nirex report concludes that the development of the reducing conditions will be favorable for the sorption of the radionuclides. The development of the high pH and anaerobic environment ensures that the near-field chemistry will be dominated with OH^- ions; this favors the formation of oxihydroxides Birgersson and Wersin (2014). The Nirex report states that hydroxides of many radionuclides have a low solubility in high pH environs, this will reduce the rate at which these low valence radionuclides are dissolved into the pore water.

Madsen (1998) provides a description of the potential corrosion products that are likely to develop on the steel surface and discusses that when the absorbed water accesses the interface, wet corrosion will develop and magnetite as well as hydrogen will be formed.

Hydrogen is produced when all free oxygen is consumed in the system, producing hydroxides; hydrogen gas is a byproduct of deprotonated H_2O . The corrosion reaction that governs the production of hydrogen gas is displayed in Equ (2):



Therefore, in the presence of an alkaline and anaerobic environment, which is expected in the later stages of the near-field evolution, will favor the formation of ferrous hydroxide (Madsen, 1998; Charpentiera et al, 2006; Carlson et al, 2007; Wersin et al, 2007; Wersin et al, 2008; King, 2008; Delage et al, 2010; Kumpulainen et al, 2010; Börjesson, 2011; Ollila, 2011; Bradbury et al, 2014; Hofstetter et al, 2014; Leupin et al, 2014). The formation of the ferrous hydroxide can be readily oxidised to form magnetite and additional hydrogen gas, the magnetite is formed due to it being more thermodynamically stable, the reaction pathway displayed below (Equ. 3) given by Wersin et al (2008):



Delage et al (2010) predicts that the resulting anaerobic phase may last around 1000 years, therefore the process of the resaturation stage is said to last in the order of $\times 10^4$ years. Delage et al (2010) describes that the resaturation phase will be prolonged by the generation of hydrogen gas, maintaining the barrier in an unsaturated state. Additional corrosive compounds within the barrier resulting from the presence of secondary minerals in the Bentonite may accelerate the corrosion process. Leupin et al (2014) discusses the initial state of the barrier and concludes that the content of the agents that accelerate corrosion should be kept low, except for the unavoidable oxygen resulting from the construction phase. They state that the presence of pyrite as a secondary mineral may accelerate corrosion due to the formation sulphides. Many studies have reported the development of metaTable green rust compounds and Siderite (Iron carbonates) after prolonged hydrothermal exposure at the Bentonite/ carbon steel interface (Tamaura et al, 1984; Antunes et al, 2003; Refait et al, 2003; Wersin et al, 2003; King, 2008). Other studies have also reported the development of Magnetite, hematite and goethite on the C-steel surface (Smart et al, 2004; Carlson, 2007). These however may be pseudomorphs of the other thermo-dynamically unstable minerals such as feroxyhyte formed in the post-mortem phase of the experimental procedures when exposed to atmospheric conditions. For more information on the THC development and Fe/ Bentonite interaction studies see section 2.2.

2.1.6. Thermal evolution and thermal impact within the near-field:

The near-field thermal limits are subject to each specific concept by considering the waste form and the thermal parameters of the surrounding rock/ barrier. The thermal flux due to the decay of the radioactive waste in the HLW/ SF repository will lead to significantly high temperatures at the interface (Leupin et al, 2014). Leupin et al (2014) states that the high thermal exposure in the barrier will influence the thermodynamic stability and the alteration kinetics of the montmorillonite. Delage et al (2010) investigated some of the thermo-mechanical behaviors of various European concepts. They highlight that the French concept (ANDRA) predicts that the peak thermal temperatures will rapidly reach 90°C after approximately 15 years (Delage et al (2010)). It is also stated that investigations into the thermal perturbation period of the barrier, investigated by Agus and Schaz (2005), shows that thermal homogeneity around the canister array will initiate around 1000 years and complete homogeneity at around 3000 years with a background temperature of 35-30°C in crystalline host rocks (Figure 26). The peak temperature for the Andra concept is lower than the hard rock concepts. The thermal profile for the Argillaceous concept is presented by Delage et al (2010) and Agus and Schaz (2005), displayed in Figure 27. Delage et al (2010) further confirms that the predicted higher thermal limits are present due to the Bentonite backfill, profiles show that the initial peak temperature is as high as 160°C after 10 years decaying to 100°C after 1000 years. Higher thermal near-field exposure in argillaceous host rock repositories is justified due to the presence of thick layer of clay from the canister surface to the outer extent of the host rock (Leupin et al, 2014). This is because the surrounding Bentonite isn't the only physicochemical barrier in the system, and the host rock also plays a role in low permeability, chemically adsorbing medium. Therefore, temperatures at the interface can be inherently higher as some mineral alteration and loss in functionality in the immediate area can be compensated by the remaining phyllosilicate rich host rock.

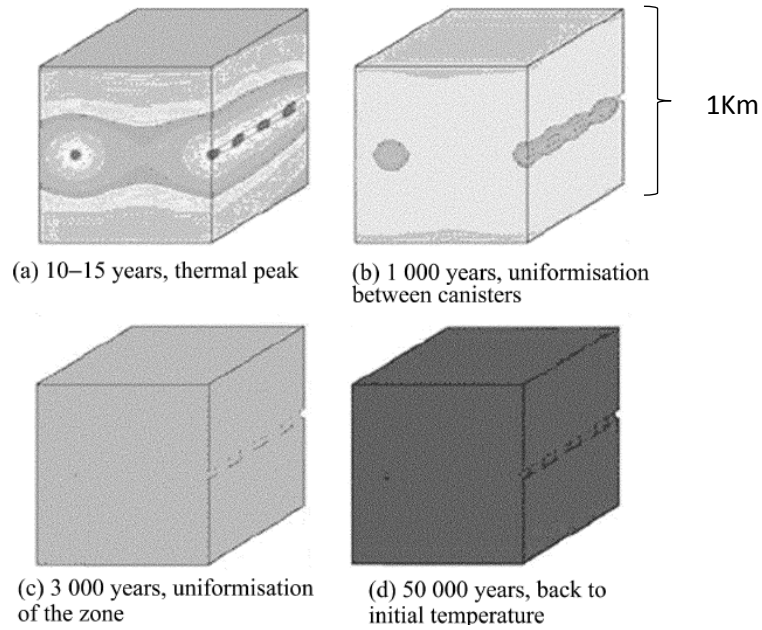


Figure 26: Thermal-temporal evolution from canister heat dissipation showing less contours when thermal homgenisation occurs (after Agus and Schaz, 2005)

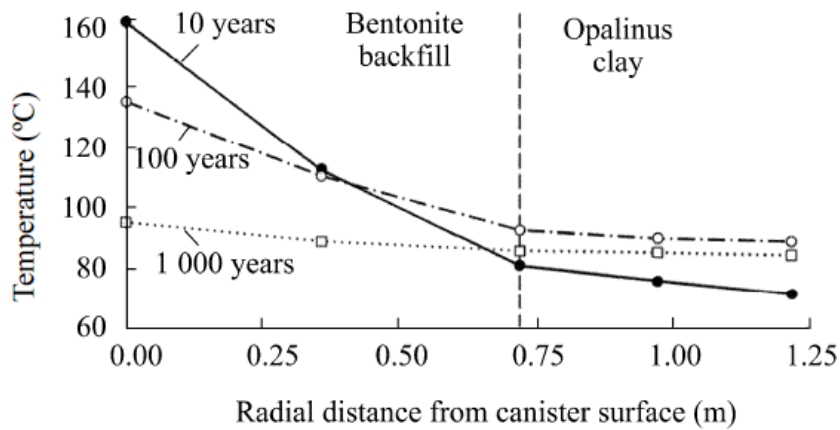


Figure 27: Temperature profile for the Swiss concept (after Agus and Schaz, 2005)

The high thermal gradients present within the barrier in the unsaturated early phase of the repository life are thought to induce complex thermo-hydro-chemical conditions. The Bentonite will undergo high thermal loading, salt enrichment and dissolution/ precipitation processes over a period of approximately 1000 years (Pusch et al, 2014). Therefore, this indicates that this environment will be highly heterogeneous. Sena et al (2010b) uses numerical analysis to predict the solute transportation within the engineered barrier system and states that early phase conditions result in a system driven by suction and a “piston-like” flow. They also observed that the elevated temperatures and gradients present do not result in evaporation of the pore water within the Bentonite barrier, concluding that this may be due to the high capillary forces and hydraulic gradients present. Any solute present within the Bentonite during the early phase is advection driven, once saturation is complete then

diffusion is the dominating transport conditions (Sena et al (2010b). Idiart et al (2013) studied similar conditions to that of Sena et al (2010b), for the Finnish concept (POSIVA) and concluded that their models displayed a geochemically stable environment over their simulated time-scale. However, simulations must be considered with uncertainty due to input error and simplification of the considered environment.

Idiart et al (2013) state the peak interface temperature of 90°C for the POSIVA crystalline host rock repository. They predict the thermal evolution of the engineered system up to 20000 years after emplacement. Figure 28 displays the thermal evolution profile for the Posiva concept. The prediction used the assumption that resaturation was achieved after 260 years and the profiled points in Figure 28 correspond to the following coordinates a) r: 0.53m & d: 2.9m, b) r: 0.875m & d: 2.9m, C) r: 0.275m & d: 6.55m and d) r: 2.9m & d: 2.9m within the EBS system.

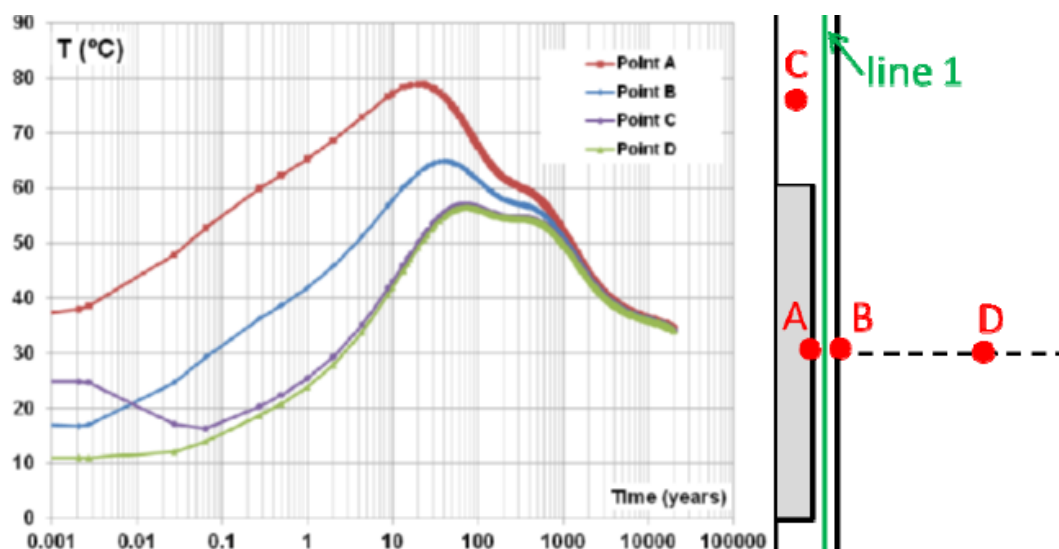


Figure 28: Predicted thermal profile for the Posiva concept. A) Canister/ Bentonite interface, B) Bentonite/ host-rock interface, °C) borehole cap and D) host rock (after Idiart et al 2013)

The Posiva concept predicts that the interface temperature will reach its peak after 20 years, reaching approximately 80°C while the Bentonite/ host-rock interface will reach 65°C resulting in a thermal gradient across the buffer of 40°C/m. Below in Figure 29, displays the thermal evolution of the barrier at key intervals in the barriers life-span. Leupin et al (2014) states that these elevated thermal gradients that will be present in the early phase of the barrier system will cause internal mass redistribution when the groundwater begins to re-saturate the buffer. The high temperatures and hydraulic gradients are thought to facilitate the dissolution and re-precipitation processes such as silica and carbonate redistribution.

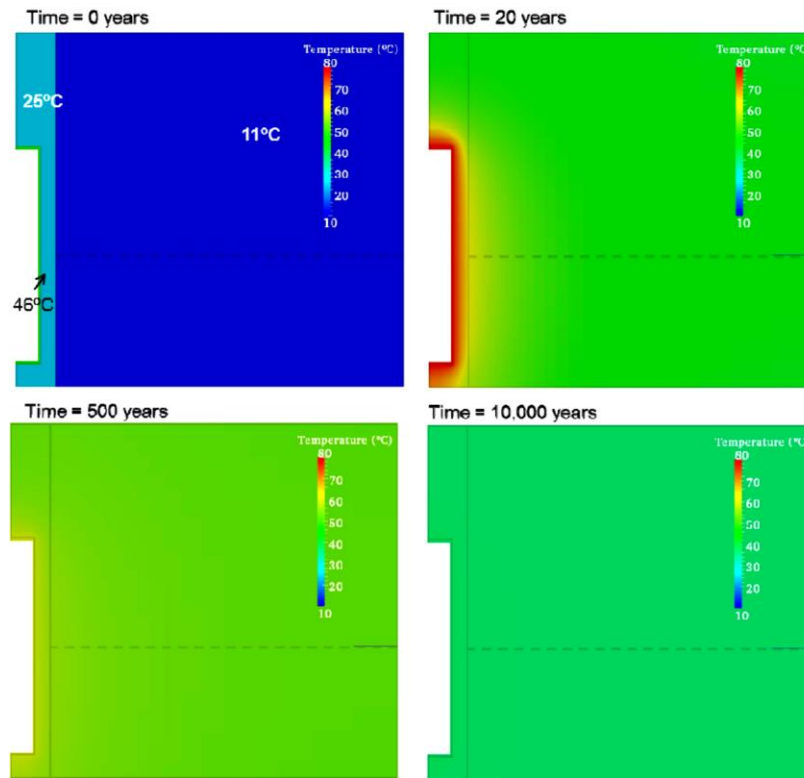
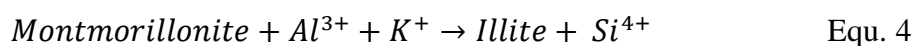


Figure 29: Thermal contour profile of the Posiva repository concept (after Idiart et al 2013)

The Swedish KBS-3V concept predicts a peak interface temperature of 100°C (Börjesson, 2010). Pusch et al (2014) gives the thermal profile of the KBS-3V concept and predicts that the temperature will drop from 100°C to 30°C after 1000 years, assuming a linear temperature drop. Illitisation is a commonly observed by-product in hydrothermal systems resulting from increasing temperature and diagenesis; it is widely known that it requires an increase in charge and access to potassium (Meunier & Velde, 2004). Any potential silification and illite formation would be initiated in the first 500 years of heating, with the inner zones being subject to the most transformation. This is due to extensive research conducted on the hydrothermal interaction of the bentonite barrier and the near-field environment. Pusch and Kasbohm (2002) describe the precipitation/ dissolution to be an alternative illitisation mechanism. They explain that several studies show that heat-exposed smectite displays two physical forms, 1) A flakey or mossy appearance indicating interstratified I/S and 2) Lath shaped minerals indicating that Illite has formed within the Bentonite pores (Inoue et al, 1987; Geuven, 1987). The latter is thought to be a result of the release of Si and Al from the smectite with the uptake of K in replacement. The more traditional approach of the illite to smectite conversion process is also given in the report by Pusch and Kasbohm (2002) and displayed in Equ 4, below.



The above formula indicates that during the process of hydrothermal exposure the transformation to illite as well as silica will be precipitated. This indicates that clay particle cementation could also occur once cooling of the near-field is initiated. Pusch et al (2014) display a comparison of Bentonite mineralogy after hydrothermal exposure after high thermal loading of 130°C (Figure 30). At these temperatures, it is thought that mineralogical changes and dissolution/ precipitation processes are expected. Figure 30, indicates that the presence of gypsum, feldspar and quartz is reduced with the increase of illite.

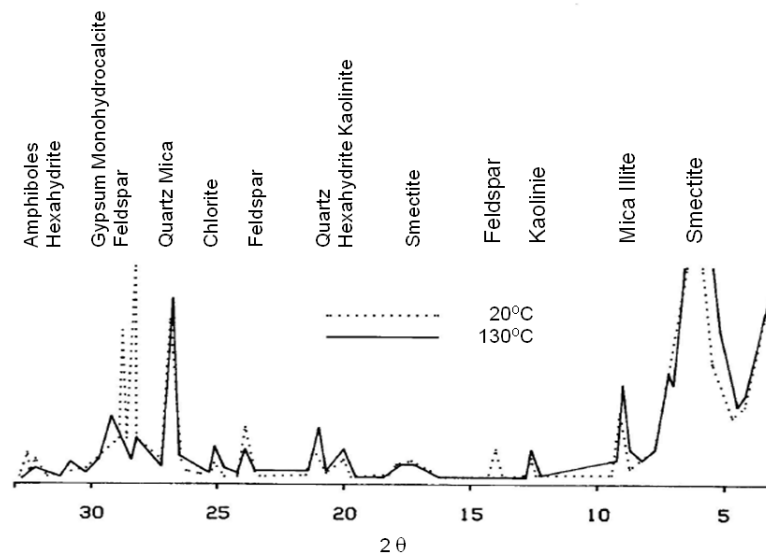


Figure 30: Comparison of MX-80 exposed to hydrothermal treatment and ambient temperatures, a comparison (after Pusch et al, 1993)

Pusch and Kasbohm (2002) conclude that saturated clay with NaCl solutions at 110°C display minor alterations. Observations of the minor development of collapsed montmorillonite stacks, formation of beidellite and stable aggregates were observed. Reports of the process that leads to the illite formation within smectite under hydrothermal conditions state that the intermediate process is the alteration to beidellite and saponite, both of which have higher layer charges (Sato et al, 1996 and Meunier et al, 1998). Push and Kasbohm (2002) also state the collapse of the stacks is believed to be partially caused by the neo-formation of sodium illite. Sodium illite could be the formation of the illite analogue, Brammallite. Initially the short-term alteration is thought to be the formation of the potassium rich bentonites, Madsen (1998) and Müller-vonmoos et al (1994) state that as the interlayer charge is augmented by the isomorphous substitution of Si and Al will increase the cation exchange. They state that the adsorption of potassium, present within the pore-water, into the interlayer will cause a collapse within the inter-lamella spacing. Thus, giving rise to the neoformation of a high charge mixed k-smectite/ illite layering, resulting in an end member

of the illite transformation further supported by Matt et al (2008). Beaufort et al (2001) presented experimental results that support the transformation process, after high thermal loads over 1 year the smectites displayed formation of high-charge beidellite, agreeing with Müller-vonmoos et al (1994), Sato et al (1996), Meunier et al (1998), Madsen (1998) and Matt et al (2008). Matt et al (2008) states that temperatures more than 100°C accelerate the illite transformation process, this is further explained by Pusch et al (2014). They highlight that increasing the interface temperature from 100 to 150°C will increase the reaction kinetics by 100 times. This reaction kinetic acceleration is using the assumption that the activation energy of the Bentonite is 27Kcal/mol, see Figure 31.

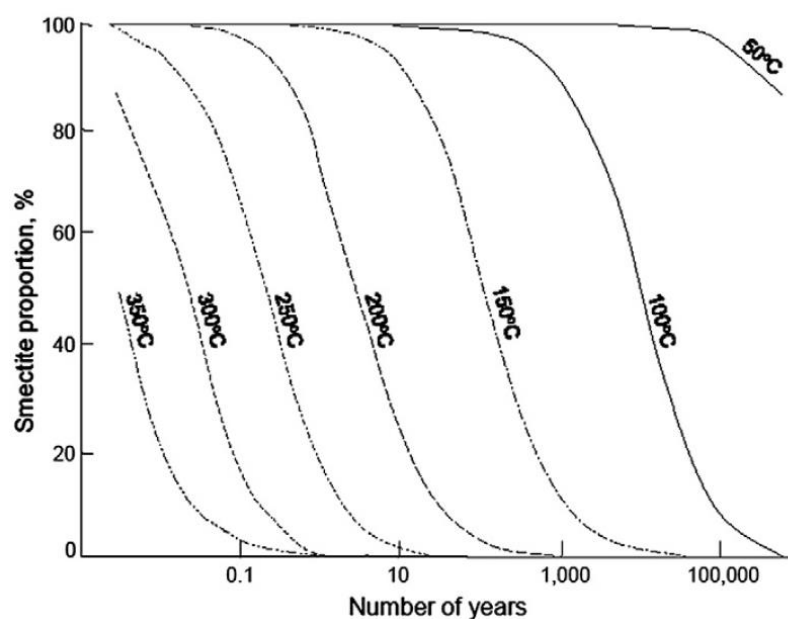


Figure 31: Conversion rates of Smectite to Illite according to the Pytte/ Reynolds model using an activation energy of 27Kcal/mol (After Pusch et al, 2014)

One other potential alteration process is the development of Chlorite as mixed smectite/ chlorite/ illite formations. Many studies suggest that Chlorite formation requires slightly higher temperatures, somewhere in the region of 150°C+ (Hoffman & Hower, 1979; Velde, 1995; Guillaume et al, 2003; Lantenois, 2003; Carlson, 2008; Leupin et al, 2014). It is known that the formation of chlorite occurs in conjunction with the dissolution of smectite with the release of Mg and Fe, the formation of Al- hydroxides within the interlayers at high temperatures 250° have been observed (Leupin 2014). Various studies have found that this dissolution and formation of the Al-hydroxide complexes displayed a reduced CEC along with the associated reduction in the geomechanical parameters i.e. swelling capacity etc., even at lower temperature exposure (Howard & Roy, 1985; Johnston and Miller, 1985; Leupin et al, 2014). However, the general conclusion provided by many of the

aforementioned studies state that for this to occur at lower temperatures, lower pH environments would need to be present (≤ 6). This disagrees with current understanding of the near-field geochemical environment under the inferred conditions (Idiart et al, 2013; Leupin et al 2014; Bradbury et al, 2014) (For more on the Illitisation or chloritisation potential, see section 2.3).

2.1.7. Near-field pH and its associated impact:

The pH evolution surrounding the canister is thought to be quite dynamic until after approximately 5000 years when reducing conditions, temperature and hydro-chemical conditions stabilise (Kumpulainen et al, 2010; Idiart et al, 2013). Bildstein et al (2006) states that pH conditions at the very interface of the carbon steel/ Bentonite interface will stabilise at 10-11, these are slightly higher than the computational results of Idiart et al (2013) as can be seen from Figure 32. However, these higher values are realistic and agree with most thermodynamic data. The high pH values are also in agreement with the pH values measured post iron/Bentonite exposure during the studies conducted by Kumpulainen et al (2010), who subject the samples to 8 and 10 years under ambient conditions (25°C), measuring a pH of 12 (see Table 14 & Figure 33). Kumpulainen et al (2010) also measured the REDOX potential (Eh) of the samples which further confirmed the strong reducing environment after 8 & 10 years under ambient conditions (Table 14). The cause for the pH to be lower is the buffering effects of secondary mineral dissolution and lower pH groundwater inflow (Idiart, 2013).

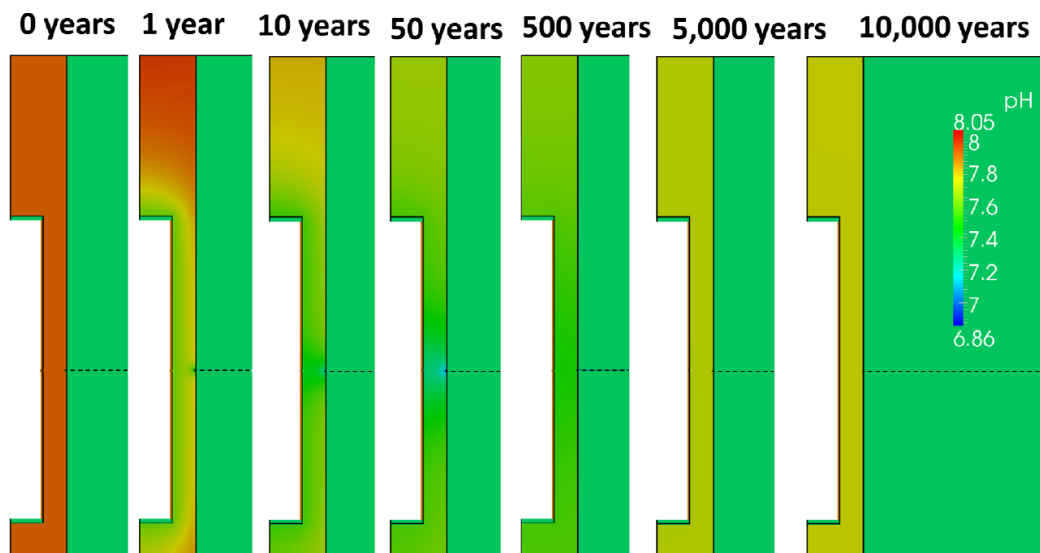


Figure 32: pH temporal distribution profile of the near-field (after Idiart et al 2013, POSIVA concept)

Table 14: pH and redox potential measurements (after Kumpulainen et al, 2010)

<u>Sample #</u>	<u>Temp (°C)</u>	<u>pH</u>	<u>Eh (mV)</u>
62	22.9	12.7	-583
63	23.2	12.96	-639
64	23.3	12.8	-637

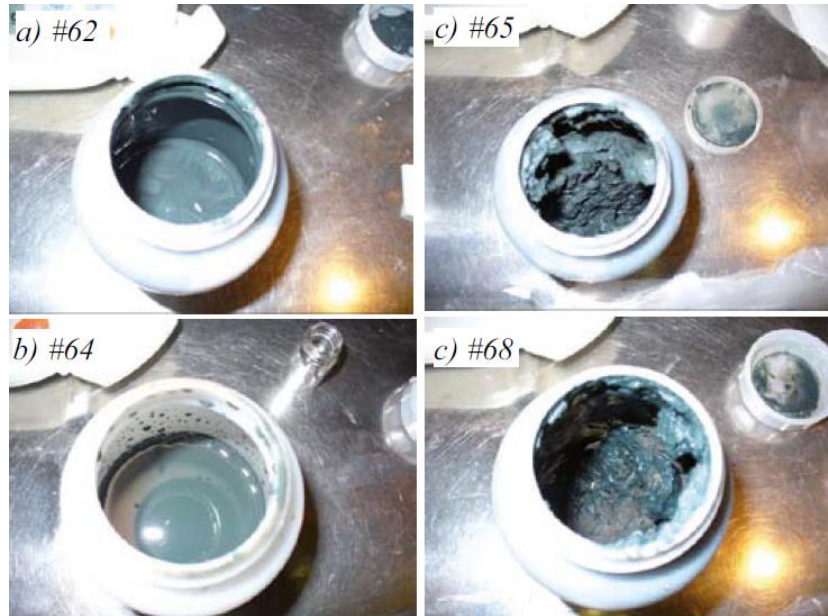


Figure 33: Corresponding photos of the samples supplementing the data in Table 14 (after Kumpulainen et al, 2010)

What is seen from the pH evolution profile, Figure 32, is that the pH will initially increase due to the oxidation of the canister and high temperatures. Once the temperature starts to drop and anaerobic/ reducing conditions are present the pH will slightly drop and stabilise (Idiart et al, 2013). Bildstein et al (2006) and Leupin et al (2014) both state the elevated pH environments will destabilise the montmorillonite and the reaction pathway to Fe-rich serpentine mineral phases such as cronstedidte and berthierine as well as beidellite and zeolites are probable. The solubility of the smectite and silica is increased with increasing pH, which are released into solution thus increasing the charge of the tetrahedral layers and supporting the discussed mineral changes (Mosser-Ruck & Cathelineu, 2004; Bouchet et al, 2004; Karnland et al 2007).

2.1.8. Natural analogues:

There are many natural and anthropogenic analogues that can be, and have been used, to study the effects of the near-field environment. The study of these environments is beneficial to the understanding of the long-term temporal behavior of the near-field, and can be used in conjunction with laboratory and computational research. Madsen (1998) and a report by the IAEA in 1999 provided details on the use of natural analogues, both highlight the beneficial nature of these case studies due to the impracticality of the long-term experimental replication of the near-field environment. There are two most commonly occurring natural analogues in literature that are used as case studies in experimental work 1) the Kinnekulle Bentonite (Sweden) and 2) Montanna Bentonite (USA). These are considered to be similar to the conditions of the Bentonite in the long-term repository, as well as the geological thermo-

mechanical history similarities. Madsen (1998), Kamei et al (1999) and King and Watson (2010) all state that these two natural analogues have been determined to be representative of the long-term nature of the repository due to the temperatures and degree of diagenesis as well as the duration of the elevated temperatures. From ten samples from the American and Swedish analogues respectively, they demonstrated that there has been little to no conversion of the original bulk montmorillonite to pure illite (Madsen, 1998). What was found from the natural analogues is that the Bentonite had become enriched in potassium, agreeing with Pusch and Kasbohm (2002), illustrating that the formation of K-Bentonite is probable. The degree of the transformation was found to be a function of the distance from the clay beds to the surrounding host rock. The Kinnekulle natural analogue is arguably the most studied case with respect to the nuclear waste disposal concept. Wilson et al (2010) details the geological history of the respective natural analogues and state that the Ordovician Kinnekulle Bentonite is approximately 400 million years old. The initial thermal exposure of the beds was approximately 120°C after the initial magma intrusion. Wilson et al (2010) explains how the temperature successively dropped to 90°C after 1000 years, and hence the examination of these bentonites is considered very close to the repository conditions. Madsen (1998) and Wilson et al (2010) both state that the content of the montmorillonite is approximately 25%, that's 25% of expandable phyllosilicate, with illite making up 50%, the remaining composition consists of chlorite/ kaolinite, carbonates, quartz and feldspar.

2.1.9. Overview of the microbial considerations of the near-field:

The microbial influence on the near-field components of the engineered system, particularly the corrosion evolution, is of concern. Wilson et al (2010) states that the microbial influence has been approached from various viewpoints, such as Bentonite microstructure, corrosion and cation/ actinide migration. They state that it is known that microbes will be active within the Bentonite as well as the groundwater, and many studies have expressed that the magnitude of structural voids should be limited to avoid or reduce the microbial growth within the clay barrier (Wersin, 2008; Hicks et al, 2009; Wilson et al, 2010; Börjesson, 2010; Leupin et al, 2014). Leupin et al (2014) states that the density should be suitably low to minimize this, the geomechanical parameters are set out in section 2.3.3.

The electrochemical influence on the REDOX states of the accessory minerals present within the clay has been most explored by Leupin et al (2014). They provide the most up to date details on the current understanding of the effects of microbial activity as well as Stroes-

Gascoyne, 2011. The most discussed aspect of the microbial interaction on the secondary minerals is the reduction of oxides and sulphates, Leupin et al (2014) states that the reduction rates decrease as the saturated density increases. Leupin et al (2014) states that sulphate reducing bacteria within the barrier is likely to produce sulphides, other microbes are a function of the available nutrient within the circulating groundwater and buffer minerals. One potential issue that is highlighted within the report by Leupin et al (2014) is the unintentional nutrient support provided by construction activity within the GDF. It is thought that the use of super-plasticisers or even the hydrogen gas given off during the chemical reduction of Fe(III) may support microbial colonies within the Bentonite and accelerate the production of corrosion aggressors.

Other potential alteration pathways have been developed and presented within literature with respect to the microbial illitisation pathway within smectites (Kim et al, 2004; Zhang et al, 2007; Ribeiro et al, 2009). However, Leupin et al (2014) states that these investigations were not representative of the conditions that are predicted to be present within the repository, and states that the aforesaid papers presented results that used non-realistic experimental boundary conditions. Such conditions used microbial/ Bentonite suspensions with free access to nutrient supplies and unrealistically high K^+ concentrations.

2.1.10. Concluding statement:

The steel-Bentonite interface will give rise to a highly dynamic environment in the first several hundred years after emplacement. Temperatures are likely to rapidly increase to the concept limiting value. Concept specific thermal limits are a function of the spacing between canister, quartz fraction within the buffer, moisture content and waste thermal enthalpy. The temperature is said to remain at the peak temperatures for approximately 50 years, after which the temperatures will reduce to background levels, specific to the individual concept over a duration of 1×10^5 years. Corrosion of the canister during the early phase is likely to produce oxidation corrosion products, Fe(III) oxides, during which the available oxygen will be consumed. As the barrier is slowly re-saturated and the temperature reduces, the formation of hydroxides will form once the oxygen is consumed the reducing phase will occur. The pH of the near-field environment at this stage is expected to be between 10-12 and thus accelerating the dissolution of the smectite, SiO_2 and the corrosion products. Diffusion of silica and Fe into the Bentonite will occur, migrating away from the higher temperature zone to the cooler outer zones. The dissolved silica is then thought to re-precipitate within these

cooler regions, and it is expected to contribute to the alteration of hydraulic conductivity and stiffness. Meanwhile reducing conditions are thought to result in the formation of hydrogen gas and other Fe (III)/Fe (II) hydroxides such as magnetite, goethite and “metastable” Iron carbonates (Siderite). Pyrite present as a secondary mineral within the Bentonite barrier is likely to yield the formation of sulphides that may accelerate the corrosion process. Microbial colonies present may also contribute to the production of sulphides due to the reduction of sulphite initially present. Furthermore, the electron transfer and energy gain from hydrogen liberated from deprotonated water during reduction may also accelerate microbial growth. Electron transfer from Fe (III) hydroxides may also aid the microbial development and thus result in an accelerated reducing environment. The resulting environment is extremely complex with the potential for smectite alteration due to many of the aforesaid reaction pathways. Such alteration is expected to yield a clay barrier that has inhibited geomechanico-chemico properties such as swelling, hydraulic conductivity and cation exchange.

2.2. Thermo-Hydro-Mechanico-Chemico investigations on MX-80 Bentonite:

This section covers research that has been conducted on Bentonite with respect to interface conditions, namely MX-80 type Bentonite. The research explored within this section has closely looked at both the physicochemical behaviour of Bentonite and the geomechanical parameters after thermo-hydraulic and iron corrosion exposure. The conditions have explored more than just the boundary conditions that are expected insitu of a long-term repository, thus allowing the uppermost limits of the Bentonite functionality to be explored. Experimental methods have also varied largely due to the generic nature of the long-term disposal concepts of many countries.

2.2.1. Montmorillonite mineralogy and heterogeneity:

The unit cell arrangement of Montmorillonite is referred to as a 2:1 phyllosilicate that is frequently denoted by the term. T-O-T structured clay (Tetrahedral-Octahedral-Tetrahedral) (Carlson, 2004; Railsback, 2006; Wilson et al 2010; Bradbury, 2011). There are two tetrahedral sheets above and below one octahedral sheet (Figure 34).

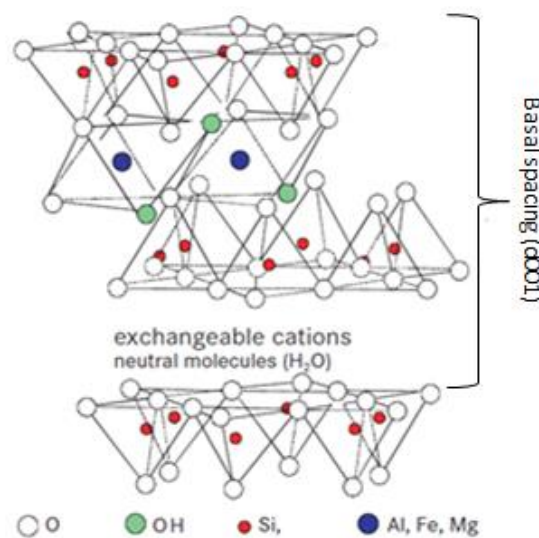


Figure 34: Unit cell configuration of the montmorillonite mineral and reference points for basal spacing measurements (After Koch (2008))

The net charge on the surface is always considered negative due to ionic substitutions within the structure. Caused by lower charge ionic species in either the tetrahedral sheets (i.e. Fe^{3+} or Al^{3+} replacing Si^{4+}) or within the central octahedral sheets (i.e. Fe^{2+} or Mg^{2+} for Al^{3+}). Odom (1984) states that the surface can be assumed to have an overall negative charge even though the edge zones may have positive charges. This is however dependant on the pH of the pore water occupying the Bentonite i.e. protonation and deprotonation of the

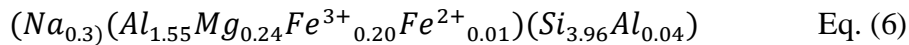
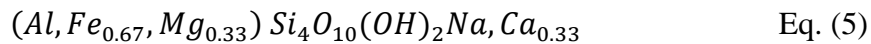
hydroxyl groups determines the charge type at the edge sites (Hicks, 2009). Generally, low pH solutions give rise to a net positive charge whereas with higher pH solutions there is a net negative charge. Ultimately, the pH of the pore solution plays a major role in the materials CEC capacity. The exchange site between each 2:1 assemblage is, in the case of montmorillonite, weakly bonded by cations. Typically, Na^+ and/ or Ca^{2+} . However, it can be replaced by higher valence cations or by order of replacing power in accordance with the lyotropic series. Permanent collapse, potassium fixation and hydrogen bonding, all lead to permanent clay alteration. The type of alteration is again dependant on the pore solution pH, dominant cation and concentration, exposure time and temperature. For example, kaolinisation is likely to occur in low pH solutions due to the abundance of hydrogen, whereas higher pH solutions with an abundance of K^+ , induction of illitisation is likely. The exchange site is denoted as nH_2O ; n being a cation of a specific valence. The amount of water that is held within the Bentonite is a function of the total layer charge and concentration of cations (Foster, 1953; Howard, 1966), the type and valence of cation in the interlayer (Glaeser & Mering, 1968; Schultz, 1969), the partial pressure (Kehren & Schainberg, 1975; Ormerod & Newman, 1983) and temperature (Rowland et al, 1956; Colton, 1986).

The MX-80 generally has a significant montmorillonite content, containing ≥ 70 Wt.%. (Milodowski et al, 2009; Hicks et al, 2009; Wilson et al, 2010 and Bradbury, 2011). This mineral is considered highly unstable when compared to the other more stable mineral groups i.e. illite and kaolinite. Naturally occurring Bentonite deposits are not solely made up of pure montmorillonite, but also from additional framboidal micro-aggregates such as Pyrite, Calcite, Dolomite, Feldspars and Plagioclases as well as other minor mineral constituents (Table 15).

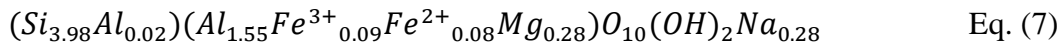
Table 15: Mineralogical composition of two batches of MX-80 Bentonite (%), Bradbury (2011)

<u>Mineral</u>	<u>(%) From Müller-vonmoos & Kahr (1982)</u>	<u>(%) From Karnland (2010)</u>
Montmorillonite	75	81.4
Illite	-	0.8
Kaolinite	<1	-
Calcite	0.7	0.2
Cristobalite	-	0.9
Gypsum	-	0.9
Muscovite	-	3.4
K-Feldspar	5-8	-
Plagioclase	-	3.5
Pyrite	0.3	0.6
Siderite	0.7	-
Quartz	15.2	3
Tridymite	-	3.8

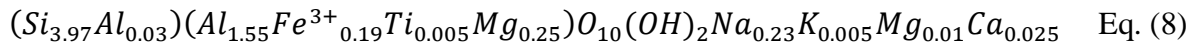
Typical aluminosilicate compositions are broadly provided in literature (Müller-vonmoos & Kahr, 1982; Sautzéat et al, 2001; Carlson, 2004; Karnland, 2010; Bradbury, 2011) although it must be noted that slight variations are expected due to the heterogeneous nature of the naturally occurring material. The supplier of the raw MX-80 (RS minerals®) provided a specification sheet detailing generic structural formulae for Bentonite displaying the two predominant exchangeable cations (given in Equ. 5). Wilson et al (2010) displays a more specific structural formula for MX-80, originally formulated by Madsen (1998), as given below in equation 6.



A report by Bradbury (2011) for the NAGRA concept emphasised that variations are present in studies that yield the structural formula for the T-O-T structure for Na-Bentonite. Overall the formulae yield very similar results except from the Fe present, e.g. Sautzéat et al (2001) produced:



Whereas Karnland (2010) presented, the structural formula is used as the SKB reference:



The minor variations may be attributed to batch/ sampling, storage and analytical heterogeneities. However, the highly anisotropic nature of the Bentonite with respect to the batch may yield slightly different results i.e. swelling pressures and bulk mineralogical compositions etc. Additionally, smectite rich clays are generally configured in the turbostratic orientation i.e. clay platelets are arranged in an end to face arrangement Figure 8 (a). In contrast, and what has been obtained from studies investigating the permeability and compaction of the Bentonite by Holmboe et al (2012) and Lee et al (2012), is that the permeability of the Bentonite when subject to anisotropic compacted gives very different permeability and swelling pressure magnitudes in the respective axial references (Figure 35 (b)).

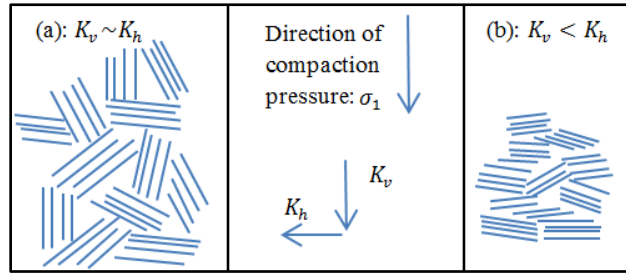
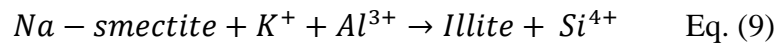


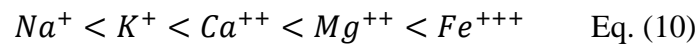
Figure 35, (a) Concept of the Turbostratic configuration of clay platelets; (b) more ordered configuration of the clay platelets with anisotropic compaction (K annotates the coefficient of permeability)

2.2.2. THCM studies and their effects on the geomechanical/ physicochemical properties of the MX-80:

A key factor that has a direct effect on the engineering properties of the barrier is the transition of smectite->illite, Wersin et al (2010) indicates that the Illite is the likely long-term alteration product of the Montmorillonite when in contact with the deep groundwater. Therefore, it is probable that the reaction kinetics will be somewhat complex, not only at the interface where the clay will be altered due to the Fe-rich environment under high temperatures but the outer sections of the Bentonite are likely to experience alteration due to complex saline water systems. High K^+ ion concentrations within the ground water under elevated temperatures could be the causative factor for illitisation. Investigations into geological systems have confirmed that upon intense heating as well as cations with higher replacing power present, smectite may slowly transform due to the isomorphic substitution, in the case of K being dominant, the transformation is displayed in equation 9.



The principle behind this transformation is the cation exchange due to the ion replacing power defined by the lyotropic series in equation 10:



The structure of illite and montmorillonite are the same (i.e. 2:1 T-O-T structure) apart from their respective interlayer bonds. Sodium Bentonite and a ground water rich in potassium increases potential for this transformation as well as being under elevated temperatures illitisation may occur. The structural similarity also supports the ease of conversion to illite rather than 1:1 minerals such as Kaolinite or Chlorite. See Figure 36 detailing a montmorillonite 2:1 structure with interface for exchangeable cations.

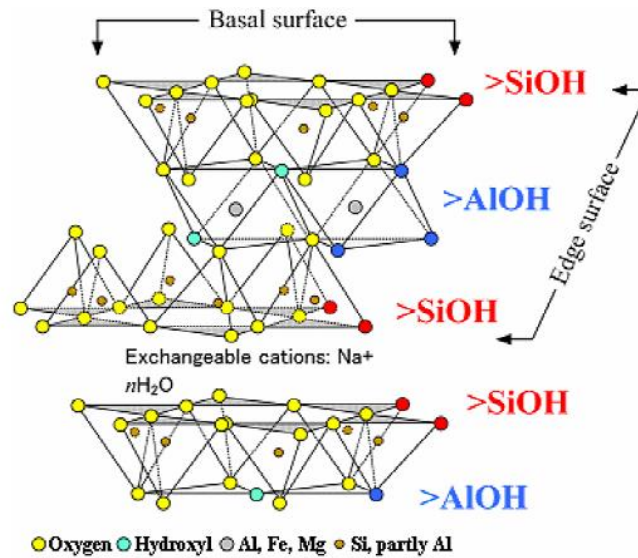


Figure 36: Layered structure of montmorillonite. Al, Mg and Fe ions are located between two inward pointing sheets of linked SiO₄ tetrahedra. The space linking the 2:1 sheets are occupied by cations and H₂O. (After Hicks et al, 2009)

Schmitz et al (2007) presents the effect of various salt concentrations on the consistency parameter, explicitly the liquid limit. Figure 37 shows the results by Schmitz et al (2007), these index alterations also have a direct effect on the engineering parameters i.e. Hydraulic conductivity and Consolidation coefficient etc. Figure 37.b also further demonstrates the potential of clay mineral stabilisation/ illitisation due to the presence of high K^+ concentrations within the groundwater, as it can be seen that the colloidal spacing is almost reduced to roughly a fifth of the original value with increasing K^+ concentrations. This, in turn, will impact the geomechanical characteristics of the bentonite (Mitchell, 1993). Potassium fixation decreases the DDL and drops the d-spacing to approximately 10Å (Schmitz et al, 2007), effectively reducing the water uptake capacity of the MX-80.

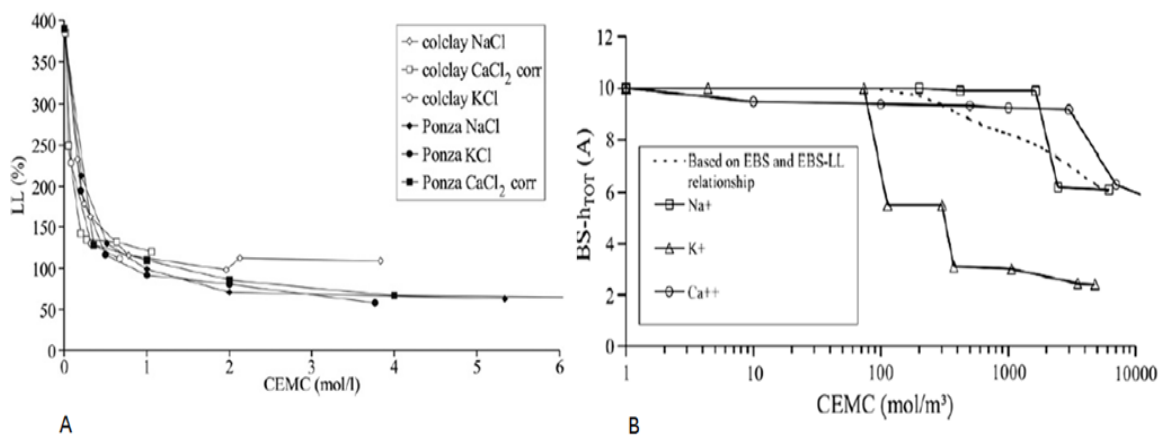


Figure 37: Liquid limit reduction of two smectite clays with increasing salt concentration. A) LI vs. Concentration Coefficient Monovalent Cations, B) The basal spacing of an oriented clay sample- thickness of a TOT/TO layer vs. concentration. (After Schmitz et al, 2007)

Studies have shown that K-rich ground water in the presence of high pH conditions gave rise to the development of non-swelling layers, considered to be illite, which formed after heating under 50°C and 60°C for periods longer than 6 months (Drief et al, 2002; Claret et al, 2002). Other studies have also found that calcium silicate hydrates in a NaOH fluid at 60°C had precipitated (Taubald et al, 2000; Claret et al, 2002). The studies correlate well with the findings of Ruck & Cathelineu (2004) who also investigated the thermo-saline interaction for 2 months. Ruck & Cathelineu (2004) included a more complex saline solution during a thermal exposure of 150°C. The resulting XRD analysis of the run products displayed no alteration of the expandability, displaying a d-spacing of $\sim 17\text{\AA}$ when glycolated. However, the development of quartz and feldspars precipitated in higher pH solutions was observed (Figure 38 & 39). Furthermore, CEC measurements of the run products displayed a reduction to 57.4meq/100g, compared to 90- 100meq/100g for the starting material. This was due to the development of the siliceous by products (Ruck & Cathelineu, 2004; Pusch et al 2010).

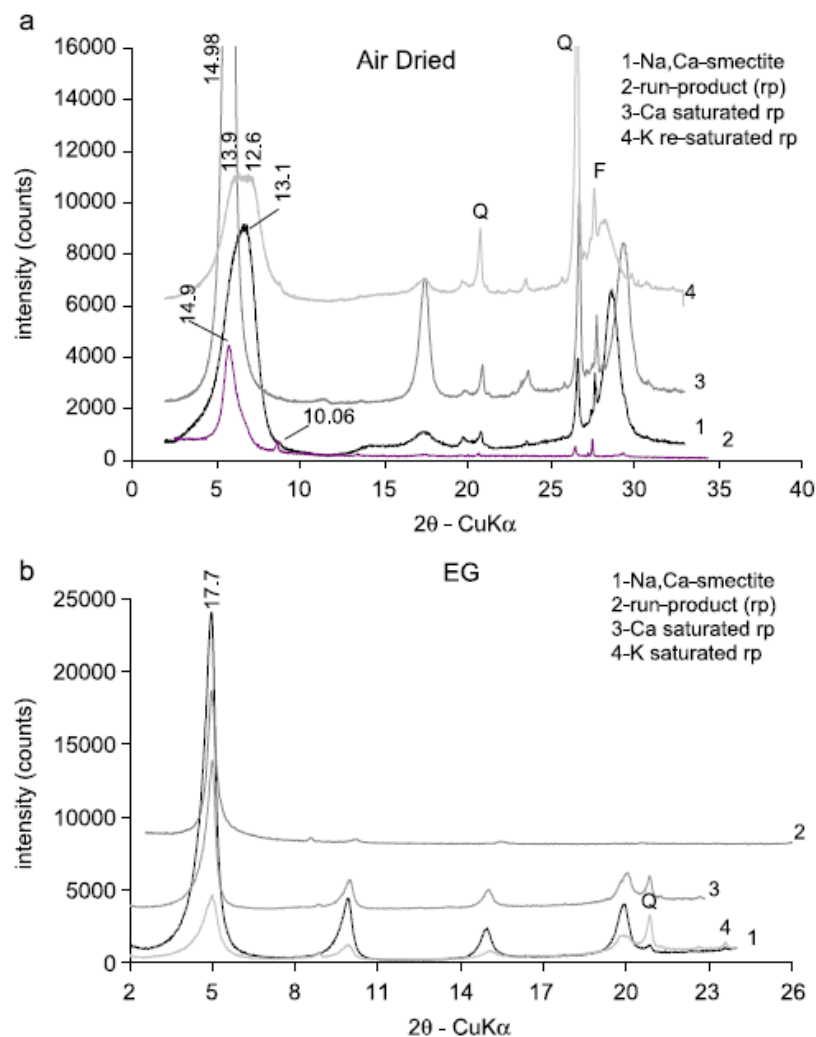


Figure 38: XRD patterns from the THC Bentonite NaOH reaction, Q: Quartz, F: Feldspars after 150°C for 2 months (After Ruck & Cathelineau, 2004)

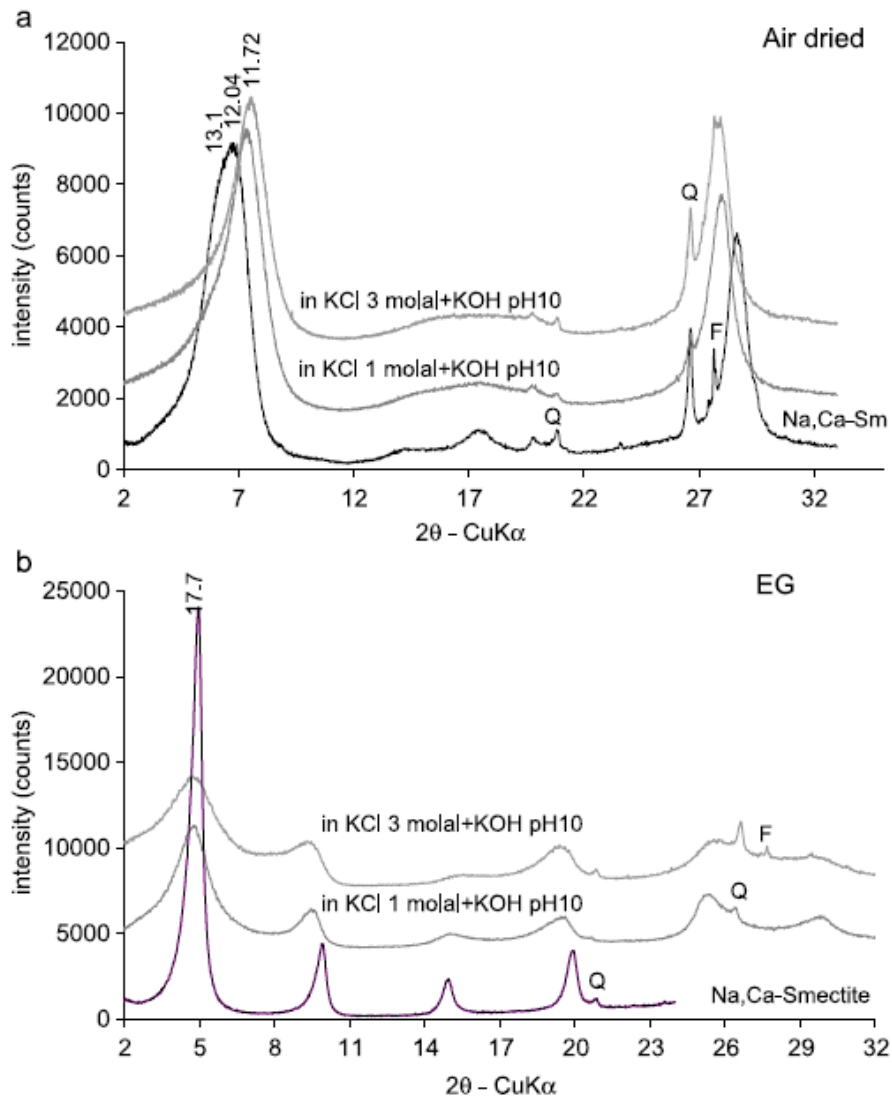


Figure 39: XRD patterns after THC Bentonite reaction with KCl and KOH after 150°C for 2 months (After Ruck & Cathelineau, 2004)

Ruck & Cathelineau (2004) explain that there is a significant drop on the d_{001} spacing when reacted with K solutions and movement toward higher angle reflections is attributed to K fixation. EG treatment of the post THC sample also displayed significant swelling reduction for the most affected sample (KCO_3 test), displaying a strongly affected interlayer and little expansion upon EG treatment, Figure 40.

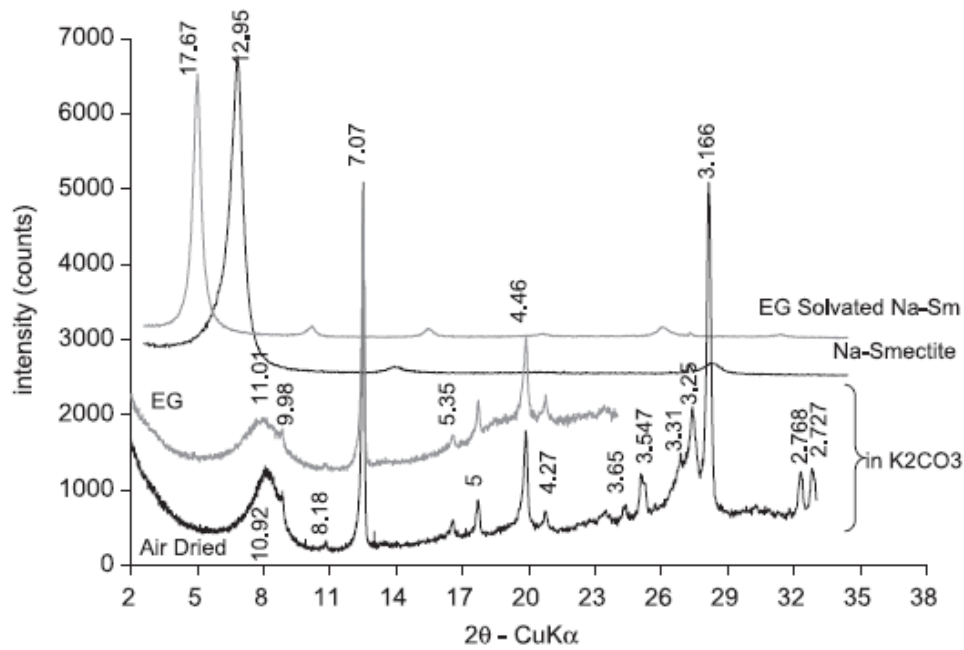


Figure 40: Na-smectite reacted with KCO_3 displays run product and starting material XRD patterns (After Ruck & Cathelineau, 2004)

Ruck & Cathelineau (2004) also discovered that reaction with KCl and NaOH resulted in montmorillonite dissolution and precipitation of zeolite (A merlinoite- like phase in Na rich smectite, Figure 41), feldspars and calcium silicate hydrates.

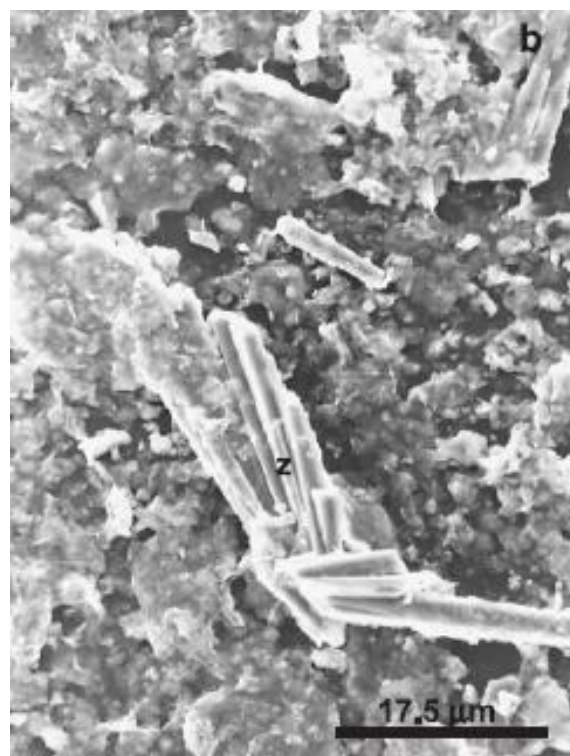


Figure 41: TEM image of zeolite development in Na-smectite after THC exposure to 150°C in a KCO_3 solution (After Ruck & Cathelineau, 2004)

Ruck & Cathelineau (2004) indicated that zeolites can form at lower temperatures, which is on the contrary to the findings of Charpentiera et al (2006) who found that after heating Bentonite to 300°C in the presence of Fe (0) resulted in zeolites and Fe-rich vermiculite after 9 months of reaction time (Figure 42).

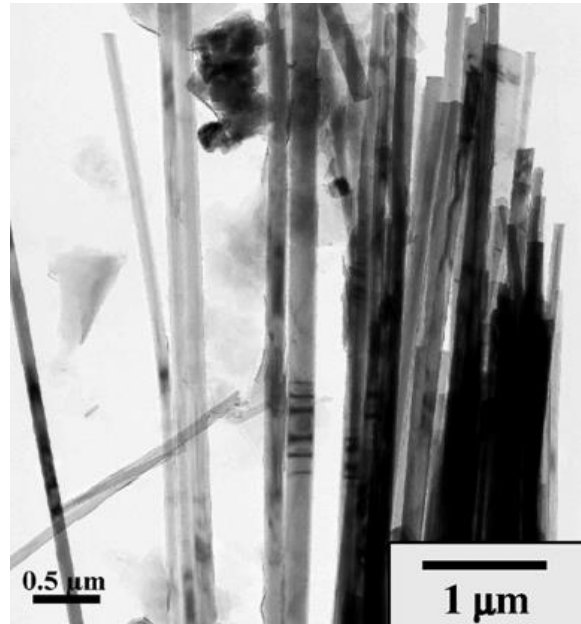


Figure 42: TEM image of zeolite development in MX80 after 300°C (After Charpentiera, 2006)

Whereas samples heated at temperatures 150°C and 80°C resulted in di-octahedral smectite enriched with Fe and the formation of Fe_3O_4 . Solution pH was high in post THC samples which resulted in higher dissolution of the montmorillonite, the observations were also observed by Bauer & Berger (1998) and Huertas et al (2001). After the dissolution/recrystallization, the crystal shape is altered. Nonetheless the mineralogy displays no considerable change (Charpentiera et al, 2006; Taubald et al, 2000). XRD and TEM analysis displayed that the calcium silicate hydrate was dominated by a Tobermorite phase in Calcium rich smectite (Figure 3).

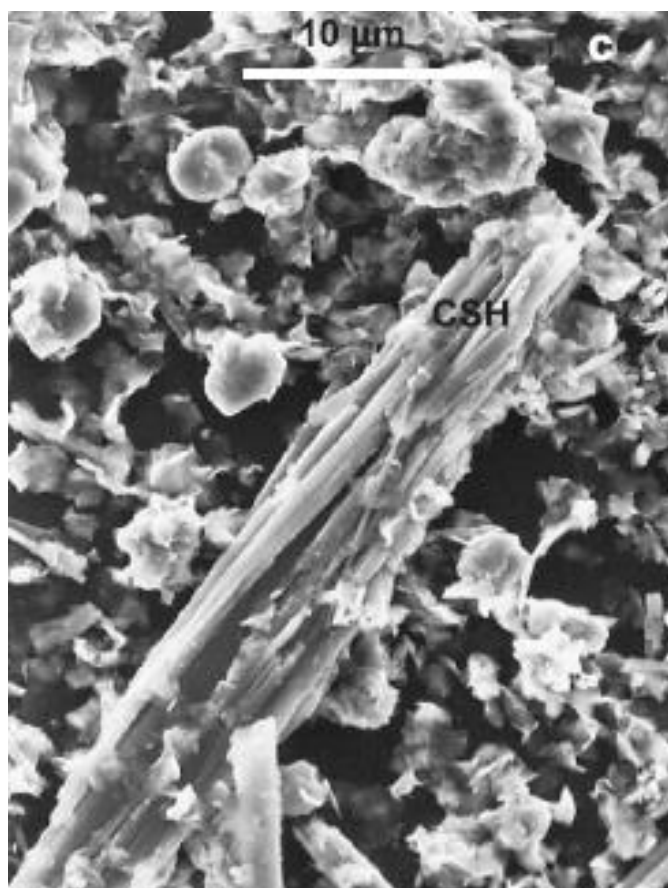


Figure 43: TEM image of the calcium silicate hydrate development in Na,Ca-smectite after 150°C THC exposure (Tobermorite- like phase) (After Ruck & Cathelineau, 2004)

Ruck & Cathelineau (2004) and Charpentiera et al (2006) found that the Bentonite exhibited complete Na^+ replacement for K^+ and partial replacement in Ca^{2+} sites. Other precipitates were concluded to be related to the release of Al and Fe from the octahedral layer that resulted in the development of SiO_2 and Feldspars. This cation release from octahedral sites increased the layer charge. Charpentiera et al (2006) stated that dissolution and alteration of the morphological properties of the detrital grains in experiments conducted below 300°C displayed minor changes, Figure 44-46. They do however comment that the observed mineral development, palygorskite, could be a transition phase from the 80°C and 150°C samples. Overall heating at 80°C under all durations displayed little alteration of the d001 characteristics and compared well with the starting material XRD patterns (Table 16 and see classification chapter), which indicates that little physicochemical alteration occurred. Broadening of the XRD patterns for the study conducted by Charpentiera et al (2006) is suggested to be attributed to the alteration of interlayer composition (Figure 47). They also state that the shoulder of the air-dried sample after 150°C displayed some vermiculite development. The runs conducted at the highest temperature of 300°C gave rise to chlorite (Figure 47) and rehydrated vermiculite for the air-dried samples.

Table 16: Average d-spacing's of MX-80 post hydrothermal treatment (80°C) for 3, 6 and 9 months (After Charpentiera et al, 2006)

<u>XRD treatment</u>	<u>Average d001 spacing (Å)</u>
Air dried	12.4
Ethylene glycol	17
Heat treated 550°C	9.7-9.8

The two predominant minerals observed by Ruck and Cathelineu (2004) are defined below:

- **Tobermorite- Calcium silicate hydrate phase:**

Has a distinct d-spacing of 11Å and 14Å with a structural formula of $Ca_5Si_6O_{16}(OH)_2 \cdot 4H_2O$, formation of this mineral phase results in pore fluid pH increase which will accelerate the Bentonite dissolution rates (Ruck & Cathelineu, 2004).

- **Merlinoite- Zeolite phase:**

Has a d-spacing of 10Å and 4.5Å however peaks are difficult to differentiate in a clay matrix and can be mistaken for Phillipsite. Merlinoite has a structural formula of $(K, Na)_5(Ca, Ba)_2Al_9Si_{23}O_{64} \cdot 23H_2O$. The development of Merlinoite phase is likely to develop in K rich environments (Mineral data.org, 2016)

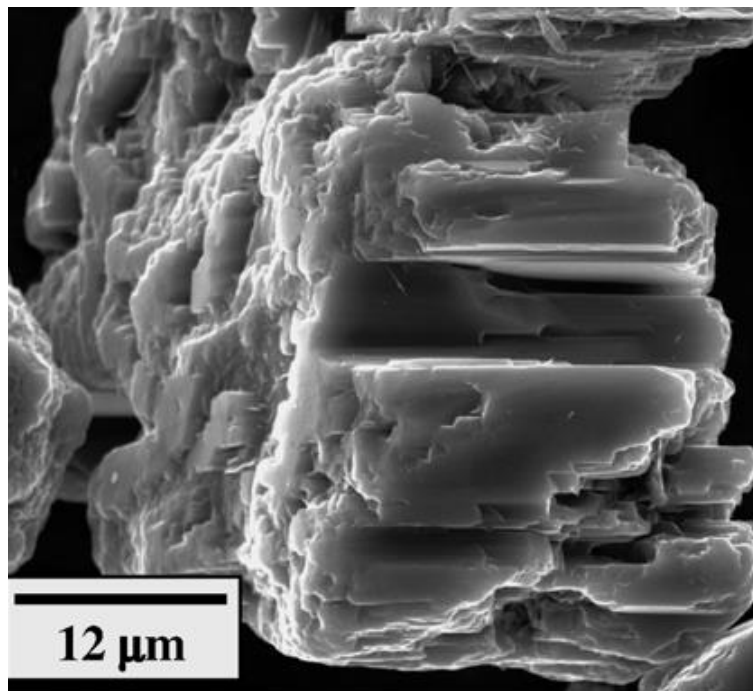


Figure 44: Plagioclase dissolution after 300°C exposure via SEM (After Charpentiera et al, 2006)

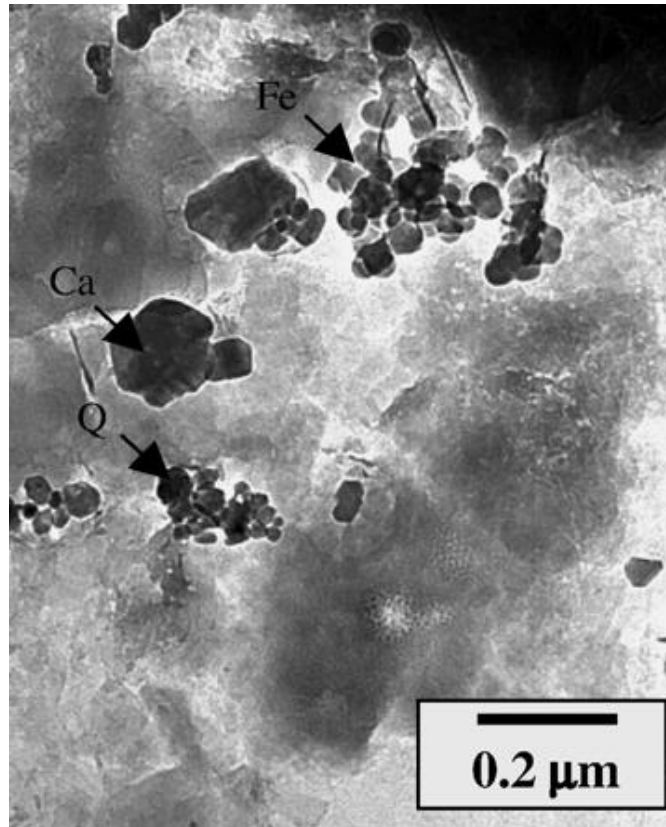


Figure 45: TEM imaging of calcite, quartz or cristobalite (Siliceous compounds) and Fe oxyhydroxides within the Bentonite matrix after 80°C and 150°C (After Charpentiera et al, 2006)

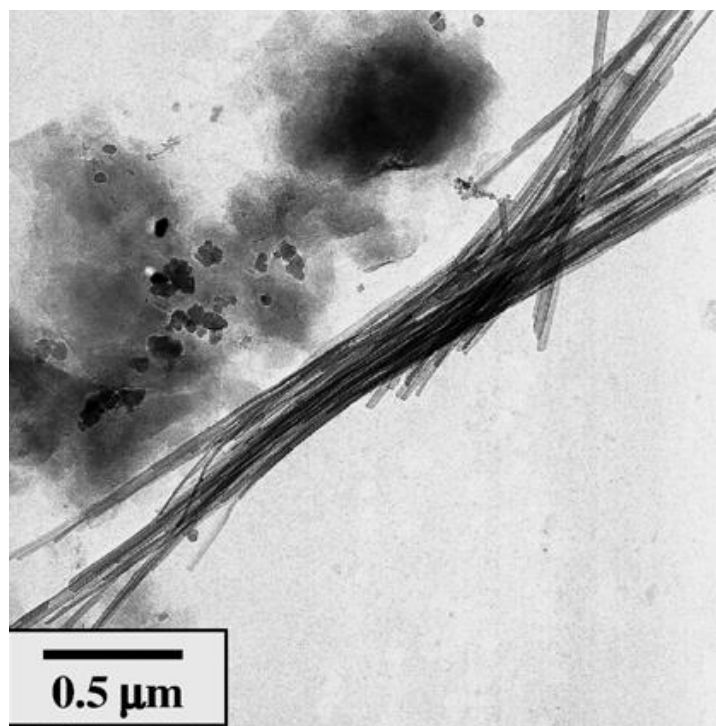


Figure 46: TEM image of Neoformed palygorskite-type minerals after 80°C (6 months) and 150°C (3 months) (After Charpentiera et al, 2006)

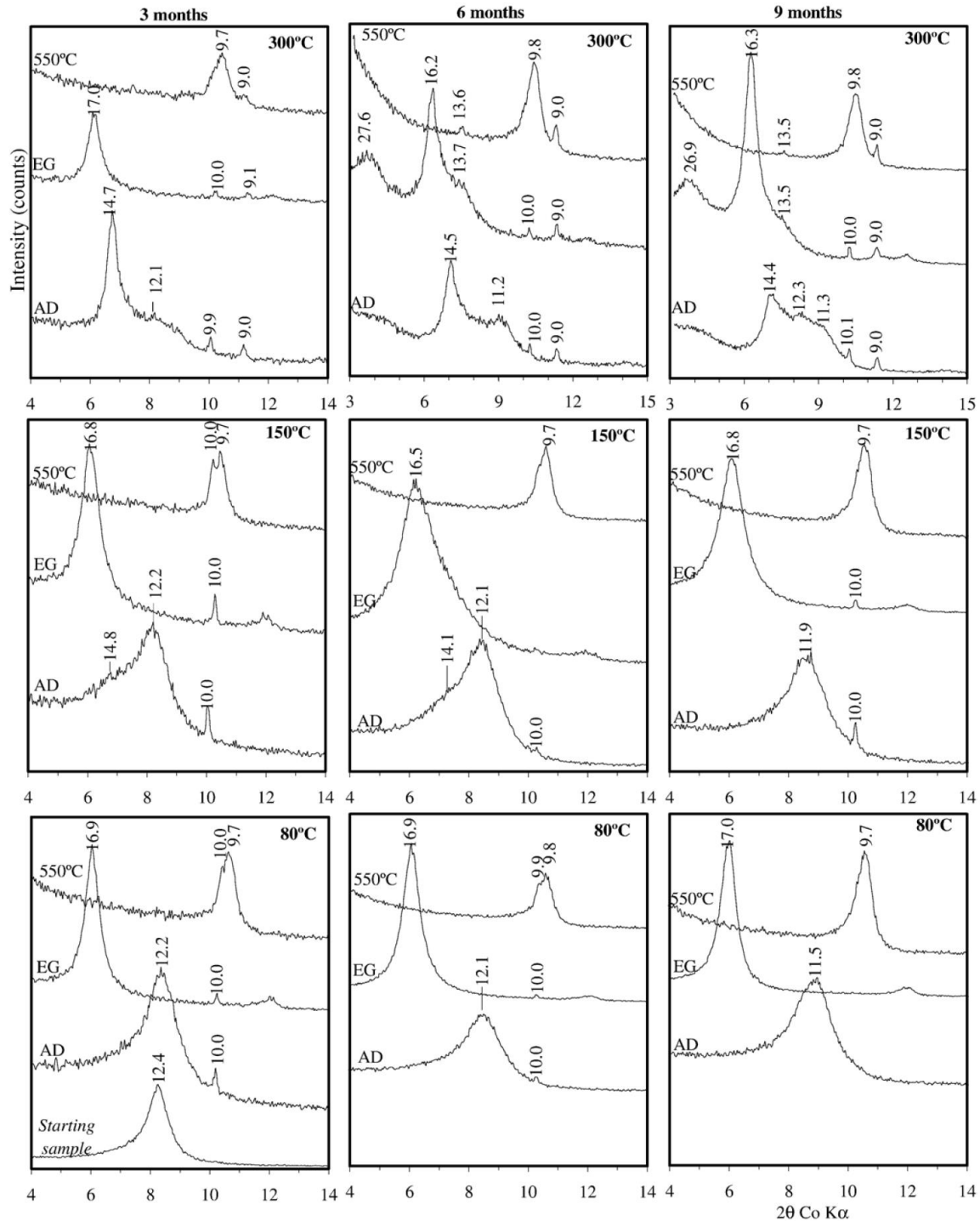


Figure 47: XRD spectra of MX-80 exposed to three thermal loading and duration increments (After Charpentiera et al, 2006)

A study conducted by Shariatmadari et al (2011) found that there is a prominent increase in material dry density with increasing salt valence and replacing power (Figure 48), this indicates that there is a higher degree of compaction which can be related to the close degree of packing between particles and interlayer spacing. Figure 49 displays their swell index measurements that agree with the proctor curve in Figure 48. Likewise, the liquid limit results that are given in Figure 50 all point toward a reduction in the DDL that correlated with an

increase in density and reduction in free swell. It can be seen that the liquid limit reduces by 20% corresponding to the highest salt concentration of 1N. The permeability is also thought to increase with increasing salt concentration and valence, Shariatmadari et al (2011) measured an increase via consolidation tests (Figure 51), this is thought to be related to the reduction in the DDL which influences the viscosity and kinetics of the absorbed water as well as an increase in intra-layer voids due to layer aggregation (Mersi & Oslon, 1970; Alther et al, 1985). The permeability however was dependent on the normal stress exposed to the sample, at lower normal stresses there was a significant reduction in the materials permeability, the opposite was observed at higher normal stresses. Tests conducted by Ahn and Jo (2009) found a similar effect on permeability with increasing concentration of Na^+ cations (Figure 52) at low confining pressures. They state that this decrease may be due to the increase in the materials swelling pressure. This may be true since they used much lower NaCl concentrations compared to Shariatmadari et al (2011). Therefore, the osmotic pressure would have driven water into the interlayers rather than causing flocculation at higher concentrations thus resulting in higher intra-layer permeability.

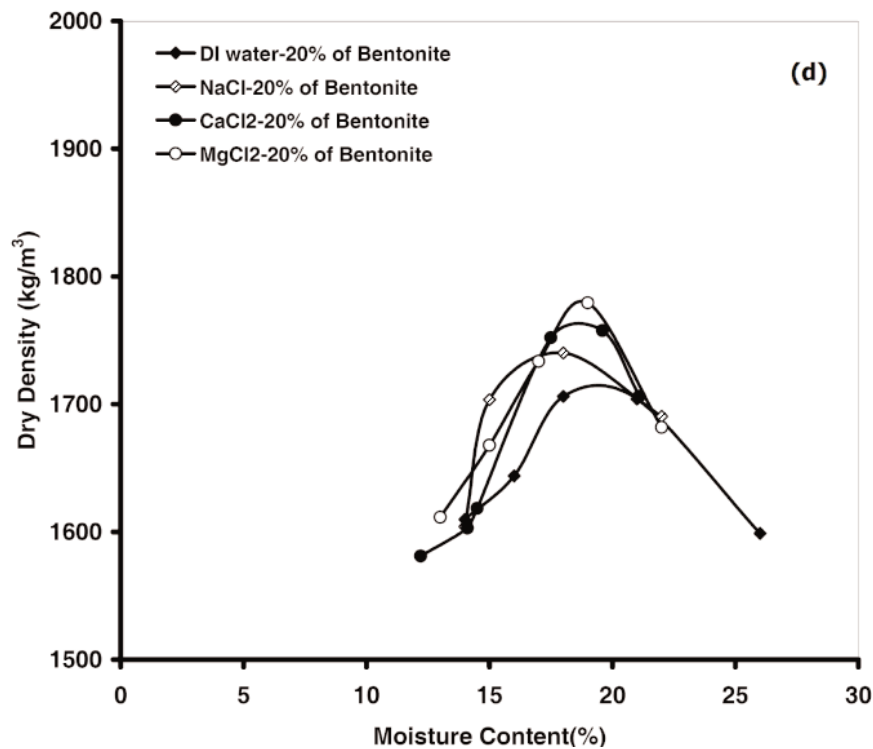


Figure 48: Proctor compaction curves displaying dry density of MX-80 with different salt solutions (After Shariatmadari et al, 2011)

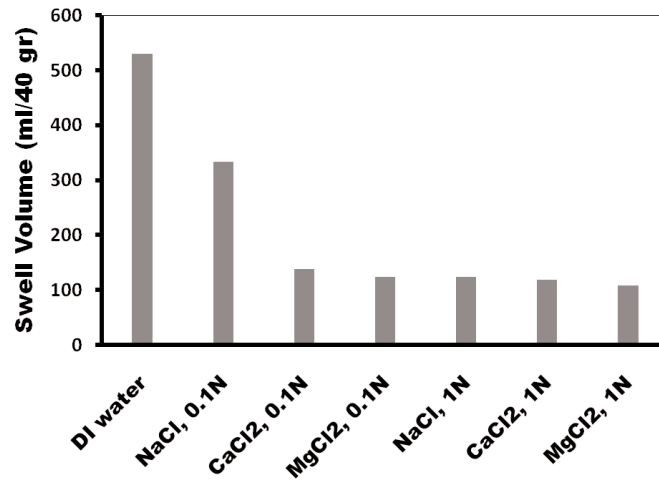


Figure 49: Free swell measurements of MX-80 with different salts and concentrations (After Shariatmadari et al, 2011)

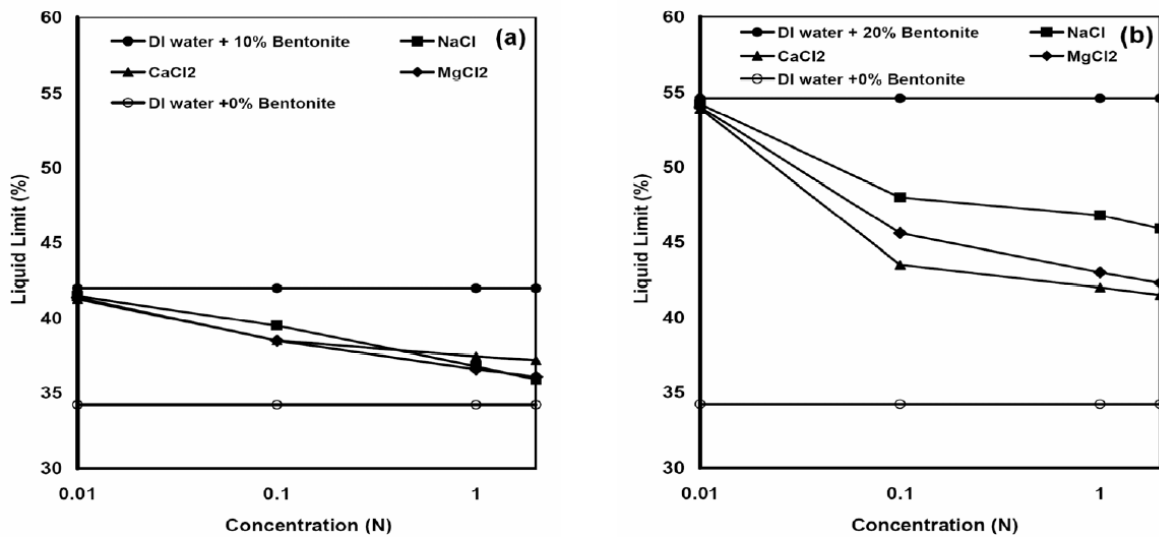


Figure 50: Liquid limit vs. salt concentration, a) 10% MX-80 and b) 20% MX-80 (After Shariatmadari et al, 2011)

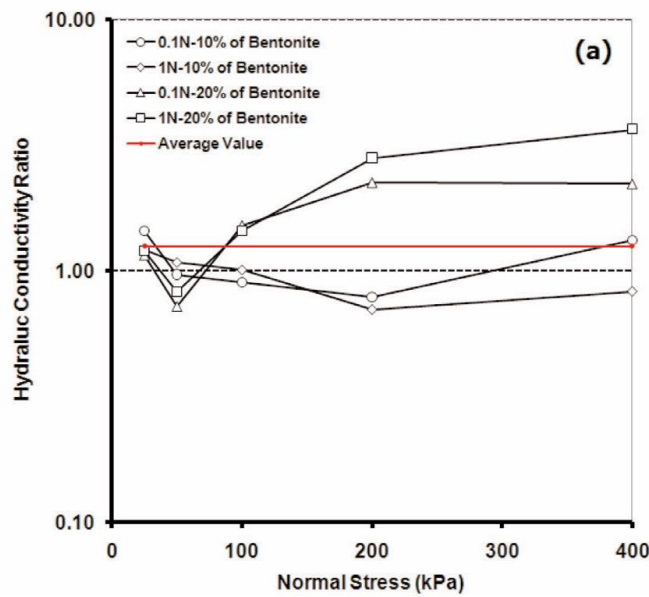


Figure 51: Permeability measurements from consolidation tests with increasing salt CaCl and NaCl (After Shariatmadari et al, 2011)

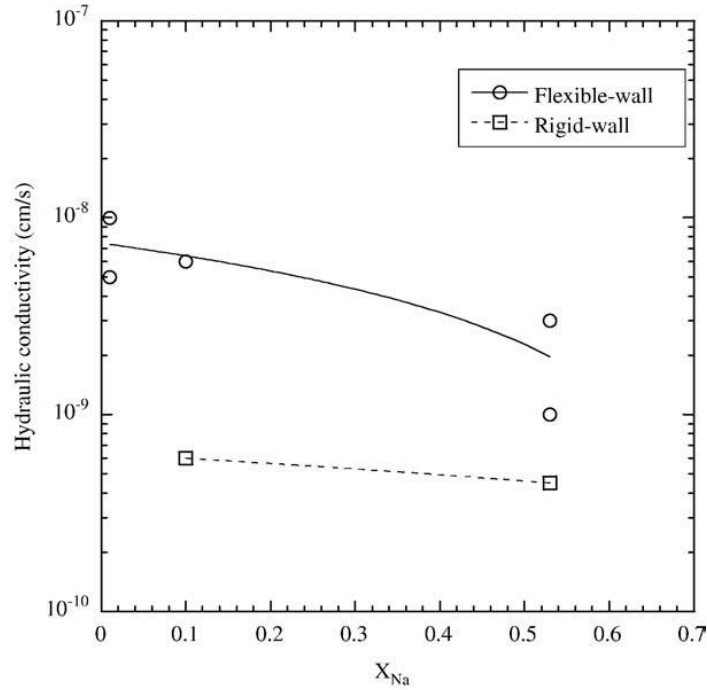


Figure 52: Hydraulic conductivity of compacted MX-80 with increasing concentration of Na cations (After Ahn and Jo, 2009)

Schmitz and Passen (2003) investigated the effect of salt solution concentration on the liquid limit of MX-80, using two salts NaCl and KCl they derived an empirical formula to predict the decay of the liquid limit with respect to the monovalent cation, equation 11. Figure 53 displays experimental data that fits well with the exponential decay function. They discovered that concentrations greater than 0.1M started with a 50% reduction of the liquid limit agreeing with Ahn and Jo (2009) and Shariatmadari et al (2011), this also indicates that the higher concentration of salt in solution will largely reduce the expandability.

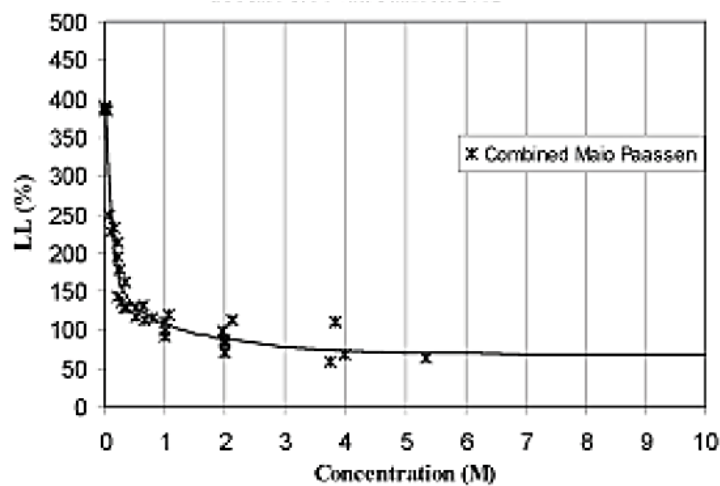


Figure 53: Liquid limit on MX-80 vs. monovalent cation concentration (after Schmitz and Passen, 2003)

$$L_l = 57.5 + 241 \times e^{\left(\frac{-c}{148}\right)} + 69.3 \times e^{\left(\frac{-c}{2.85}\right)} \quad \text{Equ. 11}$$

where:

LI= liquid limit (%)

C= concentration of monovalent cations (M)

$R^2= 0.937$

Liu (2010) investigated the thermal impact on the MX-80's liquid limit, after heating at 80°C and 95°C under differing timescales, the results indicated the liquid limit of the Bentonite reduced with heating duration. They found mineralogical changes were prominent after several months of heating, however, the changes were insignificant. A possible explanation of gradual reduction of the liquid limit could be change in the mineralogy and change in double-layer (Agreeing with Guillaume et al (2009)). The expandability of the Bentonite will be affected by the liquid limit reduction with thermal loading, this was also demonstrated by Pusch et al (2007). They found that the long-term THCM testing from the Äspö HRL has a significantly reduced swelling ability in the sub-samples taken from the innermost section (nearest to the heater). Figure 54, displays a reduction in the abundance of well-formed montmorillonite crystals indicating the development of a more amorphous structure and/or dissolution.

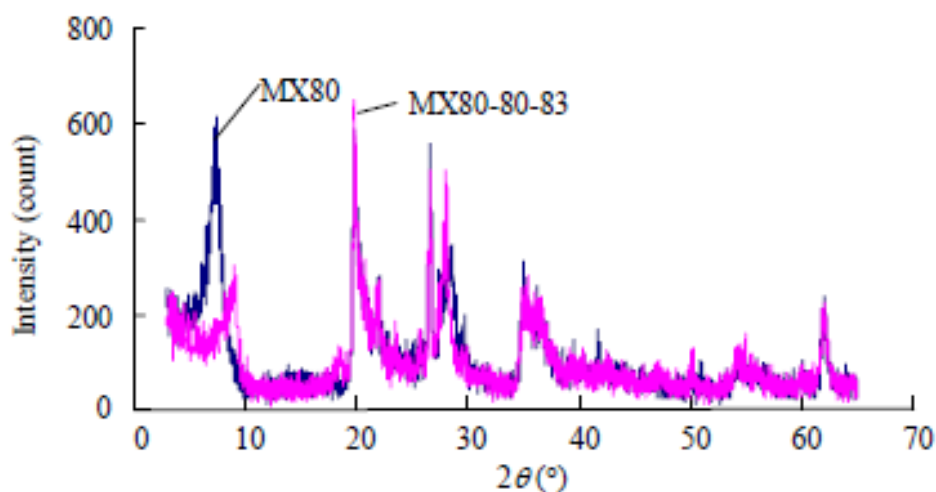


Figure 54: Random mount XRD of Bentonite before and after thermal exposure (After Liu, 2010)

Marcial et al (2003) stated that the permeability of the Bentonite when at high suctions induces a higher permeability which was put down to the effects of the suction gradient. They discovered that the intrinsic permeability dramatically reduced as the suction reduced which occurs along side a reconfiguration of the microstructure (Figure 55). They conclude that the reduction in permeability in the partially saturated state was due to the surface forces and physicochemical retention of the water within the soils voids. They also state that the slight increase at/ near full saturation is due to a “piston-like” effect that essentially pushes the

water through the voids. This trend was also observed and is supported by the study conducted by Ye et al (2012) and Wang et al (2013), Figure 56 & 57. From figures 56-59, it is seen that the unsaturated hydraulic conductivity of the Bentonite deviates more than at near saturated states. This is thought to be due to the partial pressure within the voids causing dilation, the hydraulic conductivity is also thought to increase due to the kinematic viscosity of the water with increasing temperature.

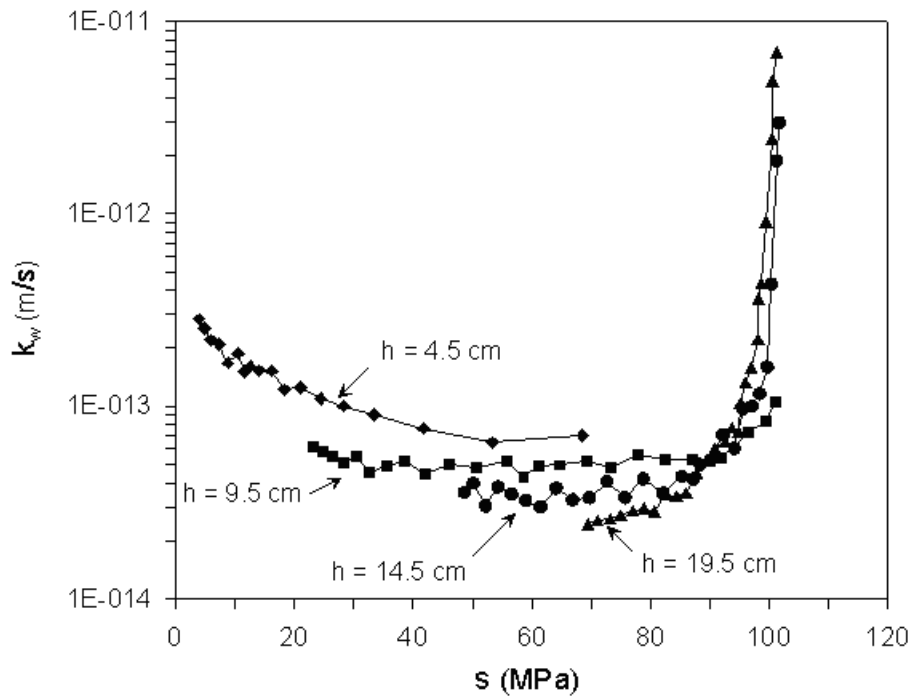


Figure 55: Change in permeability with increasing suction (after Marcial et al, 2003)

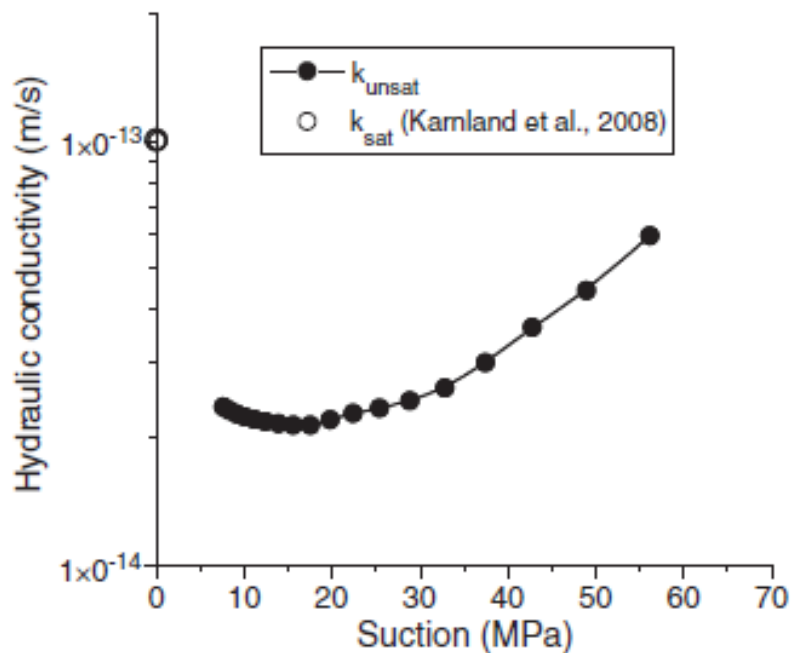


Figure 56: Hydraulic conductivity with respect to the suction and state of saturation of the MX-80 (After Wang et al, 2013)

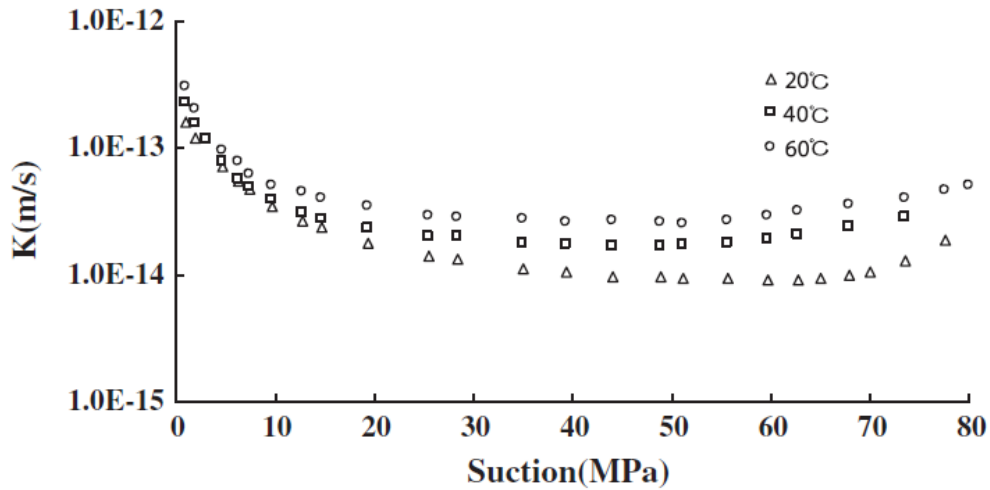


Figure 57: Unsaturated hydraulic conductivity measured under confined conditions and different temperatures as a function of the suction (After Ye et al, 2012)

Cuevas et al (2002) also studied the effects of temperature and varying salt concentrations on MX-80 for 80 days with granitic-type brine solutions under several different thermal gradients. They discovered that the hydraulic conductivity of the Bentonite was increased slightly when inundated with high saline solution, their results given in Figure 58. The granitic composition displays a similar trend compared to the control, however when increasing the concentration of the permeant the K values significantly increase. A comparison of the individual tests is further demonstrated in Figure 59, this shows the trend more prominent, what is also notable is that the high saline water/ high temperature samples indicate a 70% increase in the permeability (Cuevas et al, 2002).

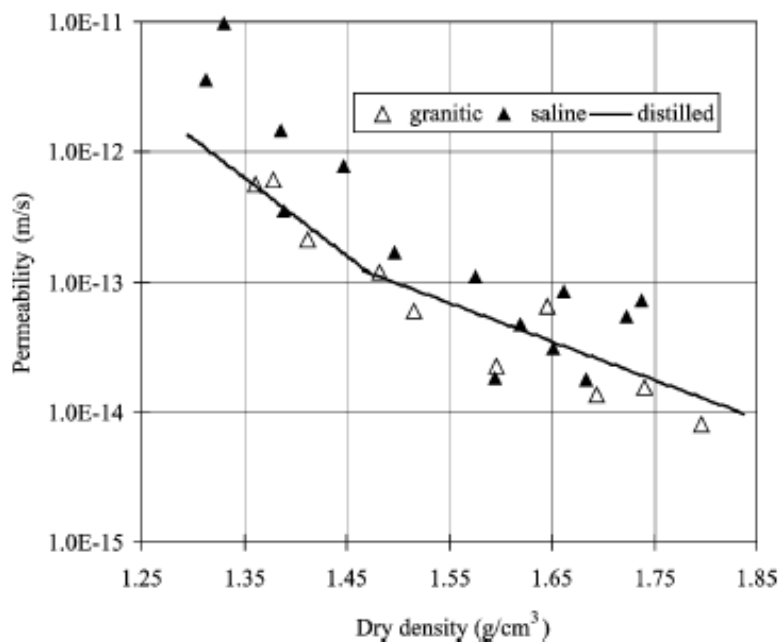
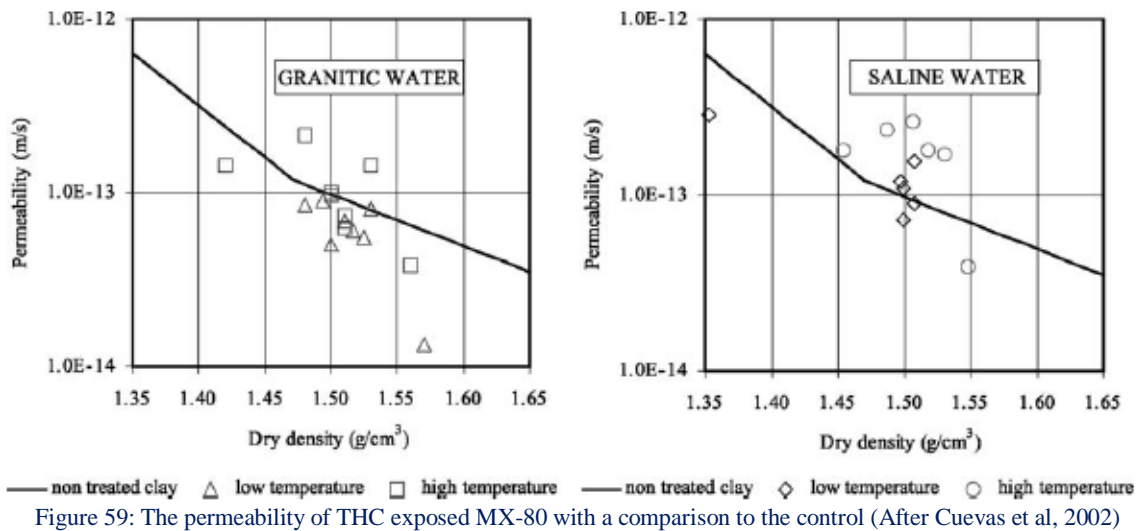


Figure 58: Influence of permeant composition on the materials permeability with density (After Cuevas et al, 2002)



The macro volumetric behaviour was also found to be very different when heated under various saturated states as well as under high and low confining pressures (5MPa and 0.1MPa respectively). Dilation of the Bentonite under lower suctions/ higher confining pressures was observed whereas higher suctions/ higher confining pressures gave rise to contraction, Figure 60. The observations made by Tang et al (2008) is in close agreement with other studies that also found plastic contraction under the aforesaid conditions (Burghignoli et al, 2000; Sultan et al, 2002; Cekerevac et al, 2003). However, it is thought that the expansion occurs up to an upper thermal limit after which permanent contraction occurs. The overall conclusion to the above studies is that the contraction was irreversible whereas the expansion was recoverable, and that higher initial moisture contents display larger irreversible compressibility. The expansion is thought to be due to the increase in the interlayer pore water pressure as well as the increase in the pore water dilation coefficient. This induces expansion in higher suctions due to the partial pressure increase, whereas lower suctions induce thermal consolidation due to higher kinematic viscosities. This combined with the effects of the siliceous and Fe corrosion cementation between particles has detrimental and permanent effects on the materials expandability.

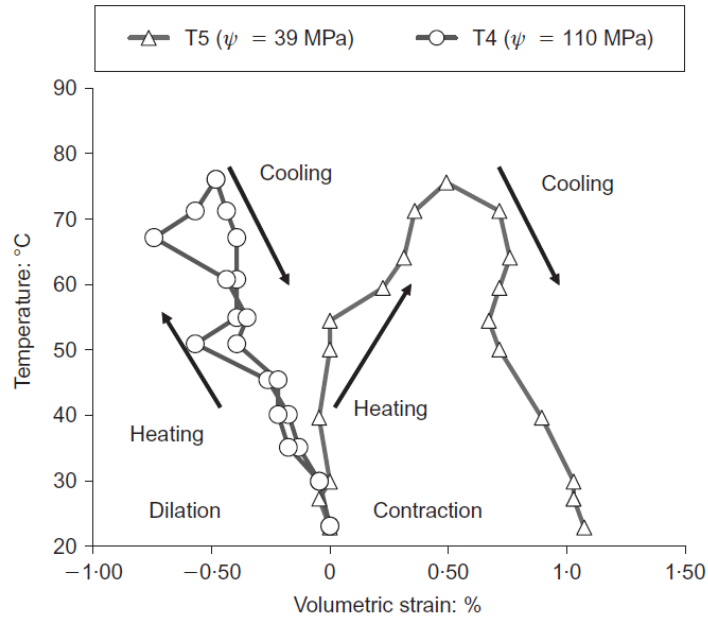


Figure 60: Volumetric strain of confined Bentonite under thermal loading (After Tang et al, 2008)

Gomez and Villar conducted long-term testing (>1-year) primarily looking at the effect of temperature on compacted Bentonite. The hydrochemistry was kept simple allowing only for the Bentonite to alter the pore fluid, therefore DI water was used and injected under a pressure of 0.001MPa. They subject the column of Bentonite to a heated side of 140°C and the opposite side was 30°C. Measurements such as the CEC, specific surface area, dry density, mineralogy were examined post hydrothermal exposure. Observations to the specific surface area close to the heater via BET, Figure 61, which displayed a reduction correlating to a reduction in CEC, thus agreeing with literature Figure 62 (Kamei et al, 1999; Guillaume et al, 2003; Ruck & Cathelineu, 2004; Milodowski, 2009; Pusch et al 2010).

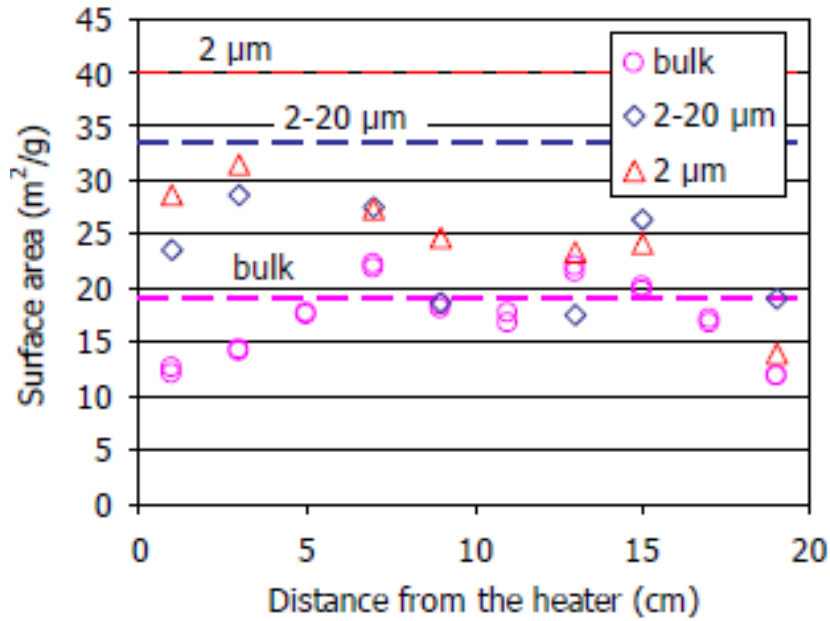


Figure 61: BET measurements of the MX-80 with distance from the heated interface (After Gomez and Villar, 2010)

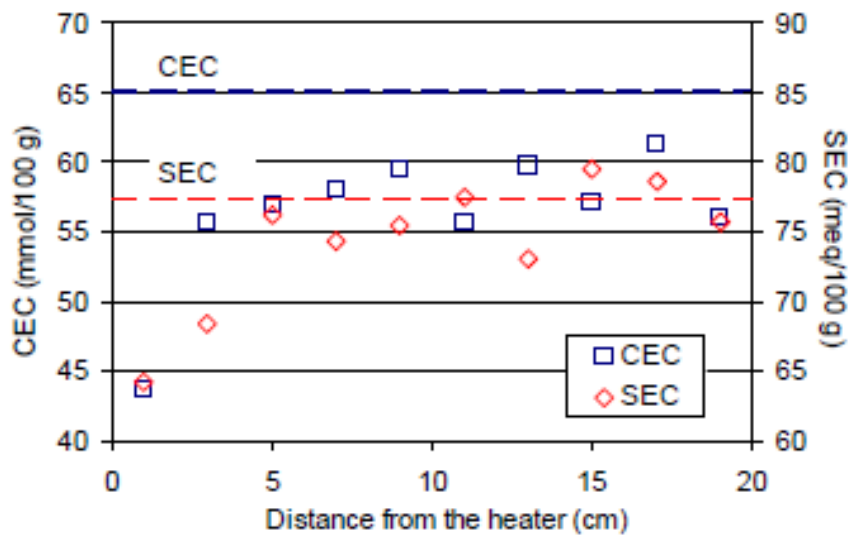


Figure 62: CEC and exchangeable cation concentration measurements with distance from the heated interface (After Gomez and Villar, 2010)

Guillaume et al (2009) used low salinity solutions under extremely high thermal loading conditions with a Bentonite/ Fe(0) boundary. The saline solutions used were NaCl and CaCl under a 300°C loading phase for 9 months. High dissolution rates of the di-octahedral smectite was observed and newly formed clays namely chlorite and saponite were seen. Sub-sampled zones of the bulk sample found Iron rich chlorite at the interface and a mixed Fe-Mg-chlorite greater than 2mm from the interface. Guillaume et al (2003) found that after exposure there was some randomly interstratified smectite/illite/chlorite with a reduced CEC (Table 17). It appears that temperature has a large effect on the materials CEC which is in

line with the precipitation of Silica under high thermal loads, Figure 63, Also discussed by Liu (2010).

Table 17: CEC measurements post THC exposure (after Guillaume et al, 2003)

Sample	CEC
Starting	79
Thermally exposed MX-80 (300°C, 3 months)	75
Thermally exposed MX-80 (300°C, 9 months)	66
Thermally exposed MX-80/ Fe (300°C, 3 months)	73
Thermally exposed MX-80/ Fe (300°C, 3 months)	30

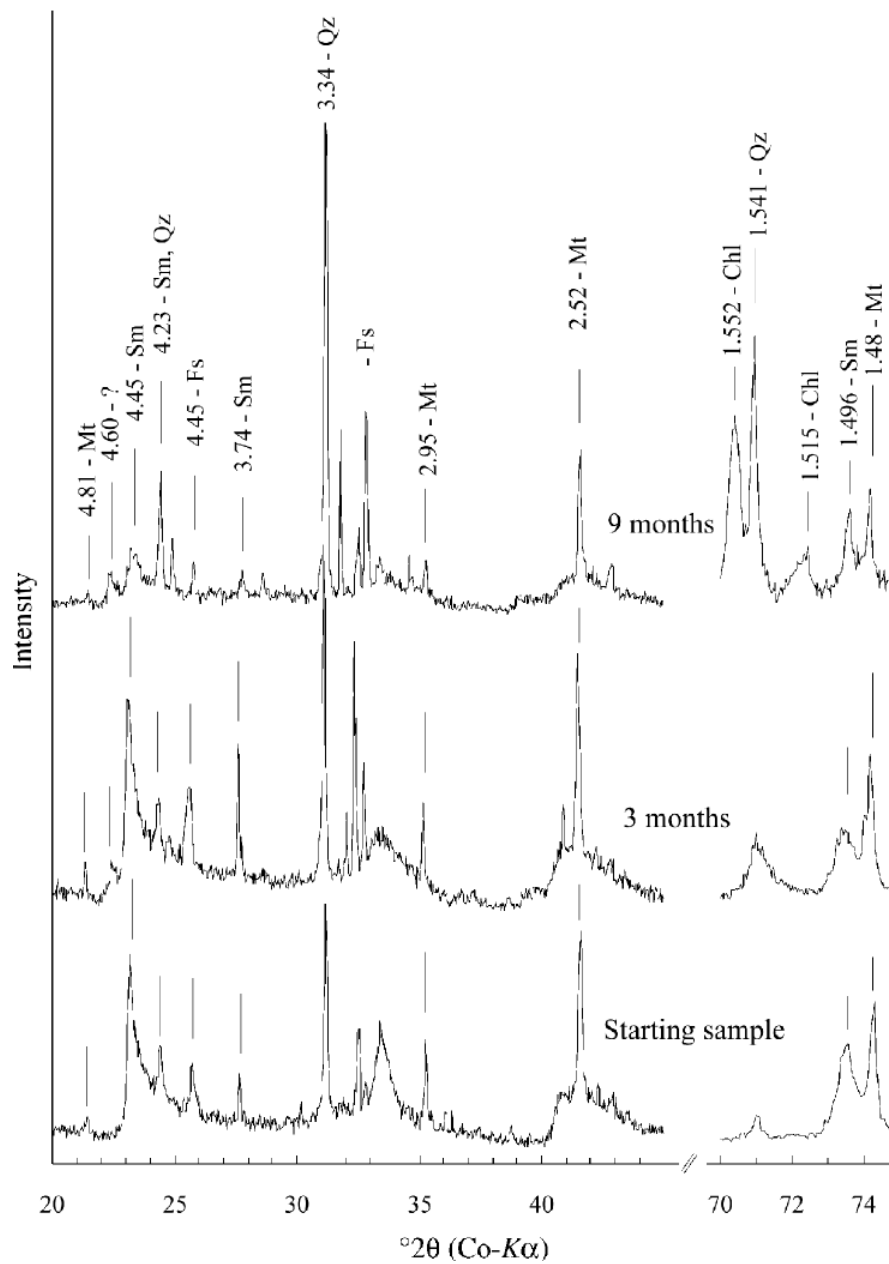


Figure 63: Bulk powder XRD patterns for the Mx-80/ Fe THC samples (after Guillaume et al 2003)

Additionally, Cuevas et al (2002) found that the CEC was significantly affected by temperature, Table 18 displays the CEC data conducted on the post hydro-thermal exposure samples. What is seen is that the CEC reduces with temperature and is independent of the saline conditions. Overall the results are limited and display little change to the MX-80's ability to exchange cations and layer charge. Furthermore, little deviation was observed in the specific surface area of the MX-80 after exposure to high and low temperatures and saline solutions over a period of 80 days, Figure 64.

Table 18: Average values of CEC properties post THC exposure (After Cuevas et al, 2002)

<u>Water type</u>	<u>Temperature</u>	<u>Ph.</u>	<u>CEC (meq/100g)</u>	<u>Mg²⁺ (meq/100g)</u>	<u>Ca²⁺ (meq/100g)</u>	<u>Na⁺ (meq/100g)</u>	<u>K⁺ (meq/100g)</u>
Granitic	High	8.1	96	35	50	26	1.6
Granitic	Low	8.1	104	36	50	27	1.6
Saline	High	7.2	97	38	49	28	1.7
Saline	Low	7.9	101	40	50	32	1.8

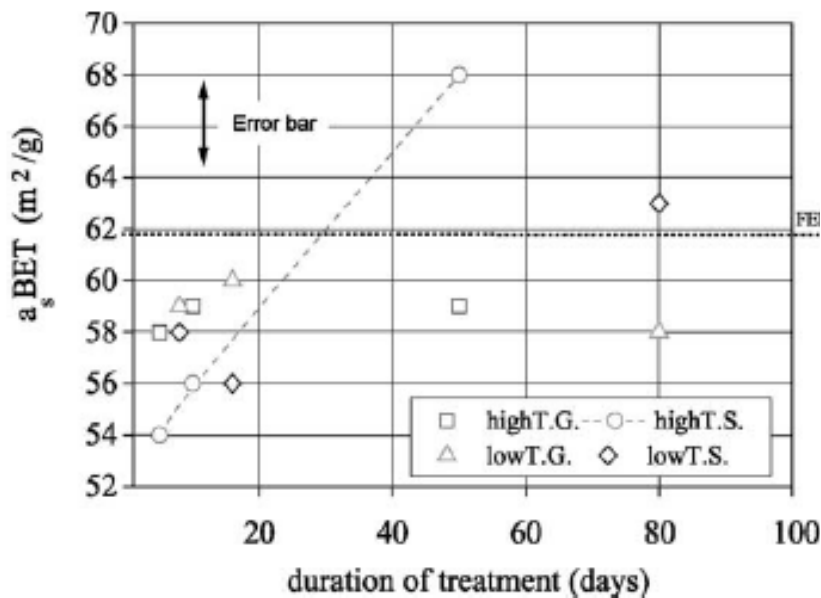


Figure 64: BET measurements on MX-80 with respect to Thermal duration, (T) temperature, (G) granitic solution, (S) Saline solution (After Cuevas et al, 2002)

From Figure 65, the MX-80 exposed to 300°C is seen to have a strong decrease in the 12Å peak with and overall increase in the 14Å peak for the air-dried samples; characteristic of the presence of a divalent cation at the interface (Guillaume et al (2003). However, upon glycolation it indicates that even after 9 months of high thermal exposure (300°C), the soil swells characteristically to that of a montorillonite-rich clay. Guillaume et al (2003) also state that the samples were slightly more calcic after the 9-month exposure.

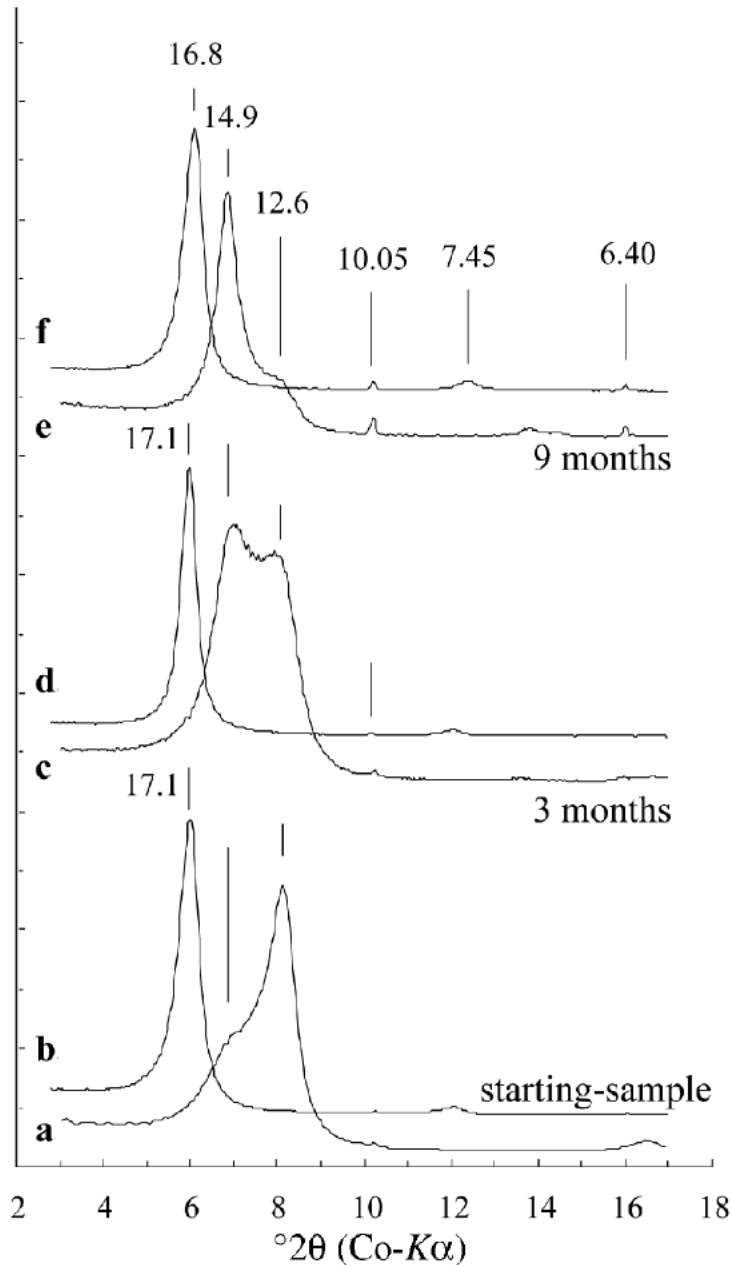


Figure 65: XRD patterns for THC exposed samples (MX-80, 300°C) with a comparison to the “starting” MX-80 (a,c,e: Air dried and b,d,f: EG treatment) (After Gullaume et al, 2003)

Their findings are also in agreement with that of the findings from Pusch et al (2010) that prove the formation of Siliceous compounds are formed at the heated interface, but the overall mineralogical composition maintained its similarity to the starting material. Some halite and calcite also formed nearer to the heated zone but had no effect on the mineralogy. This is characteristic of the Na to Ca replacement, displayed in Figure 65. Given the results from Shariatmadari et al (2011) and Schmitz et al (2007) the effect of the increased salt concentration upon resaturation will significantly impact the expandability of the inner zone. Due to the dissolution of the carbonates and salts into solution.

Herbert et al (2004) reacted MX-80 with two saline solutions (NaCl and MgCl) at 25°C, 90°C and 150°C for approximately two years. Material crystallinity, surface area and octahedral layer composition was discovered to have significantly changed. Their results contest the results from other studies that indicated partial transformation to illite under hydrothermal conditions for long time scales (Pusch et al, 1993; Claret et al, 2002; Drief et al, 2002; Guillaume et al, 2003; Wilson et al, 2006a, b; Gaudin et al, 2009; Pusch et al, 2010; Wersin et al, 2010). Their results indicated that Kaolinites and pyrophyllites will form rather than illite. The capacity of water uptake was reduced to ~50% compared to the DI water experiments, this occurred with time and thermal loading magnitude, displayed in Figure 66.

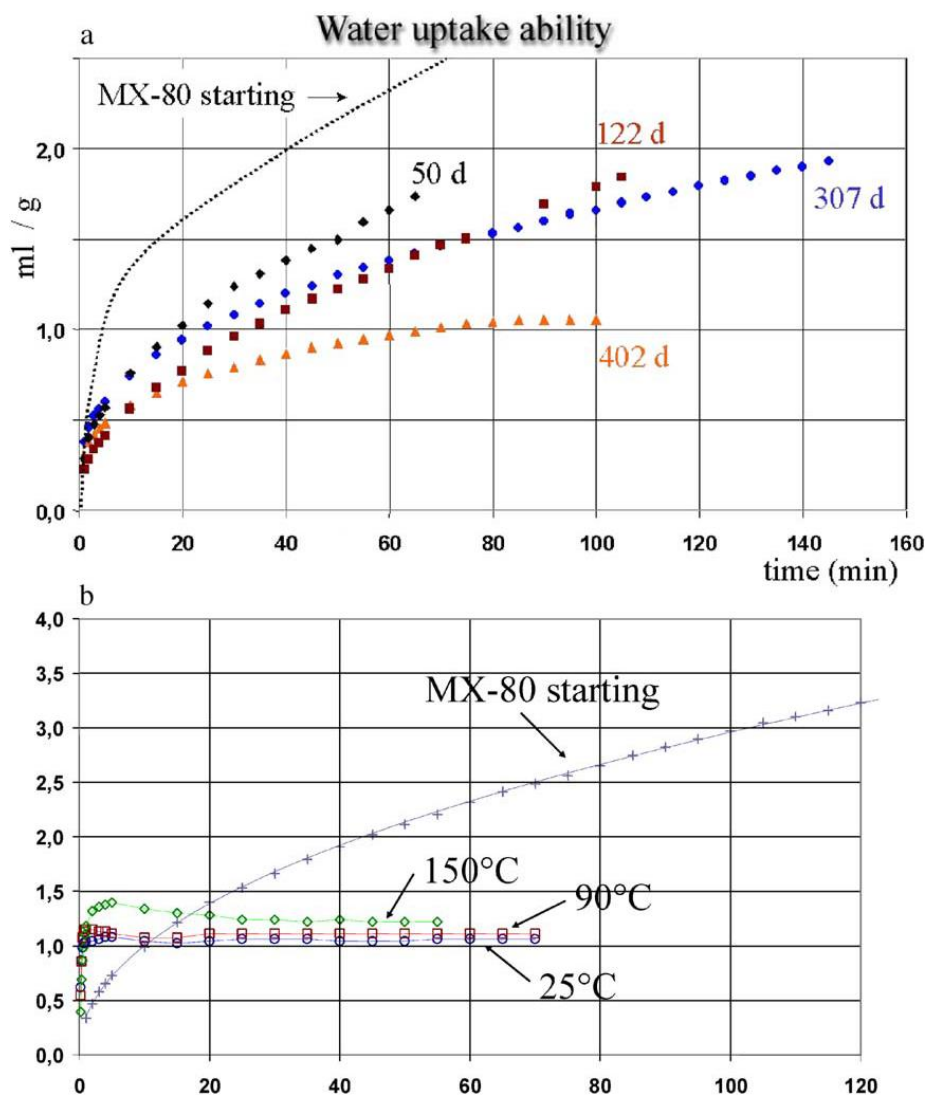


Figure 66: MX-80's water absorption capacity in an NaCl solution a) water absorption with duration at 25°C b) water absorption capacity with thermal exposure for 120 days (After Herbert et al, 2004)

What is seen from Figure 66 is that duration and thermal loading are significant to the behaviour of the material, higher thermal loading can reduce the materials water uptake ability in significantly less time than that of lower temperatures. These findings are supported

by the findings of Pusch et al (2010) that displayed the permanent layer collapse with thermal loading. Herbert et al (2004) also discovered that along with a reduction of interlayer charge the increase in octahedral Al^{3+} was comparable to pyrophyllitisation (a 2:1 sheet silicate) or kaolinisation (1:1 sheet silicate). The Si solutes were high enough to support this reaction pathway (Lippmann, 1979). Si dissolution of the tetrahedral layer was observed to be greater in experiments that involved a hydraulic gradient compared to the closed hydrostatic system. Herbert et al (2004) states that closed hydrostatic systems have a higher potential of kaolinisation and pyrophyllitisation due to the higher Si concentrations, these conditions are however unlikely for the barrier system. Overall there was no significant alteration to the expandability of the THC exposed samples, giving comparable d-spacing to that of the starting material and therefore it was concluded that montmorillonite was still the dominant mineral (Figure 67).

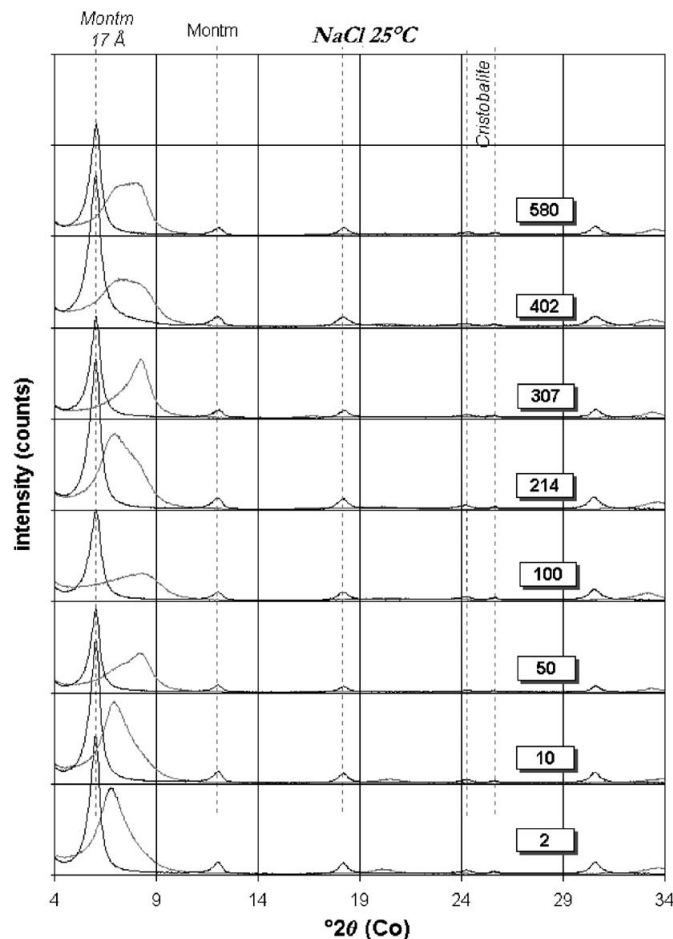


Figure 67: Oriented XRD patterns from the NaCl saturated tests at 25°C after a reaction time of 2, 10, 50, 122, 214, 307, 402 and 508 days (After Herbert et al, 2004)

What is noticeable from the glycolated samples is that the intensity of the pattern reduces with exposure time, this may be that there is more disordering or reduction in the abundance of the montmorillonite with reaction time.

Xiaodong et al (2011) also conducted similar tests to Gomez and Villar (2010) by subjecting a column of Bentonite to 50°C for 3 weeks with a 3.5% CaCl solution. They discovered that the MX-80 lost a significant proportion of its swelling pressure, permeability and stiffness compared to Ca dominant clays. The other material tested was the German friedland clay with consists of a mixed illite/smectite, which displayed the least alteration, conducted for comparative analysis. However, relative to the control measurements, for MX80, the German friedland clay has an inherently lower swelling capacity, which correspondes to a mineral component that is much more stable. Therefore, alterations are likely to be less prominent in this clay in comparison to the MX-80. Gomez and Villar (2010) found that neoformed gypsum (Calcium sulfate) was observed in the MX-80 (Figure 68), other studies have also stated that the neoformation of gypsum is present due to the oxidation of pyrite (Joeckel et al, 2005; Martin et al, 2007; Kolarikova et al, 2010). The neoformation of gypsum was also confirmed by Herbert et al (2008) and Madsen (1998) due to the presence of pyrite as a secondary microaggregate within the starting material. There was a small amount of illite present in the study however it was unclear if the illite was already present within the starting material, FTIR analysis did show silica formation in the form of cristobalite. Overall, Gomez and Villar (2010) demonstrates that there was no significant deviation from the expansive mineral, however the timescales of the test were rather short.

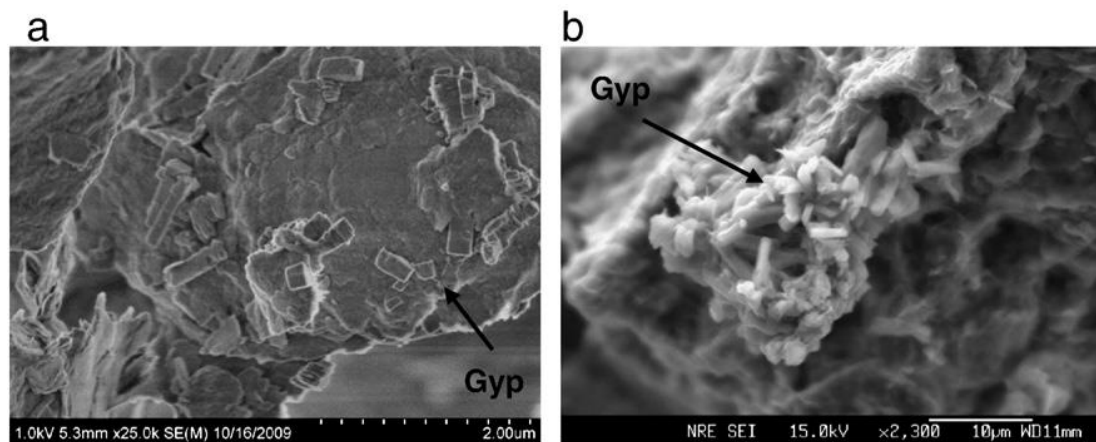


Figure 68: a) Gypsum formation on the surface of the montmorillonite crystals and b) Aggregated gypsum within the intra-layer voids (After Xiaodong et al, 2011)

Pusch et al (2010) investigated the precipitation of siliceous by-products after long-term hydrothermal exposure, the results were supported by natural analogues, namely the Kinnekulle analogue. Interaction with Fe corrosion and the development of quartz and cristobalite resulted in the Bentonite undergoing some inter-particle cementation. As can be seen below in Figure 69, silica particles were observed via SEM from samples taken at the Kinnekulle analogue (Muller-von-moos et al, 1990).

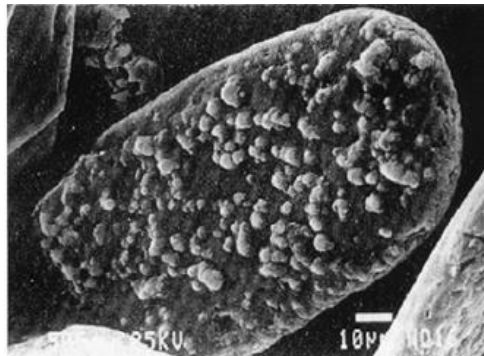


Figure 69: Siliceous by-products precipitated on the Bentonite particle taken from the natural analogue in Kinnekulle (After Muller-von-moos, 1990)

A study conducted by Pusch et al (1993) discovered that significant stiffening occurred in the sub-sampled Bentonite exposed to the hottest zone of heating. Stress controlled rheological tests displayed significant reduction in the strain as the thermal loading increased. The samples that were exposed to a thermal loading of 130°C compared to 90°C and displayed strains that were three times smaller after 1-year exposure (Figure 70). Muller-von-moos (1990) also discuss that there is some illitisation of the Kinnekulle Bentonite, leaving approximately 25% Bentonite, despite the long-term heating (over 500 years) at 120°C followed by a further 90°C for 1000 years.

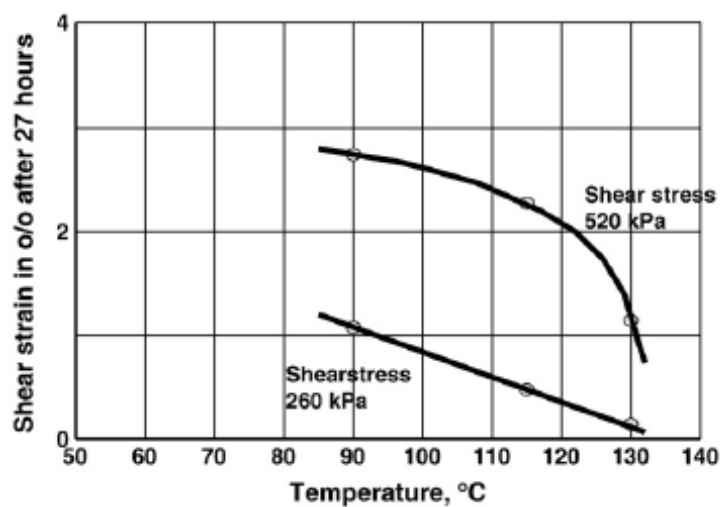


Figure 70: Rheology data displaying the reduction in strain with increasing thermal exposure (1 year) (After Pusch et al, 2010)

Push et al (2008) stated that during mock-up testing of the SKB-3V system, there were anhydrous compounds accumulated at the interface as well as chloride crystals during and immediately after the hottest phase but this is a reversible reaction. This however indicates that during the peak thermal process there is a high concentration front of salts and carbonates that crystallise, which upon resaturation, will yield a highly heterogeneous system of concentrated salt solution. This will have a large impact on the expansion capability of the clay in this zone (Shariatmadari et al (2011), Schmitz et al (2007)). These studies conclude that there are three main mechanisms, that lead to the loss of Bentonite expandability and ductility after short-term exposure. 1) very high thermal loading which induces a permanent interlayer collapse and 2) the concomitant precipitation of siliceous compounds and hydroxides and 3) DDL and osmotic gradient reduction due to high electrolyte concentration. Together these cause losses in volumetric uptake and partial fusing of the particles which are irreversible in lower temperature environments. The phenomenon of the fusing of plates during and immediately after the high thermal loading period was also hypothesised by Villar and Gomez (2010) and Xiadong et al (2011), who illustrate why this effect also impacts the permeability and swelling pressure (Figure 71 & 72).

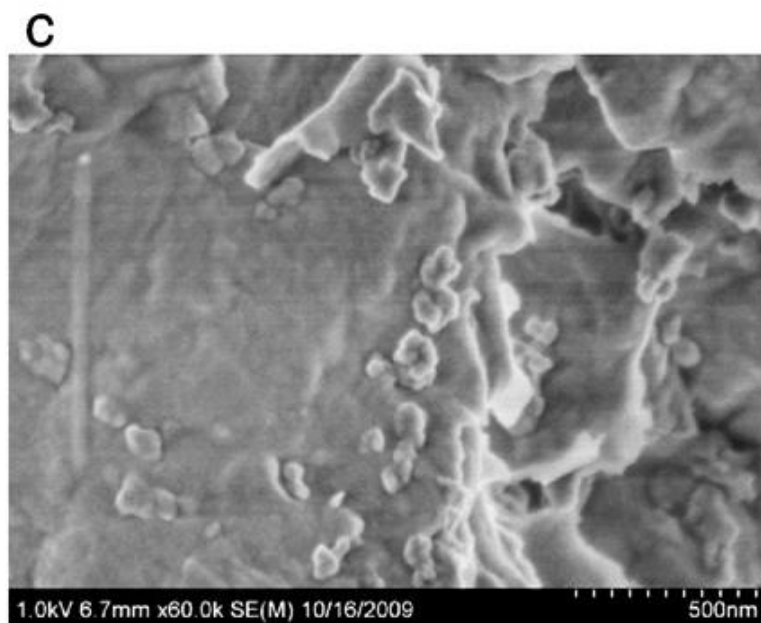


Figure 71: Silica particles formed on Montmorillonite particles (After Xiaodong et al, 2011)

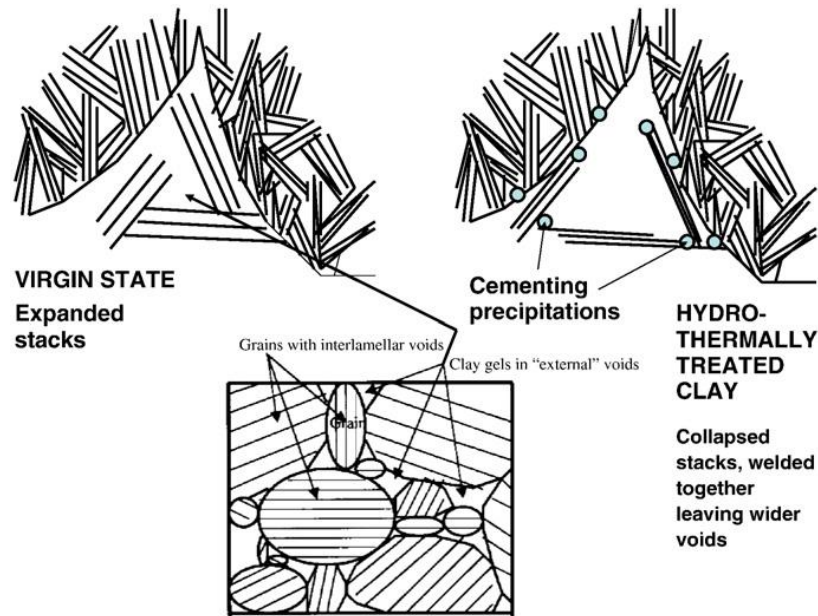


Figure 72: Illustration of the cementation of particles which causes increased hydraulic conductivity as well as reduced stiffness and swelling pressure (after Xiadong et al, 2011)

Fernandez and Villar (2010) conducted 8 year simulations with boundary conditions similar to the KBS-3V concept, the simulation subject the model to 100°C after-which the geochemical evolution was assessed. The permeant being Na-Mg-Cl type of 0.2M concentration. DRX, SEM and FTIR analysis demonstrated minimal evidence of smectite alteration Figure 73. Calcium concentration was observed to increase within the interlayer site agreeing with Gullaume et al (2003) and Pusch et al (2010). There appears to be a general trend of increasing cation concentration within the sampled pore water as the sub-sample approached the heated end (Figure 74), this supports the hypothesis of a loaded front of salt upon rehydration observed by Cuevas et al (2002). In addition, development of Ankerite, an Ca-Mg-Fe carbonate that developed at the innermost zone of the heated sample was observed, however this has crystallographic similarities to siderite, both are Iron-carbonates but contain varying amounts of Fe^{2+} . This could indicate partial dissolution of the montmorillonite, thus liberating Fe or by aiding the diffusion of Fe from the C-steel, this agrees with other studies (Carlson et al, 2007; Schlegal et al, 2008; Ishidera et al, 2008; Wilson et al, 2015).

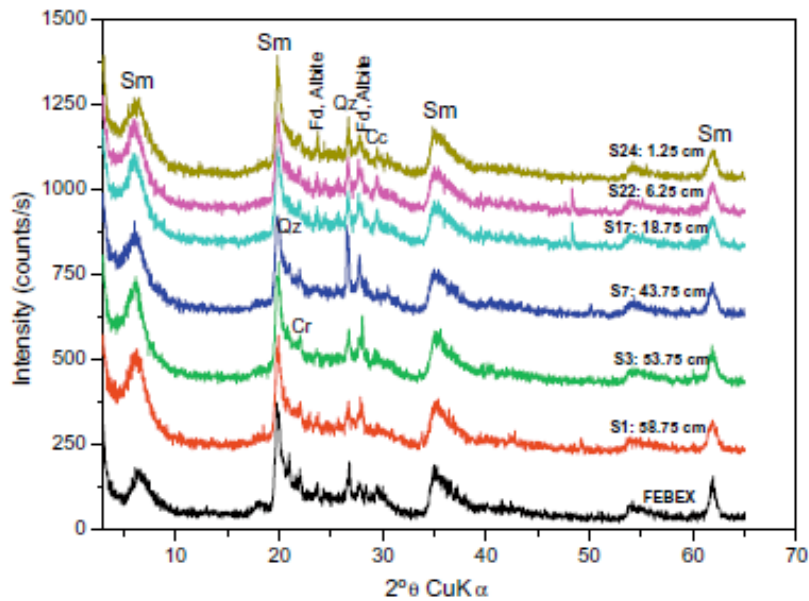


Figure 73: Random powder XRD on samples taken at different distances from the heater (S24 being the closest) (Sm: Smectite, Qz: Quartz, Cc: Calcite, Dol/Ank: Dolomite-ankerite, Fd: Feldspars, Cr: Cristobalite) (After Fernandez and Villar (2010))

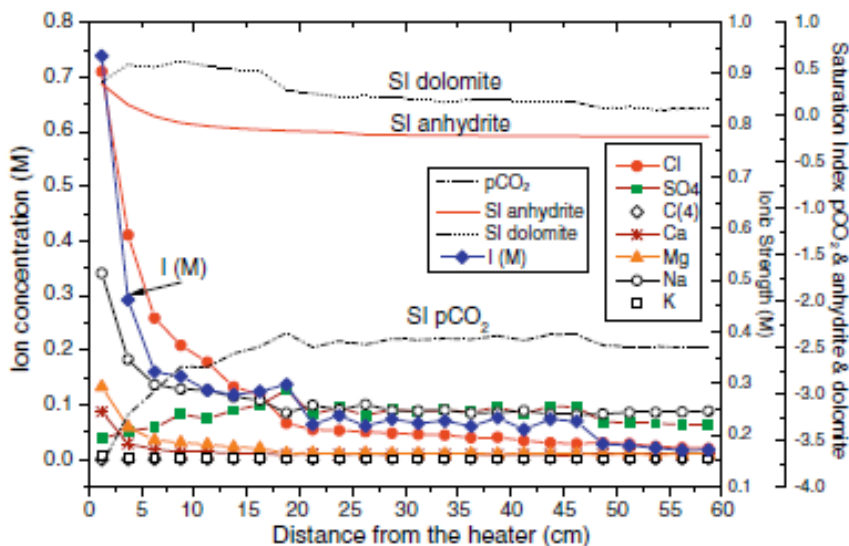


Figure 74: Cation concentration with respect to distance from the heated surface (After Fernandez and Villar, 2010)

The above studies discovered that anhydrite and calcite dissolution at the cooler end resulting in a higher CEC, whereas the CEC was lower in the heated zone due to Calcite and anhydrite precipitation (Figure 75). The studies concluded that two processes occurred, 1) in the cooler area the pore water was diluted and dissolution of highly soluble minerals (i.e. sulphates and carbonates) occurred and 2) precipitation and dissolution of sulphates and carbonates was controlled by gypsum and carbonate solubility, these mineral phases occurred at the innermost part of the Bentonite system. Nonetheless the pH of the near field was still basic.

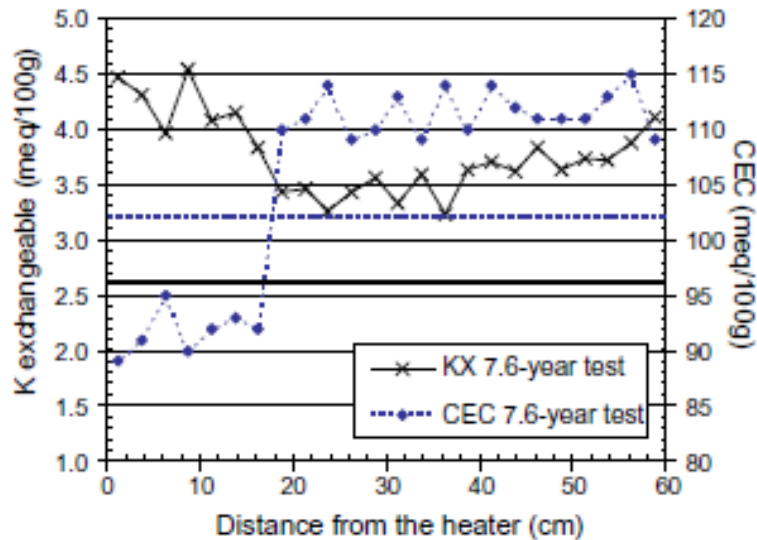


Figure 75: CEC measurements (Blue line) over the Bentonite block with respect to distance from the heater (After Fernandez and Villar, 2010)

With respect to the swelling pressure of the Bentonite Pusch et al (2010) and Pusch et al (1993) indicated that the swelling pressure of the Bentonite in the zone of the least thermal loading for the Äspö tests displayed swelling pressures twice that of the highest thermally loaded zone. They concluded that for their experimental work that the most significant alterations within the highest thermally loaded zone was the partial alteration to illite and Fe precipitation due to dissolution, forming Fe complexes during cooling adding to the cementation between particles. Silica was also higher in concentration in this zone and was thought to be the key cementing agent. The partial illitisation in the heated zone may have been due to the dissolution of vermiculite liberating K into soliton during this phase. This was due to the simplicity of the pore-water used, which meant that potassium could only be obtained from the K-bearing minerals after dissolution. Overall, they state that long-term heating under 150°C-300°C under isothermal conditions display nodular formation of SiO_2 rich compounds with some Fe nuclei, the occurrence of amorphous silica formation occurred immediately after heating in the cooling phase.

Herbert et al (2008) conducted a 3-year exposure of Bentonite under high saline conditions at varying pH conditions, that investigated the swelling pressure alteration with different ionic concentrations. Control swelling pressures were measured to be around 4MPa at the target dry density of $1.56Mg/m^3$, the samples in contact with low ionic solutions displayed swelling pressures of 2MPa and in higher ionic concentrations reduced the swelling pressure to below 1MPa. Their primary observations of the study concluded that partial dissolution of the montmorillonite was evident with higher concentrations of Mg, Al and Si

in solution agreeing with Pusch et al (1993), Schmitz et al (2007), Pusch et al (2010), Villar and Gomez (2010), Xiaodong et al (2011) and Shariatmadari et al (2011). Observations were also made of the replacement of Al for Mg within the octahedral layer, thus reducing the layer charge. This impeded the swelling ability of the clay as well as the additional replacement of Na^+ by Mg^{2+} within the interlayer, thus influencing the DDL. This mechanism that impedes the swelling ability was observed in a system free of Fe and therefore is more representative of the system further away from the interface. As it is observed by other studies using Fe/ Bentonite indicate the same dissolution but partial replacement by Fe in the octahedral sheet and interlayer (Kohyama et al, 1973; Badaut et al, 1985; Pusch et al, 2010). Similarly, the insitu Äspö retrieval test indicated the that Fe partially substituted Al^{3+} within the octahedral layer. This replacement induces higher lattice stress which increases montmorillonite dissolution (Pusch et al (2010)), nonetheless the dominant mineral was montmorillonite after hydrothermal exposure for 2 years in the Äspö HRL.

Shariatmadari and Saeidijam (2012) also found that high thermal loading reduced the free swell magnitude which correlated to a reduction in the basal spacing i.e. a reduced DDL when thermally exposed, Figure 76. The plasticity was also irreversibly reduced correlating to the loss in expandability, Figure 77. These results indicate that the ability for the MX-80 to uptake water and swell was inhibited by ~18%.

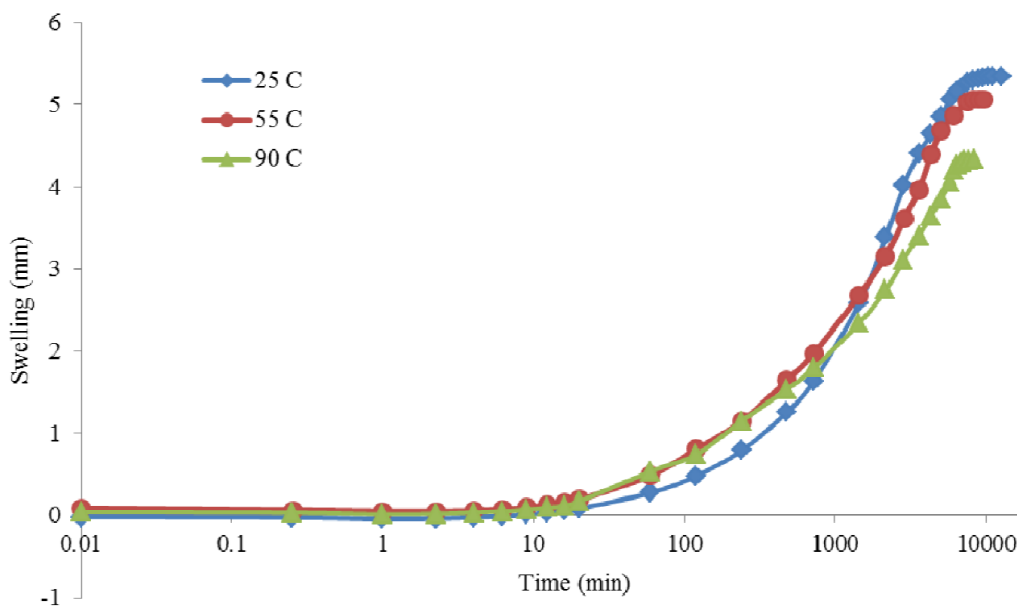


Figure 76: Free swell of MX-80 with temperature (Dry density during thermal exposure $1.5Mg/m^3$), 1:1 MX-80/ Sand mixture (After Shariatmadari & Saeidijam, 2012)

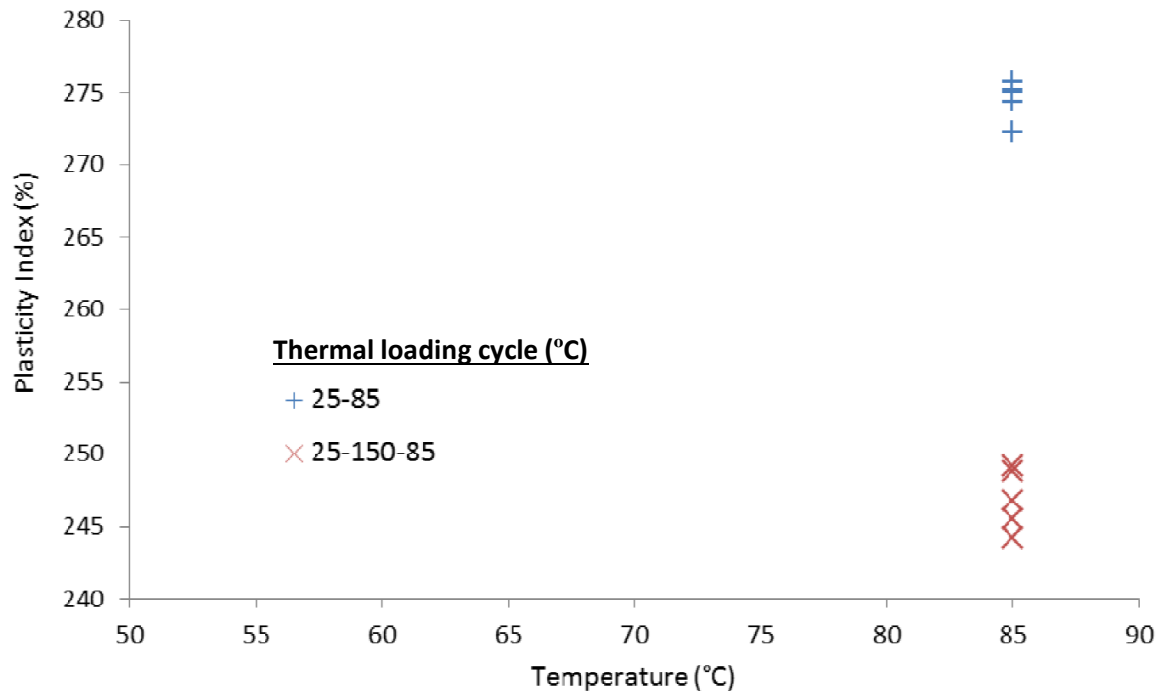


Figure 77: PI Vs. thermal loading (thermal loading increment 48hrs) (After Shariatmadari & Saeidijam, 2012)

William and Crerar (1985) stated that smectite dissolution produces an increase of Si in solution during thermo-hydraulic exposure this results in the precipitation of amorphous silica. They highlight that temperature, pressure and high pH environments increase silica solubility which is also supported by Fritz (1981), Pusch et al (2010), Xiaodong et al (2011). All the aforementioned studies conclude that the high pH environments and high thermal loading produces the following predominant minerals, Quartz, feldspars, zeolites. Furthermore, in calcium rich bentonites the development of Calcium silicate hydrates is likely. Nonetheless smectite remained the predominant mineral that is only partially altered to high-charge smectite with reduced expandability. Surface area of the smectite, porosity and fluid diffusion reduction is also demonstrated by Savage et al (2002) in line with the above conditions. Charpentiera et al (2006) found that their experiments conducted at 80°C for all durations indicated a progressive reduction of Si and Al content while Fe increased. These results indicate that an evolution of a low-charge montmorillonite to saponite or mixing of montmorillonite/ vermiculite layers. The samples collected more than 15mm away from the Fe and heating source display distinct crystal phases. The Si, Mg content was lower closer to the Fe source, with the Fe increasing. The reverse was observed the further away from the Fe source. Overall the samples at the interface displayed a Si poor/ Fe-rich clay that was characteristic of Fe-vermiculite. Whereas the samples taken further away from the interface displayed di-octahedral smectite and Mg-rich vermiculite. It was only for the experiment that experienced a thermal loading of 300°C which displayed the most significant deviation from

the starting material. The most predominant mineral in this case was vermiculite with a small amount of Tri-octahedral saponite. Their overall conclusion from experimental testing was that the most significant alterations occurred in the initial three months of hydrothermal exposure. Thus, indicating that there is a non-linear evolution of the interface physicochemical environment with respect to ongoing time. The formation of magnetite on the steel surface is presumed to act as a “passivation” layer on the carbon steel in the closed environment, thus reducing the diffusion of Fe cations into the Bentonite. However ongoing dissolution of the montmorillonite and accessory minerals occurs over the longer time scales, such as the dissolution of siliceous minerals increase diffusion rates (Bauer & Berger, 1998; Huertas et al, 2001; Taubald et al, 2000; Claret et al, 2002; Charpentiera et al, 2006; Wilson et al, 2006; Pusch et al, 2010).

Research has speculated that the abundance of Iron (ii) ions may potentially replace the native ions of the Bentonite resulting in alteration and reduced performance properties, such as Nontronite Milodowski (2009). Bentonite also contains framboidal aggregates of microcrystalline minerals (including pyrite) which may also potentially affect the integrity of both the Bentonite and canister by reacting with the groundwater (Schmitz et al (2007), Milodowski (2009), Hicks et al (2010)). There is an abundance of literature detailing the alterations of natural analogues and experimental data of the iron-Bentonite interactions. The comparison of the long time-scale physicochemical conditions of the natural analogues and the experimental data provides unequivocal conditions that will promote non-swelling clay minerals (Such as berthierine) rather than Fe-rich swelling clays (such as Fe-Saponite) (Wilson et al 2015). Kamei et al (1999) conducted experiments of Fe^{2+} adsorption in NaCl solutions to understand the effects of C-Steel corrosion products with respect to the alteration of the Bentonite in a GDF setting. As well as the study of a natural analogue i.e. a study of a C-Steel/ Bentonite interaction within a Bentonite mine. Kamei et al (1999) found that the Bentonite observed a colour alteration from grey to green around the immediate interface. XRD analysis was conducted on the sub-samples and the “starting” MX-80. They found via XRD analysis that the predominant site of Fe^{2+} sorption was in the interlayer by comparison of d001 and d060 reflections. They found that the expandable behaviour of the Fe^{2+} cation has similar characteristics to that of Ca^{2+} -Smectite (Sato et al, 1992), Figure 78. CEC measurements of the sub-samples appeared to be reduced to approximately 48meq/100g from 60meq/100g. Comparison of the d001 and the d060 indicated that no Fe^{2+} had replaced the

structural Al^{3+} within the octahedral layer, therefore predominant alteration was due to the sorption of Fe^{2+} within the interlayer.

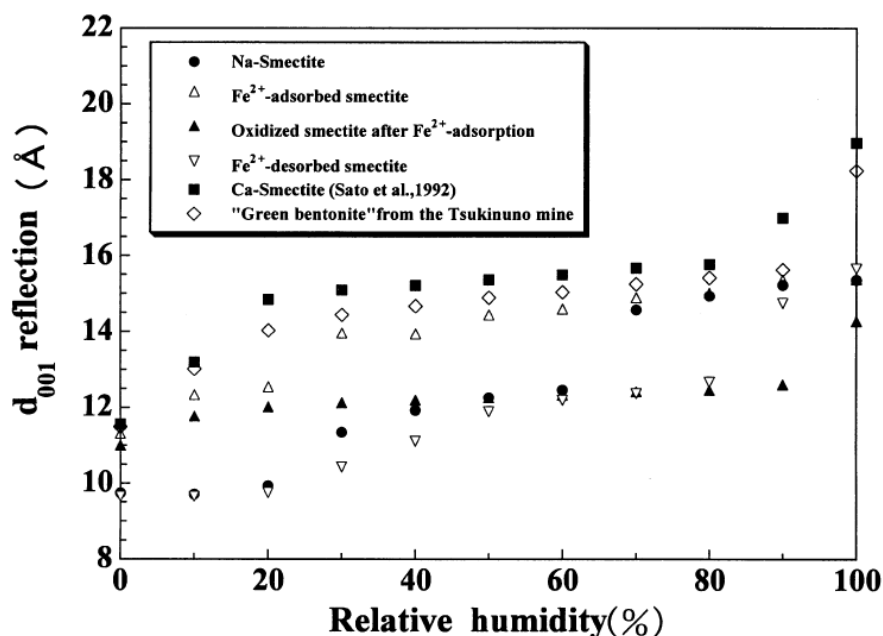


Figure 78: d_{001} reflections with respect to RH (%) with different chemically exposed samples (after Kamei, 1999)

Wilson et al (2006a, b) also states that the reaction pathway producing Fe^{2+} could replace the Na^+ bonds in the interlayer clay structure; this is due to the lyotropic series (as stated earlier). They discovered from tested specimens that the predominant mineral was berthierine ($(Fe^{2+}, Fe^{3+}, Al, Mg) ((Si, Al)_2O_5(OH)_4)$) but also emphasised that oxidation of Fe to produce magnetite (Fe_3O_4) coincides with predicted thermodynamic models. Wilson et al (2006a, b) concludes with the implications associated with the alteration potential of the Bentonite within the immediate zone of corrosion precipitation, the most likely alteration will be Fe rich smectite (saponite). Iron has a higher alteration capacity than magnetite; hence the prevailing speculated alteration could be phyllosilicate non-swelling sheets (illite or chlorite) with reduced swelling capacity.

Carlson et al (2005) conducted a long term testing programme that exposed carbon steel coupons in Bentonite at a constant temperature of 30-40°C in an anearobic environment. These conditions are not representative of early environmental phases, also the study did not consider the physicochemical by-products that would be present from early stage conditions which would be carried into the latter anaerobic phase. If the NAGRA near-field assumptions are accurate (presented by Landolt et a, 2009) then the experimental boundaries replicated the long-term conditions. Calson et al (2005) discovered that under these anareobic

conditions a green precipitant was present on the coupon surface, hence given the reducing conditions of the test it indicated that Fe^{2+} was dominant. Carlson et al (2005) noted that chlorite or berthierine had developed under the aforesaid conditions and the hydraulic conductivity had increased but no conclusive evidence was presented. The increase in hydraulic conductivity was perhaps due to the volume increase of the corrosion products related to the material porosity (Bildstein et al, 2006), or the higher saline concentration (as stated earlier). There is however speculation of the conditions required for chlorite to form, in that it is thought that extremely high temperatures are required within an environment with very high Fe^{2+}/H^+ ratios; this has seldom been experimentally achieved (Bowers et al, 1984; Small et al, 1992; Guillaume et al, 2003). The presence of the Chlorite may be already within the Bentonite due to the geological history and hydrothermal exposure during formation of the Bentonite. Schlegel et al (2008) used the same analytical methods as Carlson et al (2007) and Ishidera et al (2008), i.e. XRD, SEM, Mössbauer transmission spectroscopy, FTIR etc. for chemical and mineral alteration analysis. The results were somewhat similar and it can be inferred that the common mineral precipitants observed in these tests were goethite ($FeO(OH)$) and magnetite (Fe_3O_4). Results from the analysis conducted by Schlegel et al (2008) confirms Carlson's et al (2007) findings, such findings included Magnetite and Fe-rich phyllosilicates on the internal layers, precipitation of (Ca, Mg)-containing siderite and Goethite was also detected but not abundant.

Milodowski (2009) further confirmed the findings made by Carlson et al (2005) and Wilson et al (2006 a,b) by detailing that Dioctahedral Monmorillonite transforms into Fe rich Dioctahedral Monmorillonite, and a reduced Cation Exchange Capacity (CEC) was also observed. Furthermore Ishidera et al (2008) conducted similar tests using carbon steels under reducing conditions and speculates that smectite can be destabilised from a 2:1 structure to form 1:1 phyllosilicates of the serpentine group under basic pH conditions. Ishidera et al (2008) also stated that magnetite formed over the interface during the tests due to the redox development. Overall Ishidera et al's findings were inconclusive when compared to the more comprehensive reports such as Carlson et al (2007), Wilson et al (2006a,b & 2010), Wersin et al (2006) and Landolt et al (2009).

Schlegel et al (2008) used the same analytical methods as Carlson et al (2007) and Ishidera et al (2008), i.e. XRD, SEM, Mössbauer transmission spectroscopy, FTIR etc. for chemical and mineral alteration analysis; results were similar and it can be inferred that the common mineral precipitants observed in these tests were goethite and magnetite. The test

was conducted in a comparable method but with pure Fe coupons and with a hydrostatic pressure of 5Mpa. A realistic factor to the investigation is that Shlegel et al (2008) assumes that the highest temperature at the interface will be $\approx 90^{\circ}\text{C}$. Schlegel et al (2008) does highlight however that smectite destabilisation is more likely to occur at greater temperatures ($\geq 150^{\circ}\text{C}$). Results from the analysis conducted by Schlegel et al (2008) confirms Carlson's et al (2007) findings. Such findings included Magnetite and Fe-rich phyllosilicates on the internal layers, precipitation of (Ca, Mg)-containing siderite and Goethite was also detected but not abundant.

The principle mineral development at the interface due to corrosion precipitants are thought to be Magnetite, Hematite and Goethite. With respect to the changes due to corrosion products, past experiments (A Milodowski et al (2009) phase 1 & 2, Carlson et al (2007), Wilson et al (2005)) have underlined that the occurrence of Fe-rich clay is likely due to Fe substitution. Chloride concentrations were also observed within the Fe oxidation layer; a potential causative factor is that salt deposition due to residual high saline pore water can occur.

The quantity of virgin Fe present within the clay structure is dependent on many natural factors, prior to extraction, as well as the underlying chemistry the Bentonite deposit was subject to during its geological history. Redox conditions are a vital factor that determines the structural makeup and consequently the physical and physicochemical properties. Neumann (2013) states that the structural content of Iron in clays can vary massively from trace amounts to $\geq 30\%$. Mid to high percentages of structural iron is comparable to that of Saponite, Nontronite and Ferrosaponite. Both types are 2:1 phyllosilicate minerals of the smectite group and are considered to be likely candidates for transformation within an iron rich environment. The transformation is considered simple as it has a very similar structural configuration to montmorillonite.

Wilson et al (2006a, b) investigated the stability of montmorillonite in the presence of native Fe(0), Fe_3O_4 and high electrolyte solutions under hydrothermal conditions. The solutions included FeCl_2 and NaCl under 80°C , 150°C and 250°C . They observed the development of Fe_3O_4 on the Fe coupon surface under NaCl and 250°C , with the MX-80 partially transforming to an Fe-rich smectite. XRD analysis displayed loss of swelling of the d-spacing upon EG treatment (Figure 79). The transformation to Fe-rich clay was only

observed when the initial conditions used Fe(0), not Fe_3O_4 . When the Fe-smectite was exposed to the atmosphere is readily oxidised, indicating a non-stable Fe^{2+} bearing mineral.

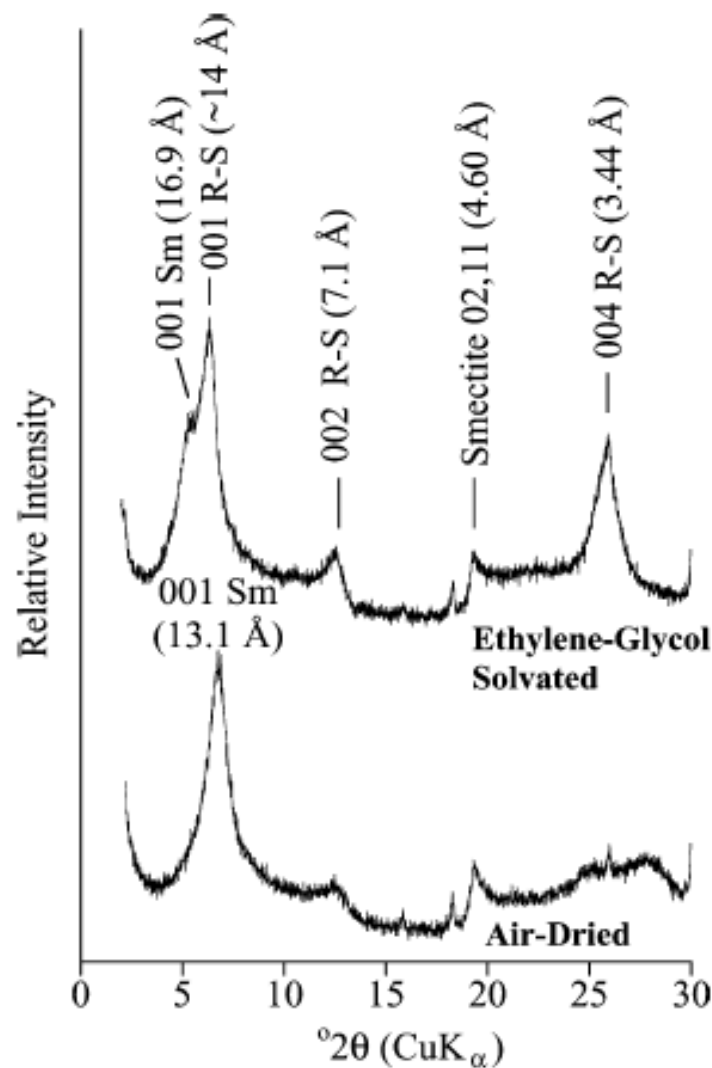


Figure 79: XRD pattern on post Fe/MX-80 exposure after heating at 250°C in NaCl solution for 92days (After Wilson et al. 2006a,b)

What is seen from Figure 79 is that much of the specimen remains at 14-14.4Å, the broad peaks also indicate the transformation to a more amorphous crystal structure. There is however, some original expansion indicated by the slight shoulder on the 14Å peak indicating some original, high charge, smectite at 16.9Å. Furthermore, Wilson et al (2006a, b) examined the XRD spectra of the partially and fully oxidised Fe-smectite Figure 80, these results are also in agreement with other studies for Fe-saponite (Kohyama et al, 1973; Badaut et al, 1985). All of the studies discovered that the Fe^{2+} bound within the trioctahedral layer is readily oxidised and the peak (06,33) is shifted from 1.55Å to 1.53Å. This result was supported by other literature that stated Fe^{3+} rich smectite will have a broad peak at ~1.53Å (Kodama et al, 1988; Sherman and Vergo, 1988) however it was reported by Sherman and

Vergo (1988) and Manceau et al (2000a) that Nontronite displays a slightly lower d(06,33) spacing of $\sim 1.52\text{\AA}$.

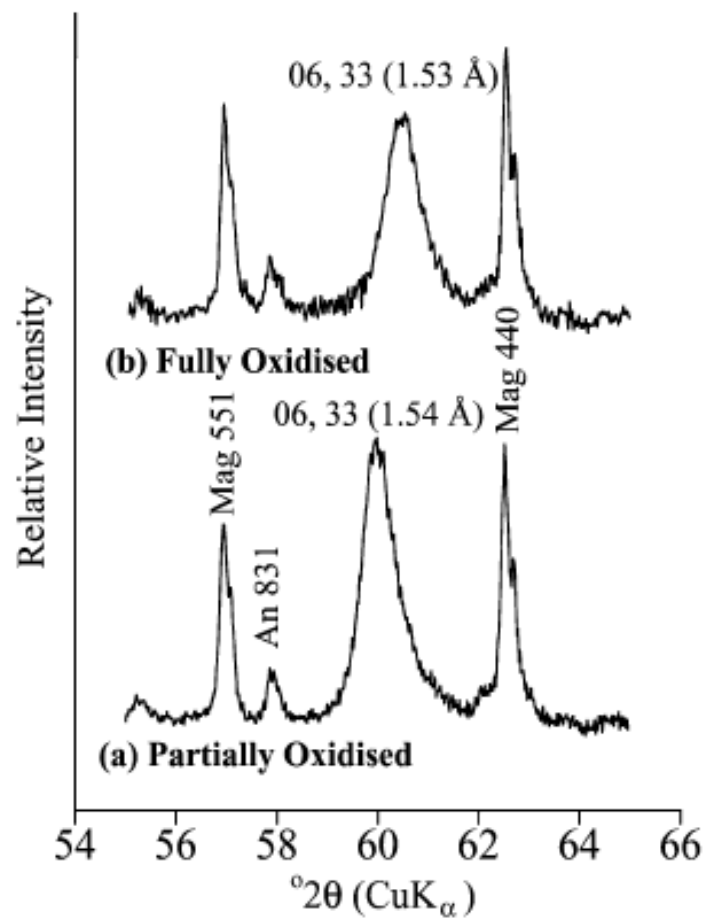


Figure 80: Structural Fe oxidation patterns for post THC Bentonite (After Wilson et al, 2006a,b)

Lower temperature studies (80°C and 150°C) indicated much less alteration with d(001) peaks at 14\AA - 15.4\AA and EG treatment 16.5\AA - 17.2\AA which did indicate some interlayer cation exchange, Na for Fe. There was a much higher quantity of silica and Al^{3+} displayed in higher temperature tests where smectite dissolution proved to be more extensive. Imaging via TEM displayed partial dislocation at the edge sites, thus forming 1:1 layers, Figure 81. This TEM image indicates that edge and tetrahedral dislocation occurs with the partial formation of berthierine-type mineral with a 7\AA spacing. Green rust was discovered in the THC exposed samples and they conclude that it is likely to be metasTable with respect to the magnetite under the experimental conditions used. Fe-rich smectite is known to be more likely to develop due to it being less kinetically constrained rather than the transformation of a 1:1 mineral such as berthierine and it is only likely to occur if the pH was low (Wilson et al, 2006a,b; Guillaume et al, 2004).

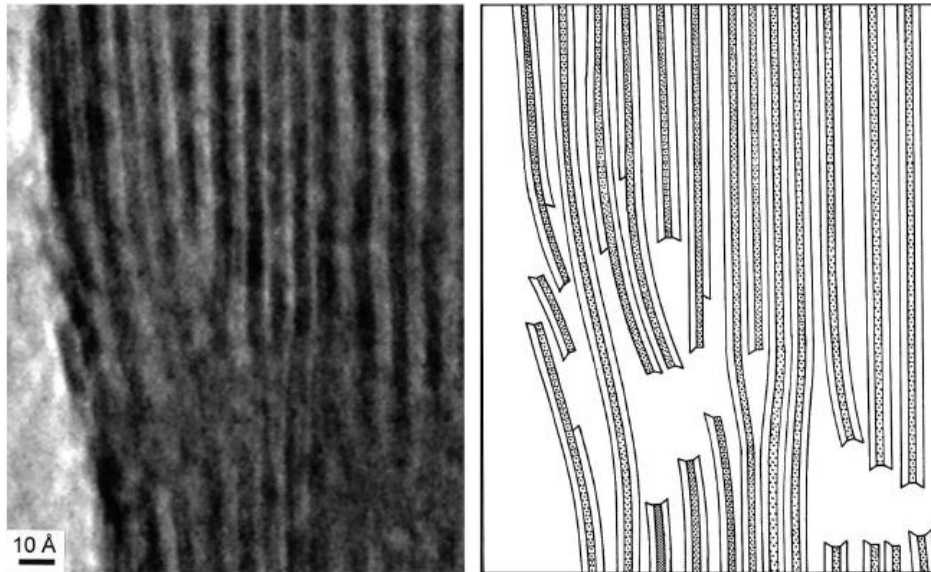


Figure 81: TEM image of the Fe altered smectite, displaying 2:1 to 1:1 modification, due to tetrahedral dislocation indicating berthierine type alteration (after Wilson et al 2006a,b)

Overall the measured solute activities coincide with berthierine, the experiments employed by Wilson et al (2006a, b) allowed sufficient concentration of Fe in the system to allow chlorite development.

Neumann (2013) discusses various mechanisms for the alteration potential of montmorillonite that contains some Fe^{3+} through the chemically induced reduction of the structural Fe^{3+} due to sorption of Fe^{2+} under reducing conditions. Neumann (2013) describes the mechanism as two separate processes depending on the solution pH, as can be seen from Figure 82, the sorption of Fe^{2+} on either the edge site or the basal plane results in the possible reduction of the structural Fe^{3+} via two electron transfer processes. For edge sorption, the electron transfer is via a moving front of electrons into the octahedral structure, whereas basal plane sorption results in a pseudo-electron transfer through the tetrahedral unit and into the octahedral unit. Neumann also stipulates that smaller cations are known to migrate into the structure of smectites upon heating, possibly suggesting that this is an alternative pathway for montmorillonite alteration.

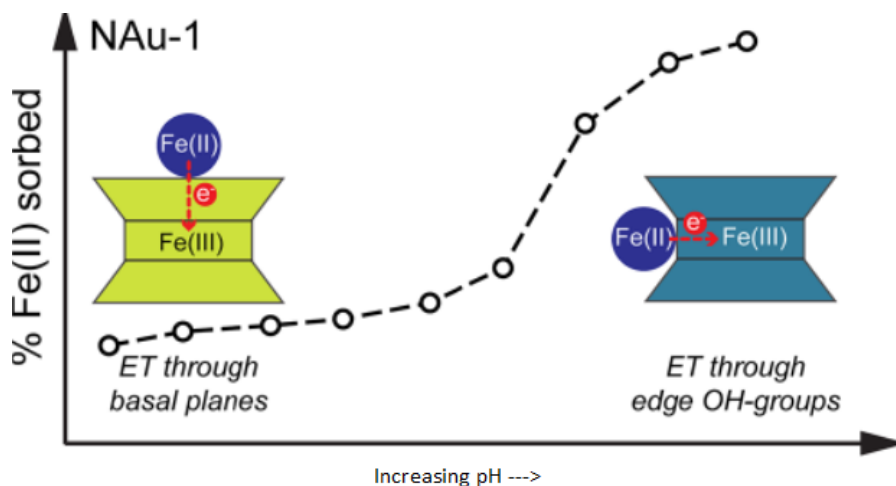


Figure 82: Sorption sites for Fe (II) cations as well as structural iron reduction via electron pathways (After Neumann, 2013)

Gaudin et al (2009) investigated the mineralogical condition of argillaceous clay after being in contact with carbon steel for 6 years. The study used both carbon and stainless steels. Their results indicated no significant alteration with the stainless-steel samples over the experimental duration. However, the carbon steel tests indicate crystal alteration. They discovered Fe-enrichment in the form of a diffusive front propagating away from the interface. The enriched area of the clay was accompanied by the crystallisation of a significant amount of goethite and magnetite. The Fe^{2+} integration into the clay is perhaps the pathway to the development of the trioctahedral cation replacement of Mg by Fe^{2+} . This pathway could lead toward the destabilising of the montmorillonite which is supported by Latenois et al (2005). A disadvantage of the experiment conducted by Gaudin et al (2009) was that the REDOX conditions were limited by the maintaining the samples in the oxidation state. Their study found strong dissolution of illite/ smectite minerals as well as high amounts of FeOOH phases and magnetite.

2.2.3. Concluding statement:

There are large discrepancies within literature with regard to the alteration transformations that are likely to occur under repository conditions for each specific disposal concept. This is understandable due to the early phase of many long-term disposal programs and the generic nature of the site parameters. However, many concepts have put large emphasis on the thermal limitation, mostly considering 100°C as the upper thermal limit for the canister arrays. Therefore, studies that investigated the THC impact under high temperatures ($\geq 150^\circ\text{C}$) are not necessarily representative of the insitu conditions. Furthermore, the alteration products from many of the studies are likely to be a “worst” case

scenarios. Reaction kinetics might be accelerated for higher temperatures, although it must be noted that considering unrealistic temperatures may yield mineral phases that will not occur at lower temperatures over geological time scales. Overall, experimental studies are useful to understand the intrinsic coupling between the Bentonite and the corrosion products, but absolute replication is impossible and therefore the by-products must be investigated with some degree of scientific judgement.

From the studies, it is evident that high saline ground water has a large impact on the montmorillonite activity by reduction of the DDL, cation fixation and osmotic pressure imbalance between the free and absorbed pore solutions. When combined with high temperatures, the physicochemical parameters appear to be permanently reduced arguably due to cementation by precipitation of Silica, cristobalite, calcium silicate hydrate, gypsum and oxy-hydroxides within the pore spaces (i.e. the Intra-aggregate voids). Liberation of Silica, Iron, Magnesium and Aluminium has been observed to occur in solution that will aid the formation of the cementitious compounds, Fe integration into the octahedral layers as well as the development of feldspars. The increase in salt content, carbonates and sulphates at the interface is thought to occur due to the initial heating and drying, leaving behind salts that were already present in the Bentonite. Then with the eventual ingress of the higher saline waters, there is likely to be a “loaded” front of high saline water near to the steel/ Bentonite interface, which will act as a corrosion aggressor to the carbon steel. Consequently, over the cooling period, the silica in solution from the dissolution of silicate minerals will crystallise to form silica cement, thus affecting the barriers physical performance. If this is to occur then the engineering performance will be affected in terms of its hydraulic and thermal conductivity, plasticity, swelling and strength/ stiffness characteristics.

Charpentiera et al (2006) as well as Ruck & Cathelineu (2004) both conclude that the Bentonite does undergo some alteration but the main mineral phase is still highly swelling smectite or vermiculite for thermal exposures of 80°C and 150°C. This was achieved through observation of the XRD EG treatment stage, where the dominant mineral is montmorillonite. However, heat treatment under 300°C after 6- 9 months, indicated some mineral alteration to a mixed smectite/ chlorite/ vermiculite layering with a lower structural charge. This was concluded to be due to loss of surface area due to particle fusing, densification by altered surface charge potential (Ma and Hueckel, 1992) and loss of the 2:1 layer dielectric constant Mitchel and Soga (2005).

As for the development of the oxy-hydroxides, from the above studies, magnetite (Fe_3O_4) is the most thermo-dynamically stable corrosion product. The development of the

Fe_3O_4 layer is known to inhibit the diffusion rate, due to the layer acting as a “passivating” layer in non-dynamic environments. However, it is speculated that Bentonite in direct contact with the C-steel will inhibit the Fe_3O_4 , thus allowing free diffusion of Fe ions into the Bentonite until complete corrosion of the canister has occurred (Wilson et al, 2010). The type of corrosion product is ultimately a function of the redox conditions. The most relevant conditions with respect to the interface environment will result in a front ferric oxy-hydroxide compounds (i.e. the possibility of maghemite, lepidocrocite, goethite, hematite etc. formation) in the outermost zone, with a ferrous-rich zone immediately behind it. The type of corrosion products is dependent on the hydrothermal history of the system (Sawicki et al, 1995). This environment will likely give rise to the integration of Fe into the octahedral layer as well as complexation of Fe in the exchanger and edge sites. Electron transfer between the exchange sites and Fe integrated cations will cause a dynamic redox environment. Studies have found that Fe-rich smectite, such as saponite, Nontronite or ferrosaponite, are kinetically more likely to develop, depending on the amount of structural Fe, over 1:1 mineral development such as bertherine type layering (Pusch et al, 1993; Ruck & Cathelineu, 2004; Charpentiera et al, 2006; Schmitz et al, 2007; Gullaume et al, 2003; Pusch et al, 2010; Villar and Gomez, 2010; Xiaodong et al, 2011; and Shariatmadari et al, 2011).

Pusch et al (2003) also speculated a swelling pressure reduction after cooling under partially saturated conditions initially at temperatures between 125°C and 150°C. It is therefore likely that the reaction kinetics are highly dependant on the ground water, buffer composition and thermal-loading/ gradient. Schmitz et al (2007) suggest areas for further study by indicating that more attention should be paid to the micro-scale interaction on which alteration of the clay minerals could occur. Hence as well as the engineering and interparticle considerations the colloidal changes must also be deliberated under elevated pressures and temperatures. Clay structure stability may change under such conditions when paralleled to the stable colloidal conditions under ambient temperatures and atmospheric pressure environments. Overall it is evident that due to complex and vastly dynamic factors of the EBS intrinsic environment, a combination of boundary conditions will need to be investigated to accurately replicate such conditions and, hence, improve the physicochemical and engineering understanding.

3. Experimental and post analysis testing methodologies

The experimental methodologies conducted as part of the research as well as the associated post THCM exposure testing protocol is set out. The steel/ Bentonite interface (Section 3.2) and constant volume (section 3.3) experiments form the focal approach of the study and are defined in the following sections below. Sections 3.1, 3.4 and 3.5 describe the supplementary batch tests conducted alongside the main testing. The aim of the supplementary batch tests was to gain an insight into the boundary conditions that may impact the Bentonite and to carry them forward into the interface and subsequent constant volume experiments for more comprehensive analysis. The thermal loading and duration tests, presented in section 3.4 and 3.5, were conducted to isolate the effects of temperature on the geomechanical properties. Thermo-saline experiments, presented in section 3.5, were implemented to investigate the coupled exposure of high temperatures, duration and salinity exposure. The batch tests were used to isolate the effects of different variables which can then be used alongside the more complex interface and constant volume tests to determine what parameters most significantly affect the engineering functionality of the barrier.

Experimental boundary parameters have been inferred from the NAGRA concept for steel/ Bentonite interface evolution phases by Landolt et al (2009) and the thermal limits defined by Holton et al (2012) and Hicks et al (2009). All of the experimental parameters were confirmed during synergy meetings with other academic and industrial institutions that included support from the RWM ltd (Radioactive Waste Management limited), a wholly-owned subsidiary of the NDA. The interface experimental protocol used high salinity water of NaCl composition and concentration of 0.45M of sodium chloride (1x the average concentration of sea water). It is recognised that this is a simplified representation of the more complex groundwater that is expected at depths associated with the GDF. It is deemed suitable for investigatory purposes to use simplified experimental variables. By using water compositions that are too complex, multifaceted alterations may obscure the results. Therefore, using a simplified saline solution will allow the research questions to be investigated within the timescale of the project. Alongside the interface and constant volume batch tests, several pilot batch experiments under varying exposure parameters for prolonged exposure times were also conducted. The pilot batch tests investigated the more complex ground water compositions as well as the standard solutions i.e. deionised water and NaCl

solution for comparison with the project experimental variables used in the main testing protocol (section 3.2 and 3.3).

MX-80 Bentonite, a Na- type Bentonite, was implemented for the experimental procedures and has been adopted throughout the entire SAFE Barriers research consortium investigations. The powdered MX-80 was obtained from RS minerals® and was used for the constant volume and supplementary batch tests. SKB (the Swedish concept) supplied the consortium with pre-compacted Bentonite rings at the concept target density ($\rho_{dry} = 1.56 Mg/m^3$) around the saturated moisture content (I.e. $S_r \approx 100\%$ at 27%). The rings were compacted and supplied by ClayTechAB®, a subcontractor for the SKB concept and were used in the interface testing regime; both materials are classified to be Wyoming MX-80 Bentonite. All experiments in this study were implemented with the principle focus of investigating/ inferring the effects of high temperature, corrosion and saline groundwater on the clay barriers’ intended functionality of the clay barrier. A comprehensive material classification has been conducted, presented in section 4, a full suite of geochemical and geotechnical tests was conducted under standard conditions (Controls) to obtain control parameters, to allow a direct comparison with “altered” specimens. All post THC exposed samples were sub-sampled at the zone of visible alteration i.e. zones of discolouration due to corrosion. These zones varied due to the initial state of the bentonite i.e. degree of compaction and porosity, the zones were also controlled by the density evolution throughout THC exposure.

The following experimental methodologies were developed to aid in answering the key research questions, the following Table (Table 19) outlines the methodologies employed to answer these questions.

Table 19: Methodology and key research questions matrix

Method	Key research questions addressed*
Pilot batch tests	2,3,4
Interface tests	3,4,5,6,7
Constant volume batch tests	3

* Refer to section 1.2 for complete key research questions

3.1. Pilot batch test methodology:

Several batch tests were conducted over a comprehensive temperature range, between 20°C- 300°C. The initial temperatures were chosen for initial characterisation purposes as the upper limit of 100°C has been selected for the current UK disposal concept. The thermal upper-limit has been also expressed in many technical and safety case reports such as Wersin

et al (2007), King & Watson (2010), Karnland et al (2011), Holton et al (2012). Higher temperature testing was implemented as a comparative study to see if any significant alterations started to occur once beyond the 100°C boundary under the time scale imposed by the experimental study. These higher thermal loading scenarios along with the use of more complex electrolytic solutions were considered necessary for experimental exploration. It is widely thought that higher temperatures may succeed in yielding potential alterations that would naturally occur over geological time-scales at lower temperatures due to the activation energies involved. The purpose of running the preliminary batch tests was to provide an initial insight into the potential adverse alterations to the MX-80 Bentonite under variable exposure scenarios. The initial preliminary batch tests conducted at 20°C and 100°C were carried out to aid the development of the interface tests by investigating the most significant experimental boundaries. The alterations were measured with respect to the geomechanical and physicochemical properties and compared to the “unaltered” material properties (See section 4).

The experimental conditions were varied to gain a broad spectrum of situational circumstances. All pilot batch samples, except for batch #3, could free swell upon hydration with no volumetric constraint imposed. Generally, most pilot batch tests were only exposed to the experimental variables for a duration of 1-month, however batch tests 5- 9 were either run for 4, 12 or 24 months respectively. This was to gain a profile of the effects of thermo-chemical exposure and duration. Ultimately, the primary experimental variables in the batch tests were electrolytic concentration and composition, compaction state, the presence of Fe(0) in the form of a C-Steel coupon (80mm diameter) and thermal loading and duration (Figures 83-88). Table 20 reports the details of the respective batch tests and the associated experimental boundary conditions.

Table 20: Pilot batch test details

Batch No.#	Batch	Test conditions
1	<u>Saline profiling batch tests</u> Batch ref: (SalineSolutions-Mx80-20)	-x1 Control with x5 increasing saline concentration solutions (for NaCl, KCl and CaCl respectively) -Duration 1 month -Temperature: 20°C - Liquid solid mass ratio: 10 after Guillaume (2003)
2	<u>Steel- Comp Clay-Saline batch tests</u> Batch ref: (S-Mx80-NaCl-Comp-20)	-x1 Control with x4 increasing saline solutions -S275 steel compacted into Bentonite blocks: target dry density: 1.56Mg/m ³ -Duration: 1 month -Temperature: 20°C

		- Liquid solid mass ratio: 10 after Guillaume (2003)
3	<u>Steel- Comp Clay batch tests</u> <u>Batch ref:</u> (S-Mx80-Comp-105)	-x3 Samples compacted to a dry density of 1.56 Mg/m ³ at 27% moisture -S275 steel -Distilled water -Sealed batch cells and hydrostatic conditions -Duration: 1 month -Temperature: 105°C
4	<u>Steel- Uncomp Clay-NaCl batch tests</u> <u>Batch ref:</u> (S-Mx80-NaCl-Uncomp)	-x1 Control with x4 increasing saline solutions -S275 plate in contact with uncompact clay -Duration: 1 month -Temperature 20°C - Liquid solid mass ratio: 10 after Guillaume (2003)
5	<u>Thermal loading and duration tests (No C-Steel/ No Salt)</u> <u>Batch ref:</u> (Mx80-HT/D)	-x3 Controls with x3 samples per thermal load (20°C, 50°C, 70°C, 90°C, 110°C, 150°C, 200°C, 230°C, 300°C for 24hrs duration) -x3 Controls with x3 samples per thermal duration (1 day, 4 days, 1 week, 2 weeks, 4 weeks, 8 weeks, 12 weeks at 105°C) - Liquid solid mass ratio: 10 after Guillaume (2003)
6	<u>Thermal loading and duration with high saline solution tests (No C-Steel)</u> <u>Batch ref:</u> (MX80-HT/D/HS)	-Powder batch tests - Batch#1: x3 samples per thermal load each with NaCl, KCl, CaCl and a synthetic groundwater solution mix (20°C, 100°C and 150°C for 8 Wks) - Batch#2: x3 samples with CaCl and synthetic groundwater solutions respectively per thermal load (80°C and 100°C for 8 and 12 weeks) - Liquid solid mass ratio: 10 after Guillaume (2003)
7	<u>Steel/ Bentonite/ Saline under very high thermal loading tests</u> <u>Batch ref:</u> (S/Mx80-HT/D-HS)	-x6 batch samples exposed to (x3) 20°C and (x3) 150°C for 4 months, each sample varying the boundary conditions i.e. Steel/ clay with DI Water, Steel/ clay with synthetic groundwater, Clay/ synthetic groundwater and Clay with DI water - Liquid solid mass ratio: 10 after Guillaume (2003)
8	<u>1-year steel/ Bentonite interaction tests</u> <u>Batch ref:</u> (1yr-S-Mx80)	-x6 batch samples steel/clay interface interaction under ambient thermal loading -x3 with DI water for 1 year at 20°C -x3 with NaCl 0.45 for 1 year at 20°C - Liquid solid mass ratio: 10 after Guillaume (2003)
9	<u>2-year steel/ Bentonite interaction tests (No Saline Solution)</u> <u>Batch ref:</u> (2yr-S-Mx80)	-x3 batch samples steel/clay interface with DI water for 2 years at 20°C - Liquid solid mass ratio: 10 after Guillaume (2003)



Figure 83: Batch test #1 (x1 month saline batch tests), MX-80 in contact with increasing saline solution (left to right) no volumetric constraints

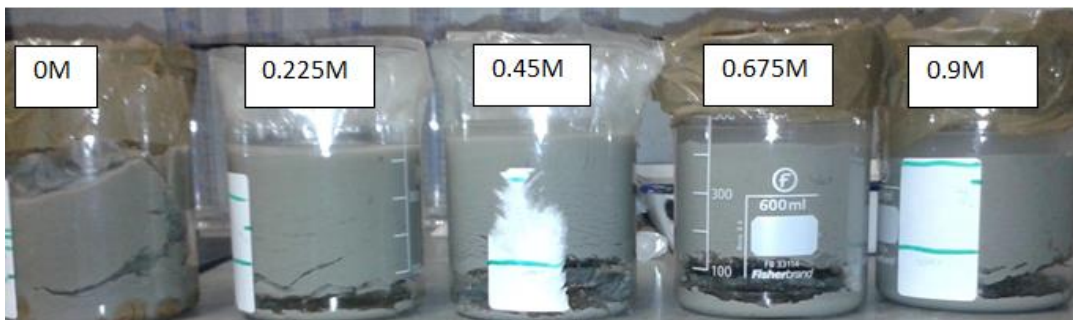


Figure 84: Batch test #2 (x1 month Steel/Mx-80 & increasing saline solution), compacted with no volumetric constraints



Figure 85: From Batch test #3 (x1 month Steel/Mx-80 & increasing saline solution), C-Steel plate in contact with uncompact Bentonite



Figure 86: From Batch test #4 (x1 month Steel/Mx-80 & distilled water), compacted and heated to 100°C within a constant volume cell



Figure 87: From Batch test #5 (x4 months), Synthetic groundwater batch test set up for 150°C, right; distilled water+ steel coupon, left; Synthetic groundwater+ steel coupon



Figure 88: From Batch #6 (Steel/Mx-80 & distilled water), C-Steel plate in contact with uncompact Bentonite at 20°C for 1 year

After completion of the THC exposure, the samples were processed and prepared for the allocated post testing protocol for geomechanical and physicochemical testing (Table 21 for post testing allocation for the respective batch samples as well as sections 3.7 and 3.8 for

geomechanical and physicochemical post exposure testing protocols). Salinity concentrations for the first two Batch tests were increased in increments of 0.225M. The saline concentrations used were 0.225M, 0.45M, 0.675M and 0.9M. This was used to achieve a spread of results over a large range of salinities. Guillaume et al (2003) used a mass ratio of 10 in their research, and this mass ratio was adopted in some of the abovementioned batch tests for an analogous examination.

Table 21: Pilot batch test post analysis details

Batch No.#	Post exposure testing
1	<ul style="list-style-type: none"> • Atterberg limits • Swell index
2	<ul style="list-style-type: none"> • Atterberg limits • Swell index
3	<ul style="list-style-type: none"> • Atterberg limits • Swell index • CEC
4	<ul style="list-style-type: none"> • Atterberg limits • Swell index • CEC
5	<ul style="list-style-type: none"> • Atterberg limits • Swell index • CEC
6	<ul style="list-style-type: none"> • Atterberg limits • Swell index
7	<ul style="list-style-type: none"> • Atterberg limits • Swell index • XRD
8	<ul style="list-style-type: none"> • Atterberg limits • Swell index • XRD
9	<ul style="list-style-type: none"> • Atterberg limits • Swell index • XRD

Batch tests 6 & 7 used a synthetic groundwater composition derived from the borehole data presented by Manning et al (2007), as given in Figure 89. The data represents a groundwater chemical analysis taken from the Eastgate borehole, County Durham, UK (Easting: 395500 and Northing: 538500). Na^+ , K^+ and Ca^{2+} was selected to keep the synthetic composition simple. However, by introducing a more complex groundwater other than just NaCl it is possible to see more comprehensive alteration characteristics, with or

without the presence of C- steel. These cations were chosen due to the dominance within this type of ground water. A comprehensive thermal range has been chosen with the same liquid/mass ratio as the previous preliminary batch tests using distilled water and NaCl. Table 20 displays the experimental boundary conditions for the synthetic groundwater batch test. Each salt concentration was obtained from the relative concentrations presented in Figure 89 and are given in terms of concentration in Table 22. These pilot batch samples are used for comparative analysis with the simplified interface and constant volume Batch tests, to investigate the physicochemical characteristics when introducing a more complex inorganic electrolyte solution. A groundwater composition relative to a crystalline rock environment was chosen within this study, this was primarily due to the experimental study keeping in line with the KSB-3V concept as well as the likelihood for emplacement within a crystalline host rock within the UK. It was recognised that other groundwater compositions that are representative of other host rock types would be beneficial for scientific investigation from a research point of view, the project was required to keep in line with the requirements of the consortium interests. Furthermore, due to time constraints it was not feasible to obtain real groundwater samples from the Eastgate borehole and therefore key cations were chosen to replicate the groundwater via the elemental analysis provided by Manning et al (2007).

Sample:	E21	E22	E23	E24	E25	E26	E27	E28	E29	E29A	E30	E31
Date (2004):	8/10	19/10	27/10	28/10	29/10	2/11	6/11	9/11	25/11	30/11	1/12	2/12
Depth (m):	335	411.5	485	561	590	674	725	770	847	910	951	995
Temperature (°C):	19.2	26	24.5	26	25.5	26.2	26.6	26.5	26.6	26	27	-
Cond. (field) ($\mu\text{S cm}^{-1}$):	26010	181000	181200	188900	190100	279600	210903	221014	212000	215000	239000	-
pH:	6.9	6.2	6.4	6.4	6.3	6.4	6.4	6.4	5.8	5.9	6	6
Cond. (lab) ($\mu\text{S cm}^{-1}$):	23210	65400	65700	66200	66500	66800	63200	64000	65800	66500	66200	65200
Alkalinity:	130	60	56	56	58	54	56	50	54	58	47	56
Nitrate	<5	<5	<5	<5	<5	<5	<5	<5	<5	<5	<5	<5
Chloride	9486	28750	25840	26970	25660	28560	25730	25700	28400	30000	31200	27800
Sulphate	255	48.5	52.2	44.7	46.9	47.8	68	69	41.2	44.3	43.4	45.3
Bromide		140	140	150	160	140	140	130	160	150	150	140
Ammonium		11	-	-	-	-	-	-	11	12	11	11
Calcium	1595	5285	5256	5424	5345	5250	5410	5620	5312	5375	5264	5009
Magnesium	28.6	72.4	71.9	72.8	72.1	73.1	68.9	69.1	79.2	79.2	78.2	75.3
Sodium	3333	9630	9580	9940	10000	9790	9930	9940	10100	10300	11000	10100
Potassium	201	631	642	646	667	656	782	551	689	708	646	638
Iron	<0.1	0.4	<0.1	0.1	<0.1	<0.1	<0.1	<0.1	<0.1	<0.1	<0.1	<0.1
Manganese	4	20.3	19.1	18.3	19.8	17.6	21.5	22	19	18.7	19.4	19
Zinc	<0.1	<0.1	<0.1	<0.1	<0.1	<0.1	<0.1	<0.1	<0.1	<0.1	<0.1	<0.1
Copper	<0.1	<0.1	<0.1	<0.1	<0.1	<0.1	<0.1	<0.1	<0.1	<0.1	<0.1	<0.1
Lead	<0.2	<0.2	<0.2	<0.2	<0.2	<0.2	<0.2	<0.2	<0.2	<0.2	<0.2	<0.2
Lithium	30.7	90.6	91.7	93.2	93	93.5	92.8	94.8	94.3	91.3	91.3	89.5
Silicon	5	6	4	4	3	3	6	4	5	4	5	6
Strontium	103	343	344	352	350	353	304	313	311	315	313	305
Barium		12.9	13.6	12	13	13.3	12.5	14.7	13.8	12.3	12.2	11.5
Charge balance (%)	-7.0	-5.6	-0.5	-1.0	1.5	-4.8	1.4	1.8	-3.4	-5.3	-5.8	-3.5

Figure 89: Groundwater elemental analysis taken from the Eastgate borehole, highlighted indicates ions used, equivalent to 995m BGL (Manning et al, 2007)

Table 22: Calculated salt concentrations for a crystalline rock mass at 995m BGL

Salt	Concentration (Molar)
NaCl	0.34
KCl	0.135
CaCl ₂	0.017

All batch Batch tests (excluding batch 3) were run within pyrex glass beakers and sealed to prevent excess moisture evaporation for the duration of exposure. These tests did not maintain constant volume conditions on the specimen but did allow observations to be made

on the interactions between corrosion products and the Bentonite as well as high salinity solutions on the clays intrinsic geotechnical and physicochemical properties. Heated Batch tests were either conducted within the constant volume batch cell or heated within a pyrex beaker on a hot plate (as displayed in Figure 87).

3.2. Carbon steel/ Bentonite interface experimental study:

Carbon-steel/ Bentonite interface tests were implemented to observe the corrosion precipitation dynamics and mineralogical changes within the localised zone. Namely the first 0~ 10mm from the carbon steel- compacted Bentonite interface under key environmental phases. The environmental boundary conditions derived from literature are outlined in Table 23. Each specific experimental condition was run for a 4-month THC exposure period and a total of three phases were complete within 12 months. The duration of each experimental phase was deemed to be the longest feasible exposure time due to the time constraints of the project. This indicates that the analysis may not yield results that would be entirely comparable to a system that has been exposed to the near-field parameters over a geological timescale i.e. 1000 to 10000-year period. Nonetheless the experimental data can give an understanding of the interaction between the near-field conditions and the engineered Bentonite barrier, and thus allowing an extrapolative understanding of the potential alteration output.

Table 23: Experimental matrix for interface replication tests inferred from Landolt et al (2009), Holton et al (2012) and Hicks et al (2009)

Phase 1- Initial conditions (Replicating emplacement -> 50 yrs.)	Phase 2- Mid-life conditions (Replicating 50 yrs. to $\times 10^4$ yrs)	Phase 3- Late-life conditions (Replicating $\times 10^4$ yrs +)
<ul style="list-style-type: none"> • Temperature (Maxima)= 100°c • Duration: 4 Months <p><u>Initial barrier parameters</u> <u>(Emplacement):</u></p> <ul style="list-style-type: none"> • Dry density: 1.56Mg/m³ • Moisture content: \approx 23% • Degree of saturation \approx 98% <p><u>Inferred replication state:</u></p> <ul style="list-style-type: none"> • Partially saturated progressing to initial dry phase (Aerobic) • Atmospheric pressures present 	<ul style="list-style-type: none"> • Temperature \approx 80°c • Duration: 4 Months <p><u>Inferred replication state:</u></p> <ul style="list-style-type: none"> • Dry progressing to Saturated conditions (Aerobic to Anaerobic): oxygen consumption used in additional corrosion of the coupon. • Saturation of sample progressing hydrostatic conditions maintaining constant dry density: final moisture content corresponding to \approx99-100% (Sr) (24% moisture) • Development of reducing conditions upon saturation • NaCl solution (0.45M) 	<ul style="list-style-type: none"> • Temperature (Minima)\approx 35°c • Duration: 4 Months <p><u>Inferred replication state:</u></p> <ul style="list-style-type: none"> • Saturated/ anaerobic conditions • System hydrostatic conditions using high salinity water (NaCl- 0.45M)

The experimental protocol used inferred near-field environmental phases obtained from industrial synergy and leading international research (RWM ltd, Landolt et al, 2009, Hicks 2009 & Holton et al, 2012). An outline of the interface environmental phases derived by Landolt et al (2009) as illustrated in Figure 20, section 2.1.1. The Bentonite interface samples were obtained from the blocks provided by SKB and were machined to fit the cells designed for the steel- Bentonite T-H-C exposure, Figure 90. The samples provided were in a compacted near-saturated state; this is not representative of the early stage emplacement conditions. Bentonite sample dimensions were 80mm in diameter and 11mm in depth, total depth of the interface cell was designed to be 20mm. Therefore, the steel coupons were machined to be 80mm diameter and 9mm deep to make up the remaining depth difference (see Appendix for full cell design). The interface sample was situated within a stainless-steel cell for structural stability and a PTFE lining for chemical isolation. Figures 91-94 depicts the interface schematic, dimensions and Bentonite phase relationship for the barrier for emplacement to the long-term physical states. Figure 93 displays the overall experimental concept. The figures illustrate the use of the interface cells and were designed to withstand a combination of internal swelling pressure, hydrostatic pressure as well as being operational under elevated working temperatures. The carbon steel coupon was machined from a structural beam to fit the interface cell, groves were machined into the rear of the coupon, this was to aid the flow of water through the Bentonite and past the coupon to replicate the groundwater flow within the EBS interface.

During the initial cell set up and calibration, seal integrity was observed to be malfunctioning. Subsequently, a series of pressure/ volume tests were conducted to locate the leak, after retrofitting new sealant seal integrity testing was repeated to ensure no leakage. The tests were also conducted under temperatures that the interface cells would experience during the main testing. Ultimately, the cell seal integrity was fully achieved by using Viton® O-rings with additional three bond gasket seal around the connections and interfaces to ensure that the internal system was completely isolated. Viton® type O-rings were chosen due to their high temperature rating, low compression index and high chemical resistance. Complete cell integrity testing details and post-repair seal integrity details are outlined within the Appendix.



Figure 90: Pre- compacted Bentonite block supplied by ClayTechAB®, used in the interface exposure experiments

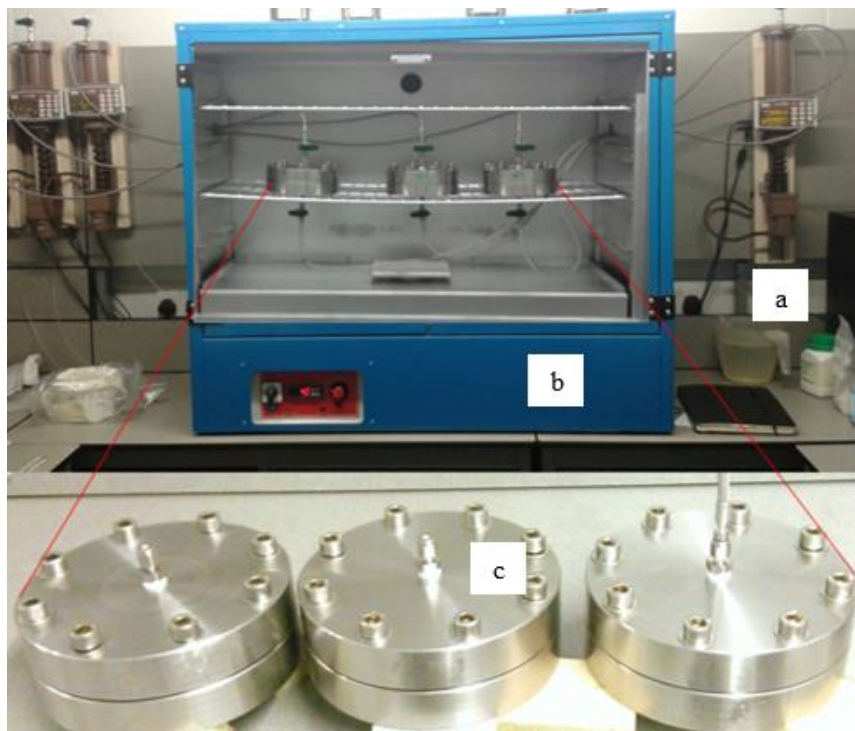


Figure 91: Steel- Bentonite interface experimental configuration for THC exposure, a) Pressure volume controllers for induced hydraulic gradient, b) Thermostatically controlled oven, C) Stainless steel interface cells that accommodate the Bentonite- carbon steel coupons

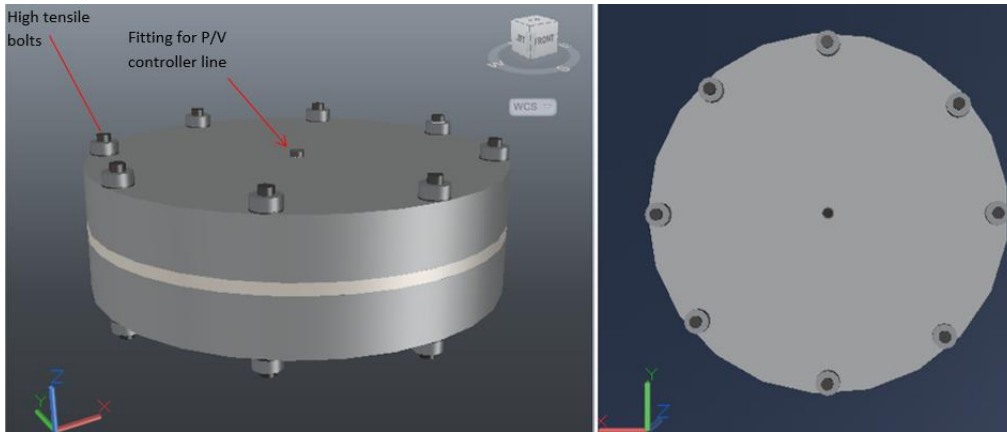


Figure 92: 3D concept of the interface cell

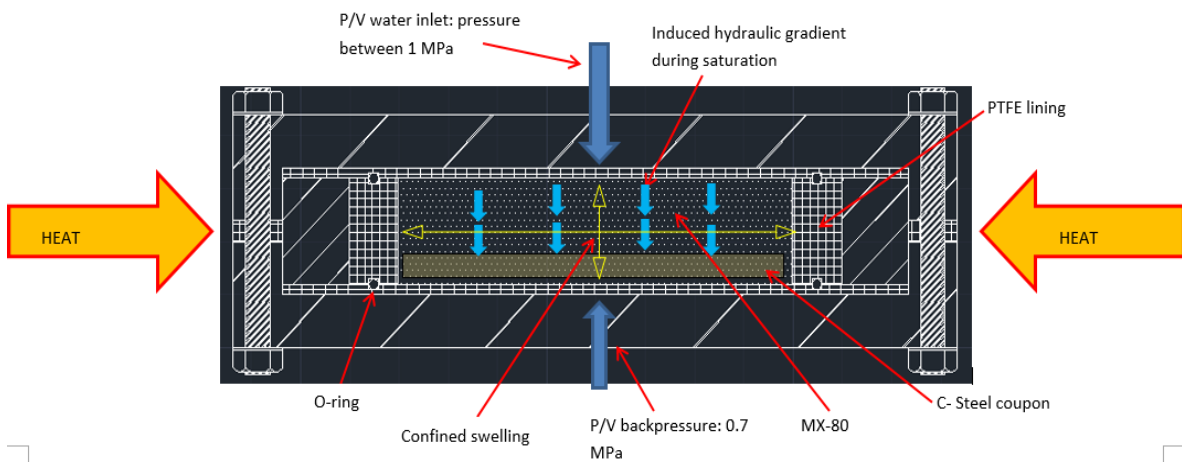


Figure 93: Fully annotated schematic of the interface concept

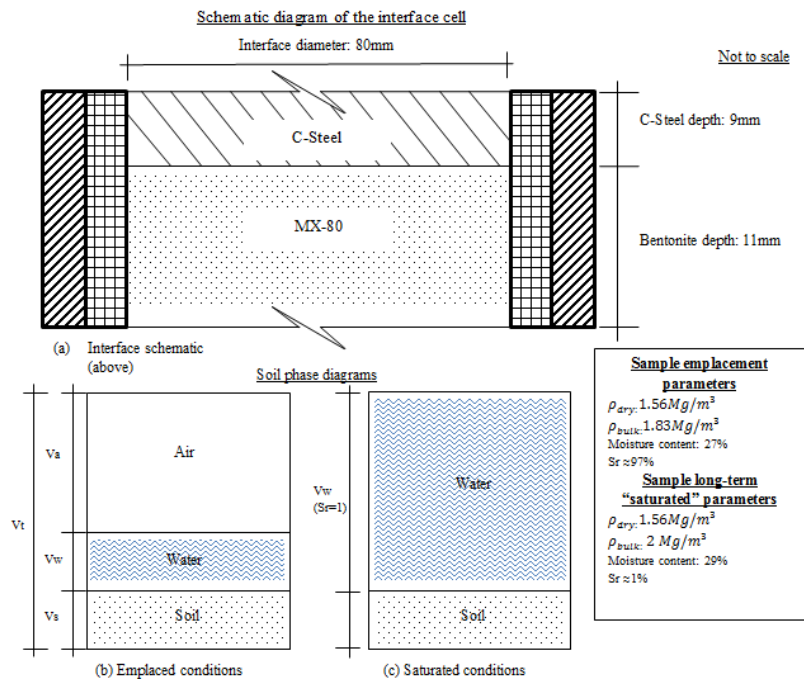


Figure 94: Bentonite physical phase state representative of early to long-term conditions. (a) Interface schematic, (b) "Early-life" emplaced conditions and (d) "Late-life" saturated conditions

Peak temperatures have been restricted to 100°C as this correlates with other UK leading research in the field of geo-waste disposal (Holton et al, 2012 and Wilson et al, 2015). The steel used as a representative canister interface material is the structural grade S275 C-steel, the general compositional analysis given in Table 24. The corrosion state of the steel was dependent on the life-phase being replicated i.e. using the coupon from the previous phase to ensure surface conditions are as close as possible to the initiation of mid & late-life phases respectively. The hydraulic pressure used for saturation of the Bentonite was 0.3 MPa, this pressure was chosen as it should not have a negative effect on the mechanical properties of the clay i.e. density and swelling capability of the Bentonite (BGS meeting 2013, J. Harrington).

Table 24: Elemental composition of the S275 grade steel (Source TataSteel @, 2015)

Grade/ composition	C%	Mn%	P%	S%	Si%
S275	0.25	1.6	0.04	0.05	0.05

Interface post-mortem and sub sampling was conducted within a nitrogen (n_2) purged glove box, Figure 95. This was done to preserve any unstable Fe^{2+} bearing minerals/ ferrous oxi- hydroxides that have formed under the interface replication phases. The interface Bentonite samples were separated into sub-sampled zones of visible corrosion precipitation for further post physicochemical analysis. This enabled a geotechnical and physicochemical profile to be generated for the respective phases over the entire depth of each interface sample. By doing so, it was possible to see the extent of corrosion and/ or temperature exposure effects to the Bentonite and if mineralogical and mechanical alteration was evident.

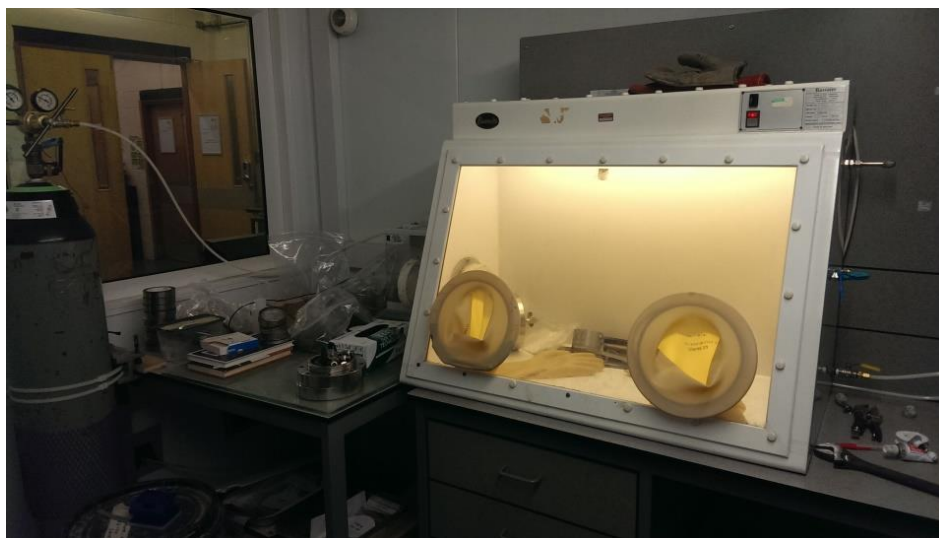


Figure 95: Nitrogen purged glove box for interface sub- sampling and post testing sample allocation

Allocated post analysis tests included quick geotechnical tests as well as comprehensive physicochemical analysis. Table 25 displays the post testing conducted on each sub- sampled zone from the respective phase allocation (See sections 3.7 and 3.8 for detailed methodologies for the geomechanical and physicochemical post analysis tests). Furthermore, post analysis of the C-Steel coupon surface via SEM-EDX for surface analysis as well as semi-quantitative elemental analysis was conducted.

Table 25: Post THC exposure testing allocation for the interface samples

Thermo-chemical interface tests
<p><u>Geotechnical measurements:</u></p> <ul style="list-style-type: none"> • Swell index • Atterberg limits <p><u>Physicochemical analysis:</u></p> <ul style="list-style-type: none"> • XRD • CEC • Digestion + absorbance spectrophotometry • Mossbauer • ICP-AES • SEM

3.3. Constant volume experimental structure and post analysis test methodology:

The constant volume batch experiment investigated how Fe-corrosion products relevant to S275 C-steel, elevated temperature and high salinity solution (NaCl: 0.45M) may induce geomechanical performance alterations to the Bentonite under prolonged time scales. Overall, 12 Oedometer sized samples were used in the constant volume batch test series (Figure 96). The cell confined the Bentonite within a sealed environment; the sample was refrained from changing in volume. Each test underwent 4 months of thermo-chemical exposure. The cells comprised of stainless steel outer walls with a PTFE inner lining to ensure that the sample does not interact with any external corrosion from the stainless steel etc. (Figure 97). To maintain a sufficient seal between interfaces the use of ThreeBond® (Type TB1207B) gasket sealant was applied around the outer edge prior to cell closure. This make is a silicon based, non- acidic, solvent free compound with a fast cure time as well as high temperature resilience, thus making this ideal for a sealant for the experimental cells as minimal interaction will occur between the Bentonite and the sealant. Table 26 displays the batch test Batch tests with the experimental conditions outlined.

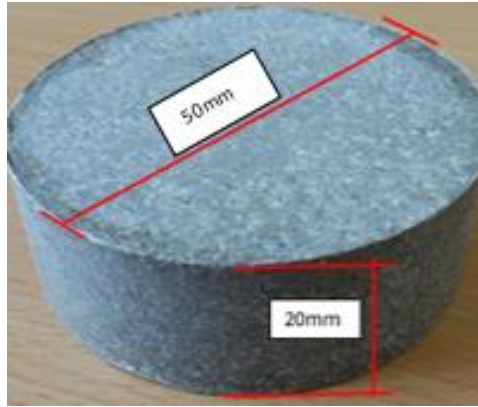


Figure 96: Constant volume batch sample dimensions



Figure 97: Constant volume batch thermo exposure cell

Table 26: Constant volume (CV) batch experimental boundary conditions, all batch tests were exposed to a thermal limit of 680°C for x4 months

<u>CV#1</u>	<u>CV#2</u>	<u>CV#3</u>	<u>CV#4</u>
<u>Control specimen</u>	<u>NaCl pore water Batch sample</u>	<u>Corrosion + NaCl pore water batch sample</u>	<u>Corrosion batch sample</u>
$\rho_{dry}: 1.56Mg/m^3$	$\rho_{dry}: 1.56Mg/m^3$	• 2mm Layer of Fe_2O_3 and Fe_3O_4 + compacted Bentonite	• 2mm Layer of Fe_2O_3 and Fe_3O_4 + compacted Bentonite
$\omega=27\%$	$\omega=27\%$	Fe/MX80 mass ratio 0.1	Fe/MX80 mass ratio 0.1
Sr \approx 97%	Sr \approx 97%	$\rho_{dry}: 1.56Mg/m^3$	$\rho_{dry}: 1.56Mg/m^3$
Distilled water	Saline solution 0.45M (NaCl)	$\omega=27\%$	$\omega=27\%$
		Sr \approx 97%	Sr \approx 97%
		Saline solution 0.45M (NaCl)	Distilled water

A temperature of 80°C was chosen for the 12 batch Batch tests, in line with the peak mid-life temperature from the baseline assumptions for current UK wastes and the near-field

evolution temperatures in the NAGRA report (Landolt, 2009). It is thought that the saturated, latter part of the mid-life phase, should have significant pore water evolution due to the presence of corrosion products and ingress of high-saline ground water. Additionally, any alteration is more likely to occur under higher temperatures due to the acceleration of reaction kinetics, supported by the abundance of literature stating the alteration significance at high temperatures (Mueller von-moos et al (1990); Karnland et al (2011); Wilson et al (2015); Pusch (2010); Ishidera et al (2008); Bildstein et al (2006); Fernandez & Villar (2010); Wilson et al (2010) et.). Therefore, 80°C was chosen as this is the highest predicted temperature of the saturated phase in the UK concept, carried forward from the derived interface evolution phases. Studies have however suggested that development of chlorites and significant illitisation will probably be more prevalent at higher temperatures of $\geq 150^{\circ}\text{C}$. Furthermore Schlegel et al (2008) highlighted that smectite destabilisation is also more likely to occur at higher temperatures ($\geq 150^{\circ}\text{C}$). However, this study looked at the realistic thermal exposure range.

Post exposure tests conducted on the constant volume batch tests are given in Table 27: these batch tests focused exclusively on the geomechanical tests. Section 3.7 provides details about the geomechanical post testing protocol.

Table 27: Post THC exposure testing allocation for the constant volume batch samples

Constant volume batch sample post analysis tests
<p><u>Geotechnical measurements:</u></p> <ul style="list-style-type: none"> • Swelling pressure measurements • Swelling kinetic measurements • Rheological testing

3.4. Thermal loading and Duration experiments:

A set of powder batch tests were conducted with the aim of isolating the effects of elevated thermal loading and elevated thermal duration on the intrinsic engineering parameters of the MX-80. The experimental protocol did not use the Bentonite as would be found in-situ. This instead used a powder form to measure intrinsic geomechanical alterations over a range of temperatures and durations. Simple geotechnical tests were implemented for post analysis of these samples as means of a fast determination of any adverse alterations. For the thermal exposure testing, eleven bulk powdered samples were exposed to temperature loadings of 20°C, 50°C, 70°C, 90°C, 110°C, 130°C, 150°C, 170°C, 190°C, 210°C and 230°C. Three samples were heated to each respective temperature and exposed for 24 hours

before being cooled to room temperature prior to post testing allocation. As for the thermal duration testing, seven bulk samples were exposed to a predetermined elevated temperature (105°C) with varying periods of thermal exposure. The periods of exposure were 1 day, 2 days, 1 week, 2 weeks, 4 weeks, 8 weeks and 12 weeks. Testing details are summarised within Table 28 as well as the allocated post exposure measurements.

Table 28: Powdered batch test matrix

Batch	Exposure details
Thermal loading (Powdered)	<ul style="list-style-type: none"> • 1-day exposure • 33 samples (500g / sample) • Temperatures used: 20°C, 50°C, 70°C, 90°C, 110°C, 130°C, 150°C, 170°C, 190°C, 210°C and 230°C
Thermal duration (Powdered)	<ul style="list-style-type: none"> • 1 day, 2 days, 1 week, 2 weeks, 4 weeks, 8 weeks and 12 weeks' exposure • 21 samples (500g/sample) • Temperature: 105°C

The powdered samples were mixed to 17% moisture using deionised water, replicating the initial moisture state of the clay blocks according to SKB, Börjesson (2010). Then they were placed into large drying trays, labelled and allocated to the respective oven for thermal exposure or duration. Once the samples had undergone their thermal/ duration cycle the samples were prepared for the geotechnical post-tests, three repeats were conducted per test, a summary of the post testing conducted is detailed within Table 29.

Table 29: Post exposure geotechnical tests

powdered batch sample post analysis tests
<ul style="list-style-type: none"> • Atterberg limits • Swell Index

3.5. Thermal loading, duration and high salinity pore water experiment:

As stated in section 3.4 additional powder batch tests were conducted to focus on the effect of combined thermal exposure and duration, however this batch test investigated the presence of additional salts in the Bentonite clay matrix was considered. These tests were also implemented to investigate the characteristic geotechnical properties of the MX80 after thermal exposure and duration with additional inorganic salts. The tests composed of powdered samples, similar to those stated previously in section 3.4 with the addition of salt solutions making up the initial moisture (17%) content prior to drying. The salt concentrations were obtained from ground water analysis of Eastgate borehole from Manning

et al (2007) as displayed in Figure 89. This section includes two sets of batch tests profiling the effects of inorganic salts on the consistency, swelling capacity, swelling kinetics and swelling pressure of the MX-80.

The first test investigated the range of salts, given in Table 30, at the concentrations obtained from the Eastgate borehole over temperatures of 20°C, 100°C and 150°C for duration of 8 weeks. Post testing analysis consisted of Plasticity index and swell index measurements, ultimately obtaining swell potential and consistency profiles over varying temperatures in the presence of individual inorganic salts, the testing matrix is presented below in Table 30.

Table 30: Batch test #1: Thermal loading and electrolyte exposure at Eastgate concentrations

Temperatures	20°C, 100°C & 150°C
Duration	8 Wks
Salt/ concentration (M)	NaCl/ 0.34 CaCl ₂ / 0.017 KCl/ 0.135

The second test initially aimed to profile the effects of the chosen salts (Table 31) by increasing salinity concentration and measuring the plasticity index in ambient conditions, ultimately obtaining a Plasticity index vs. salt concentration profile. Then from the measured profiles the salt that most significantly impacted the Bentonite at the reference borehole concentration was used in the main testing protocol. The main testing protocol consisted of three components 1) Bentonite/ salt exposure profiling, 2) powder batch tests and 3) constant volume tests.

1. Initial profiling of the effect of increasing salinity on the consistency characteristics of the Bentonite allowed insight into the salt that most impacts the Bentonite. Profiling was conducted through a series of batch tests at room temperature (20°C) for duration of 1 month, the batch samples were exposed to a range of salt solution concentrations respectively (Table 31).

Table 31: Batch test #2 part 1: Bentonite/ salt concentration profiling

Temperature	20°C
Duration	1 month
Salt/ concentrations (M)	NaCl, CaCl ₂ , KCl 0.225M, 0.45M, 0.675M, 0.9M
Post tests conducted	Plasticity index and Swell index

2. The powdered batch tests investigated thermal loading and duration as well as the effect of the chosen salt on the Bentonite (See Table 32). Using the chosen salt (Concentration given from the Eastgate borehole data) and an additional batch including a mix of all three salts I.e. the “synthetic groundwater”, formed the main powder batch tests.

Table 32: Batch test #2 part 2: Thermal loading and duration studies using synthetic groundwater and individual electrolytes

Temperature	100°C	80°C
Duration	8 & 12 Wks	8 & 12 Wks
Salt	Chosen electrolyte from profiling tests + synthetic groundwater mix*	Chosen electrolyte from profiling tests + synthetic groundwater mix*
Post tests conducted	Plasticity index, Swell index and XRD/CEC	Plasticity index and Swell index XRD/CEC

*See Table 31 for salts used in the study

3. The constant volume batch tests were run under “mid-life” conditions i.e. 80°C for the longest duration (12Wks) and used the synthetic salt mix comprising of the concentrations based on Eastgate borehole. The samples were mixed to 27% (reference moisture), and compacted into the CV cells (section 3.3) to the reference dry density ($\rho_{dry}: 1.56 Mg/m^3$). Once the samples had undergone the thermal duration the samples were transferred to the high-pressure odometer for swelling pressure measurements and then on to the modified shear box for rheological measurements. See Table 33 for the constant volume test matrix.

Table 33: Powder batch test #2: Thermal duration studies using synthetic groundwater in compacted Bentonite samples

Temperature	80°C
Duration	12 Wks
Salt	Synthetic groundwater mix*
Post tests conducted	Swelling pressure, swelling kinetics, Rheological measurements

*See Table 31 for salts used in the study

3.6. Bentonite compaction methodology:

The principal objective of the compaction tests was to achieve the target density based on the reference concept and RWM ltd suggestions. This was in order to understand the magnitude of compaction pressure required to compact the constant volume samples to the reference dry density. The Swedish SKB concept is currently one of the leading organisations in the field of geological disposal of nuclear waste of all levels. Therefore, this project and the other SAFE barriers consortium investigations based the barrier physical parameters

using similar initial conditions to enable future international synergy. Presented in Table 34 are the geomechanical boundary conditions, these were used when compacting the sample to replicate a specific phase. The pre-emplacment parameters are considered, at present, to be the most suitable based on the barrier storage and insitu safety functions respectively. The long-term parameters, used throughout the study, are used in interface and constant volume tests as the blocks provided by SKB were formed in this state and therefore compaction to replicate the blocks enable consistency throughout the experimental procedures. The inferred long-term parameters have been estimated on the basis that no erosion of the Bentonite will occur as well as the maintenance of constant volume conditions when insitu.

Realistically, there will be some deviation from the intended values due to “seating” during canister emplacement, as well as drying during the initial heating phase and swelling during resaturation, in addition to other anisotropic factors in the system.

Table 34: MX-80 block storage/ emplacement parameters and inferred long- term parameters (inferred from Borjesson, 2010)

<u>Constant parameters</u>	
MX-80 Specific gravity (Mg/m^3)	2.7
Density of water (20°C) (Mg/m^3)	1
<u>Barrier storage/ emplacement parameters</u>	
Porosity (n)	0.34-0.38
Void ratio (e)	0.52-0.63
Dry density (Mg/m^3)	1.56 ±0.05
Bulk density (Mg/m^3)	1.85
Moisture content (%)	17 ±2
Degree of saturation (%)	62
<u>Long- term parameters</u>	
Porosity (n)	0.41 – 0.44
Void ratio (e)	0.71- 0.8
Dry density (Mg/m^3)	1.56 ±0.05
Bulk density (Mg/m^3)	1.9 – 2
Moisture content (%)	27
Degree of saturation (%)	98-99

Initially the empirical formula from BS1377 Pt: [4] was used to obtain the dry densities corresponding to 10, 5 and 0% air voids. These were approximated by using the average particle density and a moisture content of 27%. Particle density values were obtained from Tang and Cui (2010) who gave a GS of $2.65Mg/m^3$, Lajudie et al (1996) gave a GS of $2.7Mg/m^3$, Sauzeat et al (2001) gave a GS of $2.65Mg/m^3$ and Madsen et al (1998) gave a GS of $2.76Mg/m^3$. Therefore, the resulting average particle density was

approximately $2.7\text{Mg}/\text{m}^3$, this was used for density calculations. The dry densities corresponding to the aforesaid phase relationship state were calculated using equation 10 and are displayed in Table 34 and 35.

$$\rho_d = \frac{1 - \frac{Va}{100}}{\frac{1}{\rho_s} + \frac{W}{100 \times \rho_w}} : \text{units} \left(\frac{\text{Mg}^3}{\text{m}} \right) \quad \text{Equ. 10}$$

where,

$\rho_d = \text{dry density (Mg/m}^3\text{)}$

$\rho_s = \text{particle density (Mg/m}^3\text{)}$

$\rho_w = \text{density of water; assumed to be 1 (Mg/m}^3\text{)}$

$Va = \text{the volume of air voids (\%)}$

$W = \text{the moisture content (\%)}$

Table 35: Dry densities at 27% moisture and corresponding air voids

Air voids (%)	Density (Mg/m ³)
10	1.411
5	1.49
0	1.57

Subsequently this gives an indication that full saturation at 27% moisture relates to a dry density of $1.57\text{Mg}/\text{m}^3$, hence if pressure exerted on the sample resulted in a density equal to or greater than this density then the pore water pressure will increase resulting in pore water being expelled. This then would indicate a deviation of the proposed initial moisture state and density range.

Tests were conducted to measure the compaction pressure needed to achieve the target dry density. These preliminary tests were conducted using the small Aggregate Crushing Value (ACV) mould and the Instron apparatus (Max permissible pressure of 55MPa, Fig 98). The initial pilot tests simply used an arbitrary mass of the Bentonite to compact. This enabled preliminary compaction pressures to be estimated. In order to establish a baseline limiting value of pressure to begin the compaction procedure, pressure magnitudes were obtained from literature that had previously conducted studies on the same or similar (i.e. Na-Bentonite) material. Villar et al (2009) and Madsen (1998) both state pressures in the range of 40 to 60 MPa to achieve the target density range chosen for their study. Villar et al (2009) states that compaction pressures up to 43 MPa at 16% moisture could achieve a nominal dry density of $1.7\text{Mg}/\text{m}^3$, as well as earlier studies by Madsen (1998) who presented a graph of a comparison between montigel and MX-80 bentonites at $\approx 8\%$ moisture (Figure 99).

Furthermore, it is well theorised that compaction is somewhat assisted by intra-pore water, mainly due to the lubricating effect it has between the soil particles upon the application of the major principle stress and the subsequent expulsion of air and the rearrangement of soil particles resulting in densification. That said, it can clearly be seen from Figure 100 that the pressure required to achieve the same nominal dry density is somewhat higher than that of Villar et al (2009), instead pressures of around 60 MPa were required. Therefore, the chosen moisture content for the SAFE barriers baseline study was $27\pm 2\%$ would therefore require less pressure to achieve the same nominal density of $1.56\text{Mg}/\text{m}^3$. The Instron apparatus compacted the first two pilot samples to its maximum permissible pressure, then by plotting the dry density vs. pressure graph and measuring the magnitude of rebound, the characteristics of the Bentonite were evaluated. All the samples observed for rebound were placed within a sealed environment at approximately $20^\circ\text{C}\pm 2^\circ\text{C}$; this was to prevent moisture loss and hence reducing the deviance in density due to drying or moisture uptake.



Figure 98: Compaction pilot test mould and Instron apparatus

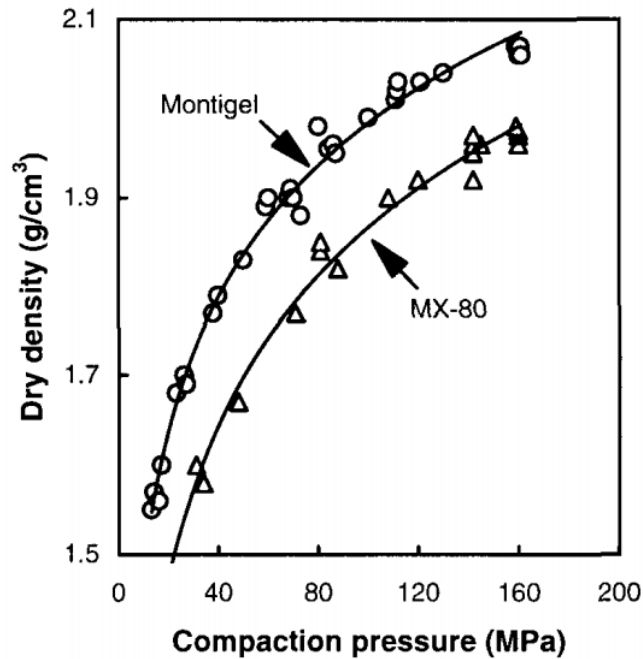


Figure 99: Dry density Vs. compaction pressure of two types of Bentonite at 8% moisture (After Masden et al, 1998)

The first four compaction tests were conducted at a moisture content of 27.3 % (after mixing and homogenisation). Initially an arbitrary mass was poured into the compaction mould and the piston placed with a maintained level surface, the initial dry densities of test #1 & #2, with only the self-weight of the piston acting over the sample area, was $0.992Mg/m^3$ and $1Mg/m^3$ respectively. The mould was placed onto the Instron apparatus and subsequently the sample was loaded in increments of 2kN per 10 minutes and held for 10 minutes per increment to observe any secondary compression. The two samples were loaded to 250KN, max permissible force exerted by the Instron, corresponding to a pressure of 55MPa. The samples were then unloaded in increments of 10KN with a rebound hold period of 5 minutes. The displacement was also measured by the Instron apparatus and hence the intrinsic density change at each loading stage was obtained. The immediate unloaded final dry densities of the samples (in-mould) after applying and holding at a peak pressure of 55MPa was approximately $1.84Mg/m^3$ and $1.83Mg/m^3$ respectively; corresponding to a degree of saturation near 100% (assuming no moisture was lost). Furthermore, 15 minutes after extruding the samples from the mould, the densities were $1.82Mg/m^3$ and $1.8Mg/m^3$ correspondingly. Hence indicating some stress relief rebound had occurred. After 15 minutes, test #1 specimen displayed a 1.4% height increase in comparison to the compacted in-mould final height. Consequently, test #1 specimen was left to oven dry for 4 days' due low permeability. The moisture content was measured to be approximately 27%, hence indicating

roughly a 0.3% difference between the initially measured moisture and the moisture after compaction. Hence indicating that some moisture was lost either during handling or more likely throughout compaction, similar results were also observed for the second test. Both tests #1 & #2 are displayed in figures 100 and 101 respectively.

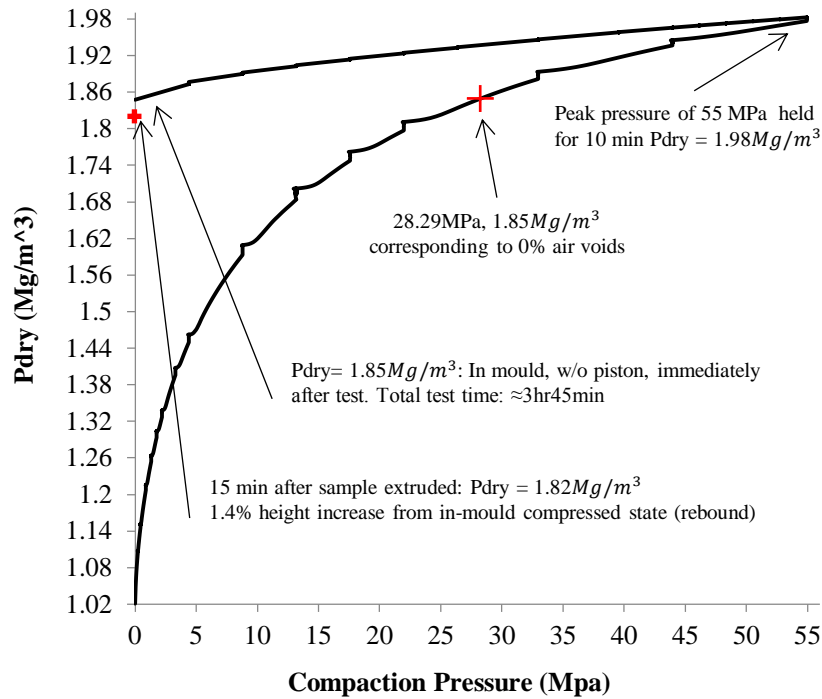


Figure 100: Test #1 of the pilot compaction tests, σ_1 : 55MPa

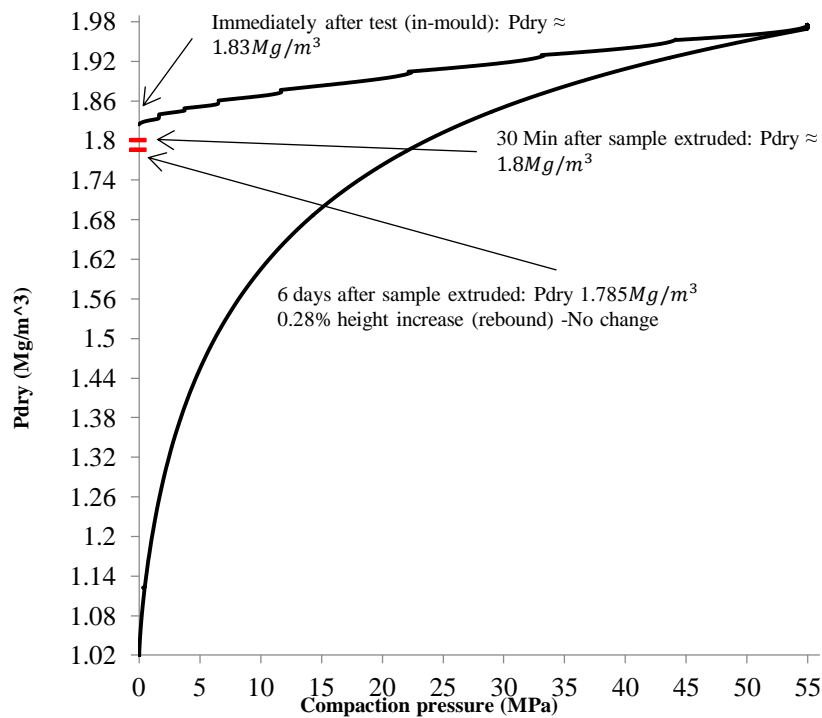


Figure 101: Test #2 of the pilot compaction tests, σ_1 : 55MPa

Specimen #2 in Figure 101 was left for 7 days to measure the rebound magnitude due to stress relief on the sample. After 6 days, the rebound stabilised resulting in a final dry density of $1.785Mg/m^3$, this rebound effect is perhaps due to the excess pore-water pressure generated by the very high compaction pressures and/ or elastic rebound of the soil grains. During the compaction procedure, the densities achieved greatly exceeded the theorised 0% air voids density. This resulted in rapid high pore-water pressure development, subsequent partial moisture loss (consolidation) and water viscosity alteration. However, due to the very brief application of such pressures, significant moisture loss because of the process of consolidation is negligible. Consequently, it was hypothesised that much lower pressures will generate the required target dry density range with reduced unpredictable rebound; hence test #3 was piloted. Using the power trend equations from tests #1 & #2 loading curves, displayed in equations [11] & [12] respectively, the average pressure predictions corresponding to a dry density of $1.56Mg/m^3$ were consequently used to conduct test #3:

$$\sqrt[0.113]{\frac{\rho_{dry}}{1.2544}} = \sigma_{max} (test \#1) \quad Equ [11]$$

$$\sqrt[0.117]{\frac{\rho_{dry}}{1.2248}} = \sigma_{max} (test \#2) \quad Equ [12]$$

The resulting pressure predictions obtained from equations were 7MPa and 8MPa respectively, therefore an extrapolated average peak pressure of 7.5MPa was chosen to test the hypothesis; the dry density vs. compaction pressure plot is displayed in Figure 102 for test #3. This shows that the initial inferred pressure achieved a density close to the intended target. The sample was then measured for rebound in the radial and axial geometries to the major stress over 7 days. Figure 102 illustrates that some rebound occurred immediately after unloading, which is expected due to creep effects, but the density did not deviate from the final extruded density after 15 minutes when measured periodically over four days.

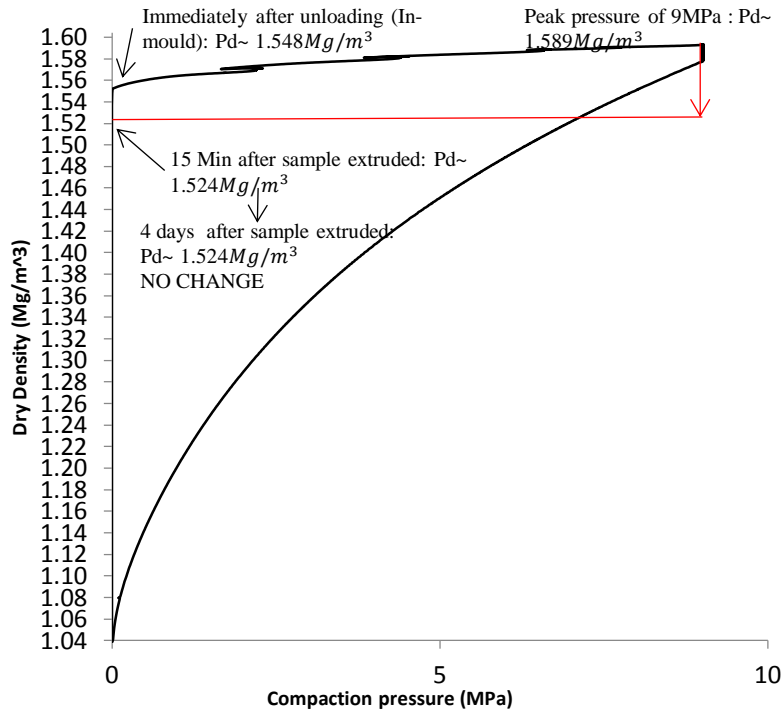


Figure 102: Test #3 of the pilot compaction tests, σ_1 : 9MPa

To obtain a comprehensive understanding of the rebound characteristics, it was necessary to run the fourth test to a much higher pressure than in tests 1, 2 & 3. It was decided to subject sample #4 to a maximum principle stress of 100MPa (Figure 103), a little higher than the pressures stipulated within Villar et al (2009) and Madsen (1998). Additionally, rebound was measured periodically to observe axial and radial displacement magnitudes until they stabilised (Figure 104 & 105).

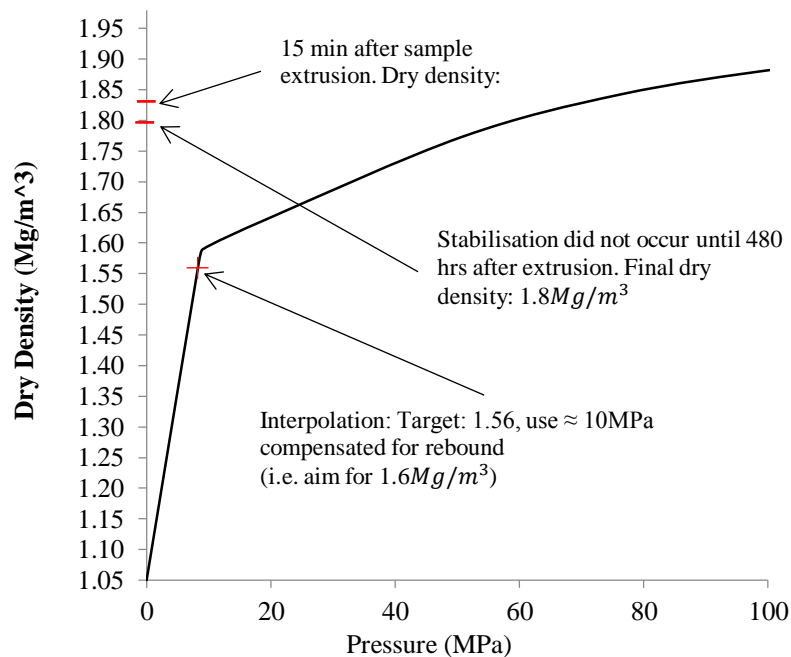


Figure 103: Test #4 of the pilot compaction tests, σ_1 : 100MPa

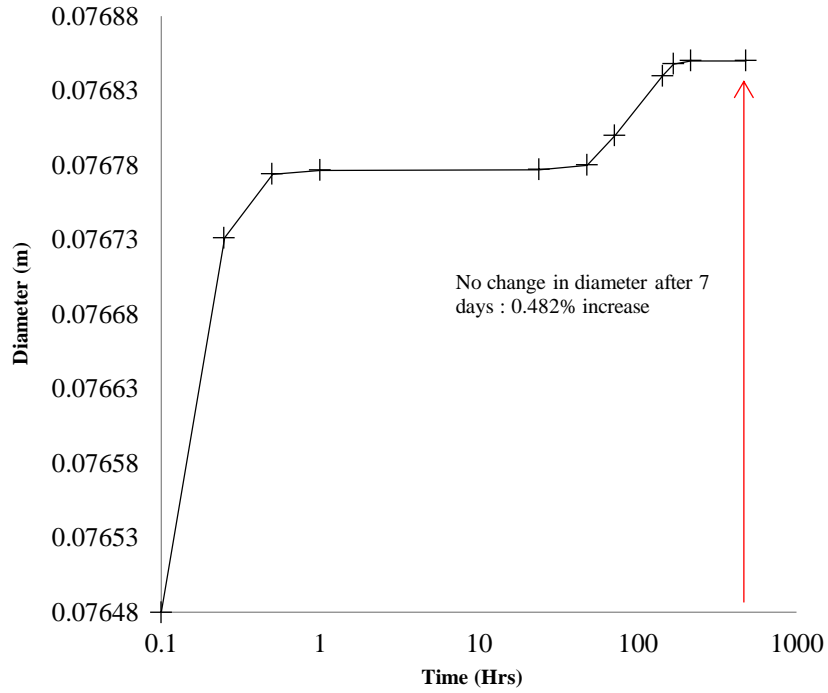


Figure 104: Measured rebound of sample diameter over 9 days after peak pressure of 100MPa

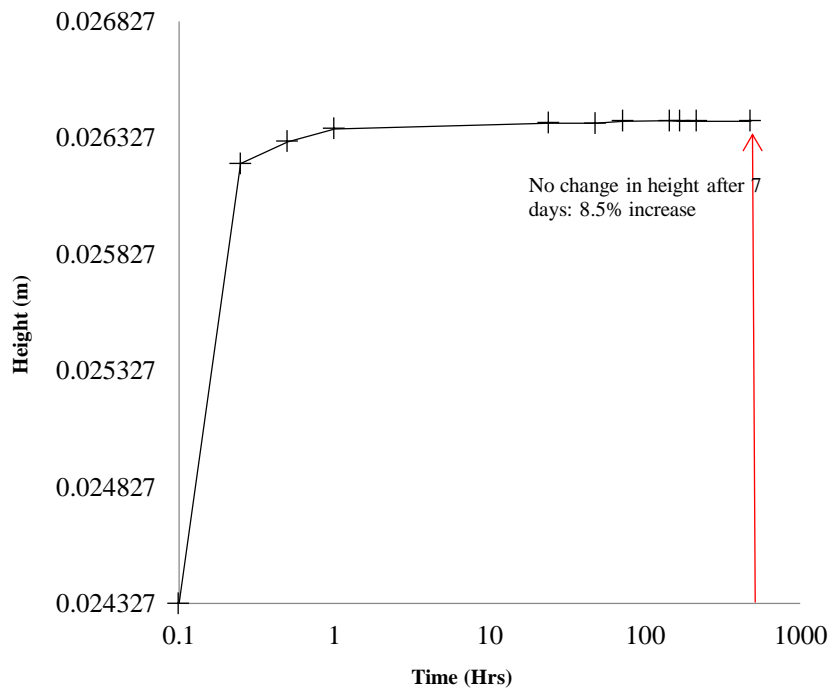


Figure 105: Measured rebound of sample height over 9 days' after peak pressure of 100 MPa

Rebound of the sample from test #4 was periodically measured in both the radial and axial directions. Since this sample had the greatest magnitude of pressure applied the rebound was predicted to be greater. As can be seen it was observed that axial rebound was

significantly larger than the radial rebound i.e. rebound perpendicular to axial loading (Figures 104 & 105).

Interpolation of the compaction pressures from test #4 were used in conjunction with trends from tests #1 & #2 respectively. This enabled a pressure range in which suitable densities should be achieved. The range in which it is deemed suitable and meets the criteria set out by the SKB concept is between $1.56\text{Mg}/\text{m}^3$ and $1.6\text{Mg}/\text{m}^3$. Therefore, using the power trends and interpolated values from tests #1, #2 and #3 correspondingly, gave a pressure range to compact future samples; minima and maxima pressures are given below:

Minimum pressure extrapolation: @27% + 1%

Equ [13]: @ $1.56\text{Mg}/\text{m}^3 = 7 \text{ MPa}$

Equ [14]: @ $1.56\text{Mg}/\text{m}^3 = 8 \text{ MPa}$

interpolated from test #4 = 8.3 MPa

∴ Average minima pressure $\approx 8 \text{ MPa}$ to achieve a dry density of $\approx 1.56 \text{ Mg}/\text{m}^3$

AND:

Maximum pressure extrapolation: @27% + 1%

Equ [15]: @ $1.6\text{Mg}/\text{m}^3 = 9 \text{ MPa}$

Equ [16]: @ $1.6\text{Mg}/\text{m}^3 = 10 \text{ MPa}$

Interpolated from test #4 = 10 MPa

∴ Average minima pressure $\approx 10 \text{ MPa}$ to achieve a dry density of $1.6 \text{ Mg}/\text{m}^3$

Therefore, the pressure range to achieve the target density is between 8MPa and 10MPa. Compensating for the effects of the stress rebound immediately after the test, by compacting the sample under 10MPa is deemed suitable. It was calculated that for a target density of $1.56\text{Mg}/\text{m}^3$ within the volume of an oedometer ring i.e. $\approx 20\text{mm}$ high and 50mm Ø, the required bulk mass of soil (at $27\% \pm 1\%$) is approximately 77.84g.

It is firmly established in soil mechanics that individual soil grains will display some crushing and elastic distortion during compaction as well as the pore water pressure increasing due to the compaction of soil grains as air is expelled i.e. S_r approaches 1. Hence, when the sample is loaded and unloaded relatively quickly, the granular elastic distortion and positive pore water pressure will need to equilibrate. Hence displaying some rebound in the samples geometry, nonetheless this is primarily due to the residual elastic rebound. To overcome this effect, however significant/ insignificant the magnitude of rebound may be, by holding the sample for a prolonged period should eliminate these effects. Providing the

pressure is kept low enough not to induce primary consolidation i.e. densities below the corresponding values of $S_r < 1$.

Through interpolation, a compaction pressure of $\approx 10\text{MPa}$ was found to be suitable to achieve a density range of $\approx 1.56 - 1.6\text{Mg}/\text{m}^3$, corresponding to $\approx 98\%$ saturation with minimal rebound during storage. Predominantly, rebound of the samples occurred at less than one week depending on the magnitude of pressure applied, the rapidity of the compaction and the excess pore water pressure generated when approaching saturation; greater rebound occurred in the direction of the axial pressure (σ_1). The tests that applied the highest pressures exceeded the saturation dry density at 27% moisture, therefore inducing slight moisture loss and/or greater unpredictable rebound. It is more than likely that the small rebound of the sample when compacted to $1.56-1.6\text{Mg}/\text{m}^3$ is due to the elastic recovery of the sample, including the intrinsic elastic recovery of the individual soil grains within the sample.

3.7. Geotechnical post testing methodologies:

The following section details the geotechnical post testing protocol as well as the conforming standards that were adhered to. All geotechnical post exposure tests were conducted at room temperature ($20^\circ\text{C} \pm 5^\circ\text{C}$) and followed the guidance of the British standards: 1377, or American standards: D5890.

3.7.1. Atterberg limits:

Atterberg limits were measured in compliance with BS1377 Pt: [2] and were conducted on samples post THC exposure at room temperature. Samples were dried, hand ground, passed through a $425\mu\text{m}$ sieve and re-mixed to consistencies using deionised water that meet the plastic limit and liquid limit sample requirements. The liquid limit measurements used approximately 300-400g (However less can be used depending on the amount of available material) of bulk material. The cone penetrometer apparatus measured penetration by measuring 4 penetration points over an increasing moisture range. Subsequently the line of best fit plotted through the points gave the liquid limit corresponding to 20mm of cone penetration. The plastic limit sample used approximately 10-20g of dry material, the sample was rolled into a 3mm thread until cracking occurred transversely and longitudinally, at which point the moisture content was determined, thus corresponding to the plastic limit. The difference between the two values gives the plasticity index (Equ 17) which is a measure of the range that a soil can take in moisture and still exhibit shear resistance as well as

volumetric change i.e. higher the PI the more expandable a clay is with an ability to resist shear stresses imposed over a higher moisture range. The liquid limit can also be used as indicator of the point at which the material has lost its shear strength ten-fold. The plasticity index can also be used with the sedimentation test results to measure the activity value proposed by Skempton (1953). A change in PI also indicates that the soil has altered its physicochemical state by alteration to the dominant interlayer cation and thus alteration to the DDL, or a layer charge alteration due to cation substitution and mineralogical modifications. All fundamentally affecting the soils ability to uptake and retain moisture while remaining plastic.

$$L_l - P_l = P_i \quad \text{Equ [17]}$$

where:

Ll= Liquid limit

Pl= Plastic limit

Pi= Plasticity index

3.7.2. Swell index:

Swell index measurements conformed to the American standards used for free swell volume measurements of compacted clay liners used in landfill applications D5890-11. The sample was dried in a thermostatically controlled oven at $105^{\circ}\text{C}\pm 5^{\circ}\text{C}$, hand ground in agate mortar and then a dry mass of 2g, passing $150\mu\text{m}$ was measured. To conduct the test a 100ml graduated cylinder- class A, with 1mL subdivisions, was filled with either deionised water or NaCl solution (depending on the test, relating to the samples experimental history) to the 90mL mark. Subsequently the 2g mass is added in increments of 0.1g over 10 minute intervals, allowing each mass increment to saturate and deposit to the bottom. Once all the mass is added the remaining 10ml is added, thus washing in any particles on the glass into the solution. The sample is allowed to free swell/ saturate over a 16-24 hr period, upon which the volume of the clay is measured in mL. The overall free swell index measurement is expressed as $\text{mL}/2\text{g} \equiv \text{cm}^3/2\text{g}$ of dry material.

3.7.3. Swelling pressure:

Swelling pressure measurements conformed to the BS1377 Pt: [5], the method used the constant volume method otherwise known as the zero-displacement method using the oedometer apparatus. Once the sample was taken from the constant volume THC cell, it was placed into the oedometer ring, 50mm in diameter, 20mm high. The sample is confined laterally by a rigid ring, with a porous discs positioned on the top and base of the sample allowing free water uptake, a loading platen is placed on the top disc which is in contact with the loading assembly. The loading method was dependant on the apparatus being used, both the manual (Fig. 106) and the automatic (Fig. 107) oedometer was used to obtain swelling pressure measurements (the latter being more accurate by eliminating human and some systematic error, namely deflection). The manual ELE25-0402 and the AOS GDS automated Oedometer were both used during testing. Both chosen for their high-pressure capabilities up to $\approx 8.8\text{MPa}$ (due to the swelling pressures anticipated from literature). The automated Oedometer allowed the testing completion rate to be increased due to the advantage of setting up and leaving the test run with no manual intervention. For the ELE25-0402 Oedometer the loading beam ratio was set to 11:1 to reduce the quantity of direct masses required. A total maximum load was calculated for the manual apparatus, the resulting load was $\approx 1.413\text{kN}$ equal to 15.54kN exerted on the sample at a ratio of 11:1. Therefore an applied maximum mass of 144kg was required to exert a maximum permissible pressure of 8MPa on the sample and within the safe working limits of the apparatus.

The theoretical principle between the two apparatuses is the same, apart from the manual loading aspect of the axial stress. The reaction force is applied to the top of the disc that is proportional to the axial swelling pressure. Ultimately, when the displacement is maintained at zero ($\pm 0.01\text{mm}$) and once the displacement becomes constant, after a 24hr period, the applied stress is in equilibrium with the axial stress exhibited by the soil. Therefore, the applied stress is known as the swelling stress of the soil mass within the ring. Elimination of systematic deflection must be eliminated when using the manual lever arm apparatus, therefore before running the tests a calibration stage must be conducted on an incompressible “sample”, therefore eliminating elastic systematic deflection with increasing mass. This calibration curve is used by subtracting from the displacement results and therefore reducing the systematic error. The automatic GDS AOES is a much more accurate and less time-consuming system, the swelling pressure is applied via a mechanical stepper motor, by having a load cell directly fed back into the system the oedometer cell itself is raised or lowered thus controlling its own axial stress. Two displacement transducers are used on the

automated system, one built in and one external RFM maintain the displacement to within ± 0.01 mm subsequently giving an instantaneous swelling pressure readout.



Figure 106: ELE manual oedometer apparatus

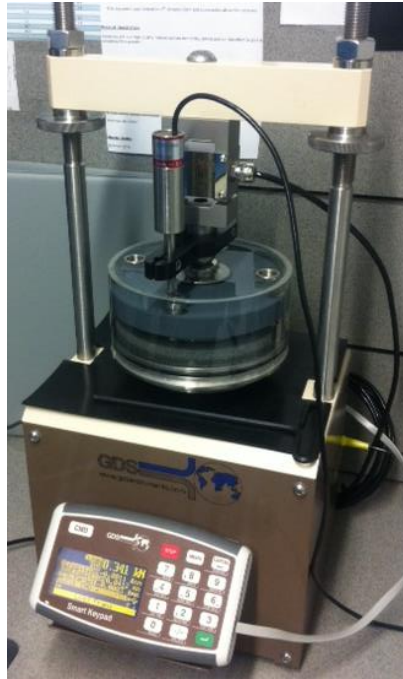


Figure 107: GDS AOES apparatus

Before commencing the swelling pressure tests, it was first necessary to calibrate the displacement read out and correct for system deflection for the manual ELE system, see Figure 108 for the systematic calibration graph. System calibration was not necessary for the automated system as the systematic deflection was minimal.

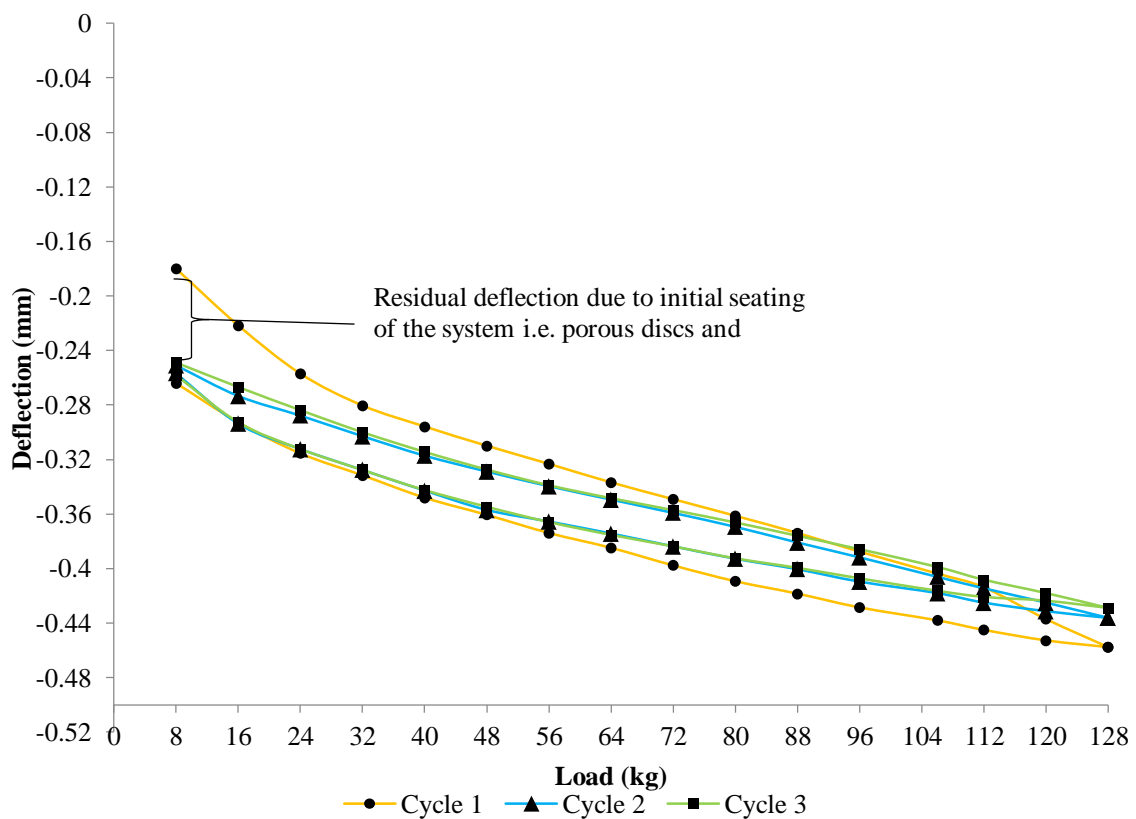


Figure 108: ELE oedometer calibration curves

From Figure 108 it can be concluded that the apparent residual deflection after unloading from the maximum load is fundamentally due to initial seating of the loading platen within the ring. Therefore, secondary and tertiary cycles were conducted to eliminate the seating deflections. Therefore, cycles 2 and 3 display the elastic hysteresis within the system.

3.7.4. Swelling kinetics:

Swelling kinetics is a measure of axial rebound i.e. how the sample can “bounce” back with a reduction in axial stress. This gives a rough indication of the materials ability to self-heal. There are no exact standards set out for the test to conform to, but the test was conducted on the automated GDS AOES oedometer designed to British Standard requirements. Once the axial swelling pressure was determined it was reduced by 10%, the subsequent axial strain was measured over 2.5 days. The gradient of the recovery curve indicates the swelling kinetics of the material i.e. the greater the gradient the faster the recovery mobilisation and hence a faster self-healing process.

3.7.5. Rheology:

Rheological testing was conducted on the automated ShearScan2, a direct shear box constructed by VJ Tech®. This apparatus was modified to allow for stress controlled tests required for rheological testing. A pulley system was fabricated to allow a stainless steel braided wire to be hung with a loading assembly for mass application (Fig. 109 & 110). The braided wire was attached to the horizontal load cell that attached to the shear box, this enabled a direct measurement/ readout of the force applied (Fig. 111). This direct readout of horizontal force enabled an instantaneous compensation of applied mass due to the loss over the pulley system. Once the sample was taken from the oedometer (post swelling pressure and kinetics) the sample was weighed and its dimensions were measured and then transferred to the direct shear box. A normal stress of 4MPa was applied and the sample was allowed to consolidate. After the displacement stabilised a stress increment of 20% of the materials ultimate shear strength was applied. This increment was run over a period of 48hrs measuring accumulated shear strain over time, the subsequent creep curves were obtained. The curves were used as a comparison to the control sample measurements as a proxy of sample stiffness i.e. any deviation from the control indicates that there is either a loss or increase in ductility. The low stress increments are considered low enough to measure the microstructural creep. Therefore, any precipitation of intra-particle cementitious compounds will be picked up by a lower accumulated strain after 48hrs.



Figure 109: Direct ShearScan2 with modifications



Figure 110: Fabricated pulley with loading assembly (Red arrows indicate direction of force)

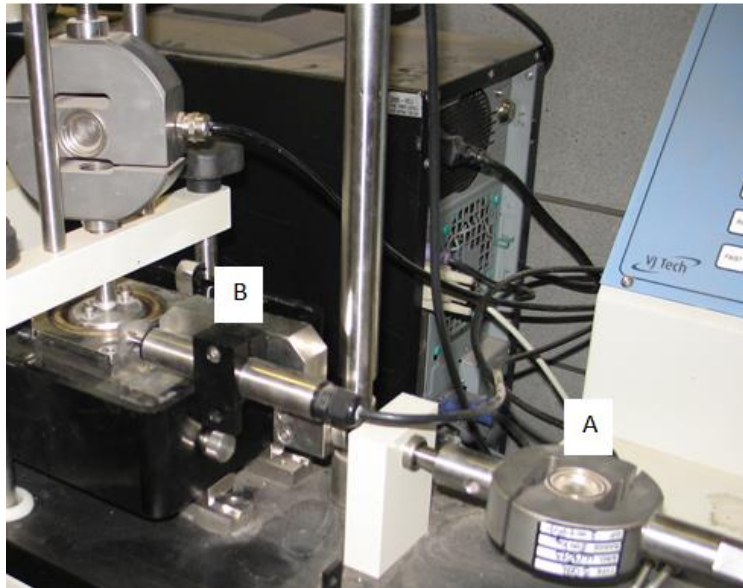


Figure 111: A: Load cell measuring applied force and B: Displacement transducer measuring sample creep

3.7.6. Permeability:

Permeability measurements were also determined using the consolidation curve from the shear-box data via the root time method, conforming to BS1377 PT: [5]. The consolidation stage of the rheology tests yielded characteristic consolidation curves (Fig. 112), therefore when plotted on a root time scale as well as knowing the physical parameters of the sample i.e. consolidation coefficient (C_v), coefficient of compressibility (M_v) and void ratio (e), it was possible to estimate the permeability. The following equations and method displays how the permeability was estimated:

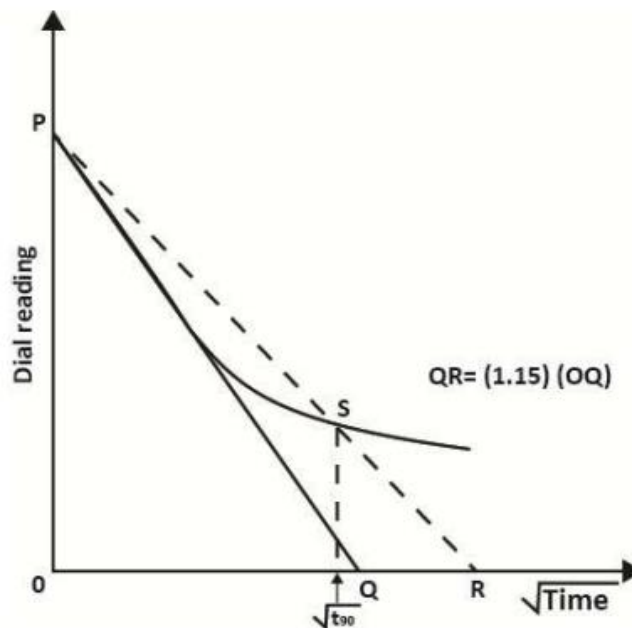


Figure 112: Consolidation curve on a root time axis displaying t_{90}

From the graph, the value corresponding to the linear part of the consolidation curve on the x axis:

$$R = 1.15 \times Q \quad \text{Equ [18]}$$

T_{90} was determined by the line PR intersecting the consolidation curve, with the corresponding value read off from the x axis. Then the consolidation coefficient (Cv) was determined by the following:

$$CV = \frac{0.848 \times d^2}{T_{90}} \left(\text{Convert units to } m^2/\text{yr}: \times \frac{1440 \times 365}{1 \times 10^6} \right) \quad \text{Equ [19]}$$

Where:

d^2 : is the length of the drainage path squared.

To obtain d, the average sample height (AvH) and change in sample thickness (ΔH) are required.

$$A = \frac{\Delta H}{2} + AvH \quad \text{Equ [20]}$$

Then,

$$d = \frac{A}{2} \quad \text{Equ [21]}$$

To obtain the coefficient of compressibility (Mv) the following equation is applied:

$$Mv = \frac{1}{1 + e_{Ini}} \times \frac{e_{Ini} - e_{fin}}{\sigma_{Ini} - \sigma_{fin}} \quad \text{Equ [22]}$$

Where:

e_{Ini} : Void ratio initial (before compression)

e_{fin} : Void ratio final (after compression)

σ_{Ini} : Initial stress increment

σ_{fin} : Final stress increment

Subsequently the parameters were then plugged into the permeability equation to obtain K (m/s) (Dividing by $60 \times 1440 \times 365 \times 1 \times 10^3$ to get correct units):

$$K = Cv \times Mv \times \gamma_w \quad \text{Equ [23]}$$

3.8. Physicochemical post testing methodologies:

The following section details the post THC physicochemical analyses conducted primarily on the interface tests as well as some batch tests. Most of these tests were conducted under their respective environmental conditions in the presence of a suitably trained laboratory technician.

3.8.1. Clay digestion, Fe^{2+}/Fe_{Tot} and Fe^{3+} quantification via UV absorbance spectrophotometry:

This method was employed to assess and quantify the abundance of Fe_{Tot} , ferrous (Fe^{2+}) and ferric (Fe^{3+}) cations within the interface sub-samples. The method has been extensively developed by many researchers, namely Stucki et al (1984 a,b,C) but further adapted by Neumann (2013). The method utilises the REDOX sensitivity of element Fe as well as the ligand 1,10 Phenanthroline employed to be used for the colorimetric indicator for Fe^{2+} within the HF digested clay solution. The addition of the 1,10 Phenanthroline to solution complexes to form a red/ orange coloured tris(1,10-Phenanthroline)- μ -oxodiiron(ii) and a transparent tetrakis(1,10-phenanthroline)- μ -oxodiiron(iii) (Stuki et al, 1984a, b, C). The UV absorbance conducted using a wave length of 512nm was measured and then compared to a set of standard solution concentrations of ferrous ethylenediammonium sulfate. With subsequent absorbance measurements allowing inference of solution concentration of Fe^{2+} and Fe_{Tot} . Two runs were conducted on each respective sample, one in the non-reduced “raw” state and the other in the totally reduced state, this enabled the measurement of Fe^{2+} and Fe_{tot} respectively. Ultimately the difference between the two inferred concentrations resulted in the quantification of Fe^{3+} . Reduction of the solutions can be achieved via two main methods, 1) by photochemical reduction or 2) chemical reduction using Hydroxylamine, the former being considered to be a much higher risk due to the handling of HF solutions within a darkened environment plus the reduction time is lengthy. Therefore, the chemical reduction method was employed (2) within this study; the method followed the protocol set out by Neumann (2013). Below is the test schedule for the digestion and Hydroxylamine reduction:

Test schedule for digestion/ UV adsorption experimental work

Samples run:

- In 125mL HDPE bottles
- x9 from interface tests (3 per phase) + x2 reference controls (SKB & RS)
Total: 11 samples
- To be run alongside the digestions are x5 standards plus x1 blank- **per run**
- **25-50mg** of solid material per digestion: Total mass of solid material used **275-550mg**

Standards- per run:

- In 125mL HDPE bottles
- Ferrous ethylenediammonium sulfate (FES) (**Total: 150mg**): for standards/ calibration in increments of 10mg, 20mg, 30mg, 40mg and 50mg (More concentrations can be used if higher proportions of Fe are expected within the samples.)

Digestion solution:

- In **250mL HDPE bottle** prepare total volume of digestion solution
- **12mL** Sulfuric acid (10%)- per sample
- **2mL** 1,10 Phenanthroline - per sample
- **1 mL** HF concentrate- per sample
- Total volume per sample **15mL**
- Total volume required for interface and control samples: **165mL** (additional volumes dependant on number of runs i.e. practice runs, standards and blanks)

Neutralising solution:

- **10mL** Boric acid (5%)- per sample (Total for interface and control samples: **110mL**)
- Total for standards and blank: **60mL**

Reducing agent:

- 1% Hydroxylamine

Buffer:

- 1% Sodium Citrate

Additional additives:

- **50mL** of DIW per sample (Total of 850ml)

Note: Once the digestion is complete the solutions are sub- divided into two for Fe^{2+} and reduced Fe_{Tot} determination (See Table 36).

- Samples are split into 30mL HDPE bottles
- So, number of samples double: **22 in total** (Without standards and blanks)

Table 36: Fe^{2+} and Fe_{Tot} sample allocation

<u>Fe (ii)- 30mL HDPE bottle /sample</u>	<u>REDUCTION- Fe (Tot) 30mL HDPE bottle /sample</u>
10ml Sodium Citrate (1%) + 1mL Digestion solution	10mL Sodium Citrate (1%) in (1%) Hydroxylamine + 1mL Digestion solution

To ensure that the active Hydrofluoric acid is made inert the samples were mixed with sulfuric acid, post digestion. Once the solutions are left overnight they are then immediately transferred to cuvettes and inserted into the UV-Vis spectrophotometer, model Genesys 10s by thermo-scientific, for absorbance measurements under a wavelength of 512nm (See Figure 113). The concentrations are obtained through regression analysis using the calibration curves obtained from the standard solutions.



Figure 113: UV-Vis spectrophotometer (Image courtesy of Thermo-Scientific, 2016)

- **Calibration:**

The standard samples and the blank were run under the same protocol as defined for the digestion of the sub-samples, above. These standard solutions of ferrous ethylenediammonium sulfate were used to produce concentration/ absorbance plots, used to infer the abundance of Fe^{2+} and Fe_{tot} within the interface sub-samples. Stucki et al (1984) states that 8.7mg of ferrous ethylenediammonium sulfate approximate to $1\mu\text{g Fe/ mL}$ from spectrometric measurements. Stucki et al (1984) expresses the formula to calculate the nominal concentrations of Fe^{2+} and Fe_{tot} in the ferrous ethylenediammonium sulfate standard solutions, given in equ [24].

$$C_{STD} = \frac{(1 \times 10^6 \times W_{STDsample} \times AW_{Fe})}{(EW_{FES} \times F \times V_{dig})} \quad \text{Equ [24]}$$

where:

C_{STD} : Nominal concentration in standard solution ($\mu\text{g/mL}$)

AW_{Fe} : Atomic weight of Fe (55.847g/mol)

EW_{FES} : Equivalent weight of the FES standard (both Fe^{2+} and Fe_{tot} in g/mol)

F: Are the appropriate dilution factors for Fe^{2+} and Fe_{tot} determinations respectively

V_{dig} : Final volume of digestate (mL) - Calculated from Equ [25]

The dilution factors for the Fe^{2+}/Fe_{tot} samples are determined from measured net masses and densities of the digestates, also including the masses and densities of the 1% citrate solution or 1% citrate in 1% hydroxylamine sulfate solution.

$$V_{dig} = \frac{(GW_{acid} - (TW + W_{sample}))}{\rho_{acid}} + \frac{W_{BoricAcid}}{\rho_{BoricAcid}} + \frac{W_{H2O}}{\rho_{H2O}} \quad \text{Equ [25]}$$

where:

GW_{acid} : is the gross mass of the bottle after sample and acid matrix has been added (g)

TW: is the bottle mass (g)

W_{sample} : Mass of the soil sample (g)

$W_{BoricAcid}$: Mass of the 5% boric acid solution (g)

W_{H2O} : Mass of the DI water (g)

ρ_{acid} : Density of the acid matrix (g/mL)

$\rho_{BoricAcid}$: Density of the 5% boric acid solution (g/mL)

ρ_{H2O} : Density of the DI water (g/mL)

Note: The density of the total digestate is determined from the net mass and volume.

The calibration is conducted by regression of the nominal standard concentrations vs. observed absorbance (A_{Std}), this is then used to obtain values for the slope (m) and the intercept (b) for each analysis stage i.e. Fe^2 and reduced Fe_{tot} . The concentration values for the sub-samples ($C_{SampleDil}$) (those including the digested soil) are then calculated for their respective REDOX stages from the observed absorbance values (A_{Sample}) using the following equation [26]. The regression values used are determined corresponding to the analysis type i.e. sample REDOX state.

$$C_{SampleDil} = m \times A_{Sample} + b \quad \text{Equ [26]}$$

The wt.% of Fe (C_{Sample}) (either Fe^2 or Fe_{tot}) present in the soil sub-sample can be determined using the concentration values $C_{SampleDil}$ ($\mu\text{g Fe/mL}$). The sample dilution factor and volume of digestate used in Equ [27] corresponds to each individual sample.

$$C_{Sample} = \frac{(C_{SampleDil} \times F \times V_{dig})}{(1 \times 10^4 \times W_{sample})} \quad \text{Equ [27]}$$

3.8.2. Mössbauer procedure:

Mössbauer is becoming a more common method of Iron speciation and a phase identification tool for clay researchers the principles have been explored and set out by many (Murad, 1987, 1988, 1998; Murad et al, 1990; Randcourt, 1998; Stucki, 2006; Neumann, 2013). The method required the analysis of several parameters, isometric shift, quadrupole shift and the magnetic hyperfine parameters to identify the presence and phase of the iron (hyd)roxides. Stucki (2006) provides an example of the identification of iron (hyd)roxides within smectitious clay using the Mössbauer spectrum, Figure (114 and 115). The difficulty associated with the analysis is that clay is an aggregation of several minor constituent minerals with a phyllosilicate matrix i.e. the clay is rarely monomineralic in nature. This is

the case with many physicochemical techniques that attempt to quantify singular component within a highly heterogeneous material.

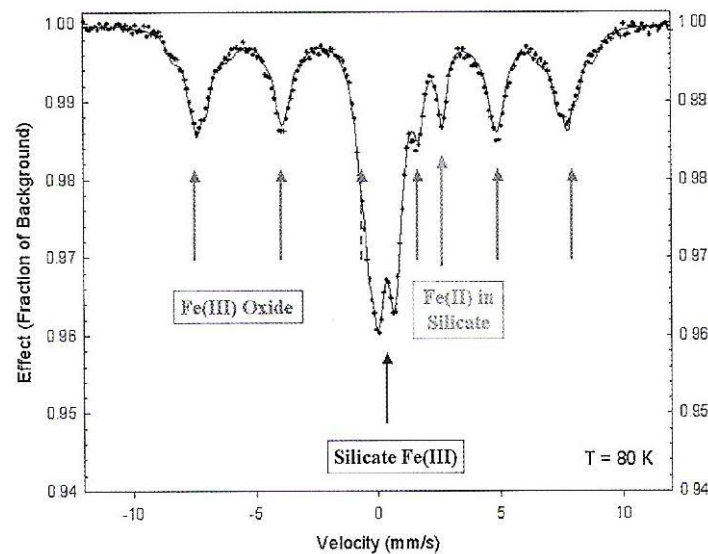


Figure 114: Mössbauer spectra for a saprolitic soil containing Fe oxides within the clay matrix and within the structure Stucki (2006)

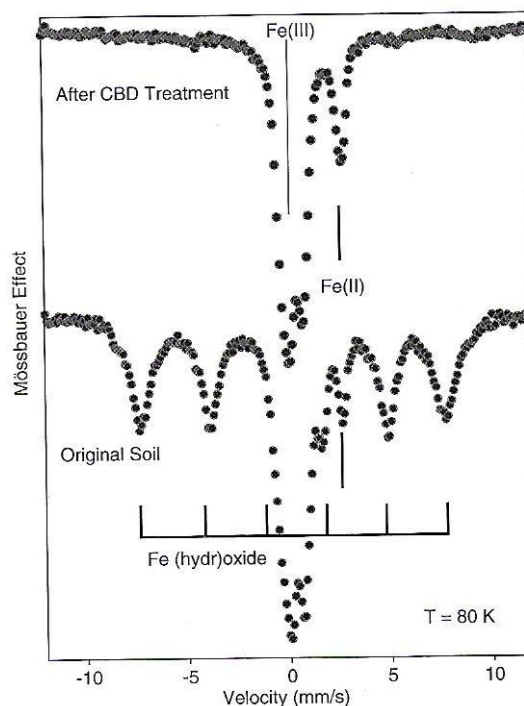


Figure 115: Spectra before and after “washing” of the interlayer oxides Stucki (2006)

Figure 115 shows that (Hyd)roxides are identified by the sextet formation with the silicate iron doublet occurring around 0.3mm/s, with an additional peak at 2.2mm/s. Magnetically ordering the iron within iron (Hyd)roxides is achieved by lowering the temperature to almost absolute zero (-273.15°C). By doing so it is possible to distinguish between structural Fe^3 and Fe^2 . Also, identification of the Fe^2 peak at a larger quadrupole

split at $\approx 3.5\text{mm/s}$ can be concluded to be predominantly basal bound Fe^{2+} . Moreover, it is possible to isolate the structurally located cis- and trans-octahedral/ tetrahedral Fe from the (Hyd)roxides through chemical “washing” known as the CBD method (Citrate-bicarbonate-dithionite), highlighted in Figure 116. However, the washing process is likely to alter the Fe phase state, an unwanted result in REDOX sensitive analysis. On the contrary, this “washing” can give an insight into the integration of Fe into the octahedral or tetrahedral sites from the external system, therefore differentiating between the extent of alteration due to the increased Fe presence in the system and the unaltered specimen. Washing of the sample is conducted by repeated mixing and centrifuging of CBD solution with the supernatant being taken after each run.

3.8.3. CEC procedure:

The Cation Exchange Capacity (CEC) is a method widely used in soil analysis to measure the materials ability to retain positively charged ions i.e. Mg^{2+} , Ca^{2+} , K^+ , Na^+ etc. In the case of the engineered barrier around the HLW/ SF canister this determines the potential to retain/ sorb radionuclides from potential leachate. Cations are electrostatically held within the interlayer of the clay platelets and are exchanged by replacing power of the lyotropic series. The method used in this study was the barium chloride method to ISO 11260- standardised in 1994, initially proposed by Gillham (1979) and further modified by Gillham and Sumpter (1986).

- **Procedure:**

A representative sample of approximately 2.5g is taken, mixed with 30mL of 0.1mol/L $BaCl_2$ and shaken for 1 hour. The sample is then centrifuged and the supernatant is decanted and collected, the process is repeated two or three times with each supernatant being collected for the determination of the CEC. The soil is then equilibrated within a 30mL solution of 0.0025mol/L $BaCl_2$. The sample is once again shaken but in a 30mL 0.02mol/L of $MgSO_4$ two centrifuge runs are conducted at 2hrs and 12hrs respectively. The principle is that the adsorbed Barium (Ba^+) is exchanged with the Magnesium (Mg^{2+}) due to its replacing power, the resulting compound in solution is precipitated as Barium sulphate ($BaSO_4$). The concentration is determined through flame atomic adsorption spectroscopy and is subtracted from the initial content thus giving the CEC measured in $\text{cmol/kg} \equiv \text{Meq/kg}$.

3.8.4. ICP-AES:

Inductively coupled plasma atomic emission spectrophotometry (ICP-AES) is a common method used to determine elemental concentrations within solutions. The problem with soil analysis is that it is very difficult to dissolve the silicate structure and therefore hydrofluoric acid digestion was required to put all elements into solution. This therefore gives total elemental analysis and is difficult to differentiate between initial sites.

- **Principle and procedure:**

The principle behind the ICP-AES analysis is that each element has a characteristic energy gain and decay, thus returning to its original base state. Therefore, by exciting the atom to higher energy states and allowing it to decay the excess energy is given off by means of a photon with characteristic wavelengths. Isolation of the characteristic wavelengths can allow elemental identification and concentration determination within the solution. The sample solution is introduced into the plasma via a peristaltic pump and nebuliser, after which the elements are excited once entering the plasma. The plasma is produced by an ionised argon stream; the temperature profile of the plasma displayed in Figure (116). The samples chosen for elemental analysis was the sub-sampled interface specimens after post THC exposure as well as the two control materials.

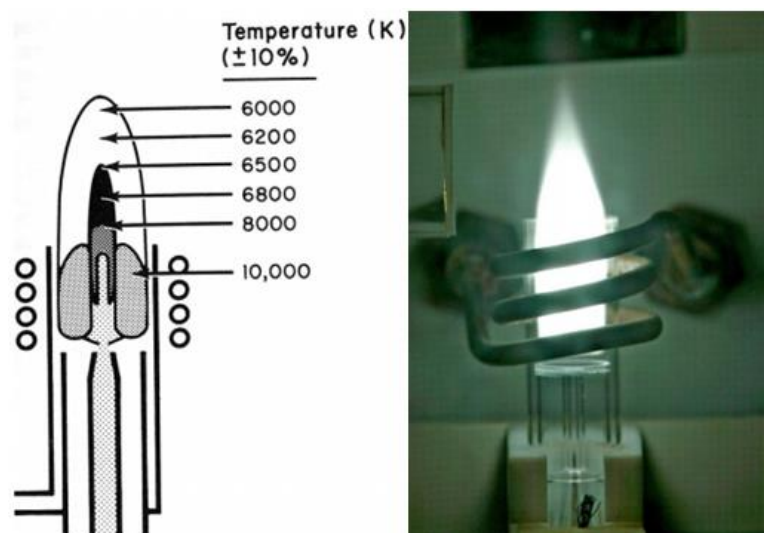


Figure 116: Ionised argon plasma jet and temperature profile at nebuliser outlet

The interior prism and echelle set-up separates the wavelengths into measurable emission sections. The different elements present will emit different wavelengths and intensities depending on the group i.e. alkali metals are generally weakly emitting whereas the earth metals are much stronger. Common problems are interfering spectra, matrix solutions and sample prep. Therefore, calibration runs were conducted using the elements chosen for the

analysis as displayed in Table 37. The matrix solution was stated to the operator prior to running the experiments as well as a blank sample i.e. just the matrix solution to negate the interference.

Table 37: Chosen elements for concentration profiling of the interface experimental samples

Elements chosen for ICP-AES analysis
Na
Mg
Ca
Si
Al
<i>Fe_{tot}</i>

To put the silicate into solution it was required that HF digestion was conducted, the procedure for digestion and neutralisation is set out below.

Test schedule for digestion for ICP-AES analysis

Samples run:

- x9 from interface tests (3 per phase) + x2 reference controls (SKB & RS)
Total: 11 samples run
- The solutions were digested within 250mL HDPE bottles

Digestion solution:

- In **250mL HDPE bottle** prepare total volume of digestion solution
- **12mL** Sulfuric acid (10%)- per sample
- **1 mL** HF concentrate- per sample
- Total volume per sample **13mL**
- Total volume required for interface and control samples: **143mL**
- **25-50mg** of soil mass per digestion (Total mass≈275mg- 550mg)

Neutralising solution:

- **10mL** Boric acid (5%)- per sample (Total for interface and control samples: **110mL**)

Remaining solution make up:

- **50mL** of DIW per sample (Total of 550mL)

Solutions to eliminate solution matrix effects during ICP-AES analysis:

- **100mL** of 10% Sulfuric acid
- **100mL** of 5% Boric acid

3.8.5. XRD preparation and procedure methodology:

X-ray powder oriented diffraction analysis is one of the most common practices in the analysis of crystallographic soil structures and subsequent determination of mineralogical species. XRD was employed as part of the physicochemical suit of tests due to the grain size of powdered MX-80, other optical methods are considered unsuitable for direct

observation. For the soil analysis the target metal used in the procedure was Copper (Cu), thus giving a characteristic radiation ($K\alpha$) with a specific wavelength (λ) of 0.154nm. A simplification of how this analysis works is displayed in Figure 117, this diagram is a common simplification to explain how the diffracted X-rays are then related to the mineralogical makeup of the material under question.

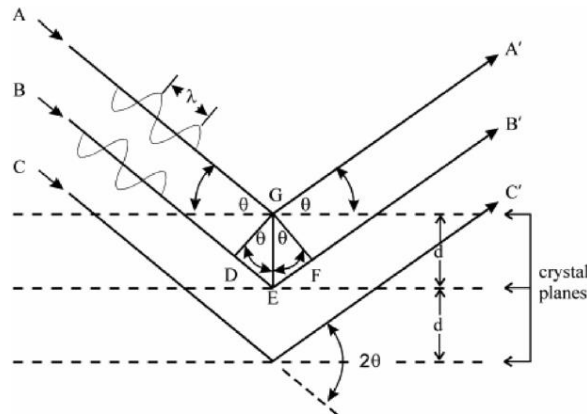


Figure 117: A simplification of a mineral structure with consistent spacing displaying the incidence X-ray and associated angle (after Moore and Reynolds, 1997)

From the simplification of the atomic schematic, Figure 117, depicts a simplified arrangement of crystal planes with incident X-rays and the resulting diffracted waves. Figure 118 indicates that the distance in between the crystal planes can be measured, this is achieved by the underlying principles of the Bragg equation (Equ. 28) obtained from Moore and Reynolds (1997).

$$n\lambda = 2d_{hkl}\sin\theta \quad \text{Equ (28)}$$

$$\therefore d = \frac{\lambda}{2\sin(\theta)} \quad \text{Equ (29)}$$

Where:

d: d- spacing (\AA)

2θ : Beam deviation ($^\circ$)

h,l,k: dimensional components for the lattice planes

n: an interger that represents higher order scattering (for MX-80 analysis 1 is assumed)

Therefore by solving for d (Equ.28) and using the wavelength relevant to the characteristic radiation and measured incident x-ray angles, the crystallographic d-spacings can be obtained. The angle used in the determination of the d-spaing was gained by observing the intensity over a range of angles, the peak intensity angles are therefore inputted into the Bragg equation. Using the mineral database the d-spacings are linked to the material under analysis. This method can be used as a tool in determining the mineral phases present in the bulk material as well as a direct measurement of the swelling ability of the clay. An example

of such databases are presented in Table 38. Nonetheless, despite the use of digital databases fitting candidate minerals to the d- spacings, an understanding of what the original material composition is and what the expected alteration minerals could be, greatly decreases the time needed for database searches and probable error.

Table 38: D-spacing database for common soil minerals, published by the international centre for diffraction data (Harris, 2007)

Mineral groups	Minerals	Major d-spacing's
Amphiboles	Hornblende	8.52, 3.16, 2.73
	Riebeckite	8.4, 3.12, 2.73
	Tremolite	8.38, 3.12, 2.71
Calcite	Aragonite	3.4, 1.98, 3.27
	Calcite	3.03, 1.87, 3.85
	Dolomite	2.88, 2.19, 1.8
Chlorites	Chamosite	7.05, 3.53, 2.52, 14.1
	Clinochlore	3.54, 7.07, 4.72, 14.1
Expandable phyllosilicates	Montmorillonite	18, 9, 4.49
	Vermiculite	14.4, 7.18, 4.79, 3.6
Feldspars	Albite	3.19, 4.03, 3.21
	Anorthite	3.20, 3.18, 4.04
	Microcline	3.24, 3.29, 4.22
	Orthoclase	3.31, 3.77, 4.22
Kaolin	Halloysite	10.7-10 (hydrated), 7.6, 4.4, 3.4
	Kaolinite	10, 3.33, 5
Mica	Muscovite	10.1, 3.37, 2.06
Oxides, hydroxides	Anatase	3.51, 1.89, 2.38
	Gibbsite	4.85, 4.37, 2.39
	Goethite	4.18, 2.45, 2.7
	Hematite	2.69, 2.59, 1.69
	Ilmenite	2.74, 2.52, 1.72
	Quartz	3.34, 4.26, 1.82
	Rutile	3.26, 1.69, 2.49
Phosphates	Fluorapatite	2.8, 2.7, 2.77
	Strengite	4.38, 5.5, 3.11
	Variscite	4.29, 5.39, 4.83
	Wavellite	8.67, 8.42, 3.22
Pyroxenes	Augite	2.99, 3.23, 2.95
	Enstatite	3.18, 2.88, 2.54
Serpentines	Antigorite	7.29, 2.3, 3.61
	Chrysotile	7.31, 3.65, 4.57
Sulfates	Epsomite	4.21, 5.35, 2.68
	Gypsum	7.56, 3.06, 4.27
	Jarosite	3.08, 3.11, 5.09
Sulfites	Marcasite	2.69, 3.43, 1.75
	Pyrite	1.63, 2.71, 2.43
Zeolites and related minerals	Anaclime	3.43, 5.60, 2.93
	Clinoptilolite	3.97, 8.99, 3.91
	Heulandite	3.92, 2.96, 8.85
	Palygorskite	10.4, 4.47, 4.2
	Sepiolite	12.1, 2.56, 4.31

Samples were subject to bulk and oriented scans. Bulk scans enabled the principle mineral identification and the oriented scans gave insight into the inter-lamella spacing after serval treatments. These treatments involved several steps to investigate the clays intrinsic shrink swell behaviour. After THC exposure, the selected samples were air dried where possible and gently hand ground within an agate mortar. Gentle hand grinding during preparation is encouraged because phase changes in the mineral present are more probable

when forceful grinding is conducted (Moore and Reynolds, 1997). Poor preparation can lead to crystallographic strain accumulation with subsequent broadening of the XRD line. Moore and Reynolds (1997) state “[Aggressive hand grinding can lead to] the production of X-Ray amorphous material”. A disadvantage of XRD is that non-clay aggregates within the sample will mask the clay peaks if present in large quantities, such minerals are quartz, feldspars, gypsum, pyrite, zeolites and Fe. One possible disadvantage of using a Cu as a source metal is given in Moore and Reynolds (1997), the fluorescence of Fe could be problematic by producing a high background noise. Hence, smaller peaks are potentially masked and a method of overcoming this is using a monochromator in the beam path. Thereby doing so, the beam is diffracted through the crystal spacing. Generally graphite is used as this allows only waves with the specific wave lengths to reach the detector. This abovementioned methodology for Fe interference may be conducted when clay alteration analysis is necessary from the interface samples.

Preparing oriented clay specimens:

The sample, after hand grinding, is put into a clay/ deionised water suspension. The suspension concentration should be approximately 57- 60mg/ml according to Moore and Reynolds (1997). The samples must be smooth and thick enough to allow mineralogical homogeneity. Moore and Reynolds (1997) give an in-depth description of the four-common oriented sample preparation methods as well as their ease of preparation, preparation speed and their outcomes. The principle method employed for the XRD analysis was clay slurry mounted on a glass slide. For the initial oriented scan, the glass slide is allowed to air dry, with subsequent treatments being conducted on the same sample.

Analysis procedure:

In order to fully set apart what clay mineral is present, due to the fact that many minerals shall share similar d-spacings, several types of XRD analysis was conducted i.e. bulk, oriented air dried, oriented glycolated and oriented heat treated at 440°C and 550°C respectively. Firstly, the bulk analysis will allow the determination of non-clay constituents such as iron-rich minerals, Fe oxide-hydroxides, quartz, feldspars etc. Subsequent orientation of the specimen will allow analysis of the clay component with air dried sample being used as the reference. Glycolation of the sample is generally used on expandable soils as Mg^{2+} produces analogous d-spacings, in the region of 14Å, therefore solvation is needed to eliminate this phenomenon. Thus identification of expandable phyllosilicates and

elimination of Mg-bearing minerals (i.e. Vermiculites) is differentiated due to the development of a d-spacing of approximately 18Å. This increase is due to the resistance of solvation of the vermiculites, whereas smectitious materials easily solvate within the interlayers and expand. Therefore the expanded d-spacing can enable insight into the bentonites ability to swell and determination into the affect of THC exposure. Futhermore, the heat treatment of the material also differentiates particular minerals due to thermal dehydration/ decomposition. Therefore along with d-spaing databases the thermal limits of common minerals are also used in the classification (Table 39). The d001 alteration involves solvation with ethylene glycol and two high heating increments, generally 440°C and 550°C. Solvation enables the soil to swell to its highest d-spacing relevant to the layer charge thus allowing an examination of the swell/ shrink characteristics. Interface spectra were compared to “unaltered” control spectra to measure any permanent alteration i.e. partial Smectite to Illite and/ or chlorite.

Table 39: Thermal limits and associated d-spacing’s for clay minerals used in XRD analyses (Harris, 2007)

Mineral	Diagnostic d-spacing’s					
	Mg	Mg+ glycerol	K, 25°C	K, 110°C	K, 300°C	K, 550°C
Smectites	14-15	15-18	10-14	10-12	10	10
Hydroxy-interlayered smectite	14-15	17-18	11-14	12-14	11-12	10-11
Vermiculites	14	14	10-12	10-11	10	10
Hydroxy-interlayered vermiculite	14	14	14	13-14	11-13	10-12
Chlorites	14, 7	14, 7	14, 7	14,7	14, 7	14, 7
Dioc mica	10	10	10	10	10	10
Trioc mica	10.3	10.3	10.3	10.3	10.3	10.3
Halloysite	10	10	10	7.2	7.2	No peak
Kaolinite	7.2	7.2	7.2	7.2	7.2	No peak
Gibbsite	4.86	4.86	4.86	4.86	No peak	No peak
Goethite	4.18	4.18	4.18	4.18	No peak	No peak
Gypsum	7.56	7.56	7.56	7.56	3.5	3.5

Preparation of the oriented samples was conducted within a N_2 purged glove box to prevent any further oxidation. The sample was hand ground and placed into a glass vessel with a rubber sealed cap to ensure reduced exposure to atmospheric O_2 . The stock sample is then sub-sampled for analysis and further eliminates unnecessary exposure to the atmosphere. For oriented XRD analysis approximately 15-20mg was taken, mixed into a slurry suspension with deionised water (Milli-Q, $18M\Omega/cm$ resistivity) on a watch glass and then dabbed onto a glass slide, after which the sample is air dried (see Figures 118 & 119). To solvate, the sample it is exposed to the reagent for 12 hours at 60°C. The samples are placed above a container containing approximately 200ml of the ethylene glycol allowing the vapour to

contact the sample, the samples are then immediately analysed. The vapour method is considered the most suitable by Moore and Reynolds (1997) for clays with high Smectite compositions. The subsequent heating increments allow analysis of complete water loss and hence collapse of the d-spacing; this makes clay mineral analysis somewhat easier as well as indicating changes to its swelling ability. Characterisation is conducted using LabVIEW software and enables fast matching with mineral databases. The results and conclusions are determined via operator judgement with an understanding of likely alteration products. This is due to the fact that minerals often share similar d-spacing and therefore false identification is possible if the mineralogy of the control sample is not fully understood.

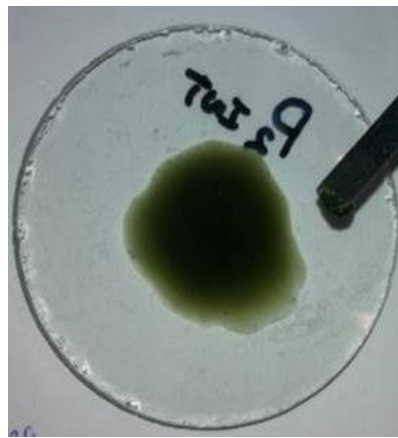


Figure 118: Oriented sample preparation for XRD analysis- clay suspension on watch glass

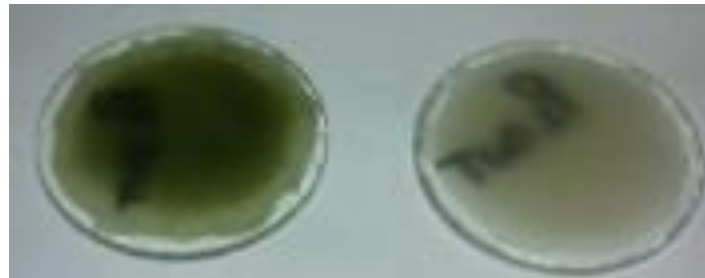


Figure 119: Oriented air dried sample on glass slides

3.8.6. SEM-EDX:

SEM-EDX analysis was conducted on the post-THC sub-samples and the post THC C-steel coupon surface for semi-quantitative elemental analysis as well as microstructural imaging. This method again relies on energy state excitation via an X-ray source, subsequently each element will have characteristic x-rays given off as the electrons return to the ground state. This allowed a detailed analysis of the microstructure and the corresponding mineral phase present after hydro-thermo-chemico exposure.

3.9. Concluding statement:

This section discussed the testing methodologies employed to meet the research objectives. The suite of geomechanical tests allows observations of the Bentonite from an engineering perspective, it is appreciated that clays are a highly heterogeneous and are a physicochemical dependant material with respect to its bulk properties and behaviour. Therefore, alterations observed on a macro scale are a combined result of microstructural and mineralogical alterations. The tests were developed to compliment one-another to gain an understanding of their symbiosis within the engineered barrier system. The results of the tests outlined within this section are presented in the following sections. A summary Table is presented which outlines all the tests conducted, see Table 40.

Table 40: Summary of experimental investigations

Test	Description	Total No. of samples	Duration (Days)	Temp (°C)	Analysis
Batch tests	See Table 20	114	Between 60 and 1	Between 300 and 20	SI, PI, CEC, XRD
Interface replication tests	See Table 23	9	90 per phase replication	100, 80 and 35	SI, Plastic limit, CEC, XRD, SEM, ICP, Mossbauer, UV spectrophotometry
Constant volume tests	See Table 26	16	90 per run	80	Swelling pressure, Rheology, Permeability

4. Material Characterisation

The following chapter provides the characterisation of the unaltered Bentonite used in the investigation. Two separate sources have been used for the MX-80 classification, consignment #1 is a powdered MX-80 (Bentonex WB) supplied by RS minerals® and consignment #2 was provided as compacted blocks of (MX-80) supplied via SKB's supplier ClayTech AB®. Both materials are conditioned to be Na homoionised and are used in the interface and batch testing methodologies outlined in the previous chapters. The powdered bulk Bentonite obtained from RS minerals® (UK) was used in the batch test experiments and constant volume experiments respectively (See testing methodologies chapter for preliminary batch tests and constant volume batch tests). The blocks supplied by ClayTech AB® were employed for the interface replication experiments, focusing on the physicochemical alterations (See testing methodologies chapter for interface testing). Standard geotechnical tests to characterise the two Bentonite consignments were conducted such as Atterberg limits, PSD and Swell Index (SI). Additional control measurements on consignment #1 (Bentonex WB) were conducted such as swelling pressure, swelling kinetics, permeability and rheological tests. The standard characterisation parameters obtained for the two materials are compared for homogeneity analysis. Furthermore, physicochemical tests were run on both consignments of MX-80 enabling comparison of bulk mineralogy and composition.

4.1. Geomechanical classification and comparison between two MX-80 sources:

In this section, the geotechnical results from both consignments of MX-80 are presented and are compared to one another. Standard characterisation has been conducted on both consignments in order to assess the consistency between sample consignments, this was in order to validate and justify the use of these materials within the testing protocol. The results presented here will also be used as control parameters, to be compared to the THCM affected samples. Swelling pressure, swelling kinetics, hydraulic conductivity and rheological results are presented at the end of this section and were only measured using the Bentonex WB MX-80 (Consignment #1). The additional measurements using the Bentonex WB form the control parameters for comparison to the constant volume and batch test results.

4.1.1. Particle size analysis:

It can be seen from the particle size distribution, Figure 120 (Saba et al, 2014), that 80-90 % of the mass of MX-80 falls within the 2µm fraction for the hydrometer test. The poorly graded larger aggregated fraction i.e. quartz grains and other micro-aggregates, is seen from the two profiles denoted as Bentonite grains and sand grains. The poor grading can be inferred from parameters Cu and Cc (Equations 30-33).

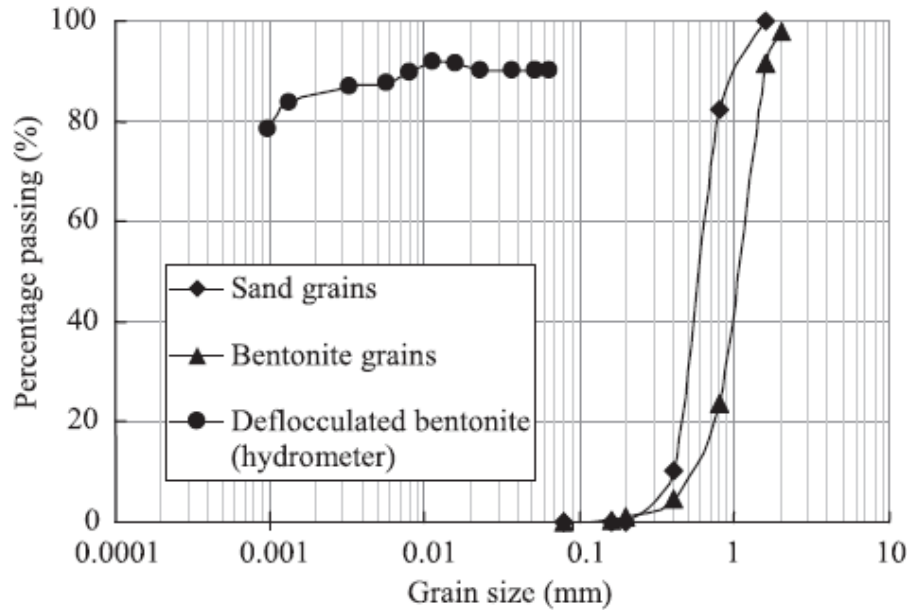


Figure 120: PSD for MX80 Bentonite (Saba et al (2014))

For the Bentonite grain fraction:

$$Cu = \frac{1.3}{0.6} = 2.1 \quad \text{Equ (30)}$$

$$Cc = \frac{0.85^2}{0.6 \times 1.3} = 0.93 \quad \text{Equ (31)}$$

For the sand grain fraction:

$$Cu = \frac{0.65}{0.4} = 1.63 \quad \text{Equ (32)}$$

$$Cc = \frac{0.5^2}{0.4 \times 0.65} = 0.96 \quad \text{Equ (33)}$$

Where, Cu and Cc are the coefficients of uniformity and curvature respectively and the D parameters are the grain sizes passing the percentage stated.

Particle size analyses were run in accordance with BS1377: Pt [2], sedimentation by pipette, on consignment #1 and #2. The method conducted was the sedimentation analysis as nearly 100% of the sample passed the 63µm sieve. Results of the sedimentation analysis are tabulated below (Table 41 & 42) and are presented in Figure 121. Due to the initial compacted state of consignment #2, the sample was dried and hand ground prior to conduction the PSD analysis.

Table 41: Sedimentation results on powdered MX-80, consignment #1 (Supplied by RS minerals®)

<u>Average particle diameter (µm)</u>	<u>Average percentage passing (%)</u>
63	98.63
20	96.37
6	94.01
2	89.41

Table 42: Sedimentation results on powdered MX-80, consignment #2 (Supplied by ClayTechAB®, SKB)

<u>Average particle diameter (µm)</u>	<u>Average percentage passing (%)</u>
63	99.88
20	99.04
6	94
2	89

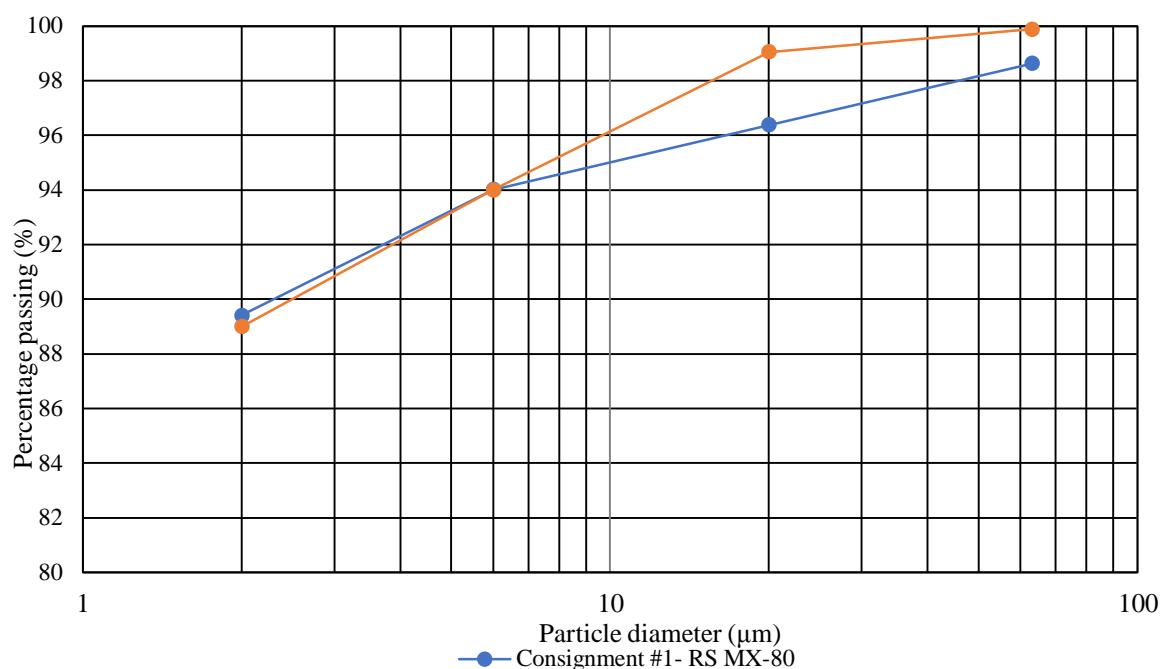


Figure 121: Particle size analysis comparison of both MX-80 consignments

For each consignment, two tests were run and the average particle sizes were taken. It is seen that 89% of the bulk material passes the 2µm fraction i.e. according to BS5930, 89% of the material falls within the clay size fraction. Both material consignments are very similar in the particle size distribution with the clay supplied by RS® containing slightly more fines (passing the 2µm fraction) than the ClayTechAB® material, the difference is considered negligible. However, the ClayTechAB® material contains larger diameter particles ($\geq 20\mu\text{m}$), this is presumably due to the presence of more secondary minerals such as quartz etc. The difference in particle size content above 20µm could be due to the screening procedures from the different sources. The results obtained for the sedimentation tests are also in agreement with the results obtained by Saba et al (2014).

The presence of minor impurities is further confirmed by the mineralogical analysis provided by RS minerals (2014) displayed in Table 43, for consignment #1. Also, a report published by Karnland (2006) for ClayTechAB® provided a mineral content analysis for the material supplied for consignment #2, Table 44. The secondary minerals presented in Table 43 and 44 explain why there is small proportion that is retained on the 63µm sieve. The results displayed in the compositional analysis also agree with the PSD results, in that there is slightly larger diameter aggregates in consignment #2 than there is in consignment #1. It is also evident in the percentage passing the clay fraction that is greater for consignment #1 which correlates to a high weight percent content of Montmorillonite in Table 43.

Table 43: Typical bulk composition of consignment #1 MX-80 (Results obtained from RS minerals, 2014)

Mineral type	%wt.
Montmorillonite	94
Gypsum	≤ 1
Feldspars	≤4
Quartz	≤2%

Table 44: Mineralogical composition of ClayTechAB®, average from 6 samples, consignment #2-MX-80 (Results from Karnland, 2006)

Mineral	%wt.
Montmorillonite	81.4
Illite	0.8
Anatase	0.2
Calcite	1.1
Goethite	0.1
Hematite	0.4
Lepidocrocite	0.5
Magnetite	0.2
Microcline	0.1
Muscovite	3.4
Plagioclase	3.5
Pyrite	0.6
Quartz	3
Tridymite	3.8
Cristobalite	0.9
Gypsum	0.9

4.1.2. Atterberg limits and activity:

Atterberg limit tests were conducted on the unaltered material for control measurements and classification of the unaltered material. The tests were conducted in accordance with BS1377: Pt [2]. The liquid limit testing was carried out using the cone penetration apparatus. Three repeats were run for the plastic and liquid limits respectively. The results for both consignment of MX-80 are tabulated below in Table 45 and 46; the averages of the three tests are presented.

Table 45: Average Atterberg limit values for the powdered MX-80, consignment #1 (Supplied by RS minerals®)

<u>Av. Plastic limit</u>	<u>Av. Liquid limit</u>	<u>Av. Plasticity index</u>	<u>Activity</u>
32	395	363	4.08

Table 46: Average Atterberg limit values for the powdered MX-80, consignment #2 (Supplied by ClayTechAB®, SKB)

<u>Av. Plastic limit</u>	<u>Av. Liquid limit</u>	<u>Av. Plasticity index</u>	<u>Activity</u>
33	387	354	4

Given the high plasticity index, it is evident that this material is classified as highly plastic clay. From a conventional ground engineering point of view these parameters would indicate an unsuitable material to use for conventional construction. However, from an environmental engineering point of view i.e. use in waste disposal geo-liners; these high PI clays are ideal. With respect to the MX-80's ability to self-heal, self-healing is a function of the clays swelling ability which means that a high PI indicates that the material will take up large quantities of water with subsequent large volumetric changes. This swelling potential is also demonstrated by the relatively high activity value (tables 45 and 46) obtained via the activity ratio equation expressed by Skempton (1953), equation 34. This further demonstrates the materials ability to swell and effectively seal any preferential pathways upon hydration due to its ability to massively change in volume, as well as maintaining some shear resistance with the plastic index range.

$$A = \frac{I_p}{\% \text{ Clay}} \quad \text{Equ (34)}$$

where:

Ip: The materials plasticity index (%)

%Clay: The percentage of material passing the 2µm sieve

The dimensionless parameter, termed activity, can be used to understand a clays stability. Table 47 displays some boundary parameters for pure minerals and common clays. By comparison, it is seen that Kaolinite, the most stable clay mineral form has an activity of ≤ 0.4 whereas Montmorillonites activity is ≥ 1 . Consequently, any activity value greater than 1 is considered highly unstable with moisture uptake. The measured values for the MX-80 from both consignments are significantly greater than 1.

Table 47: Generic activity values for standard clay minerals and common clays (From Principles of geotechnical engineering 7th ed, Braja, M and Atkinson, 2000)

<u>Mineral</u>	<u>Activity</u>	<u>Soil</u>	<u>Activity</u>
Muscovite	0.25	Kaolin clay	0.4-0.5
Kaolinite	0.4	Glacial clay and loess	0.5-0.75
Illite	0.9	Most British clays	0.75-1.25
Montmorillonite	>1.25	Organic estuarine clay	>1.25

4.1.3. Control swell index:

Savage (2005) expresses the intrinsic mechanisms of swelling, there are two accepted processes that enables the bulk material to swell, 1) the “inner-crystalline” swelling (dominated by the cation species hydration) and 2) osmotic swelling (controlled by the ion concentrations within the respective bulk pore water and the inter-lamellae void). This test enables a characterisation of, and correlation between the material’s ability to occupy a large volume upon hydration (i.e. its self-healing ability). Thus, with the aid of other chemical analyses interpretation of the swell index test may indicate that a possible physicochemical alteration of the barrier material has occurred during THCM exposure (i.e. occupancy and concentration of certain cation species and/ or mineralogical / structural alteration etc).

The tests conformed to the ASTM specified swell index test (ASTM D5890:11), implemented to quantify the volumetric free swelling capacity upon hydration, expressed as ml/2g ($\equiv Cm^3/2g$). The experimental conditions when conducting the swell index tests are kept constant, i.e. room and water/ solution temperature is maintained at 20°C \pm 0.5°C. Through examination of Figure 122 it can be interpreted that both consignments are highly expansive.

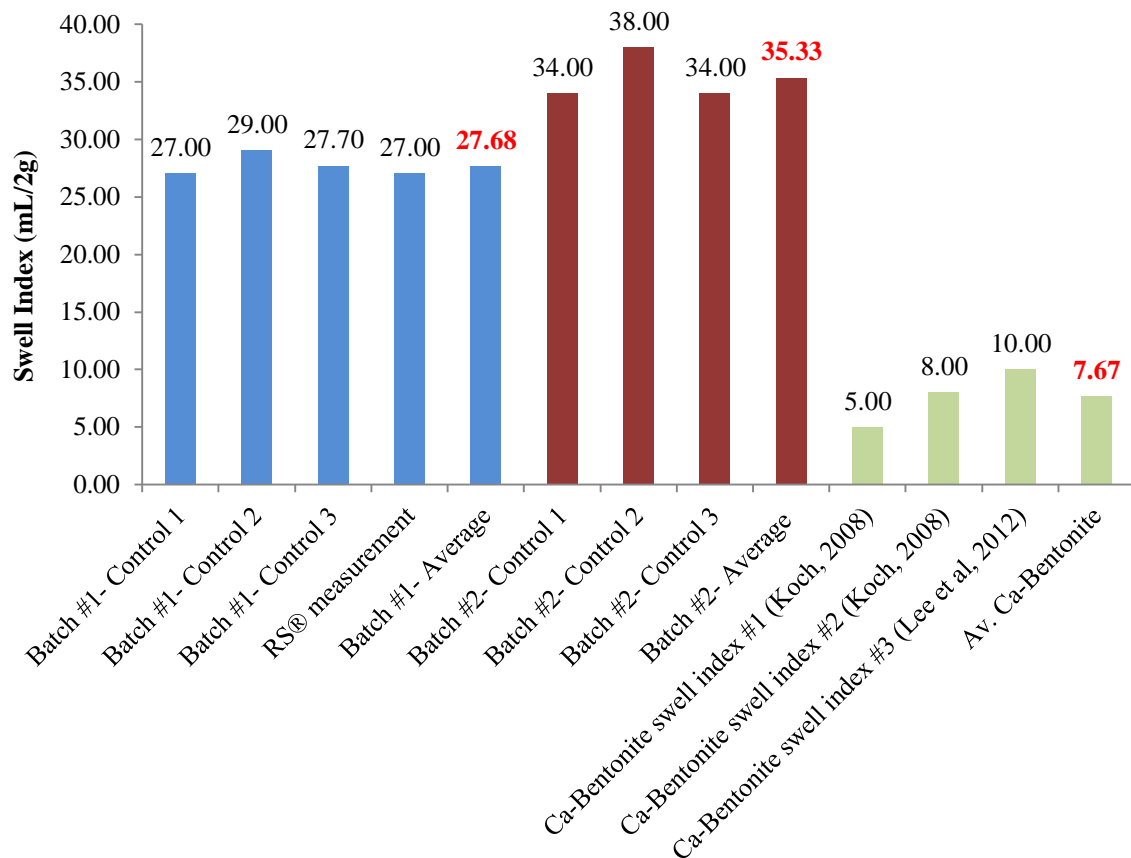


Figure 122: Control swell index results for consignment #1 (RS® MX-80; blue bars) and #2 (ClayTechAB® MX-80; Red bars), along with a comparison to the Ca-type Bentonite (Green bars)

Consignment #1, the RS® MX-80, averages $27.7\text{cm}^3/2\text{g}$ and consignment #2, the ClayTechAB MX-80, averages $35\text{cm}^3/2\text{g}$. Comparably, the swell index of Ca-Bentonite is significantly lower, showing an average of $7.67\text{cm}^3/2\text{g}$. Koch (2008) and Lee et al (2012) provide an extensive characterisation of Na^+ and Ca^{2+} bentonites respectively. Their classification gives a resulting swell index of $5 - 10\text{cm}^3/2\text{g}$ for the latter homoionic Bentonite. Swell index measurements of the Ca^{2+} -Bentonite demonstrate the abnormal expansibility of Na^+ -bentonites and therefore such material is more favourable for barrier self-healing capabilities.

By comparison, the ClayTechAB® consignment #2 is considerably greater than the Ca-homoionic Bentonite by nearly a factor of five and is slightly higher than the RS® MX-80. This could be due to the conditioning heterogeneities in the processing stage from the suppliers i.e. varying relative amounts of Na present in each clay consignment. This potential concentration variation could have an effect on the osmotic swelling component.

4.1.4. Control swelling pressure and swelling kinetics:

One-dimensional Odometric swelling tests have been conducted in accordance with BS1377 [5]:1990. This technique, known universally as the constant volume method, involves maintaining the axial displacement to within $\pm 0.01\text{mm}$ until equilibrium is reached (i.e. no change in displacement under an applied load for 24hrs). Subsequent unloading and reloading is then carried out to complete the swelling test cycle. The swelling pressure and kinetics were only conducted on consignment #1- RS® MX-80, as the testing methodology used only this batch in the constant volume THCM experiments. From Figure 123 is it clear that the swelling pressure for the compacted control specimens is on average 4.11MPa corresponding to an average dry density of $\rho_{dry}=1.512\text{Mg}/\text{m}^3$.

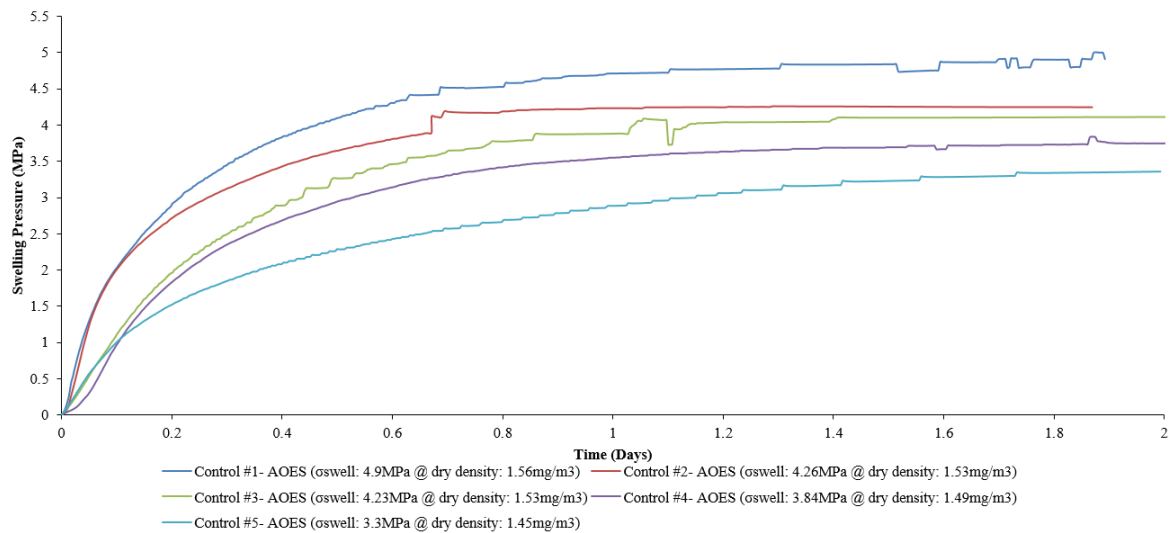


Figure 123: Control swelling pressures for the RS® MX-80- Consignment #1

Operator error during compaction may have resulted in a very minor deviation in the resultant densities for the respective samples. Nonetheless a tolerance of $\pm 0.05\text{Mg}/\text{m}^3$ with a corresponding maximum of $1.6\text{Mg}/\text{m}^3$ and a minimum of $1.51\text{Mg}/\text{m}^3$ is acceptable. The measured swelling pressures corresponded to the measured pressures by Börjesson (2010) with respect to the reference dry density; these are in the range of 4.2-5.2MPa displayed in Figure 124.

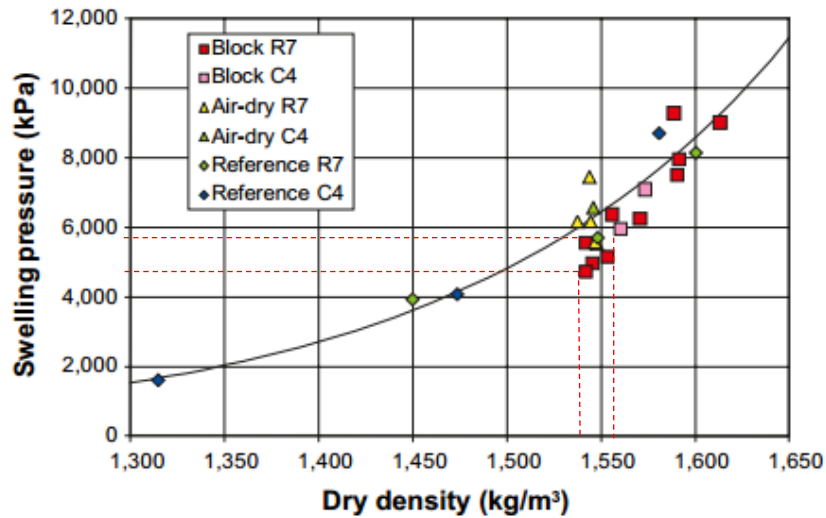


Figure 124: Oedometric swelling pressure tests conducted on samples under reference properties (After Borjesson, 2010)

Figure 125 displays the results by Dueck et al (2011) displaying the magnitude of swelling pressures expected under constant volume saturation. The results presented were for reference (control) samples for an insitu thermo-hydraulic cycle study conducted on a full-scale test within the Swedish hard rock laboratory (HRL). The measured swelling pressures appear not to be as high as those swelling pressures presented by Dueck et al (2011). The swelling pressures given by Dueck et al (2011) are higher than expected and increase dramatically between $\rho_{dry}=1.48Mg/m^3$ and $\rho_{dry}=1.56Mg/m^3$. That is, over a range of $\rho_{dry}=0.08Mg/m^3$ the swelling pressures measured by SKB increase by 1.61MPa, which is a considerable deviation. This demonstrates the diversity of results for the same material within literature. The swelling pressure methodologies vary between sources which may be a cause of the variations observed i.e. confined uniaxial or biaxial measurements.

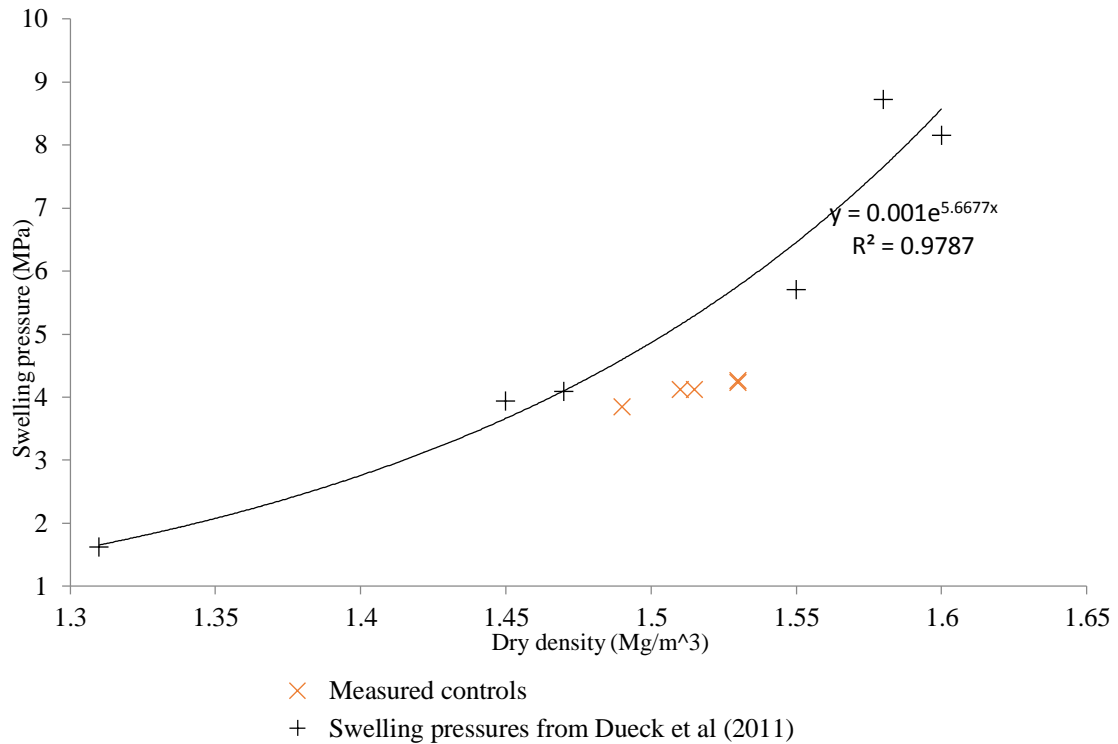


Figure 125: Swelling pressure Vs. dry density results presented are from a study on the long-term thermos hydraulic experiments for the SKB concept (after Dueck et al, 2011) and the measured controls as a comparison (orange crosses)

Once the swelling pressure stage was complete the axial stress was reduced by 10% of the swelling pressure. The axial strain versus time was logged i.e. the swelling kinetics. Figure 126 displays all control swelling kinetics measurements, it is seen that the sample, on average, could swell by 0.74% over a 2.5-day period. Table 48 displays the swelling pressures obtained for control samples along with the axial strain after 2.5 days. From this Table, the average of the values was used as the reference control parameters.

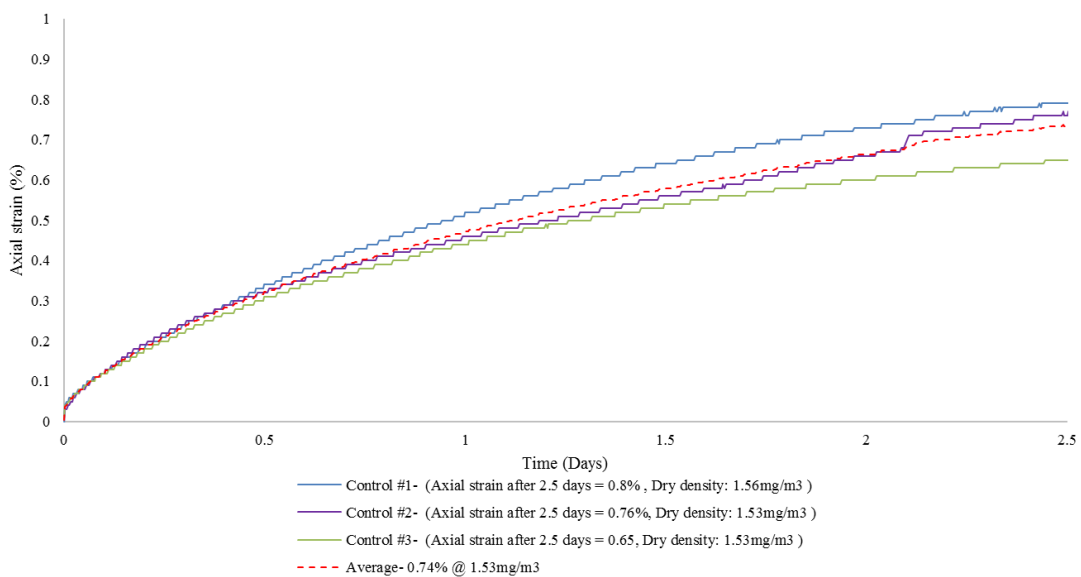


Figure 126: Swelling kinetics measurements for the control samples on the RS® MX-80 (Consignment #1)

Table 48: Control swelling pressure and kinetics values

Sample no. #	Swelling pressure (MPa)	Swelling kinetics (%)
1	4.9	0.8
2	4.26	0.76
3	4.23	0.65
Average	4.11	0.74
10% of average	0.41	-

4.1.5. Rheological control tests:

Rheological tests were conducted to observe the intrinsic changes to the samples stiffness; the controls allowed a comparison of the initial deformation characteristics to the Thermo-Chemically exposed samples. The rheology measurements can be used as a material stiffness proxy, any changes can then be related to the exposed “near-field” conditions and the impact on the soil structure i.e. cementation or mineral dissolution etc.

Shear strength tests were initially conducted to obtain the ultimate shear strength in order to conduct stress controlled tests for creep measurements on the constant volume samples. The sample was initially allowed to saturate under a normal stress of 4MPa, chosen to approximately correspond to the swelling pressure for the desired dry density. The swell stage was allowed to run until the sample height did not deviate by $\pm 0.1\text{mm}$ for 200 consecutive logging increments (Figure 127). The sample was then sheared at a rate of 0.01mm/min to ensure that no excessive pore water pressure is built up and that the shear stress is essentially “effective”. These ultimate strength measurements are necessary for the rheological creep tests i.e. a stress increment of 20% of the total shear strength was then applied with subsequent creep measured over 48hrs per increment.

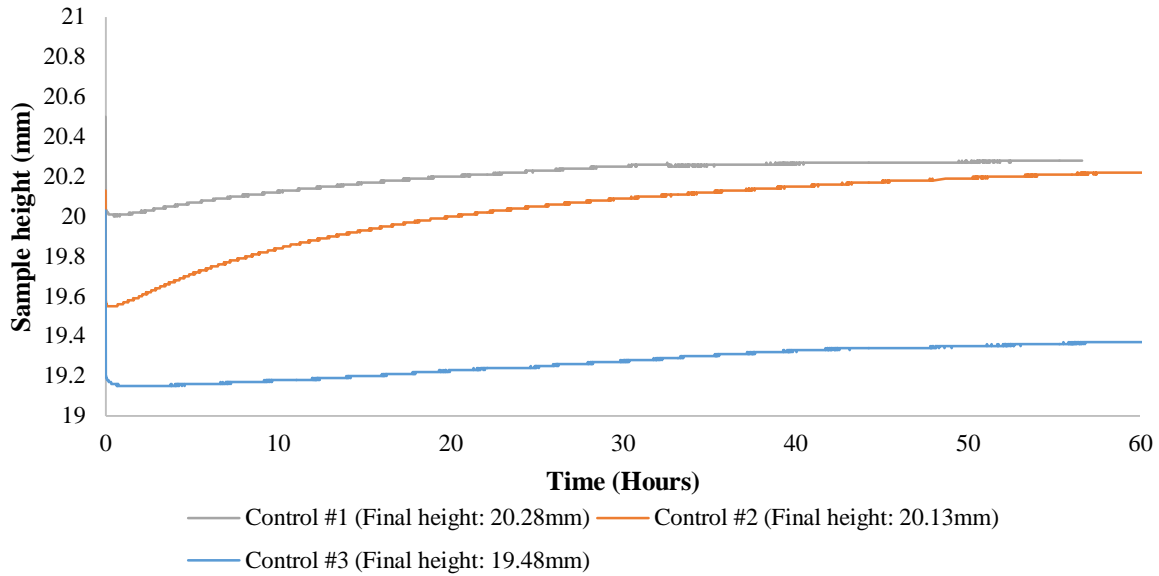


Figure 127: Swell stage graphs for control USS samples under a 4MPa normal stress

It is assumed in conventional direct shear tests that the cross-sectional area of the shear plane remains constant. This is in fact incorrect, but the assumption is widely accepted. If we correct the area change, using the equation 36 (proposed by Lai, 2004), the resulting stress path is corrected as is illustrated in Figure 128 (b); the true stress path is therefore modified from AB to AB'. This is because the normal stress does in fact increase as the area reduces under the horizontal displacement and therefore the resulting stress path follows the modified stress vector. Therefore, the results obtained for the ultimate shear strength used the area correction factor (F).

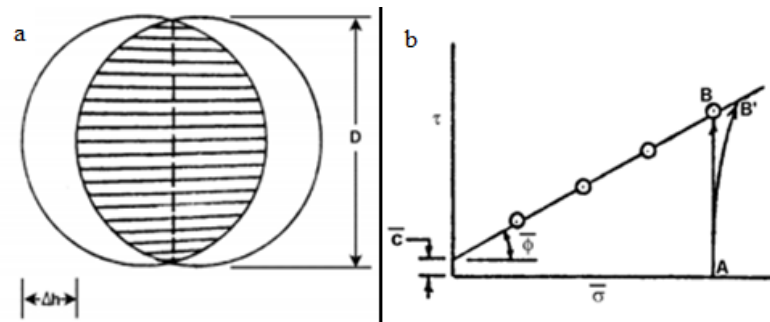


Figure 128: Area correction illustration for circular shear box, a) differential contact surface that changes with time and b) modified stress path AB' (After Lai, 2004)

$$A_o = \frac{\pi}{4} D^2 \quad \text{Equ (35)}$$

$$F = \frac{\pi}{2} \left\{ \cos^{-1} \left(\frac{\Delta h}{D} \right) - \left(\frac{\Delta h}{D} \right) \sqrt{1 - \left(\frac{\Delta h}{D} \right)^2} \right\} \quad \text{Equ (36)}$$

where:

- F: Area correction factor
- \cos^{-1} : Inverse cosine (radians)
- D: Diameter

ΔH : Change in length

Once F is obtained for each displacement increment, it is multiplied by the original area, this then results in the reduced area for the respective increment being used in the normal stress and shear stress calculations.

Below in Figure 129 displays the total shear strength results for control samples #1, #2 and #3. What is evident is that assuming a constant area the resultant stress results are conservative, Table 49 displays a comparison between the ultimate shear stress values for constant area and corrected area calculations.

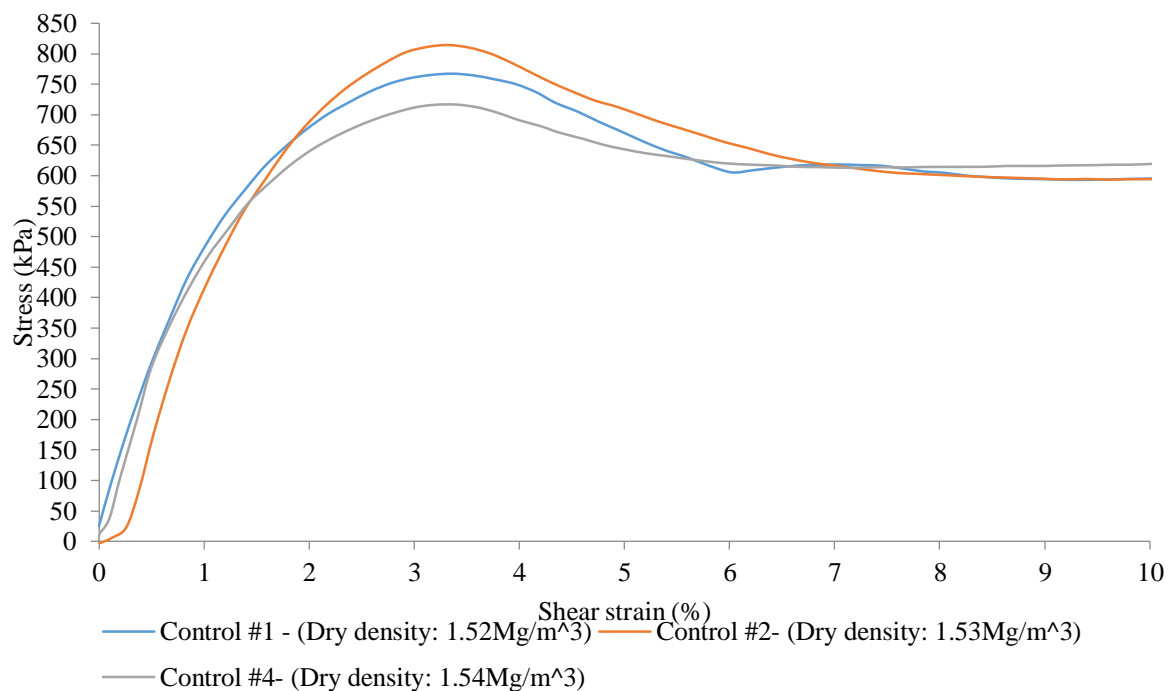


Figure 129: Compiled stress vs. strain graphs for the control specimens

Table 49: Ultimate shear strength comparison with and without applied area correction

Control sample no. #	Ultimate shear strength- w/o area correction (KPa)	Ultimate shear strength- area correction (KPa)	Shear strain at failure (%)	Dry density (Mg/m^3)
1	707.4	767.42	3.36	1.52
2	780.8	814.46	3.32	1.53
3	682	716	3.4	1.54
Average	723.4	765.96	3.36	1.53
20% of USS	144.68	153.2	-	-

Once the control shear strength graphs were complete additional samples were tested for the control rheology measurements. The samples were confined within the shear cell and submersed within water after which it was consolidated under a normal stress of 4MPa, a

horizontal stress corresponding to 20% of the ultimate shear strength was applied to the system (as indicated in Table 49). Thus, measuring shear strain vs. time over a 48hr period. The resulting graph displayed in Figure 130, allowed the rheology of the sample to be measured which can be used as a proxy of stiffness when compared to the THC samples. The rheology values are presented below in Table 50.

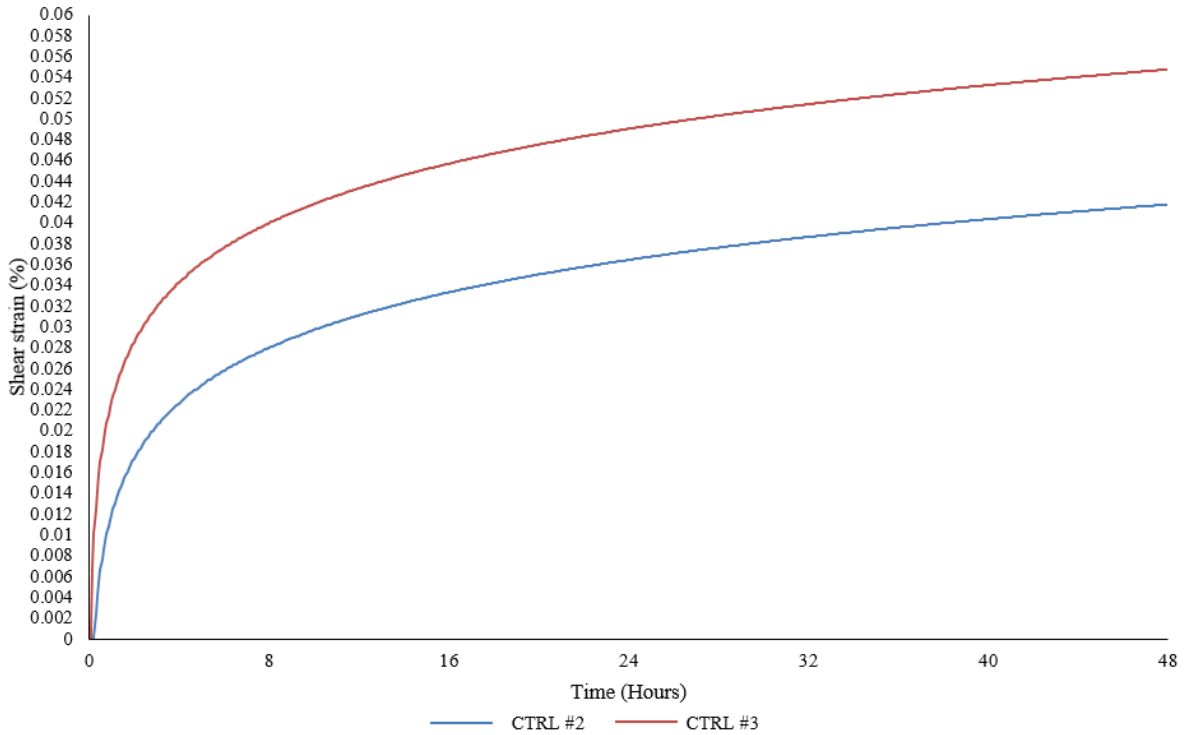


Figure 130: Control rheology results

Table 50: Rheology measurements on control samples

Control sample no. #	Axial strain (%) after 48 hours
1	No recovery
2	0.042
3	0.054
Average	0.048

4.1.6. Permeability estimates:

Using data from the consolidation stage of the rheology tests it was possible to calculate a permeability estimate for the constant volume samples using the root time method (method outlined in section 3). Below in Table 51 displays the estimated permeability results for the control samples. Example of the consolidation curve used to estimate the permeability is presented in Figure 131 as well as the data calculated for that sample, Table 52, the data presented is only for control sample #2 to display the method employed.

Table 51: Estimated permeability values for the control samples at target density

Control sample no. #	Permeability (K) m/s
1	8.4×10^{-15}
2	5.5×10^{-15}
3	5.65×10^{-15}
Average	6.52×10^{-15}

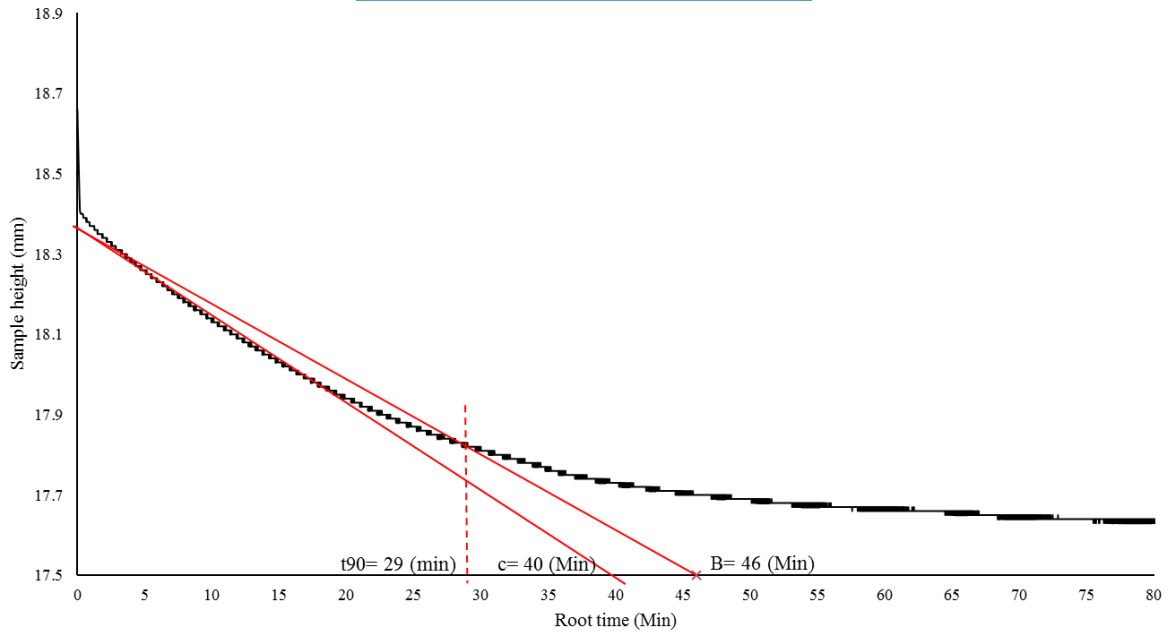


Figure 131: Example Consolidation graph for control sample #2

Table 52: Example of calculated parameters for control permeability, sample 2 (pre and post rheology)

Parameter	Value
Initial dry density (Mg/m^3)	1.4
Final dry density (Mg/m^3)	1.5
Initial bulk density (Mg/m^3)	1.871
Final bulk density (Mg/m^3)	1.951
Initial void ratio (e)	0.96
Final void ratio (e)	0.85
t90 (Min)	29
C (Min)	40
b (Min)	46
Av Thickness (mm)	17.71

Change in height (mm)	1.03
A	18.22
d	9.11
d²	83.03
CV (m²/yr)	1.28
Mv (m²/KPa)	9.81
K (m/s)	5.5× 10 ⁻¹⁵

4.2. Comparison of geotechnical results- Concluding statement:

Both Bentonite consignments have had several classification tests conducted on them in an unaltered state to provide a reference to which the Thermo-Hydro-Chemical affected samples can be compared. Both materials have been provided by separate sources and state that the material is Wyoming MX-80, a Na-homoionic Bentonite. Presented in Table 53 is an overview of the results obtained for the geotechnical classification. Excluding the Swelling pressure, kinetics, rheology and permeability results, as these were only conducted on consignment #1- The RS MX80 for comparison to the constant volume experimental series. The values presented are averages taken from several repeats for each test; this was to allow for any mineralogical heterogeneity within the bulk sample.

Table 53: Average measured control parameters for the “starting” materials

Material/ parameter	LI (%)	PI (%)	PI (%)	% CLAY (≤2µm)	Activity	SI (Cm³/2g)
Consignment #1 RS® MX80	397	32	365	89.41	4.08	28
Consignment #2 ClayTech® MX80	387	33	354	89	4	35

It can be seen that the samples are very similar in terms of their engineering behaviour, this justifies the use of both materials within their respective testing methodologies and it can be assumed to be the same material. The minor experimental dissimilarities are likely to be due to bulk material heterogeneities and operator error. It must also be noted that the preparation methodology varied between the clay consignments. This is due to the state in which the starting material was provided, i.e. consignment #1 was supplied in powdered form whereas consignment #2 was provided in a highly compact state, relevant to the Swedish concept’s engineered barrier specification. Hence it was necessary for the clay consignment #2 to be dried, hand ground and sieved before running any classification tests. Thus, any

dissimilarity may be related to crushing of particles, various quantities of micro aggregates present and potential physicochemical alteration due to the compaction pressure.

4.3. Physicochemical classification of consignments #1 and #2:

This section provides an extensive chemical classification of both consignments of MX-80. This is provided to compliment the geotechnical classification section. This was also conducted to form an analytical basis to compare to the THCM altered specimens. The following sections have covered several physicochemical parameters such as CEC, XRD, Mossbauer, ICP-AES and Fe speciation.

4.3.1. Cation Exchange Capacity:

A CEC analysis was run on both consignments of MX-80 using the the centrifugal extraction method. The CEC parameter is expressed as milliequivalents per 100 grams. The preliminary runs will give a reference measurement for comparison to future THC affected samples. The CEC results are tabulated in Table 54. To put this into perspective, Dorothy (1959) presents CEC values for several phyllosilicate minerals, tabulated below (Table 55). It indicates that the Bentonite exhibits superior cation exchange capacity in comparison to the other main clay mineral types. Ruck and Cathelinew (2004) stated that “impure” Bentonite (i.e. Bentonite with a high proportion of quartz) displayed a CEC of 64.1(meq/100g) whereas after washing with NaCl resulted in an increase to 101(Meq/100g. The material used in this study will be an excellent candidate for slowing/ preventing the transportation of radionuclides due to sorption to the clay platelet surface. On the contrary, it can be anticipated, with supporting evidence from swell index measurements, the sorption of higher valence cations may significantly reduce the clays swelling ability.

Table 54: CEC values measured for both clay consignments

<u>Consignment</u>	<u>CEC (meg/100g)</u>
Material #1: RS MX80	78
Material #2: SKB MX80	80

Table 55: CEC values of the three-main clay mineral groups (Dorothy, 1959)

<u>Mineral</u>	<u>CEC (meg/100g)</u>
Kaolinite	3-15
Illite	10-40
Montmorillonite-group	70-100
Measured control value (MX-80)	78

The CEC results are slightly different; this is however considered negligible. Both CEC measurements correspond well to other literature sources using the same Bentonite. Other studies have obtained control CEC values in the range of 75-90meq/100g (Kumpulainen et al (2010), Pusch et al (1992), Karnland et al (2011)).

It is vital to the overall assessment of the barrier's ability to retain or slow certain radionuclides that are released after canister failure. Thus, a parameter that quantifies the material's ability to exchange its original cations with other species is the cation exchange capacity (CEC). The cation exchange capacity is measured in meq/100ml ($\equiv \text{cmol/kg}$) i.e. a concentration value per unit volume or mass of the material. Subsequent alterations to the CEC of a soil may indicate possible mineral alterations. It is well established that smectites display one of the highest CEC characteristics in the clay mineral groups. This is primarily due to the large surface area of the montmorillonite mineral. The physicochemical benefits of the aforesaid phyllosilicate mineral are observed though its high CEC value and the related specific surface area (the theoretical surface area for Montmorillonite is calculated at $\approx 750 \text{ m}^2/\text{g}$ Karnland (2010)). Smectites are considered to have the greatest surface area available for cation sorption. As highlighted in Figure 132, illustrated by (Eslinger and Pevear, 1988), the zones for sorption to occur are far greater than that of the most stable clay mineral, e.g. kaolinite. Interactions between Fe corrosion products (i.e. Fe^{2+}) and the unaltered clay structure may induce alterations such as changes to layer charges etc. as well as the induced effects of thermal loading.

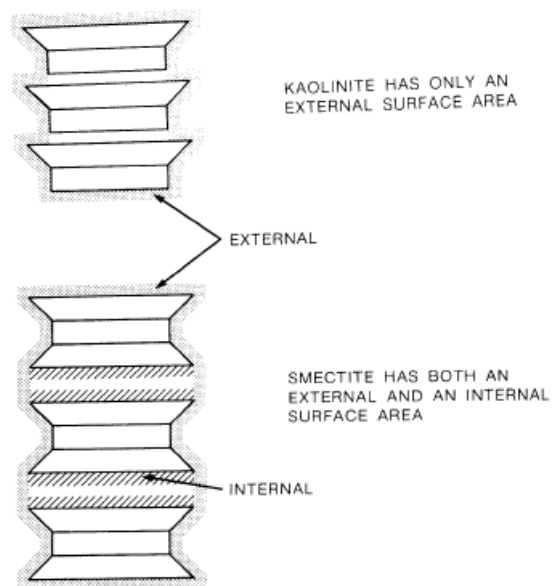


Figure 132: Available zones for cation sorption and surface area comparison between smectite and kaolinite (after Eslinger and Pevear, 1988)

The CEC can be affected in two ways, firstly, alteration to the “permanent” charge due to isomorphous substitution or cation reduction due to electron transfer within the T-O-T structure. In the case of the Bentonite/ Fe integration, Fe^{2+} released by the anaerobic corrosion processes may result in structural reduction of Fe^{3+} within the octahedral layer. Alternatively, isomorphous substitutions may occur, by the replacement of $Al^{3+} \rightarrow Fe^{2+}$. Secondly, pH dependent charge also influences the material’s CEC. This pH dependent charge is focused at the “edge” hydroxyl sites. The charge is governed by the protonation and deprotonation of these OH groups. The latter charge mechanism is governed by the solution pH. Additionally, all materials will have a pH value that correlates to a point of zero charge (PZC); hence at this pH edge charge is neutral and either side of this point the charge deficit is either positive or negative. Neumann (2013) reports that the point of zero net proton charge for an Fe-containing smectite is approximately at a pH of 7.2. This measurement is founded on electrolytic titrations. At low pH values, the edge sites tend to hold an anion exchange capacity whereas at higher pH values a cation exchange capacity is predominant. These OH groups are considered to be amphoteric in nature i.e. these can act as acids or bases. Therefore, the CEC value of the material will increase with increasing pH. This is because there fewer hydrogen anions available to displace the cations from the colloidal zone into the bulk water. It can be said that the CEC is dependent on the pH of the solution and subsequently the lyotropic series is only obeyed in alkaline solutions. Ultimately a measure of the CEC can display the material’s self-healing ability as an increase or decrease can indicate that some ionic alteration has occurred with a subsequent DDL modification.

4.3.2. X-ray diffraction analysis:

Preliminary XRD (oriented- unfractionated) analysis was run on the unaltered Bentonite supplied by RS minerals (RS- Material #1) for mineral characterisation. Courtesy of Edinburgh University (Rigonat, 2015), Figure 133. The analysis provides a baseline composition for comparative analysis to the thermo-chemical exposure samples. Carlson (2004) has previously conducted a semi-quantitative analysis using XRD spectra as well as other methodical analyses. Carlson (2004) discovered that through comparison of several types of Bentonite mined from various sources globally (i.e. MX-80, FEBEX/ MILOS, Kutch and Czech) all contain, to some degree, Fe (III) ranging between 4- 13.2% in concentration. According to the technical report for Posiva produced by Carlson (2003) the Iron is partly incorporated into the two types of iron oxy/hydroxides and edge/ basal sorped iron. These

are, Ferrous hydroxide and Goethite respectively, but also include partial replacement of Fe within the octahedral layer.

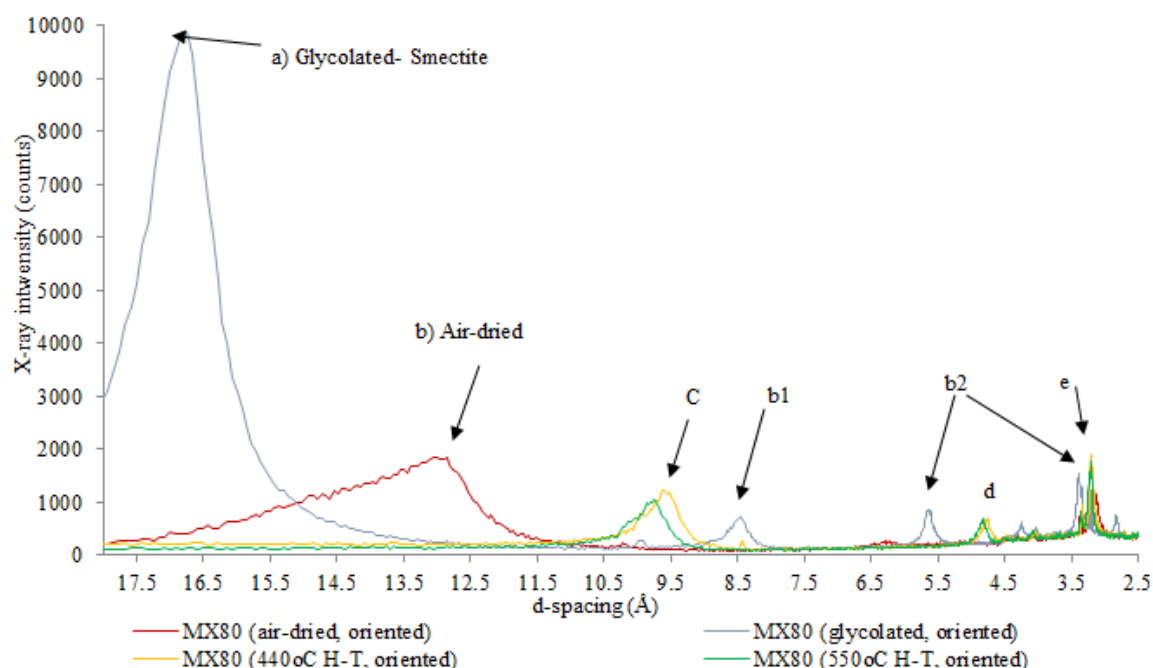


Figure 133 Oriented XRD spectra for the RS-MX80 control (Courtesy of Edinburgh University, Rigonat (2015))

Carlson (2004) and Moore and Reynolds (1997) give advice on clay mineral and other aggregate identification and state that sample saturation with ethylene glycol shifts the smectite 001 spacing from 12-15Å to 16-17Å depending on the hydration state and dominant interlayer cation, presence and ordering of other interstratified clay minerals. Smectite hydration states can vary due to the varying degrees of moisture content, vapour pressure and electrolytic type, ion size and concentration within the interlayer. Bergaya et al (2006) refer to the varying water layers as “pseudo-layers” when referring to the hydration state of 2:1 phyllosilicate minerals. The hydration states were given by Bergaya et al (2006) and are displayed in Table 56.

Table 56: Hydration states of 2:1 silicate, d- spaces taken from Villar et al (2011) and Bergaya et al (2006)

Hydration state	d- spacing (Å)
0	~10
1 (Pseudo- monolayer)	~11.8- 12.5
2 (Pseudo- bilayer)	~14.5- 15.5
3 (Three water pseudo- layers)	~18.5
4 (Four water pseudo- layers)	~19- 20

From Figure 133 (peaks a, b), it is observed that there is a predominant peak of 12.9Å (peak b) with a subsequent jump to 16.8Å (peak a) upon glycolation. Using table 56, it is evident that the air-dried sample was in a 1-2 hydration state. This confirms the presence of

the smectite mineral. Moore and Reynolds (1997) give step-by-step identification guidelines for interstratified clays e.g. Illite/Smectite (I/S) or Chlorite/Smectite (C/S). It may be inferred that there is a small presence of randomly interstratified Illite/Smectite, firstly by examining the characteristic (001) reflection for the glycolated smectite at 16.9Å. This peak is fairly broad and Moore and Reynolds specify that interstratification is likely to be random and rich in Smectite if there is a prominent broad peak around 16.9 Å. The peak at (b1, Figure 133) is also characteristic for a composite Illite (001)/ glycolated Smectite (002) reflections. Lastly, the peaks corresponding to (b2, Figure 134) further reinforce the argument for presence of composite I/S with the broad peak at $\approx 5.56\text{Å}$. Moore and Reynolds (1997) also state that a sharp peak at $\approx 3.4\text{Å}$ for the glycolated run is due to juxtaposition of the (003) Illite and the (005) Smectite reflections. They further state that the presence of interstratification within a smectite rich material produces peaks near $5.2(2\theta)$ [16.98Å] for the glycolated run along with a reflection near the $16(2\theta)$ [5.53Å] to $17.7(2\theta)$ [5Å]. This profile, if present, is due to the reflection (002/003) of the interstratified Smectite/Illite. Therefore, it is rational to conclude that there is a small amount of Illite present within the material, it is also possible to semi-quantify the likely amount of Illite in the clay matrix presented in Table 57 provided by Moore and Reynolds (1997). Therefore, using table 57, the peaks in Figure 133 (above) at (b1 & b2) indicate that there is $\sim \leq 10\%$ Illite.

Table 57: The positions of useful reflections for estimating percent Illite/EG- Smectite (Moore and Reynolds, 1997)

%Illite	001/002(Å)	002/003(Å)
10	8.58	5.61
20	8.67	5.58
30	8.77	5.53
40	8.89	5.5
50	9.05	5.44
60	9.22	5.34
70	9.4	5.28
80	9.64	5.2
0	9.82	5.1

The final heating increments of the sample is the final run for XRD analysis, this dehydrates the sample inducing a collapse of the layers. This spacing, used in conjunction with the other measured spacing's from the air-dried and glycolated runs allow a conclusive mineral identification. Heating at temperatures greater than or equal to 300°C induces dehydration and thus the (001) peak drops to $\approx 10\text{Å}$ or slightly below. Figure 134 (point C) is supported by Table 58.

Table 58: Thermal limits and associated d-spacing for clay minerals (Harris and white, 2008)

Mineral/ Treatment	Mg	Mg + glycerol	K, 25°C	K, 110°C	K, 300°C	K, 550°C
Smectites	14-15	15-18	10-14	10-12	10	10
Hydroxy- interlayered smectites	14-15	17-18	11-14	12-14	11-12	10-11
Vermiculites	14	14	10-12	10-11	10	10
Hydroxy- interlayered vermiculites	14	14	14	13-14	11-13	10-12
Chlorites	14, 7	14, 7	14, 7	14, 7	14, 7	14, 7
Di-octahedral mica	10	10	10	10	10	10
Tri- octahedral mica	10.3	10.3	10.3	10.3	10.3	10.3
Halloysite	10	10	10	7.2	7.2	-
Kaolinite	7.2	7.2	7.2	7.2	7.2	-
Gibbsite	4.86	4.86	4.86	4.86	-	-
Goethite	4.18	4.18	4.18	4.18	-	-
Gypsum	7.56	7.56	7.56	7.56	3.5	3.5

The findings given by Carlson (2004) coincide with the XRD spectra displayed in Figure 133. The peak drops to around 9.5/ 9.7Å (C) after undergoing the subsequent heating increments with little change between the two. Indicating that dehydration of the smectite has occurred, also another characteristic that Illite is present is that upon dehydration of the material the spacings resemble that of Illite. This peak decay is attributed to moisture loss with the supporting evidence from Table 56 (above). Additionally, Midgely and Gross (1956) state that water is lost, reversibly, when heated between 0-200°C that corresponds to a basal layer change from 14Å to 9.6Å. They also argue that if Na^+ is the predominant cation present within the interlayer, heating results in an immediate drop in basal spacing to $\approx 9.5\text{Å}$ with no intermediate stage. Given this evidence, it highlights that the peaks displayed in Figure 133 (C) for the 440° and 550° spectra are attributed to the Na-rich smectite component of the MX-80 with some Illite determined from the glycolated spectra. Two distinct peaks occur upon heat treatment around 4.7Å (d); these may be attributable to the 003-chlorite peak, more specifically the Fe- bearing chamosite. The high concentration of high angle peaks (Figure 133: e) is attributable to non-clay aggregates in the clay matrix. Figure 134 looks more closely at this end of the diffraction pattern.

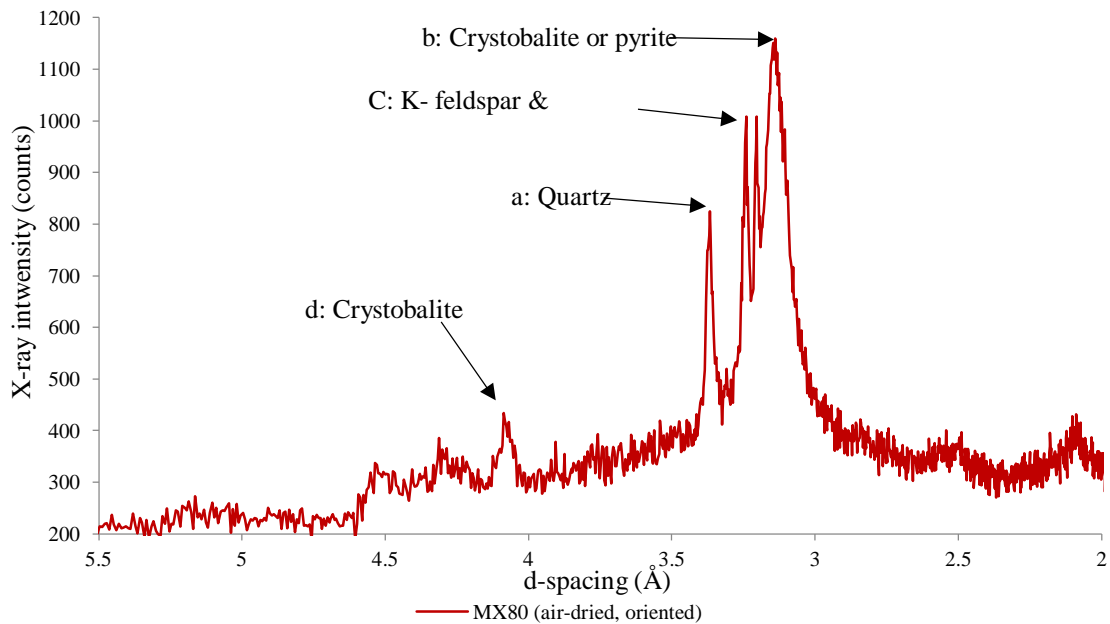


Figure 134: Oriented XRD spectra for the RS-MX80 control (Courtesy of Edinburgh University, Rignonat), focusing more closely on the high angle peaks

With an approximate composition from other analyses (Müller- vonmoos & Kahr, 1982; Karnland, 2010 etc.) it is easy to focus in on the probable minerals present with help from Moore and Reynolds (1997). It is difficult to precisely identify what the exact mineral is in an oriented mount and therefore random powder analyses are beneficial for this purpose. Moore and Reynolds (1997) give specific checks when examining the 2θ angles in search for particular minerals. Firstly, point (a) in Figure 134 is indicative of a quartz peak, whereas peaks corresponding to (b) may be characteristic of the quartz polymorph, crystobalite or alternatively, pyrite. However, it is suggested that orthoclase mineral peaks overlap some crystobalite peaks, therefore one way of identifying crystobalite is by a strong peak at $4.04\text{\AA} \approx$ (d) and a weak peak at 3.14\AA . In this case, the opposite is observed and therefore this peak may be due to the presence of pyrite. Moore and Reynolds (1997) discuss the identification of Feldspars by explaining that when observing XRD reflections from oriented samples, and indicate that the only decent reflections will be at $27.5 (2\theta)$ for K-feldspars and $28 (2\theta)$ for plagioclase respectively. The sharp peaks correspond to $\approx 3.24\text{\AA}$ and 3.2\AA respectively, therefore the peaks at point (C) indicate the presence of Feldspars.

Further bulk XRD as well as oriented runs was conducted on air-dried and glycolated samples for both consignments, displayed in figures 135 and 136. Analysis on the bulk samples was accompanied with the aid of the Table 59.

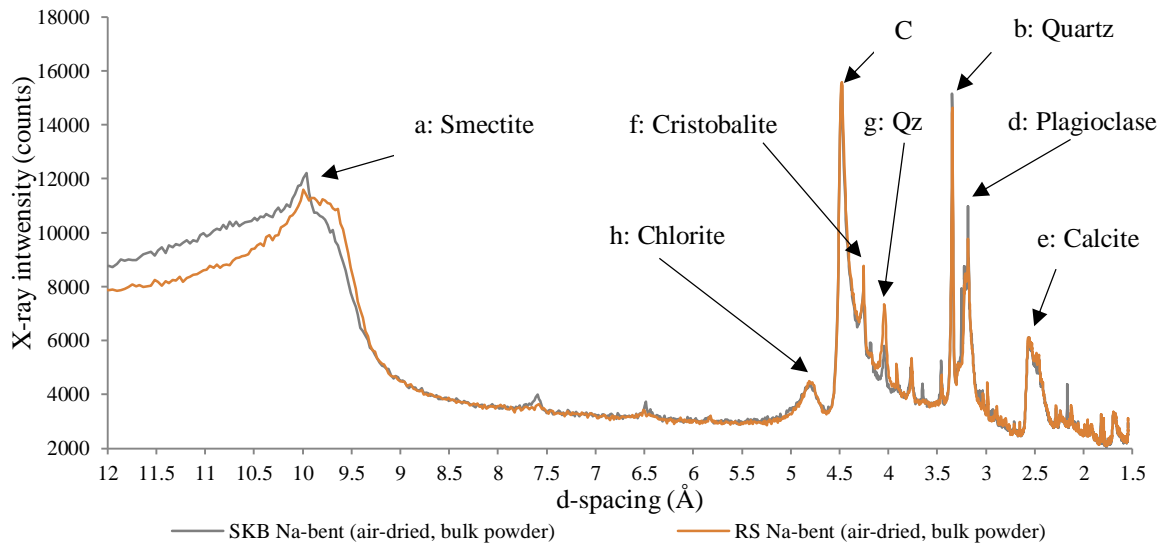


Figure 135: Bulk XRD spectra run on both RS-MX80 and SKB- MX80 materials

Table 59: X- ray diffraction mineral peaks for bulk analysis sample spectra, d-spacing values from Moore and Reynolds (1997)

Mineral	d-spacing (Å)
Quartz	2.128, 2.23, 2.28, 2.45, 3.34, 4.27
K- Feldspar (Orthoclase)	4.77, Main peak: 3.24
Plagioclase	3.18, 3.19, 3.33
Crystobalite	4.04, 3.14, 2.49
Illite	3.38, 5, 10.1
Chlorite	3.55, 4.7, 7.1, 14.2
Montmorillonite	(Dry) ~9.5-15, (Glyc) ~16-17
Gypsum	2.87, 2.68, 3.07, 4.28, 7.61
Pyrite	1.63, 1.92, 2.21, 2.43, 2.71, 3.13
Calcite	2.10, 2.29, 2.5, 3.04, 3.68

What is observed is that for both materials, XRD traces correlate very well, and thus it can be inferred that they are compositionally similar. From Figure 135, point (a), a d-spacing of approximately 10 Å, equivalent to that of Illite is measured. It should be noted that the “air-dried” sample was in fact oven dried at 105°C for a period of 24hrs and therefore it can be concluded that this is in fact predominantly smectite (with support from the glycolated runs (Figure 136). This therefore indicates that the sample was in a zero-hydration state inferred from tabulated data presented by Villar et al (2012) and Bergaya (2006) above in Table 59. Furthermore, Figure 136 displays peaks (b & g) that correspond well to quartz (≈3.34, 4.27Å respectively), and additionally the peak at (d) indicates the presence of a plagioclase. Calcite is also thought to be present in both samples given by the obvious peak at

(e) $\approx 2.55\text{\AA}$. There is also a shoulder towards the lower d-spacing side that may indicate a Crystobalite or pyrite peak overlap ($\approx 2.45\text{\AA}$). Also at (f), this is thought to be Crystobalite ($\approx 4.04\text{\AA}$). At (h) there is a broad peak at around $\approx 4.7\text{\AA}$, which may indicate the presence of chlorite within the material. Moore and Reynolds (1997) support this observation by explaining that peaks on chlorites are at 6.2 and 18.8 (2 θ), weak peaks are predominating when there is a low concentration of the Fe content. This may indicate why this peak was not detected in the oriented runs in figures 136 & 137, perhaps due to the high concentration of Montmorillonite masking the 001 reflection. If Chlorite and Illite are in fact present, this may indicate that there may be some amount of Fe already present in the clay. Mossbauer analysis is presented in the next section and determines the presence of Fe within the bulk materials, further supporting the presence of Fe^{3+}/Fe^{2+} already within the Bentonite structure. Figure 136 displays reflections for the clay fraction, which are almost identical to the XRD conducted at Edinburgh. The same peaks (a-e) correspond to a mixed I/S with the Illite being $\leq 10\%$.

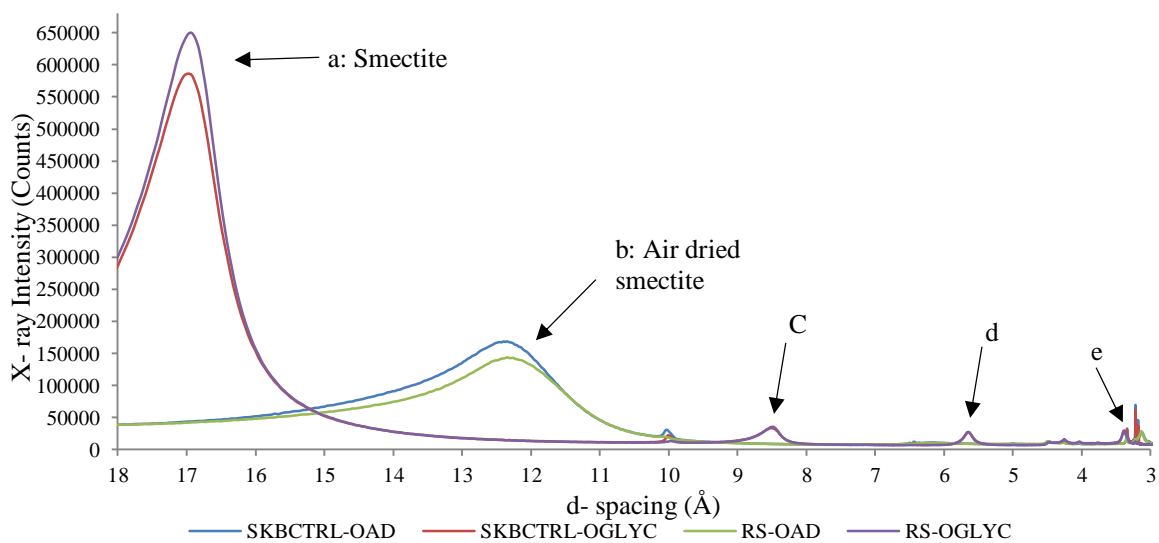


Figure 136: Oriented air- dried and glycolated control runs for both RS and SKB materials (Conducted at Newcastle University)

In addition, the smectite peaks at (C, d and e) are characteristic to a saponitic type smectite. It appears that the smectite component of both materials is Mg-rich and tri-octahedral in nature, the glycolated profiles for both materials fit the saponite profile well given by Moore and Reynolds (1997). Looking more closely at the higher angle reflections, Figure 137, it is seen that the characteristic peaks are very similar to that of Rigonat (2014) XRD on consignment #1 (RS® MX-80).

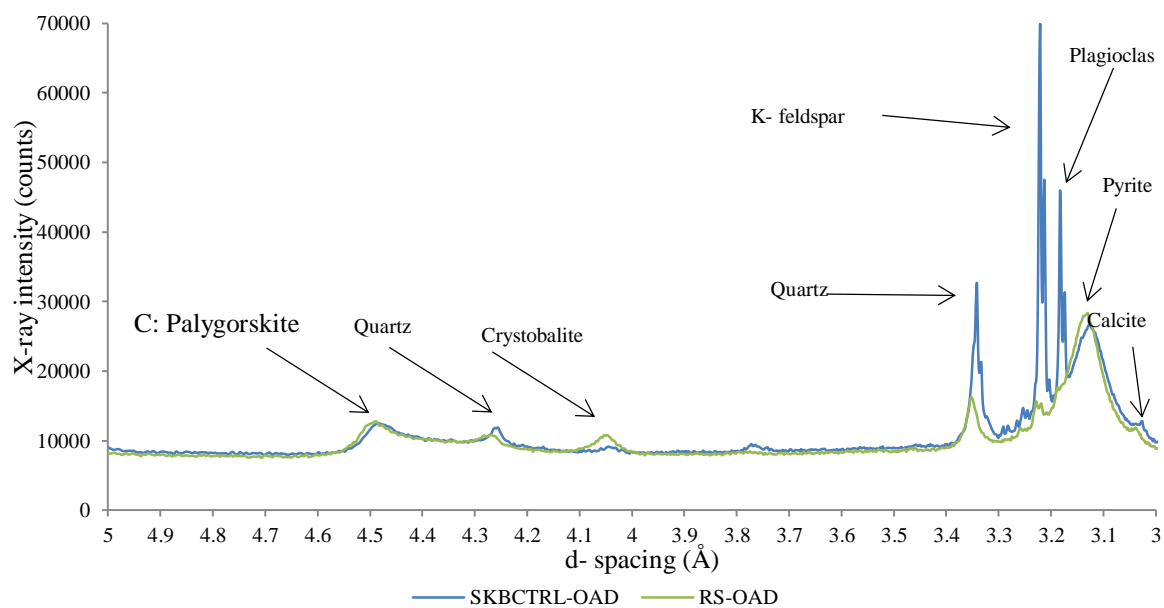


Figure 137: Air-dried oriented high angle peaks for both control materials

Interestingly, the intensities measured for consignment #1 (RS MX-80) are lower than that of the SKB material for the accessory minerals range (Figure 137). This may be due to the screening, processing and conditioning of the Bentonite post-extraction. Therefore, it seems that consignment #1 MX-80 contains fewer secondary minerals or they are more amorphous than that in the consignment #2 (ClayTechAB® MX-80). Overall it can be concluded that both materials used are similar in mineral composition, with slight compositional and concentration heterogeneities, as is expected with any extracted earth materials.

Additionally, examination of the 002/003 reflections indicate the degree of electron scattering from within the octahedral layer due to the increased density of electrons present. This can be used to infer the type of smectite due to the presence of Fe within the octahedral sheet. The 002/003 intensity ratio indicates the magnitude of back scattering from the incident X-rays i.e. higher intensity ratios indicate higher amounts of electron present. Figure 138 displays a comparison of the respective materials Fe composition.

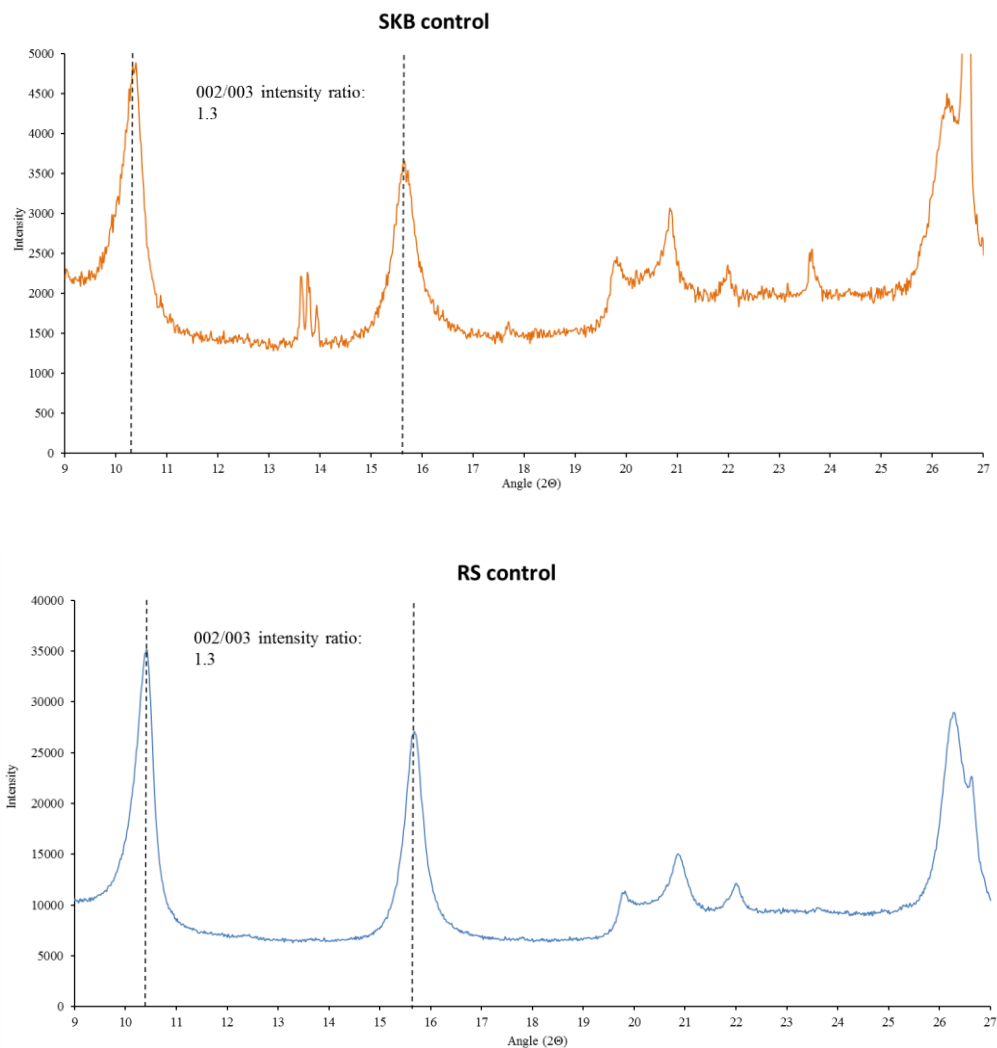


Figure 138: 002/003 intensity ratios for both control materials

It is seen from Figure 138 that the Fe scattering from the octahedral sheet are identical between sample sources. The material resembles a saponitic smectite, which is Mg-rich as displayed in Moore and Reynolds (1997). It is difficult to determine whether the octahedral layer is Fe or Mg rich as both cations can display electron scattering, therefore the 060 measurements are necessary to differentiate this.

4.3.3. Mossbauer:

Mossbauer analysis was conducted on both the unaltered material, consignment #1 from RS® and consignment #2 supplied ClayTechAb®. Mossbauer was conducted by Dr. Neumann from the school of civil engineering and geosciences. The comparison of the hyperfine parameters enabled some quantification into the presence of Fe^{2+} and Fe^{3+} already within the unaltered material.

From figures 139-140 it can be seen that the silicate iron, identified by the isometric shift and central doublets are characteristically similar. The doublet at approximately 0.3mm/s and the additional peak approximately around 2.2mm/s is indicative of iron within the silicate structure. The runs took a long time to complete, indicating that the content of iron is low and the long run time was necessary to get a suitable profile. The Mossbauer profiles indicate that Fe species, Fe^{2+} and Fe^{3+} is present, slightly less in consignment #2 but nonetheless similar. At 4 Kelvin when the Fe-Oxy(hydroxides) are magnetically ordered the true presence of the silicate Fe is more evident from the doublet profiles for both materials. When examining the profiles conducted at near absolute zero, there is the development of a weak sextet profile that is characteristic of the presence of Fe-(hydr)oxides the fitting is close to hematite. The fitting resembled ferroxyhyte but this mineral is not known to be stable under atmospheric conditions. However, the signal is weak and therefore indicates that the presence of iron (hydr)oxides is low enough to have weak a magnetic interaction upon 4k ordering.

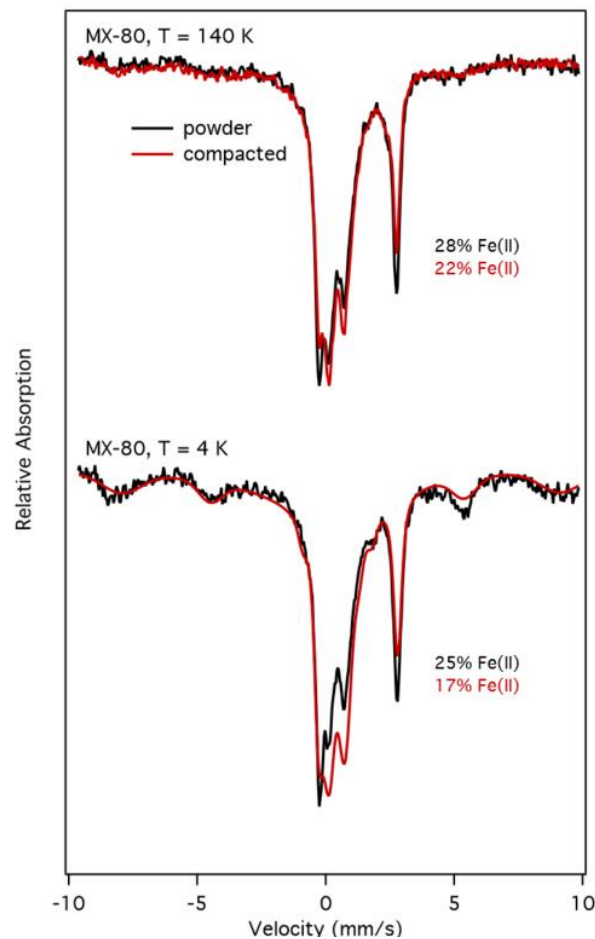


Figure 139: Mossbauer comparison of the two starting bentonites at -133°C and -269°C

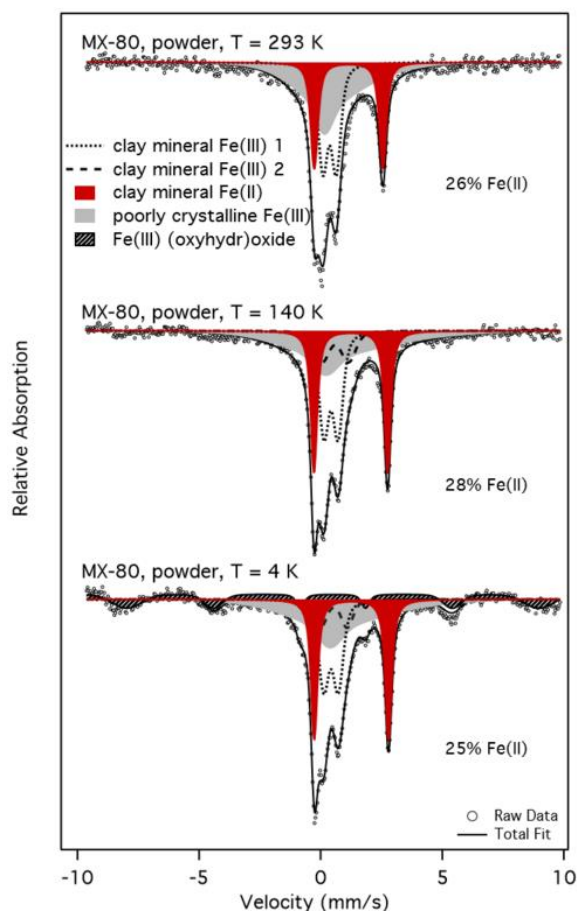


Figure 140: Several temperature Mossbauer profiles of the RS MX-80 Bentonite at 20°C, -133°C and -269°C

Below in Table 60, is the data obtained for both control samples under temperatures 4K and 293K. The hyperfine parameters indicate that the material is similar in Fe composition with no (Hydr)oxides present within the Bentonite matrix due to the single/ collapsed profile. The parameters indicate some octahedral bound Fe also supported by the SEM-EDX measurements; this is expected for Bentonite.

Table 60: Mossbauer hyperfine parameters at 4K and 293K

Sample	%Fe(ii)	%Fe(iii)	% Magnetically ordered Fe(iii)	Quadrupole split (mm/s) (Fe(iii))	Quadrupole split (mm/s) (Fe(ii))	Sextet Quadrupole split (mm/s)
Control SKB	17	83	17	1.01	3.03 (2.87 at 293K)	Collapsed
Control RS	25	76	16	1.09	3.05 (2.82 at 293K)	Collapsed

4.3.4. UV absorption spectroscopy for Fe^{2+}/Fe_{Tot} analysis:

UV absorption studies allow the quantification of the abundance of Fe species within the Bentonite pre-and post THC exposure. The method employed for Fe quantification is set out

in the methodology chapter, section 3. Below presented in Table 61 is the starting abundance of Fe present within the MX-80.

Table 61: Fe species abundance in control (starting) materials

Sample consignment	FeTotal (mg/mL)	Fe^{3+} (mg/mL)	Fe^{2+} (mg/mL)
SKB control	4.13	3.2	0.9
RS control	4.1	3.9	0.2

As can be seen from Table 61, the abundance of the relative iron species present within the sample are very similar, even though both materials come from different sources. This further confirms the compatibility for use within this study with the assumption that they are of similar composition. The total amount of Fe^{3+} is much greater than Fe^{2+} which is understandable as the material and accessory minerals are exposed to atmospheric conditions post extraction from its source. Also, the abundance of Fe^{2+} is slightly higher for the compacted SKB material, this could be due to the compaction pressures causing mineral alteration. Furthermore, the measurements were conducted on digested bulk material and therefore the total abundance of Fe species given here is a combination of structural and mineral Fe. The amount of clay mineral and accessory mineral Fe could not be determined in this test, but nonetheless the materials are comparable to one another.

4.3.5. ICP- analysis:

To further examine the material compositional similarities, ICP analysis was conducted on the control materials to determine elemental abundance and composition. Below are the measurements of the total elemental abundance in both starting materials in Figure 141.

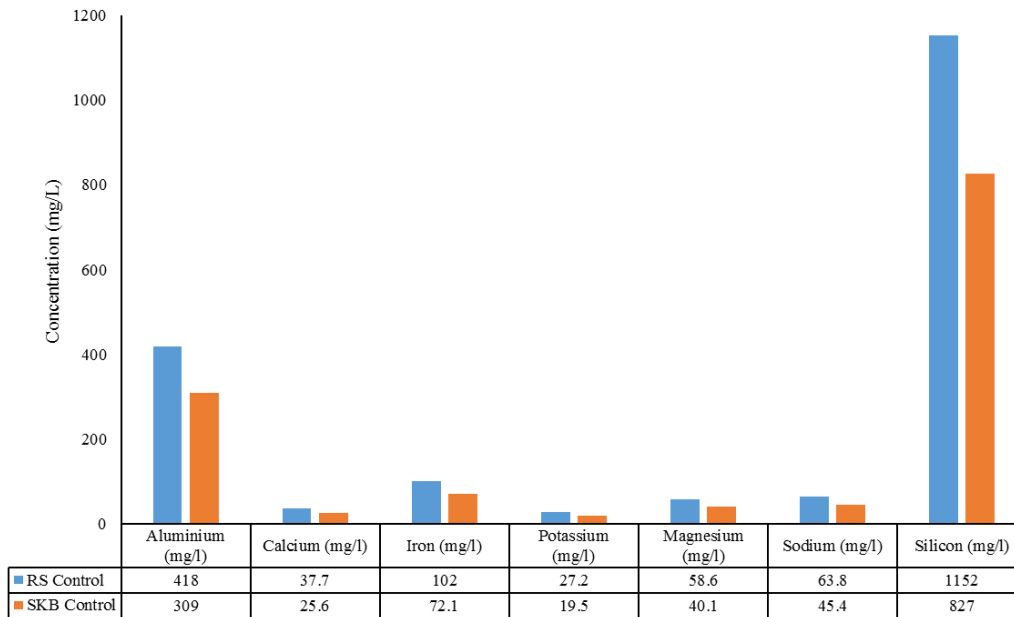


Figure 141: Elemental composition of the starting materials, digested samples

The composition of the two materials is very similar with the compacted, SKB sample showing a total element concentration profile that is slightly lower than the RS material. The difference is negligible for all elements except for the silicon abundance. This higher concentration of Silicon in the RS sample is probably due to slightly higher quartz abundance in the bulk sample matrix. Also, the screening process of the SKB material by ClayTechAB is much more accurate than the material procured in bulk for the RS source which probably contains more accessory minerals.

4.3.6. SEM-EDX:

Energy-dispersive X-ray spectroscopy was conducted on both starting materials to provide a bulk elemental analysis for compositional comparison. Figure 142 below displays the measured elements and their respective quantities by % wt.

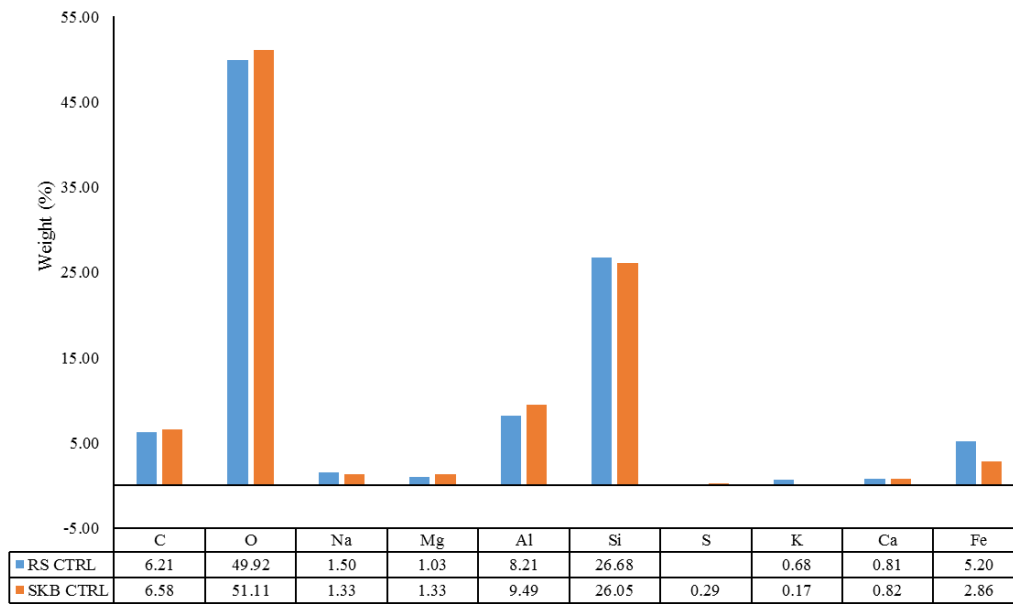


Figure 142: SEM-EDX analysis on the starting materials

The composition of each material is very similar with slight elemental heterogeneities, which is understandable for naturally occurring material. The minor amount of Sulphur indicates the presence of sulphide most likely in the form of FeS₂ (Pyrite). The amount of Fe corresponds well to the level found in the naturally occurring “unaltered” MX-80 (Kiviranta and Kupulainen, 2011; Karnland, 2010; Carlson, 2004).

4.4. Concluding statement:

This section presents a series of classification and physicochemical results conducted on the MX-80 obtained from two different sources. This enabled a comparison to determine the compositional similarity prior to the main testing. The interface replication experiment used the pre-compacted Bentonite (consignment #2), obtained from the clayTechAB. Whereas the batch test and constant volume test experiments used the powdered MX-80 (consignment #1), obtained from RS minerals. Hence, it was necessary to determine that both clay consignments were compositionally similar.

The results indicate that both clay consignments display minor mineral compositional heterogeneities. This is expected from naturally sourced materials. The minor particle size variance observed between consignment #1 and #2 can be attributable to the processing, conditioning and compaction state of the clay. Consignment #1 appears to contain less secondary minerals and slightly less clay sized particles compared to consignment #2. This is perhaps due to consignment #1 being subject to a more stringent processing or that the clay obtained from claytechAB (consignment #2) was compacted, these high pressures may induce mineral alteration/ formation. Furthermore, the presence a higher percent of clay size particles in consignment #2 might be related to the drying and hand grinding preparation of the initially compacted sample prior to the sedimentation tests. Nonetheless, bulk geomechanical classification tests indicate that both consignments are generally similar and therefore can be treated as the same. This validates using these two individually sourced materials within the respective testing methodologies.

Results of the batch tests, canister-Bentonite interface tests and the constant volume tests are presented in the next sections. The results are compared to the “control” measurements presented within this section to determine the extent of geomechanical or physicochemical deviation.

5. Batch test results

Several batch tests have been conducted under several temperatures (ranging from 20°C to 300°C). The two key temperatures of 20°C and 100°C were chosen for initial characterisation purposes. This was in line with the upper thermal limit of the UK disposal concept of 100°C. This upper thermal limit has been supported via industrial and academic synergies. Additional temperatures exceeding 100 °C (Maximum temperature 300 °C) have been explored to investigate the impact of higher thermal loading scenarios to investigate potential alteration by accelerating any reaction kinetics, resulting in any alterations that may yield over geological timescales. This is interesting from an experimental exploration perspective. The purpose of running the preliminary batch tests was to provide some initial insight into the potential adverse alterations to the MX-80 Bentonite under variable exposure scenarios. The alterations were measured for basic geomechanical tests and some limited physicochemical analysis, the results were compared to the “unaltered” control material properties to see the extent of the alteration (outlined in the classification chapter- 4). The batch tests were run under a limited range of scenarios i.e. redox conditions (aerobic conditions were present in most batch consignments). To gain a comprehensive insight into alterations under aerobic conditions the experimental conditions were varied to gain a broad spectrum of situational circumstances. For instance, batch series #1 investigated the effects of the solution salinity on the materials consistency, salinity was incrementally increased from zero to unrealistically high concentrations (2M). With other batch tests looking at the effects of corrosion integrated into the Bentonite or just Bentonite with or without saline solutions under thermal loading and different durations (See table 62). Ultimately, by varying these experimental boundary conditions it was possible to conduct a comparative analysis, to isolate the most significantly altered specimens and relate the alterations to the most influential boundary conditions.

Table 62: Batch testing regime

Batch No.#	Batch	Test conditions
1	Saline profiling batch tests <u>Batch ref:</u> (SalineSolutions-Mx80-20)	-x1 Control with x5 increasing saline concentration solutions (for NaCl, KCl and CaCl respectively) -Duration 1 month -Temperature: 20°C - Liquid solid mass ratio: 10 after Guillaume (2003)
2	Steel- Comp Clay-Saline batch tests <u>Batch ref:</u>	-x1 Control with x4 increasing saline solutions -S275 steel compacted into Bentonite blocks: target dry density: 1.56Mg/m ³

	(S-Mx80-NaCl-Comp-20)	-Duration: 1 month -Temperature: 20°C - Liquid solid mass ratio: 10 after Guillaume (2003)
3	<u>Steel- Comp Clay batch tests</u> Batch ref: (S-Mx80-Comp-105)	-x3 Samples compacted to a dry density of 1.56 Mg/m ³ at 27% moisture -S275 steel -Distilled water -Sealed batch cells and hydrostatic conditions -Duration: 1 month -Temperature: 105°C
4	<u>Steel- Uncomp Clay-NaCl batch tests</u> Batch ref: (S-Mx80-NaCl-Uncomp)	-x1 Control with x4 increasing saline solutions -S275 plate in contact with uncompact clay -Duration: 1 month -Temperature 20°C - Liquid solid mass ratio: 10 after Guillaume (2003)
5	<u>Thermal loading and duration tests (No C-Steel/ No Salt)</u> Batch ref: (Mx80-HT/D)	-x3 Controls with x3 samples per thermal load (20°C, 50°C, 70°C, 90°C, 110°C, 150°C, 200°C, 230°C, 300°C for 24hrs duration) -x3 Controls with x3 samples per thermal duration (1 day, 4 days, 1 week, 2 weeks, 4 weeks, 8 weeks, 12 weeks at 105°C) - Liquid solid mass ratio: 10 after Guillaume (2003)
6	<u>Thermal loading and duration with high saline solution tests (No C-Steel)</u> Batch ref: (MX80-HT/D/HS)	-Powder batch tests - Batch#1: x3 samples per thermal load each with NaCl, KCl, CaCl and a synthetic groundwater solution mix (20°C, 100°C and 150°C for 8 Wks) - Batch#2: x3 samples with CaCl and synthetic groundwater solutions respectively per thermal load (80°C and 100°C for 8 and 12 weeks) - Liquid solid mass ratio: 10 after Guillaume (2003)
7	<u>Steel/ Bentonite/ Saline under very high thermal loading tests</u> Batch ref: (S/Mx80-HT/D-HS)	-x6 batch samples exposed to (x3) 20°C and (x3) 150°C for 4 months, each sample varying the boundary conditions i.e. Steel/ clay with DI Water, Steel/ clay with synthetic groundwater, Clay/ synthetic groundwater and Clay with DI water - Liquid solid mass ratio: 10 after Guillaume (2003)
8	<u>1-year steel/ Bentonite interaction tests</u> Batch ref: (1yr-S-Mx80)	-x6 batch samples steel/clay interface interaction under ambient thermal loading -x3 with DI water for 1 year at 20°C -x3 with NaCl 0.45 for 1 year at 20°C - Liquid solid mass ratio: 10 after Guillaume (2003)
9	<u>2-year steel/ Bentonite interaction tests (No Saline Solution)</u>	-x3 batch samples steel/clay interface with DI water for 2 years at 20°C - Liquid solid mass ratio: 10 after Guillaume (2003)

	<u>Batch ref:</u> (2yr-S-Mx80)	
--	-----------------------------------	--

The batch tests using a synthetic groundwater composition was derived from the borehole data presented by Manning et al (2007), the data presented is a groundwater chemical analysis taken from the Eastgate borehole at incremental depths to 1000m BGL in a crystalline rock (See Figure 89- Section 3). Na^+ , K^+ and Ca^{2+} were selected to keep the synthetic composition simple, but by introducing a more complex groundwater other than just NaCl it is possible to see the alteration characteristics with a slightly more realistic water composition.

5.1. Batch series results:

Post analysis involved a series of relatively fast tests that can yield preliminary measurements on the materials altered functionality. Measurements were correlated to the characteristic unaltered material parameters, thus enabling an analysis of the extent to which the materials intended use is affected. The preliminary geotechnical classification tests consisted of Atterberg limits and swell index measurements, run to investigate the physical alteration. The fundamental aim of these initial batch analyses was to construct an alteration hypothesis under initial aerobic conditions corresponding to the initial GDF conditions. The alteration classification was achieved via a correlation between both the physicochemical and geotechnical measurements. Limited physicochemical analysis was conducted on select samples, these will be presented in their respective section, primarily CEC and XRD was conducted to provide insight into mineral/ structural changes. These batch tests were able to provide an insight into the “short-term” alteration effects when the exposure of the aerobic corrosion products have integrated with the MX-80 soil matrix, along with initial increased temperatures and saline water concentrations. NaCl was used as the main salt with reference to 0.45M concentration throughout the experimental testing as agreed by the research consortium, however some batch tests using KCl and CaCl for comparative analysis were considered.

5.1.1. Batch #1 (SalineSolutions-Mx80-20) results:

Firstly, profiling the impact of saline solutions on the bentonites free swell and consistency was explored. These tests were based on a hypothesis presented by Lee et al (2012), they subject homoionised Ca-Bentonite to increasing saline solution concentrations

(NaCl) and thus reported on the alterations the materials ability to free swell. This was used as an initial comparison between the characteristics of the two bentonites when under such hydraulic boundary conditions. MX-80 was subject to static saline conditions for approximately one month under ambient conditions (20°C). The saline solutions consisted of NaCl, CaCl, KCl types and a synthetic ground water mix (A mix of all three salts under borehole reference concentrations. Simply through observing the uncompact material submersed within the solutions, as the electrolyte concentration increased so did the density of the solid material (Fig 143). The mass of the material was maintained the same as well as the mass of saline solution, with a liquid to soil ratio of 10 being used (after Guillaume et al, 2003).

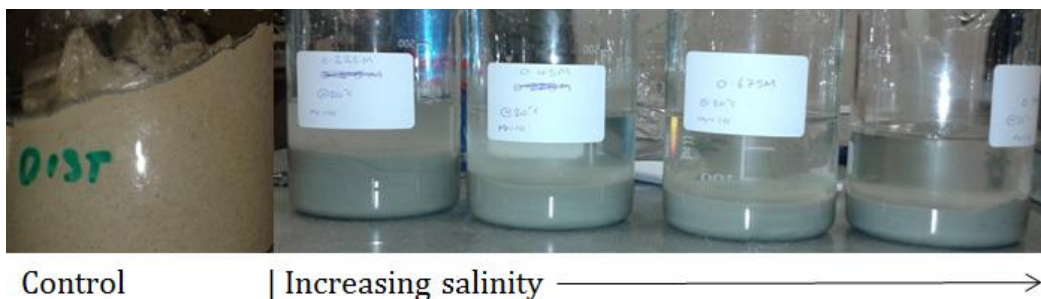


Figure 143: Saline/ MX-80 batch tests (NaCl tests pictured) 1-month duration (Liquid/ solid mass ratio: 10)

The swell index values were plotted along with the results from Lee et al (2012), these are displayed in figure 144. The slight peak in the Ca-Bentonite swell index is comprehensively explained by Lee et al (2012) and is diagrammatically represented in figure 145. In brief, the slight increase is due to the exchange of Ca^{2+} ions with Na^{+} ions, ultimately increasing the diffuse double layer in the interlayer. Furthermore, water is driven into the inter-lamella spacing under an osmotic gradient in dilute NaCl solutions. However, upon increasing the electrolyte concentration the osmotic pressure is reduced and subsequently the interlayers are “pressed” together, this ultimately causes densification/ flocculation of the clay platelets and colloidal layer respectively. Eslinger and Peaver (1988) also discuss the impact of salt solution concentrations on the diffuse double layer of clays, it is necessary to highlight is the effect on the double layer, in that the diffuse double layer reduces with an increase in the electrolyte concentration and as the valence of the dominant cation species increases. Eslinger and Peaver (1988) use an example of a smectite suspension within a dilute solution, it is expressed that the distance of the diffuse layer of cations reduces with increasing solution concentration thereby causing a reduction in spacing between the clay platelets. Ultimately the clay will aggregate/ flocculate and settle, this confirms what is

observed in this batch test. Consequently, this diminishes the materials ability to free swell, otherwise known as the barriers “self-healing” capacity. As for relating this to the MX-80, the process essentially begins at point (A) in figure 145. As Na^+ is already the dominate cation within the interlayer, as the concentration of Na within the bulk solution increases the osmotic pressure reduces thereby reducing the volume of water accessing the interlayer. This as well as the high concentration of Na reducing the DDL, manifests itself by inhibiting the bulk volumetric capacity of the Bentonite.

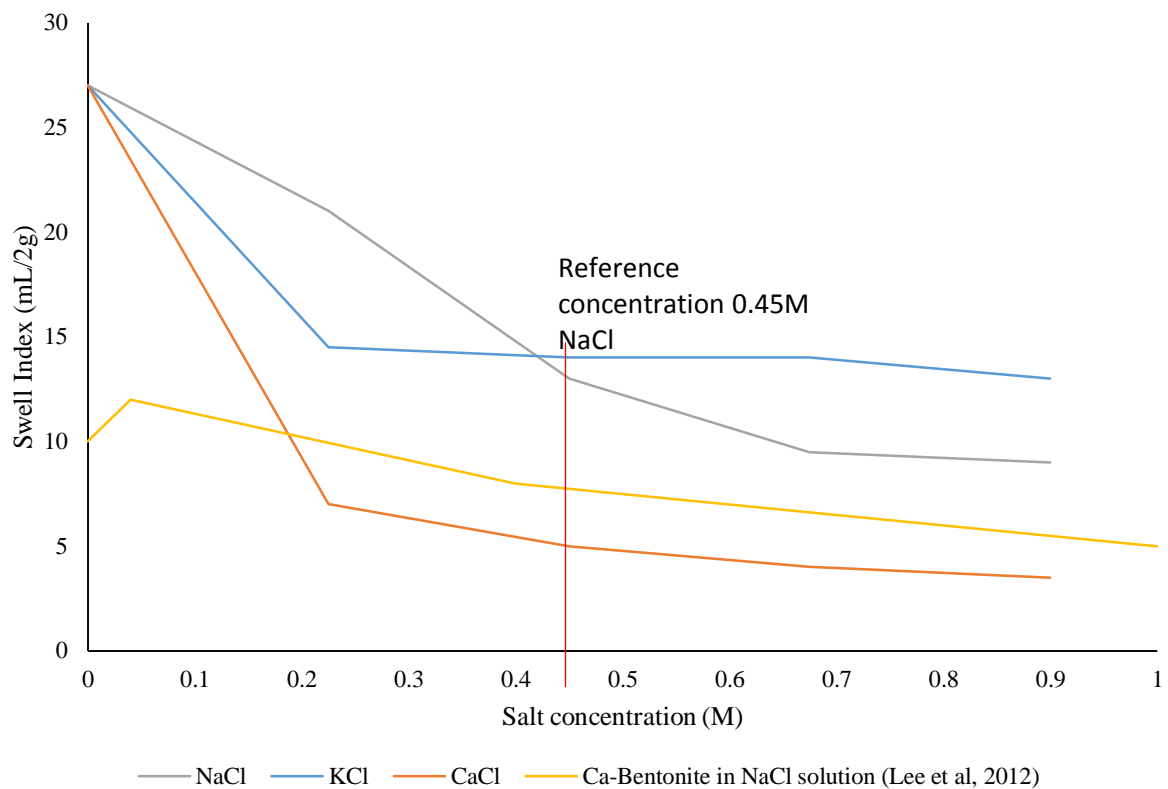


Figure 144: Swell index results for the MX-80/ salt exposure and the Ca-Bentonite in NaCl solution (Ca-Bentonite results after Lee et al, 2012), the red line highlighting the reference salinity concentration for the SAFE Barriers concept

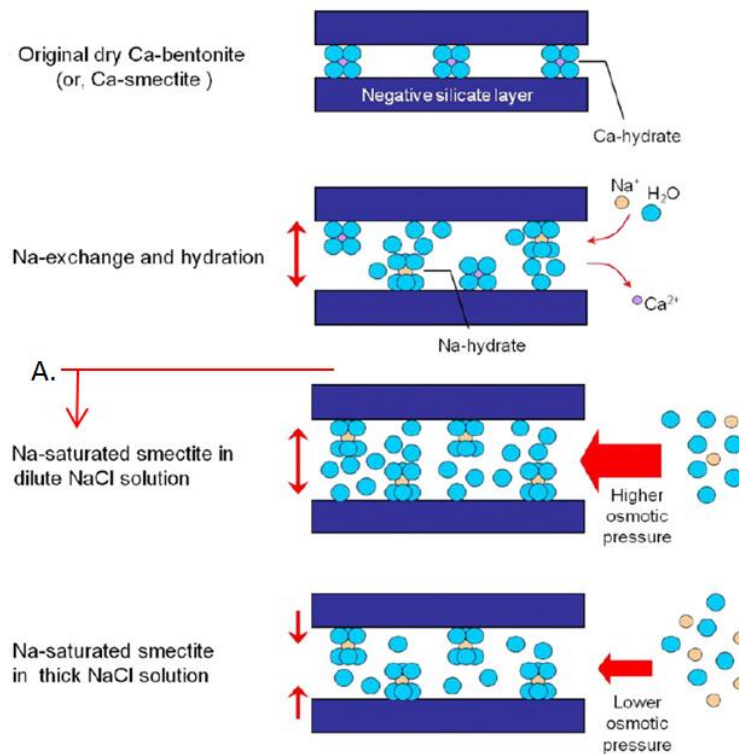


Figure 145: Diagrammatic representation of the swelling hypothesis given by Lee et al (2012), beyond point (A) applies to Na-bentonites (After Lee et al, 2012)

Nevertheless, the MX-80 still intrinsically exhibits a higher free swelling ability under NaCl and KCl solutions, even at the reference concentration (Red line, fig 144). However, using a higher valence cation as the dominant electrolyte, it displays preferential ion exchange and large reductions in the DDL, the MX-80s activity is significantly reduced in high CaCl solutions. Overall there was a drop of 52%, 49% and 81% for NaCl, KCl and CaCl respectively at the reference concentration. Thus, indicating that NaCl and KCl reduces the swelling ability by half whereas CaCl will almost completely inhibit the materials swelling ability.

The plasticity index and activity as a function of the increasing saline concentration is given in figure 146. The PI describes the moisture range over which the soil can exhibit shear resistance while still exhibiting ductile characteristics. This parameter also indicates the materials ability to uptake water over its plastic range with a subsequent increase in volume i.e. the swelling capacity. The activity index was obtained using the PSD curve given in the material classification chapter and the plasticity index values. As can be seen from figure 146, the PI has reduced, as well as the materials activity, therefore its overall characteristic bulk volumetric capacity as well as its plastic behaviour has been impeded. At the reference concentration, the PI is reduced by 76%. Nonetheless, the activity of the clay remains at 1 or above which is considered in soil mechanics as an “active clay” in comparison to a more

stable soil such as a glacial till. Table 47 (Section 4), gives some comparable activity values from literature for other clays and minerals.

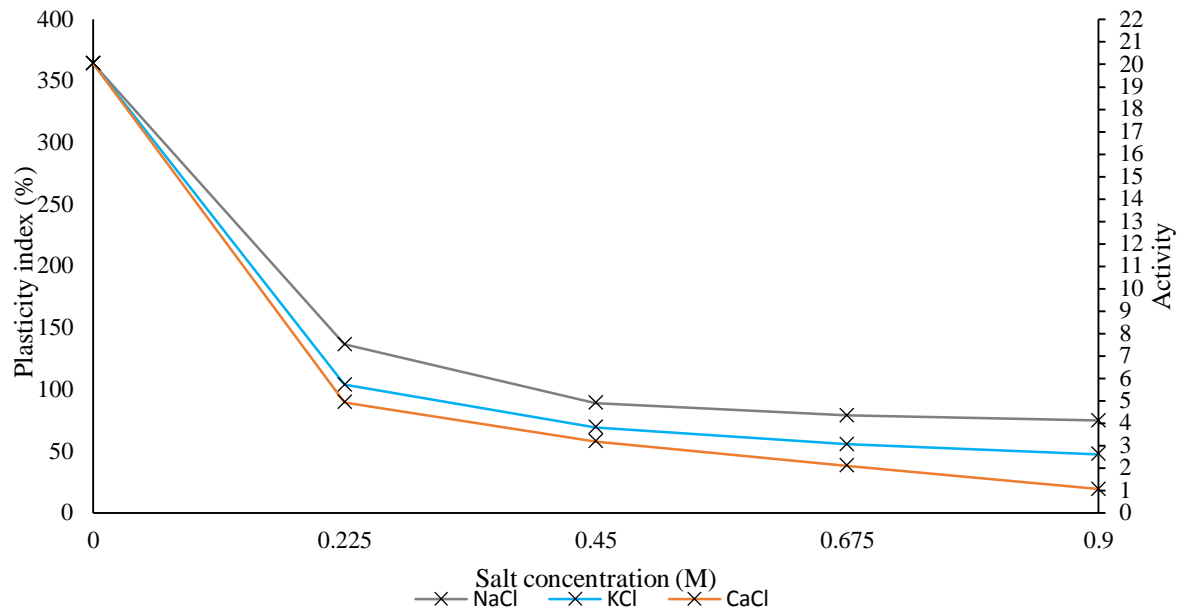


Figure 146: MX-80 PI and Activity vs. Saline solution concentration for the individual electrolyte batch tests

This demonstrates the impact of salt on the clay consistency and its colloidal properties such as the DDL. It is proven here that elevating the salt concentration will essentially make the clay progressively inert, however after a certain concentration the parameters appear to level off. Low to mid saline concentrations seem to induce to most impact, once the solution is saturated the DDL layer becomes rich in the dominant cation and is reduced as well as the osmotic pressure driving the pore fluid into the inter-lamella voids. A combination of these reactions induces flocculation/ densification of the material which ultimately causes loss of volumetric expansion, water uptake capacity and plasticity.

Therefore, caution must be taken when investigating a potential repository site with respect to the deep high salinity groundwater. High saline groundwater appears to have a significant detrimental effect on the barriers ability to uptake higher volumes of water while still displaying shear resistance along with maintaining the high swell capacity for the self-healing functionality. As is seen from figure 146 the plasticity index at the reference salinity has reduced to one quarter of the control value i.e. from approximately 360% to 90% respectively for the NaCl solution. KCl and CaCl displayed a reduced PI by 70% and 58% respectively. Nevertheless, at the reference salinity (0.45M) the clay activity of

approximately 5, 3 and 2 for NaCl, KCl and CaCl respectively, still somewhat classifies the Bentonite as being an highly active clay.

5.1.2. Batch #2 (S-MX80-NaCl-Comp-20) results:

The series of batch tests conducted here introduced the chosen steel, namely structural carbon steel, type S275. This batch investigated the interaction of corrosion of the C-Steel with distilled and low to high saline solutions- NaCl type. The batch used compacted Bentonite “pucks” (See figure 147) which was compacted to the reference dry density (ρ_{dry} : 1.56 Mg/m^3). Upon exposure to DI water or saline solution, the Bentonite could free-swell within the solution at 20°C for 1 month. Swarf from the machined carbon-steel coupons was implemented within this batch test, this was to increase the exposed surface area between the bentonite and the carbon-steel to maximise corrosion integration.



Figure 147: Compacted MX-80 with S275 particles (Swarf)

From figure 148, it appeared that the Bentonite lost its ability to adsorb as much water with increasing salinity. Moreover, an interesting point to be made is that the saline samples, upon hydration, appeared to migrate up the glass vessel towards the saline solution, which is likely due to the osmotic pressure. However, this migration looks to be hindered by the upper zone of Bentonite. This is conceivably due to a localised reduction in porosity due to particle flocculation and a differential concentration of NaCl concentration over the sample depth. Whereas the sample that was able to free swell in DI water, appears to saturate in a much more uniform manner.

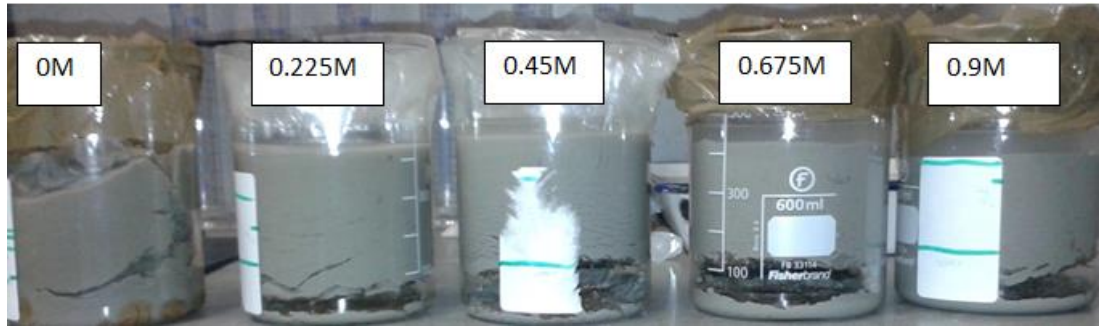


Figure 148: Batch samples after 1 month of saturation with increasing saline solution (NaCl)

It is acknowledged that the corrosion and the Bentonite was exposed to an aerobic environment and the redox conditions could not be controlled. Nonetheless the batch series allowed an insight into the extent to corrosion integration into the Bentonite as well as the alteration under such conditions. Post-mortem of the samples displayed that the extent to which visible corrosion had precipitated was approximately 3mm. The batch specimens were separated at the 3mm zone from the C-steel, the objective behind this was to obtain a property alteration profile throughout the sample.

Figure 149, displays the post analysis free swell index for the batch series, two measurements were taken less than 3mm and greater than 3mm from the C-steel zone. Figure 150 displays the Plastic limit results for the batch series, due to the lack of sample mass, only the plastic limit was obtainable.

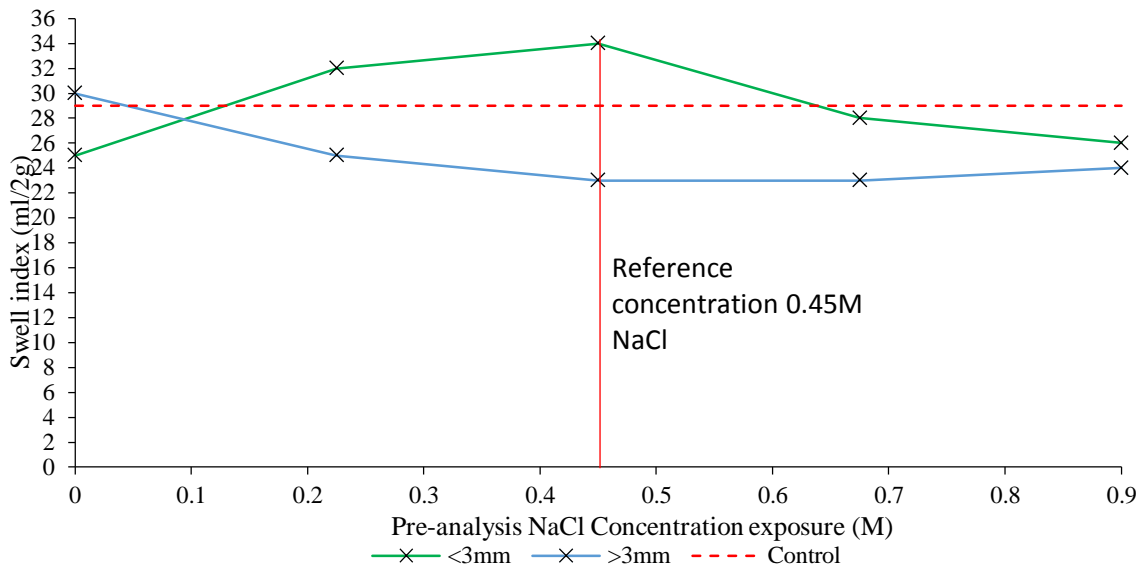


Figure 149: Swell index results for batch #2, the green line represents the sample from the interface zone and the blue line represents the outer zone (Red line indicates reference concept saline concentration)

It appears that the outermost section of the sample (>3mm) is affected by the saline solution, the profile displays the characteristic decline in swelling ability, with a 20% reduction at the reference concentration. The reduction in the swell index is however much

higher than the previous batch, this is due to the post testing procedure. In the previous test the salt solutions were used in the free swell methodology. Whereas the free swell results here used DI water on the samples, post saline exposure, thus meaning that the salt within the Bentonite has been diluted giving rise to a recovered swell index. This indicates that there is no irreversible alteration to the smectite, but the salt that remained in the sample has impeded the swelling. What is more, the sub-sampled zone closed to the C-steel has an increased SI in the mid saline range, Fe corrosion products are known to have a higher volume than in its zero-valent state, and can therefore be attributable to this. At the reference concentration, the swell index increased by 17%, this increase indicates that in fixed volume conditions the pressure would be greater due to the combined effects of the swelling component of the Bentonite and the corrosion products. It also appeared that the extent of the corrosion integrated more into the Bentonite in the mid salinity concentration range, which is likely due to the loss in gelling characteristics and reduction in the DDL, thus allowing more free movement/ diffusion throughout the intra-lamellae pores.

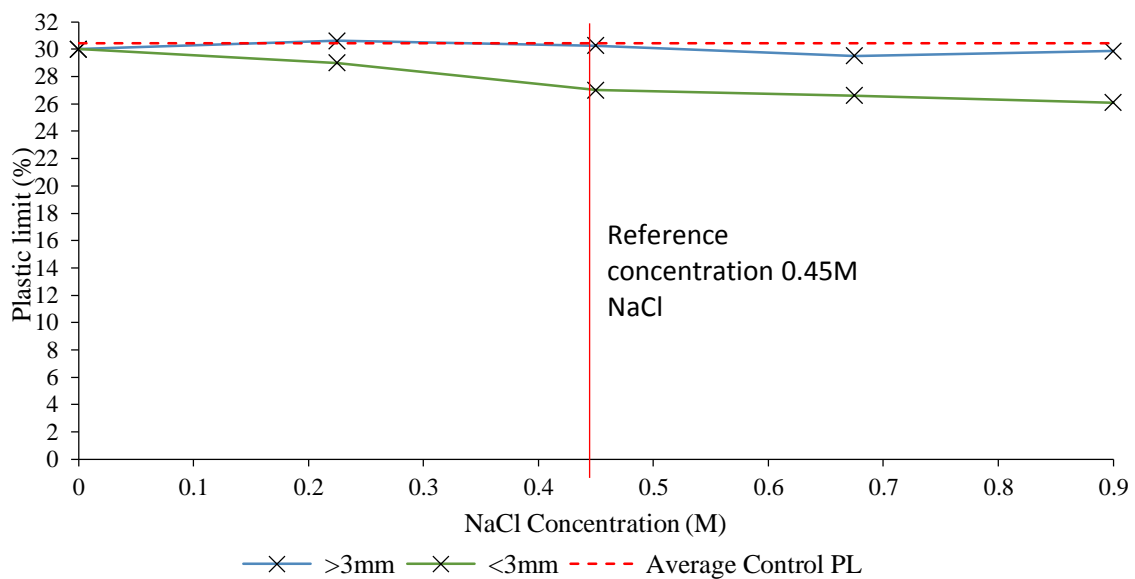


Figure 150: Plastic limit results for batch #2, the green line represents the sample from the interface zone and the blue line represents the outer zone (Red line indicates reference concept saline concentration)

As stated previously, plastic limit measurements could only be obtained due to the lack of material used. However, for the interface sub-sample that the reduction in the plastic limit is greater with little change to the outer zone consistency. The reduction in the plastic limit is thought to be related to the reduction in size of the diffuse double layer, in this case due to the higher valence cation, Fe^{3+} . Thus, indicating that the soils capability to uptake as much free water is inhibited by the inter lamella spacing reduction, which is governed by the distance of

the diffuse double layer from the platelet to the weakly held solution in the centre. Nevertheless, at the reference concentration the sample with the integrated corrosion products only displays a plastic limit reduction of 10%.

5.1.3. Batch #3 (S-MX80-Comp-105) results:

This batch tests implemented the constant volume cells which allowed the steel/Bentonite to be exposed to high thermal loading under confined conditions, more realistic to the early phase interface conditions (See Figure 151). The samples used compacted Bentonite using DI water in contact with the C-steel coupon, exposed to 105°C for 1 month. The following graphs display the results from each sub-sampled zone for the swell index and plastic limit respectively. Again, only the plastic limit was measurable due to the limited mass of material used.

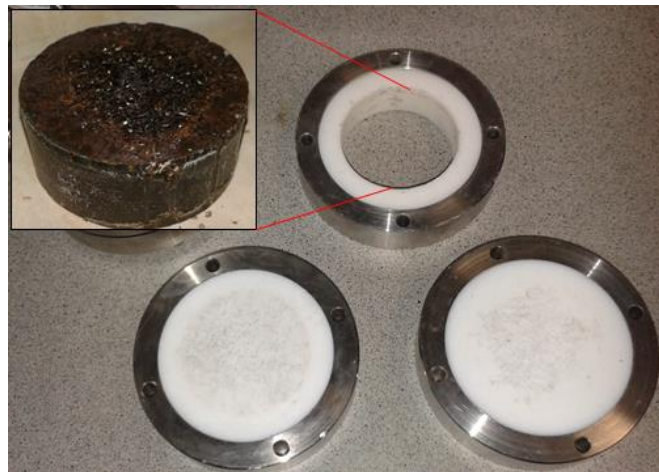


Figure 151: From batch #3 (Steel/Mx-80 & distilled water), compacted and heated to 105°C within a constant volume cell
(The sample picture is post THC exposure)

There is a large variation in the free swell index measurements for the interface and outer zones, figure 152. Whereas the plastic limit, demonstrates an overall reduction with little change over the sample profile, figure 153. The small difference in the plastic limit is most likely due to the sampling distance between the sub-sample zones. There is a little drop which indicates that temperature and corrosion has some influence but no conclusive deviation. However, what is seen in figure 152, the free swell index displays higher discrepancy between the sub-sampled zones. The higher temperature zone affected by the corrosion product integration displays a 38% drop which could be due to the sampling post THC exposure. In that the sample was dried before the swell index sample was taken and therefore the sample may have contained more oxides than actual Bentonite by mass. In the outer zone the free swell index displayed a 38% increase in the free swell index, perhaps indicating that

there is an increased concentration of cations that have migrated away from the interface thus influencing the DDL.

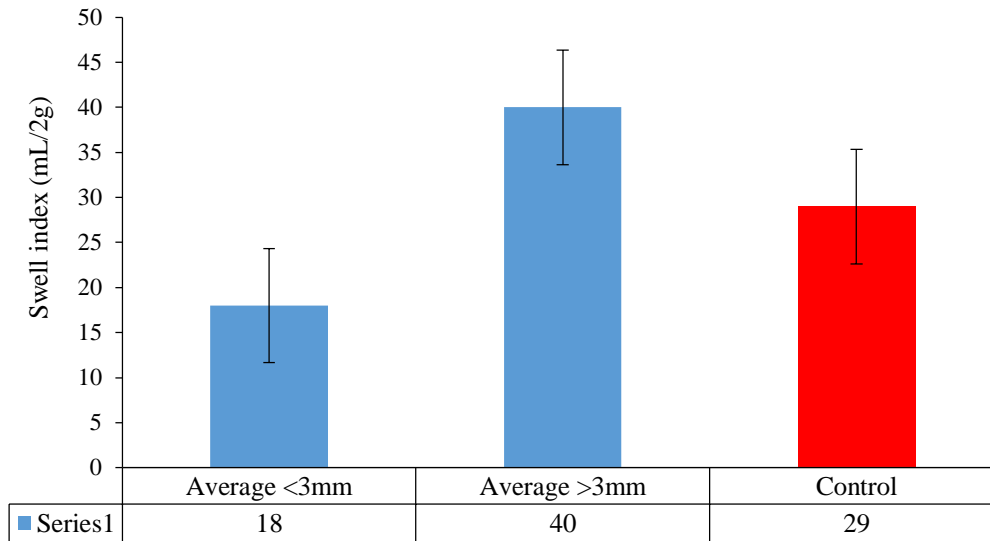


Figure 152: Batch #3 swell index measurements post THC exposure

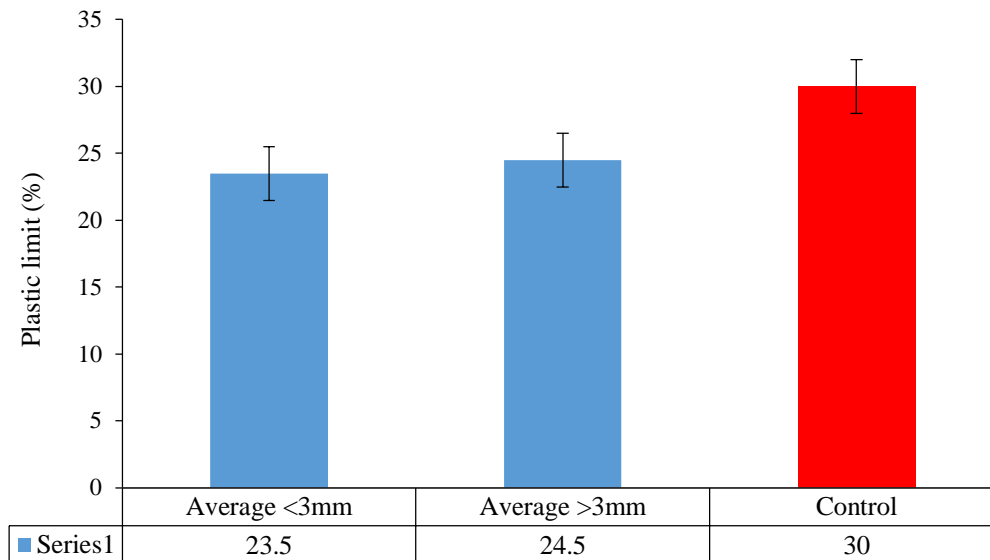


Figure 153: Batch #3 plastic limit measurements post THC exposure

CEC measurements were taken post thermal exposure the results indicate a minor drop, figure 154. Nonetheless after short-term thermo-chemical exposure the materials ability to exchange cations is barely influenced.

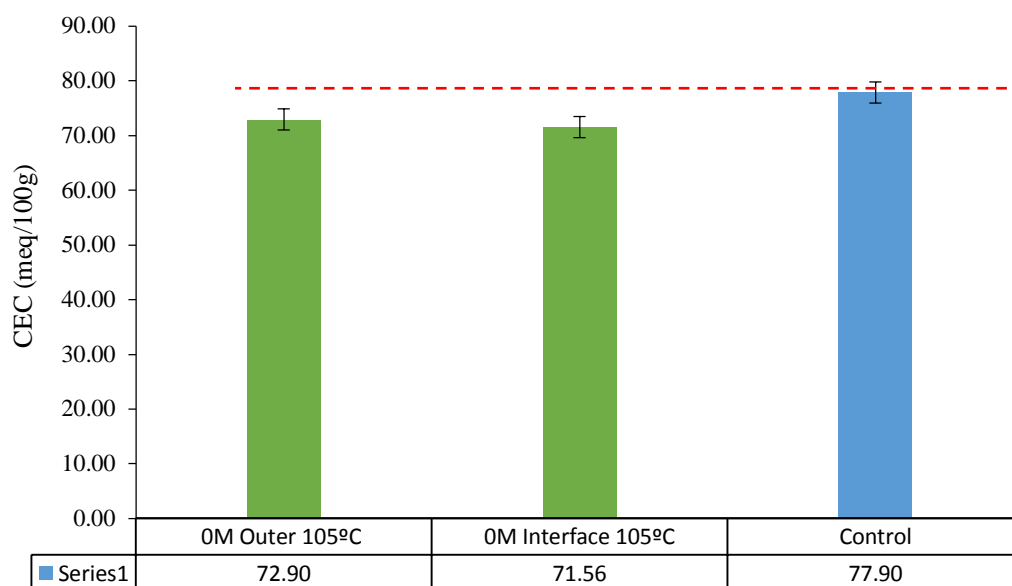


Figure 154: CEC measurements on interface and outer sub-samples from batch test #3

5.1.4. Batch #4 (S-MX80-NaCl-Uncomp-20) results:

This consignment implemented the same boundary conditions as batch #2, except for the initial conditions of the Bentonite. The Bentonite was in powdered form with the steel coupon inserted into the powder in contact with the respective solution (figure 155). The liquid to solid mass ratio was the same as before.



Figure 155: From batch #4 (Steel/Mx-80 & increasing saline solution), C-Steel plate in contact with uncompact Bentonite (DI water sample)

The purpose of this test was to observe differences to the extent of which the corrosion products precipitated throughout the uncompact sample. The same post exposure sub-sampling methods were adopted as before, as well as post exposure analysis. After the THC exposure period, it was observed that the uncompact Bentonite resulted in a much greater extent of visible corrosion precipitation from the interface (see figure 158). This is

understandable as the Bentonite structure will be overall less compact and randomly oriented. The structure difference between compacted and uncompact Bentonite was expressed by Holmboe et al (2012) and Lee et al (2012) with figure 156 illustrating their hypothesis.

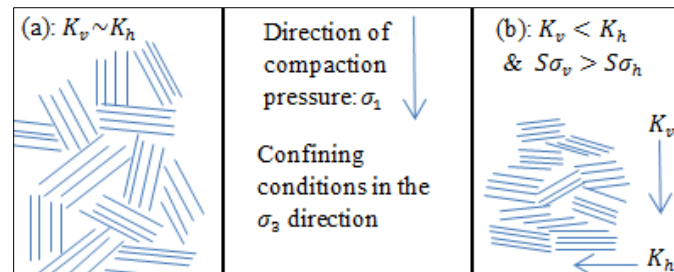


Figure 156: Effects of anisotropic compaction on the structure of the Bentonite, A) uncompact Bentonite, turbostratic formation with somewhat isotropic permeability (K) and B) after compaction displaying a more ordered structure with anisotropic swelling pressure ($S\sigma_x$) and permeability (K).

A more compact structure, as evident in batch series #2, results in a lower porosity and void ratio along with the rest of the associated geotechnical and physicochemical properties i.e. hydraulic conductivity and diffusion rate. With respect to the uncompact state, an interesting point to highlight is the extent to which the visible corrosion is transported away from the coupon over the salinity range. Through direct observation the extent to which the discolouration penetrated the sample was reduced at either end of the salinity concentration spectrum. A conceivable postulation for this phenomenon may perhaps be due to two completely different mechanisms for the respective samples. For instance, the 0M batch, the clay essentially develops its characteristic colloidal gelatinous form that appears to visually limit corrosion precipitation into the sample. It can be seen in figure 160, the 0M sample shows a large extent of oxide built up on the base. This is not through the sample but over the glass layer in a void caused upon the Bentonite hydration within the sample containing distilled water. The extent to which corrosion precipitated into the uncompact sample was measured to be approximately 15mm under static, zero saline conditions (Figure 157) compared to approximately 3mm for batches 2 and 3 respectively.

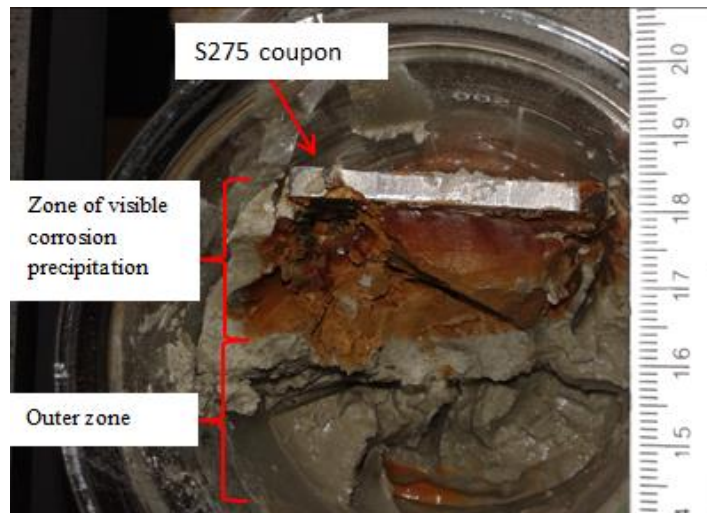


Figure 157: Steel/ clay batch test sub-sample locations for post- tests, sample picture of the uncompact batch #4 (OM)

Whereas the highest molarity batch sample destroys the structure of the Bentonite causing flocculation and loss in the materials ability to form the thixotropic consistency. The higher the concentration of saline solution the more changes to the colloidal characteristics of the clay is recognised. Increasing saline concentration results in increasing densification, this appears to inhibit visual corrosion transport from the coupon into the surrounding outer zone. Additionally, from a qualitative point of view and by observation of figure 158, the Bentonite loses its ability to hold the coupon upright. Thus, indicating that with the same volume of solution for each sample, the liquid limit decays with increasing salinity (apparent from the results obtained from batch consignment #1). Ultimately the shear resistance of the thixotropic material is largely lost at very high salinity's. This signifies a potential adverse circumstance for canister displacement tolerances and the self- healing ability at the higher end of the salinity range. Furthermore, the extent of visible corrosion was greatest in the batch sample relevant to the reference salinity (0.45M), thus demonstrating the rate of diffusion is greatest at this salinity range as well as possible alterations due to iron/ montmorillonite structural interaction may be at elevated risk.

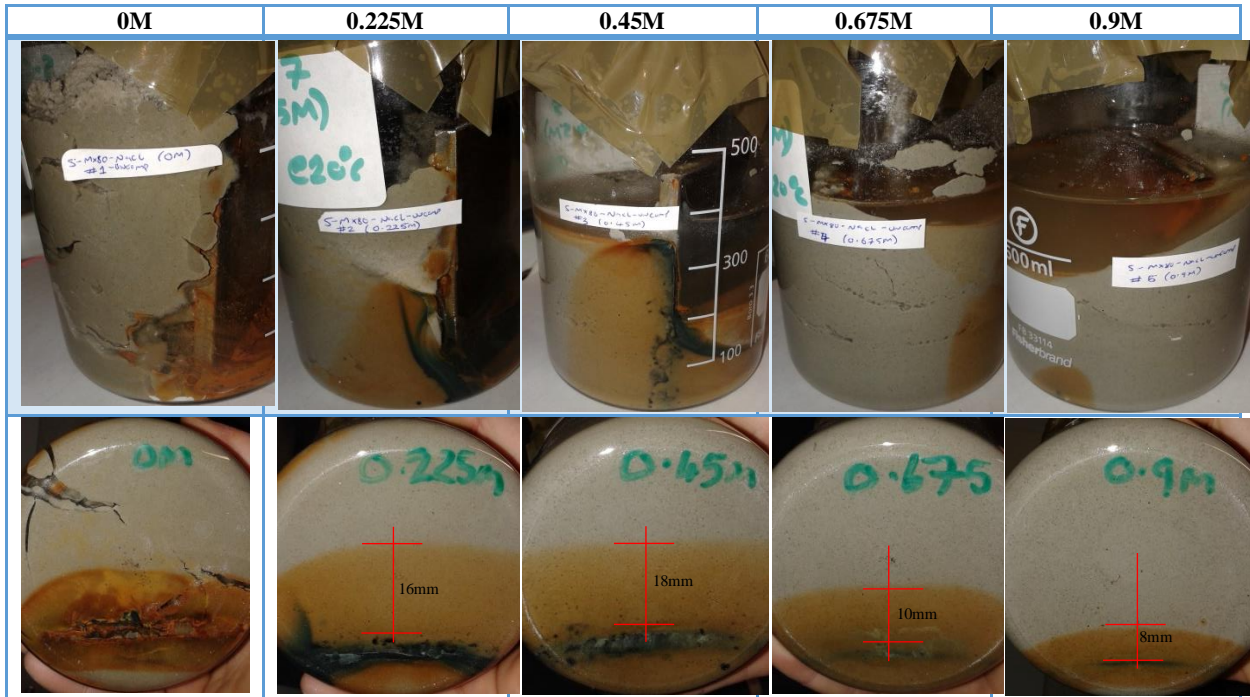


Figure 158: Batch test #4 (S-MC80-NaCl-Uncomp-20°C)

Swell index results conducted on batch #4 consignment samples are displayed in figure 159, once more the characteristic decay of volumetric uptake upon access to free water is observed.

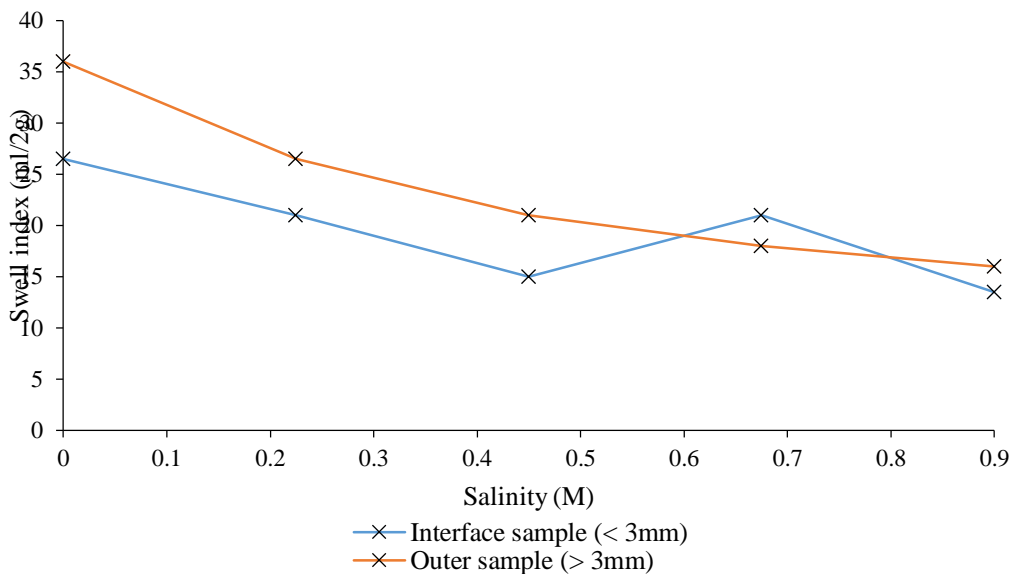


Figure 159: Batch #4 swell index measurements

By comparison of the interface swell index measurements for batches' #2 and #4 (figure 160), the initially compacted sample displays an increase in the mid- salinity range at the interface zone. Whereas the uncompact samples display a progressive deterioration with a

slight anomaly 0.675M sample. This anomaly may perhaps be down to sampling heterogeneities during sample dissection.

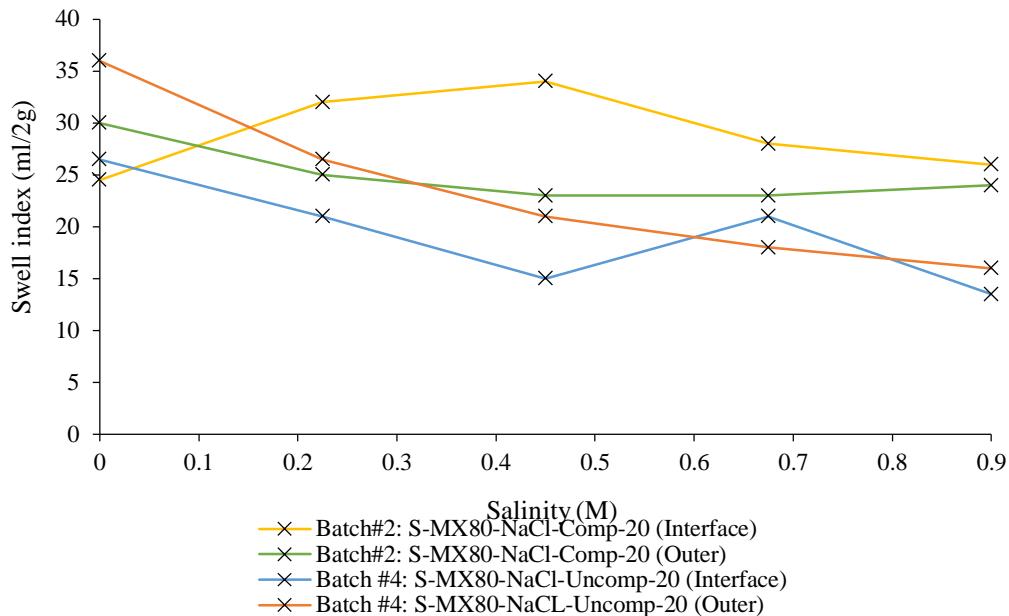


Figure 160: Swell index comparison of batch #2 (initially compact sample) and batch #4 (Initially uncompact sample)

Difficulties in sub-sampling were also experienced for the uncompact batch (#4) samples due to the loss of integrity at higher salinities, thus getting an exact boundary without disturbing and mixing the inner and outer areas of the loose material was difficult. Nonetheless for the majority of the results closely correlate with one another. A plausible explanation for the difference between the two interface results is the accessibility of saline solution into the sample during saturation. For instance, the compact sample slowly re-saturates, progressively saturating and expanding from the outer zones first, this may perhaps act as a barrier for sodium ions accessing the inner areas of the Bentonite. Whereas the uncompact Bentonite when saturated with a saline solution, will saturate much more uniformly and therefore the effects of increasing salt solution can be seen right into the sample and not just in the outer zones. The increase in the swell index for the initially compacted sample (batch #2) could be the presence of more corrosion products, thus increasing the volume. As for the outer zone sub-samples, the swell index measurements display the characteristic decay as displayed in batch #1 and #2. The gradient of the slope presented in figure 160 (above) is somewhat steeper for the uncompact samples than the outer swell index measurements for compact samples in batch test #2. This may be a result of the loosely arranged nature of the powered samples and the ability for sodium to access the interlayers throughout the sample. Furthermore, the zero-salinity batch for batch #4 is slightly higher than batch #2 (0M NaCl), 36 ml/2g and 30 ml/2g respectively, a difference of 6 ml/2g.

Thermal influence and clay structure can be further demonstrated in figure 161. This displays a comparison of the results from batch tests #2, #3 and #4 for the DI water samples. There is negligible change in the swelling index for both the interface and outer zones for the ambient batch samples (20°C). Batch #3 that received the highest thermal exposure displays the most prominent deviation between the sample zones. It appears that temperature greatly influences the colloidal characteristics of the Bentonite and the diffusion rates of the corrosion products.

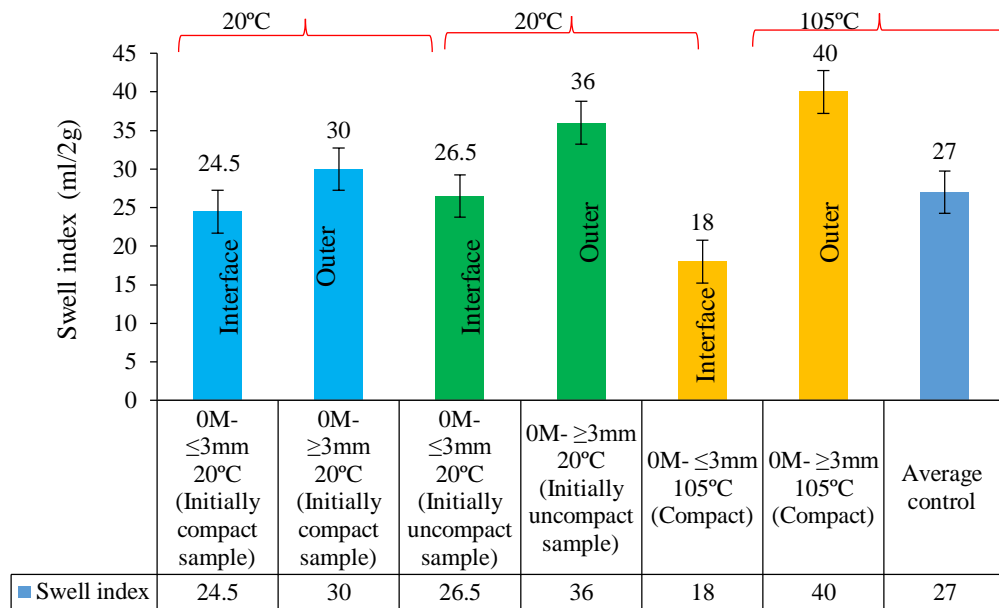


Figure 161: Swell index comparison of batch tests #2 (Blue), #3 (Green) and #4 (Yellow) displaying the influence of structure and thermal exposure

Plastic limit measurements conducted on the samples taken from the un-compacted specimens (batch #4) are displayed within figure 162. Comparing these results to the plastic limit measurements from batch #2, display little deviation from the average control, figure 163.

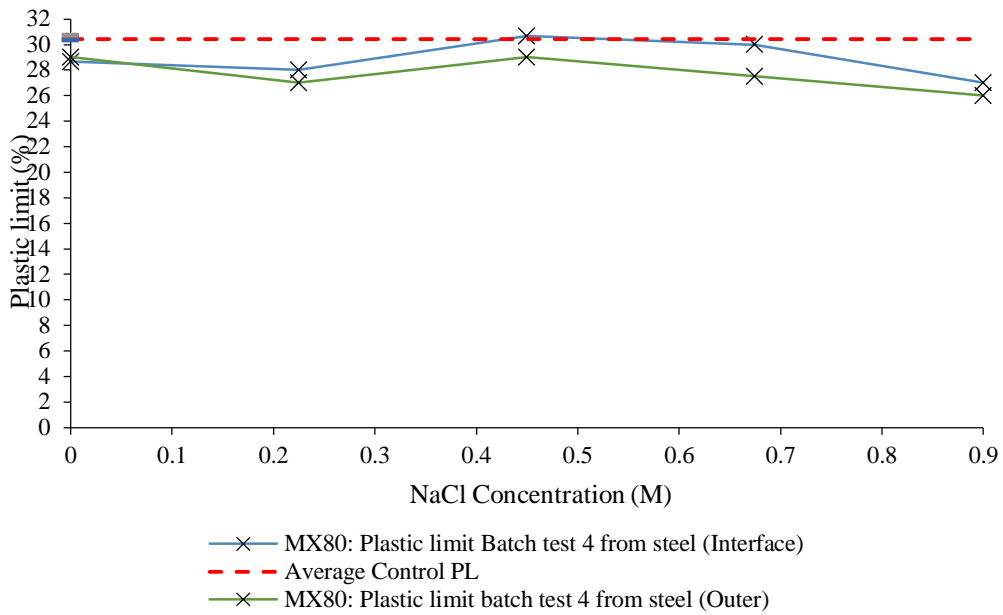


Figure 162: Plastic limit results for batch test #4 sub-samples

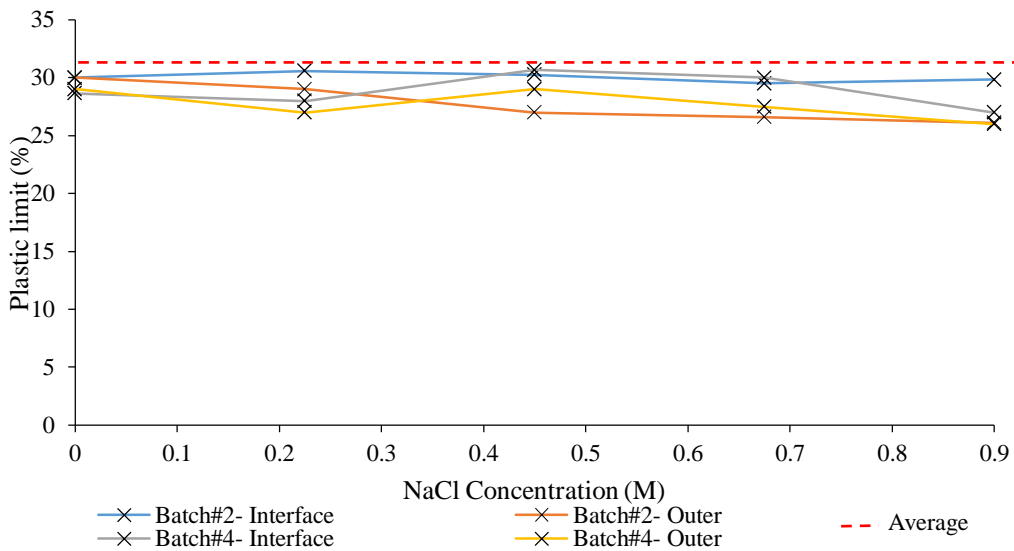


Figure 163: Plastic limit comparison between batch tests #2 and #4

Additionally, CEC measurements were conducted on batch series #4, figure 164, to see if high salinity and corrosion integration affected the ability of the Bentonite to retain cations. The higher the value the more the material will act as a “molecular sieve” to external cations and more importantly, with respect to the nuclear barrier system, the ability for the barrier material to sorb/ slow any radionuclides.

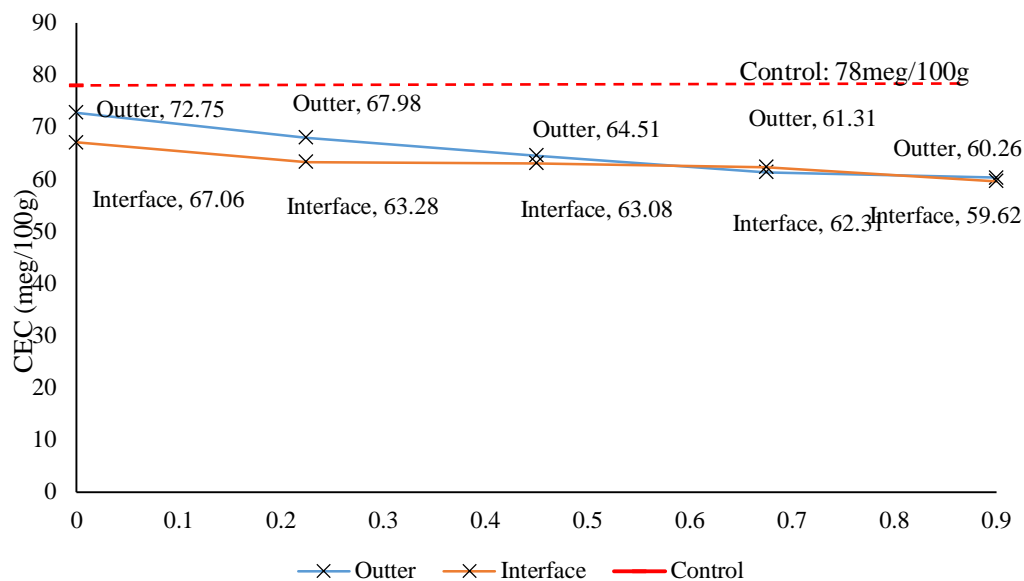


Figure 164: CEC measurements on batch series #4

Figure 164 indicates that exposure to NaCl solution and carbon steel does somewhat impact the materials overall CEC capabilities, however the CEC measurements are still very high. Both the outer and interface zones display a steady decay other the increasing salinity range, additionally the 0M batch indicates a drop from the control value of almost 5 meg/100g and 11 meg/100g for the outer and interface samples respectively. Thus, indicating that purely iron present within the system slightly influences the materials sorption ability, consequently the additional reduction is a combination of NaCl solution concentration and the Fe cations present. Nonetheless the CEC of the highest salinity concentration (approx. 60meg/100g) is still considerably high in comparison to other more stable clay minerals such as illite and kaolinite. Table 63 displays the respective CEC values for the common clay mineral types for comparative purposes.

Table 63: General CEC values of the most common clay minerals (F.G.Bell, 1996; Weaver et al, 1973)

Material	Cation exchange capacity (meq/100g)
Montmorillonite	60-120
Illite	10-15
Kaolinite	2-5

Figure 165 below displays the 0M samples from the 105°C and the 20°C exposure batch tests (Batches #2, #3 and #4). What is clear is that there is an inherent reduction in the CEC under exposure solely to an iron source with no saline solution. However, it is also evident that thermal loading during contact with an iron source doesn't necessarily impact the CEC of

the material under short-term THC exposure (1 month). The most significant difference is noticed between the control and the interface sub-sample for the 20°C specimen of approximately 11 meq/100g, the short-term thermal loading impact seems to be negligible due to the minor difference between the two outer measurements of 72.89 and 72.75 meq/100g for the 105°C and 20°C respectively.

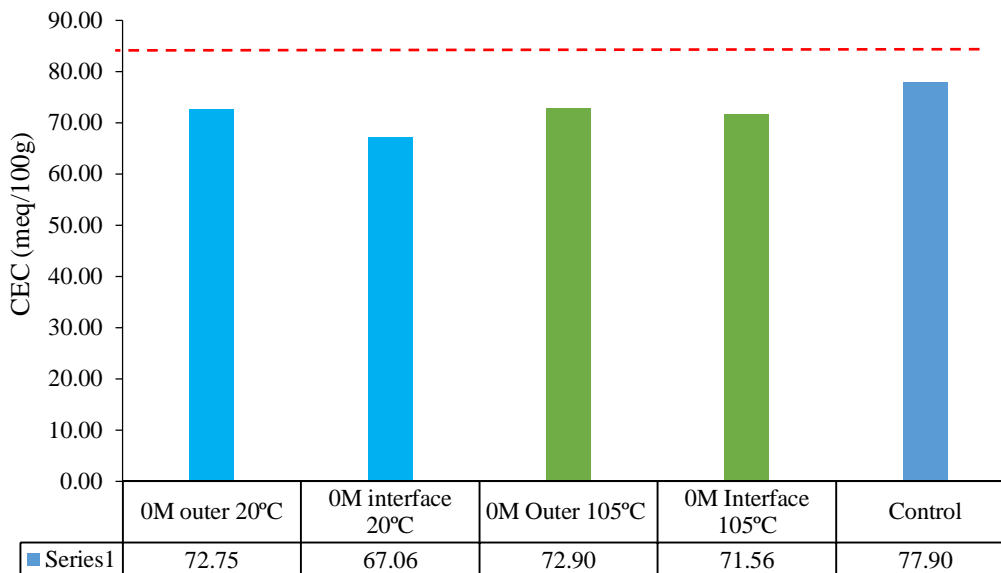


Figure 165: Batch #4 (Uncompact) and batch #3 (Compacted, heated) CEC comparison

5.1.5. Batch #5 (MX-80/HT/D) results:

This batch consignment focused exclusively on the effects of temperature exposure and duration on the Bentonite. Temperature exposure increments ranging between 50°C and 300°C were implemented over a 24hr exposure period (each increment increasing by 20°C). Thermal duration under 105°C for 1 day to 12 weeks were also implemented with the thermal loading tests (each duration increment increasing by 1 week). This investigation allowed a systematic comparison to duration and thermal loading exposure thereby allowing a conclusion on what boundary condition more significantly affected the consistency, free swell and CEC of the Bentonite.

Firstly, the results from the thermal loading under short timescales are presented, the free swell index results presented in figure 166 and plasticity results in figure 167. Interestingly, the swell index measurements appear to remain unaltered to a temperature of 90°C (a, figure 166) after-which the free swell volume of the Bentonite appears to increase to a temperature of 150°C (Point b, figure 166). After reaching this thermal load the free swell ability of the Bentonite declines with increasing temperature increment. Between the two points where

temperature appears to increase the swell index, the maximum increase over this thermal range was 27%. At a thermal exposure of 300°C the swell index was reduced by 22%. The increase here is likely attributable to the DDL and the surface potential charge, it is known that higher temperatures will increase the DDL (Mitchel and Soga, 2005), this can be quantified via XRD analysis in a fully expanded state. The subsequent drop is likely due to the combined temperature effect on the layer charge, fusing of platelets due to the precipitation of siliceous minerals (Xiadong et al, 2011) and the development of disordered amorphous crystallites. However, results for the plasticity index do not deviate significantly with little trend between the PI and increasing temperature. Therefore, short-term thermal loading does not affect the bentonites' ability to uptake water as well as its plastic range.

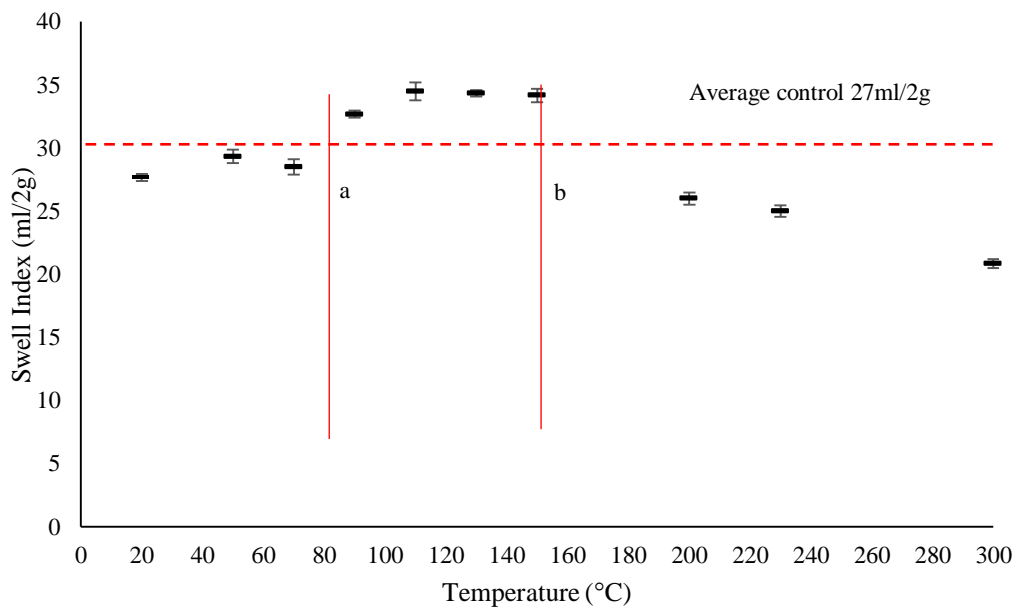


Figure 166: Average swell index measurements with increasing thermal exposure for 24hrs

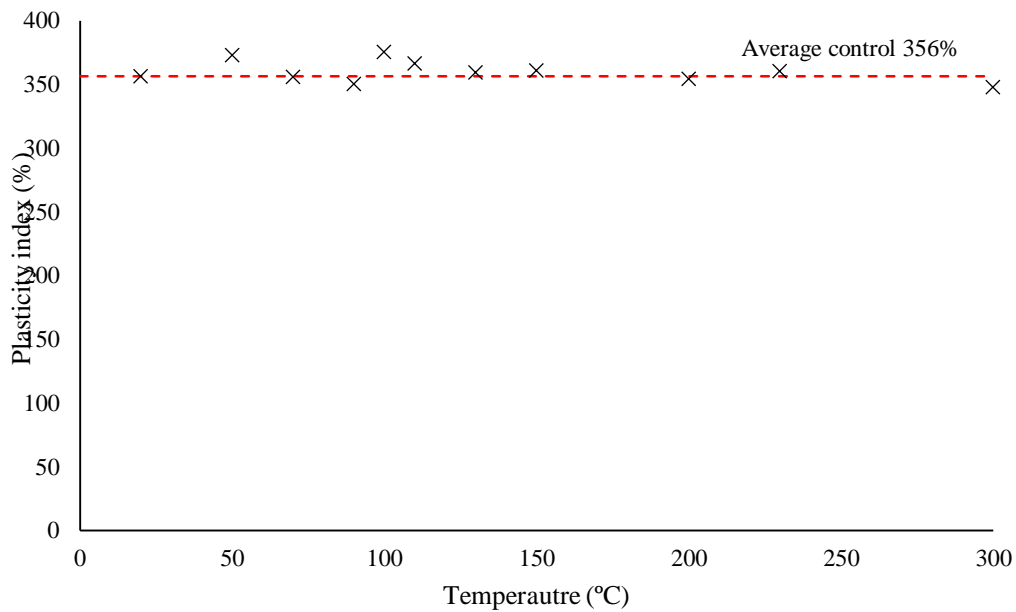


Figure 167: Average plasticity index with increasing thermal exposure for 24hrs

Secondly, the thermal duration swell index and plasticity results are displayed in figures 168 and 169 respectively. What is seen is that there is a correlated increase in the swell index and plasticity index for the lower duration increments, up to two weeks of thermal exposure. It appears that the plasticity index of the materials is largely reduced after 84 days of thermal exposure of 100°C, a drop of 32% was measured. The initial increase in the swell index for the lower durations correlate to the thermal exposure measurements in figure 165, which indicate that the results are in fact systematic and not due to operator error. Therefore, thermal exposure initially increases the DDL and layer charge. However, duration appears to allow microstructural/ mineralogical alterations to take place and had a greater influence on the consistency of the Bentonite rather than thermal loading.

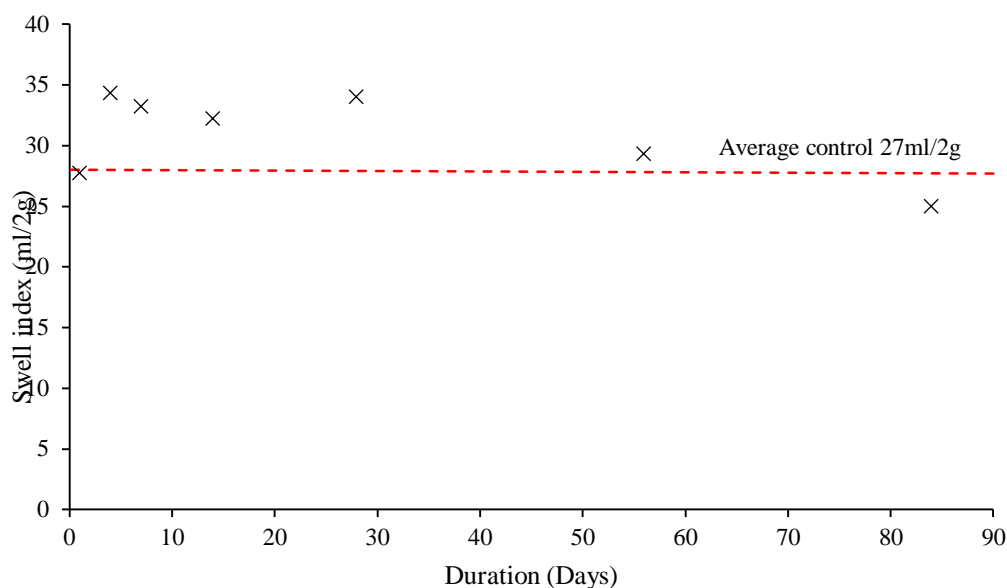


Figure 168: Average swell index after thermal loading (100°C) and duration

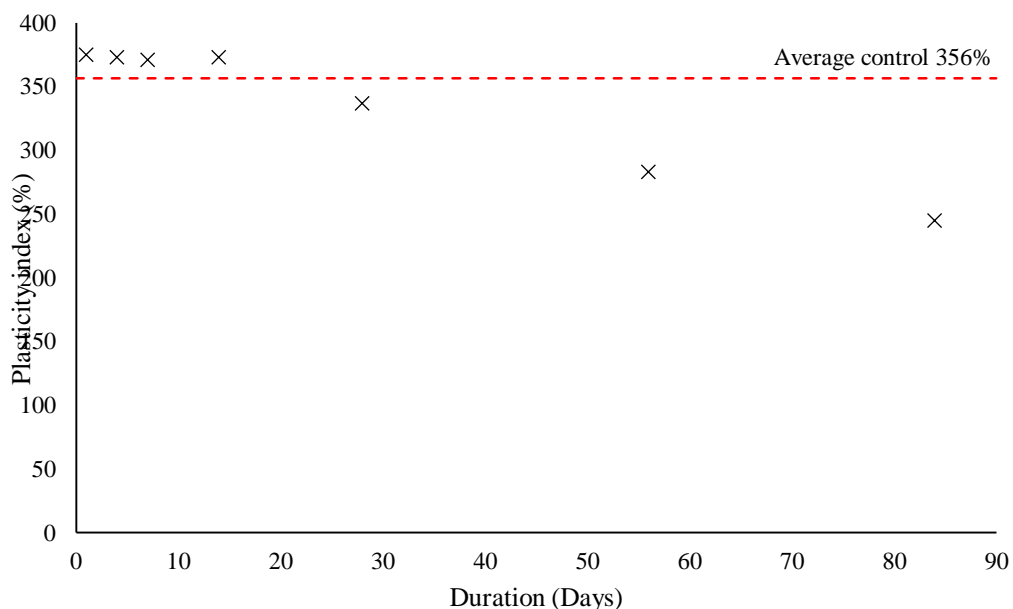


Figure 169: Average plasticity index after Thermal loading (100°C) and duration

CEC measurements were also conducted to investigate if there was layer charge alteration after loading and duration testing, figures 170 and 172. Short-term thermal loading displays negligible change to the layer charge characteristics of the MX-80. However, interestingly, there is a very similar profile for the duration measurements, initially increasing with a slight reduction, this profile is not as prominent as the PI or SI vs. duration measurements. This supports the idea that there is a degree of alteration to the layer charge due to the influence of thermal exposure. Layer charge alteration is primarily due to the vacancy state of the TOT layers. Therefore, it is possible that cation exchange is occurring i.e. Al^{3+} or Fe^{3+} for Si^{4+} in the tetrahedral layer at the higher temperatures in the short term

due to an increase in the kinetics by higher thermal energy input. Exchange for Si^{4+} can cause an excess negative layer charge. The subsequent drop in the SI and PI for longer durations and higher thermal exposure could be due to higher dissolution and recrystallisation of amorphous products, likely siliceous in nature. This latter reaction pathway may explain the reason for loss of CEC due to Si loss from the tetrahedral layer or fusing of stacks by Si products.

With respect to the functionality of the barrier, any loss in swelling capacity or PI indicates that the Bentonite has lost its ability to “self-heal” or maintains suffice plastic characteristics with respect to canister positioning and stress distribution/ absorption if host rock displacement was to occur. However due to the short time scales conducted here, a loss of 32% in PI after 86 days does not mean that the barrier will continue to linearly decay. Hence longer time scales are required to understand the nature of this parameters decay function with temperature.

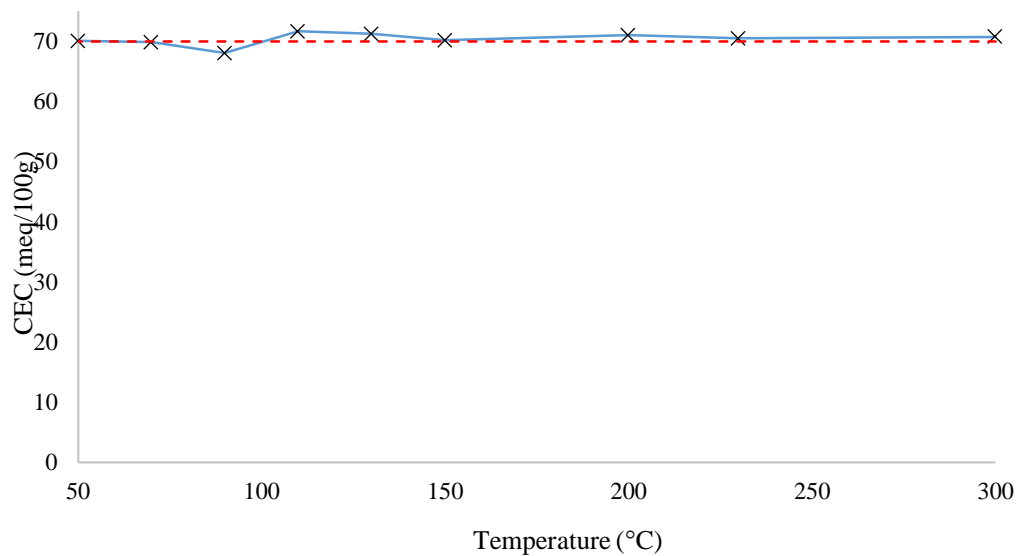


Figure 170: CEC measurements for thermal loading tests (Red line: average control)

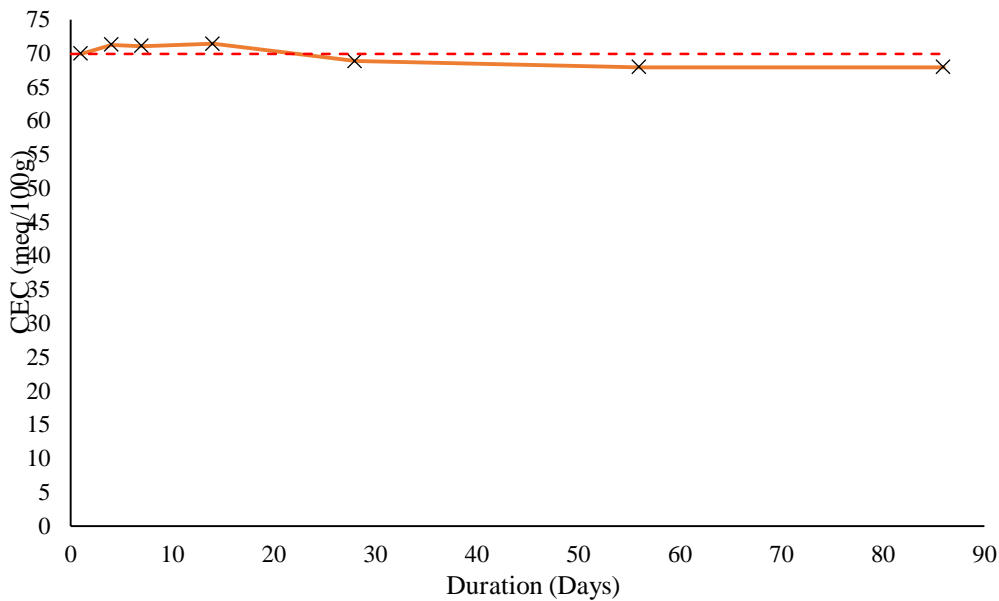


Figure 171: CEC measurement for thermal duration tests (Red line: average control)

5.1.6. **Batch #6 (MX-80/HT/D/HS) results:**

This powder batch tests investigated thermal loading (20°C, 105°C and 150°C) for 56 days with four separate inorganic salt solutions (NaCl, KCl, CaCl and a synthetic groundwater mix). The second part of this batch consignment used the salt that had the most significant impact on the consistency of the MX-80, obtained from the PI vs. salt concentration profiling from batch #1. Consequently, CaCl was chosen to carry forward into this batch consignment, along with the synthetic groundwater mix under three thermal loads (20°C, 80°C and 100°C) for two durations (8 and 12 weeks).

The plasticity index results for the first powder batch analysis are displayed below in figure 172. The concentration of the respective salt solutions was based on the calculated concentrations from the Eastgate borehole data (the respective concentrations are displayed below in table 64). The purpose of these tests was to investigate the influence of more realistic concentrations on the consistency of the MX-80 as well as a more complex saline solution i.e. the synthetic groundwater. The composition of the synthetic groundwater was a mix of the three chosen salts at their respective concentrations. By comparison, the reference concept concentration for NaCl is similar to the calculated concentration from the borehole data. Therefore, the effects are somewhat comparable to previous tests for this particular salt.

Table 64: Calculated salt concentrations for a crystalline rock mass at 995m BGL (After Manning et al, 2007)

Salt	Concentration (Molar)
NaCl	0.34
KCl	0.135

CaCl_2	0.017
-----------------	-------

From figure 172, the individual salt concentrations under ambient temperatures have a direct impact on the consistency of the salt, with the greatest impact being from the Di-valent calcium. Understandably, this greatly reduces the DDL with a subsequent loss of the materials ability to uptake moisture. Furthermore, the combined effect of all three salts display a much greater initial drop of due to the much higher initial concentration. All four salt solutions follow a similar trend with increasing temperature. The synthetic groundwater appears to immediately reduce the plasticity index by ~29.3%. Temperature appears to have a negligible impact from 20°C to 100°C with a ~7% decrease between the two. Additionally, and interestingly, the KCl at 20°C does not appear to impact the PI of the Bentonite, however as thermal loading increases there is a reduction in the PI. It appears that temperature could accelerate K fixation/ illitisation i.e. higher temperatures increase the interlayer exchange capacity. At 100°C KCl reduces the PI by ~21% with no change after this thermal boundary. This could be due to the limited availability and low concentration of K cations in solution. The green line in figure 172, displays the effect of temperature without the presence of salt for comparative purposes.

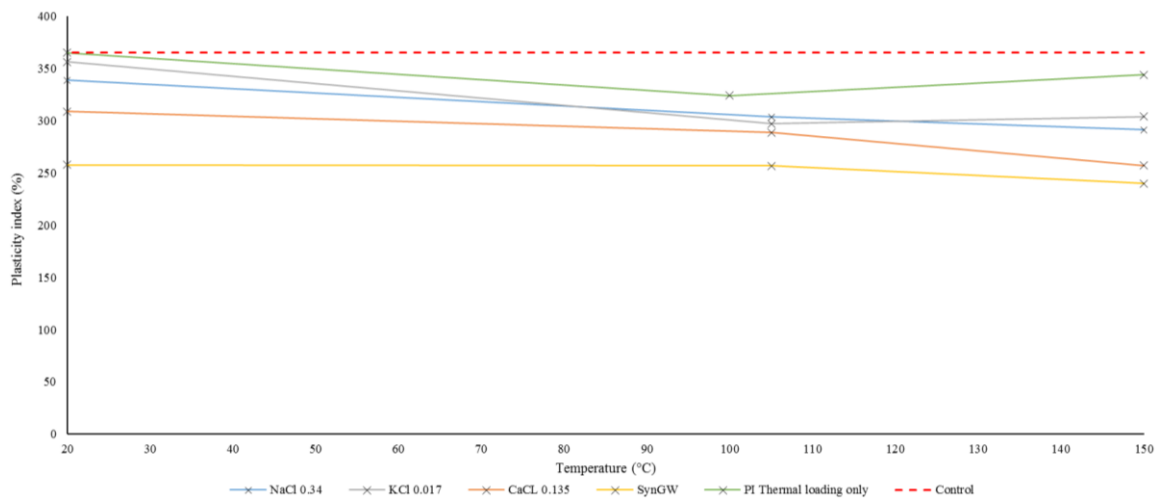


Figure 172: Plasticity index Vs. Temperature exposure for 56 days with different salt solutions

Furthermore it is seen, from figure 172, that temperature alone does have an impact on the MX-80s consistency. But the effect of temperature, at this duration, appears to have little negative impact after 100°C. The addition of salt has a much larger impact, with a continuous decreasing trend at higher temperatures. The combined effect of temperature on the DDL and layer charge as well as the impact of salt held within the interlayer displays a large reduction in the plasticity index. Temperature appears to amplify the effects of salt on the consistency of the MX-80 due to the exchange and fixation kinetics increasing with thermal exposure.

5.1.7. Batch #7 (S/MX-80/HT/D/HS) results:

This batch series investigated the effect between steel/ Bentonite and Bentonite with and without the synthetic groundwater under ambient and elevated temperatures (20°C and 150°C) over a period of 4 months. This allowed an insight into the impact of salt and corrosion products over longer time-scales at the lowest and highest thermal exposure used in this study. Below in figures 173 and 174, display the free swell and plasticity index measurements, post THC exposure.

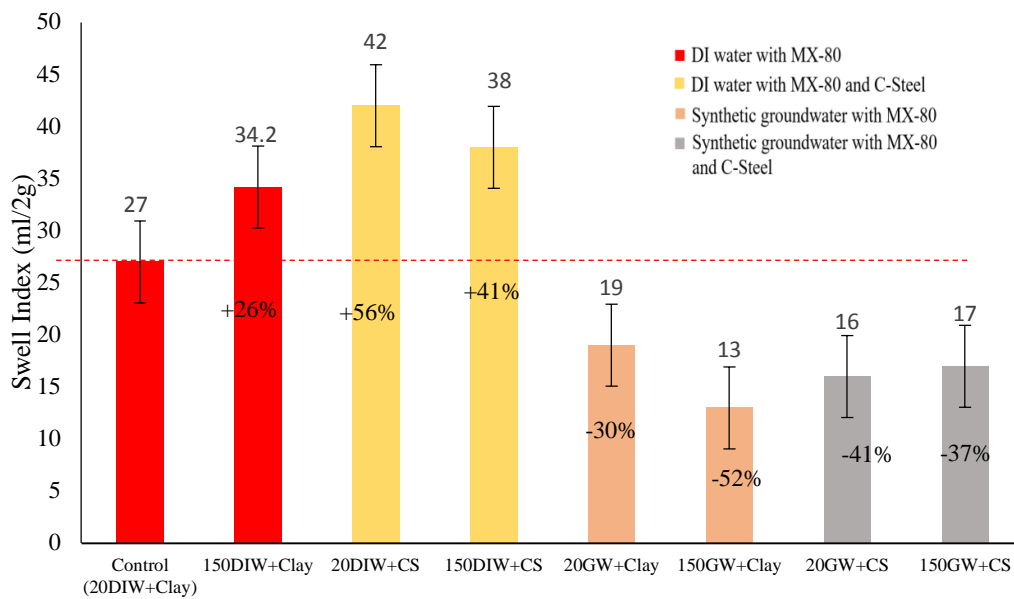


Figure 173: Swell index measurements for batch series #7

Figure 173, shows a systematic increase in the free swell in the presence of temperature and temperature and carbon steel plus DI water. The increase in the free swell index that involved temperature alone correlates to the result given for batch#5, 150°C (Section 5.1.5). This increase is due to layer charge alteration due to isomorphous substitution of the tetrahedral layer. Even after 4 months of thermal exposure the swell index remains 26% higher than the control, identical to the result in batch #5. MX-80 with corrosion products and DI water display a significant increase (DIW+CS, figure 173), this is noted even at higher temperatures, corrosion rich samples display an increase in the swell index by ~56% and 41% respectively. The increase displayed for this batch is due to the combination of the thermal effects on the layer charge and DDL thickness as well as the integration of voluminous Fe oxy-hydroxides. With respect to the integrity of the barrier, this increase due to corrosion product integration, could indicate that the porosity of the MX-80 will increase thereby increasing chemical transport rates and potential mechanism i.e. diffusion to advection.

However, when a high saline solution is added to the experimental boundary conditions, the impact of this salt is significant. With little difference between corrosion and non-corrosion batch samples, the saline solution with temperature impacts the MX-80 free swell by -30% and -52% for 20°C and 150°C exposure respectively. The addition of C-steel appears to have little effect on the overall free swell capacity in the presence of high saline solution

The plasticity index values, displayed in figure 174, displays that there is little effect on the bulk consistency of the MX-80 with temperature and temperature plus corrosion, however there is a trend in a slightly more reduced PI with higher thermal loading. The addition of the complex synthetic ground water displays a significant drop, indicating that cation exchange/fixation has a much greater impact on the early phase consistency of the barrier by inhibiting its ability to uptake as much free water and swelling capacity. The Swell index and plasticity index is still considerably higher than most clays and non-montmorillic minerals. However, Börjesson (2009) states that the liquid limit must not drop below 250%, clearly the impact of temperature and saline solutions with/ without C-steel drops well below this limiting value (See section 2.3.3 for limiting barrier parameters for the SKB concept).

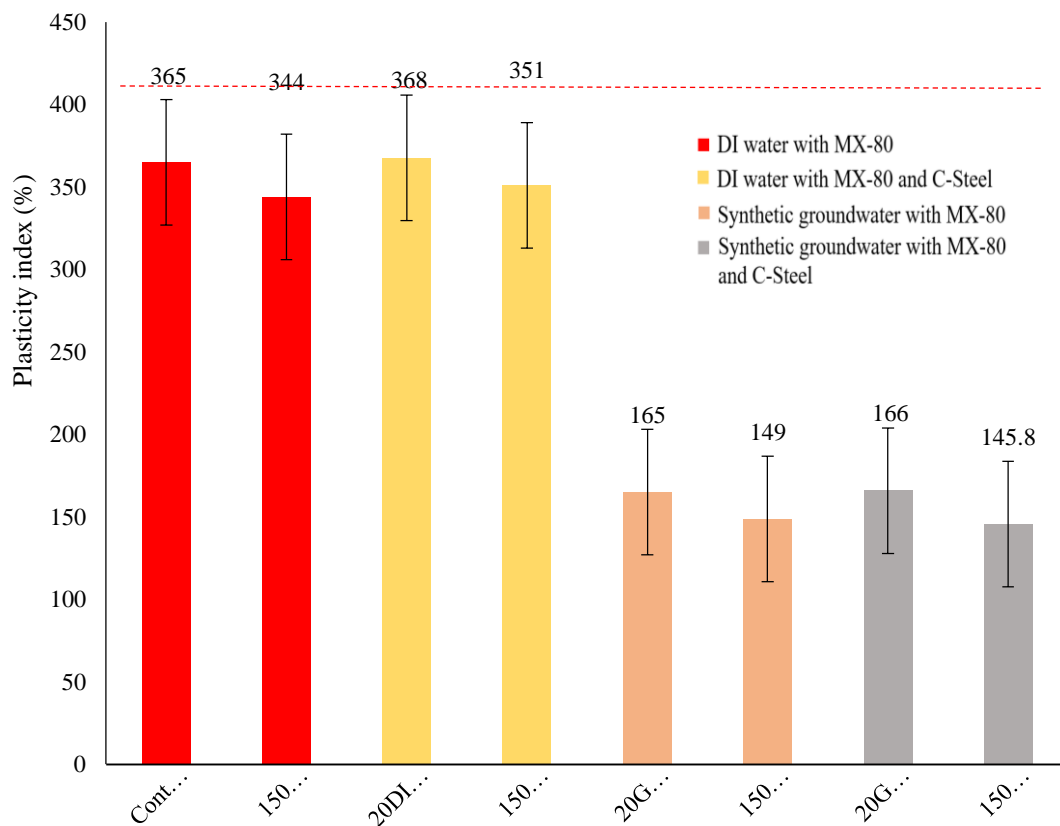


Figure 174: Plasticity index for batch series #7

Furthermore, XRD analysis was conducted on the interface and outer zones of the batch samples to investigate if there was significant mineralogical and accessory mineral alteration. Below in figures 175 to 180 displays the low angle measurements for the tests, each with a comparison the control. These were used to determine if the smectite component has altered by examining the glycolated d-spacing.

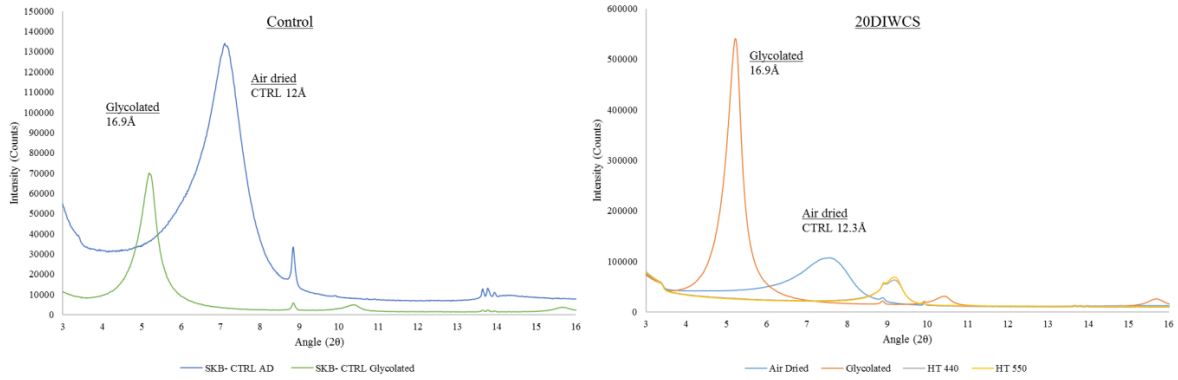


Figure 175: Low angle XRD pattern for batch MX80 + DI water and C-steel at 20°C

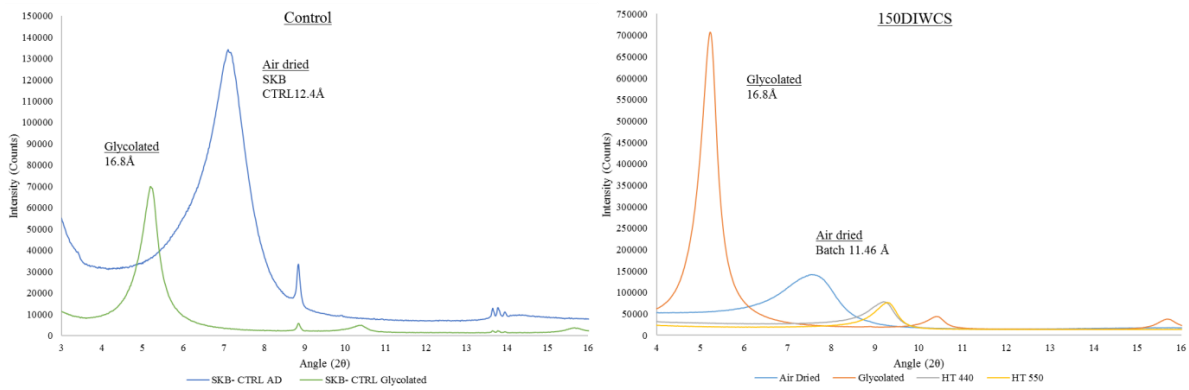


Figure 176: Low angle XRD pattern for batch MX80 + DI water and C-steel at 150°C

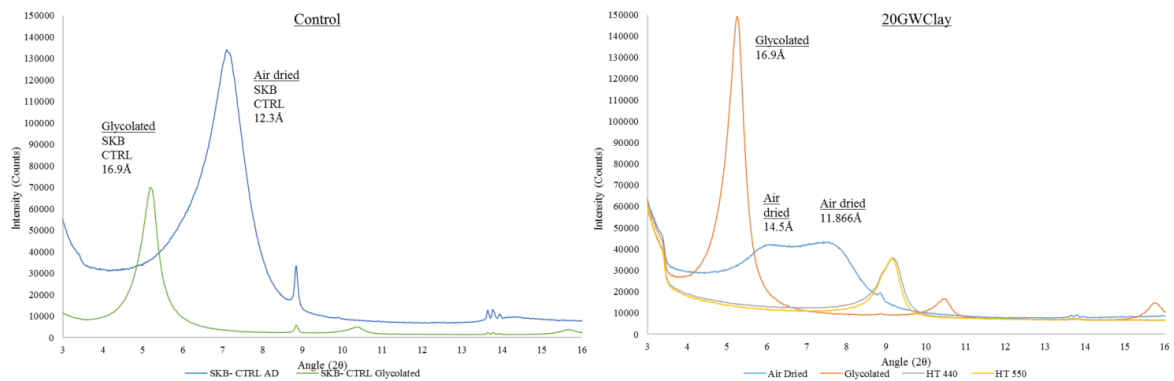


Figure 177: Low angle XRD pattern for batch MX80 + synthetic groundwater at 20°C

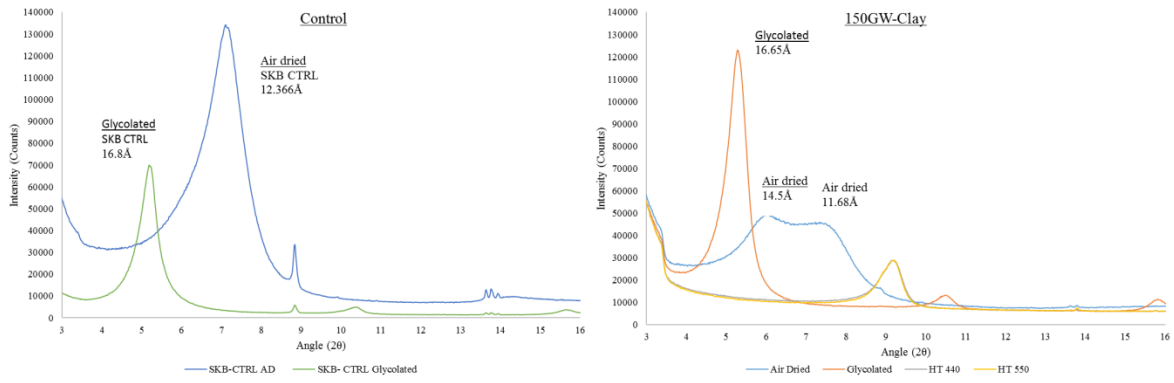


Figure 178: Low angle XRD pattern for batch MX80 + synthetic groundwater at 150°C

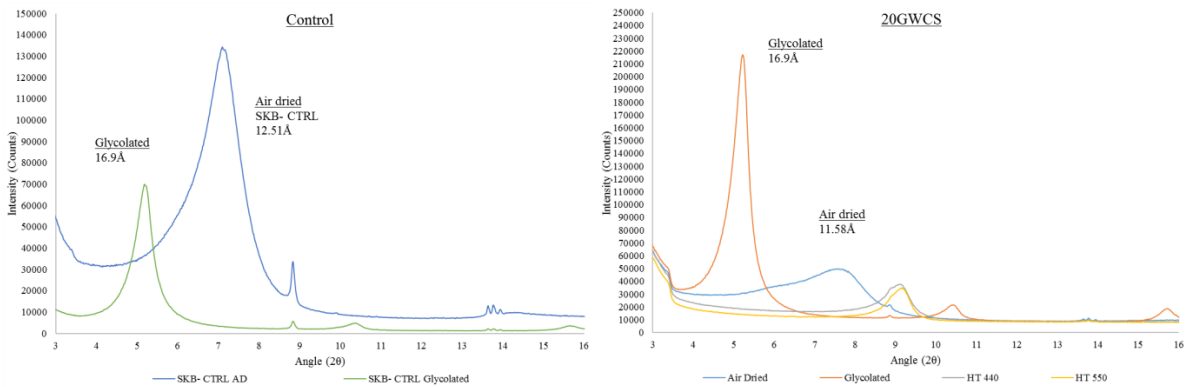


Figure 179: Low angle XRD pattern for batch MX80 + synthetic groundwater and C-steel at 20°C

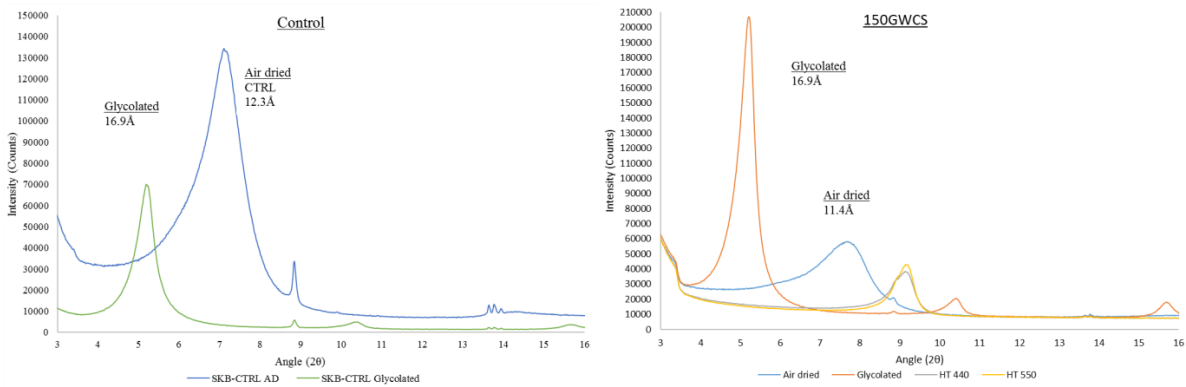


Figure 180: Low angle XRD pattern for batch MX80 + synthetic groundwater and C-steel at 150°C

It is clear from the above figures that the smectite component is not altered, with mineral d-spacings comparable to that of the control XRD patterns. MX-80 with C-steel and/or complex groundwater when exposed to a high temperature environment after 4 months' results in no conclusive alteration to the swelling component. One noticeable feature of the above XRD patterns is in figures 177 and 178, the batch that contained only the MX80 and synthetic groundwater only, shows distinctive air dried peaks. The shoulder becomes broad with an additional peak developing around 14.5Å, which is accentuated in the higher temperature batch, this is characteristic of interlayer cation exchange. More specifically, exchange of mono-valent cations for Di-valent cations, this is what is likely causing the

observed peak shift, also supported by Guillaume et al (2003). The exchange rate is clearly increased by the thermal loading, due to increased kinetics from thermal expansion of the interlayer, kinematic viscosity of the solution as well as the increased activation energy of the system. Furthermore, the batch which contained all the components, figure 180, i.e. the synthetic groundwater, C-steel and MX80 under the two thermal loads indicate no alteration. This is opposite to what is expected/ observed in the aforesaid batch XRD pattern. It should be noted that the air-dried peaks are sensitive to environmental conditions such as humidity and temperature, also sampling/ human error may also result in this difference in results. The exchanged sites may not be uniformly distributed, with zones of di-valent rich cations and zones with mono-valent cations.

Through examination of the 002/003 glycolated peaks of the Bentonite it is possible to observe any Fe exchange within the octahedral layer; the analytical method is given by Moore and Reynolds (1997). Higher 002/003 intensity ratios indicate increased scatter from the higher number of electrons present within the octahedral layer, hence indicating that Fe is present. This measurement can be used as an indicative tool for smectite alteration to Fe-rich smectites as well as the alteration to the layer charge characteristics. Figures 181-186 displays the respective 002/003 peaks for the batch samples.

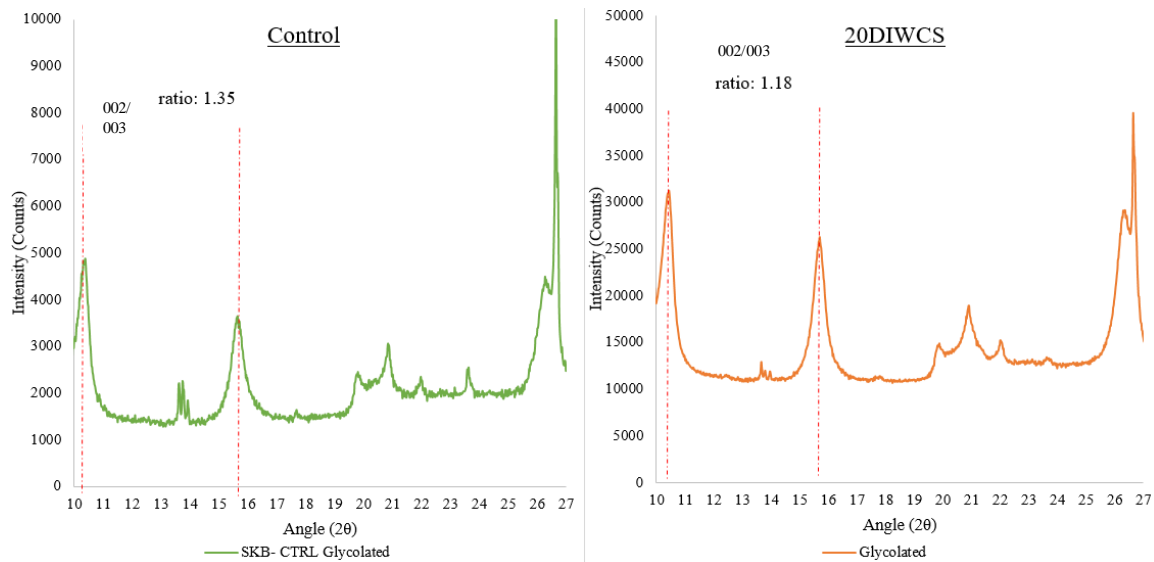


Figure 181: 002/003 intensity ratio for the DI water + C-steel at 20°C batch

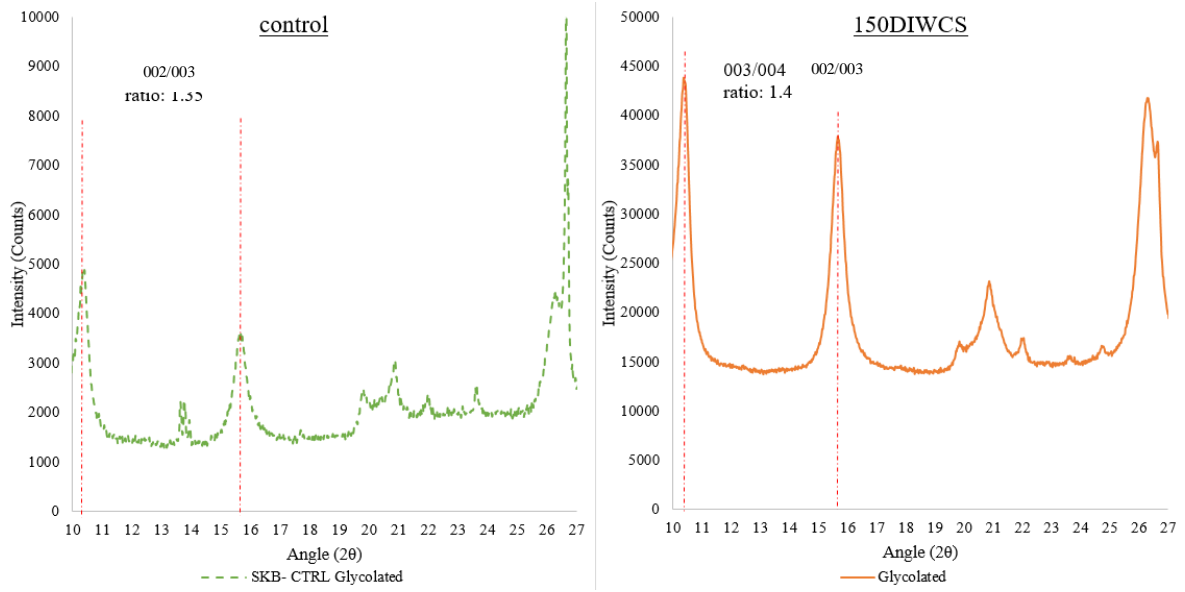


Figure 182: 002/003 intensity ratio for the DI water + C-steel at 150°C batch

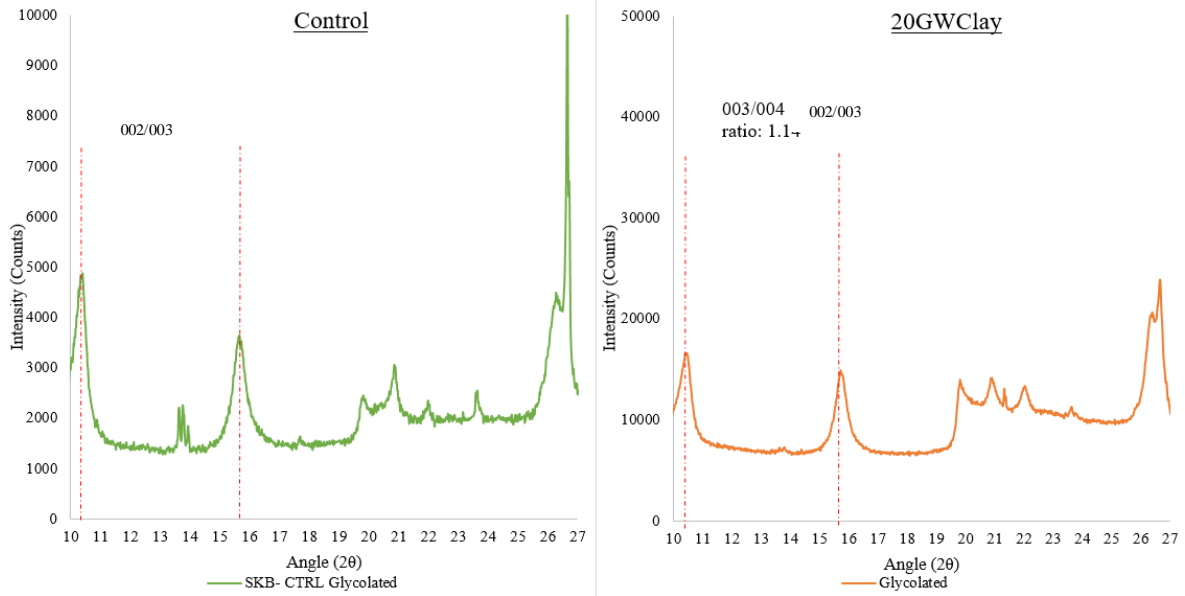


Figure 183: 002/003 intensity ratio for the Groundwater + clay only at 20°C batch

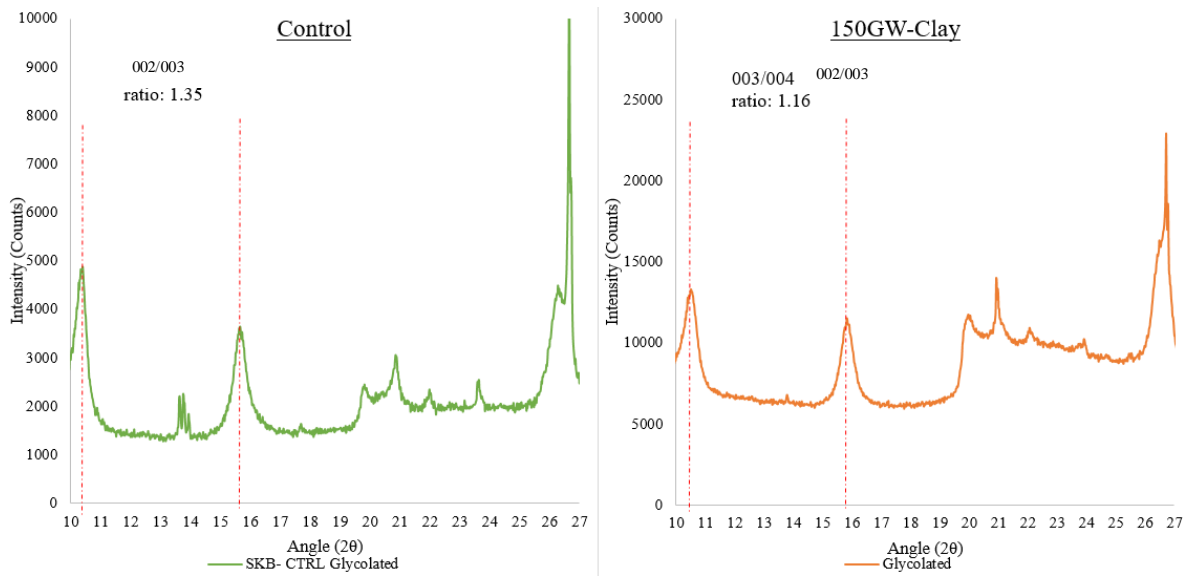


Figure 184: 002/003 intensity ratio for the Groundwater + clay only at 150°C batch

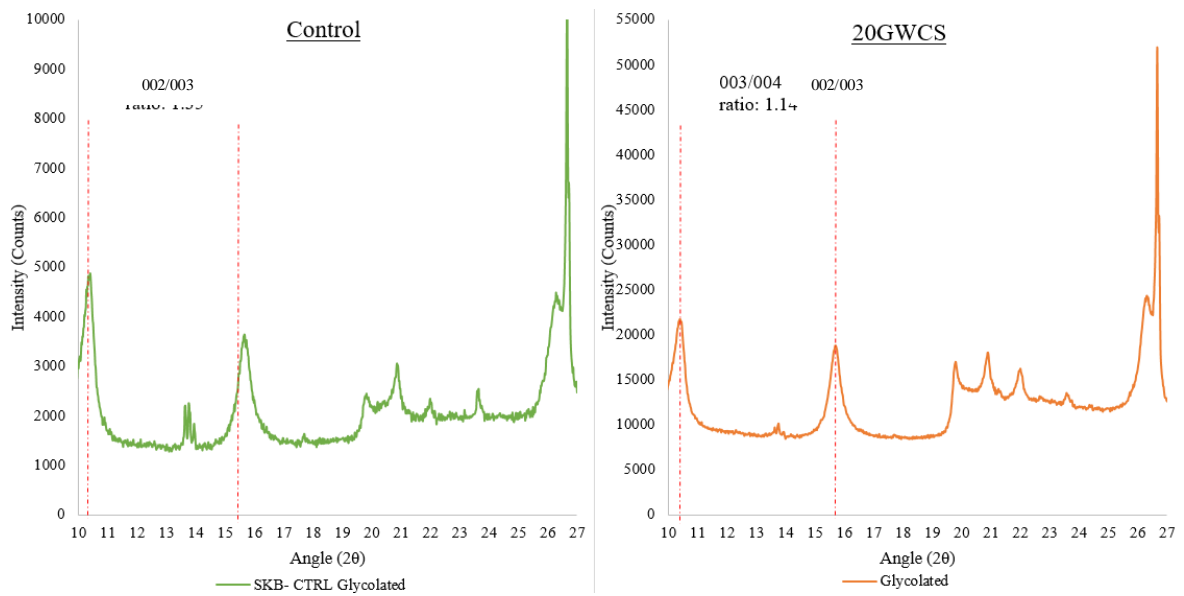


Figure 185: 002/003 intensity ratio for the Groundwater + clay + C-steel at 20°C batch

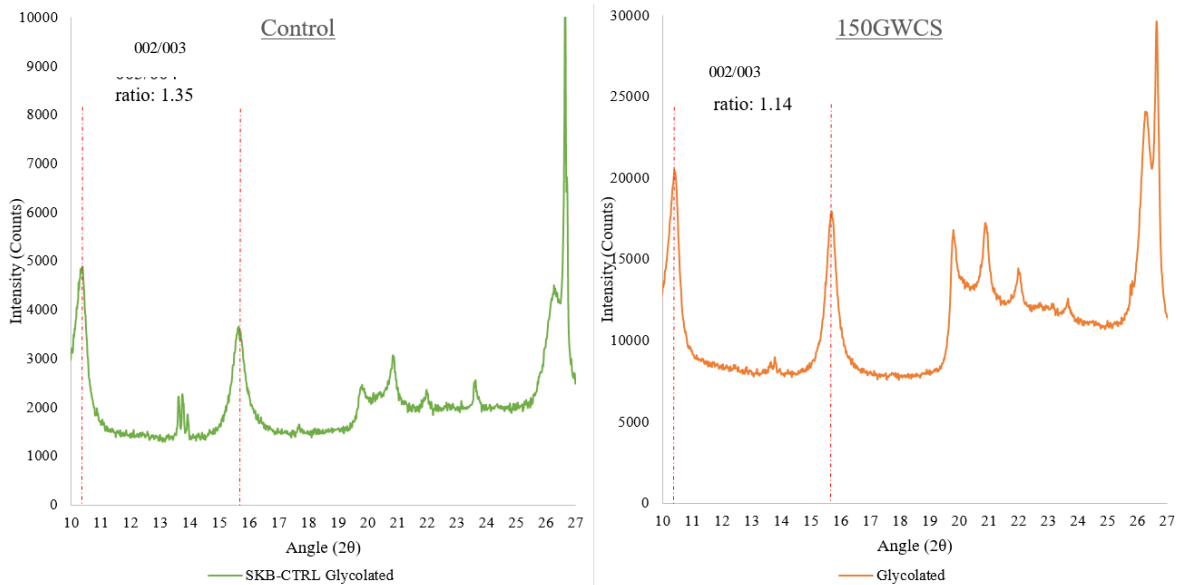


Figure 186: 002/003 intensity ratio for the Groundwater + clay + C-steel at 150°C batch

Below are the intensity ratios in tabulated format, to enable comparative analysis, see table 65. Interestingly, the results mostly indicate that there is no octahedral exchange of Fe^{3+} , and display a lower intensity ratio compared to the control. The lower intensity ratios are more prominent in the groundwater batch samples which indicates that there is some exchange of a preferred cation over the Fe^{3+} either in the clay matrix or what is already present within the octahedral layer. This is further supported by the batch sample that included the DI water, MX80 and C-steel at the higher thermal load (150°C), which displays a slight increase in the intensity ratio. This indicates that in a non-complex saline solution system the Fe^{3+} remains the preferred exchangeable cation for the octahedral layer. Moreover, the peak at ~ 26.64 (2θ) is indicative of an orthoclase feldspar peak (K-feldspar), as this peak does not change upon glycolation and heating (see high angle XRD patterns, figs 187-192). However, the intensity of the peak is greatly lost upon exposure to temperature, corrosion products and DI water. This is presumably due to the dissolution of the mineral as the pH increases as well as the presence of a dilute soil matrix solution. The shoulder of the k-feldspar peak becomes prominent upon glycolation (around 26.3 (2θ)) which indicates a swelling clay mineral. This is characteristic of interstratified (saponite) smectite-illite, this peak is largely impacted by the presence of temperature and the complex groundwater solution without the corrosion products. This correlates to the air-dried peak in figure 180, which indicates the preferential exchange of Ca^{2+} which may also mask the little illite present. Although the rest of the batch XRD patterns display similar glycolated peaks characteristic of mixed layer (saponite) smectite/illite when compared to the control.

Table 65: compiled 002/003 peak intensity ratios for each batch consignment

Batch	003/004 Intensity ratio
Control	1.35
20°C, DI Water, MX80 and C-steel	1.18
150°C, DI Water, MX80 and C-steel	1.4
20°C, Groundwater and MX80 only	1.14
150°C, Groundwater and MX80 only	1.16
20°C, Groundwater, MX80 and C-steel	1.14
150°C, Groundwater, MX80 and C-steel	1.14

Below displays the high angle peak XRD patterns for the above batch tests, the accessory mineral analyses displayed in figures 187-192. Additionally, figure 195 displays a high angle XRD pattern for a sub-sample of a white precipitant which formed on the surface of the sample conducted under 150°C with the synthetic groundwater and the carbon steel.

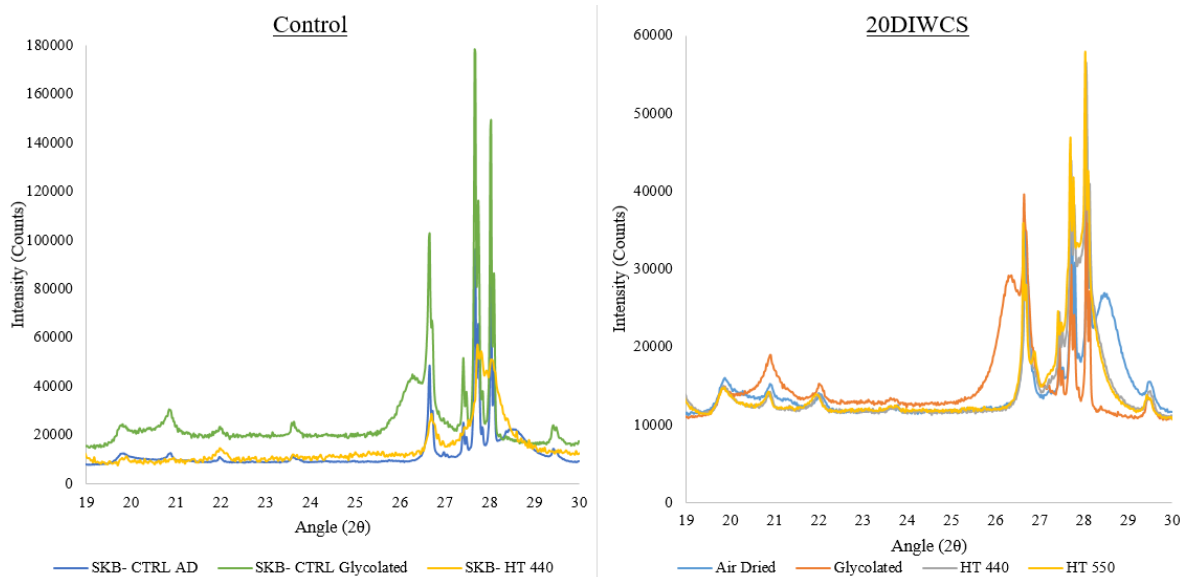


Figure 187: High angle peak pattern for the DI water + C-steel at 20°C batch

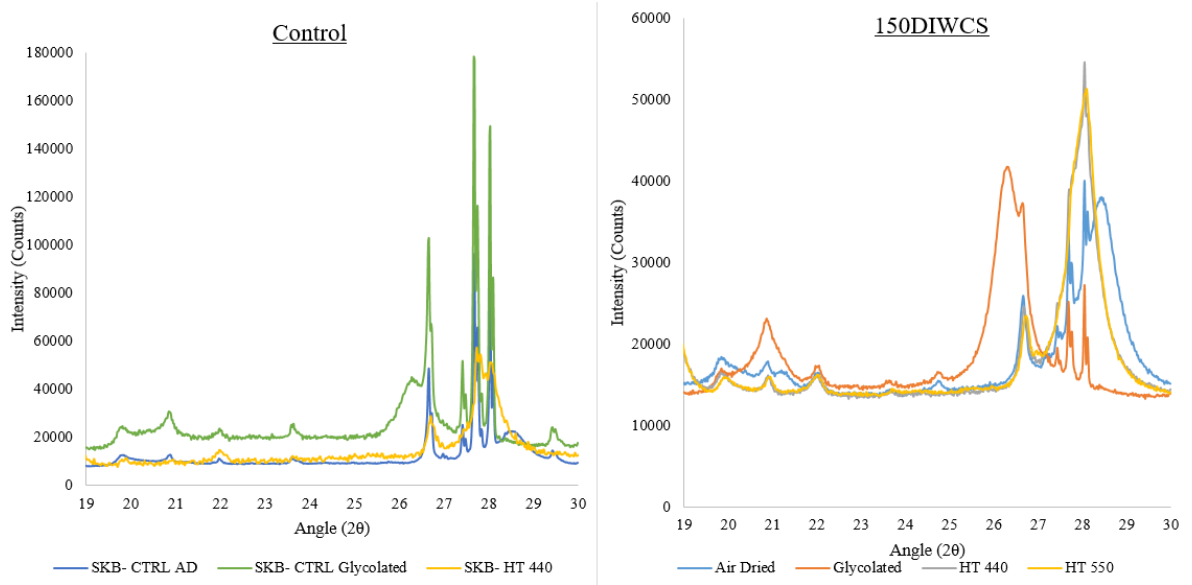


Figure 188: High angle peak pattern for the DI water + C-steel at 150°C

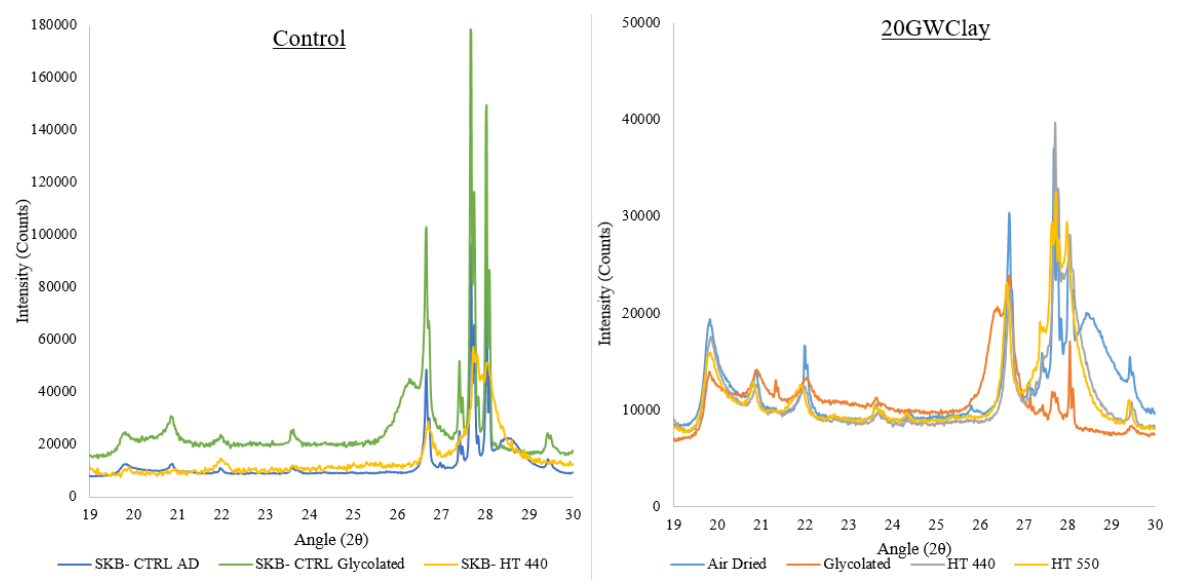


Figure 189: High angle peak pattern for the Groundwater +clay only at 20°C

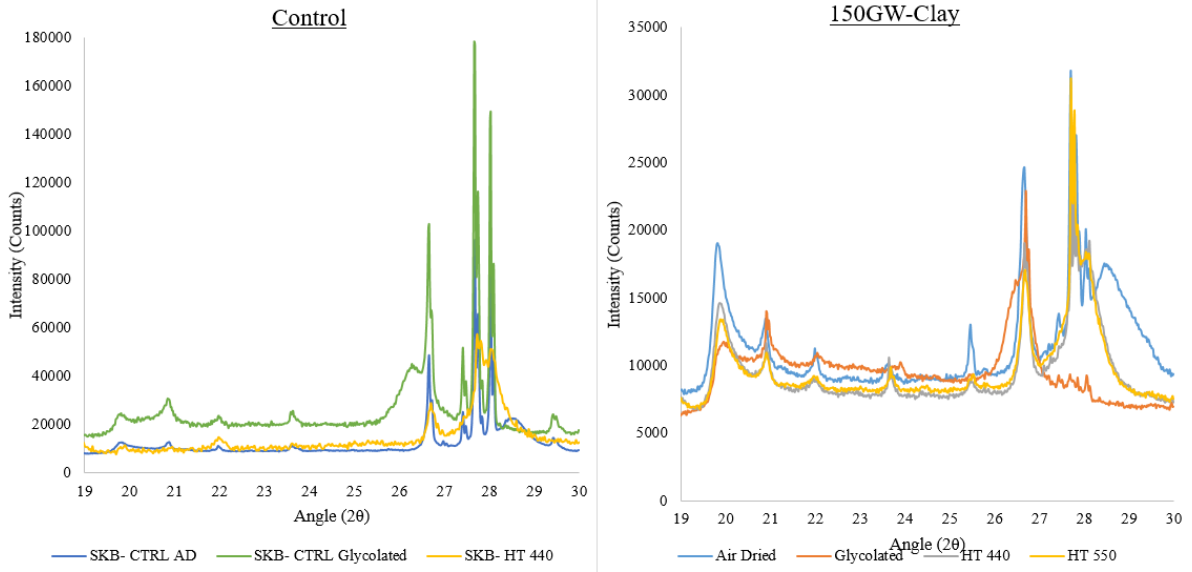


Figure 190: High angle peak pattern for the Groundwater +clay only at 150°C

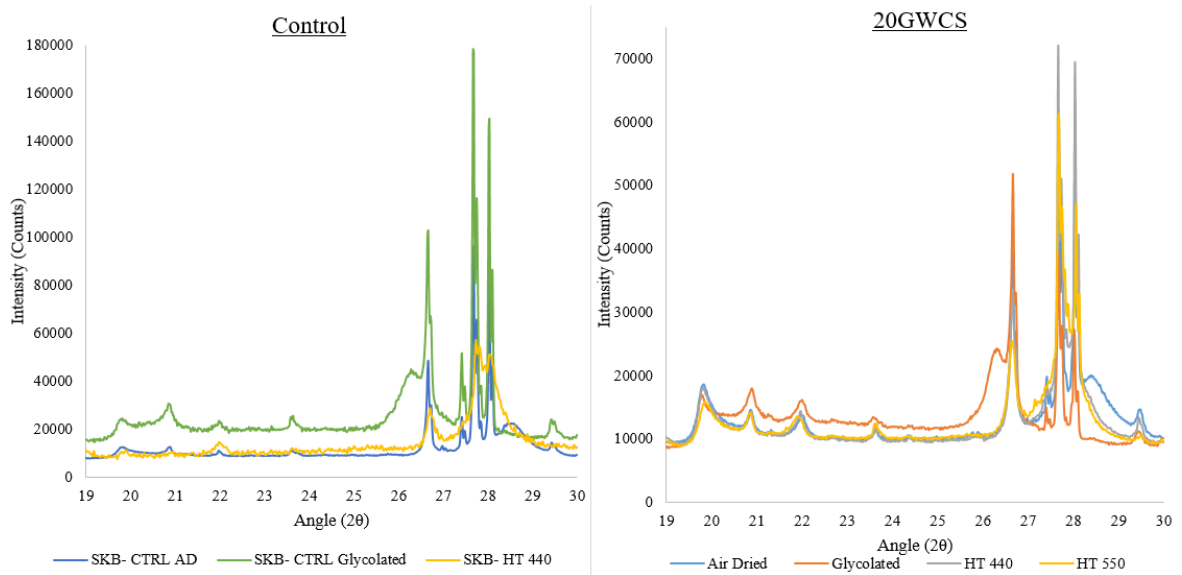


Figure 191: High angle peak pattern for the Groundwater + clay + C-steel at 20°C

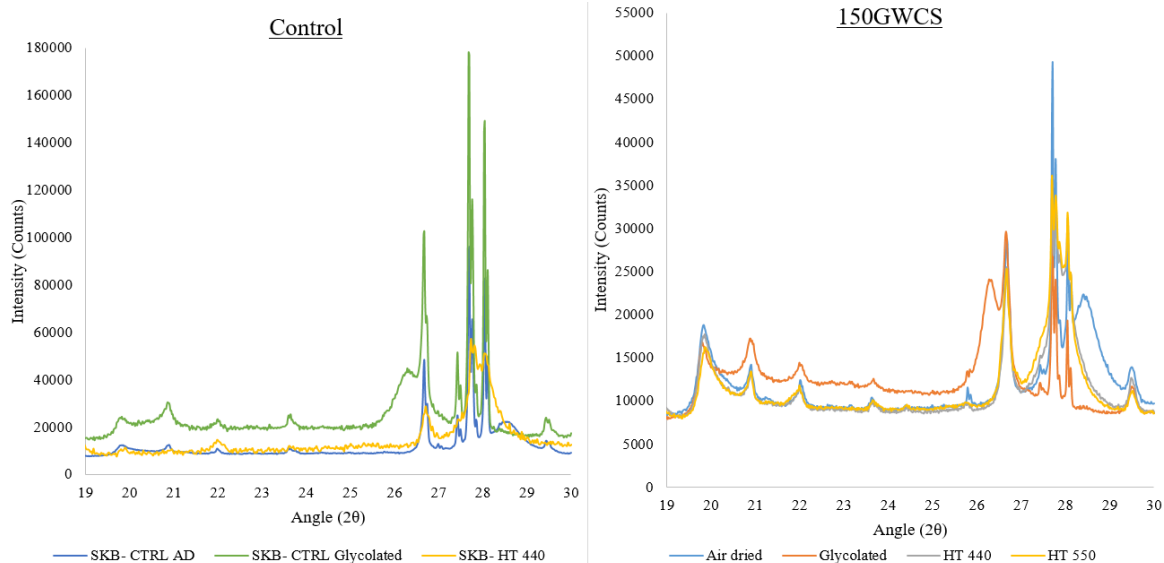


Figure 192: High angle peak pattern for the Groundwater + clay + C-steel at 150°C

From inspection of figures 187-192, there is significant peak deviation of the post THC accessory mineral profiles compared to the control XRD pattern. There are few newly formed peaks but the intensities have significantly altered respectively. Observation of the glycolated peaks show that the intensity of the feldspar peaks between 27-28(2θ) is effected by temperature and the presence of the synthetic groundwater. This is due to the disordering and increase dissolution rates at higher temperatures. Furthermore, development of a peak at 19.8(2θ) for the samples containing the synthetic groundwater is indicative of the 2:1 Ca-silicate mineral Palygorskite, this agrees with other studies (Bailey, 1980; Charpentiera et al, 2006). This is again accentuated by the presence of thermal loading. The Quartz peak at ~26.7(2θ) diminishes with higher temperatures, indicating silica dissolution at the interface, with more intense silica peaks occurring in the outer/ cooler zone. This is observed by figure 190 and 193, which displays that after thermal exposure of 150°C with synthetic groundwater and C-steel. The quartz peak is greatly diminished at the interface with a more intense peak at the outermost/ cooler zone. The XRD patterns also indicate that calcite forms in the complex groundwater systems with peaks at 29.5(2θ). Lastly the higher temperature batches, particularly with the C-steel, display much broader peaks which indicates higher crystallite disordering and amorphous corrosion products within the clay matrix.

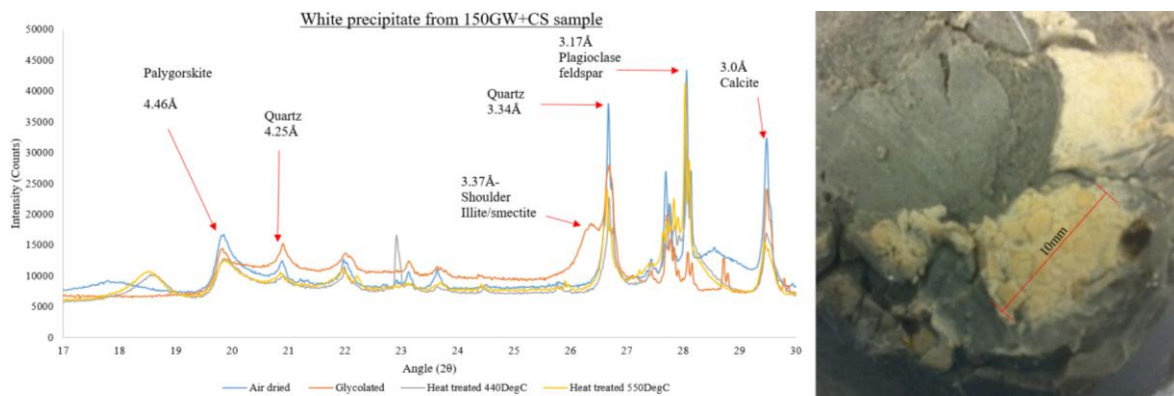


Figure 193: High angle peak pattern for the Groundwater + clay + C-steel at 150°C batch top precipitate

At the outermost surface of the 150°C, groundwater and C-steel batch displayed a white precipitate on the surface furthest away from the heat source. High angle XRD conducted on this indicated a similar trend to its associated XRD pattern except for the increased Calcite peak. Thus, indicating that the precipitant is calcic in nature, confirming the dissolution of carbonates at the interface and migrating away with subsequent precipitation in the cooler regions.

5.1.8. Batch #8-9 (1yr-S-Mx80 and 2yr-S-Mx80) results:

The last two batch consignments were run in conjunction with the batch tests. These tests investigated the longevity characteristics of the interface with and without the presence of saline solutions. Thermal loading was kept low (20°C), to observe the integration of the corrosion products into the Bentonite matrix with little kinetic acceleration. The consignments were run for a duration of 1 and 2 years respectively, the 1-year consignment was run in two batches with and without the presence of NaCl solution but both with C-steel. Unfortunately, for the 2-year consignment, an accidental loss of samples without the NaCl solution occurred, this resulted in the 2 year samples with NaCl being analysed. SI, PI and XRD were conducted on all samples post THC exposure. Therefore, samples containing NaCl could only be compared.

Below in figure 194, demonstrates that after 1 year under ambient conditions (20°C) the corrosion products integrated into the Bentonite does not affect the free swell capacity MX80. Interestingly, the corrosion products of this batch series appeared to demonstrate an anaerobic corrosion cell at the interface, figure 195. It was approximated that corrosion penetration of 20mm into the uncompact Bentonite after 2 years of ambient thermal exposure was achieved. Even though the sample was within a sealed bag within a Pyrex beaker i.e. anaerobic conditions were not expected as it could not be controlled. It appears that the Bentonite above

the interface formed a seal, therefore allowing only the oxygen to be consumed within the immediate zone of the C-steel. The colour development appeared to go from blueish/ green to orange in the outer regions, this is characteristic of an Fe^{2+} rich environment with an Fe^{3+} corrosion front, as indicated in Figure 195. Hence it seems that the corrosion products were using up the available oxygen in the Bentonite and developing a sub-oxic zone behind the oxic front. This may be further aided by the electron transfer from the Fe^{3+} to the Fe^{2+} zone, thus further expanding the reduced corrosion zone. Nonetheless, this corrosion integration does not appear to affect the bulk free swell characteristics of the Bentonite. It appears that there is a slight increase in the parameter, more so for the DI water sample which is understandable due to the increase concentration of Na from the saline solution in the corresponding batch. The increase is due to the volumetric increase of the corrosion products. This could be because there was only a small volume of Bentonite affected by the corrosion products (~20mm into the Bentonite) compared to the potentially uncompromised Bentonite.

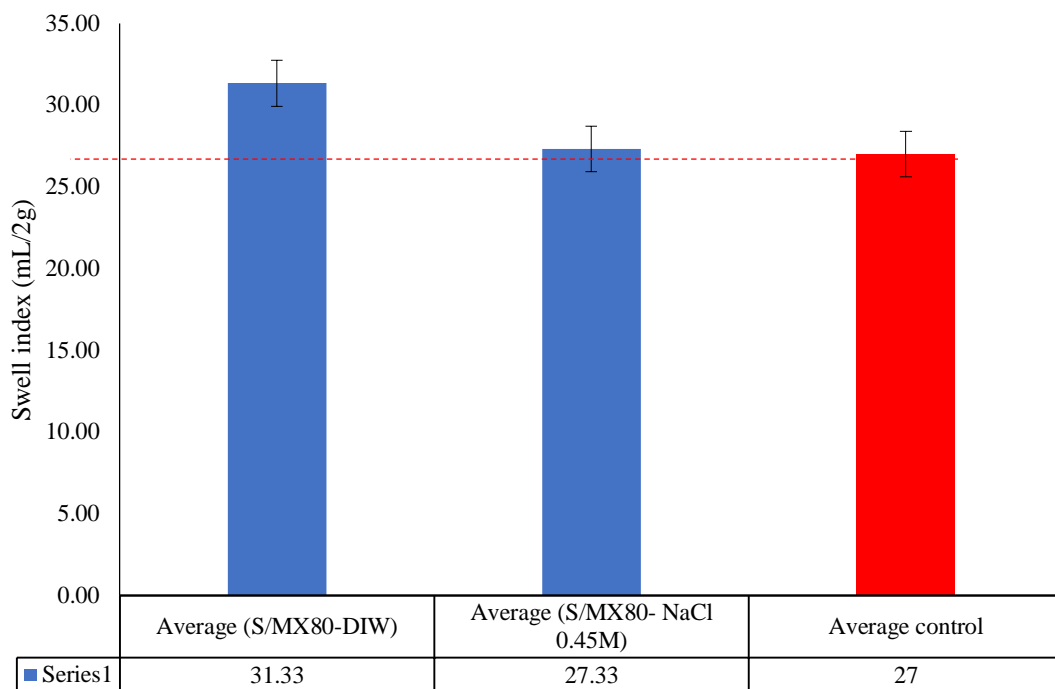


Figure 194: Swell index results for the 1-year ambient batch test series

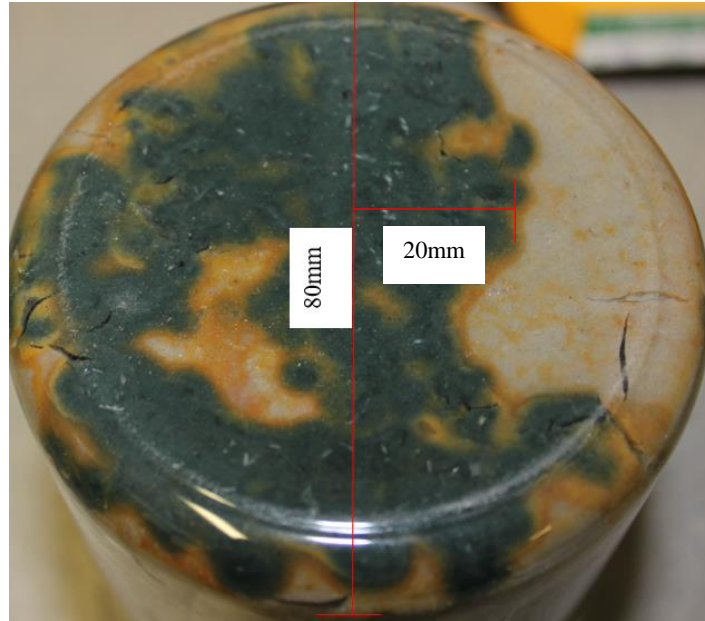


Figure 195: 1-Year batch series displayed a colour development at the Bentonite- C-Steel interface from blue to orange in the outer zones characteristic of Fe^{2+} rich environment

Figure 196, displays the average plasticity index results for the 1-year batch test. It appears that the corrosion exposure alone reduces the PI by ~10% which indicates that there is some alteration to the layer charge due to the potential exchange of Fe in the octahedral layer and interlayer sites. What is more, the plasticity index of the NaCl solution batch samples resulted in an average reduction of ~46%. It appears that the combined effects of the higher saline solution and the corrosion products significantly reduces the materials ability to uptake and retain water, while still exhibiting some shear strength. This is due to the area of exposure of the integrated corrosion products into the Bentonite, thereby increasing the area of influence. Recalling the results from batch #4 (section 5.1.4) it was observed that the corrosion could diffuse faster into the Bentonite due to the loss of the gelling/ thixotropic structure.

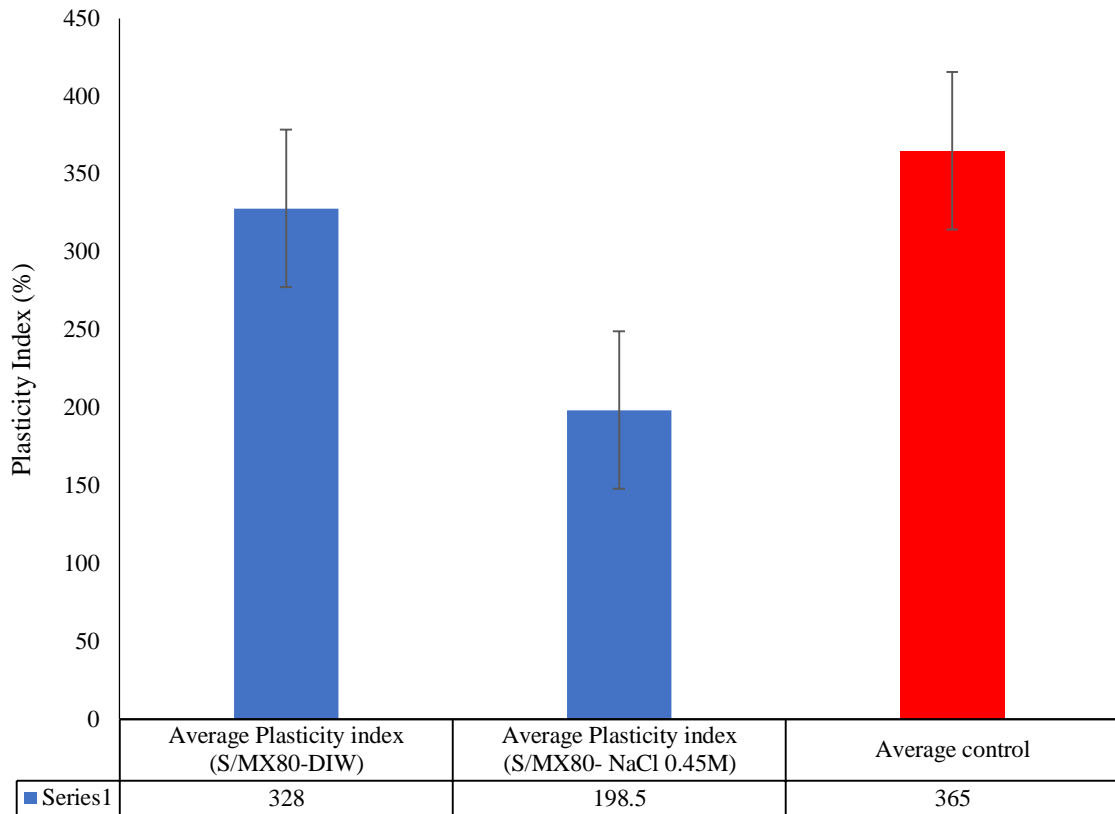


Figure 196: Plasticity index results for the 1-year batch test series

The second part of these batch series, was the 2- year consignments, unfortunately the tests including the saline solution were accidentally lost, therefore only the DI-water batch results are presented below. It appears that after 2-years of THC exposure there is little impact on the materials free swelling capacity (figure 197). The interface sub-sample has been reduced by 11.1%, nonetheless the sample still has a very high swell index, whereas the outer zone has a slight increase of 11.1%. Therefore, it can be said that there is no significant impact on the materials volumetric swelling ability. Furthermore, the extent of visible corrosion penetration into the uncompact Bentonite after 2 years was measured to be approximately 35mm, 15mm more than the 1 year DI water batch sample.

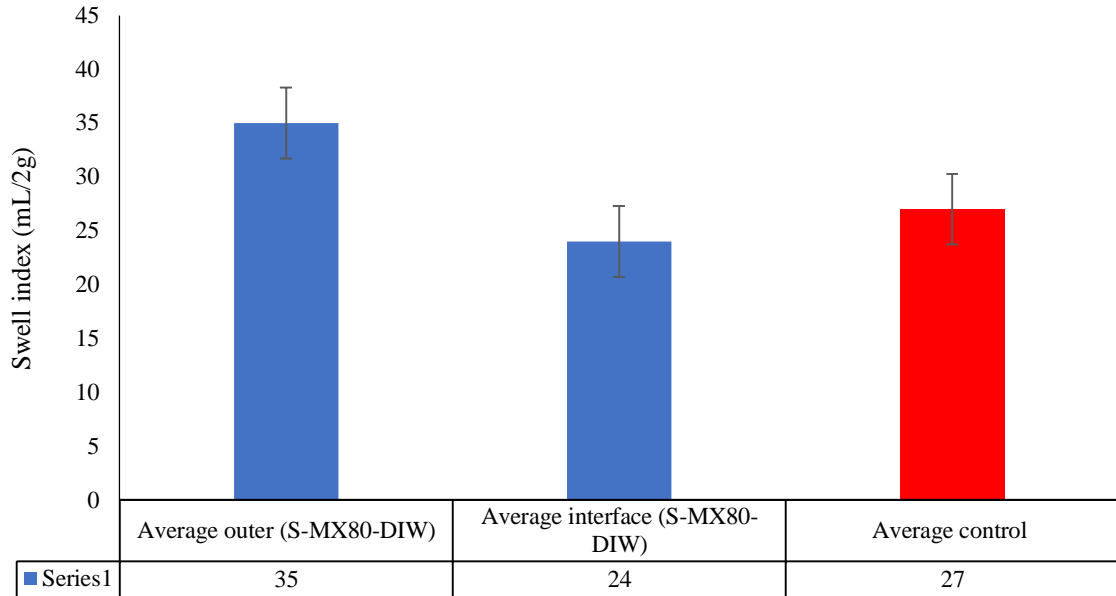


Figure 197: Swell index results for the 2-year batch consignment with only DI-Water

Figure 198 shows that the plasticity index of outer sub-sampled zone of the 2-year batch samples has not been affected during the THC exposure. Whereas the plasticity index of the sub-sampled zone at the interface sample displays a reduction of ~22%. This indicates that the corrosion products have influenced the materials ability to uptake water. These results also indicate that the temporal dimension is an important factor in the interaction between the corrosion products and the Bentonite and the integration of Fe into the Bentonite structure. Fe^{2+} appears to have exchanged in the interlayer sites thereby reducing the DDL. Furthermore, Fe^{3+} may have altered the layer charge by integration into the octahedral site, however without XRD it cannot be confirmed.

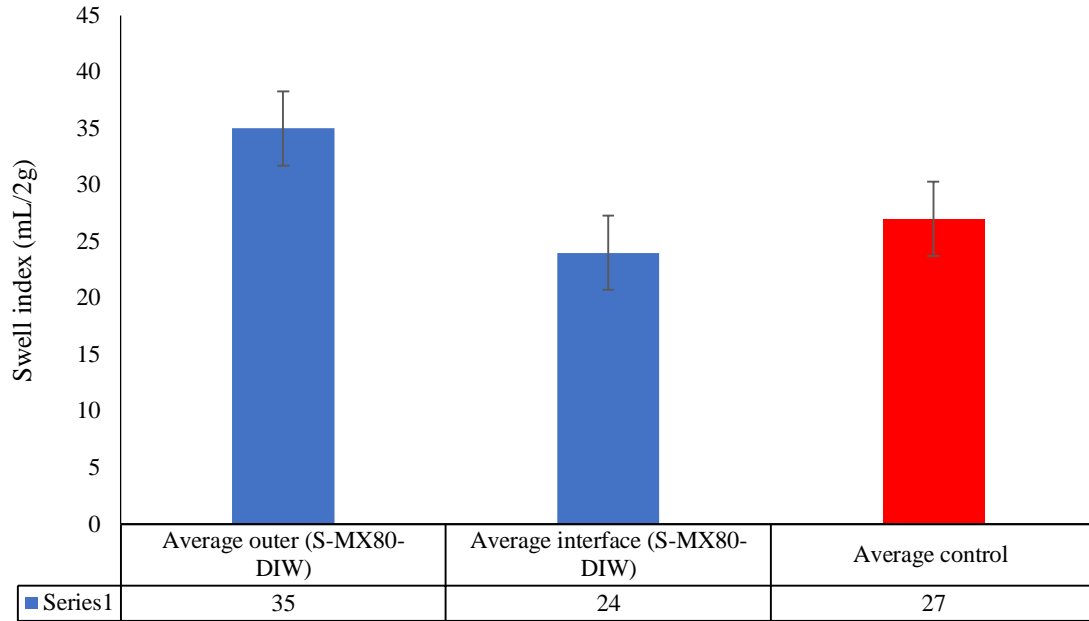


Figure 198: Plasticity index results of the 2-year batch samples with DI-Water

5.2. Discussion:

Using the data measured from the above batch test series it was possible to combine the measurements to gain an understanding of the interaction between various systematic factors that have an influencing role on the EBS barrier. The conditions explored in the corresponding tests may not be completely replicable of the EBS interface. Nonetheless the intrinsic interaction between the corrosion and the Bentonite, saline solution and the Bentonite or a combination of factors under several thermal loading and duration regimes, allows insight into reaction and alteration kinetics.

Comparison of results from batch consignments 2, 3, 4, 8 and 9 provides insight into the combination of temperature, duration and compaction state on the plastic limit and swelling properties. Non-saline batch measurements were chosen to explore impact of corrosion within the Bentonite matrix. The plastic limit is presented for comparison due to the limited amount of material making a measurement of the liquid limit impossible. It must be noted that any alteration may be more prominent with complete consistency data, however the plastic limit is useful in indicating alteration to the dominant cation and layer charge. Figures 199 and 200, compare the short and long-term batch consignments with an additional high temperature test to compare the effects of higher thermal loading. Swell index results display little change for the short-term samples whereas the long-term samples i.e. 1 and 2-year exposure durations display an elevated swelling capacity. This increase is presumably due to the higher volumetric uptake of the corrosion products within the Bentonite, the neutral pore

solution allows only the effect of corrosion to be assessed. Comparably, the higher thermal loading does not appear to significantly reduce the materials volumetric capacity. Moreover, the compact specimens appear to have a lower swell index compared to the respective counterpart sample, thus supporting the proof that higher porosity results in an increased abundance of corrosion products within the intra aggregate voids.

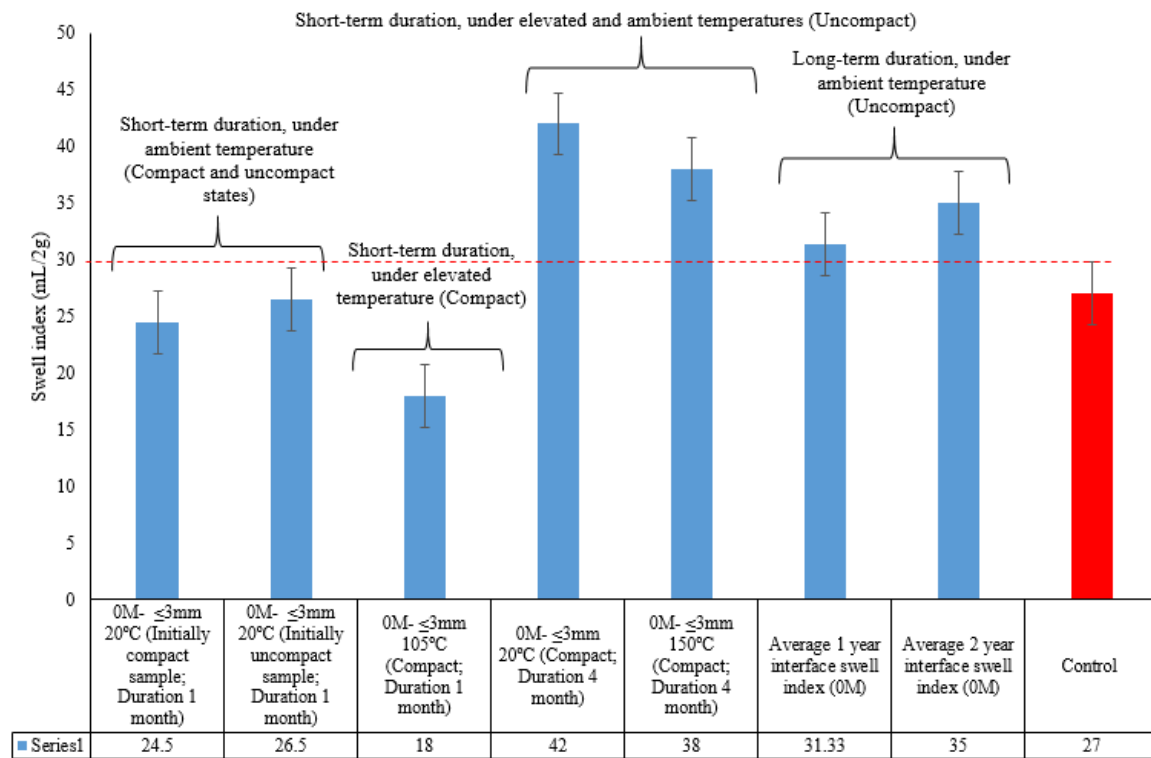


Figure 199: Swell index comparison of DIW samples with respect to temperature and duration

Comparison of the plastic limit, figure 200, displayed negligible alteration expect for the longest duration explored in the testing regime. This indicates that the liquid limit is significantly more sensitive to physicochemical changes. The large drop in the plastic limit for the 2-year batch consignment is likely due to the volume of corrosion products within the Bentonite. Due to the plastic limit being the moisture content at which the material displays characteristic cracking when rolled, the moisture content is a function of the bulk and dry masses. Therefore, if a large proportion of the material contains corrosion products then the PI and SI measurements are not conducted on the Bentonite alone but the corrosion/ clay mix.

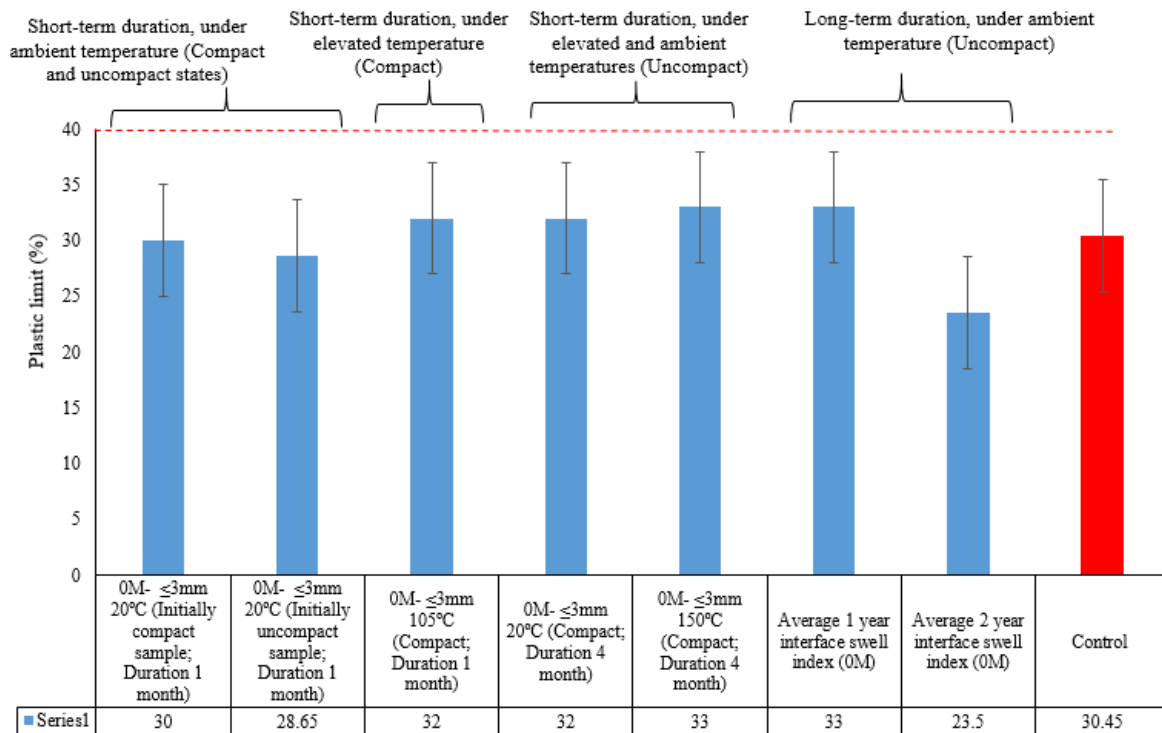


Figure 200: Plastic limit comparison of DIW samples with respect to temperature and duration

Temperature aids the rate of kinetics, but the most significant results are displayed when comparing the longer duration tests to the 4-month exposure test see table 66 and figure 200. Additionally, table 66 includes the measured penetration of visible corrosion into the Bentonite enabling insight into the diffusion rates under ambient conditions. However, it must be noted that the Bentonite was in an uncompact/ non-volume constrained system and therefore it is not necessarily realistic to the EBS barrier. Maintaining the Bentonite in a relatively confined system will yield lower spatial diffusion magnitudes due to the low porosity of the material. Hence the reason for comparing tests using uncompact and compacted Bentonite samples.

Table 66: Plasticity index results comparison of duration Vs. C-steel/ Bentonite interface exposure at 20°C, also includes one 150°C result for comparison

Batch	Plasticity index (%)	Extent of visible corrosion integration (mm)
Control	365	0
DI- Water+MX80+C-Steel (x4 months) at 150°C	351	-
DI- Water+MX80+C-Steel (x4 months) at 20°C	368	15
DI- Water+MX80+C-Steel (1 year) at 20°C	328	20
DI- Water+MX80+C-Steel (2 years) at 20°C	286	35

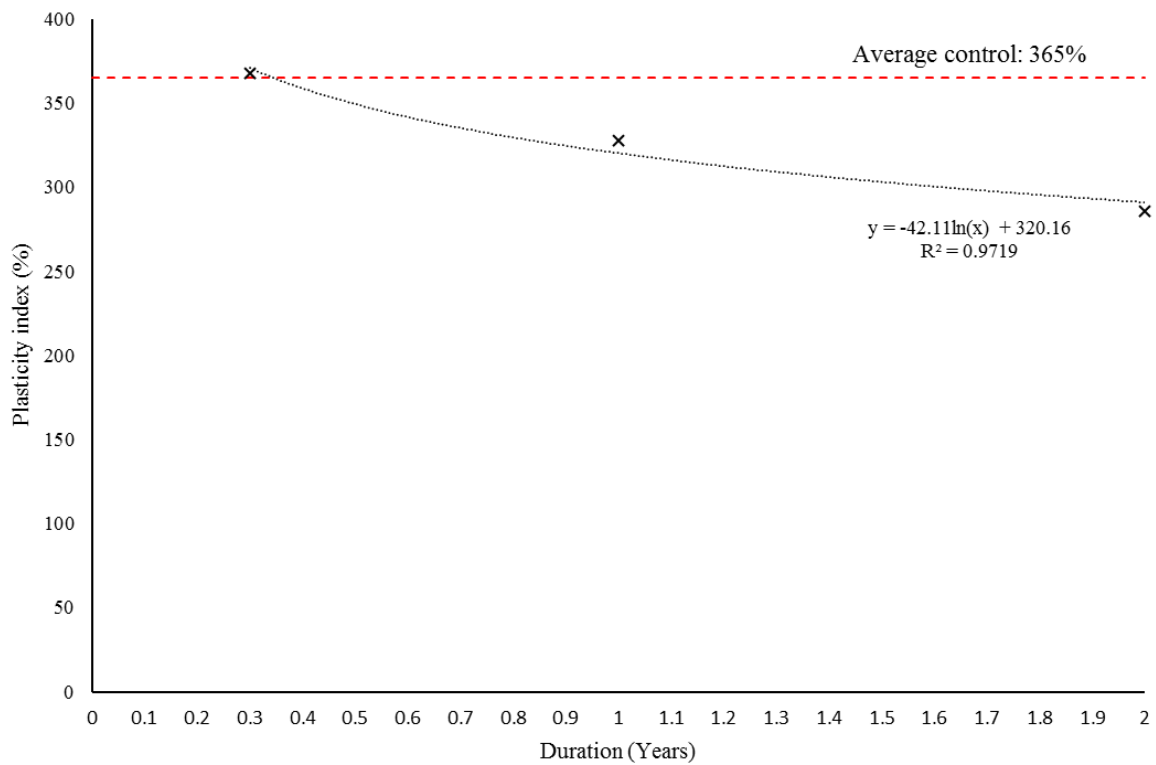


Figure 201: Plasticity index vs. exposure duration under ambient conditions (20°C)

Figure 201 demonstrates that duration plays an essential role with respect to the interaction between Fe and the Bentonite. The corrosion products appear to reduce the plasticity index by ~10% after one year and by ~21% after two years.

Using the SKB borehole and barrier geometry, highlighted below in figure 202, it is possible to calculate the minimum swell index required to maintain the design geometry. Below sets out the calculations using the Bentonite physical parameters and insitu geometry used to obtain this limit. Assuming the total volume of the UKs' concept is to be comparable to that of the proposed design of the SKB concept (Börjesson, 2010).

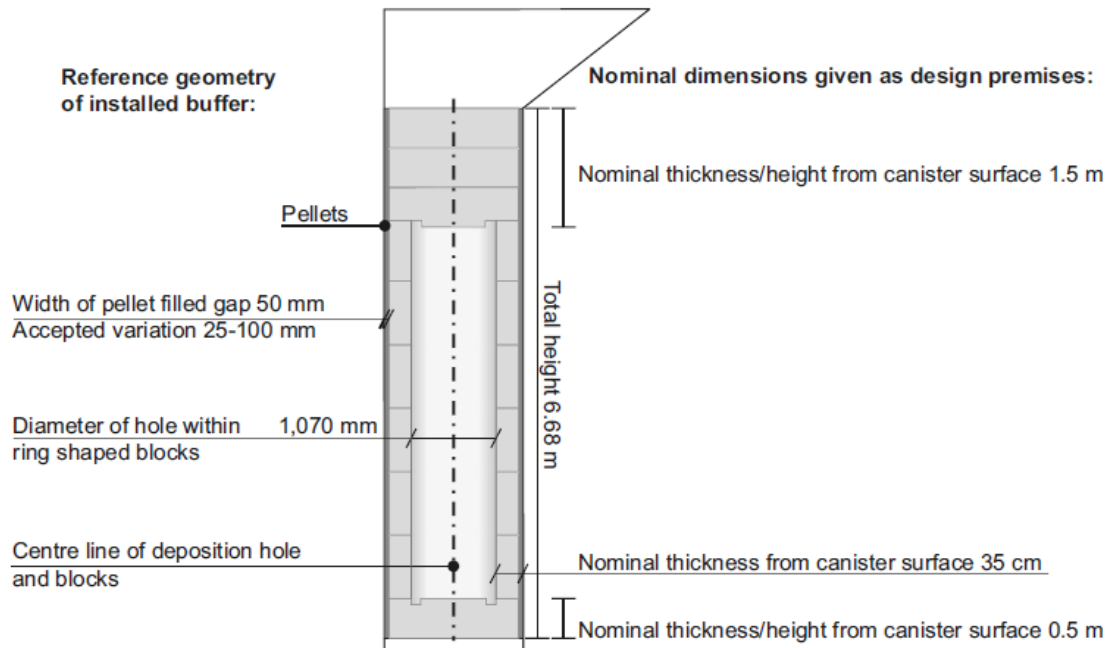


Figure 202: Reference buffer geometry for the SKB concept (After Borjesson, 2010)

Using the above dimensions set out for the SKB concept the total Bentonite volume can be obtained. Using the target saturated bulk density an insitu minimum volume can be defined. By comparing the measured swell index parameters to the limiting insitu index, the self-healing capacity can be determined i.e. If the measured swell index is \geq the limiting insitu index, then self-sealing is maintained. This notion however assumes that the entire surrounding buffer is subject to the specific experimental boundary conditions set out in the above batch tests, nonetheless this provides an additional method of assessing the materials self-healing ability post THC exposure. Below details the method of obtaining the total buffer volume and how the index parameters were converted.

- **Volume of top block:**

$$Area = \pi \times radii \text{ from hole center } (88.5^2) \text{ (cm}^2\text{)}$$

$$Volume \text{ of top block} = \text{height of top block (150)} \times Area(24605) = 3690750 \text{ cm}^3$$

- **Volume of bottom block:**

$$Volume \text{ of top block} = \text{height of bottom block (50)} \times Area(24605) = 1230250 \text{ cm}^3$$

- **Volume of ring blocks:**

$$\begin{aligned} Total \text{ volume of ring blocks } (V_t) &= \text{height of ring blocks (468)} \times Area(24605) \\ &= 11515140 \text{ cm}^3 \end{aligned}$$

Total volume of ring block annulus (V_a)

$$= \text{height of ring blocks (468)} \times \text{Area(8992)} = 4208256 \text{ cm}^3$$

$$\text{Volume of ring block} = V_t - V_a = 7306884 \text{ cm}^3$$

- **Total volume of Bentonite:**

$$\text{Volume of bentonite} = 7306884 + 1230250 + 3690750 = 12227884 \text{ cm}^3 (12.221 \text{ m}^3)$$

Using the corresponding dry density of 1.56 Mg/m^3 and the total volume of the Bentonite (in m^3), the total dry mass can be obtained.

$$1.56 \times 12.221 = 19.06 \text{ Mg (or } 1906500 \text{ g)}$$

$$\therefore \frac{1906500}{2} = 953250 \text{ (amount of 2 grams within the total barrier volume)}$$

- **Barrier swell index limit:**

The total dry mass (in grams) was divided by 2 to obtain the same index units as the measured free swell index. Then the volume (in cm^3) was divided by the total dry mass (2g) to determine the insitu swell index limit.

$$12227884(\text{cm}^3) \div 953250(2\text{g}) = 12.83 \text{ cm}^3 / 2\text{g} \left(\frac{\text{mL}}{2\text{g}} \right)$$

From the calculations, this limiting value was derived with the assumption that the emplacement borehole maintained the bentonite within fixed volume conditions. It is understood that a natural system contains many uncertainties which is far from an idealised system assumed here. Nonetheless, this limiting value can be used as a comparison to post THC exposed Bentonite to see if volumetric loss is likely. Deviation below this limiting value therefore indicates that the barriers self-healing and density will likely deviate below design parameters. The limiting index value is lower than the Bentonite free swell index measurements for most the batch test consignments that implemented the reference temperature and salinity. Therefore, the barrier under the reference environmental conditions satisfies the minimum free swell criterion. However, the batch test which explored the range of salinities and concentrations (batch consignment #1- Figure 203) indicated that high concentrations of Calcium will impact the barrier to the point where self-healing will be lost. This is due to the instantaneous impact of the high valence cations of the DDL. Monovalent cations still have a higher swell index compared to the limiting value, even at very high concentrations in the sort-term exposure period. These results do not factor in long-term

physicochemical interactions that may occur over longer time scales such as Illitisation or mineral alteration i.e. 2:1 to 1:1 etc.

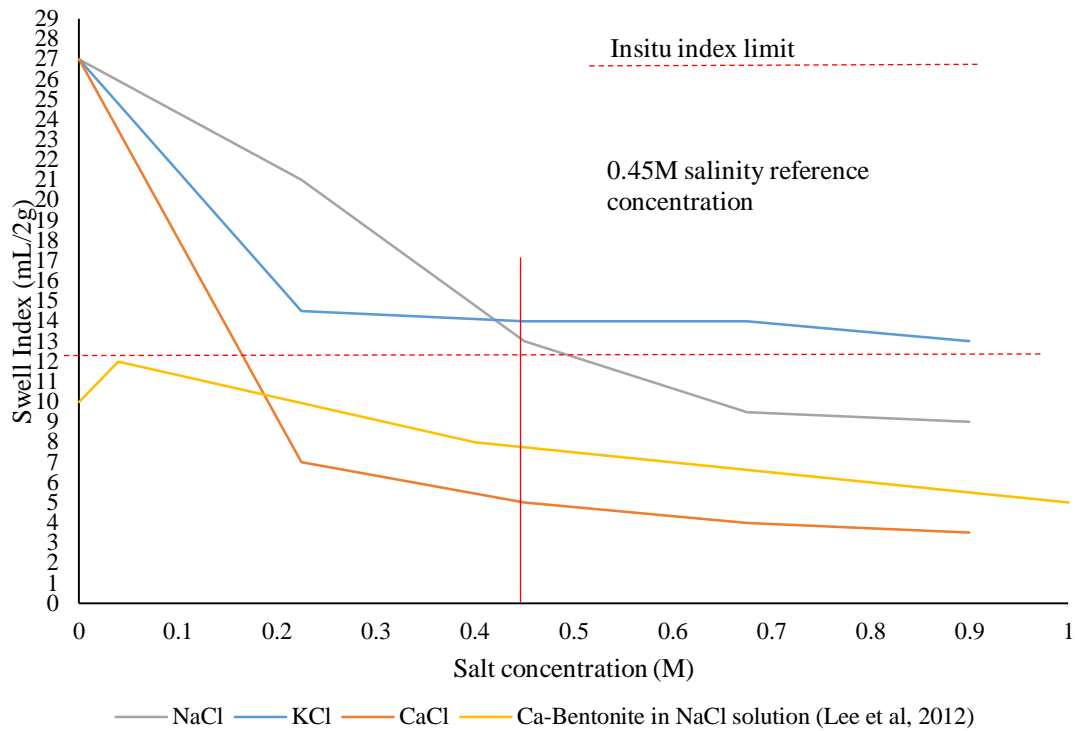


Figure 203: Swell index results for the MX-80/ salt exposure and the Ca-Bentonite in NaCl (Ca-Bentonite results after Lee et al, 2012), the solid red line highlighting the reference salinity concentration for the SAFE Barriers concept

5.3. Conclusion:

The data presented within the above sections indicates that salt alone, particularly from batch consignments 1, 6 and 7 has an instantaneous impact on the bentonites' ability to free swell and maintain its plasticity. Saline concentration exposure equivalent to that of the reference salinity (0.45M- NaCl) reduces the swelling ability by approximately 50%. Nonetheless the swell index measurements are still above than the determined limiting swell index parameter. One significant issue raised from the saline/ Bentonite interaction studies is the impact of higher valence cations. Calcium reduces the materials swell index by 82% (to ~ 4.5 ml/2g) at a concentration of 0.45M, which could be problematic for the barrier if the circulating groundwater is rich in higher valence cations.

It appears that thermal loading under the reference temperature (100°C) reduces the swell index and plasticity index as duration of thermal loading increases. Short-term thermal loading causes an increase due to the thermal dilation coefficient of the Bentonite, with a subsequent drop with long durations which is due to the combined effect of particle fusing by dissolution/ precipitation of siliceous minerals and reduction of the layer dielectric constant.

Much higher thermal loading i.e. above 100°C, displays a large impact on the swell index and consistency for longer durations. There was a measured 23% reduction in the swell index after 24hrs under a thermal load of 300°C compared to a 23% drop after 55 days under a thermal load of 100°C. The swelling ability is a function of the thermal loading and duration exposure.

Tests conducted on the multiple variations of saline solutions under varied temperatures and durations in the presence of carbon steel. Indicate that high saline groundwater influences the barrier much more than the corrosion and temperature alone. Through examination of the XRD patterns conducted on the mid-term synthetic groundwater and DI water samples, Fe exchange in the octahedral layer was not evident. However, broadening of the clay peaks containing C-Steel indicates formation of poorly crystalline corrosion products within the clay matrix. Long-term duration tests (1 and 2 years) further support that the impact of the corrosion is a long-term phenomenon. The alteration of these effects was unobtainable under short-term conditions. XRD demonstrated that higher temperatures resulted in higher disordering of the smectite and secondary mineral composition. However, the swelling component remained largely equivalent to the smectite characteristic peak. Samples with the synthetic groundwater solution indicated a predominant interlayer exchange of Ca, with air-dried peaks corresponding to the divalent interlayer occupation. Furthermore, samples also displayed a calcic composition, upon post exposure analysis, which also appeared to form a new peak possibly corresponding to Palygorskite. Quartz peaks were largely reduced after high thermal exposure, with increased/ prominent peaks at cooler/ outer zones, indicating and supporting the premise of siliceous compound dissolution and precipitation upon cooling which will impact the swelling and stiffness characteristic of the barrier. Dissolution of secondary minerals such as feldspars and calcite show dissolution within the higher temperature exposed samples. Also, indicating possible alteration towards porosity and density.

6. Experimental interface results

The interface testing protocol consisted of the C-steel/ bentonite interface subject to a series of inferred experimental boundary conditions which closely replicated the near-field environment. Each phase corresponded to a specific period after the canister is emplaced within the GDF. Literature data and industrial/ academic collaboration enabled each life-phase to be determined, with the subsequent experimental design based on the aforesaid results and data. As previously stated, each phase was conducted over a 4-month duration, this was the longest feasible time-scale within the project completion constraints. Based on this, the alteration products may not necessarily be completely replicable of the real EBS system. However, the reaction kinetics and subsequent inference of probable outcomes after longer durations i.e. on geological time-scales can be achieved with the aid of literature results. For clarity, table 67 is recalled which displays the experimental testing matrix which outlines the boundary conditions of each respective phase.

Table 67: Inferred key life phases for interface replication experiments

Phase 1- Initial conditions (Replicating emplacement -> 50 yrs.)	Phase 2- Mid-life conditions (Replicating 50 yrs. -> 1×10^4 yrs)	Phase 3- Late-life conditions (Replicating 1×10^4 yrs +)
<ul style="list-style-type: none"> • Temperature (Maxima)= 100°C • Duration: 4 Months <p style="text-align: center;"><u>Initial barrier parameters</u> <u>(Emplacement):</u></p> <ul style="list-style-type: none"> • Dry density: 1.56Mg/m³ • Moisture content: ≈ 23% • Degree of saturation ≈ 98% <p style="text-align: center;"><u>Inferred replication state:</u></p> <ul style="list-style-type: none"> • Partially saturated progressing to initial dry phase (Aerobic) • Atmospheric pressures present 	<ul style="list-style-type: none"> • Temperature ≈ 80°C • Duration: 4 Months <p style="text-align: center;"><u>Inferred replication state:</u></p> <ul style="list-style-type: none"> • Dry progressing to Saturated conditions (Aerobic to Anaerobic): oxygen consumption used in additional corrosion of the coupon. • Saturation of sample progressing hydrostatic conditions maintaining constant dry density: final moisture content corresponding to ≈99-100% (Sr) (24% moisture) • Development of reducing conditions upon saturation • NaCl solution (0.45M) 	<ul style="list-style-type: none"> • Temperature (Minima)≈ 35°C • Duration: 4 Months <p style="text-align: center;"><u>Inferred replication state:</u></p> <ul style="list-style-type: none"> • Saturated/ anaerobic conditions • System hydrostatic conditions using high salinity water (NaCl- 0.45M)

A comprehensive suite of geotechnical and physicochemical analyses has been conducted on the THC exposed interface samples. Each cell was prepped for post analysis within a nitrogen-rich environment. Given below are the results conducted on each experimental phase, clay analysis looked into the alteration of the intended design parameters for the engineered barrier functionality as well as a brief analysis of the steel coupon used within each phase. Furthermore, the use of photographic evidence has enabled the preservation of interface sub-sampled conditions immediately after THC exposure, thus compensating for any REDOX sensitive minerals. Time-lapse photography has also been conducted on the “altered” bentonite to investigate the reaction kinetics of oxidation, post-anaerobic exposure.

6.1. Interface post-mortem inspection:

Each cell was opened within a low oxygen/ nitrogen purged environment as well as the sub-sampling protocol, subsequently samples were stored until post testing was conducted. Additionally, observations of the interface sampling were recorded for comparative analysis as well as allowing insight into the extent to which corrosion transpired throughout the sample. Sub-samples were taken at each visible zone of corrosion alteration i.e. each zone was characterised by colour alteration to the bentonite. The initial state of the bentonite is described as a grey/ white material depending on the compaction and hydration state, therefore any colour alteration was classed as a zone for post analytical measurements. Below in figure 206, 207 and 208, present the compiled interface pictures with spatial extent measurements of each affected zone.

6.1.1. Phase #1: Initial conditions:

The conditions that this phase was subject to are defined in table 67 above. This phase implemented the highest exposure temperatures with no hydraulic gradient, the phase allowed the sample to become dry, similar to emplacement conditions of the interface bentonite. After 4-months of thermo-chemical exposure the contact surface of the interface displayed a black precipitate, characteristic of Magnetite (Fe_3O_4). The immediate zone (0-0.1mm) from the C-steel interface displayed a characteristic colour change. The bentonite was green in appearance. The greenish appearance gives an indication that there is possibly Fe^{2+} enrichment within the bentonite matrix. The next zone (0.1-0.2mm) from the C-steel interface gave a characteristic orange appearance, this zone was indicative of Fe^{3+} enriched bentonite. The majority of the bentonite block had not displayed any colour alteration. The remaining 10.8mm had the same characteristic grey as the original material. Figure 204 displays each zone with depth measurements indicating the depth of alteration from the C-steel interface.

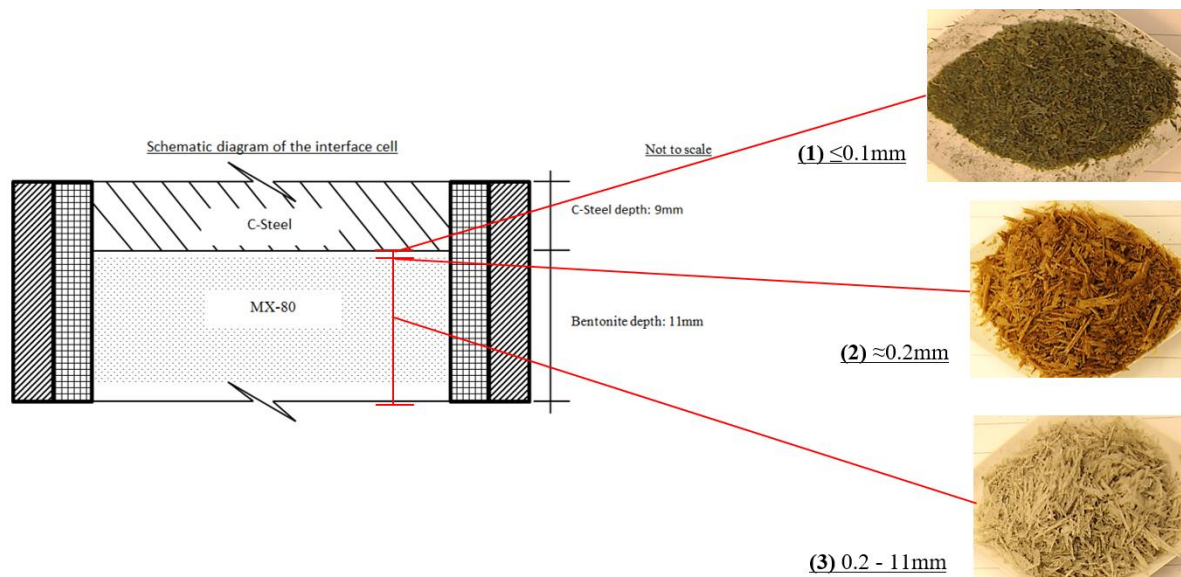


Figure 204 Interface post-mortem diagram for phase #1

6.1.2. Phase #2: Mid-life conditions:

The experimental boundary conditions implemented for phase #2 are outlined in table 67 above. This phase implemented elevated temperatures with a saline hydraulic gradient allowing for re-saturation. After the THC exposure period, the interface appeared to display the similar black precipitate on the surface. However it appeared to be higher in abundance and more uniform over the coupon surface. The colour alteration transpired in a similar fashion to that of phase #1, expect the boundaries of corrosion integration increased. The green phase was evident but penetrated to a depth of 0.5mm from the C-steel. The orange phase had integrated into the bentonite by 3mm from the C-steel with the remaining 8mm remaining grey in appearance. Below in figure 205 displays the interface post-mortem diagram for phase #2.

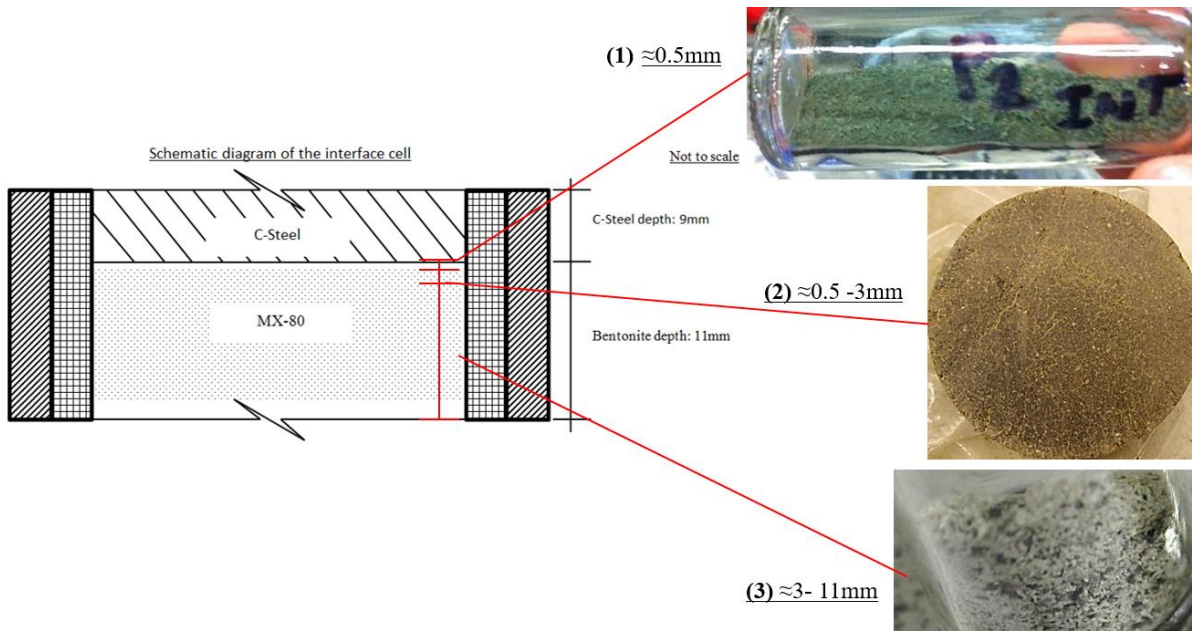


Figure 205: Interface post-mortem diagram for phase #2

6.1.3. Phase #3: Late-life conditions:

The conditions that this phase was subject to are defined in table 67 above. This phase implemented the lowest exposure temperature with a saline hydraulic gradient. The phase saturated the sample under “background” temperatures comparable to radiogenic temperatures for depths associated to the GDF emplacement vaults within a crystalline rock. These conditions are replicable to very late-life parameters, after the waste has completely thermally decayed to background levels. After 4-months of thermo-chemical exposure the contact surface of the interface displayed a black precipitate, similar to the previous interface environment phases. However, this phase did not display the greenish colour alteration in the bentonite immediately in contact with the C-steel, it did however display an orange colour integration up to 2 mm from the interface. The remaining 9mm was visibly the same as the “starting” material. Figure 206 displays the interface diagram post THC for phase #3.

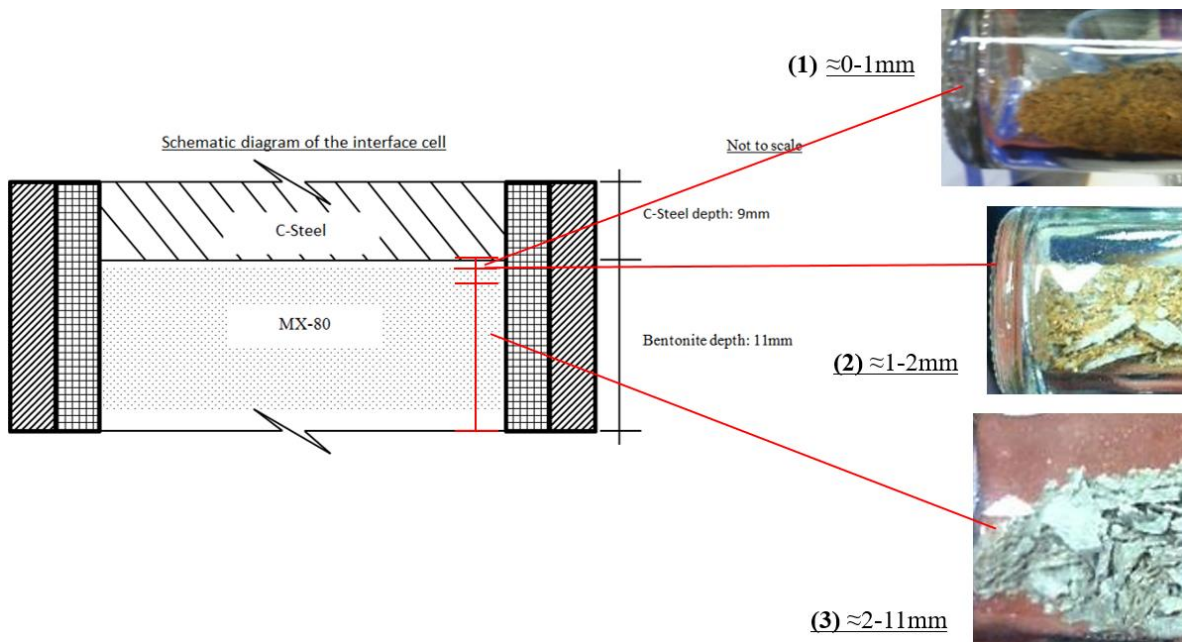


Figure 206: Interface post-mortem diagram for phase #3

6.1.4. Interface corrosion integration comparison:

A comparison of the extent to which the corrosion transpired into the bentonite is displayed in table 68. This displays the comparative data of the integration measurements taken during post-THC sampling.

Table 68: Visible corrosion integration comparison

Phase #	(1) Depth of green bentonite from C-steel (mm)	(2) Depth of orange bentonite from C-steel (mm)	(3) Depth of “Unaltered” bentonite from C-steel (mm)
1	0.1	0.2	10.8
2	0.5	3	7.5
3	N/A	2	9

From table 68 it is clear that temperature with the hydraulic gradient plays an important role in the type of corrosion product and spatial extent to which it travels into the compact bentonite. It appears that the development of the green bentonite occurs at elevated temperatures, most likely due to the accelerated consumption of oxygen in the system. When a hydraulic gradient was present the corrosion, extent appeared to be greater, even though it was opposite to the direction of the fluid flow. The saline solution appears to increase the diffusion rate into the bentonite block from the C-steel. Higher temperature phases indicated the development of the green bentonite, with phase 1 displaying the least degree of colour alteration regardless of the highest thermal exposure.

6.1.5. Oxidation study on the green bentonite taken from the interface:

The study was conducted using the green material from the bentonite directly in contact with the C-steel, time-lapse photography was implemented to observe and measure the time for oxidation to occur. It was assumed that the bentonite in this zone was rich in Fe^{2+} due to the appearance, and it was also assumed it would be REDOX sensitive. The sample was exposed to atmospheric conditions at 20°C and the time-lapse photos were taken at three hour intervals. The first time-lapse photos were conducted in a post-phase state with no additional temperature or moisture. The second set of time-lapse photos was conducted with additional water to accelerate the oxidation kinetics. Figure 207 displays the initial and final time-lapse pictures for comparison. Figure 208 displays the initial, middle and final time-lapse pictures for an additional comparison.

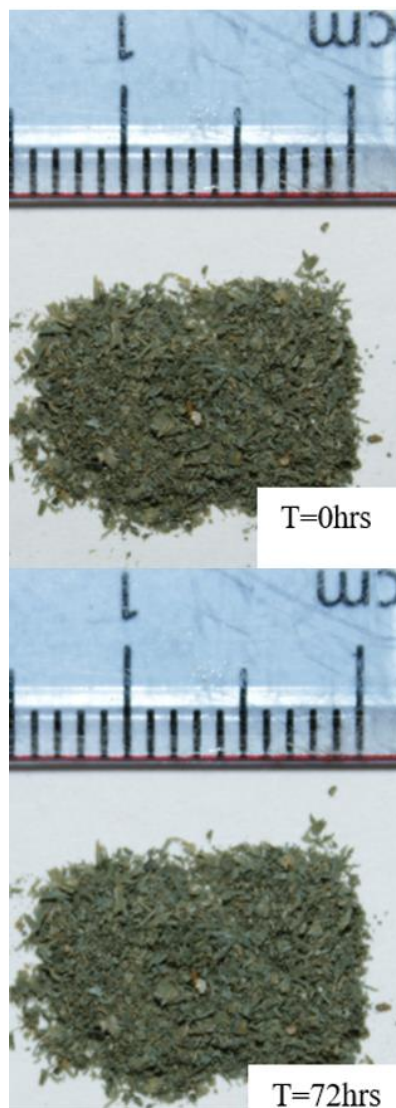


Figure 207: Time-lapse pictures for the dry ambient oxidation tests



Figure 208: Time-lapse pictures of the hydrated oxidation tests

The ambient time-lapse pictures, figure 208 above, indicate that oxidation of the green bentonite does not occur which was on the contrary to what was initially hypothesised. It was thought that exposure to atmospheric conditions would initiate oxidation and it would occur

rapidly. This was due to the findings of other studies who reported the speedy oxidation of the bluish/green altered bentonite (Kumpulainen et al, 2010; Idiart et al, 2013). However, through examination of figure 208, the addition of water accelerates the oxidation process, this is evident by the gradient colour alteration from bluish green to orange over time. After 36hrs with the addition of water under an ambient temperature (25°C), the sample appears to display some oxidation. The clay in this zone is definitely Fe^{2+} rich, complete oxidation is observed when the sample is run for XRD. Heat treatment of the sample, post glycolation, turns the sample completely orange after 24hrs under 440°C. Therefore, these observations indicate that the Fe^{2+} -rich phase is in a metastable state, further testing in the following sections investigate the likely type and location of the mineral.

6.2. Post THC exposure geotechnical testing:

Post geotechnical measurements such as the plasticity index and swell index are presented in this section. The measurements conform to BS 1377 Pt.2 and ASTM D5890 respectively. With respect to the Atterberg limit measurements only the plastic limit was obtained for the internal sub-samples due to the limited mass of dry material.

6.2.1. Plastic limit measurements:

Figure 209 displays the compiled plastic limit measurements for each sub-sampled zone and phase respectively. Each sampled zone is assigned a number which is displayed in figures 204, 205 and 206 as well as table 68.

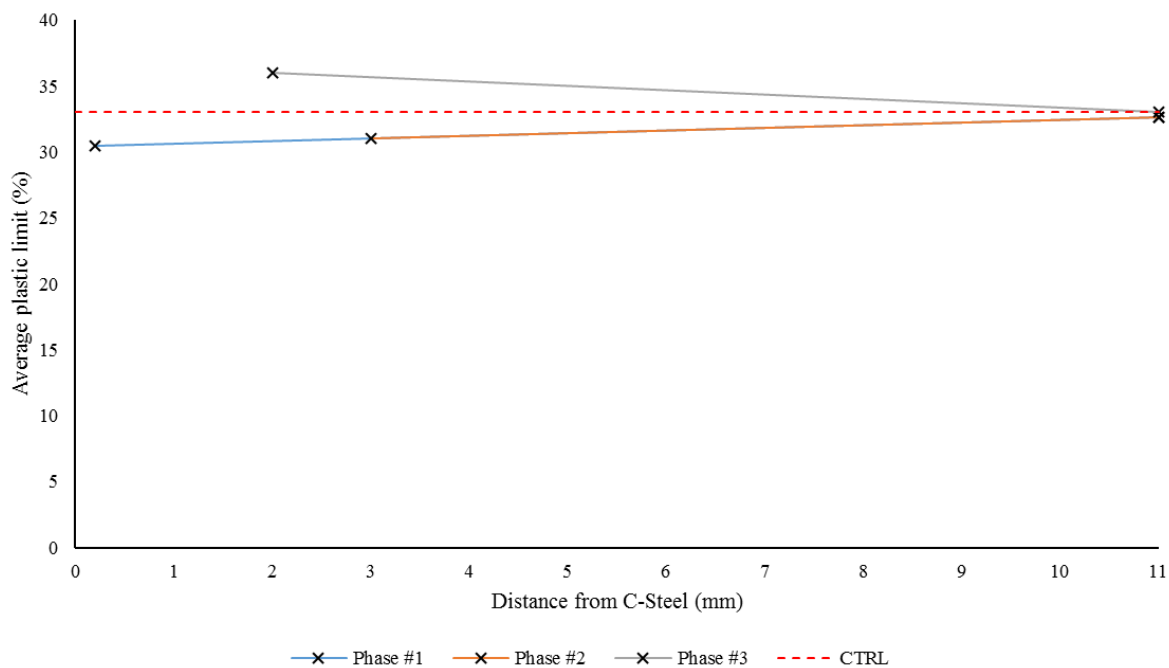


Figure 209: Average plastic limit profile for each environmental phase for interface samples

Overall there is little observed deviation of the plastic limit results. There is a general trend in reduction closer to the interface zone which may indicate that the integration of the corrosion products is having a slight impact on the consistency. It is not clear however if it is the impact of the Fe^{3+}/Fe^{2+} species on the DDL or structural consistency from these results. It could be that the oxy(hydroxides) have formed within the clay matrix and therefore the measurements for the plastic limit are affected by the non-clay component. Nonetheless, there is a very slight reduction with phase 1 and 2 displaying almost identical trends across the bentonite profile. These two phases use the highest temperatures in the interface experiments. From this higher temperature exposure with the corrosion environment influences the material more than corrosion alone. Phase 3, the lowest thermal exposure experiment, displayed an opposite trend. Overall the results indicate a deviation within $\pm 5\%$ of the control measurements for the sub-samples closer to the interface with the plasticity measurements being identical to the control in the outer zone of the interface sub-sample. Therefore no geotechnical alteration under phase 3 conditions is apparent.

6.2.2. Plasticity index measurements:

Figure 210 displays the calculated plasticity index measurements for the outer sub sampled zones only. This is due to the liquid limit being conducted on these sub-samples due to the volume of material required. The plasticity index is considered much more useful with respect to assessing the consistency of a soil. The higher the plasticity index range the higher the swelling capacity, as well as the soil displaying a larger range over which the soil can resist shear stress.

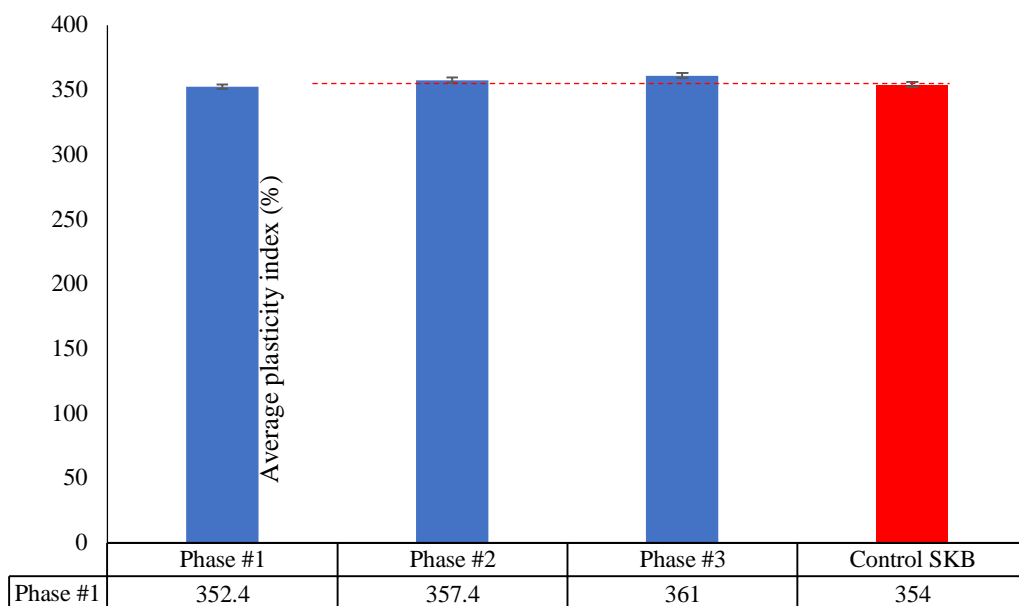


Figure 210: Outer zone plasticity index measurements for all phases with a comparison to the control parameter

The plasticity index results conducted for each phase outer sub-sampled zones indicate that there is negligible deviation from the control parameter. This indicates that temperature, corrosion and saline solution (0.45M- NaCl) has little impact on the consistency parameters. It was assumed, based on the results from the batch test measurements (section 5), that the impact of electrolyte rich solutions would have an impact on the consistency parameters. However, it appears that in a constant volume system with the presence of corrosion products the plasticity index is not affected. This is possibly due to the compensating trend of the Fe within the system. However, a gradual reduction with increasing temperature is observed, nevertheless the parameters do not drop below the control measurement.

6.2.3. Swell index measurements:

Figure 211 displays the free swell index profiles for the sub-sampled zones with respect to each interface phase.

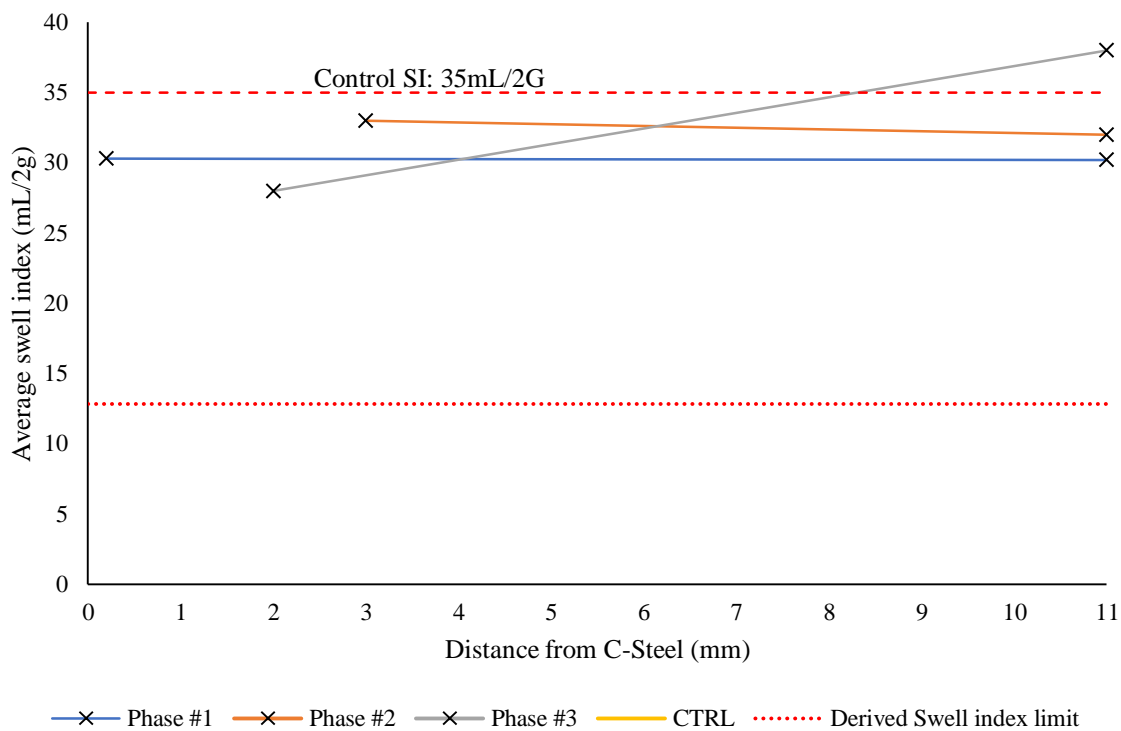


Figure 211: Average swell index profile for the interface sub-sampled zones

The swell index measurements displayed in figure 211, show a systematic reduction with respect to the thermal exposure. Phase 1 results display an overall reduction of approximately 14% from the control measurement, the reduction appears to be uniform over the entire soil profile. This indicates that thermal loading has a higher impact on the soils swell potential corresponding to the findings from the batch test series in section 5. The same trend is observed in phase 2, with an overall reduction of approximately 6%, again indicating that

thermal loading impacts the materials volumetric uptake upon saturation. This impact is thought to be due to particle “fusing” by the precipitation of silica and alteration of the dielectric constant. Dissolution and reprecipitation of silica is evident from the XRD analyses in the higher temperature tests. However, a reduction of the dielectric constant would impact the DDL of the clay and the result would be systematic throughout all the measurements i.e. PI and SI. Whereas the deviation is only observed in the swell index test which indicates that inter-particle fusing has likely occurred. The deviation is minor for these tests however the impact is a function of exposure time, supported by the batch test series results (section 5). Therefore, the results are not representative of the real-time impact of the experimental boundary conditions but they do show a trend with respect to the probable boundary conditions the EBS will experience. Phase 3 displays anomalous measurements and the most erratic deviation compared to the other phases. This is inconsistent with the results observed here and in the batch test series. This appears to be due to a gross error in the testing protocol. Nonetheless, measurements do not deviate below the derived limiting swell index value of 12.83mL/2g, determined from batch testing (given in section 5) which would indicate that the bentonite would not maintain the volume of the deposition hole.

6.3. Post THC exposure physicochemical analysis:

This section presents the post THC chemical analysis on the interface sub-samples, this section forms the focal part of the interface results. This is because the interface testing intended to have a primary focus on the mineralogical alteration post interface replication exposure.

6.3.1. CEC measurements:

Cation exchange capacity measurements allow the observation of layer charge alteration due to the exposure to the interface replication tests. Layer charge alteration can be due to isomorphic substitution cations in either the tetrahedral and octahedral layers or occupation of interlayer cations respectively. Figure 212 displays the compiled CEC measurements for each sub-sampled zone for each respective replication phase.

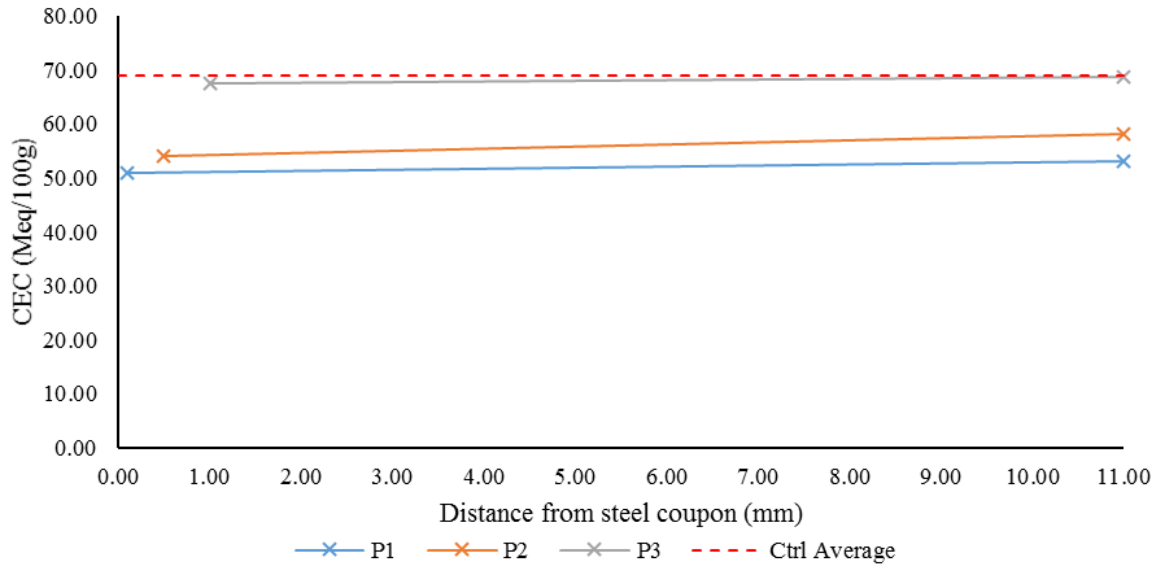


Figure 212: CEC measurements for the interface sub-samples (only measured for immediate zone affected by bentonite and outermost zone)

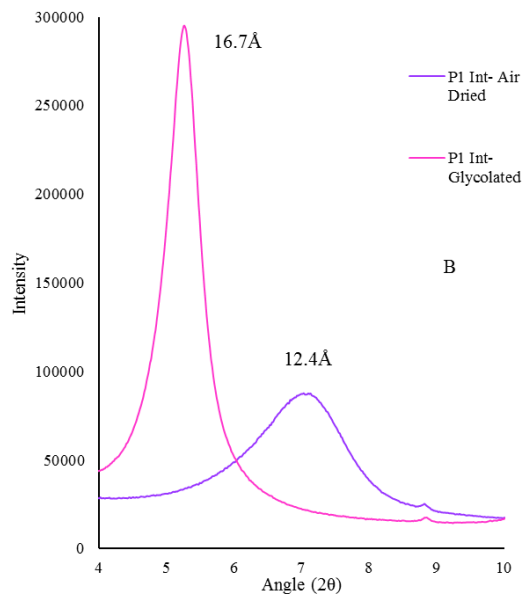
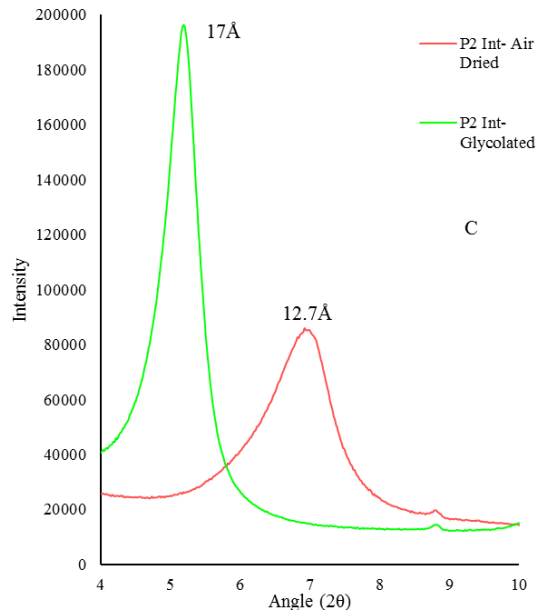
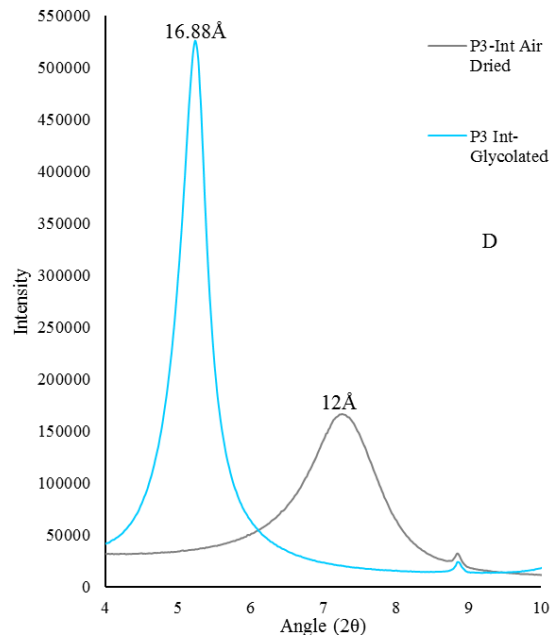
There is an overall trend in the reduction of the CEC closer to the zone impacted most by the corrosion of the steel coupon. There is also an additional trend in reduction with respect to interface exposure temperature. This is likely down to the development of layered double hydroxides at the interface zone and within the bentonite surrounding it. It is widely known that the thermodynamic kinetics of oxi-hydroxides are higher under elevated temperatures due to the activation energy change in the system. Therefore, higher temperature phases are likely to observe layered double hydroxides. Additionally, the reduced CEC may also be due to the substitution of trivalent cations for divalent cations within the octahedral layer (See XRD results section 6.3.2).

6.3.2. XRD analysis:

Crystallographic analysis has been conducted on all post THCM interface sub-samples. Various XRD treatment and post analysis data processing has enabled a comprehensive examination of the clay physicochemical state, as well as the accessory mineral composition. The XRD treatments have enabled semi-quantitative analysis of the clay composition, intrinsic expandability measurements of the smectite layers, Fe replacement within the octahedral layer and the non-clay mineral composition.

6.3.2.1. XRD examination of the clays swelling ability:

This section examines the integrity of the smectite component with a comparison to the control data. Figures 213-215 display the compiled XRD patterns for the interface, mid and outer sub-samples respectively.



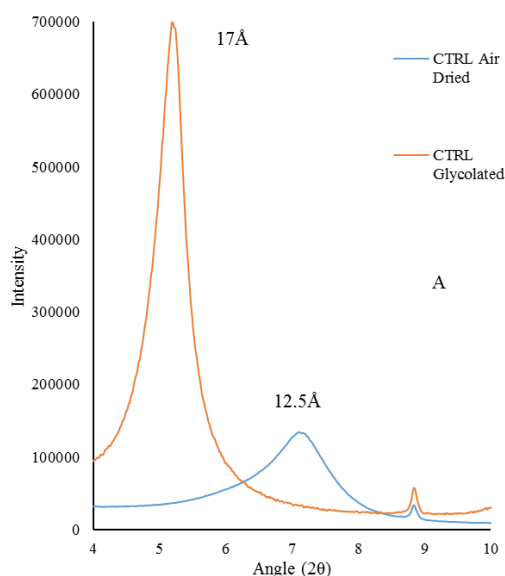


Figure 213: Clay swelling component XRD patterns for interface sub-samples A) Control data, B) Interface zone phase 1 data, C) Interface zone phase 2 data and D) Interface zone phase 3 data

Examination of the XRD patterns in figure 213, displays the low angle peaks for the clay interface sub-samples for phases 3 to 1 respectively. To assess the swelling of the smectite component the low angle range is focused on, as well as the air-dried and glycolated runs. It appears that the smectite component has not been altered, with glycolated samples swelling to the characteristic d-spacing for smectite ($\sim 17\text{\AA}$). The air-dried sample alone cannot be relied upon as change in the relative humidity during air drying can alter the d-spacing according to the hydration state. The results do however indicate little alteration to the interlayer occupancy, with d-spacing in the 12\AA region, this indicates monovalent cation occupancy. The small peak that remains stable near 9° (2θ) is characteristic of illite, as indicated within the material classification section (section 4) along with additional conformation of randomly interstratified illite/smectite. This peak appears to diminish with increasing temperature exposure i.e. from phase 3 to phase 1. What is apparent is that the air-dried peaks are broader in the higher temperature exposed sub-samples which also correlate to higher amounts of Fe, supported by UV-Vis and ICP data as well as the visual post-mortem pictures. This therefore indicates that there are more amorphous corrosion products within the clay matrix which masks smaller peaks due to Fe fluorescence effects. Nonetheless, the bentonite directly in contact with the C-steel coupon under the respective phases indicates little alteration to the smectite component, which is advantageous for the integrity of the barrier. Nonetheless, it must be noted that the time-scales involved in the experimental testing are significantly shorter than those of real insitu conditions.

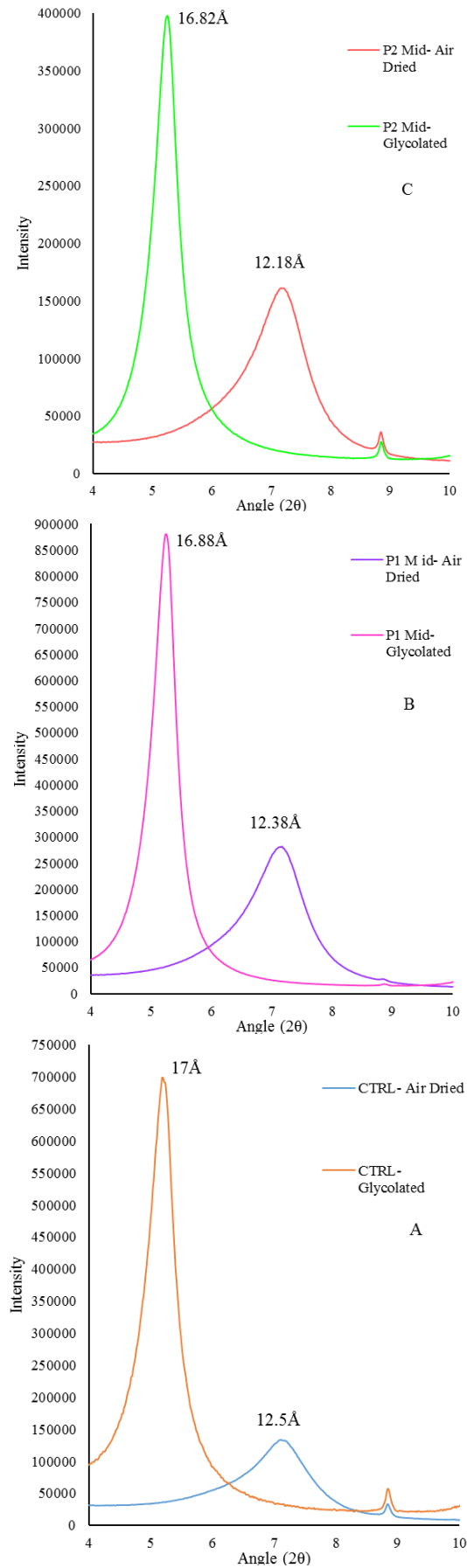
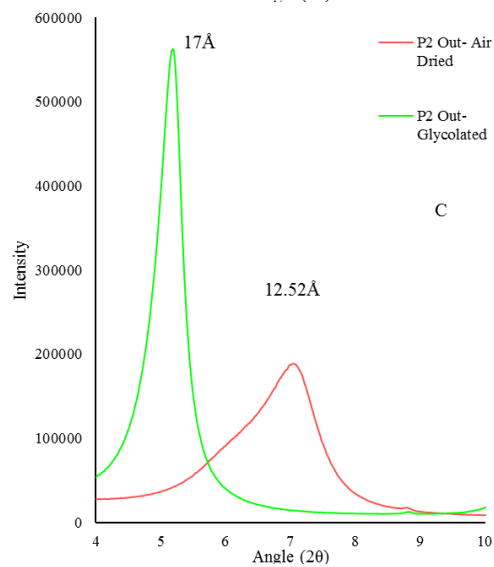
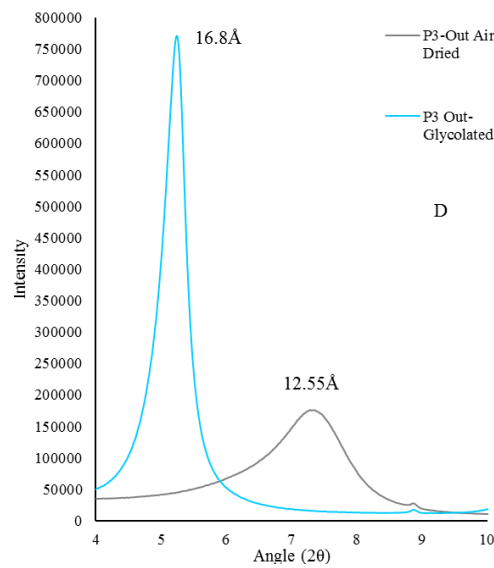


Figure 214: Clay swelling component XRD patterns for mid sub-samples A) Control data, B) Mid zone phase 1 data, C) Mid zone phase 2 data

Middle zone sub-samples for the respective interface phases are displayed above in figure 214. Similarly, the smectite component of each interface phase exposure is unaffected with d-spacing swelling remaining in the 17Å region. The characteristic illite peak is more prominent in the middle zone of phase 2 whereas the illite peak is still in phase 1. This indicates that Fe oxide amorphous compounds are present in the mid zone for the highest temperature exposed and the penetration depth is greater in phase 1 compared to the lower temperature experiments. A mid-zone sub-sample was not obtained for phase three as no clearly defined mid-zone was detected.



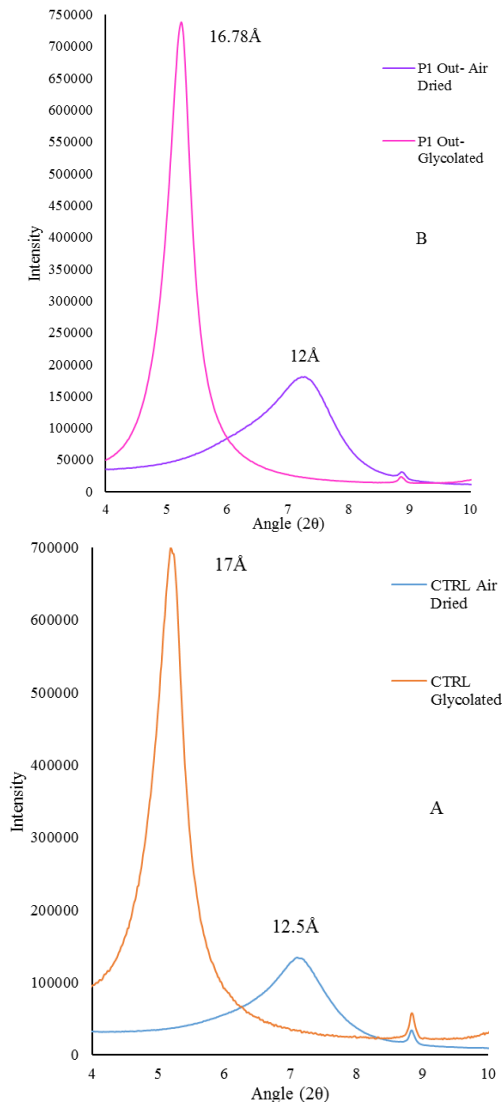
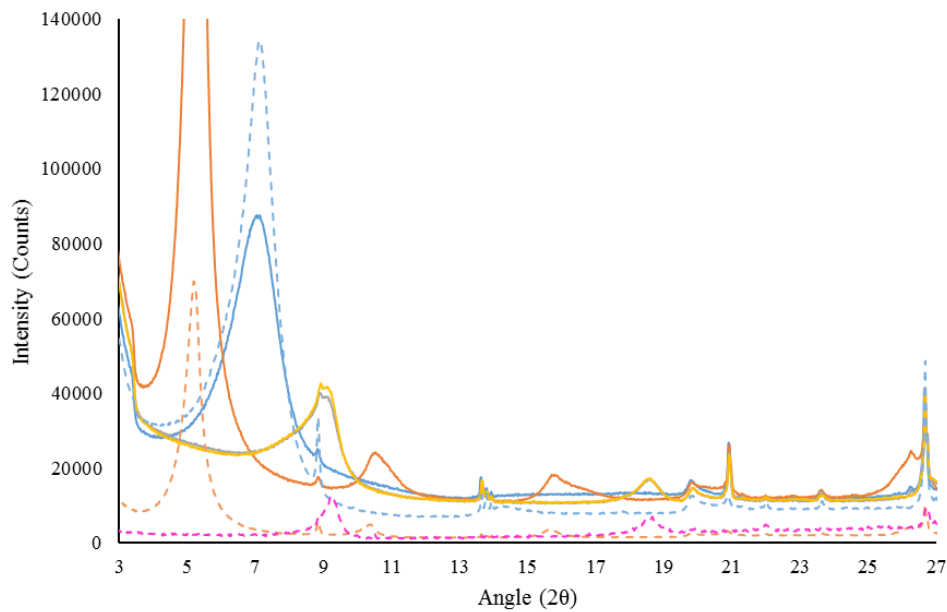


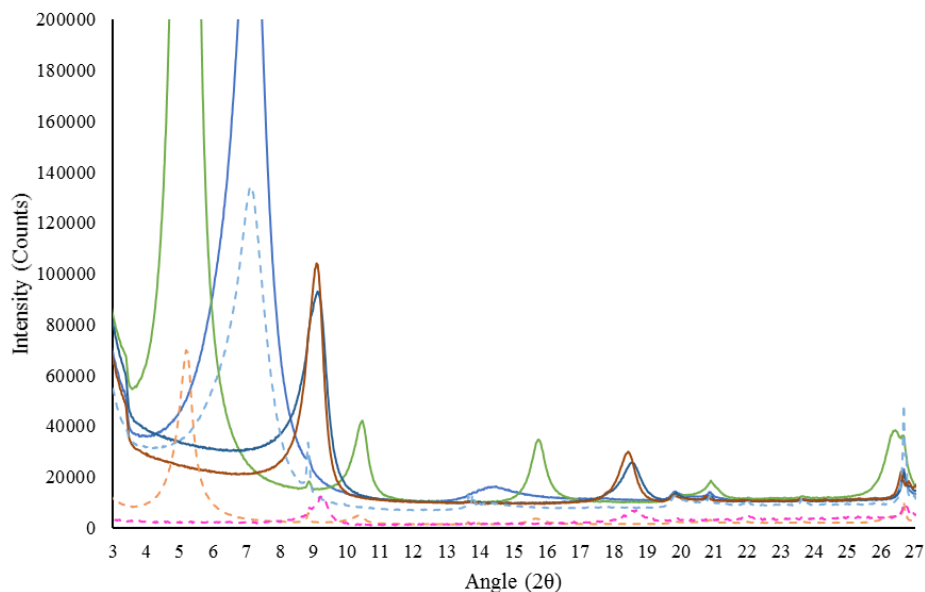
Figure 215: Clay swelling component XRD patterns for outer sub-samples A) Control data, B) Outer zone phase 1 data, C) Outer zone phase 2 data and D) Outer zone phase 3 data

The outer most sub-samples for the respective interface environmental phase conditions are presented in figure 215, above. The XRD patterns also demonstrate that there was no alteration to the smectite component on the bentonite within the interface system. The illite peak is still slightly present in all phases indicating that the extent of amorphous corrosion products didn't penetrate the outer zones. This is supported by the visual post-mortem measurements. The air dried XRD pattern for phase 2 which also was subject to a hydraulic gradient consisting of saline solution, indicates a broadening of the shoulder toward the lower angle range. This may indicate that there is some divalent occupancy of the interlayer, this is also supported by the cation concentration measurements within the following sections especially the Mg concentrations in the outer zones. The premise of the shoulder developing and shifting toward 15\AA due to exchange with divalent cations is supported by the measurements in the batch test results (in section 5) and Moore and Reynolds (1997).

Figures 216 to 218 display the overall compiled XRD treatment peak profiles for the respective interface sub-samples. It is clear that the interface sub-samples demonstrate some partial Fe substitution, especially when examining the 002/003 peaks. At the interface these peaks, 002 near 11° (2θ) and the 003 near the 16° (2θ), they are much broader and the intensity of the 003 is lower than that of the 002 thus indicating that some Fe substitution has occurred as well as the development of poorly crystalline Fe minerals. Peak intensity ratios are examined in the next section, 6.4.2.2 that quantifies the magnitude of Fe substitution.



— P1Int-AD
 — P1Int-HT440
 - - SKB-CTRL Air Dried
 - - SKB CTRL- HT 440
 — P1Int-Glycolated
 — P1Int-HT550
 - - SKB CTRL- Glycolated



— P1Mid-AD
 — P1Mid-HT440
 - - SKB-CTRL Air Dried
 - - SKB CTRL- HT 440
 — P1Mid-Glycolated
 — P1Mid-HT550
 - - SKB CTRL- Glycolated

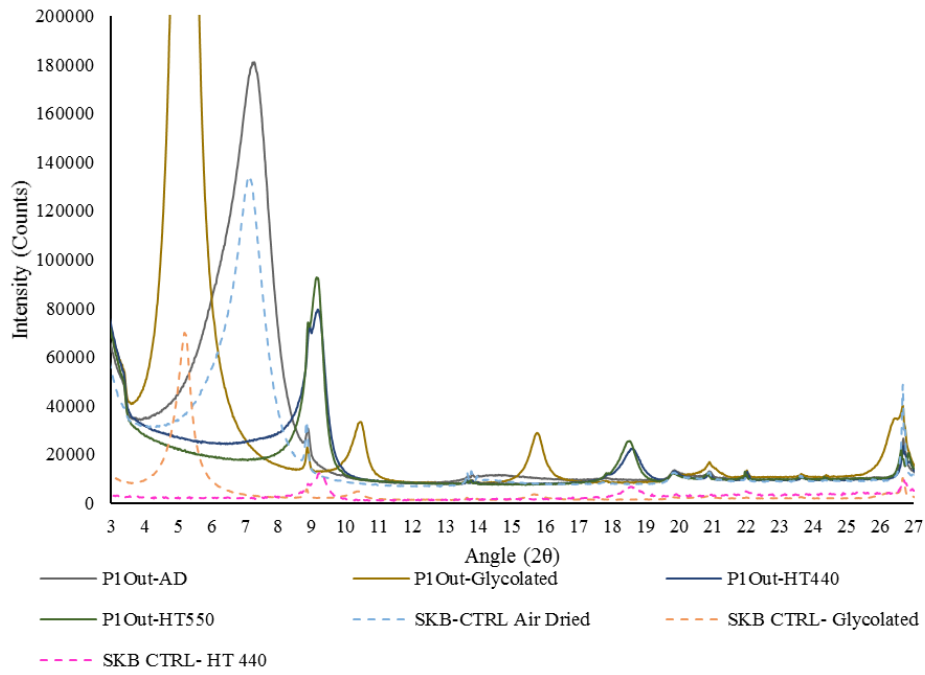
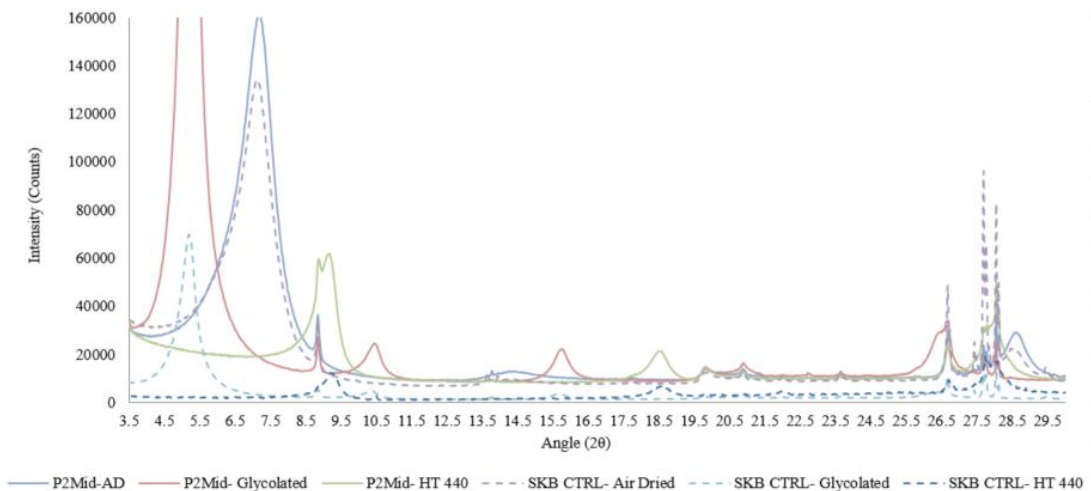
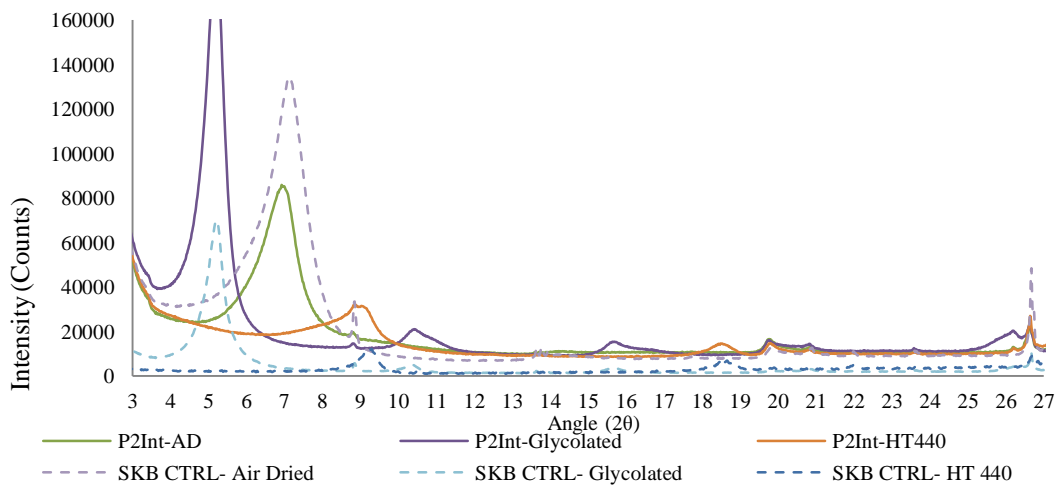


Figure 216: Clay range XRD profile for interface phase 1 sub-samples



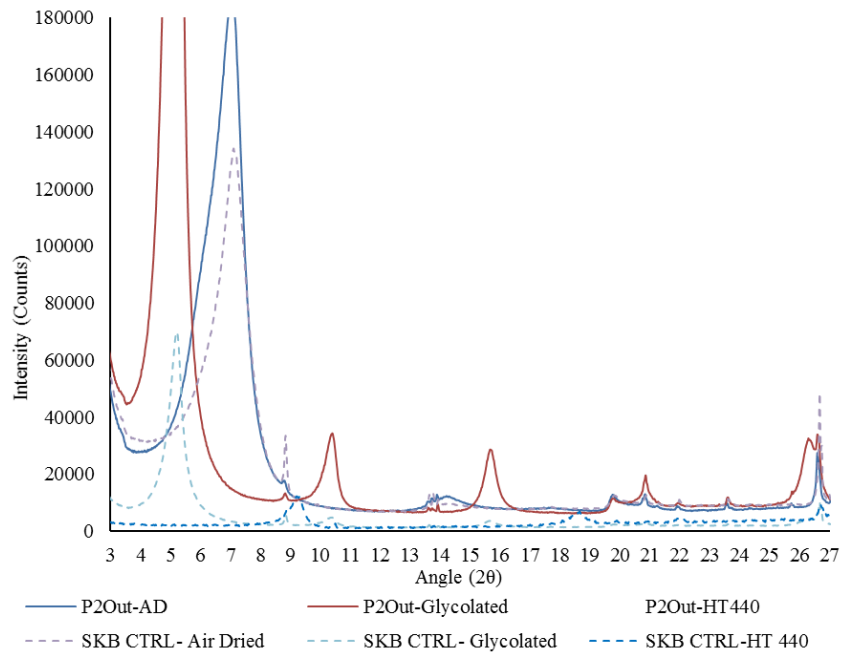
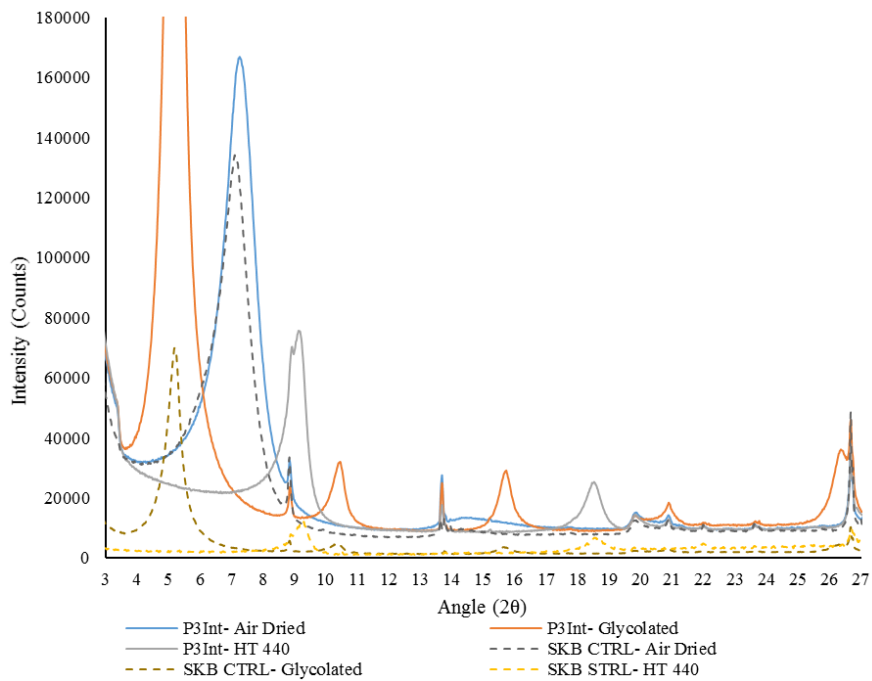


Figure 217: Clay range XRD profile for interface phase 2 sub-samples



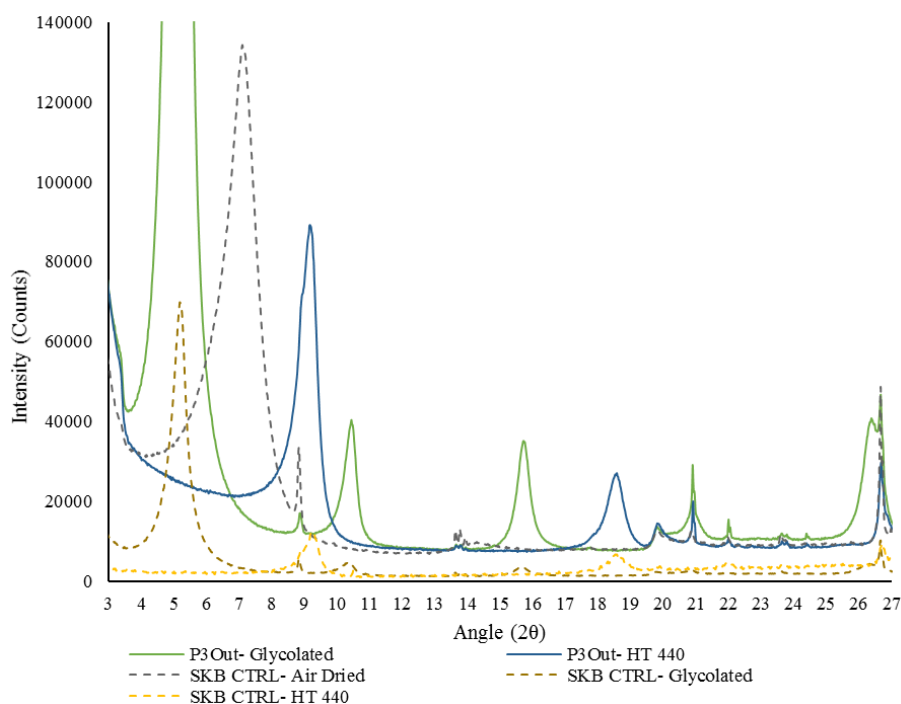


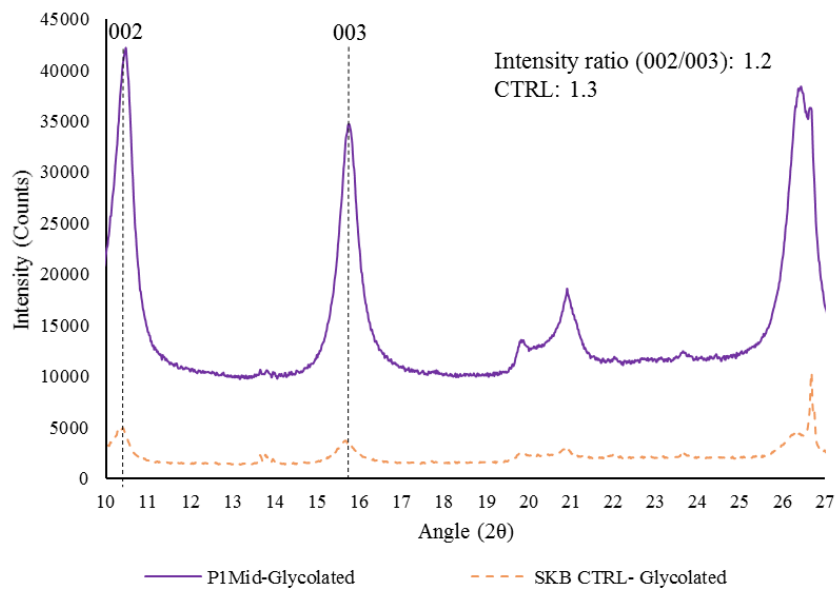
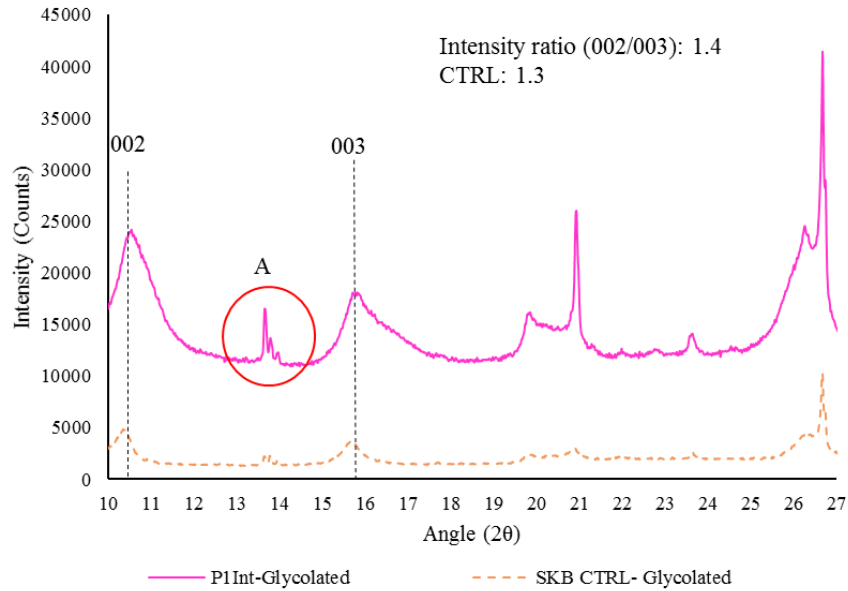
Figure 218: Clay range XRD profile for interface phase 3 sub-samples

Overall it is clear that the material still contains a high charge/ high surface area smectite component within a mix of accessory minerals and corrosion products. The profiles of the smectite peaks indicate that the material is a saponite-type smectite which is rich in Fe and Mg at the interface sub-samples with a more Mg-rich saponite type smectite further away from the coupon. The following sections will explore the iron content within the smectite structure, assessment of accessory minerals and determination of the type of corrosion products within the bentonite matrix.

6.3.2.2. XRD examination of Fe integration:

It is possible to obtain information regarding the integration and substitution of Fe within the octahedral layer. This is achieved by inference of the effects of electron scattering from the octahedral layer due to the increased presence of Fe though inspection of the 002/003 intensity ratio. Therefore, the higher the intensity ratio of the 002/003 peaks indicate higher back scattering. However, differentiation between di-octahedral and tri-octahedral smectite is harder if the 060 peaks are not present. Furthermore, Mg-rich tri-octahedral smectite can be indistinguishable to Fe Tri-octahedral smectite without the 060 measurements. Nevertheless, without the 060 measurements, the 002/003 peak intensities can be used as an indicator to the increase in electrons within the octahedral sheet. Along with the use of other analysis e.g. ICP and the UV-Vis measurements, it can be inferred which is the probable cause of the scattering effect. Both ICP and UV-VIS results indicate an increased concentration of Fe closer to the

interface with the concentration level falling as the distance from the coupon increases. The magnesium concentration levels appear to follow the same trend but to a much lesser extent, therefore the intensity ratios will indicate if there is a general increase electron density. Displayed in figures 219, 220 and 221 are the intensity ratio profiles for the individual phase sub-samples along with the control profile for comparison.



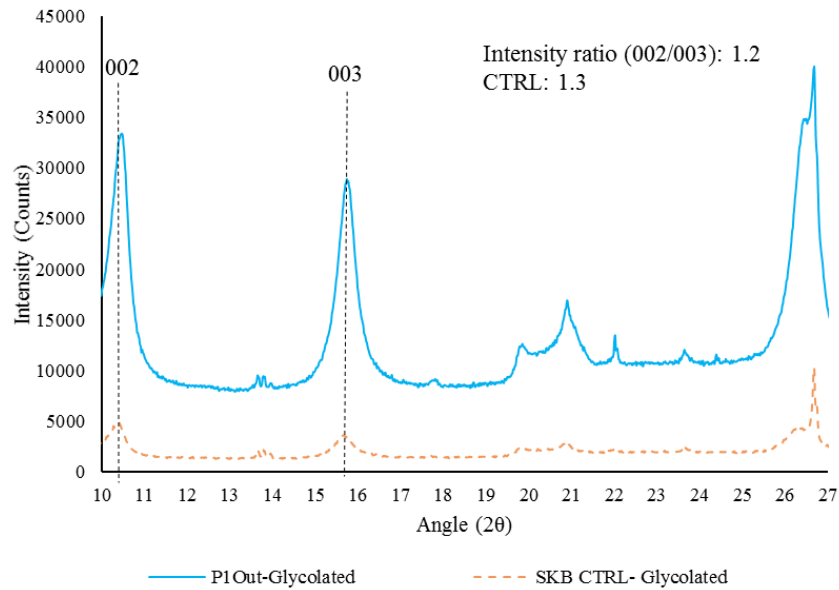


Figure 219: 002/003 peak intensity XRD patterns for phase 1 interface sub-samples

Figure 219 displays the glycolated 002/003 peaks for the interface phase 1 sub-samples. The intensity ratio does not appear to increase significantly over the sample profile, but there is a trend in higher values nearer to the interface. This could indicate that there is some substitution occurring, ICP results (Displayed in section 6.3.5) indicate a higher concentration of Fe within this zone. Interestingly, the interface sub-sample displayed a peak around 14(2θ) highlighted in point A (Red circle) in figure 219. This peak is closely characteristic to a FeO(OH) peak. The development of goethite is understandable as this phase was open to atmospheric conditions under high temperatures, therefore free access to oxygen was allowed. Furthermore, the “green” sub-sample was exposed to air upon air-drying and glycolation which would further allow oxidation to occur. This therefore provides some indication that the green layer is Fe^{2+} hydroxide rich, which reverts to an Fe^{3+} rich mineral upon oxidation

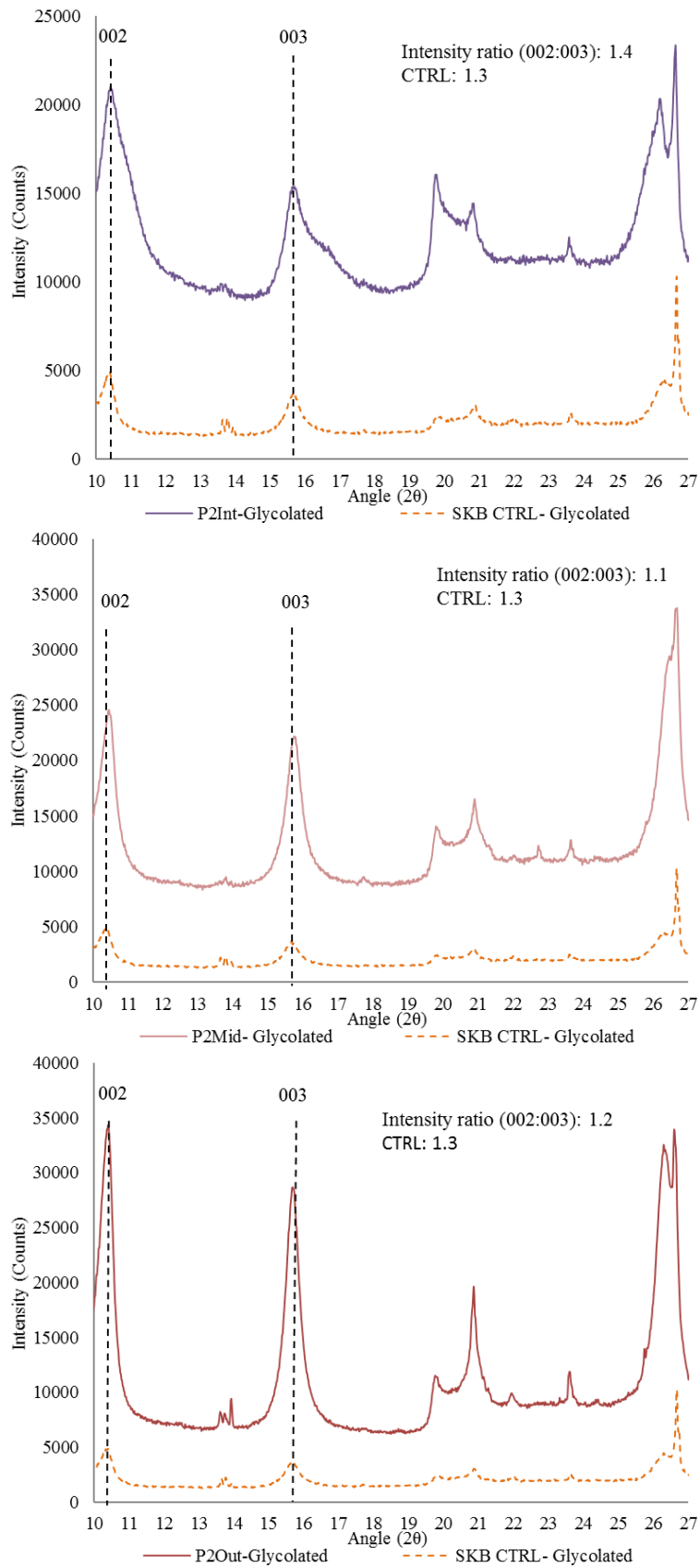


Figure 220: 002/003 peak intensity XRD patterns for phase 2 interface sub-samples

Figure 220 displays the 002/003 peaks for interface phase 2 sub-samples, similarly to phase 1 the intensity ratio is slightly higher at the interface with a gradual reduction in the

outer zones. The peak corresponding to a FeO(OH) phase is not as prominent in this phase, which corresponds to the low oxygen environment created within this interface phase. The FeOOH peak appears in the outer zones which are likely richer in oxygen.

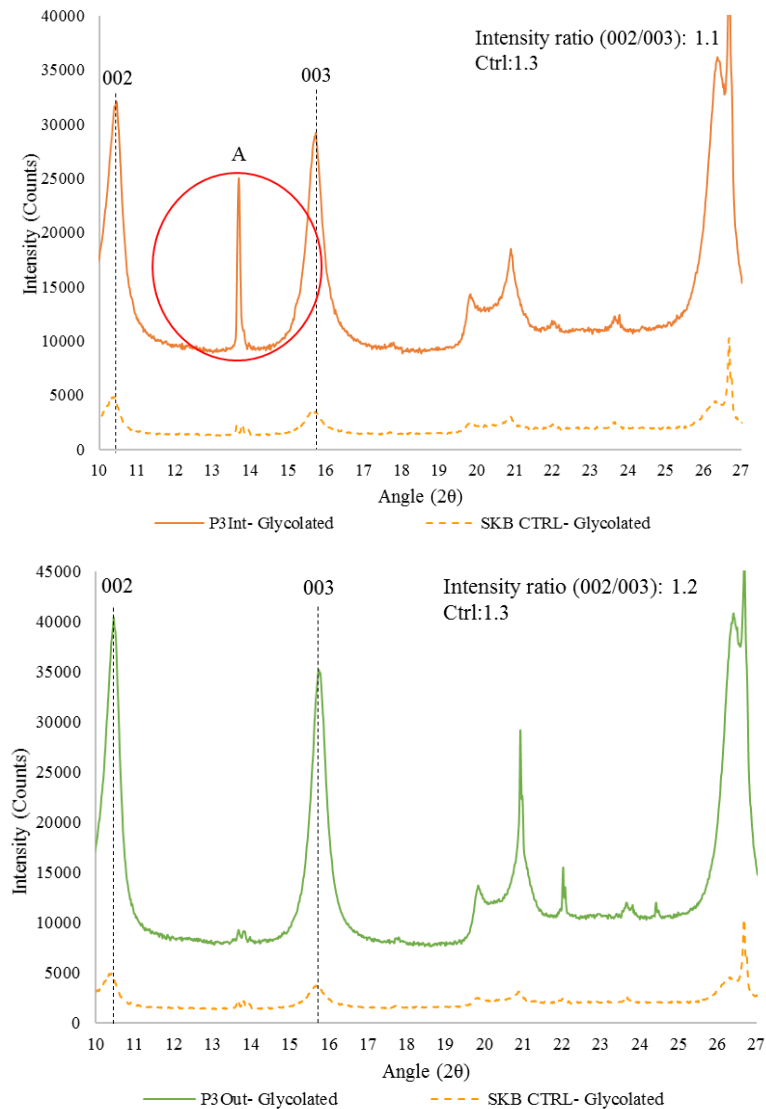


Figure 221: 002/003 peak intensity XRD patterns for phase 3 interface sub-samples

Finally, in the phase 3 interface 002/003 XRD patterns it is clear that there is very little electron back scattering from the octahedral sheet. What is noticeable is the sharp Goethite peak within the interface sub-sample which is also observed in phase 1 and 2 sub-samples. It is understandable that the FeOOH peak is present here due to the low temperature exposure within the interface system. Hence due to the low temperature, thermodynamic corrosion rates are much slower and therefore reducing conditions were not achieved resulting in a Fe^{3+} rich environment.

It is clear from figures 219, 220 and 221 that there is little Fe substitution within the bentonite across the respective interface replication phases. There is however a slight increase in the intensity ratio with increasing temperature and distance into the bentonite toward the coupon. Table 69 displays the compiled intensity ratios with the control measurement for comparison. The bentonite profile doesn't appear to change significantly from its initial Fe octahedral occupancy (as highlighted within the material classification section).

Table 69: Interface sub-sample 002/003 intensity ratios

Sample	003/004 Intensity ratio
Control	1.3
Phase 1 interface zone	1.4
Phase 1 middle zone	1.2
Phase 1 outer zone	1.2
Phase 2 interface zone	1.4
Phase 2 middle zone	1.1
Phase 2 outer zone	1.2
Phase 3 interface zone	1.1
Phase 3 outer zone	1.2

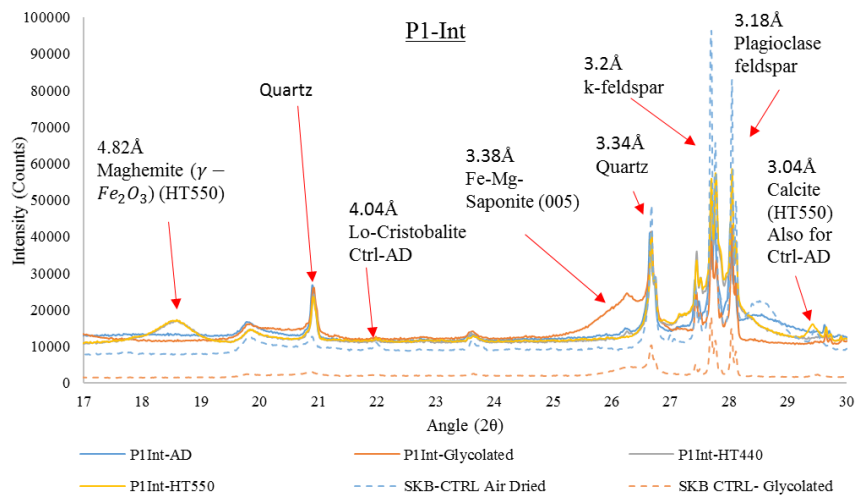
Evidently the time-scales implemented did not allow for suffice reaction/ cation structural substitution to occur to become significantly measurable. However it is clear that with time this reaction is probable. The profile still closely resembled that of the control and it appears that the clay is of a saponitic type, this may however be altered to Ferro-saponite at the interface due to the partial replacement of Magnesium for Iron.

The sharp peak indicating the presence of Goethite (FeOOH phase) within the interface zone is indicative of oxidation of Fe^{2+} minerals. The “green” bentonite indicates that some oxidation occurred either within the interface system due to incomplete oxygen consumption or upon sub-sampling/ XRD sample prep. This however confirms that the green clay observed and displayed in section 6.1 is likely due to the presence of Ferrous hydroxide $Fe(OH)_2$. Mossbauer results further confirm the presence of edge bound Fe^{2+} which have complexed to the OH^- site, additionally CEC results indicate layer charge alteration closer to the interface indicating the presence of the layered double hydroxide which is an anion exchanger i.e. lower CEC's within the interface zone.

6.3.2.3. XRD examination of non-clay mineral composition and corrosion products within the clay matrix:

Examination of the higher angles allowed characterisation of the accessory mineral composition for the respective interface sub-samples. Figures 222, 223 and 224 display the

higher angle XRD profiles for accessory mineral and corrosion product identification. Without higher 2θ angles i.e. within the $40\text{-}60^\circ(2\theta)$ range, it is only possible to use the lower intensity peak identification for the corrosion products. From inspection of figure 222, phase 1 sub-samples further indicate the swelling Fe-Mg-saponite due to the broad but sharper peak than the mid and outer zones. Also, ICP results indicate and support this premise in that Mg and Fe concentrations are higher at the interface with Fe concentrations reducing away from the coupon. Furthermore, phase 1 which did not include the progressive saturation, displayed the precipitation of calcite at the interface which is supported by literature Fernandez and Villar (2010). The high alkaline conditions at the interface can result in the formation of calcite. There is a slight reduction in the feldspar peaks closer to the interface. Maghemite peaks were picked up in all zones after heat treatment but more noticeably in the middle zone, this indicates that the corrosion product in the middle zone was Goethite (which was determined with the support of Mossbauer analysis), an Fe^{3+} rich iron mineral. However due to the black-greenish appearance at the interface and the development of Maghemite after heat treatment measured via XRD, it can be inferred that the presence of ferrous hydroxide and goethite (see Mossbauer for supporting evidence) was present on the bentonite/ steel surface and within the bentonite near the interface.



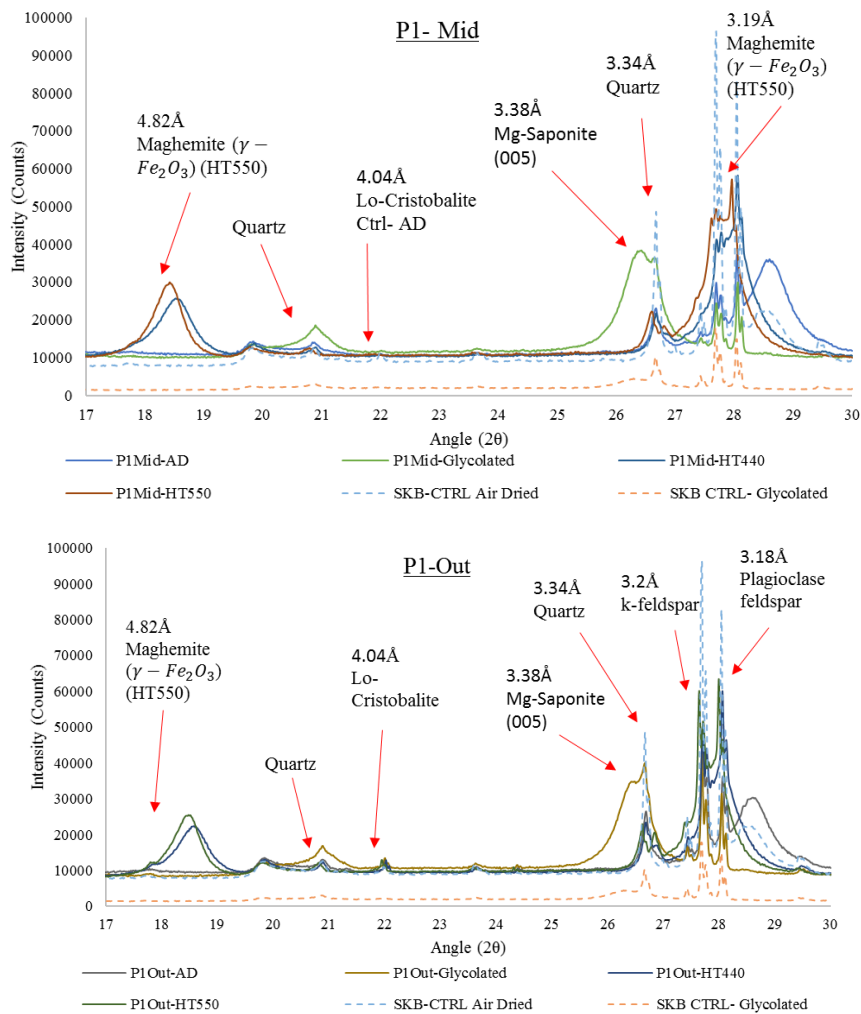
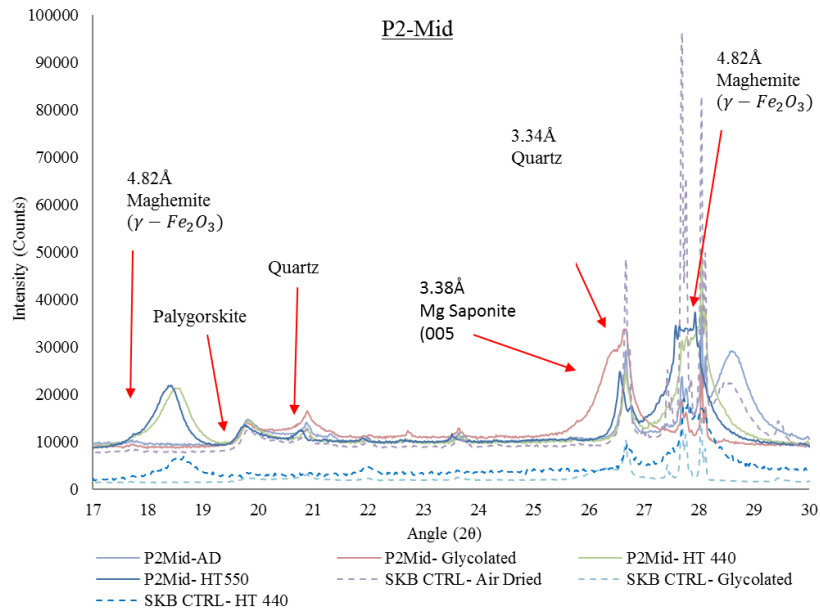
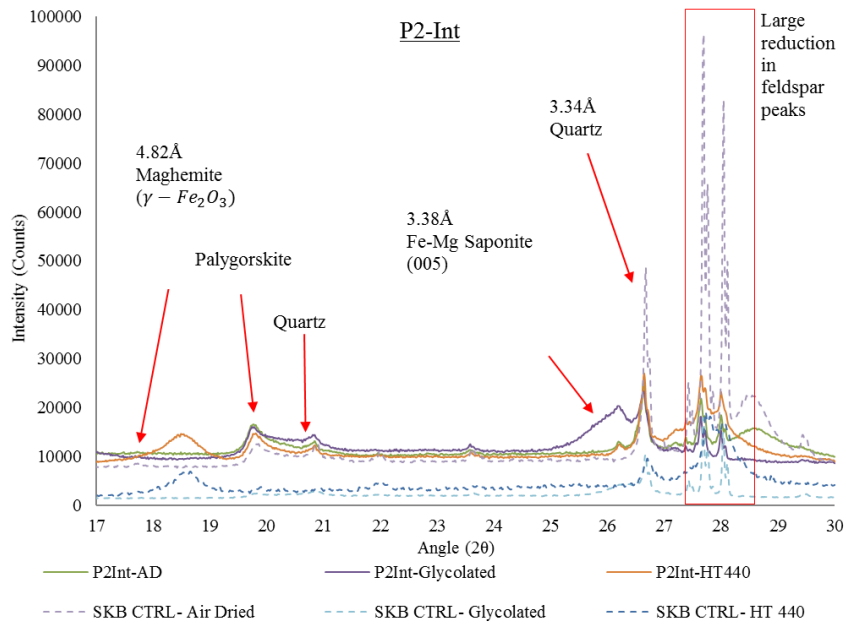


Figure 222: Higher angle peak profile for phase 1 interface sub-samples

Figure 223, displays the accessory mineral and corrosion product profile for phase 2 sub-samples. What is most predominant from this phase is the large alteration of the feldspar and quartz peaks. These progressively reduce with distance from the outer zone toward the coupon interface. High dissolution rates are indicative of this effect due to the hydrostatic flow through the bentonite as well as high temperatures and highly alkaline conditions. A similar premise can be obtained for the phase 1 interface profile for the corrosion products and Fe integration. But penetration depths and the extent of poorly developed crystalline products was greater in this phase due to the influence of a high saline solution gradient and temperature. What's more, at the interface with the sodium rich groundwater influx, an intense peak is indicative of the sodium endmember feldspar, albite. This indicates that the influx of salt solution “washes” ions from the bentonite matrix during dissolution. During this process the sodium is replaced which forms the sodium rich endmember of the feldspar type.



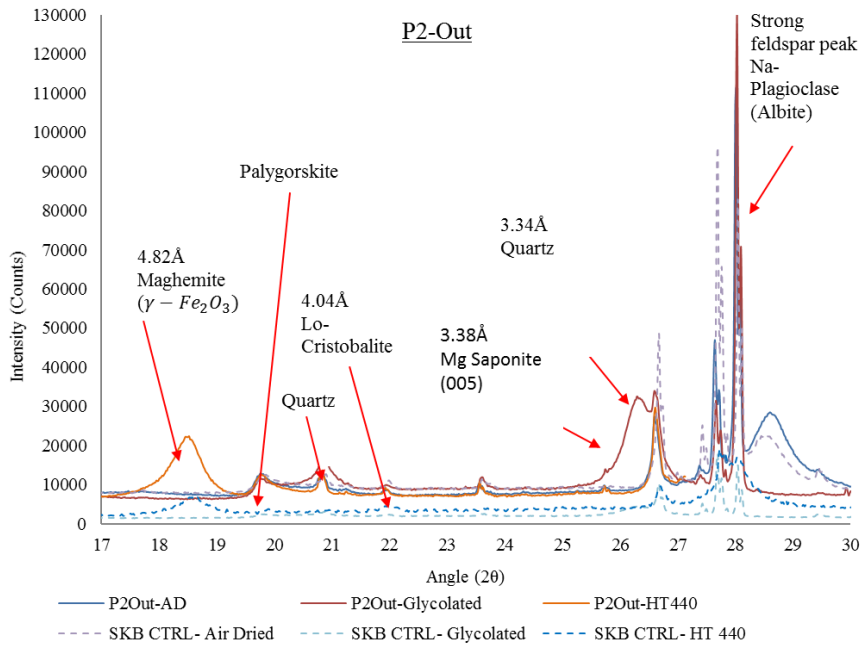
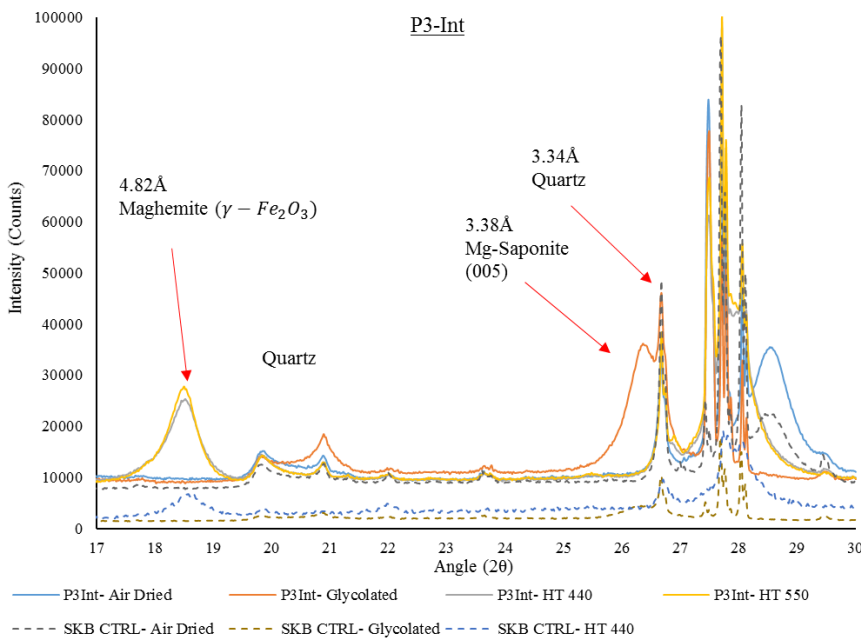


Figure 223: Higher angle peak profile for phase 2 interface sub-samples

Figure 224 shows the corrosion and mineral profile for phase 3 which was the coolest phase explored in the interface tests. The corrosion products in this phase display only maghemite indicating that goethite was the predominant corrosion phase due to the low temperatures during oxidation. The low temperature did not promote the reducing conditions as observed in phases 1 and 2 over the time-scale of the interface testing. Furthermore, Mg-saponite remained the predominant smectite phase over the entire sample profile with no observable dissolution of the accessory minerals.



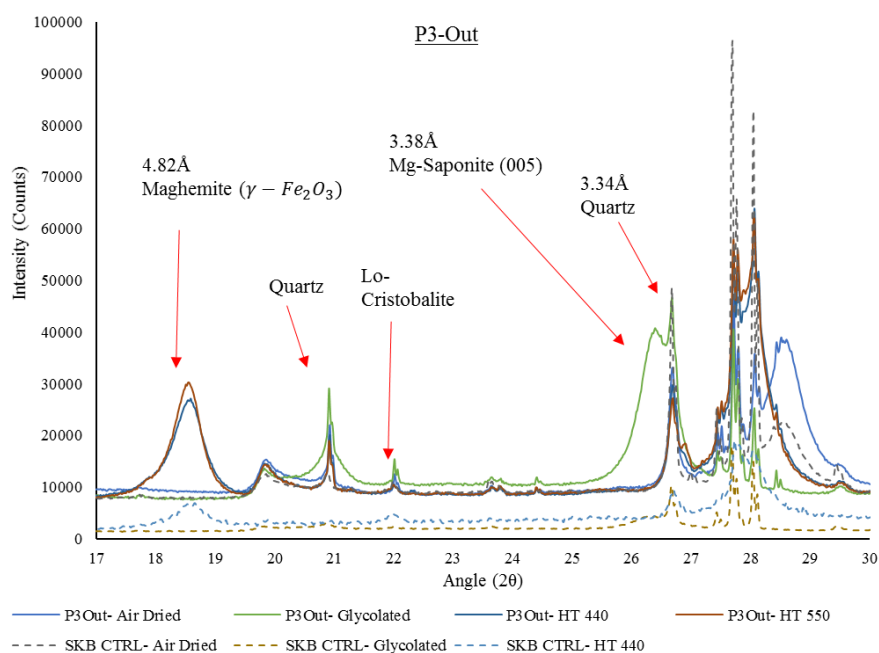


Figure 224: Higher angle peak profile for phase 3 interface sub-samples

Given the results from the XRD measurements, it is clear that the predominant saponitic smectite phase remains after the THC exposure over the explored time-scales. An Fe^{2+} -rich environment developed after the two highest thermal exposure phases with and without a hydraulic gradient. Thus, indicating that elevated temperatures accelerate the oxidation process and hastening the development of reducing conditions. Therefore, XRD profiles show that there is some partial replacement of Mg for Fe within the bentonite close to the steel coupon thus forming Ferrosaponite and Illite interstratification. With Mg-saponite and randomly interstratified Illite remaining predominant over the remaining mid and outer sub-sampled zones. Dissolution rates appear to be dependent on the thermal exposure and the ingress of water toward the interface as well as the extent to which corrosion products integrate into the bentonite. The complexing of Fe^{2+} at OH^- edge sites near the interface coupon, result in the formation of Ferrous hydroxides, a double layered hydroxide (LDH) which will impact the layer charge and overall cation retention capacity. Results from previous literature and computational models, indicates the development of LDH and the transformation to Nontronite as well as layer dissociation causing some 1:1 mineral development Pusch et al (1993), Manceau et al (2000a), Ruck & Cathelineu (2004), Charpentiera et al (2006), Schmitz et al (2007), Gullaume et al (2003), Milodowski (2009), Pusch et al (2010), Villar and Gomez (2010), Xiaodong et al (2011) and Shariatmadari et al (2011). From the results obtained via XRD and supported by the other physicochemical data, ferrosaponite and the iron minerals within the bentonite matrix are precursors to the development of more Fe rich clays given longer time-scales.

6.3.3. SEM analysis:

Scanning electron microscopic measurements have been conducted on the C-steel coupon surface as well as the bentonite sub-samples. This enabled a semi-quantitative analysis of the abundance of elements present as well as a topographical imaging of the particle surfaces.

6.3.3.1. SEM analysis on the C-Steel interface surface:

Analysis conducted on the carbon steel surface allowed preliminary insight into the interface replication impact on the steel and the corrosion/ clay remnants. Below in figure 225 displays.

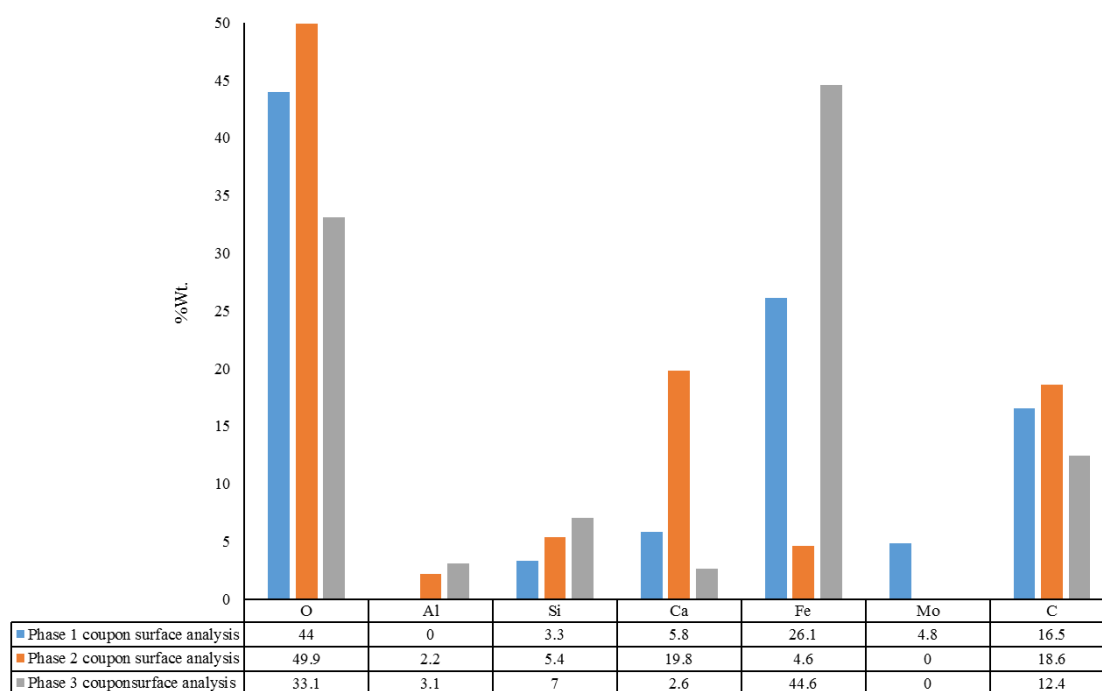


Figure 225: Coupon surface EDX elemental measurements compiled for all phases

From the EDX analysis conducted on the respective interface coupon surfaces, the elemental composition indicates a high concentration of oxides i.e. given the high proportion of oxygen and Fe. Aluminium, Silicon, Oxygen and Calcium is also detected due to residual clay and non-clay minerals left on the surface after post-mortem sub-sampling. The higher concentration of Al, Si, O and Ca for the phase 2 analysis is supported by figure 229 which displays MX-80 on the coupon surface. Additionally, the small proportion of molybdenum and carbon which are compositional elements of the steel coupon was picked up in the background measurements. Furthermore, it appears that magnetite formed over the surface with what appears to be some siderite crystal formation which also supports the element measurements and SEM observations, figures 226-230. Figure 230 (a) also displays stress

corrosion cracking (SCC) on the coupon surface. It is however difficult to determine if this was formed before or after interface testing. It may be that the steel, which experienced elevated temperatures, induced surface cracking during machine preparation for the interface cells. However, the observed cracking correlates to highest thermal exposure phase which relates to the higher corrosion rates. Comparison to the surface of the lowest phase coupon indicates no surface cracking, figure 230 (b). Also, it is supported that a highly alkaline and chloride rich environment will accelerate SCC. The Fe %Wt. is measured lower on the interface phase 2 analyses resulting in approximately 5%Wt, this correlates the surface deposit of bentonite rather than the magnetite/ oxide surface exposed on the other interface coupons. This corresponds to the %Wt. measurements for Fe on the MX-80 sub-samples given in section 6.3.3.2. This measurement is slightly higher than the control measurement, thus indicating some Fe integration.

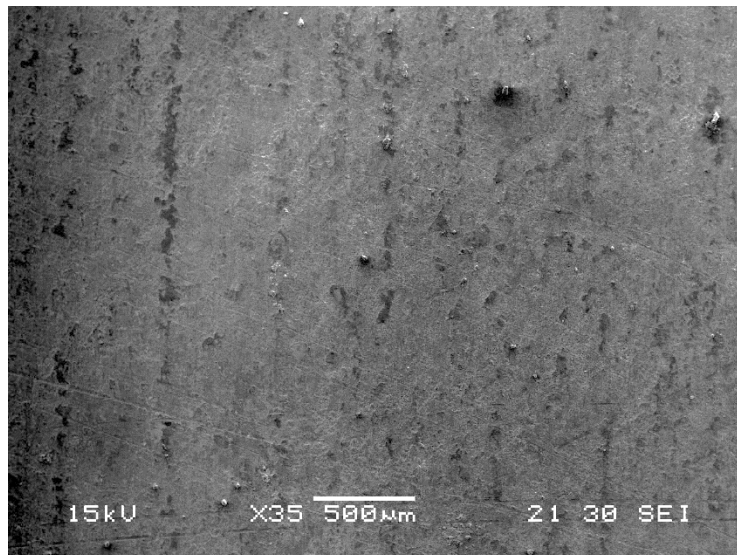


Figure 226: Magnetite on the surface of the interface phase 1 coupon (Black sections)

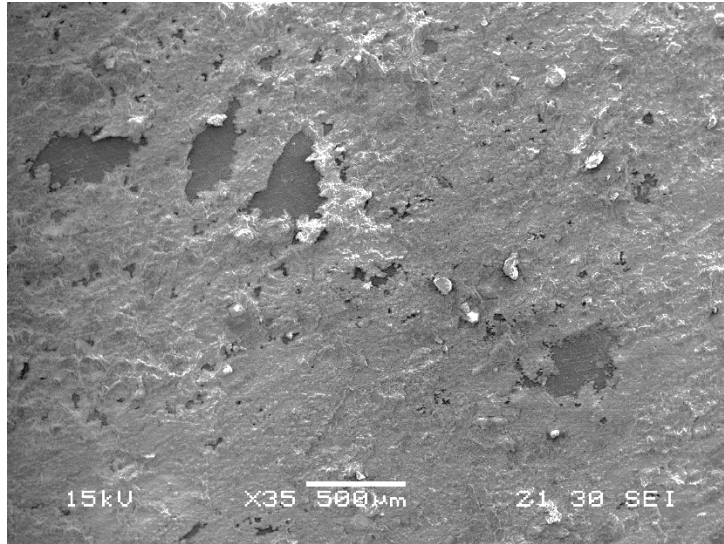


Figure 227: Magnetite on the surface of the interface phase 2 coupon (Black sections), lighter sections displaying Fe oxides

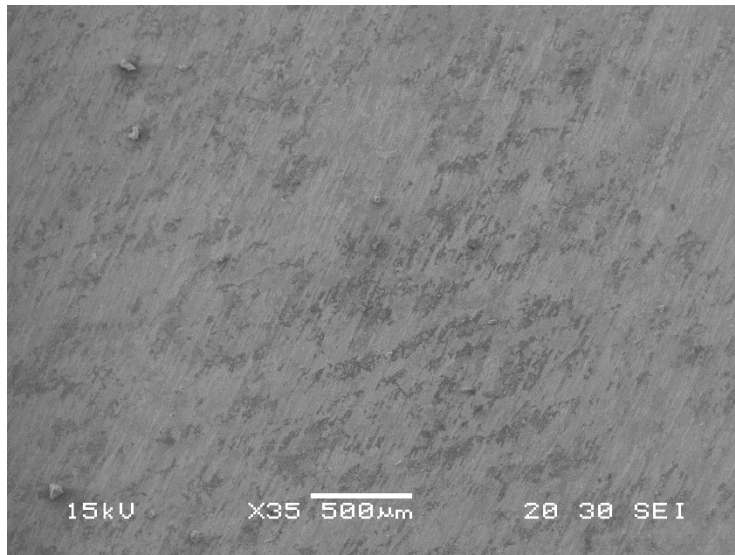


Figure 228: Magnetite on the surface of the interface phase 3 coupon (Black sections)

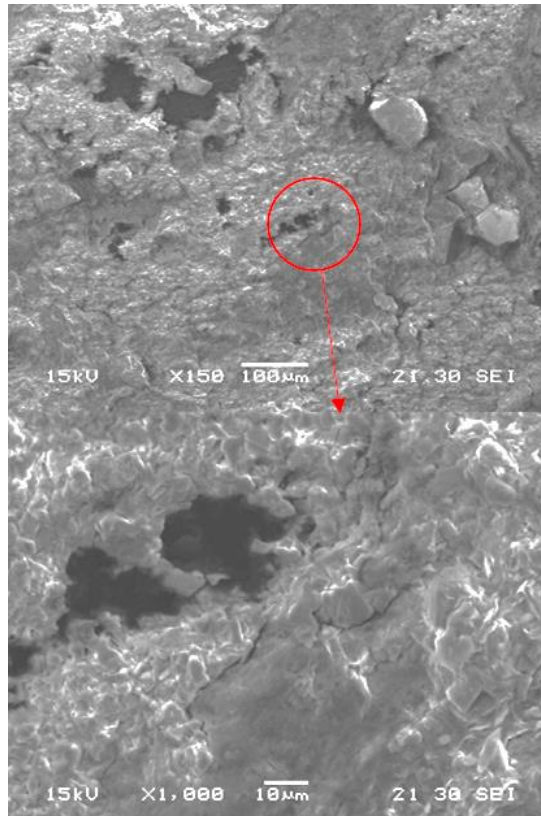


Figure 229: SEM image of the coupon surface taken from the phase 2 interface experiment showing bentonite with oxides

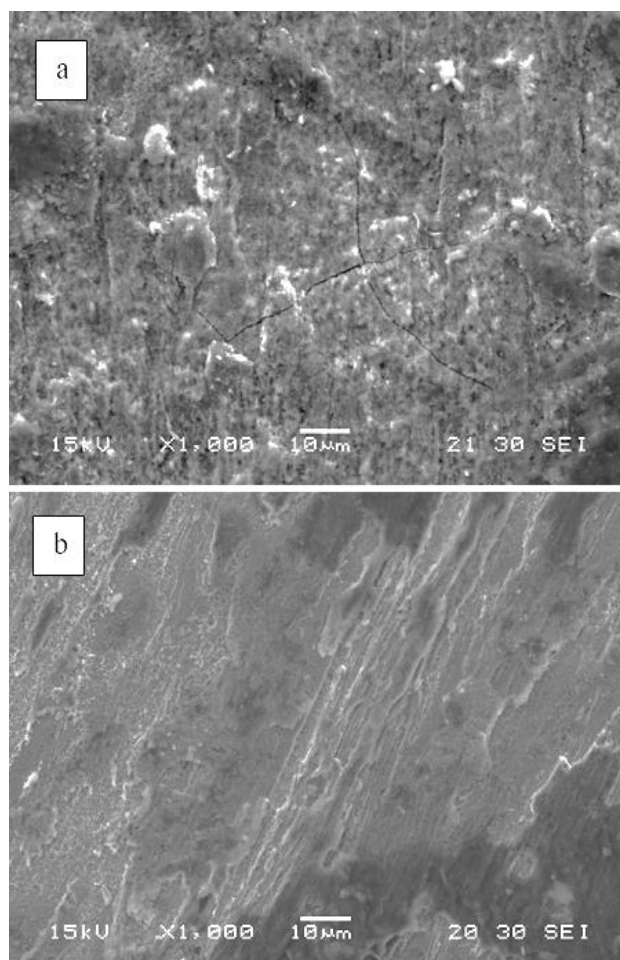


Figure 230: a) Phase 1 interface coupon displaying stress corrosion cracks and b) Phase 3 interface coupon surface lowest thermal exposure

6.3.3.2. SEM analysis on the MX-80 sub-samples:

Below in figures 231, 232 and 233 display the compiled SEM-EDX elemental composition data for the respective interface sub-samples. The elemental profile appears to support the mineral evolution measured in the XRD patterns. All phases indicate that sodium concentrations increase with distance from the interface which indicates that there is partial replacement due to Fe within the exchanger. Aluminium and magnesium also slightly reduces near the interface which supports the XRD examination of 002/003 intensities indicating some Fe substitution within the octahedral layer. Calcium is also higher in the corrosion zone which supports the hypothesis that calcite will form after cooling within the interface zone due to the higher PH conditions (Fernandez and Villar, 2010), as observed also in XRD and ICP analysis. Furthermore, the concentration of sodium is higher in the outer zones of phases 2 and 3, this is understandable as these phases included the saline solution inflow from the outer zone into the bentonite. This also supports the preservation/ development of the sodium rich end-member feldspar (Albite). Potassium and sulphur concentrations appear lower in the

high hydrothermal experiment (phase 2), indicating that there is more mineral dissolution in the non-static fluid flow and high thermal conditions, also supported in the XRD analysis.

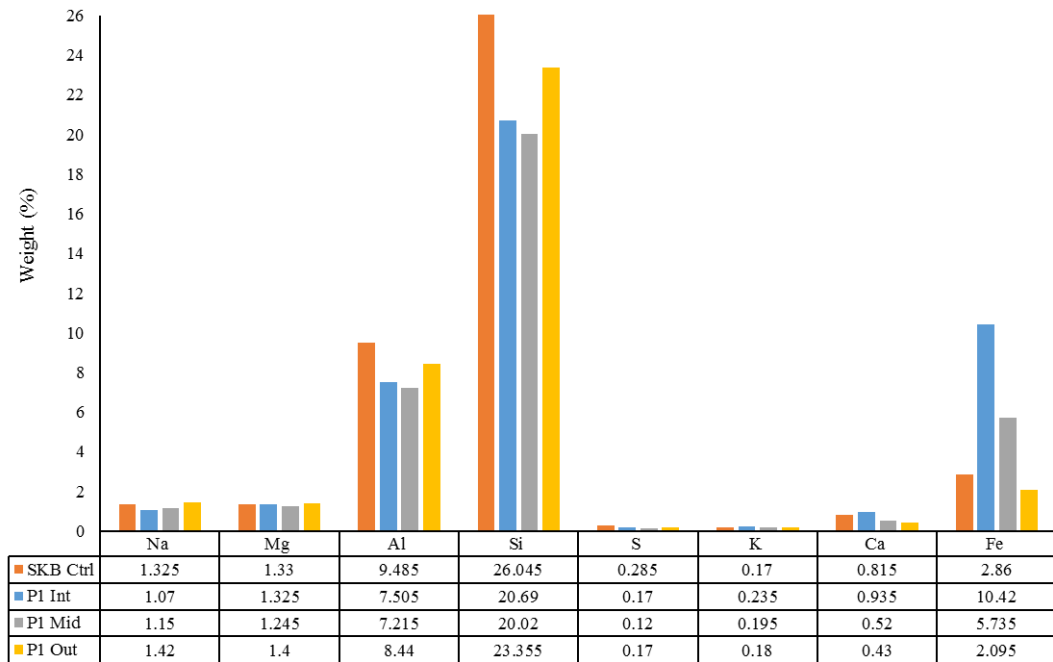


Figure 231: EDX analysis on interface phase 1 sub-samples

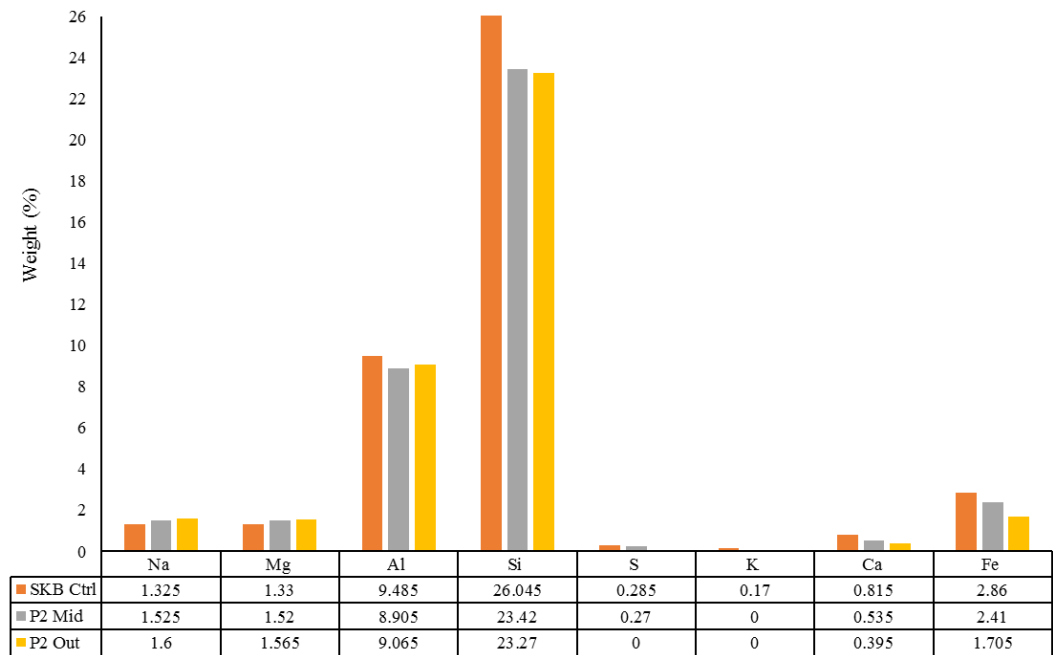


Figure 232: EDX analysis of phase 2 interface sub-sample

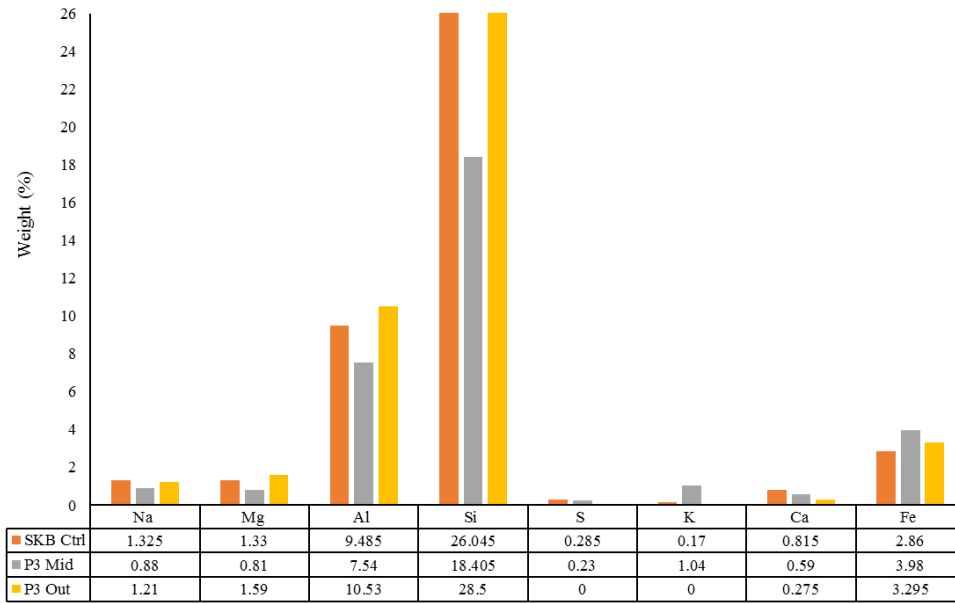


Figure 233: EDX analysis on phase 3 interface sub-samples

6.3.4. UV-Vis spectrophotometric analysis:

Displayed in this section is the Fe speciation measurements conducted via the adsorption of (512nm) UV radiation on the clay samples in a digested and reduced / non-reduced state. This method enabled to calculation of the abundance of Fe as well as the species of Fe present within each sub-sampled zone for each respective interface phase. Figure 234 and 235 gives the concentration profiles of Fe^{3+} and Fe^{2+} respectively.

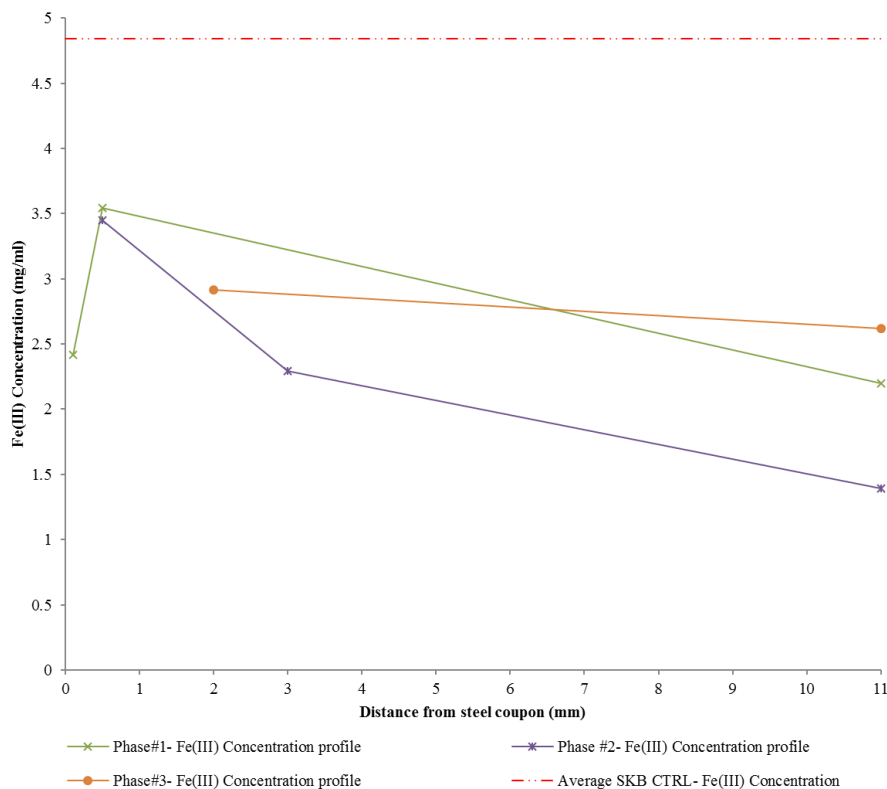


Figure 234: Fe(III) concentration profile

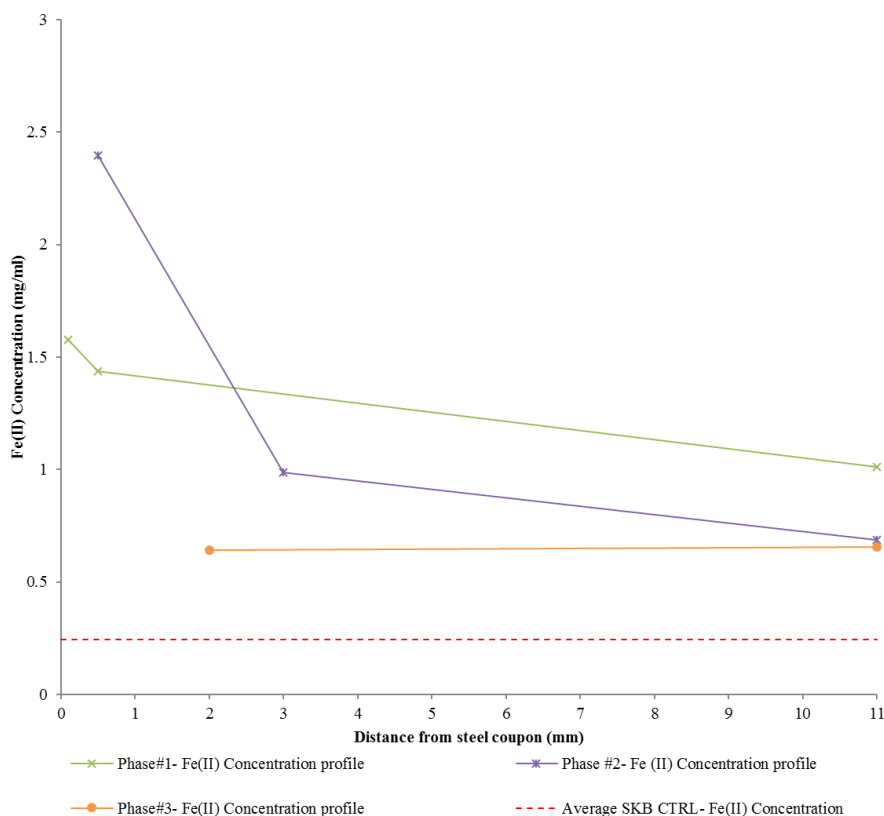


Figure 235: Fe(II) concentration profile

The UV-VIS results indicate a trend in the gradual reduction of Fe concentration from the interface to the outer zones for phases 1 & 2. Whereas phase 3 displays an overall increase in Fe^{2+} but is much more uniform throughout the sample. Generally, the higher temperature phases display an increased Fe^{2+} concentration profile, which indicates that the conditions within the interface zone were reducing. The presence of the hydraulic gradient in phase two appears to have an impact on the concentration of Fe(II). The corrosion is accelerated due to the high temperature and saline solution causing an increase in diffusion rates. This is also observed within the direct spatial measurements during post-mortem subsampling as well as the ICP results for total iron analysis, displayed in section 6.3.5. There is a general increase in the amount of Fe(II) present within the samples with an overall reduction in the amount of Fe(III) compared to the average control concentration. This indicates that there is reduction occurring corresponding to the development of Fe(II) rich phases, which is also supported by XRD data in section 6.3.2.

6.3.5. ICP elemental analysis:

ICP was conducted on the clay samples, post digestion. Table 70 displays the list of measured elements.

Table 70: List of measured elements conducted via ICP analysis

Elements
Al
Ca
Fe
K
Mg
Na
Si

Figures 236-242 display the elemental concentration profiles for the sub-sampled zones for each interface phase respectively.

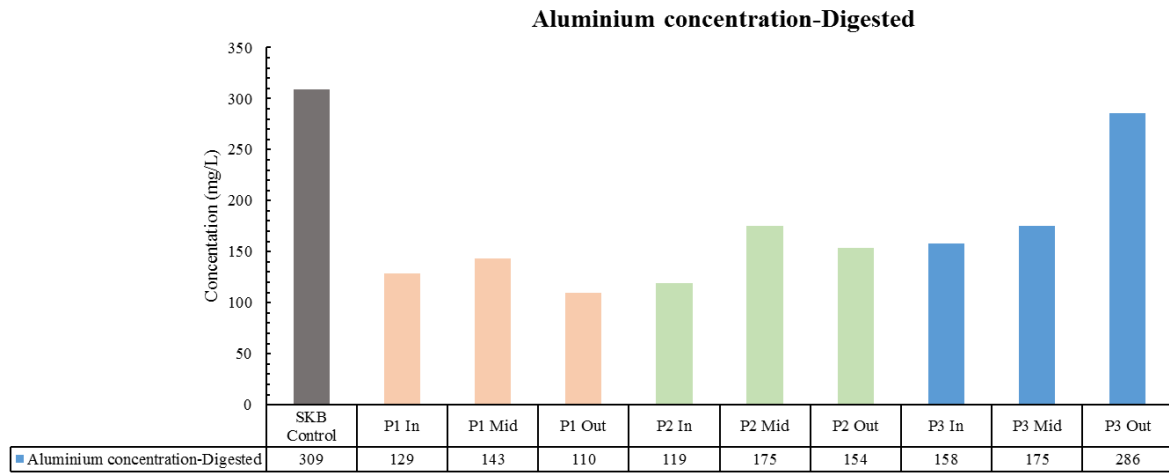


Figure 236: Compiled ICP results measuring Aluminium concentration for each interface sub-sample and phase respectively

As can be seen, the higher temperature phases display a reduced aluminium concentration across the bentonite profile. This could be due to the partial replacement of Al for Fe within the octahedral layer, as observed in section 6.3.2 for XRD 002/003 intensity measurements. Interestingly, the outermost sub-sample for phase three has an increased concentration, which is anomalous to the rest of the data. This sub-sample also experienced the least thermal loading intensity and therefore reaction kinetics would be slower than the other phases. For this reason, this elevated measurement is likely a systematic anomaly.

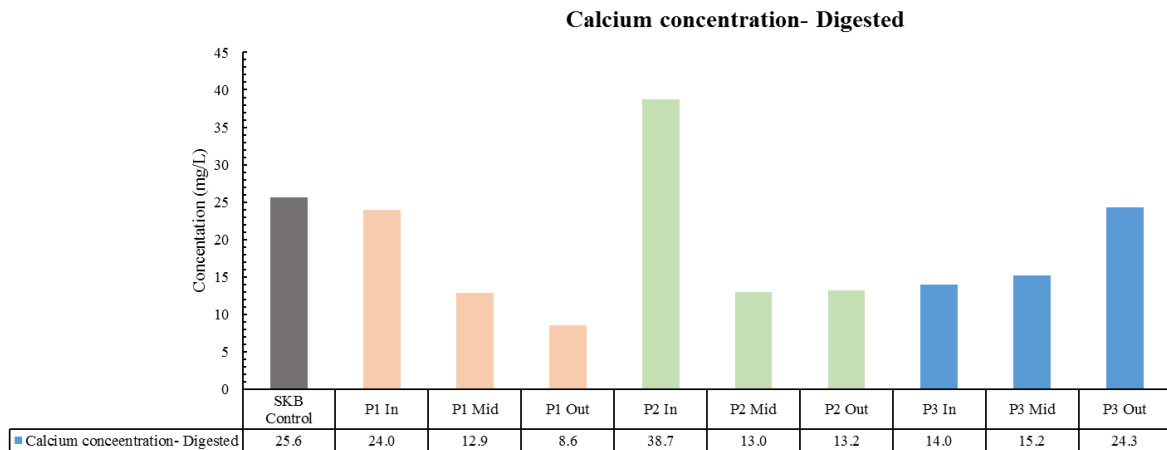


Figure 237: Compiled ICP results measuring Calcium concentration for each interface sub-sample and phase respectively

The calcium concentration appears to increase within the interface zone for the higher temperature phases, this correlates to XRD supporting the precipitation of calcite upon cooling within this zone due to the higher alkaline environment. The prominence isn't as excessive for interface phase 3, which were also the lowest thermal exposed experimental conditions. The elevated concentration of Ca near the interface is also observed by Pusch et al (2010), Fernandez and Villar (2010). The dissolution of calcite in the outer zone and precipitation within the inner zones also explains the lower CEC values measured at the interface.

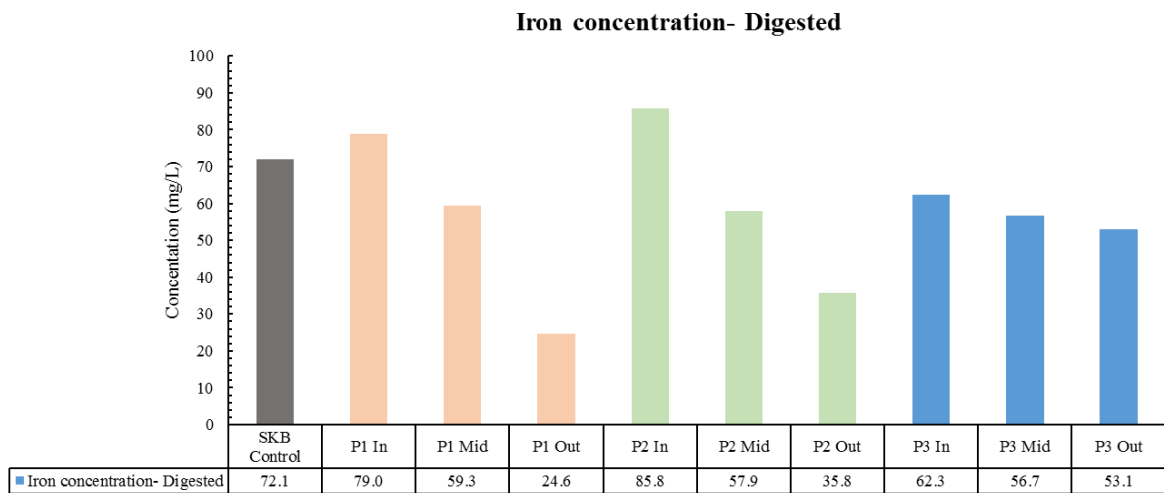


Figure 238: Compiled ICP results measuring Iron concentration for each interface sub-sample and phase respectively

The concentration profile of iron (Figure 238) in all interface phases correspond to observations made during post-mortem sub-sampling, UV-Vis, SEM, XRD and Mossbauer i.e. high concentrations at the interface and reducing with distance from the C-Steel. The two highest thermal phases 1 and 2, display the highest Fe concentrations in the interface zones as well as a gradual reduction of Fe with distance from the corrosion source. However, the

second phase shows a slightly higher concentration than phase 1 which implemented the highest thermal loading. This correlates to the UV-VIS measurements for Fe^{2+} concentration for the interface sub-sample when comparing phases 1 and 2. The measurements also made during the post-mortem sub-sampling correlate to these observations, the extent to which the “green” layer transpired into the bentonite was greater for phase 2 than phase 1. It was concluded that the introduction of a hydraulic gradient with a saline solution increases the diffusion rates at the interface. Furthermore, the reduction of Fe at the outermost zone corresponds to the concentration profiles of Aluminium (Figure 236) and Magnesium (Figure 240), it appears that Fe replacement within the octahedral layer displaces any Mg or Al which diffuses away from the interface and therefore increasing in concentration within the outer zones either by filling vacant sites or staying in solution. Additionally, the overall concentration profile of Fe within phase 3 sub-samples was much lower than the higher temperature phases.

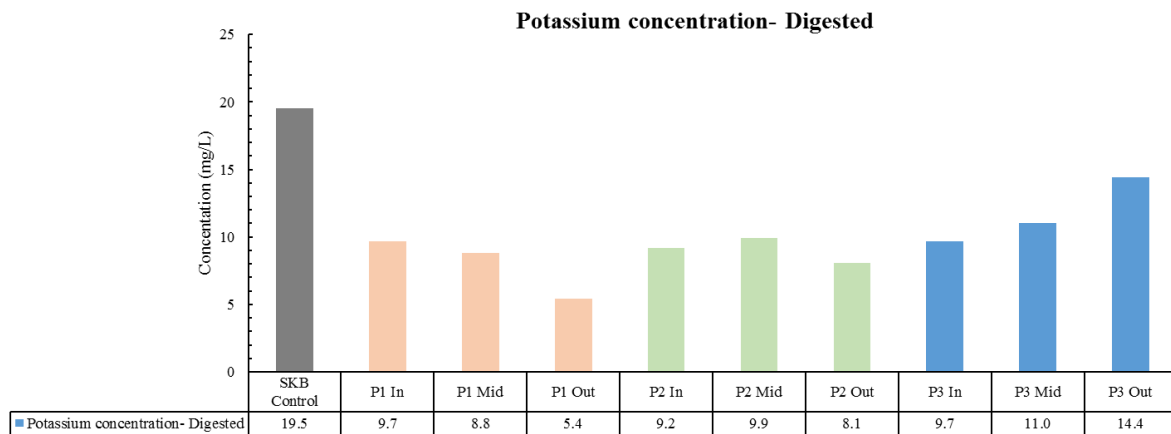


Figure 239: Compiled ICP results measuring Potassium concentration for each interface sub-sample and phase respectively

Again, the concentration profile of potassium (Figure 239) present within the solutions indicates that there is more dissolution occurring at the interface. XRD also supports this by observation of the peaks for the non-clay mineral patterns. XRD analysis indicates dissolution of feldspars in the corrosion rich/ higher temperature phases.

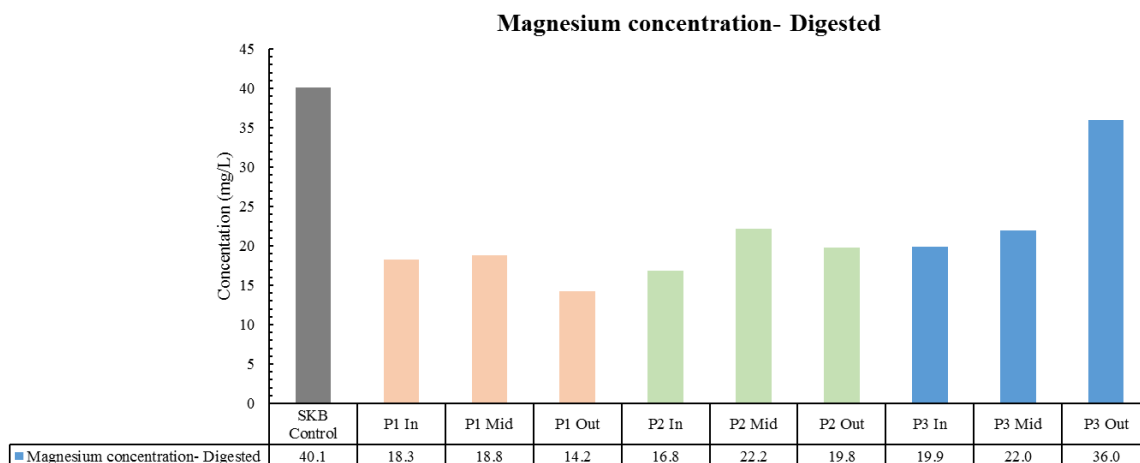


Figure 240: Compiled ICP results measuring Magnesium concentration for each interface sub-sample and phase respectively

As stated previously, it appears that the magnesium profile follows a similar trend to that of the aluminium profile (Figure 240). Similarly, analogous to the aluminium data, the concentration measurements are lower in the higher temperature phases which also indicate that dissolution of accessory minerals is very likely.

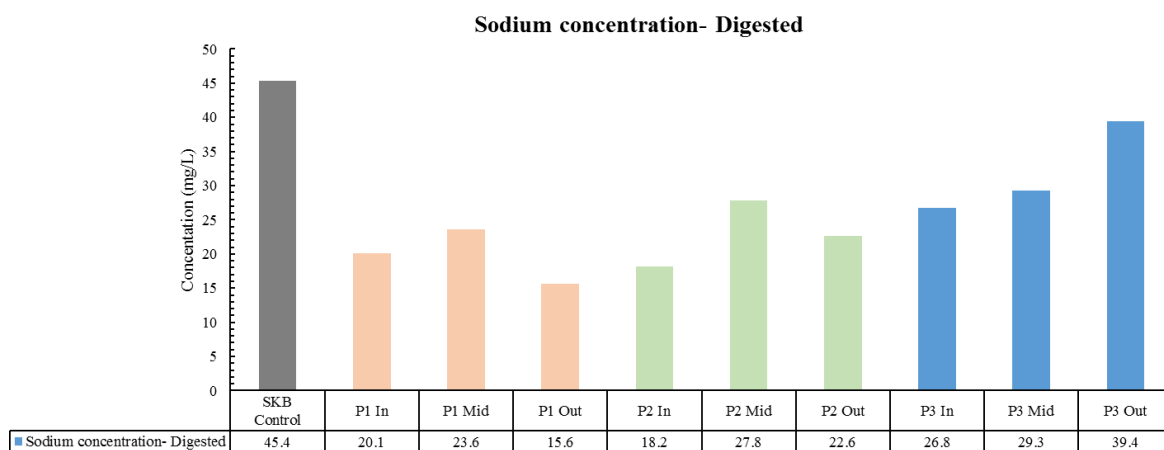


Figure 241: Compiled ICP results measuring Sodium concentration for each interface sub-sample and phase respectively

The sodium concentration measurements (Figure 241) are important to understand the dominant interlayer occupancy. The bentonite used within this study is a sodium-rich type smectite which has been conditioned to have an almost homoionic interlayer composition. Therefore, from figure 241 it is clear that the concentration of Na is reduced at the interface which can be correlated to the interlayer replacement by higher valence cations, namely Fe^{2+} and Fe^{3+} becoming dominant within the interface zones and Mg^{2+} and Al^{3+} in the outer zones. This reduction in concentration increases with thermal exposure, which suggests that the interlayer exchange rate is accelerated with temperature. The increase in interlayer exchange rate with higher valence cations at higher temperatures is also observed in XRD patterns within the batch test results (section 5).

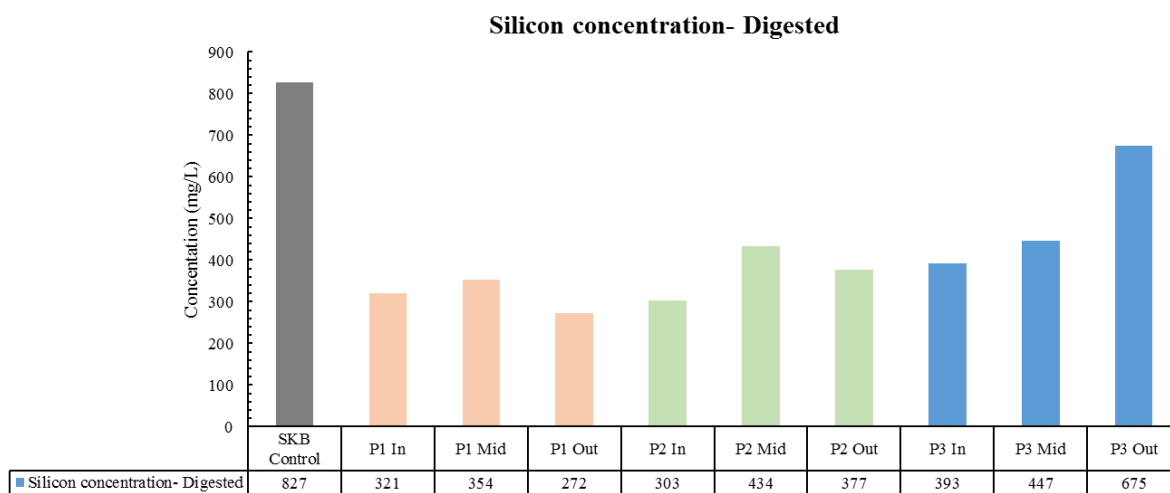


Figure 242: Compiled ICP results measuring Silicon concentration for each interface sub-sample and phase respectively

Silicon concentrations are significantly higher in the control compared to all of the interface phases presented. The silicon measurements presented in figure 242 is the total concentration and therefore it is difficult to differentiate between siliceous minerals and phyllosilicates. What can be said is that the overall trend in reduced concentrations is expected to be due to dissolution rates being higher within the higher temperature phases. Generally, with support from XRD data, the silicon content is greater in the mid/ outer zones which also points toward the precipitation of siliceous compounds away from the heated/ corrosion rich zone. This also indicates that this supports the likely “stiffening” effects as seen in constant volume tests (section 7) and literature Guillaume et al (2010); Gomez and Villar (2010); Xiaodong et al (2011); Pusch et al (2014); Leupin et al (2014).

6.3.6. Mossbauer analysis:

Mossbauer analysis has been carried out on the unaltered bentonite as well as the mid-life phase sub-samples only. Project time constraints have resulted in limited data collection due to the length of time required for complete thermal profiling. Therefore, the most interesting phase was chosen, which was the phase 2 sub-samples i.e. the “green” layered sample. Mossbauer analysis allowed the location of Fe, speciation and type of corrosion that was present within the bentonite matrix by examining the hyperfine parameters. Bergaya et al (2006) states that it is easier with Mossbauer to determine Fe location of the general phases than to determine the exact location of Fe sites, therefore the analysis will examine the quadrupole split as well as the isometric shift to determine the type and presence of Fe.

Tabulated below in table 71, is the hyperfine parameters obtained from the Mossbauer spectra at 4K, only the 4 Kelvin results are displayed here as Fe phases are considered to become magnetically ordered at this temperature allowing differentiation between Fe location

sites. Furthermore, the hyperfine field parameters indicate no superparamagnetic components therefore simplifying the analysis.

Table 71: Mossbauer hyperfine parameters at 4K for phase 2 interface sub-samples

Sample	%Fe(ii)	%Fe (iii)	% Magnetically ordered Fe (iii)	Quadrupole split (mm/s) (Fe(iii))	Quadrupole split (mm/s) (Fe(ii))	Isomer shift (Fe(ii)) (mm/s)	Isomer shift (Fe(iii)) (mm/s)	Sextet Quadrupole split (mm/s)	Hyperfine field interaction (Tesla)
Control	17	83	17	1.01	3.03 (2.87 at 293K)	1.23	0.41	Collapsed	52.9
P2 Int	27	73	41	1.14	3 (2.72 at 293K)	1.24	0.52	-0.02	45.4
P2 Mid	15	85	40	1	2.97 (3.37 at 293K)	1.31	0.42	-0.07	49.7
P2 Out	28	72	32	1.37	3.04 (2.76 at 293K)	1.27	0.46	0.05	51.3

Bergaya et al (2006) states that Fe rich smectite such as nontronite displays a relatively small quadrupole split around ~0.4mm/s. Looking at the hyperfine parameters within table 71 and based on Bergaya et al (2006) statement, the material does not appear to have altered to a Fe rich clay as the quadrupole split is higher than that of Fe clays. Furthermore, the presence of a sextet for all sub-sample phases indicate the presence of Fe (hydr)oxides within the sample. This is further supported by the percentage of magnetically ordered Fe^{3+} there is an overall significant increase in the abundance of magnetically ordered Fe which reduces with increasing distant from the interface. This indicates that the interface and mid sub-sample are rich in (hydr)oxides within the bentonite matrix. XRD also indicates that a FeOOH metastable phase is present. Inspection of the quadrupole split at room temperature (293K) indicate that Fe^{2+} is located within the interlayer exchanger (basal) for the mid- zone sub-sample. The interface sub-sample displays a slightly higher abundance of structurally bound Fe^{2+} and a lower quadrupole split (nearer to 2.54mm/s) indicating that the immediate zone near the coupon has Fe^{2+} substitution in the octahedral sheet and edge sorped Fe^{2+} . Fitting of the hyperfine parameters in the interface and mid-zone sub-samples closely relate to Goethite. Also, Maghemite is observed in heated XRD interface and mid zone sub-samples which also support the alteration of phases upon oxidation. Overall the percentage concentrations of Fe^{2+}/ Fe^{3+} correspond to the measurements made via ICP and UV spectrophotometry.

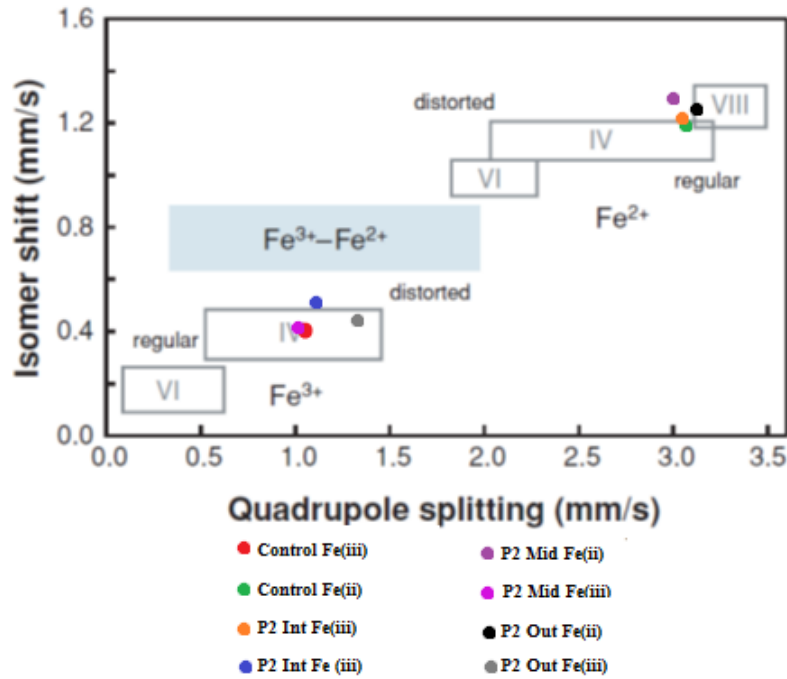


Figure 243: Hyperfine parameter field identification of Fe speciation (After Dyar et al 2006)

Figure 243 displays the fitted hyperfine field parameters given in table 70, onto a Fe speciation and phase identification plot derived by Dyar et al (2006). What is seen, is that Fe^{3+} and Fe^{2+} phases for the phase 2 sub-samples are poorly ordered with low crystallinity, this is also displayed by the broad peaks in the XRD patterns. Comparably the control parameters fit into the regular fields for both Fe species. Therefore, it is clear that mid-life conditions cause large disordering within the composition of the crystallite structure, most likely due to the rapid formation of oxides and dissolution/ precipitation of the secondary minerals under the rapid thermal loading/ cooling cycle. Furthermore, looking at the hyperfine field interaction parameter, all phases do not deviate significantly above 50 Tesla. This indicates that there are no superparamagnetic components in the clay matrix, this would add to the complexity of oxide phase identification. Given the results from the heat treated XRD patterns for phase 2 and using the hyperfine field interaction parameter, the interface sub-sample displays a measurement close to that of Goethite (using identification methods in Dyar et al, 2006).

6.4. Conclusion:

Interface tests were conducted for three inferred near-field conditions representative of the EBS. However, the experimental conditions were time constrained. The longest possible time for interface exposure for the respective phases was 4 months. This was due to project time restraints. Therefore, the results presented here are only short-term interactions and display possible precursors to further mineral developments over longer time-scales.

Additionally, the interface tests used NaCl as the chosen saline solution which further simplified the testing conditions. More complex and realistic groundwater interactions were briefly explored within the batch testing (presented in section 5) and the constant volume testing (presented in section 7). However, more realistic conditions are still open for examination under longer time-scales, but that's not to say that the results presented here are not representative of the interface conditions as the correlation between other studies can be made. Thus, allowing the observed alterations made in this study to be linked to observations made in long-term tests, geochemical simulations and studies on natural analogues.

Post hydro-thermo-chemical analysis indicated that the magnitude of corrosion diffusion increased with increasing temperature. Furthermore, tests that implemented the mid-phase temperatures with percolating saline solution indicated higher diffusion rates. The hydraulic gradient was implemented toward the coupon interface, realistic of insitu conditions, the diffusion of the corrosion products occurred opposite to the direction of flow. Therefore, the impact of high temperature and high saline pore solution appears to accelerate the rate of diffusion that is independent of the bulk flow conditions. Direct observation of the coupon surface post THC exposure indicated a black layer covering the steel, this is characteristic of magnetite (Fe_3O_4). Magnetite appears to form over the steel surface with the diffusive front of Fe ions occurring into the bentonite. This indicates that contact between the bentonite and steel causes progressive corrosion diffusion to occur with the normally passive magnetite layer losing effectiveness; this phenomenon was also observed by Sawicki et al (1995), Wilson et al (2010) and Kumpulaninen et al (2010). Wilson et al (2010) states that the bentonite could act as a “pump” for corrosion products which inhibits the development of partial passivation by magnetite formation, this appears to be the case within the studied interface experiments. Over the 4-month period the higher temperature phases indicated that immediate layer of bentonite turned green which indicated that this was rich in Fe^{2+} . The extent to which the green sample integrated into the sample was greater in the mid-phase conditions, supporting the diffusion rate increase with thermo-saline conditions present. The sub-sampled “green” bentonite did not appear to oxidise upon exposure to atmospheric conditions, the oxidation study indicated no colour alteration after 72 hours. The sample was further exposed to moisture for an additional 72 hours which appeared to induce oxidation, this indicates that the green rust and structurally bound Fe^{2+} is in a metastable state also supported by Wilson et al (2010) and Kumpulaninen et al (2010).

With respect to the physical geomechanical properties of the bentonite, it appears that the plastic limit is reduced for the “green” sub-sample. Only the plastic limit was possible to conduct on this sub-sample due to the volume obtained from the post-mortem sub-sampling. Outer zones appear to display little alteration in plastic limit, which indicates that the interface sub-samples contain more corrosion products by mass which explains the reduction in plastic limit closer to the coupon. The PI results were only obtained within the outer zones of the interface sample. The outer zone PI results appear to have small change but there is a reduction with increasing temperature. Temperature appears to impact the materials moisture adsorption characteristics more so than the corrosion which also correlates to the findings in sections 5 and 7 respectively. Temperature appears to induce inter-particle cementation as well as a reduction in the surface potential. The macro free swelling characteristic of the post THC exposure also appears to reduce with increasing temperature. This correlates with the impact of thermal exposure on the PI measurements. The measurements display minor trend in reduction of PI closer to the coupon, this further supports that short-term THC impact is more significant for temperature than corrosion. Swell index measurements taken from the interface sub-samples display no reduction below the calculated minimum (12.83mL/2g), determined from the physical borehole geometry and MX-80 barrier parameters for the SKB concept (Calculations set out in section 5).

CEC measurements for the interface sub-samples indicate bulk charge alteration with temperature, with only a slight reduction closer to the coupon. The lower CEC measurements indicate that there is a combined influence of corrosion products and temperature on the MX-80 agreeing with Wilson et al (2010). It appears that the bentonite containing the meta-stable green rust is rich in double layer hydroxides (FeOOH) which overall have a net positive charge, thus reducing the materials bulk CEC. Furthermore, other studies have indicated that temperature reduces the layer charge which correlates to a reduced CEC (Ma and Hueckel, 1992; Mitchell and Soga, 2005). These also relate to the reduced free swell capacity. It is also seen that the development of a tri-octahedral smectite as observed in XRD studies, also reduces the structural layer charge.

Crystallographic analysis indicates that all interface sub-samples are rich in high charge smectite, with glycolated analysis resulting in d-spacing that correlate to smectite. Therefore, the macro swelling characteristic observed in PI and SI measurements indicate that alterations occur on an inter-particle level. Inter-particle interactions such as cementation and DDL reduction reduced the geomechanical characteristics. However the material remains

structurally smectic in composition. Overall the bentonite appears to remain mixed layer smectite/illite clay. Air-dried analysis also displays slight shift/ shoulder toward the 15Å spacing thus indicating some divalent cation exchange within the clay exchanger. Broader peaks are observed in corrosion rich sub-samples which also point toward to development of poorly crystalline/ amorphous corrosion products. Also, perhaps the dissolution of minerals has become more amorphous in nature. This indicates that ordering of the crystalline material becomes less ordered with higher temperature, saline and corrosion exposure. Overall all phases indicate that the predominant component is still a high charge/ high surface area smectite. Looking at the glycolated 002/003 profiles and intensity ratios, these indicate a saponitic smectite with Fe being substituted in the octahedral sheet nearer to the coupon surface. UV spectrophotometry and ICP further support the findings of green rust and integrated Fe^{2+} , with Fe^{2+} concentrations higher nearer to the coupon. Therefore, it is clear that the bentonite near to the steel coupon is a Ferro-saponite with Mg-saponite becoming more predominant with distance away from the coupon with ferrous hydroxides within the clay matrix. Madsen (1998) also discovered that the smectite was not transformed under THC exposure with Magnetite being predominant on the steel surface, Guillaume et al (2003) found that clay alteration only occurred in very high temperatures ($\geq 300^{\circ}C$).

Inspection of the non-clay component indicated the predominant development of Goethite within the mid to outer zones, further heat treatment (at $440^{\circ}C$) for XRD analysis confirm this by the peaks indicating maghemite alteration. Overall, it appears that there is a corrosion “front” rich in Fe^{3+} which is preceded by a reducing zone rich in ferrous hydroxides with a diffusing layer of magnetite on the steel coupon surface. SEM-EDX also indicates the surface development of magnetite on the steel surface. Quartz appears to reduce in the immediate bentonite zone near the steel surface and increases in the mid/ outer zone which supports the dissolution during THC exposure and precipitation on cooling. This explains and supports the premise of interparticle cementing and the associated influence on the geomechanical properties. Mid-phase conditions that experienced thermo-hydro flow conditions displayed the largest degree of feldspar dissolution at the bentonite near the coupon surface. It appears that the high thermo-hydro conditions accelerate the dissolution rate with solution flow essentially “washing” elements away from the interface. Strong plagioclase peaks in the outer zone where the saline solution inflow was located indicate that the Na rich water supplemented the development of Albite type feldspar post THC exposure.

XRD and coupon surface SEM-EDX also indicate the development of some calcite precipitation post THC exposure, also indicating dissolution of minerals containing Ca.

SEM inspection of the coupon surface indicates that stress corrosion cracking occurs in the higher temperature phases. This phenomenon may induce a reduced integrity of the canister as a barrier and structural component of the containment system. EDX analysis of the interface sub-samples correlate to the results observed of ICP analysis. Sodium appears to be displaced from the exchanger in the corrosion rich zone which implies that there is some Fe substitution at the exchange sites, supported by Mossbauer measurements conducted on phase 2 sub-samples. The degree of exchange is higher in the higher thermal loading conditions and much higher in non-static flow conditions. Magnesium and Aluminium concentrations are also reduced closer to the interface which also supports the premise that Fe is partially substituted into the octahedral layer, XRD also shows this. Again, the degree of Mg and Al displaced is higher in the high temperature non-static flow conditions. Calcium is higher in the high pH corrosion zone indicating calcite formation post hydrothermal exposure. EDX further confirms other analysis in that feldspar and other sulphur containing minerals indicate more dissolution in the high thermo-saline tests. The results indicate that mid-life conditions are significant to the barriers alteration characteristics. The mid-life period which will experience corrosion-saline-thermal loading conditions will exhibit most alteration. The next chapter (chapter 7) examines the impact of the mid-life boundary conditions on the barriers geomechanical properties related to the critical functionality. Mid-life conditions were chosen due to the conditions being the most complex in terms of the THC environment.

Mossbauer analysis support the identification of meta-stable Ferrous (hydr)oxides. Furthermore, the location of Fe^{2+} supports the evidence that Na is displaced from the basal sites thus indicating that Fe^{2+} is sorbed in this zone. Fe^{2+} also appears to have complexed to the edge site supporting the development of hydroxides. Fe^{2+} also appears to have replaced the Mg within the octahedral layer with the relative abundance measured via Mossbauer indicating this. These Mossbauer measurements support observations made via ICP, UV spectrophotometry, XRD and CEC etc. Overall, interface sub-samples under high thermo-saline conditions indicate partial replacement of Mg by Fe^{2+} with meta-stable ferrous (hydr)oxides and magnetite. Both mid-sample and interface zones displace Fe^{2+} replacement for Na within the basal exchange site, more so for the mid-zone indicating a REDOX sensitive front of Fe^{2+} moving into the bentonite. The temporal factor appears to be

important for the interaction of Fe^{2+} and the octahedral layer, thus interactions observed in this study indicate precursor exchanges.

Overall it is clear that the results from the interface experiments display little change from the overall desired design functionality. Even though the geomechanical results indicate that macro scale intrinsic properties of the bentonite are slightly inhibited by influence of temperature, salt and corrosion products but overall the properties are still relatively high and meet the design limitations set out by SKB Börjesson (2010). Large rates of dissolution are observed over the relatively short time-scales involved in this study. High thermal and saline fluid flow conditions as well as a high pH environment due to the corrosion at the interface accelerate the dissolution of accessory minerals. This results in the development of a poorly crystalline corrosion rich zone at the interface with some calcite precipitation upon cooling. Crystallinity is also reduced over the sample profile due to the thermal interactions, and amorphous silica also precipitates within the outer zones. Bergaya et al (2006) states that Fe^{3+} can partially replace Si^{4+} in the triocahedral sheets, this is not directly observed but it may support the displacement of Si into the outer zones as well as the dissolution of quartz. Furthermore, physicochemical analysis displays that the clay remains rich in smectite with intrinsic swelling of the d-spacing due to layer charge remaining unchanged. Interface sub-samples display some Fe substitution within the octahedral sheet, with XRD profiles resembling a Ferro-saponitic type smectite. This substitution is also supported by other physicochemical analysis conducted in this study. Thus, indicating that the material is still relatively tri-octahedral in composition. However, it must be noted, and as has been stated previously, a fundamental restriction in the testing is the time-scales involved. However previous simulations and analysis on natural analogues display the development of Fe-rich clay which indicates that the results observed here is the precursor mineral/ corrosion interaction development. Time appears to be a critical component of the interactions with higher temperatures not necessarily accelerating the alteration products but on the contrary changing the type of minerals produced.

From the inferred near-field/ interface predictions and the results from this section of interface tests, the mid-life phase will involve the most significant combination of environmental variables. Therefore, the next section used the mid-life near-field variables outlined in this section to investigate the impact on the barriers geomechanical properties.

7. Constant volume test results

This experimental methodology was assigned the name of constant volume tests, primarily due to the fact that the samples were sealed within cells that prevented the loss of moisture during thermal exposure, thus enabling a chemically isolated environment. The fundamental purpose of the constant volume batch tests was to replicate the initial period of complete resaturation, where temperatures are likely to be the highest with corrosion products present in the pore water as well as the bentonite matrix. Therefore, measurements of swelling pressure and swelling kinetics enabled an insight into the bentonites ability to self-heal after thermo-chemical exposure. Several consignments were conducted to investigate what environmental factors cause the most significant geomechanical alterations. Furthermore, rheological measurements are given as a proxy of stiffness which is considered useful as an indicator of the effects of interparticle cementation. Additionally, consolidation data obtained from the consolidation stage of the rheology measurements enabled estimates of intrinsic permeability. The permeability is obtained from the root time method to obtain M_v and CV thus using the empirical formula, detailed within the methodology chapter, to obtain the intrinsic K parameter. Overall by obtaining the aforesaid parameters it is possible to isolate and observe the environmental variable that most significantly inhibits the barriers design functionality. Each batch was subject to the same THC exposure duration; table 72 displays the test matrix outlining the experimental boundary conditions. In the following sections only the compiled average results are displayed.

Table 72: Constant volume batch test matrix

B#1	B#2	B#3	B#4
<u>Control specimen-thermally exposed</u>	<u>NaCl pore water Batch sample</u>	<u>Corrosion + NaCl pore water batch sample</u>	<u>Corrosion batch sample</u>
$\rho_{dry}: 1.56Mg/m^3$ $\omega=27\%$ $Sr \approx 1$ Distilled water Duration: 4 months	$\rho_{dry}: 1.56Mg/m^3$ $\omega=27\%$ $Sr \approx 1$ Saline solution 0.45M (NaCl) Duration: 4 months	<ul style="list-style-type: none"> • 2mm Layer of Fe_2O_3 and Fe_3O_4 Fe/MX80 mass ratio 0.1 $\rho_{dry}: 1.56Mg/m^3$ $\omega=27\%$ $Sr \approx 1$ Saline solution 0.45M (NaCl) Duration: 4 months 	<ul style="list-style-type: none"> • 2mm Layer of Fe_2O_3 and Fe_3O_4 Fe/MX80 mass ratio 0.1 $\rho_{dry}: 1.56Mg/m^3$ $\omega=27\%$ $Sr \approx 1$ Distilled water Duration: 4 months

The measured parameters have been related to barrier design limits that are highlighted in leading literature. Therefore, any deviation from the geomechanical parameters measured during this study can be related to the functionality of the near-field EBS. Displayed in table 73 below are the simplified barrier design limits used for comparison, full barrier design

geomechanical parameters are given in section 2.3.3 detailing the literatures findings and suggestions. Only the swelling pressure and hydraulic conductivity can be compared as there is no data on the stiffness characteristics of the barrier. However, the rebound kinetics and rheology measurements can indicate serve as proxies for alterations in the barrier self-healing capacity and stiffness respectively. The Posiva concept appears to have a relatively higher minimum swelling pressure. This is concept specific and the SKB concept is the most relevant to the UK’s disposal methodology, therefore the SKB limits will be used as the main comparative concept.

Table 73: Simplified barrier design limitations for three leading concepts (after Leupin, 2014 and Borjesson, 2010)

<u>Geomechanical parameter</u>	<u>SKB</u>	<u>Nagra</u>	<u>Posiva</u>
Swelling pressure (MPa)	≥1 & ≤15	≥0.2 & ≤15	≥5 & ≤15
Hydraulic conductivity (m/s)	≤× 10 ⁻¹² m/s	≤× 10 ⁻¹¹ m/s	≤× 10 ⁻¹¹ m/s

7.1. Swelling pressure:

One-dimensional Odometric swelling tests were conducted in accordance with BS1377 [5]:1990. The average consignment selected swelling pressure profiles are compiled and presented in figure 244 with the average swelling pressures presented table 74 below, along with the average control measurements for comparison.

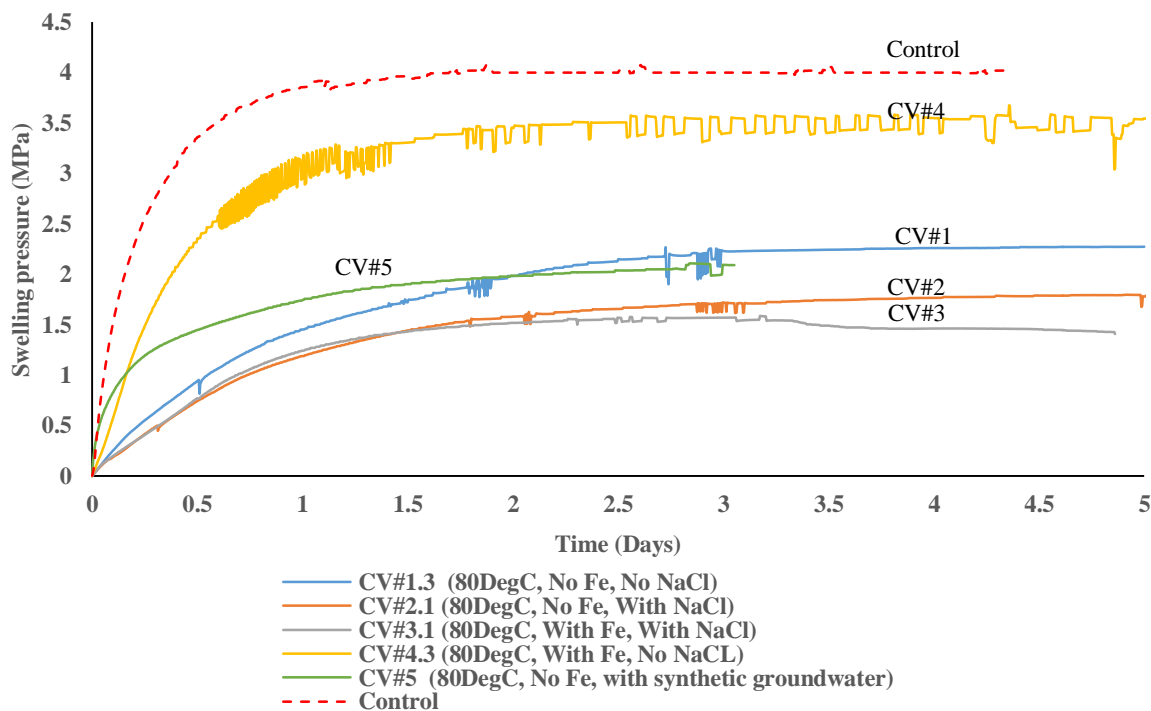


Figure 244: Characteristic swelling pressure profile for each test consignment

Table 74: Compiled swelling pressure results

Sample	Experimental boundary conditions	Average swelling pressure (MPa)
Control	20°C, DI water, No THC exposure	4
Batch #1	80°C, No Fe, No NaCl	2.6
Batch #2	80°C, No Fe, With NaCl	2
Batch #3	80°C, With Fe, With NaCl	1.7
Batch #4	80°C, With Fe, No NaCl	3.68
Batch #5	80°C, No Fe, with synthetic groundwater	2.09

Figure 244 displays the average swelling pressure results from the constant volume batch tests, the non-uniform and sporadic nature of the swelling profiles is due to the influence of external sources within the laboratory. The magnetic flux generated from a heating solenoid from the oven and the room temperature control appears to impact the resolution of the load cell. This was determined from several investigatory/ side experiments where the tests were conducted with the oven on and off to determine the impact this had. From figure 244 the control swelling pressure profile is given as the red dotted line for comparison. As stated earlier the purpose of the tests was to investigate the impact of the near-field conditions during the mid-life phase with the highest thermal load, corrosion and saline rich pore water. Furthermore, by varying the experimental boundaries it was possible to isolate the most significant variable that impacts the geomechanical parameters relevant to the barrier functionality.

In order of batch completion, constant volume consignment #1, subject the sample to just thermal loading over 4 months. The thermal influence alone reduces the swelling capacity of the bentonite. The results display a 35% reduction in swelling pressure by comparison to the control measurement. This can be correlated to literature in that the thermal influence on the bentonite causes siliceous compounds to precipitate and fuse the particles together (Pusch et al, 1993; Senal et al, 2010; Idiart et al, 2013; Leupin et al, 2014; Pusch et al, 2014). Ultimately, this inhibited the swelling capacity of the bentonite upon hydration due to the fused particles remaining in a “collapsed” state. The macro level swelling capacity displays some alteration after the comparatively short thermal exposure period with respect to the duration of the EBS. Long-term studies of natural analogues display that cementation does occur, supporting the observed measurements. Nonetheless the Kinnekulle deposit still contained at least 25% smectite with unaltered swelling properties, with the deposit succeeding the life-time of the EBS as reported by Madsen (1998) and Wilson et al (2010). XRD measurements for the interface experimental tests also display an increased presence of quartz near the interface. With comparison to the barrier design limits, displayed in table 73

(above), the swelling pressure after thermal exposure is still above the minima of 1MPa that is considered to uphold self-healing (swelling pressure and volume change), density, stiffness and permeability.

Constant volume batch consignment #2 included both thermal exposure and a high saline pore solution. The combined influence of a high electrolyte concentration and thermal loading further reduces the swelling pressure by 50% with respect to the control measurement. This can be ascribed to the combined effects of the siliceous fusing between particles and the drop in the DDL due to the higher concentration of NaCl flocculating the clay platelets. As described in the previous paragraph fusing of the bentonite platelets is supported by literature. Furthermore, the drop in the macro swelling capacity due to the impact of high electrolyte solutions is supported by the findings in the batch test experiments displayed in section 5 and in literature (Lee et al, 2012). Even though the salt concentration used was equivalent to a worst-case scenario, i.e. the concentration of NaCl was equivalent to that of sea water (0.45M), the swelling pressure remains higher than the design limit set out for the SKB concept to uphold the key geotechnical properties. Nonetheless, more complex saline pore solutions may yield more repressed swelling pressure results.

The third consignment investigated the combined influence of Fe corrosion products and saline pore water as well as the thermal loading boundary conditions. These were most representative of mid-life conditions. It appears that there is a further drop in the materials macro swelling pressure however the difference is small compared to consignment #2 which experienced thermal loading and high saline pore water. The swelling measurement was 58% lower than the control and only a 300KPa difference between the high saline/ high thermal load consignment (#3). By comparison of the two consignments the saline pore water and temperature combined have a greater impact on the materials swelling than the additional presence of corrosion products within the intra-aggregate voids. Furthermore, the consignment measurements indicate that the combined experimental boundaries still display swelling pressures greater than the design parameter limitations set out by the SKB concept.

Consignment batch #4 isolated the effects of temperature and the presence of corrosion products without saline pore-water. From figure 244, it is evident that the swelling pressure does not significantly change from the control measurement, with only a difference of -8%. This is thought to be due to the volumetric expansion of the corrosion products within the bentonite matrix, in addition to the expansion of the non-fused clay platelets upon exposure

to DI water. This further supports the premise that under the explored experimental conditions, the impact of salt and thermal exposure has a greater effect on the swelling characteristics after short-thermal exposure. The slight reduction is perhaps due to cementation effects of the corrosion products and the siliceous compounds with the bentonite due to the thermal loading.

The final consignment, batch #5, looked at the effects of thermal loading with the presence of a synthetic groundwater composition. It appears a more complex groundwater does not significantly affect the swelling pressure beyond that of the other batch tests. The swelling pressure displays a 48% reduction from the control measurement, indicating that batch #2 displays a similar reduction with the presence of NaCl.

Through observation of the swelling mobilisation profiles, this is the gradient of the initial part of the swelling profile in figure 244, it is clear that the swelling mobilisation of the respective samples is altered with influence of the various experimental boundary conditions. The initial swelling mobilisation gradients are taken from data between 0- 0.5 days and are displayed in table 74. It is clear from table 75 that the mobilisation of the swelling pressure decreases with respect to the more complex environmental boundary conditions, i.e. the more realistic scenario given by batch #3, displays the most inhibited swelling mobilisation. This indicates that upon resaturation of the barrier the initiation and completion of the self-healing of the barrier will be repressed due to the coupled influence of the saline solution on the DDL, precipitation cementation by siliceous compounds and cementation of intra-aggregates due to the presence of the corrosion products. The mobilisation potential of the barrier is reduced by over half and may prove problematic for the initial sealing of the voids within the bentonite that may develop during the initial dry phase. Nonetheless, the swelling pressure for all the consignments are above the minimum design limit for maintaining self-healing, diffusion and density etc.

Table 75: Initial swelling pressure mobilisation gradients for the respective average batch consignment profiles

<u>Batch consignment</u>	<u>Swelling mobilisation gradient (MPa/day)</u>
Control (20°C, DI Water)	4.68
Batch #1 (80°C, No Fe, No NaCl)	2.15
Batch #2(80°C, No Fe, With NaCl)	1.38
Batch #3 (80°C, With Fe, With NaCl)	1.23
Batch #4 (80°C, With Fe, No NaCl)	4.96
Batch #5 (80°C, No Fe, With synthetic groundwater)	1.58

From figure 245, the synthetic groundwater batch tests were subject to two separate conditions. After compaction of the sample with the saline solution mixed into the bentonite matrix, the first swelling test used Deionised (DI) water within the oedometer cell and the second used the synthetic solution within the cell. This enabled a comparison between the free access to the high saline solution and DI water. The purpose was to investigate the impact of free access to DI water and saline water from the oedometer cell after THC exposure. The swelling pressure for the sample that included the synthetic groundwater within the bulk cell solution displayed a lower swelling pressure than the same sample with access to DI water. It appears that the bulk saline solution inhibits the free movement of the water molecules due to the lower osmotic pressure within the bulk solution. Thus, causing inhibited expansion of the interlayers. The sample which included the DI water indicates that there is a combined effect of electrolytes reducing the DDL, thermal fusing of the platelets (with support from literature and the experimental data conducted in this study) and the change in the osmotic pressure between the interlayer solution and the bulk solution.

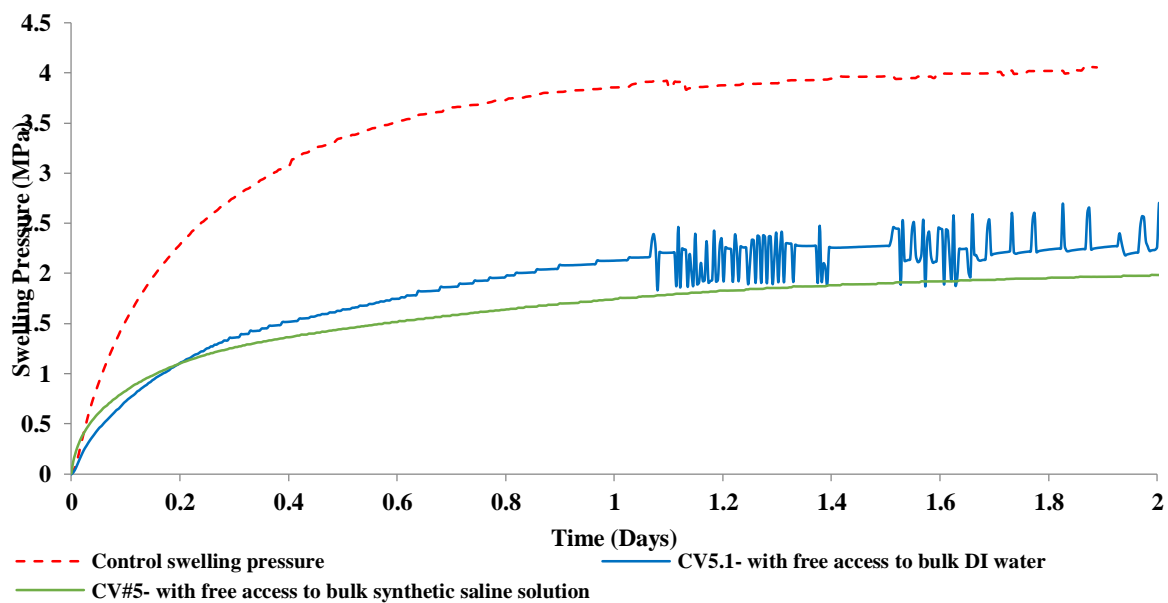


Figure 245: Comparison between free access of DI water and a high saline solution

7.2. Swelling kinetics:

The swelling kinetic measurements were obtained post swelling pressure; the axial stress was reduced by 10% after stabilisation with the subsequent axial strain logged over two days. The average compiled data along with control measurements are presented in figure 246. Furthermore, the gradient of the axial strain resulting in measurements of strain rates for the respective consignments were obtained. Thus, by comparison of the resulting strain rates an

understanding of the materials swelling (self-healing) characteristic after the higher thermal, saline and corrosion exposure can be assessed. This can also be related to the clays ability to mobilise the swelling pressure as stated in the previous section, 7.1. The compiled total accumulated axial strain after 2.5 days as well as the strain rates for the respective consignments are tabulated below, table 76.

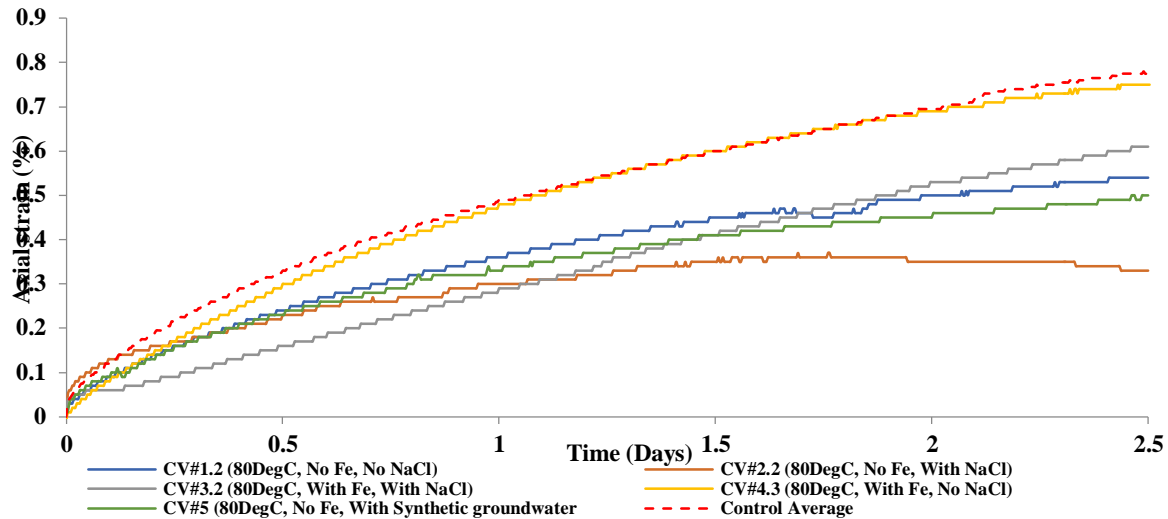


Figure 246: Characteristic swelling kinetics measurements for each constant volume consignment with average control comparison

Table 76: Compiled average accumulated axial strain and average strain rates for respective constant volume consignments as well as average control measurements

Batch	Accumulated axial strain after 2.5 days (%)	~Strain rate (%/day)
Control	0.79	0.45
CV #1	0.55	0.22
CV #2	0.35	0.16
CV #3	0.68	0.3
CV #4	0.75	0.43
CV#5	0.5	0.23

The kinetic profiles displayed in figure 246, for the respective sample consignments display an identical trend to the swelling pressure profiles. That is, the increasing complexity of the experimental boundaries for batch #1-3 follows the same reduction profiles. The impact of the thermal loading displays a 30% reduction in the axial strain rebound profile like the swelling pressure reduction. Thermal loading and the presence of a high saline solution (CV #2) further reduces the axial rebound profile by 56%. Again, the measurement correlates well to the magnitude of swelling pressure reduction displayed in section 7.1. The addition of the presence of corrosion produces within the bentonite matrix with high temperature and high saline solution, displays a much less degree of reduction, as observed in the swelling pressure profile measurements, with only a reduction of 16%. This degree of alteration does not correlate to the swelling pressure reduction, while the swelling pressure for this

consignment displays the most significant level of reduction. The rebound profile displays a higher recovery compared to consignments 1 and 2. It is evident that the addition of the corrosion products within the bentonite matrix increases the macro volumetric swelling capacity of the bentonite. This is due to the volumetric capacity of the hydrated corrosion products. This is further supported by batch consignment 4 that observed the influence of corrosion products and thermal loading alone, the macro-scale axial rebound remains almost unchanged with only a 5% reduction in the final axial strain. This is comparable to the degree of alteration in the swelling pressure for the bentonite-thermo-corrosion experiment. The synthetic groundwater batch sample included a lower concentration of NaCl with additional electrolytes in comparison to the other batch samples. By comparison of the batch which used the more complex saline solution and the batch using only NaCl it is clear that NaCl alone at higher concentrations has a much greater impact than a Calcium, potassium and sodium mix. Nonetheless, the swelling strain after 2.5 days for batch #5 is 37% lower than the control. The strain rate estimations obtained from the axial rebound profiles in figure 246 displays a similar trend which supports the premise that thermal loading and high saline pore water has a greater detrimental effect on the materials macro geomechanical parameters than the corrosion products alone.

7.3. Permeability:

As stated previously, the consolidation data was used to obtain the parameters required to empirically estimate the materials permeability via the root time method through the consolidation parameters, i.e. t_{90} , CV and MV as well as the samples physical parameters. Displayed below in table 77 are the compiled average permeability measurements along with the control permeability. The order of magnitude is considered more important to quote and consider when looking at the permeability of a heterogeneous soil.

Table 77: Compiled average permeability measurements

Batch	Average permeability (m/s)
Average control	6.52×10^{-15}
Average CV #1	2.3×10^{-14}
Average CV #2	4.3×10^{-15}
Average CV #3	6.1×10^{-15}
Average CV #4	4.8×10^{-15}

From table 77, the permeability does not change significantly between sample consignments. What is noticeable, the thermal loading test, CV#1, indicates that the permeability has increased by an order of magnitude. This is not observed in other batch consignments particularly for the corrosion and saline samples. The post THC exposure intrinsic porosity of the material is therefore not affected by any of the experimental boundary conditions. Previous research has observed an increase in permeability of the material with thermal exposure. However, the measurements were conducted during live experimental conditions and not post thermo-chemical exposure as is the case here. Thus, the increased permeability observed in previous studies (Batchelor, 1983; Cho et al, 1999; Hicks, 2009) measured the increase in the kinematic viscosity of the intra-aggregate pore water and not any physical change to the bentonite itself. The measured permeability values correlate to the controls measured by Leupin et al (2014) but do not correspond to that of Shariatmadari et al (2011) who states that there is an increase in permeability with increasing salt concentration due to particle flocculation. This is explained by the findings made by Mersi & Oslon (1970) and Alther et al (1985) who found that the permeability was dependant on the magnitude of the normal stress and confining conditions. They found that a higher normal stress in a laterally confined cell resulted in little alteration to the permeability, which is similar to the test conducted in this study, with the opposite effect observed in low confining pressures. Overall, it appears that the intrinsic permeability remains significantly below the diffusion/ advection boundary. Nevertheless, the higher thermal environment has a much larger direct impact on the physical properties of the pore solution than the potential physical alterations to the bentonite due to THC exposure. This is evident from the results given in table 77, which measured the permeability post THC compared to the results from literature that measured live permeability during thermo-chemical loading. The thermal dilation/ contraction phenomenon was observed by Tang et al (2008) who found that thermal particle dilation and particle contraction was dependent on the materials degree of saturation. High saturation states, similar to that of the samples used in this study, displayed thermal contraction which corresponds to the low permeability. Whereas low saturation states/ high suctions, opposite to the samples in this study, displayed a thermal dilation which corresponds to the higher permeability's observed in previous studies. These two factors will temporarily increase the permeability during the higher thermal phase. But there is little evidence that post high thermal exposure i.e. the late life phase permeability will increase. Therefore, upon cooling, the permeability of the bentonite appears to remain within the diffusion controlled zone. The measured parameter is within the design limits set out by the SKB concept for all

experimental conditions. However, one potential limitation to the study was that the condition under which the sample was thermo-chemically exposed was static. It is evident from the interface experiments (section 6) that an active hydraulic gradient induces mineral dissolution during THC exposure. Dissolution of feldspars and carbonates at the interface may cause a bulk mass loss which will alter the bulk physical parameters such as the density etc., which would cause a permanent permeability increase as well as loss in the bulk swelling pressure.

7.4. Rheology:

One main design function of the barrier is the ability to act as a stress buffer during the repository life. For example, if in the event of a host rock displacement the energy should not be directly transferred into the canister via the bentonite barrier. Consequently, the barrier must remain ductile enough to adsorb the energy and deform meanwhile maintaining sufficiently high shear resistance to prevent excessive canister displacement. Recalling figure 24, section 2.1.3, is presented in a combined consortia report on a critical review of bentonite in repository applications jointly published by independent research companies Quintessa, Sweco and TerraSalus ltd (Wilson et al, 2010) and illustrates why ductility within the buffer must be maintained for canister integrity. Furthermore, figure 247 displays the compiled average rheology results. Accumulated shear strain over 48 hours was measured under a constant shear stress of 20% of the ultimate shear strength. It must be noted that there are no measurements given within literature as a standard for comparison, however by testing the unaltered bentonite under the pre-emplacment design conditions allows a direct comparison. The rheological profiles given in figure 247 allow an insight into the influence of the THC experimental variables on the microstructure of the bentonite.

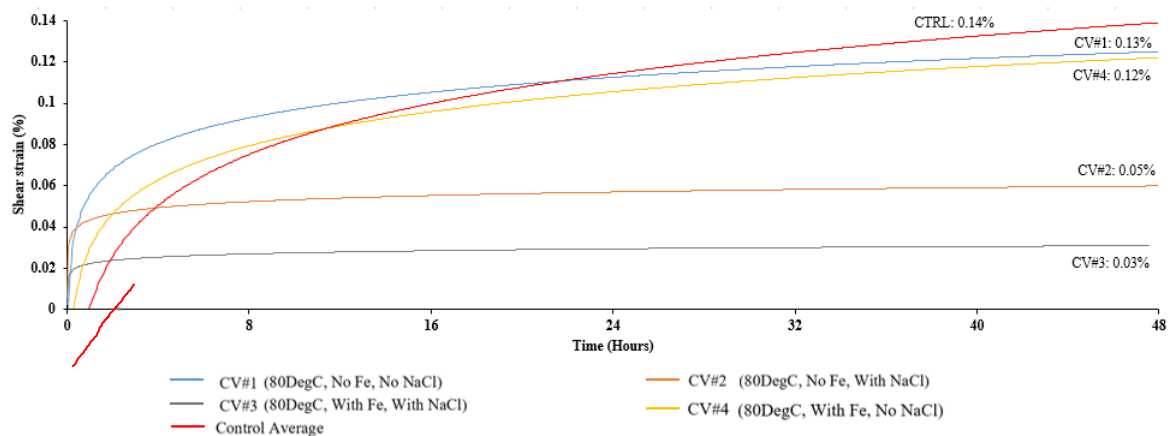


Figure 247: Characteristic rheology results under a stress of 20% ultimate shear strength for 48 hours

From figure 247, batch #1 displays a negligible reduction in the accumulated shear strain with only a 7% increase in sample stiffness. This indicates that thermal loading alone only slightly increases the stiffness of the material. This could be due to the fusing of particles due to silica precipitation within intra-aggregate voids. Batch #2 included the addition of a saline solution. There is a substantial increase in the samples stiffness with the addition of a high saline solution and thermal loading. There is a 64% increase in the sample stiffness which indicates that the reduction of the DDL is due to the influence of a high saline solution which increases the density and inter particle packing configuration. This may also increase the potential for fusing between particles as well as the degree of interlocking. The measurements post thermo-saline exposure indicates significant stiffening. Furthermore, the addition of Fe within the bentonite matrix under thermo-saline conditions (Batch #3) displays the highest degree of bulk stiffening. Batch #3 displays that there is a 79% increase in the samples stiffness or a 79% reduction in ductility. Batch #3 replicates the closest conditions from the inferred mid-life environmental conditions, and thus proves that high saline, high corrosion and a high thermal environment causes the interface bentonite to become significantly less ductile. The combined effect of salt on the DDL, the fusing on the particles and cementation induced by the corrosion products incurs a large loss in ductility. However, when examining the influence of corrosion alone (batch #4) it appears that corrosion products within bentonite do not impact the rheological characteristics, displaying a ductility loss of 14.3%. This is also demonstrated by the other bulk geomechanical properties such as the swelling pressure, kinetics and permeability. Therefore, thermal loading and salt concentration has a much larger impact on the short-term physical characteristics, this is also observed within the batch test series illustrated in section 5. Table 78 gives the shear strain after 48hrs of swelling rebound, post THC exposure.

Table 78: Shear strain after 48 hours of axial rebound

Batch	Shear strain (%)
Control	0.14
CV #1	0.13
CV #2	0.05
CV #3	0.03
CV #4	0.12

7.5. Conclusion:

This chapter presented the results that investigated several thermo-hydraulic static conditions on compacted bentonite which undergone varying THC exposure scenarios. The

testing intended to isolate the individual boundary conditions inferred from near-field predictions and observe what effect they have on the geomechanical properties. The testing conditions were limited by the exposure time compared with the insitu conditions of the EBS. Understandably, the times scales expected for the barriers exposure to mid-life conditions are considerably lengthy, however the experimental work allows real-time interactions and used along with studies on natural analogues and computational data enable a comprehensive insight into the barriers functionality.

It is evident from the geomechanical results presented above that high saline pore solution along with thermal loading impact the barriers geomechanical functionality compared to the impact of the corrosion products alone. The swelling pressure after thermo-chemical exposure, representative of insitu conditions (batch #3) result in a 58% reduction along with a 69% reduction in mobilisation rate compared to the control measurements. However, comparing the results to the thermo-saline batch consignment (batch #2) the measurements are similar, thus indicating that temperature and salt impede the physical properties in the initial short-term interactions. With support of previous studies, it is concluded that this short-term impact is due to two macro-scale and two micro-scale mechanisms. Firstly, discussing the inter-particle macro-scale alterations, thermal loading induces thermal contraction in highly saturated/ low suction compacted MX-80 (Tang et al, 2008) as well as the precipitation of siliceous minerals within the intra-aggregate voids which “fuse” the platelets together (Muller-von-moos, 1990; Villar and Gomez, 2010; Xiadong et al, 2011). This is supported by the reduction in the ductility (rheological) measurements, which also supresses the materials ability to swell, as indicated by the kinetic and swelling pressure profiles. Secondly, the micro-scale physicochemical influence of thermo-saline exposure induces collapse of the DDL due to loss in the surface potential and dielectric constant (Ma and Hueckel, 1992; Mitchell and Soga, 2005) as well as the effect of the increased electrolyte concentration (Schmitz et al, 2007; Lee et al 2012). These combined mechanisms appear to be the cause of the reduced swelling pressure, rebound (kinetics) and increased stiffness. However, post THC exposure measurements on permeability displayed no change thus indicating that the material maintained similar physicochemical and porosity parameters upon cooling. Alteration to the physical parameters of the pore solution during the thermal loading causes increased kinematic viscosity which allows higher diffusion rates. This can also be inferred from the interface results displayed in section 6, it was observed that the corrosion front extended greater into the bentonite for the high temperature/ hydrostatic

phase. It was also observed from the interface tests that hydro-thermal conditions induced accelerated dissolution rates which may cause bulk changes to the materials porosity and ultimately the permeability. However, the experimental protocol implemented here used isolated and static/ no-flow conditions thus stopping any mass loss from the system, this can explain the unchanged permeability measurements.

Overall, the mid-life conditions replicated in batch #3 display an overall reduction in swelling pressure, self-healing as well as increased stiffness but remain above the physical design parameters set out by the SKB concept (given in section 2.3.3). Furthermore, natural bentonite analogues explored and presented in previous literature has found that a large proportion of the deposit was still rich in smectite after some 1000 years of heating at 120°C decaying to 90°C with time. Some potassium enrichment and illitisation was present and was concluded to be due to the percolating ground water (Madsen, 1998; and Wilson et al, 2010). More complex interactions between the groundwater and the bentonite is not explored fully here, but the impact is demonstrated by that fact that partial alteration of the natural analogue to illite occurs. Therefore, the concentration of potassium should be low in the percolating groundwater for a site under consideration as well as the screening/ removal of high amounts of accessory minerals that may induce potassium fixation and illitisation upon dissolution. The macro and micro physicochemical alterations, as explained above, explain the cause of loss of functionality as well as the additional cementing/ interlocking effect of the corrosion products present within the bentonites voids. The conditions explored here are closely representative of the immediate interface conditions surrounding the waste canister during the mid-life phase. The outer zones of the bentonite may display more favourable parameters and may compensate for loss in ductility and swelling pressure at the interface. Thus, assuming that the interface conditions do not extend extensively into the barrier and alterations continue to evolve under longer time-scales, the results presented here indicate that bentonite within the interface zone will uphold the design requirements.

8. Conclusions and recommendations for further research

Three experimental configurations were designed with the fundamental aim to investigate and examine the physical and geomechanical performance of the bentonite barrier. Firstly, batch testing aimed to explore a range of experimental variables with respect to salinity, temperature, and duration and corrosion exposure. The experimental conditions were derived from leading literature. The conditions under which the specimen was contained were simple. The MX80 was contained within Pyrex beakers in which the experimental boundary conditions were implemented. For the samples which involved a carbon steel interface the corrosion conditions were limited with redox conditions unable to be controlled and assumed to be in the oxidation state. The post THC physicochemical and geomechanical measurements allowed brief insight into conditions that most significantly affect the performance of the barrier after short-term exposure.

The second experimental study involved the compacted bentonite block and the S275 carbon steel coupon, the bentonite was compacted to SKB concept specific parameters. The interface was subject to three inferred life-phases obtained from leading literature with agreed generic near-field variables for the UK concept. This ultimately achieved objective #1 of the study; to determine UK concept specific near-field variables. The design of this study and boundary conditions were also based on preliminary results and other research methodologies, thus achieving objective #2 and 2a; implementing a THC laboratory investigation of the clay/steel interface. The results of the initial short-term batch tests also enabled key variables to be carried through into the interface testing. The preliminary aim of the interface phase testing was to investigate the physicochemical alterations of the bentonite after “snap-shots” of the most significant phases of the barriers life were exposed to the interface; thus achieving objective 3 and 3b. Furthermore, the interface tests enabled the assessment of the extent to which corrosion integrated into the bentonite under insitu conditions, addressing objective 3c.

Lastly, the constant volume batch testing focused mainly on the mid-life phase carried from the interface testing methodology and inferred interface near-field predictions with the premise that the most significant alterations will occur during this period due to high temperatures, corrosion integration and resaturation with high saline water. This experiment looked at all of the experimental variables combined, as well as supplementary constant

volume tests looking at isolated variables i.e. thermal, corrosion or saline loading respectively. This allowed the measurement of geomechanical parameters post mid-life exposure conditions as well as post thermo and thermo-saline conditions. From the combined results and outcomes of designing and conducting the aforesaid tests, the fundamental objective (3 and 3a) set out at the beginning of the project were achieved.

The key research questions established at the beginning of the study ultimately enabled a structured experimental and research methodology to provide a well-structured and scientifically rigorous answers. The following section summarises the principle findings from the three experimental investigations as well as addressing the final research objective; to interpret the physicochemical and geotechnical factors with respect to the longevity of the EBS clay/ steel interface over the predicted THC phase evolution.

8.1. Batch tests finding summary:

From the initial batch tests, it was possible to examine the intrinsic alterations to the MX-80 bentonite under several experimental boundary conditions after relatively short-term exposure compared to the durations the barrier will be subject to in-situ. It was clear from the tests that thermal loading alone inhibits the free swell capacity of the bentonite by 20% compared to the control. Nonetheless comparing the derived minimum swell index derived from the SKB borehole geometry and clay barrier parameters (SI_{\min} : $12.83\text{cm}^3/2\text{g}$), the swell index of the MX-80 after thermal loading is not exceeded. Therefore, temperature exposure of 100°C on MX-80 powder under non-constant volume conditions after 4 months still displays high swell characteristics. Additional experiments containing thermo-saline (100°C and 0.45M NaCl) boundary conditions indicate a larger reduction in the physical properties, with the swell index and plasticity index being reduced by over 50%. The measurements still however remain above the minimum design limits set out by the SKB concept. The experiments looking at the interaction between corrosion and MX-80 powder does not appear to affect the physical characteristics, particularly in comparison with thermal loading and higher saline concentrations.

Longer thermal loading scenarios at the peak concept temperature (100°C) appear to have a greater impact on the physical properties on the MX-80 than short-term very high thermal loading scenarios. This indicates that thermal loading over long time-scales has a more significant impact on the barriers self-healing properties than temperature exposure ($\geq 100^\circ\text{C}$) under shorter durations (≤ 4 months).

Experiments which investigated the intrinsic alterations on the geomechanical and physicochemical properties after exposure to more complex saline solutions (i.e. replicating groundwater at associated depths of the GDF and of a crystalline host rock environment), indicate that more complex saline composition and corrosion exposure results in a 50% and 60% reduction in the free swell and plasticity respectively. Physicochemical analysis of these tests indicates that divalent cations are readily exchanged within the basal exchanger which reduces the DDL. This inhibits the barriers ability to swell and potentially self-heal. Hydro-thermal tests in the presence of the synthetic groundwater displayed elevated levels of feldspar dissolution as well as the potential formation of palygorskite. This may result in bulk density loss due to mineral dissolution under hydro-thermo-chemico conditions. Siliceous mineral dissolution and re-precipitation upon cooling was also observed under the aforementioned saline-hydro-thermal conditions. This also indicates that the barriers physical properties will be affected such as self-healing and stiffness linked to the fusing of clay platelets causing reduced swelling and plasticity.

Thermal loading, saline solution and corrosion exposure appears to reduce the surface potential and dielectric constant of the clay surface as well as a reduction in the DDL. High pH conditions at the interface also display that accessory minerals are subject to dissolution and re-precipitation upon cooling. With respect to the barrier, these results indicate that the barrier will be slightly inhibited with respect to its self-healing properties. Nonetheless, comparing the results to the baseline minimum design parameters, the barrier will uphold its volume and self-healing properties. The minimum limit of the swell index was calculated using information on borehole geometry and physical parameters of the bentonite block for the SKB concept. Under all the experimental conditions explored in the batch experiments the parameters did not deviate below this limiting value (SI_{\min} : $12.83\text{cm}^3/2\text{g}$). Therefore, the short-term exposure conditions, based on the results obtained within this study, indicate alteration to the intrinsic properties of the bentonite after THC exposure do not adversely affect the barriers ability to self-heal, retain radionuclides, maintain diffusive transport of percolating groundwater etc. Provided that the UK concept designs the engineered system with the intent of keeping the thermal peak sufficiently low over the entire canister array over the early stages of post enclosure, the results give here indicate that self-healing and radionuclide retention will be upheld.

As stated previously the next section will summarise the findings from the interface experiments which used the boundary conditions carried forward from the batch experimental methodology as well as the inferred key life phases from literature and consortium meetings.

8.2. Interface findings summary:

This section of the testing methodology provided the main focal point of the research which was designed to address the key research question outlined in section 1. This experiment enabled insight and radial profiling of corrosion integration and precipitation as well as mineralogical characterisation post interface replication phase. Three phases were chosen to replicate key periods of the interface during its working life. Phase 1 replicated the immediate conditions post emplacement of the canister, phase 2 replicated the mid-life conditions with high saline groundwater inflow and phase 3 resembled the late-life period after complete thermal decay and resaturation had taken place. The three phases were tested for mineralogical and corrosion characterisation with some supporting geomechanical measurements.

Upon post-mortem sampling of the respective interface samples within an N_2 -rich glove box, the extent to which corrosion had visibly precipitated into the bentonite was measured with sub-sampled zones chosen by the colour change throughout the bentonite. It was observed that corrosion diffusion into the bentonite was greatest when the interface was subject to “mid-life” conditions i.e. 80°C and percolating saline solution. It was discovered that the direction of corrosion diffusion was independent of the direction bulk fluid flow. Corrosion diffusion appeared to move away from the coupon while the saline solution moved toward the coupon. This indicates that the corrosion rich environment with a bulk saline solution environment at the interface causes the diffusion rate to increase away from the source. With respect to the implication on the barrier, this mechanism indicates that the saline pore water increases the diffusion rate which is linked to the reduction of the DDL ultimately increasing the bulk fluid transportation rates. Mid-life conditions may increase the zone of influence of Fe on the MX-80 under the time-scales involved, which could result in Fe enrichment with reduced swelling properties.

Under “early-life” and “mid-life” phases the bentonite in direct contact with the steel appears green, indicating a Fe^{2+} rich composition. Magnetite (Fe_3O_4) formed over the coupon surface observed by the black precipitant on the steel surface during post-mortem/sub-sampling. According to thermodynamic principles, the formation of the magnetite layer on carbon-steel normally acts as a passivation layer, Fe is subsequently released slowly into the bulk solution with (hydr)oxides forming. What appears with respect to the interface, is that the carbon-steel in direct contact with the MX-80 reduces the passivation effectiveness. Therefore, the bentonite acts as a “sponge” for the diffusion Fe ions. Nonetheless, magnetite formation indicates that the diffusion rate is non-linear and the rate will slow when magnetite

formation is fully established. The corrosion products within the bentonite appear to be Goethite observed by examining the hyperfine field interaction of ~48 Tesla, this is supported by the oxidised pseudomorph signature, Maghemite, in heat treated XRD samples. Both analyses indicate that Fe is partially integrated into the bentonite as well as Fe being basal edge bound. This indicates that ferrous hydroxide is also present (FeOH) due to the edge sites being occupied, this supports the observations of a meta-stable ferrous (hydr)oxide. Furthermore, XRD 002/003 intensity ratios also display that partial integration of Fe into the octahedral layer has occurred. This indicates that time is important in the alteration characteristics over longer exposure durations the bentonite is likely to become progressively enriched with Fe. This is thought to increase the lattice stress which may induce 2:1 to 1:1 mineral alteration (Berthierine) with reduced swelling and cation retention properties. ICP analysis also indicates that Na concentration increases with increasing distance from the steel coupon, this indicates that Fe ions replace and displace the basal adsorbed Na cations (i.e. Fe enrichment within the basal exchanger). ICP and EDX measurements also indicated that Mg increased in the outer zone with Fe higher at the interface which supports partial replacement within the octahedral layer. Over time, divalent cation enrichment will impact the DDL which was observed by XRD peak shift of the air-dried sample toward 15Å, ultimately reducing the plasticity and free swelling ability of the MX-80. Geomechanical measurements conducted on the sub-sample indicate there is a slight reduction in the plasticity and swell index, this is higher for high thermal exposure, but the parameters remain above the lower design limits. This however does not indicate that the temporal factor will not inhibit these parameters further. Overall the presence of double-layer hydroxides, divalent cations in the exchanger and within the octahedral layer reduces the overall negative charge supported by the lower CEC measurements. Indicating that the materials ability to retain cations are slightly inhibited, however the CEC measured here are still higher than most clay types. Time-lapse photography was implemented to examine the oxidation potential of the “green” bentonite taken from the high temperature phases. It was observed that upon exposure to atmospheric/ ambient thermal conditions, in a dry state, the sample did not oxidise. However, upon hydration it appeared that oxidation occurred, indicating that the Fe within the bentonite matrix is meta-stable. The corrosion products within the bentonite are determined to be poorly crystalline, which is likely due to the rapid formation under the “early-life” and “mid-life” conditions.

Crystallographic observations of the smectite component after the relatively short-term interface exposure indicated little alteration of the high-charge/ high surface area component.

This was concluded from the characteristic d-spacing upon glycolation (17Å). This indicates that the bulk materials ability to swell/ self-heal is not affected post exposure to the experimental conditions. Furthermore, the clay component remained interstratified with smectite-illite, similar to the control material profile. The type of smectite had changed slightly, irrespective of the unchanged swelling, interface sub-samples indicated that the smectite had become Ferro-saponitic whereas the mid-outer zones remained its Mg-Saponitic profile; this is supported by ICP, EDX and XRD as stated earlier.

Examination of the non-clay component indicated high feldspar dissolution which was greatest in the “mid-life” phase due to the dynamic hydrothermal environment at the interface. Na-rich feldspar (Albite) remained predominant in the outer zones. Cristobalite dissolution occurred at the higher temperature conditions with quartz concentrations higher in the outer zones upon cooling. Siliceous products post THC supports the premise that cementation between particles increases post THC-exposure (upon cooling).

Overall, Fe (hydr)oxides are present within the interface and mid-zones with ferrosaponite-type smectite dominating the clay phase in the interface zone. There is no Fe-rich clay alteration (i.e. 2:1 to 1:1) was observed during the interface exposure phases. (Hydr)oxides and ion exchange indicates slight layer charge alteration. However, the material remains highly swelling with other physicochemical properties remaining largely unchanged. Feldspar dissolution may indicate that insitu mass loss could occur thus resulting in an overall density loss. On a physicochemical scale, it appears that the bentonite does not change significantly, however the impact of siliceous “fusing”, reduction of the DDL and layer charge reduction will inhibit the bulk geomechanical properties. It appears from this study that the most significant stage of the barriers life is exposure to mid-life conditions, this phase experiences the highest thermal conditions as well as high saline/ corrosion rich pore composition. It was therefore necessary to carry forward the boundary conditions of the inferred “mid-life” conditions to examine the impact on the geomechanical parameters and barrier functionality. More work is necessary to further investigate the impact of a completely reduced, Fe-rich, environment on the engineering performance of the barrier. Results indicate that silica and silica rich mineral dissolution may have a direct impact on the geomechanical performance of the barrier. From a UK concept perspective, pH conditions must be kept within the neutral/ low alkalinity range as well as temperature is kept sufficiently low (<100°C) in order to prevent reprecipitation and fusing of the clay platelets. Redox conditions cannot be controlled within the insitu EBS system and therefore the effects of a Fe²⁺ rich

environment should be further investigated, provided that a carbon steel canister is implemented.

8.3. Constant volume geomechanical batch tests finding summary:

From the geomechanical testing, it appears that thermal loading and high saline exposure has a greater impact on the bulk physical properties than corrosion alone. The relatively short exposure durations conducted in this testing compared to the expected in-situ life-span may observe geomechanical alterations related to corrosion exposure. However, the immediate effects on the barrier are related to the exposure of the high thermal loading and access to high electrolyte concentrations within the bulk solution. The test which isolated the effects of thermal loading of the mid-life conditions on the geomechanical properties of the MX-80 displayed a 35% reduction in the swelling pressure, 30% reduction in the rebound kinetics and a 7% increase in stiffness. This indicated, with support from the physicochemical interface studies, that thermal exposure induces inter-particle fusing due to the dissolution and re-precipitation of silica as well as thermally induced layer collapse.

The tests that isolated the mid-life high saline/ high thermal loading conditions displayed a 50% reduction in swelling pressure, 56% reduction in axial rebound kinetics and a 64% increase in the sample stiffness. This indicates that layer collapse due to the reduction of the DDL due to osmotic pressure imbalance in high saline solutions as well as the fusing of the inter-particle fusing of the interlayer particles impact the self-healing and stiffness than thermal loading alone.

The batch which isolated the effects corrosion and thermal effects indicated the least degree of alteration to swelling. The swelling pressure displayed only an 8% reduction with a 5% reduction in axial rebound kinetics and a 7% increase in stiffness. Thus, corrosion integration and thermal exposure does not affect the bulk geotechnical properties on a short-term time-scale.

Combined boundary conditions which closely resembled the “mid-life” conditions gave rise to the most significantly affected bulk geotechnical properties of the MX-80 block. Overall this batch resulted in a 58% reduction in swelling pressure, 16% reduction in axial kinetics and a 79% increase in stiffness. Axial rebound was the only parameter that appeared not to be adversely affected which is due to the presence of corrosion and the volume uptake upon hydration.

Overall, the measurements obtained from this experimental study did not indicate that the geomechanical characteristics of the smectite deviated below the minimum design

parameters. Post THC inferred permeability appeared to remain within the control/ unaltered magnitude range. It is clear that the physical changes to the pore-water during thermal exposure such as the kinematic viscosity and interlayer expansion, results in a higher intrinsic permeability which is reversible. This is assuming that the mass loss due to erosion and mineral dissolution remains low. Overall, short-term exposure to “mid-life” conditions reduces the bulk physical properties by 50-60% with a large degree of stiffening. As stated, the swelling pressure magnitudes remain within the design limits set out by leading concepts. However, the stiffening measurements are of concern as the combined environmental factors cause the sample to become significantly less ductile than the control. At present, there is no comparable measurement in other studies or design limitations on barrier stiffness but it is widely stated that stiffening is unfavourable due to the transfer kinetics of stress into the canister via the barrier if in the event of host rock displacement.

It must be noted that the experimental conditions explored do not completely replicate the conditions that would be found in-situ of a GDF as well as the expected time-scales for the lifespan of the EBS. Therefore, alteration results given here are relevant to the intrinsic properties of the bentonite over a short duration with respect to the overall life of the EBS. However, alterations are not expected reduce linearly over geological time scales. Therefore, with the evidence from natural analogues, and computational data, the barrier is likely to uphold its design function providing thermal exposure is kept low, ground water composition is low in potassium and higher valence electrolytes and the pH of the near-field environment is kept in the neutral to mildly alkaline range. The findings presented here display little crystallite, physicochemical and geomechanical alteration after exposure to several experimental variables over relatively short durations. The findings agree with that of Ishidera et al (2008) who subject MX-80/ C-steel to 10 years. Even after 10 years of THC exposure at the interface, the physicochemical characteristics did not change significantly.

8.4. Recommended areas for further exploration:

Throughout the experimental work outlined above there was several areas highlighted for further and additional scientific exploration with respect to the longevity of the engineered barrier interface.

During interface and constant volume testing it became progressively apparent that it was difficult to maintain/ achieve completely reduced conditions. Consequently, it was clear that an additional experimental programme which chemically reduces the interface after corrosion has diffused into the bentonite is needed in order to replicate very-late life

conditions. This was evident due to the time-scales required before complete reduction is achieved that accelerated activation energies within the system are required. The difficulty in this is maintaining the reduced conditions during high thermal exposure and geomechanical testing i.e. swelling pressure measurements etc. Ultimately, the conditions need to be reduced and tested within an isolated/ oxygen free environment. By reducing the Fe within both the bentonite matrix and the structure, the material will have altered layer charge and structural lattice stresses due to ionic radii change. This will enable measurements the bulk physical characteristics as well as the realistic physicochemical characterisation of the intrinsic conditions after several thousand years of exposure. The reduction of the Fe within the bentonite is possible via chemical reduction methods such as the sodium dithionite or hydroxylamine method, with Na-citrate preserving the reduced state. By chemically reducing the bentonite within the aqueous solution, the difficulty is then either compacting the sample to the insitu parameters before conducting the geotechnical measurements or designing a system to reduce the sample while in a compacted state. The latter scenario gives rise to maintaining reduced sample homogeneity. Nonetheless, investigating the intrinsic geotechnical properties of the MX-80 after corrosion integration and reduction needs to be investigated in order to assess the engineering function of the barrier after thousands of years into the operational future. By doing so, and using the measurements obtained from this study, will gain an insight into the operational characteristics under both short and long-term (on a geological time-scale) conditions.

Additionally, it was clear from this study that the influence of microbes within the barrier and the percolating groundwater would influence the physicochemical environment. Swelling pressure measurements under a complex saline environment (high valence cations) indicated a drop below the limit set out for the SKB concept to inhibit microbial development within the Bentonite (2MPa). Microbial development is thought to influence the bulk geomechanical properties due to the influence on the density and porosity due to consumption of the secondary minerals present within clay matrix. Furthermore, Fe, sulphate reducing and hydrogen feeding/ producing bacteria are known to exist in terrestrial soils which also related to the EBS environment due to the corrosion, presence of secondary minerals and hydrogen production during the reducing environment. Therefore, microbial colonies active within the barrier/ circulating groundwater may accelerate Fe-reduction as well as causing bulk physical alterations to the barrier such as porosity increase and density reduction. These bulk physical alterations along with the impact from the thermo-chemical environmental may inhibit the barriers design functionality.

10. Bibliography

Adamcova and Kolaoikova (2006). Alteration processes in bentonites: Mineralogical and structural changes during long-term and short-term experiments. Mineralogy and mineral resources- Faculty of science and the Czech geological survey. Czech republic

Ahn and Jo (2009). Influence of exchange cations on hydraulic conductivity of compacted bentonite. Applied clay science. 44. 144-150

Akesson (2012). Temperature buffer test. SKB technical report. Report no: TR-12-04

Alther. G., Evans, C., Fang, Y., Witmer, K. 1985, Influence of Inorganic Permeants upon the Permeability of Bentonite. ASTM. STP874

Amitrano (2005). Long term behaviour of a gallery within a clay repository: impact of stress and the water saturation perturbations. Clays in natural and engineered barriers for radioactive waste confinement- International meeting. France

Alexandre S. Anastácio, Amina Aouad, Patrik Sellin, José Domingos Fabris, Faïza Bergaya, Joseph W. Stucki. (2008). Characterisation of a redox-modified clay mineral with respect to its suitability as a barrier in radioactive waste confinement. Applied clay science. 39. 172-179

Andra Dossier (2005). Andra research on the geological disposal of high-level long-lived radioactive waste- Results and perspectives

Antunes, R.A., Costa, I., de Faria, D.L.A. 2003. Characterisation of corrosion products formed on steels in the first months of atmospheric exposure. Materials Research 6, 403–408.

Arasan and Yetimoglu (2008). Effect of inorganic salt solutions on the consistency limits of two clays. Engineering environmental science. 32. 107-115

Atkinson (2002). Soil mechanics-classification. Available at:
<http://environment.uwe.ac.uk/geocal/SoilMech/classification/soilclas.htm> (Accessed on 24 August 2016)

Badaut, D., Besson, D., Decarreau, A., Rautureau, R., 1985. Occurrence of a ferrous trioctahedral smectite in recent sediments of Atlantis II Deep, Red Sea. Clay Miner. 20, 389–404.

- Min-Hoon Baik, Won-Jin Cho, Pil-Soo Hahn. (2007). Erosion of bentonite particles at the interface of a compacted bentonite and a fractured granite. *Engineering geology*. 91. 229-239
- Bailey, W. 1980. Structures of layer silicates. In: Brindly and Brown. *Crystal structures of clay minerals and their X-ray identification*. Min Soc
- Bain and Morgan (1969). The role of thermal analysis in the evolution of impure clay deposits as mineral raw materials. *Clay minerals*. 8. 171
- Barbour, S., Fredlund, D., Pufahl, D. (1991). The osmotic role in the barrier behaviour of swelling clay soils. *Proceedings of the NATO advances research workshop*. Greece. 97- 139
- N Barnel, T Lassabatère, C Le Potier, P Sémété. (2004). Sensitivity analysis on the thermal-hydraulic parameters governing the saturation of an engineered clay barrier system. *Applied clay science*. 26. 209- 217
- Bauer, A., Berger, G., 1998. Kaolinite and smectite dissolution rate in high molar KOH solutions at 35 and 80°C. *Applied Geochemistry* 13, 905–916.
- Beaufort, D., Berger, G., Lacharpagne, J.C. & Meunier, A. (2001): An experimental alteration of montmorillonite to a di + trioctahedral smectite assemblage at 100 and 200 °C. *Clays and Clay minerals* 36, 211-225.
- Belkhiri, S & Guerza, M & Chouikh, S & Boucheffa, Y & Mekhalif, Z & Delhalle, J & Colella, C. (2012). Textural and structural effects of heat treatment and gamma irradiation on Cs exchanged NaX zeolite, bentonite and their mixtures. *Microporous and mesoporous materials*. 161. 115- 122
- Bell (1996). Lime stabilization of clay minerals and soils. *Engineering geology*. 42. 223- 237
- Bergaya, F and Lagly, G. (2006). *Handbook of clay science*. Elsevier. Oxford
- O. Bildstein, L. Trotignon, M. Perronnet, M. Jullien . (2006). Modelling iron-clay interactions in deep geological disposal conditions. *Physics and chemistry of the earth*. 31. 618- 625
- Birgersson and Karnland (2009). Ion equilibrium between montmorillonite interlayer space and an external solution- Consequences for diffusional transport. *Geochimica et Cosmochimica Acta* 73. 1908-1923

Birgersson and Wersin (2014). KBS-3H reactive transport modelling of iron-bentonite interactions, an update for the Olkiuoto case. SKB technical report. Report no: 2013-02

Börjesson (2009). Design premises for a KBS-3V repository based on results from the safety assessment SR-Ca and some subsequent analysis. SKB technical report. Report no: TR-09-22

Börjesson (2010). Design, production and initial state of the buffer. SKB technical report. Report no: TR-10-15

Börjesson (2011). Long-term safety for the final repository for spent nuclear fuel at Forsmark. SKB technical report. Report no: TR-11-01

Börjesson (2014). ASPO hard rock laboratory annual report. SKB technical report. Report no: TR-15-10

Bouchet, A., Cassagnabère, A. & Parneix, J.C. (2004): Batch experiments: results on MX80. *In: Ecoclay II: Effect of cement on clay barrier performance phase II*. Final report. European contract FIKW-CT-2000-28.

Bowers T.S., Jackson K.J. & Helgeson H.C. (1984) *Equilibrium Activity Diagrams for Coexisting Minerals and Aqueous Solutions at Pressures and Temperatures to 5 kb and 600°C*. Springer-Verlag, Berlin.

Bradbury and Baeyens (2003). Nuclear energy and safety research department laboratory for waste management. NAGRA technical report

Bradbury and Baeyens (2011). Physico-chemical characterisation data and sorption measurement of Cs, Ni, Eu, Th, U, Cl, I and Se on MX-80 bentonite. NAGRA technical report 09-08

Bradbury, M., Berner, U., Curti, E., Hummel, W., Kosakowski, G., Thoenen, T. (2014). The long term geochemical evolution of the near-field repository. NAGRA technical report 12-01

Bro, A., Stewart, J., Pradel, D. (2013). Estimating undrained strength of clays from direct shear testing at fast displacement rates. Geo-congress- ASCE

Burghignoli, A., Desideri, A. & Miliziano, S. (2000). A laboratory study on the thermomechanical behaviour of clayey soils. *Can. Geotech. J.* 37, No. 4, 764–780.

Carlson (2004). Bentonite mineralogy parts 1 and 2. Posiva report. 2004-02

Liisa Carlson, Ola Karnland, Virginia M. Oversby, Andy P. Rance, Nick R. Smart, Margit Snellman, Marjut Vähänen, Lars O. Werme. (2007). Experimental studies of the interactions between anaerobically corroding iron and bentonite. *Physics and Chemistry of the Earth*. 32. 334- 345

Liisa Carlson, Ola Karnland, Virginia M. Oversby, Andy P. Rance, Nick R. Smart, Margit Snellman, Marjut Vähänen, Lars O. Werme. (2008). Experimental studies on the interactions between anaerobically corroding iron and bentonite. SKB technical report. Report no: TR-08-28

Cekerevac, C., Laloui, L. & Vulliet, L. (2003). A new temperature controlled triaxial apparatus. *Proc. 3rd Int. Symp. Deformation Characteristics of Geomaterials*, Lyon, pp. 133–137.

D. Charpentiera, K. Devineau, R. Mosser-Ruck, M. Cathelineau, F. Villiéras. (2006). Bentonite-Iron interactions under alkaline condition: An experimental approach. *Applied clay science*. 32. 1-13

W.J. Cho, J.O. Lee, K.S. Chun. (1999). The temperature effects on hydraulic conductivity of compacted bentonite. *Applied clay science*. 14. 47-58

Won-Jin Cho, Jae-Owan Lee, Heui-Joo Choi. (2012). Radionuclide migration through an unsaturated clay buffer under thermal and hydraulic gradients for a nuclear waste repository. *Annals of Nuclear Energy*. 50. 71- 81

Ciesielski, H & Sterckeman, Thibault & Santerne, M & Willery, J.P. (1997). A comparison between three methods for the determination of cation exchange capacity and exchangeable cations in soils. *Agronomie- EDP Sciences*. 17. 9-16

Claret, F., Bauer, A., Schafer, T., Griffault, L., Lanson, B., 2002. Experimental investigation of the interaction of clays with high-pH solutions: a case study from the Callovo-Oxfordian formation, Meuse-Haute Marne underground laboratory (France). *Clays and Clay Minerals* 50, 633–646.

Colten V.A., 1986. Hydration States of Smectite in NaCl Brines at Elevated Pressures and Temperatures. *Clays and Clay Minerals*, Vol. 34:4, p. 385-389

Cornell and Schwertmann (2000). The Iron oxides, properties, reactions, occurrences and uses. Wiley-VCH. Germany

CoRWM report to the government (2009). Geological disposal of higher activity radioactive wastes. CoRWM document 2550

CoRWM report to the government (2009). Report on national research and development for interim storage and geological disposal of higher activity radioactive wastes and management of nuclear materials. CoRWM document 2543

Crerar, D.A., Anderson, G.M., 1971. Solubility and solvation reactions of quartz in dilute hydrothermal solutions. *Chem. Geol.* 8, 107– 122.

J Cuevas, M.V Villar, M Martín, J.C Cobeña, S Leguey. (2002). Thermo-hydraulic gradient on bentonite: distribution of soluble salts, microstructure and modification of the hydraulic and mechanical behaviour. *Applied clay science.* 22. 25- 38

Robert J. Cuss, Jon F. Harrington, Dave J. Noy, Anders Wikman, Patrik Sellin. (2011). Large scale injection test (Lasgit): Results from two gas injection tests. *Physics and Chemistry of the earth.* 36. 1729- 1742

Delage, Pierre & Sultan, Nabil & Jun, yu. (2012). On the thermal consolidation of Boom clay. *Can Geotech.* 37. 343- 354

P. Delage, Y.J. Cui, A.M. Tang. (2010). Clays in radioactive waste disposal. *Journal of Rock Mechanics and Geotechnical Engineering.* 2. 111- 123

Department of Energy and Climate Change report (2011). Managing radioactive waste safely: Implementing geological disposal annual report.

Department of Energy and Climate Change report (2012). Managing radioactive waste safely: Implementing geological disposal annual report.

Department of Energy and Climate Change report (2014). Implementing Geological Disposal: A framework for the long-term management of higher activity radioactive waste

Dimond, S and Kinter, E. (1963), Characterisation of montmorillonite saturated with short-chain amine cations: inspection of basal spacing measurements. TENTH NATIONAL CONFERENCE OF CLAYS AND CLAY MINERALS

Domitrovic, D and Kovacevic, B. (2013) The relationship between swelling and shear strength properties and bentonites. Proceedings of the 18th International Conference on Soil Mechanics and Geotechnical Engineering, Paris

Dorothy and Starkey (1971). Reactivity of clay minerals with acids and alkalis. *Clays and clay minerals*. 19. 321- 333

Drief, A., Martinez-Ruis, F., Nieto, F., Velilla Sanchez, N., 2002. Transmission electron microscopy evidence for experimental illitization of smectite in K-enriched seawater solution at 50°C and basic pH. *Clays and Clay Minerals* 50, 746–756.

Drits and Manceu (2000). A model for the mechanism of Fe(iii) to Fe(ii) reduction in dioctahedral smectites. *Clays and clay minerals*. 48. 185- 195

Dudek, T. (2006). Interstratified kaolinite-smectite: nature of the layers and mechanism of smectite kaolinization. *American mineralogist*. 91. 159- 170

Duek, A., Johannesson, L., Kristensson, O., Olsson, S. (2011). Report on hydro-mechanical and chemical-mineralogical analyses of bentonite buffer in canister retrieval test. SKB technical report. Report no: TR-11-07

Dutton (2013). CoRWM visit to France. Meeting minutes

M. Darby Dyar, David G. Agresti, Martha W. Schaefer, Christopher A. Grant, Elizabeth C. Sklute. (2006). Mossbauer Spectroscopy of Earth and Planetary Materials. *The Annual Review of Earth and Planetary Science*. 34. 83-125

Eslinger and Peaver (1988). *Clay minerals for petroleum geologists and engineers*. Society for sedimentary. Short course notes. 22

Fernandez and Villar (2010). Geochemical behaviour of a bentonite barrier in the laboratory after up to 8 years of heating and hydration. *Applied geochemistry*. 25. 09- 824

Fernandez (2008). Geochemical analysis of samples of MX-80 compacted bentonite from block 13/ parcel A2 of the LOT experiment, ASPO hardrock laboratory, Sweden. NAGRA technical report- NAB 08-08

Forpro (2005). Long-term behaviour of argillaceous rocks: evaluation of “simulated creep”. Clays in natural and engineered barriers for radioactive waste confinement- International meeting. France

Fox (2010). Oxide fuel. NDA technical report. Report no: SMS/TS/C2/G0/001

Fredlund, D., Xing, A., Huang, S. (1994). Predicting the permeability function for unsaturated soils using the soil-water characteristic curve. Canadian Geotechnical Journal. 31 (3). 521- 532.

Fritz, B., 1981. Etude thermodynamique et modelisation des reactions hydrothermales et diagenetiques. Thesis, Universite Louis Pasteur Strasbourg, France, Sciences Ge´ologiques. MemoireNo. 65.

Galle (2000). Gas breakthrough pressure in compacted Fo-Ca clay and interfacial gas overpressure in waste disposal context. Applied clay science. 17. 85- 97

Gatmiri and Hoor (2005). Excavation effect on thermos-hydro-mechanical behaviour of geological barrier. Clays in natural and engineered barriers for radioactive waste confinement- International meeting. France

A. Gaudin, S. Gaboreau, E. Tinseau, D. Bartier, S. Petit, O. Grauby, F. Foct, D. Beaufort. (2009). Mineralogical reactions in the Tournemire argillite after insitu interaction with steels. Applied clay science. 43. 196-207

Genuchten (1980). A closed-form equation for predicting the hydraulic conductivity of unsaturated soils. Soil science society of America. 44

Ghasemzadeh and Gatmiri (2005). Nonlinear behaviour of geological and engineered barriers. Clays in natural and engineered barriers for radioactive waste confinement- International meeting. France

Glaeser R., Mering J., 1968. Homogeneous hydration domains of the smectites. Acad. Sci.,Paris 267, 436-466.

Gomez and Villar (2010). Geochemical and mineralogical changes in compacted MX80 bentonite submitted to heat and water gradients. Applied Clay science. 47. 400- 408

Goomez and Villar (2010). Geomechanical and mineralogical changes in compacted MX-80 bentonite submitted to heat and water gradients. Informe Tecnicos Ciemat 1199

Grim and Rowland (1980). Differential thermal analysis of clay minerals and other hydrous materials

Grive, M., Duro, L., Domenech, C., Salas, J. (2009). Model of the Redox conditions in the near-field of a cementitious geological disposal facility (GDF)- AMPHOS Final report

Gueven N, Carney L L., Ridpath B E, 1987. Evaluation of geothermal drilling fluids using a commercial bentonite and a bentonite/saponite mixture. Contr. Rep. Sandia 86-7180, SANDIA Nat. Labs. Albuquerque, New Mexico, USA

Guillaume, Damien & Neaman, A & Cathelineau, Michel & Mosser, Regine & Peiffert, C & Abdelmoula, Mustapha & Dubessy, J & Villiéras, Frédéric & Baronnet, A & Michau, Nicolas. (2003). Experimental synthesis of chlorite from smectite at 300°C in the presence of metallic Fe. Clay minerals. 38. 281-302

Gustavo A Cragolino, Sitakanta Mohanty, Darrell S Dunn, Narasi Sridhar, Tae M Ahn. (2000). An approach to the assessment of high-level radioactive waste containment- Waste package degradation. Nuclear Engineering and Design. 201. 289- 306

Hall and Astill (1989). Adsorbtion of water by homoionic exchange forms of Wyoming montmorillonite. 37. 355- 363

Harrington and Horseman (2003). Gas migration in KBS-3 buffer bentonite. SKB technical report. Report no: TR-03-02

Harris and White (2007). X-Ray diffraction techniques for soil mineral identification. Soil science society of America. 5. 1-36

Hedin and Börjesson (2004). Integrated near-field evolution for a KBS-3 repository. SKB technical report. Report no: TR-04-36

Hella, P., Pitkanen, P., Lofman, J., Partamies, S., Vuorinen, U., Wersin, P. (2014). Safety case for the disposal of spent fuel at Olkiluoto- Definition of reference and bounding groundwaters, buffer and backfill porewaters. Posiva report. 2014-04

Hensen and Smit (2002). Why clays swell. *Journal of physics and chemistry*. 106. 12664-12667

H.-J Herbert, J Kasbohm, H.C Moog, K.-H Henning. (2004). Long-term behaviour of the Wyoming bentonite MX-80 in high saline solutions. *Applied clay science*. 26. 275-291

Horst-Juergen Herbert, Joern Kasbohm, Heinz Sprenger, Ana María Fernández, Christian Reichelt. (2008). Swelling pressures of MX-80 bentonite in solutions of different ionic strength. *Physics and chemistry of the earth*. 33. 327-342

Hicks, T., White, M., Hooker, P. (2009). Role of Bentonite in determination of thermal limits on geological disposal facility design. *Galson sciences*. Report no: 0883-1

Hoffman, J. & Hower, J. (1979): Clay mineral assemblages as low grade metamorphic geothermometer – Application to the thrust-faulted disturbed belt of Montana. *In: P.A. Scholle & P.R. Schluger (eds.): Aspects of Diagenesis. SEPM Special Publication 26, 55-79.*

Sander, Michael & B. Hofstetter, Th & Gorski, C & Sosedova, Y & Voegelin, Andreas. (2014). REDOX properties of iron-bearing clays and MX-80 bentonite- electrochemical and spectroscopic characterisation. *NAGRA technical report 13-03*

Michael Holmboe, Susanna Wold, Mats Jonsson, Porosity investigation of compacted bentonite using XRD profile modeling, *In Journal of Contaminant Hydrology, Volume 128, Issues 1–4, 2012, Pages 19-32*

Holton, D., Dickinson, M., Hoch, A., Cowper, M., Thetford, R., Allinson, H., Corckett, G., Cairns, M., Roberts, D., Padovani, C., Johnson, M., Carr, N., Jowett, J., Finch, C., Walsh, C., Southgate, B., Wood, P., Young, A. (2012). Project Ankhiale: Disposability and full life cycle implications of high-heat generating UK wastes. *NDA/ Amec report*. Report no: RP51

Howard, J.J. & Roy, D.M. (1985): Development of layer charge and kinetics of experimental smectite alteration. *Clays and Clay Minerals* 33, 81-88.

Hoxha (2005). Mechanical behaviour of unsaturated meuse/ haute marne argillite. *Clays in natural and engineered barriers for radioactive waste confinement- International meeting. France*

- Huertas, F.J., Caballero, E., Jiménez de Cisneros, C., Huertas, F., Linares, J., 2001. Kinetics of montmorillonite dissolution in granitic solution. *Applied Geochemistry* 16, 397–407.
- Hultquist G, Szakálos P, Graham M J, Sproule G I, Wikmark G, 2009. Detection of hydrogen in corrosion of copper in pure water. In *Proceedings of the 17th International Corrosion Congress, Las Vegas, Nevada, 6–10 October 2008*. Houston, TX: NACE International, 2378–2386.
- Huo, Dongfang & Fialips, Claire-Isabelle & Stucki, Joseph. (2004). Effects of structural Fe oxidation state on physical-chemical properties of smectites: evidence from infra-red spectroscopy. *Japanese society of soil physics*. 96. 3- 10
- Hyndmann and Peacock (2003). Serpentinization of the forearc mantle. *Earth and Planetary Science*. 212. 417- 432
- Icenhower and Dove (2000). The dissolution kinetics of amorphous silica into sodium chloride solutions: effects of temperature and ionic strength. *Geochimica cosmochimica acta*. 24. 4193- 4203
- Idiart, A., Maia, F., Arcos, D. (2013). Geochemical evaluation of the near-field for future HLW repository at Olkiluoto. Posiva report. 2013-05
- Wersin, P & H Johnson, L & Schwyn, Bernhard & Berner, Urs & Curti, Enzo. (2017). Redox Conditions in the Near Field of a Repository for SF/HLW and ILW in Opalinus Clay. Nagra
- Inglethorpe, S., Morgan, D., Highley, D., Bloodworth, A. (1993). Industrial minerals laboratory manual BENTONITE. British geological survey technical report- mineralogy and petrology series WG/93/20
- Inoue A, Kohyama N, Kitagawa R, Watanabe T, 1987. Chemical and morphological evidence for the conversion of smectite to illite. *Clays and Clay Minerals*, Vol. 35 No. 2 (pp. 111–120)
- Takamitsu Ishidera, Kenichi Ueno, Seiichi Kurosawa, Tadahiro Suyama. (2008). Investigation of montmorillonite alteration and form of iron corrosion products in compacted bentonite in contact with carbon steel for ten years. *Physics and chemistry of the earth*. 33. 269- 275

Joeckel, R.M., Clement, B.J.A., VanFleet Bates, L.R., 2005. Sulfate-mineral crusts from pyrite weathering and acid rock drainage in the Dakota formation and Graneros Shale, Jefferson County, Nebraska. *Chemical Geology* 215, 433–452.

Johannesson (2002). ASPO HRL- Manufacturing of bentonite buffer for the prototype repository. SKB technical report. Report no: IPR-02-19

Lars-Erik Johannesson, Lennart Börgesson, Reza Goudarzi, Torbjörn Sandén, David Gunnarsson, Christer Svemar . (2007). Prototype repository: A full scale experiment at ASPO HRL. *Physics and Chemistry of the Earth*. 32. 58- 76

Johannesson, L., Sanden, T., Dueck, A., Ohlsson, L. (2010). Characterisation of a backfill candidate material, IBECO-RWC-BF. SKB technical report. Report no: TR-10-44

Johnson and King (2003). Canister options for the disposal of spent fuel. NAGRA technical report 02-11

Johnston, R.M. & Miller, H.G. (1985): Hydrothermal stability of bentonite-based buffer materials. AECL report AECL-8376. AECL, Pinawa, Manitoba, Canada.

Joint DEFRA, BERR and the devolved administrations of Wales and Northern Ireland report (2008). A Framework for implementing Geological Disposal. CM 7386

Jorand (2005). The thermal conductivity and hydraulic properties of the argillites. Clays in natural and engineered barriers for radioactive waste confinement- International meeting. France

G Kamei, C Oda, S Mitsui, M Shibata, T Shinozaki. (1999). Fe(II)- Na ion exchange at interlayers of smectite: adsorption desorption experiments and a natural analogue. *Engineering Geology*. 54. 15-20

Karnland (1998). Bentonite swelling pressure in strong NaCl solutions. Posiva technical report. 98.01

Karnland (1998). Bentonite swelling pressure in strong NaCl solutions. Posiva report. 98-01

Karnland (2010). Chemical and mineralogical characterisation of the bentonite buffer for the acceptance control procedure in a KBS-3 repository. SKB technical report. Report no: TR-10-60

Karnland (2010). Chemical and mineralogical characterisation of the bentonite buffer for the acceptance control procedure in a KBS-3 repository. SKB technical report. Report no: TR-10-60

Karnland, O., Olsson, S., Nilsson, U. (2006). Mineralogy and sealing properties of various bentonites and smectite-rich clay materials. SKB technical report. Report no: TR-06-30

Ola Karnland, Siv Olsson, Ulf Nilsson, Patrik Sellin. (2007). Experimentally determined swelling pressures and geochemical interactions of compacted Wyoming bentonite with highly compacted Wyoming bentonite with highly alkaline solutions. *Physics and chemistry of the earth*. 32. 275-286

Karnland, O., Olsson, S., Dueck, A., Birgersson, M., Nilsson, U., Hakansson, T., Pedersen, K., Nilsson, S., Eriksen, T., Rosborg, B. (2011). Long-term test of buffer material at the ASPO HRL, LOT project. SKB technical report. Report no: TR-09-31

Karnland, O., Olsson, S., Nilsson, U. & Sellin, P. (2007): Experimentally determined swelling pressures and geochemical interactions of compacted Wyoming bentonite with highly alkaline solutions. *Physics and Chemistry of the Earth, Parts A/B/C* 32, 275-286.

Kehren R., Schainberg I. (1975). Water vapor isotherms and heat of immersion of Na/Camontmorillonite systems. *Clays and Clay minerals* 23, 193-200.

Kim and Tan (2011). *Principles of soil chemistry*. Taylor and Francis group. London

Kim, J., Dong, H., Seabaugh, J., Newell, S.W. & Eberl, D.D. (2004): Role of microbes in the smectite-to-illite reaction. *Science* 303, 830-832.

King (2008). Corrosion of carbon steel under anaerobic conditions in a repository for SF and HLW in opalinus clay. NAGRA technical report 08-12

King and Watson (2010). Review of the corrosion performance of selected metals as canister materials for UK spent Fuel and/or HLW. Report no: QRS-1384J-1

King, F. (2008). Corrosion of carbon steel under anaerobic conditions in a repository for

Kiviranta and Kumpulainen (2011). Quality control and characterisation of bentonite materials. Posiva report. Report no: 2011-84

Klinkenberg (2005). Correlation of mechanical behaviour to mineralogical and microstructural characteristics. Clays in natural and engineered barriers for radioactive waste confinement- International meeting. France

Koch (2008). European bentonite as alternatives to MX-80. Science and technology series. 334. 23- 30

Koch, C.B., Oxborrow, C.A., Mørup, S. (1995). Magnetic properties of ferroxhyte. Physics and Chemistry of Materials. 22. 333-341

Kodama, H., De Kimpe, C.R., Dejou, J., 1988. Ferric saponite in a gabbro saprolite at Mont Blanc Magantic, Quebec. Clays Clay Miner. 36, 102–110.

Kohyama, N., Shimoda, S., Sudo, T., 1973. Iron-rich saponite ferric and ferrous forms. Clays Clay Miner. 21, 229–237.

Kolaříková, I., Švandová, J., Příkryl, R., Vinšová, H., Jedináková-Křížová, V., Zeman, J., 2010. Mineralogical changes in bentonite barrier within mock-Up-CZ experiment. Applied Clay Science 47 (1–2), 10–15.

Kristensson and Borgesson (2015). Canister retrieval test. SKB technical report. Report no: TR-14-19

Kumpulainen, S., Kiviranta, L., Carlsson, T., Muurinen, A., Svensson, D., Sasamoto, H., Yui, M., Wersin, P., Rosch, D. (2010). Long-term alteration of bentonite in the presence of metallic iron. SKB technical report. Report no: TR-10-527

Kull, H., N. Jockwer, C.-L. Zhang, Y. Wileveau, and S. Pepa. “Measurement of Thermally-Induced Pore-Water Pressure Increase and Gas Migration in the Opalinus Clay at Mont Terri.” Physics and Chemistry of the Earth. Vol. 32, Nos. 8–14. pp. 937–946. 2007.

Laaksonen (2009). MANU- Purchase of bentonite- process description. Posiva report. 2009-64

Landolt, D., Davenport, A., Payer, J., & Shoemith, D. (2009). A review of materials and corrosion issues regarding canisters for disposal of spent and high-level waste in opalinus clay. Nagra technical report 09-02

- Lantenois S. (2003). Réactivité fer métal/smectites en milieu hydraté à 80°C. Ph.D. thesis, University of Orleans.
- Youn-Myoung Lee, Chul-Hyung Kang, Yong-Soo Hwang. (2007). Nuclide release from an HLW repository: Development of a compartment model. *Annals of Nuclear Energy*. 34. 782-791
- Jae Owan Lee, Jin Gyu Lim, Il Mo Kang, Sangki Kwon. (2012). Swelling pressure of compacted Ca-bentonite. *Engineering geology*. 129- 130. 20- 26
- Leupin, Olivier & Birgersson, Martin & Karnland, Ola & Korkeakoski, Petri & Sellin, Patrik & Mäder, Urs & Wersin, Paul. (2014). Montmorillonite stability under near-field conditions. NAGRA technical report 14-12
- B.E. Lingnau, J. Graham, D. Yarechewski, N. Tanaka, M.N. Gray. (1996). Effects of temperature on strength and compressibility of sand-bentonite buffer. *Engineering geology*. 41. 103-115
- Lippmann, F. (1979).The stabilisation of clay minerals. *Neue Jahrb. Mineral*. 136, 287– 309.
- Liu (2010). Influence of heating and water exposure on the liquid limits of GMZ01 and MX80 bentonites. *Journal of Rock Mechanics and Geotechnical Engineering*. 2. 188- 192
- Ma, C. and Hueckel, T. 1992. Stress and Pore Pressure in Saturated Clay Subjected to Heat from Radioactive Waste: A Numerical Simulation. *Canadian Geotechnical Journal*, **29**, p1087-1094.
- Madsen (1998). Clay mineralogical investigations related to nuclear waste disposal. *Clay minerals*. 33. 109- 129
- Malinsky (2005). Experimental investigation of the healing and sealing capability of two clays. *Clays in natural and engineered barriers for radioactive waste confinement-International meeting*. France
- Manceau, A., Lanson, B., Drits, V.A., Chateigner, D., Gates, W.P., Wu, J., Huo, D., Stucki, J.W., 2000a. Oxidation-reduction mechanism of iron in dioctahedral smectites,1. Crystal chemistry of oxidised reference nontronites. *Am. Mineral*. 85, 133–152.

Manning, D., Younger, P., Smith, F., Jones, J., Dufton, D., Diskin S. (2007). A deep geothermal exploration well at Eastgate, Weardale, UK: A novel exploration concept for low-enthalpy resources. *Journal of the Geol soc.* 371- 382

Marcial, D., Delage, P., Cui, Y. (2007). Hydromechanical couplings in confined MX80 bentonite during hydration. *Unsaturated Soils.* Pp 249- 255

Martín, F., Diez, M., García, I., Simón, M., Dorronsoro, C., Iriarte, Á., Aguilar, J., 2007. Weathering of primary minerals and mobility of major elements in soils affected by an accidental spill of pyrite tailing. *The Science of the Total Environment* 378, 49–52.

Nicolas C.M. Marty, Bertrand Fritz, Alain Clément, Nicolas Michau, Modelling the long term alteration of the engineered bentonite barrier in an underground radioactive waste repository, In *Applied Clay Science*, Volume 47, Issues 1–2, 2010, Pages 82-90
Mesri and Olson (1971). Mechanisms controlling the permeability of clays. *Clays and clay minerals.* 19. 151-158

Meunier, A. & Velde, B. (2004): *Illite*. Springer-Verlag Berlin Heidelberg, Pp.286.

Meunier, A., Velde, B. & Griffault, L. (1998): The reactivity of bentonites: a review. An application to clay barrier stability for nuclear waste storage. *Clay Minerals* 33, 187-196.

Midgley and Gross (1956). Thermal reactions of smectites. Building research laboratory. UK

Milodowski, A. (2009a). Mineralogical investigations of the interaction between iron corrosion products and bentonite from the NF-PRO experiments (phase 1). SKB technical report. TR-09-02

Milodowski, A. (2009b). Mineralogical investigations of the interaction between iron corrosion products and bentonite from the NF-PRO experiments (phase 2). SKB technical report. TR-09-03

Mitchell, J.K. and Soga, K. (2005). *Fundamentals of Soil Behavior*, second ed. *John Wiley & Sons Inc*, New Jersey, 577pp.

Mitchell, J.K. (1993). *Fundamentals of Soil Behavior*, second ed. John Wiley & Sons Inc.

G. Montes-H, J. Duplay, L. Martinez, C. Mendoza. (2003). Swelling- shrinkage kinetics of MX-80 bentonite. *Applied clay science.* 22. 279- 293

Moore and Reynolds (1997). X-ray identification of clay minerals. Oxford university press. New York

Morgan and Lahav (2007). The Effect of pH on the kinetics of spontanrous Fe(II) oxidation by O₂ in aqueous solution- basic principles and a simple heuristic description. Chemosphere. 68. 2080- 2084

Mosser-Ruck, R. & Cathelineau, M. (2004): Experimental transformation of Na,Ca-smectite under basic conditions at 150 C. Applied Clay Science 26, 259-273.

MP Rt Hon Edward Davey (2013). Letter from leader and deputy leader of Cumbria County Council to Sexretary of state for energy and climate change

Muurinen, A. (2011). Measures on cation exchange capacity of bentonite in the long-term test of buffer material (LOT). Posiva report. Report no: 2011-10

Müller-Vonmoos M, Butcher F,. Bentonite as a containment barrier for the disposal of highly radioactive wastes. Appl Clay Sci 1990;4(2):157–77

MWRS partnership report (2012). The final report of the west cumbria managing radioactive waste safely partnership.

NDA and DECC report (2010). The 2010 UK radioactive waste inventory. Report no: URN 10D/985 and NDA/ST/STY(11)0004

NDA and DECC report (2013). 2013 UK radioactive waste inventory. Report no: URN 14D042 and NDA/ ST/STY(14)0010

NDA and DEFRA report (2008): The 2007 UK radioactive waste inventory. Report No: Defra/RAS/08.003 and NDA/RWMD/005

NDA Report (2009). The NDAs research and development strategy to underpin geological disposal of the United Kingdom's higher-activity radioactive wastes. Report no: NDA/RWMD/011

NDA report (2009). UK Radioactive higher activity waste storage review.

NDA report (2010). Geological disposal: steps towards implementation. Report number NDA/RWM/013

NDA report (2012). Managing risk reduction at Sellafield. Report no: 2012-13

NDA technical report (2014). Geological disposal: A review of the development of bentonite barriers in the KBS-3V disposal concept. Report no: 21665941

NDA transcript (2010). History of work in the UK towards a policy for dealing with radioactive waste

Neumann, A., Olson, T., Scherer, M. (2013). Spectroscopic evidence for Fe(ii)-fe(iii) electron transfer at clay mineral edge and basal sites. *Environmental science and technology*. 47. 6969-6977

Newman (1987). *Chemistry of clays and clay minerals*. Mineralogical society monograph. 6

Nicolas and Poirier (1956). *Crystalline plasticity and solid state flow in metamorphic rocks*. Wiley. London

Nirex report (2005). The viability of a phased geological repository concept for the long-term management of the UKs radioactive waste. Report number N/22

Odom (2014). Smectite clay minerals: properties and uses. *Mathematical and physical sciences*. 311. 391- 409

Ollila (2013). Copper corrosion experiments under anoxic conditions. SKB technical report. Report no: TR-13-34

Olson (1989). Direct shear testing (area correction). Lecture notes- Dept of construction engineering Chaoyang university of technology.

Orden, A. (1989). Corrosion mechanisms relevant to high-level waste repositories. *Engineering geology*. 26. 331- 349

Ortiz and Geet (2005). Self-healing capacity of argillaceous rock: review of laboratory results obtained from the selfrac project. *Clays in natural and engineered barriers for radioactive waste confinement- International meeting*. France

Ormerod E.C. Newman A.C.D., 1983. Water sorption on ea-saturated clays. *Clay Minerals* 19, 289-299.

Patel, R., Punshon, C., Nicholas, J., Bastid, P., Zhou, R., Schneider, C., Bagshaw, N., Howse, D., Hutchinson, E., Asano, R., & King, S. (2012). Canister design concepts for disposal of spent fuel and high level waste. NAGRA technical report 12-06

- Perronnet, M., Jullien, M., Villie´ras, F., Raynal, J., Bonnin, D., and Bruno, G. (2008). Evidence of a critical content in Fe(0) on FoCa7 bentonite reactivity at 80°C. *Applied clay science*. 38. 187- 202
- Poulton and Canfield (2005). Development of a sequential extraction procedure for iron: implications for iron partitioning in continentally derived particulates. *Chemical geology*. 214. 209- 221
- Powell, J., Waters, C., Millward, D., Robins, N. (2010). Managing radioactive waste safely: initial geological unsuitability screening of west Cumbria. Report CR/10/072
- Powell, J., Waters, C., Millward, D., Robins, N. (2010). Managing radioactive waste safely: Initial Geological Unsuitability Screening of West Cumbria. BGS Comissioned report
- Puls, R., Powell, R., Clark, D., Eldred, C. (1991). Effects of pH, solid/ solution ratio, ionic strength, and organic acids on Pb and Cd sorption on kaolinite. *Water, Air and Soil Pollution*. 57. 423-430
- Pusch (2002). Alteration of MX-80 by hydrothermal treatment under high salt content conditions. SKB technical report. Report no: TR-02-06
- Pusch (2004). The performance of clay barriers in repositories for high level radioactive waste. Geodevelopment international
- Pusch (2008). Geological storage of highly radioactive waste. Springer- Verlag. Berlin
- Pusch and Madsen (1995). Aspects on the illitisation of the kinnekulle bentonites. *Clays and clay minerals*. 43. 261- 270
- Pusch, R., Karnland, O., Hokmark, H. (1990). GMM- A general microstructural model for qualitative and quantitative studies of smectite clays. SKB technical report. Report no: TR-90-43
- Pusch, R., Karnland, O., Lajudie, A., Decarreau, A. (1993). MX-80 clay exposed to high temperatures and gamma radiation. SKB technical report. Report no: TR-93-03
- Pusch, R., Drawite, A., Yong, R., Nakano, M. (2010). Stiffening of smectite buffer clay by hydrothermal effects. *Engineering geology*. 116. 21-31

Pusch, R., Drawite, A., Yong, R., Nakano, M. (2014). Medium-deep or very deep disposal of highly radioactive waste. Conference paper

Pusch, R. Kasbohm, J. Thao, H, M. Evolution of the clay buffer under repository conditions. 2007. 1-12

RAWRA report (2011). Deep Geological Repository for radioactive waste and spent nuclear fuel. Czech rep

Refait, P., Memet, J.B., Bon, C., Sabot, R. and Genin, J.M.R., 2003. Formation of the Fe,II–Fe,III hydroxysulphate green rust during marine corrosion. Corrosion. Science 45, 833–845.

Report by the Federal Ministry of Economics and Technology (2008). Final disposal of high-level radioactive waste in Germany- The Gorleben repository project

International Atomic Energy Agency (IAEA). (1983). Criteria for underground disposal of solid radioactive wastes. Report no: 60

International Atomic Energy Agency (IAEA). (1989). Use of natural analogues to support radionuclide transport models for deep geological repositories for long-lived radioactive wastes. Report no: 1109

International Atomic Energy Agency (IAEA). (2011). Disposal of radioactive waste- Site safety requirements. Report no: SSR-5

International Atomic Energy Agency (IAEA). (2013). The safety case and safety assessment for the predisposal management of radioactive waste. Report no: GSG-3

Ribeiro, F.R., Fabris, J.D., Kostka, J. E., Komadel, P. & Stucki, J.W. (2009): Comparisons of structural iron reduction in smectites by bacteria and dithionite: II. A variable temperature Mössbauer spectroscopic study of Garfield nontronite. Pure and Applied Chemistry 81, 1499-1509.

Rizzi, M., Laloui, L., Salager, S., Marschall, P. (2011). Granular MX-80 bentonite as buffer material: A focus on swelling characteristics. NAGRA technical report

Rosborg (2013). Post-test examination of a copper electrode from disposition hole 5 in the prototype repository. SKB technical report. Report no: TR-13-14

Rowland R.A., Weiss E.J., Bradley W. F., 1956. Dehydration of monoionic montmorillonites: 4th National Conference on Clays and Clay Minerals Proceedings, p. 85-95.

Roxburgh (1987). Geology of high-level nuclear waste disposal- An introduction. Chapman and Hall. New York

Ruck and Cathelineu (2004). Experimental transformation of Na, Ca-smectite under basic conditions at 150°. Applied clay science. 26. 259- 273

Saba, S., Barnichon, J., Cui, Y., Tang, A., Delage, P. (2014). Microstructure and anisotropic swelling behaviour of compacted bentonite/ sand mixture. Journal rock mechanics and geotechnical engineering. 6. 126- 132

Sallfors (2015). Rheological properties of the bentonite buffer. SKB technical report. Report no: 2015:08

Sato, T., Murakami, I. & Watanabe, T. (1996): Change in layer charge of smectites and smectite layers in illite/smectite during diagenetic alteration. Clays and Clay Minerals 44, 460-469.

Sato, T., Watanabe, T., Otsuka, R., 1992. Effects of layer charge, charge location, and energy
Savage (2007). The effects of high salinity groundwater on the performance of clay barriers. Quintessa report

Savage (2014). An assessment of the impact of the long-term evolution of engineered structures on the safety-relevant functions of the bentonite buffer in a HLW repository. NAGRA technical report 13-02

Savage and Arthur . (2012). Exchangeability of bentonite buffer and backfill materials. STUK report. Report no: STUK-TR 12

Savage, D., Noy, D., Mihara, M., 2002. Modelling the interaction of bentonite with hyperalkaline fluids. Appl. Geochem. 17, 207– 223.

Sawicki, J., Price, J., Brett, M. (1995). Corrosion-product inventory: the bruce-B system. CANDU maintenance conference. Canadian Nuclear Society. 53- 60

- Schlegel, M., Bataillon, C., Benhamida, K., Blanc, C., Menut, D., Lacour, J. (2008). Metal corrosion argillite transformation at the water-saturated high-temperature iron-clay interface: a microscopic scale study. *Applied geochemistry*. 23. 2169- 2633
- Schmitz, R., Schroeder, C., Charlier, R. (2005). A general approach to assess hydro-mechanical changes of natural clay barriers due to physicochemical interaction with waste in deep seated waste disposal sites. *Clays in natural and engineered barriers for radioactive waste confinement- International meeting*. France
- Schmitz, R., Schroeder, C., Charlier, R. (2007). A general approach to assess hydro-mechanical changes of natural clay barriers due to physicochemical interactions with radwaste in deep disposal sites. *Physics and Chemistry of the Earth*. 32. 922-928
- Schmitz, R., Passen, L., (2003). The decay of the liquid limit of clays with increasing salt concentration. *Offshore, Ingeokring newsletter*
- Schultz L.G. 1969. Lithium and potassium absorption; Dehydroxylation and structural water content of aluminous smectites. *Clays and Clay Minerals* 17, 115-149
- Schwarzkopf, W., Smailos, E., Koster, R. (1988). In-situ corrosion studies on selected high-level waste packaging materials under simulated disposal conditions in rock salt formations. Institute for Nuclear engineering. Report kfk 4324
- Sena, C., Grandia, F., Arcos, D., Molinero, J., Duro, L. (2008). Complementary modelling of radionuclide retention in the near-surface system at Forsmark. SKB technical report. Report no: R-08-107
- Shariamadari and Saeidijam (2012). The effect of thermal history on thermos-mechanical behaviour of bentonite-sand mixture. *International Journal of Civil Engineering*. Technical note
- Karimpour-Fard, M., Shariatmadari, N. (2011). Effect of inorganic salt solutions on some geotechnical properties of soil-bentonite mixtures as barriers. *International Journal of Civil Engineering*. 9. 104- 110
- Sherman, D.M., Vergo, N., 1988. Optical (diffuse reflectance) and Mossbauer spectroscopic study of nontronite and related Fe-bearing smectites. *Am. Mineral*. 73, 1346–1354.

Smailos, E., Cunado, M., Azkarate, I., Kursten, B., Markx, G. (2000). Long-term performance of candidate materials for HLW/ spent fuel disposal containers. European commission report. Report no: FIKW-CT-2000-00004

Small J.S., Hamilton D.L. & Habesch S. (1992) Experimental simulation of clay precipitation within reservoir sandstones 1: Techniques and examples. *Journal of Sedimentary Petrology*, 62, 508 –519.

Smart, N.R., Rance, A.P. and Werme, L. 2004. Anaerobic corrosion of steel in bentonite. Stewart (1953). Permian evaporate and associated rocks in Texas and New Mexico compared with those of Northern England. *Proceedings of the Yorkshire Geological Society*. 20. 185-235

Stroes-Gascoyne, S. (2011): Microbiological characteristics of compacted bentonite for a dry density of 1'450 kg/m³: A literature review. Nagra Working Report NAB 11-05. Nagra, Wettingen.

Stuki, J., Golden, D., Roth, C. (1984). Effects of oxidation state of octahedral iron on clay swelling. *Clays and clay minerals*. 32. 357- 362

Stuki, J., Golden, D., Roth, C. (1984). Preparation and handling of dithionite- reduced smectite suspensions. *Clays and clay minerals*. 32. 191- 197

Stuki, J., Golden, D., Roth, C. (1984). Effects of reduction and reoxidation of structural iron on the surface change and dissolution of dioctahedral smectites. *Clays and clay minerals*. 32. 350-356

Amonette, J., Templeton, J., (1998). Improvements to the quantitative assay of nonrefractory minerals for Fe(ii) and total Fe using 1,10 phenanthroline. *Clays and clay minerals*. 46. 51-62

Sultan, N., Delage, P. & Cui, Y. J. (2002). Temperature effects on the volume change behaviour of Boom clay. *Engng Geol*. 64, 2–3, 135–145.

Taibi, S., Ghembaza, M., Sayad, C., Fleureau, J. (2005). Thermo-hydro-mechanical behaviour of clays. *Clays in natural and engineered barriers for radioactive waste confinement- International meeting*. France

- Tajeddine, L., Gailhanou, H., Blanc, P., Lassin, A., Gaboreau, S., Vieillard, P. (2015). Hydration- dehydration behaviour and thermodynamics of MX-80 montmorillonite studied using thermal analysis. *Thermochimica acta*. 604. 83- 93
- Tamaura, Y., Yoshida, T. and Katsura, T. 1984. The synthesis of green rust II, FeIII–FeII and its spontaneous transformation to Fe₃O₄. *Bulletin of the Chemical Society of Japan* 57, 2411–2416.
- Tang and Cui (2010). Effects of mineralogy on thermos-hydro-mechanical parameters of MX-80 bentonite. *Journal of Rock Mechanics and Geotechnical Engineering*. 2. 91-96
- Tang and Cui (2010). Effects of mineralogy on thermo-hydro-mechanical parameters of MX80 bentonite. *Journal of Rock Mechanics and Geotechnical Engineering*. 2. 91- 96
- Tang, A., Cui, Y., Barnel, N. (2008). Thermo-mechanical behaviour of a compacted swelling clay. *Geotechnique*. 58. 45-54
- Tang, A., Cui, Y., Le, T. (2011). A study on the thermal conductivity of compacted bentonites. *Applied Clay Science*. 41. 181- 189
- Tarnawski, V., Momose, T., Leong, W. (2009). Assessing the impact of quartz content on the prediction of soil thermal conductivity. *Geotechnique*. 59. 331- 338
- Taubald, H., Bauer, A., Scha, T., Geckeis, H., Satir, M., 2000. Experimental investigation of the effect of high-pH solutions on the Opalinus Shale and the Hammerschmiede Smectite. *Clay Minerals* 35, 515–524.
- Thakur and Sing (2005). Rapid determination of swelling pressure of clay minerals. *Journal of testing and evaluation*. 33. 239- 245
- Turner, E., Pettersson, S., Snellman, M., Autio, J. (2007). KBS-3H Development of the horizontal disposal concept
- Turnbull (2009). A review of the possible effects of hydrogen on lifetime of carbon steel nuclear waste canisters. NAGRA technical report 09-04
- Turner (2004). Fire accident performance of waste packages. NIREX presentation. Presented at the Fe-NET Annual industry meeting

- Velde, B. (1995a): Composition and mineralogy of clay minerals. *In: B. Velde (ed.): Origin and Mineralogy of Clays: Clay and the Environment. Springer, New York Chapter 2, 8-41.*
- Velde, B. (1995b): Compaction and diagenesis. *In: B. Velde (ed.): Origin and Mineralogy of Clays: Clay and the Environment. Springer, New York, Chapter 5, 220-245.*
- Villar and Lloret (2008). Influence of dry density and water content on the swelling of a compacted bentonite. *Applied clay science. 39. 38-49*
- Villar and Gomez (2010). Geochemical and mineralogical changes in compacted MX-80 bentonite submitted to heat and water gradients. *Applied Clay Science. 47. 400-408*
- Villar, M., Espina, R., Nebot, L. (2012). Basal spacings of smectite in compacted bentonite. *Applied clay science. 65- 66. 95-105*
- Villar, M., Martin, P., Barcena, I., Sineriz, J., Espina, R., Lloret, A. (2012). Long-term experimental evidences of saturation of compacted bentonite under repository conditions. *Engineering geology. 149- 150. 57- 69*
- Volkan and Bayan (2011). *Corrosion chemistry. Wiley publisher. London*
- Wang, Q., Tang, A., Cui, Y., Delage, P., Gatmiri, B. (2012). Experimental study on the swelling behaviour of bentonite/ claystone mixture. *Engineering Geology. 124. 59-66*
- Wang, Q., Cui, Y., Tang, A., Barnichon, J., Saba, S., Ye, W. (2013). Hydraulic conductivity and microstructure changes of compacted bentonite-sand mixture during hydration. *Engineering geology. 164. 67-76*
- Watson, S., Metcalfe, R., McEwen, T., Paulley, A. (2007). *International precedents for HLW/SF iron canister concepts. Quintessa. Report no: QRS-1376A-1*
- Watterson (1986). Fault dimensions, displacements and growth. *Pageoph. 124.*
- Wayllace (2008). *PhD thesis: Volume change and swelling pressure of expansive clay in the crystalline swelling regime. University of Missouri*
- Weaver and Pollard (1973). *The chemistry of clay minerals. Developments in sedimentology. Elsevier. London*

Wersin, P., Johnson, L., McKinley, I. (2007). Performance of the bentonite barrier at temperatures beyond 100°C: A critical review. *Physics and Chemistry of the earth*. 32. 780-788

Wersin, P., Birgersson, O., Karnland, O., Snellman, M., Oy, S & R. (2008). Impact of corrosion-derived iron on the bentonite buffer within the KBS-3H disposal concept. SKB technical report. Report no: TR-08-34

Wersin, P., Birgersson, M., (2014). Reactive transport modelling of iron-bentonite interaction within the KBS-3H disposal concept: The Olkiluoto site as a case study. *Geological society*. 400. 237-250

Wersin, P., Johnson, L.H., Schwyn, B., Berner, U., and Curti, E. 2003. Redox Conditions

White, M., Baldwin, T., Hicks, T., Hooker, P. (2008). Engineered barrier materials for geological disposal facilities. *Galson sciences*. Report no: 0828-1

Wilson, J., Cressey, B., Cuadros, J., Ragnarsdottir, V., Savage, D., Shibata, M. (2006). The effect of iron on montmorillonite stability. (II) Experimental investigation. *Geochimica*. 70. 323- 336

Wilson, J., Savage, D., Bond, A., Watson, S., Pusch, R., Bennett, D. (2010). A review of key properties, processes and issues for consideration in the UK context. NDA- RWMD report. No: QRS-13788ZG-1

Wilson, J., Benbow, S., Sasamoto, H., Savage, D., Watson, C. (2015). Thermodynamic and fully-coupled reactive transport models of a steel-bentonite interface. *Applied geochemistry*. 61. 10-28

Wilson, J., Savage, D., Cuadros, J., Shibata, M., Ragnarsdottir, K. (2006). The effect of iron on montmorillonite stability. (I) Background and thermodynamic considerations. *Geochimica*. 70. 306- 322

Xiaodong, L., Prikryl, P., Pusch, R. (2011). THMC- testing of three expandable clays of potential use in HLW repositories. *Applied clay science*. 52. 419-427

Yang, S., Chuan, C., Huang, W. (2005). Effect of compaction energy on soil suction of clayey soils. *Clays in natural and engineered barriers for radioactive waste confinement- International meeting*. France

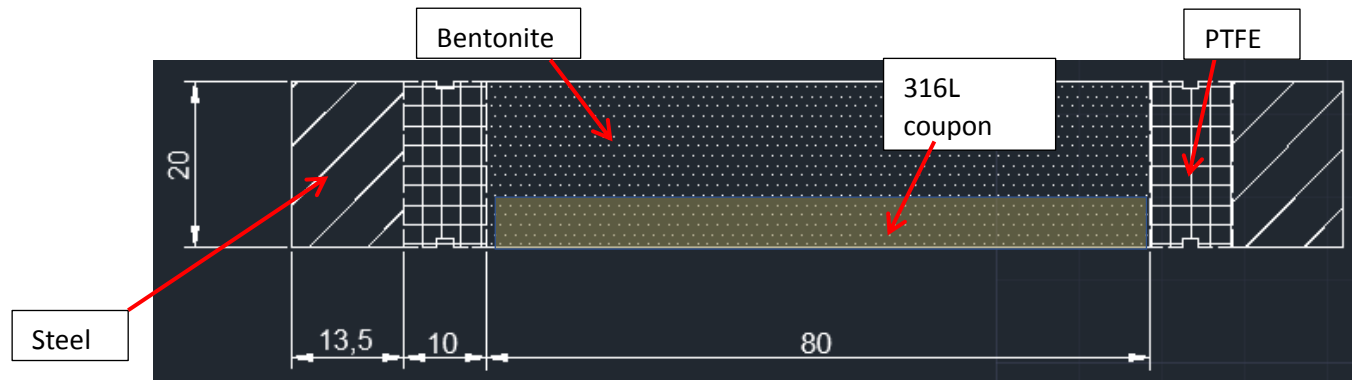
Ye, M., Wan, M., Chen, B., Chen, J., Cui, Y., Wang, J. (2012). Temperature effects on the unsaturated permeability of the densely compacted GMZ01 bentonite under confined conditions. *Engineering Geology*. 126. 1- 7

Zhang, C., Rothfuchs, T., Su, K., Hoteit, N. (2005). Experimental study of the thermo-hydro-mechanical behaviour of indurate clays. *Clays in natural and engineered barriers for radioactive waste confinement- International meeting*. France

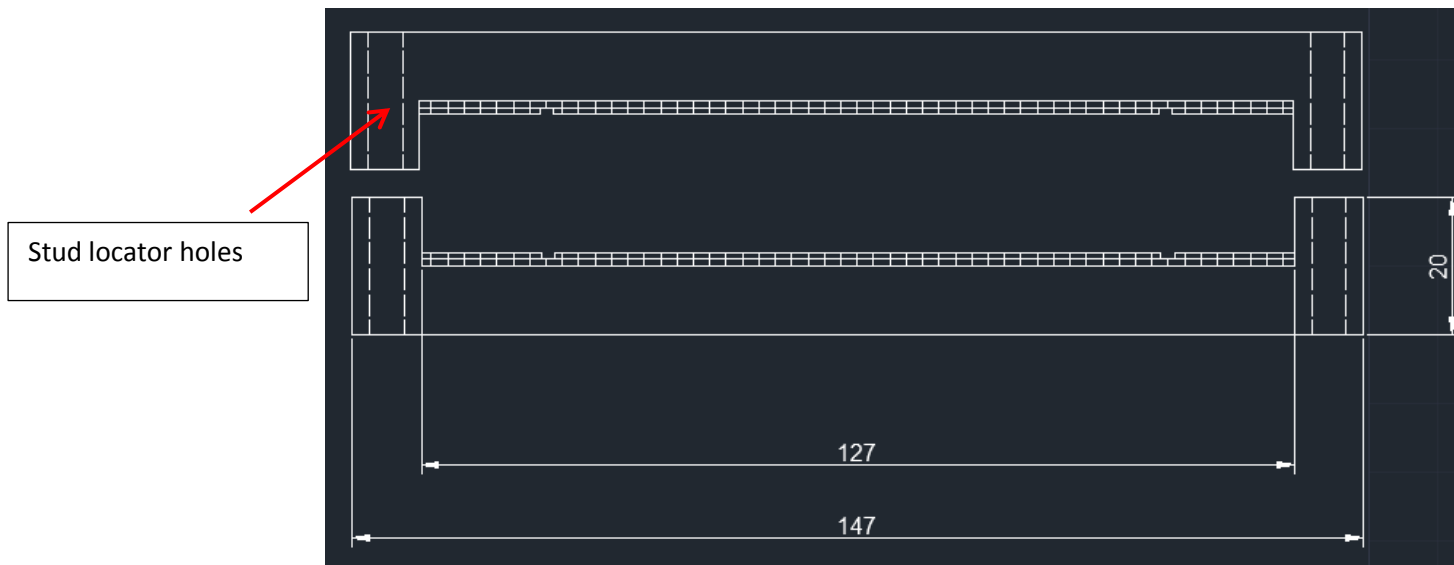
Zhang, M., Zhang, H., Jia, L., Cui, S. (2012). Salt content impact on the unsaturated property of bentonite-sand buffer backfilling materials. *Nuclear Engineering and Design*. 250. 35- 41

Zhang, G.X., Dong, H., Kim, J. & Eberl, D.D. (2007): Microbial Reduction of Structural Fe³⁺ in Nontronite by a Thermophilic Bacterium and its Roles in Promoting the Smectite to Illite Reaction. *American Mineralogist* 92, 1411-1419.

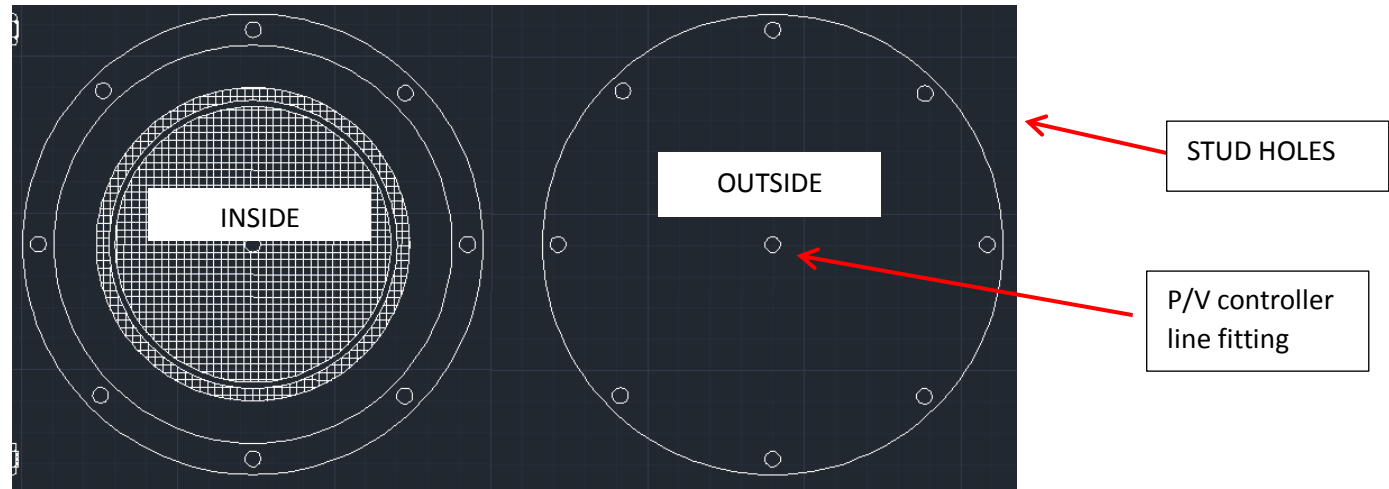
Appendix



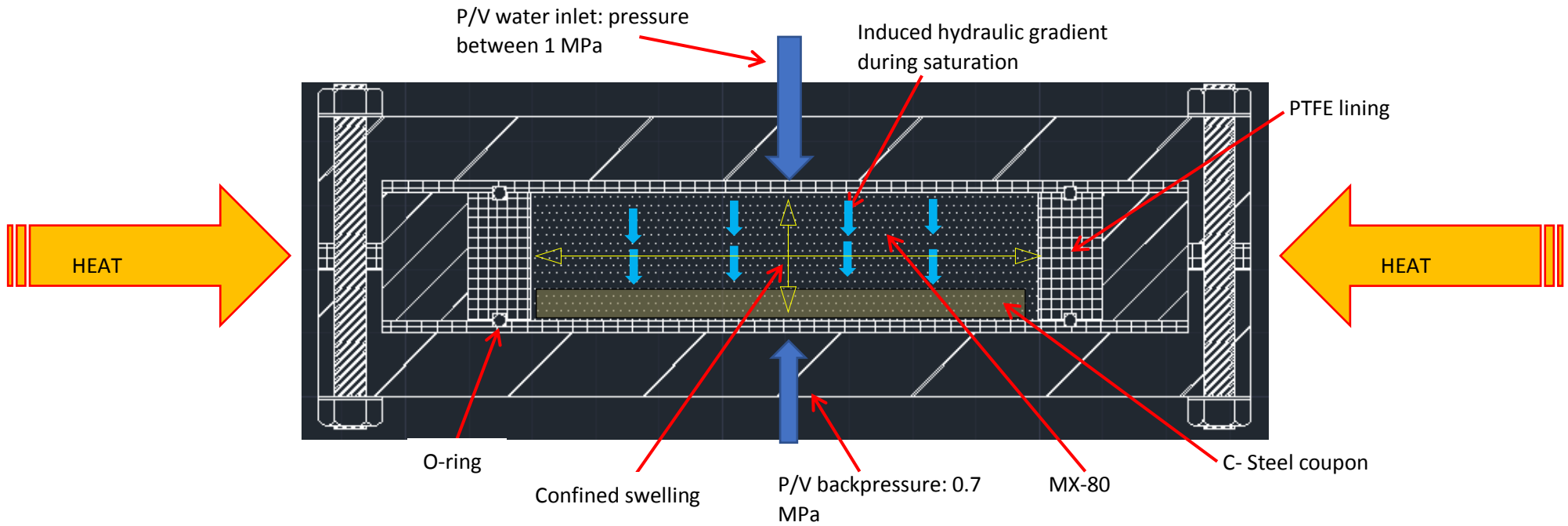
A1: TH cell inner cross-section, steel wall with PTFE lining channelled for o-ring location (Dimensions mm)

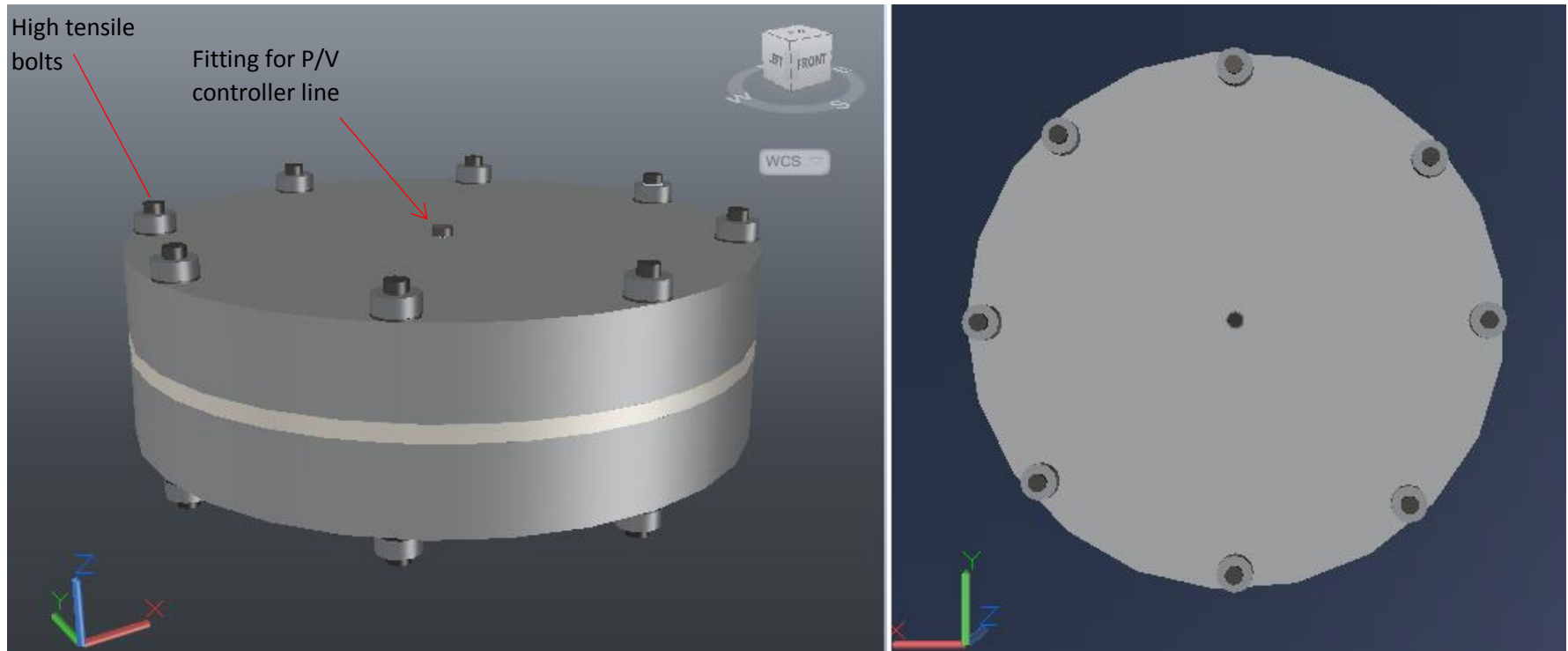


A2: Cross-section of TH cell end caps with stud locator holes, with PTFE cover



A3/4: Plan and side view of TH cell end caps and working concept





A5: 3D TH cell concept; the PTFE gasket can be left out of the design

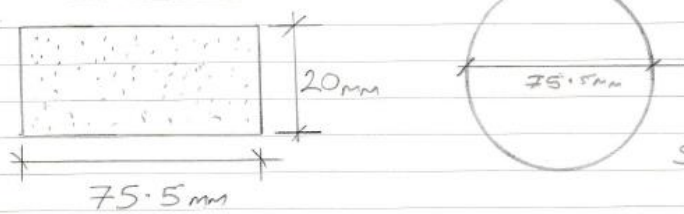
HAND CALCS

10/05/2015

CELL DESIGN #2

NOT TO SCALE

SAMPLE GEOMETRY



AREA: $\pi \times 0.03775^2$
 $= 4.477 \times 10^{-3} \text{ m}^2$

SAY NB $\approx 80 \text{ mm} \rightarrow 3''$

10/5/2015

CELL FOR THERMO-HYDRAULIC EXPERIMENTS

INTERNAL PRESSURE CONSIDERATIONS:

- * Hydrostatic pressure $\approx 5 \text{ MPa}$ (1.6 Mg/m^3)
- SWELLING PRESSURES @ REFERENCE DRY DENSITY: $\approx 8 \text{ MPa}$
- ∴ TOTAL INTERNAL PRESSURE, ASSUMED TO BE $\approx 13 \text{ MPa}$

Hoop & Longitudinal Stress (USING THIN WALLED PRESSURE VESSEL THEORY)

$$\sigma_t = \frac{P \cdot r}{t} \quad \& \quad \sigma_a = \frac{P \cdot r}{2t}$$

PTFE LINED TO REDUCE CORROSION OF CELL AND HENCE THE UNWANTED INFLUENCE OF EXTERNAL CORROSION.

- * PTFE (POLYTETRAFLUOROETHYLENE): STABLE AT HIGH TEMPS $\approx +250^\circ \text{C}$
- AMORPHOUS TRANSITION @ 32°C , LOW FRICTIONAL PROPERTIES.
- CONSIDERED A GOOD INSULATOR.
- THERMAL DIFFUSIVITY: $\approx 0.124 \text{ mm}^2/\text{s}$

PTFE:

↳ THE PLASTIC SHOP:

OD	ID	t (mm)
90	80	5
100	80	10
120	80	20

* STEEL: HOLME DODSWORTH

TYPE: 316 / BAR

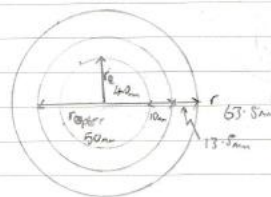
WALL THICKNESS (mm)

- ✓ $\phi: 127 \text{ mm}$ → 13.5
- ✓ 152.4 mm → 26.2
- ✓ 177.8 mm → 31.9

X [or 101.6 mm OD] ?

PTD
 ↓ CONCEPTUAL DESIGN...

* O-ring $\phi < 100 \text{ mm} \ \& \ > 80 \text{ mm}$
 CS (S) $\approx 5.33 \text{ mm}$



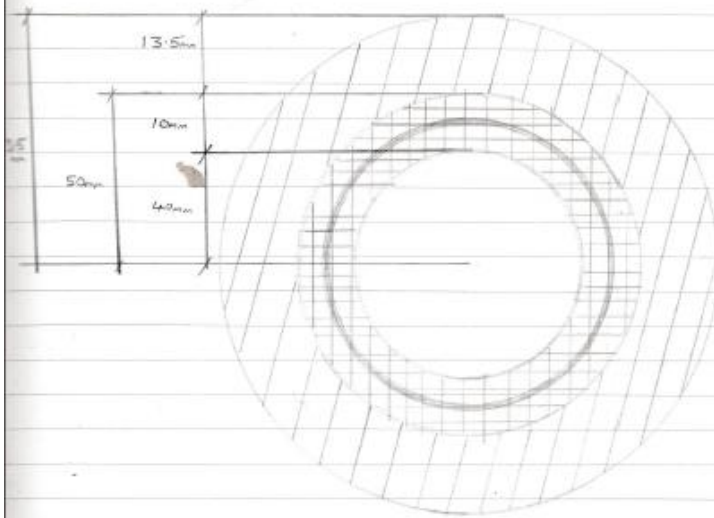
14/05/2013

COMPOUND DESIGN

$r_{fit} < 5 \cdot t_{th}$; THICK WALLED THEORY VALID

At $r = r_o$, $\sigma_{radial} = 0$ $P = P_i = 13 \text{ MPa}$, $P_o = 0$
 At $r = r_i$, $\sigma_{radial} = -P$

COMPOUND THEORY NEGLECTED AS PTFE LINER IS VITRIM HENCE RADIAL STRESS WILL BE NEGLECTABLE.



STAINLESS STEEL TUBE:

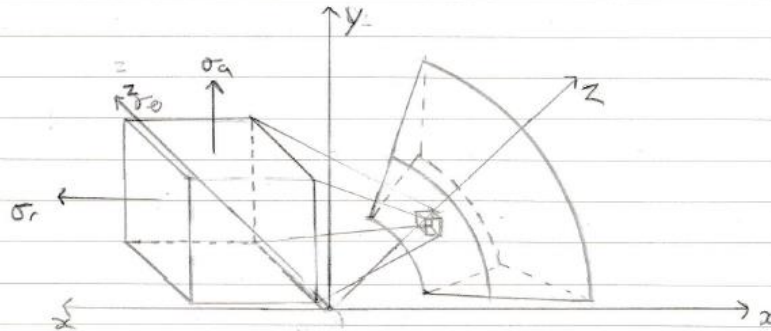
OD: 127mm, ID: 100mm

PTFE TUBE:

OD: 100mm, ID: 80mm

[SNIP FIT]

THICK WALL THEORY VALID IN STAINLESS STEEL i.e. RADIAL STRESS WILL BE SIGNIFICANT. ASSUMING TOTAL RADIAL DISTANCE TO BE ONE MATERIAL!



$$-P = A - \frac{B}{r_o^2}, \quad 0 = A - \frac{B}{r_i^2}$$

$$A = \frac{P \cdot r_i^2}{(r_o^2 - r_i^2)} \quad \& \quad B = \frac{P \cdot r_i^2 \cdot r_o^2}{(r_o^2 - r_i^2)}$$

$$\therefore \sigma_r = A - \frac{B}{r^2} = \left[\frac{P \cdot r_i^2}{(r_o^2 - r_i^2)} \cdot \left(1 - \frac{r_o^2}{r^2} \right) \right] = \sigma_r$$

$$\sigma_{\theta} = \frac{P \cdot r_i^2}{(r_o^2 - r_i^2)} \cdot \left(1 + \frac{r_o^2}{r^2} \right)$$

t

$$\sigma_a = \frac{P_i \cdot r_i^2 - P_o \cdot r_o^2}{r_o^2 - r_i^2}$$

MAX SHEAR STRESS:

$$\tau_{max} = \frac{\sigma_i - \sigma_s}{2} = \frac{\sigma_H - \sigma_r}{2}$$

τ_{max} OCCURS LOCALLY ON THE INSIDE RADIUS WHERE $r = r_o$

t

@ $r = r_i$ i.e. 40mm

$$\sigma_{\theta} = 30.1 \text{ MPa (T)}$$

$$\sigma_r = -13 \text{ MPa (C)}$$

@ $r = r_o$ i.e. 63.5mm

$$\sigma_{\theta} = 17.15 \text{ MPa (T)}$$

$$\sigma_r = 0 \text{ MPa}$$

$$\sigma_a = \frac{13 \times 40}{63.5^2 - 40^2} = 8.552 \text{ MPa}$$

$$\tau_{max} = \frac{30.1 - (-13)}{2} = 21.55 \text{ MPa on inside surface.}$$

ro	ri	r	r ²	Radial stress	Hoop stress	Axial stress
63.5	40	40	1600	-13.000	30.104	8.552
		42	1764	-10.996	28.100	
		44	1936	-9.260	26.363	
squd(ro)	squd(ri)	46	2116	-7.744	24.848	
4032.25	1600	48	2304	-6.415	23.518	
Pi		50	2500	-5.241	22.345	
13		52	2704	-4.201	21.304	
		54	2916	-3.274	20.377	
		56	3136	-2.444	19.548	
		58	3364	-1.699	18.802	
		60	3600	-1.027	18.130	
		62	3844	-0.419	17.522	
		63.5	4032.25	0.000	17.104	

σ_{yield} of

PTFE: $\approx 23 \text{ MPa}$

316: 170 MPa

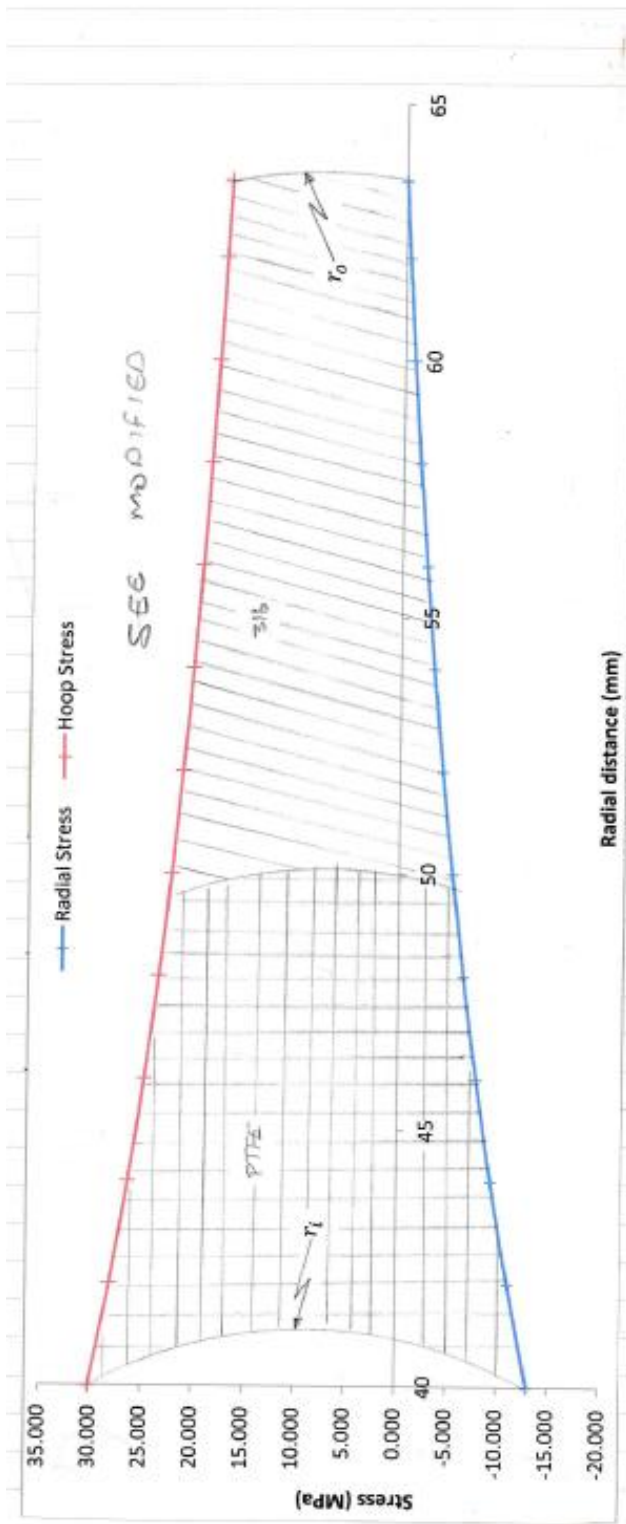
80% of σ_{yield}

$\rightarrow 18.4 \text{ MPa}$

$\rightarrow 136 \text{ MPa}$

} THIS WILL BE CONTAINED BY THE STEEL

$\Rightarrow > \sigma_{\theta} @ r_i \therefore \underline{ok}$



END FITTINGS 316L BOLTS

FITTINGS

HEXAGON NIPPLE

NOM SIZE:	EACH SIDE	
1/8 = 3.175mm	10mm	C: BOLT CIRCLE ϕ
1/4 = 6.35mm	15mm	hg: RAD DIST FROM GASKET LOAD REACTION TO BOLT CENTER = (C - G) / 2
3/8 = 9.525mm	16mm	b: GASKET SEATING WIDTH = b ₀ when b ₀ < 6.3mm 2.52 / b ₀ when b ₀ > 6.3mm
1/2 = 12.7mm	20mm	HG: COMP LOAD ON GASKET TO GASKET TIGHT FIT (2x b x 314 GMP)

* FROM BS 5500

BLIND FLANGER (C) FACTOR = 0.41

MIN THICKNESS OF END PLATE:

$$e = \sqrt{\frac{0.3 \cdot G^2 \cdot P}{Sf_0} + \frac{1909 \cdot W_m \cdot h_g}{G \cdot Sf_0}}$$

BOLTING UP COND

$$W_{m2} = 3.14 \cdot b \cdot G \cdot y$$

Required Bolt Area $A_m > A_{m1} \& A_{m2}$

ACTUAL BOLT AREA: $A_b \cdot N_b < A_m$

USE REST AREA (MIN ϕ)

b: GASKET SEATING WIDTH

HG: COMP LOAD ON GASKET TO GASKET TIGHT FIT (2x b x 314 GMP)

M: GASKET FACTOR (BS5500 3-1-4)

h: HUB LENGTH

G: GASKET ϕ

P: DESIGN PRESSURE

Sf₀: DESIGN STRESS AT WORKING PEAK TEMP

W_{m1}: MIN REQ BOLT LOAD FOR OPERATING COND (HG + H)

OPERATING COND

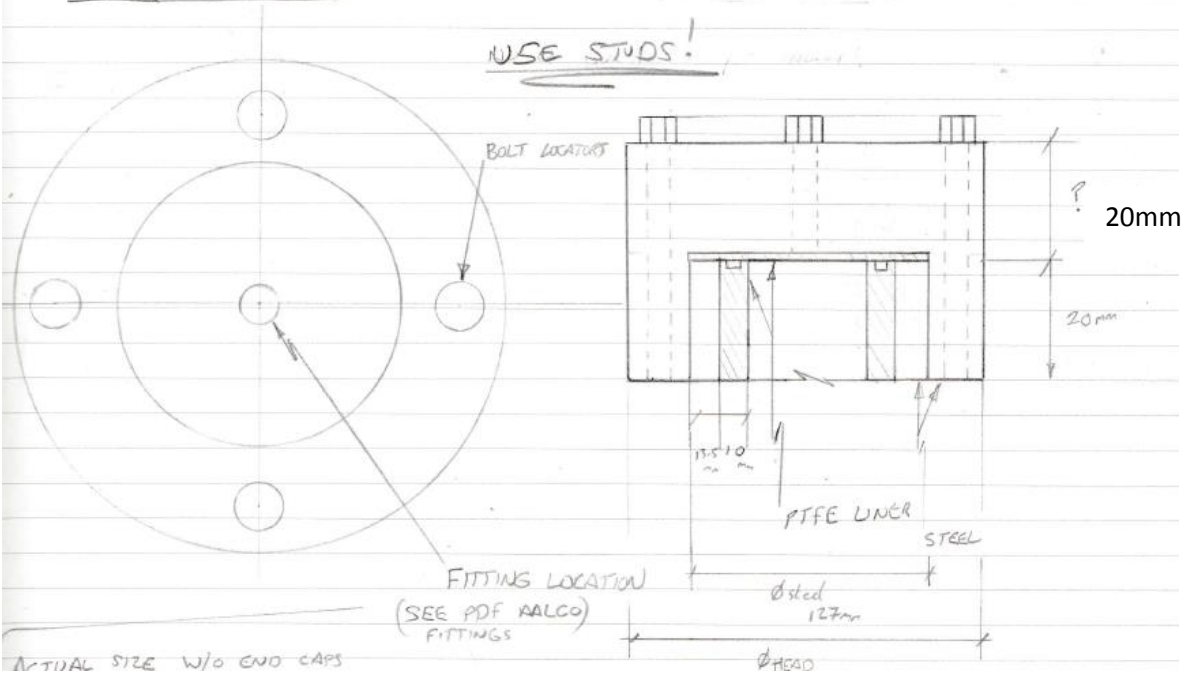
END CAP

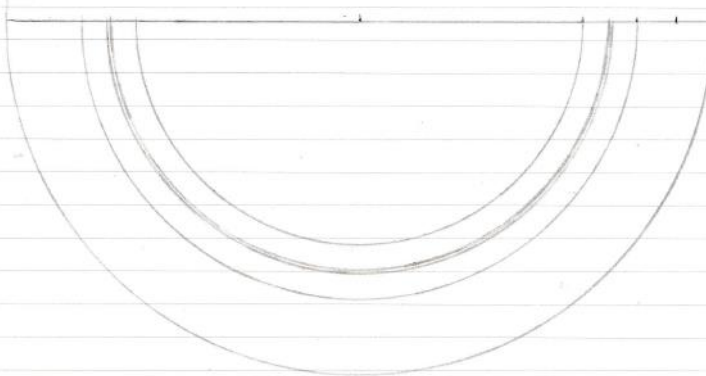
P_i acting on area $\rightarrow F_i \Rightarrow 13 \times 10^3$ kPa / area using r_{steel} 0.05m

$$\Rightarrow A = 7.854 \times 10^{-3} \text{ m}^2$$

$$F = 102.102 \text{ KN}$$

USE STUDS!





MIN BOLT AREA REQ TO RESIST END FORCES!

$$e_t = \sqrt{\frac{1.904 \times W_m \times h_G}{E \times S_{FO}}} \quad (\text{min thickness beyond gasket.})$$

WALL THICKNESS CALC (ASME B31.3 - 2008)

$$t = \frac{PD}{2(SE + PY)} \text{ valid if } \frac{P}{SE} > 0.385 \quad (B31.3 - 304.1.2)$$

SPEC NO: A312

So, $P_{int} =$ Assuming 13 MPa

$E \rightarrow$ BASIC QUALITY FACTORS (E) \rightarrow SEAMLESS TUBE = 1 (TABLE A-1B)

$S \rightarrow$ USE ALLOWABLE STRESS AT PEAK TEMPS OF 150°C
= 115.1425 MPa (TABLE K-1)

So, $\frac{P}{SE} = 0.113 < 0.385 \therefore \text{OK}$

WALL THICKNESS OF STEEL

$$t = \frac{PD}{2(SE + PY)} = \frac{PD}{2(SE + PY)} \quad \left. \begin{array}{l} y = \text{TABLE 304.1.1} \\ \rightarrow 0.4 \\ 4D = 127, 152.4, 177.8 \text{ (mm)} \end{array} \right\}$$

$\phi 127 \text{ mm}$

$$t = \frac{13 \times 0.127}{2(115.1425 \times 1) + (13 \times 0.4)} = 6.86 \times 10^{-3} \text{ m or } 6.86 \text{ mm}$$

$\phi 152.4 \text{ mm}$

$$t_{min} = 8.232 \text{ mm}$$

$\phi 177.8 \text{ mm}$

$t_{min} = 9.6 \text{ mm}$

So, max $t_{min} = 9.6 \text{ mm}$ & min $t_{min} = 5.5 \text{ mm}$
 \therefore USING TUBE OD OF 127 mm WITH ID OF 100 mm GIVING 27 mm (t)
 HENCE OK OR USING TUBE OF 101.6 mm (4") GIVES 11.6 mm (t) OK

Also,

@ $\phi 101.6 \text{ mm}$

$t_{min} = 5.49 \text{ mm}$

CONSIDERED TO BE THIN WALLED IF r is 5 times the wall thickness.

$\frac{1}{2} [r > 5 \cdot t]$ if $[r < 5 \cdot t]$ then thick walled theory is suffice.

Number of stud bolts required for end caps:

Proposed to use 10x M10 (A2, 304) stud bolts with a proof stress of $\approx 210\text{MPa}$ and Ultimate tensile strength of 520-720MPa (Aalco steel data sheets on 304 stainless).

Nominal area for one M10 bolt is $7.854 \times 10^{-5}\text{m}^2$, Total area of 10 M10 bolts = $7.85 \times 10^{-4}\text{m}^2$

Force exerted on the end plate area (Average of internal PTFE and steel radii respectively): $6.36 \times 10^{-3}\text{m}^2$ and internal pressure of 13MPa = 82.7 KN

I.e. Tensile stress in one bolt = 1053MPa **NOT SUFFICE!**

Number of bolts for plastic yielding to occur: ≈ 5 bolts.

So, ten bolts = 105.3 MPa/ bolt \therefore Ok, functioning at **50%** proof stress!

NB. END CAPS ARE TO BE TAPPED FOR ADDITIONAL PROTECTION AGAINST THREAD STRIPPING FAILURE WITH WASHER AND NUT SECURITY, HENCE ONLY CONCENTRATING ON TENSILE RESISTANCE.



A6: Pressure/ Volume controller (Max pressure 3MPa)

A.2. Interface cell Calibration, Hydrostatic and Thermo-Hydrostatic testing:

In order to have an idea of the volume of fluid going into the sample, as stated previously, the system needed to be checked for seal integrity and subsequently due to the fact that each system needed to be isolated from the outside. The initial hydrostatic test was piloted on the three interface cells at room temperature ($\approx 21^\circ\text{C}$). The purpose of this test was to investigate the cells ability to withstand the peak hydraulic pressures present during interface experimentation. In order to do this the cells were bled of internal air from the upper fitting while the hydraulic feed was attached to the opposite side (see figure A7), after which a blank fitting sealed the upper fitting.

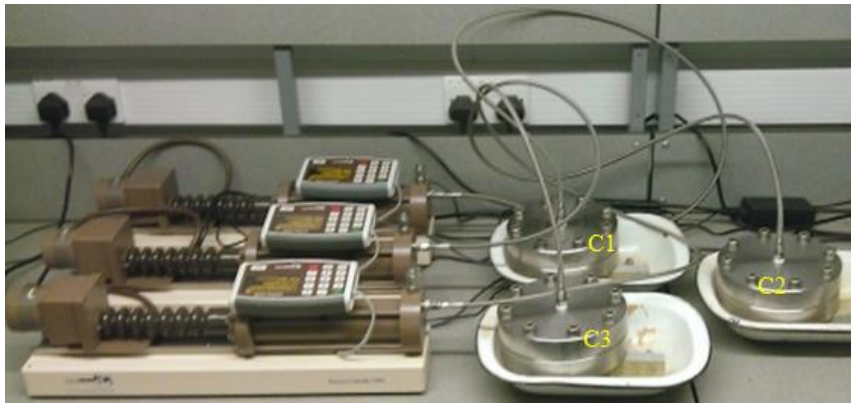


Figure A7: Initial hydrostatic test configuration at 1MPa under ambient conditions ($\approx 21^\circ\text{C}$)

The hydrostatic pressure was set to the maxima that the controller could input and subsequently volume over time was recorded via the GDS software. This was left to run for approximately 20 days to ensure the seals would resist the working pressure. Upon plotting the data, it was observed that the volume of the piston was decreasing (see figure A8), this indicated that there was some input into the cells. Hypothetically the data output should be a constant volume, thus indicating that no water is escaping from the system, the average gradient of the slopes of the three cells over the month was approximately $\frac{\Delta y}{\Delta x} = 2.058 \times 10^{-5} \text{mm}^3/\text{s}$. As can be seen the leak was somewhat consistent over the three individual cells, therefore the systematic fault can be concluded to be a design error. This output of fluid may be infinitesimal, but nonetheless the cells were not functioning as the design premise intended. This leak was concluded to be due to the seal between the O-ring and the seating groove.

Initial hydro-pressure test at 21°C

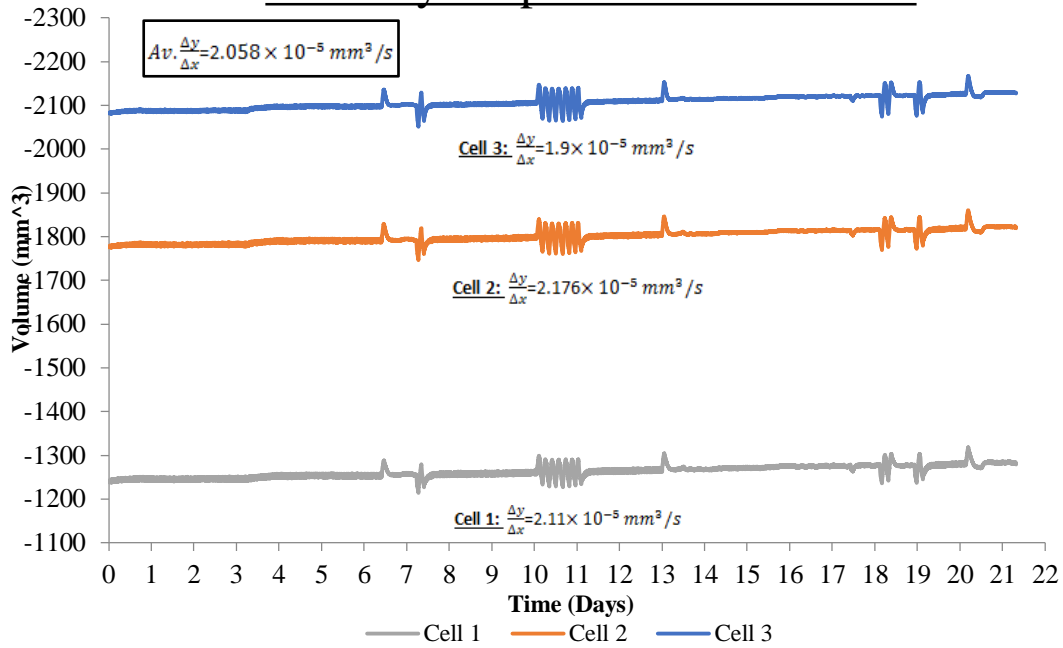


Figure A8: Hydrostatic seal integrity test at 1MPa under ambient conditions

It was also observed that comparable spiking occurred under the same time period on each isolated system. Understandably the parallel spiking between all three systems could only be established to be due to temperature deviations within the temperature controlled room where the tests were taking place. Consequently, a temperature logger was placed in the room over the latter three-day period of the testing (between days 19 and 21). The resulting temperature profile (Figure A9) confirmed the assumption and indicated that the room temperature fluctuates by $\pm 2^\circ\text{C}$. This study also validates the sensitivity of the pressure/volume controllers. Nonetheless the overall steady volume reduction can only be attributed to systematic outflow associated with the O-ring/ cell contact tolerance.

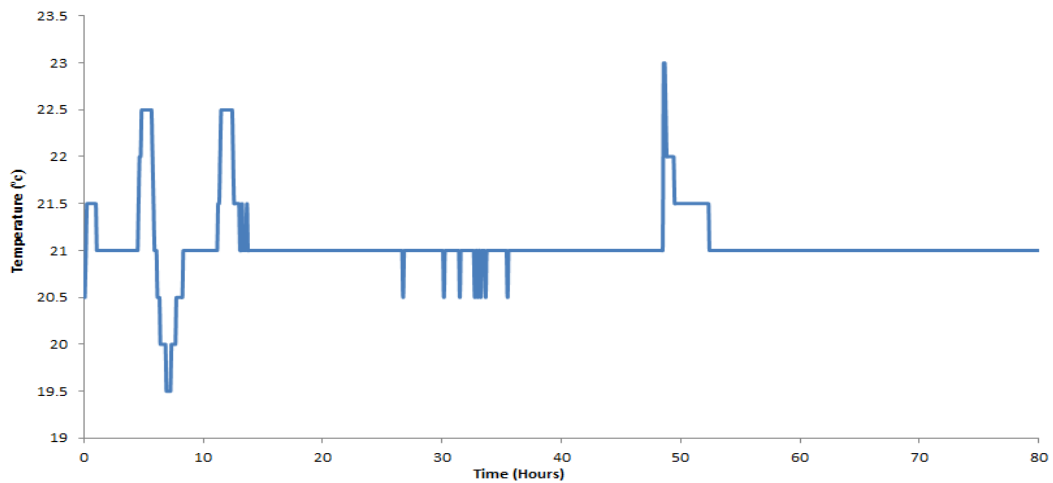


Figure A9: Room temperature sample over a three-day period

Calibration tests used a pseudo sample, a block considered incompressible under the hydrostatic conditions and therefore any volume change is assumed to be purely systematic. Furthermore, the high temperature testing was conducted to see if the problem was exaggerated. The tests were run in cycles (temperature and pressure increments) to measure volume changes, initially with the valves open (i.e. pressure/volume controllers, piping and interface cell) after which the cycles are run before interface implementation with the valves closed (i.e. pressure/volume controllers and piping volumetric measurements only). Temperature increments were 35°C, 60°C, 80°C, 90°C and 100°C, with each temperature stage undergoing 300KPa, 600KPa and 900KPa pressure increments. Consequently, it is possible to isolate and measure the cell volume by subtracting the measurements taken from the volume data with the valves closed from the data with the valves open. Volume increase was noticed during the initial stages of the thermo-hydraulic testing, it was decided to cease the testing and consider resolving these issues. Figure A10 displays the large increase in output as the temperature is increased. This is perhaps due to the reduction in the kinematic viscosity of the water as the temperature is increased. This is also recognised by the gradient increase as the temperature is increased.

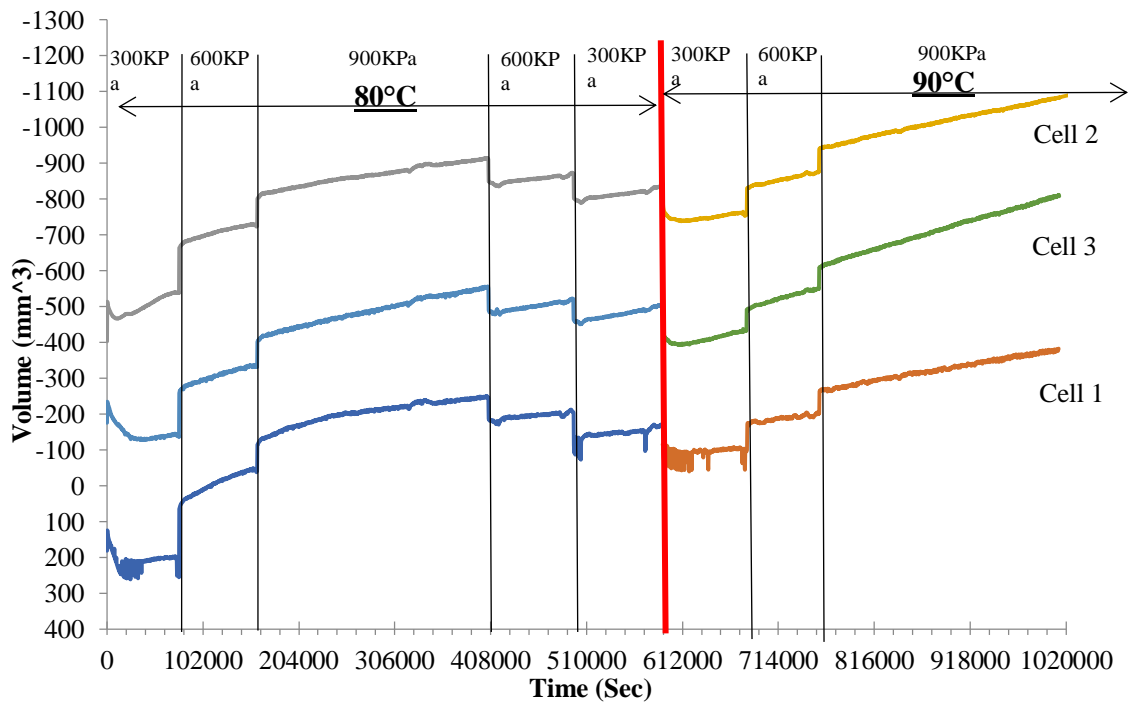


Figure A10: Thermo- hydro pressure test profile over 80°C and 90°C

As stated previously it was assumed that this volume deviation was down to water leaking from the interface cell. Therefore, a gasket sealant was used (Three Bond), a solvent free, silicon based sealant used primarily on combustion engines. Thus it can be safely

implemented under the operational pressure and temperature ranges. The sealant was applied around all O-rings and PTFE interfaces (Figure A11), ensuring that no direct contact with the internal cell occurred. Upon disassembly of the cells discoloration at the PTFE-blanking flange interface confirmed that the presence of water was almost certain. All three cells displayed some staining outside of the inlet/ outlet O-ring, the O-ring is intended to cease water flow into this area and concentrate flow into the cell.

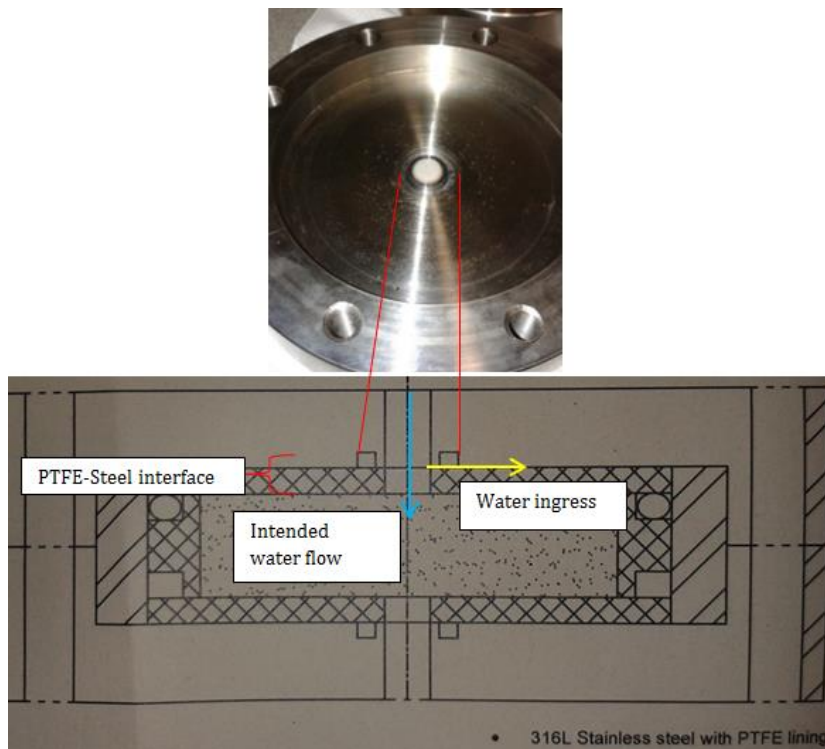


Figure A11: Interface cell blanking flange showing O-ring location, inadvertent preferential flow path and discoloration on outer section (beyond the O-ring)

Additionally, the thermal profile over the pressure volume controllers was investigated to see if the thermal output from the side pipe inlets on the oven was contributing to the issue. This was conducted using the highest temperature and hydrostatic pressure that the experimental regime intends to use, 100°C and 300KPa respectively. Instantaneous temperature measurements were taken over five discrete points from the oven outlet to the opposite wall, the profile is shown in Figure A12. Figure A12 also demonstrates that pressure- volume controller #3 (closest to the oven) has a gradient one order of magnitude higher than cells #1 and #2 respectively. Therefore, this indicated that the thermal transfer along the piping and in the surrounding air toward the controllers also affected the piston volume reading. Compound effects were determined to be contributing to the cell seal integrity, as is stated, cell #3 displays the highest leak rate and this is also accentuated with temperature. Subsequently the inlet hole on the oven was blocked with insulating fibre to

reduce the turbulent air circulating around the controllers. After the corrective measures were implemented the hydrostatic and calibration test runs were reinitiated.

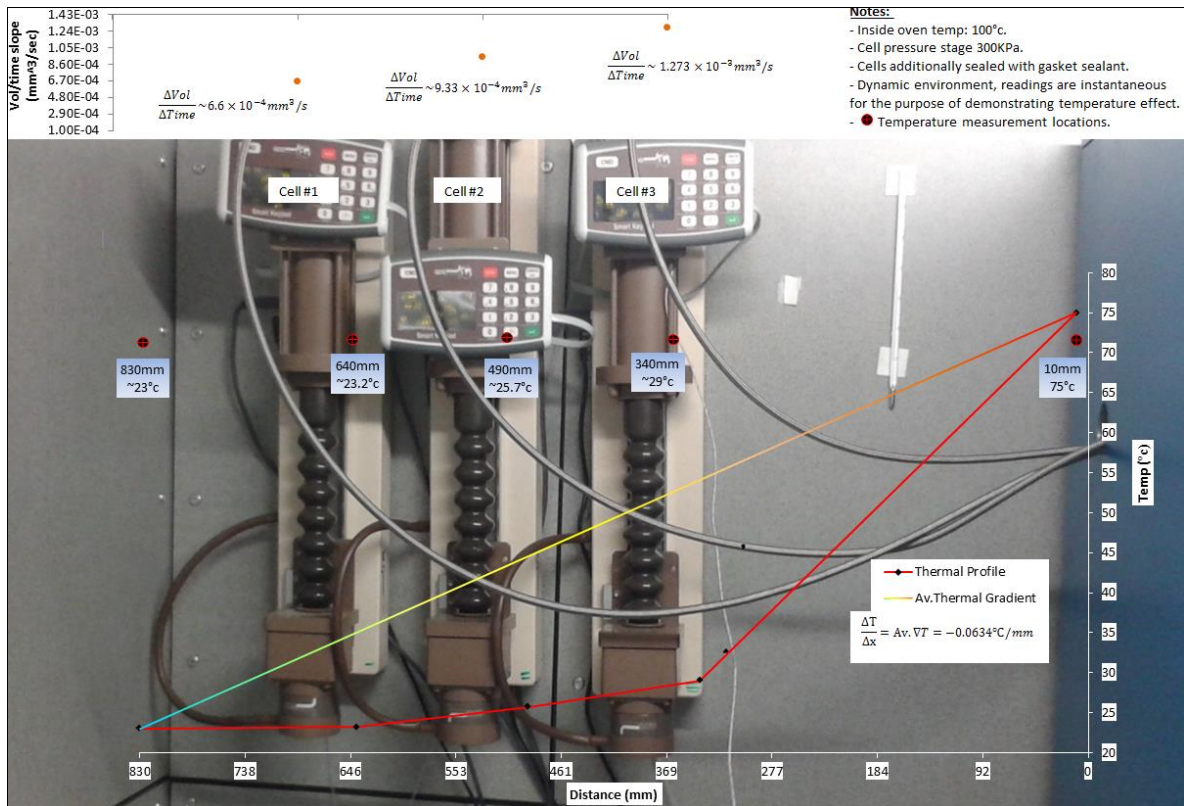


Figure A11: Thermal profile over the input pressure/ volume controllers with the corresponding gradient measurements

Figures A12 – A14 show that the ambient hydrostatic pressure tests (run for two weeks) with the sealant applied around all major interfaces displays stable volumetric data. What can be seen from these is that constant volume conditions are sustained under the respective pressure increments i.e. the seal functions suitably ($Overall \frac{\Delta y}{\Delta x} = 0$; disregarding the temperature induced sporadic spikes).

Hydro-pressure test: Cell #1 (21°C)

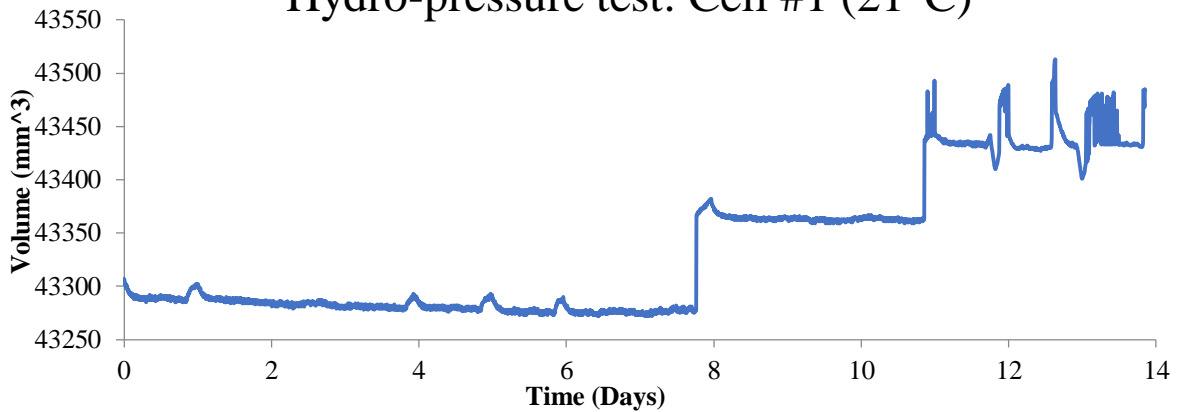


Figure A12: Cell #1 repeated hydrostatic test under ambient conditions

Hydro-pressure test: Cell #2 (21°C)

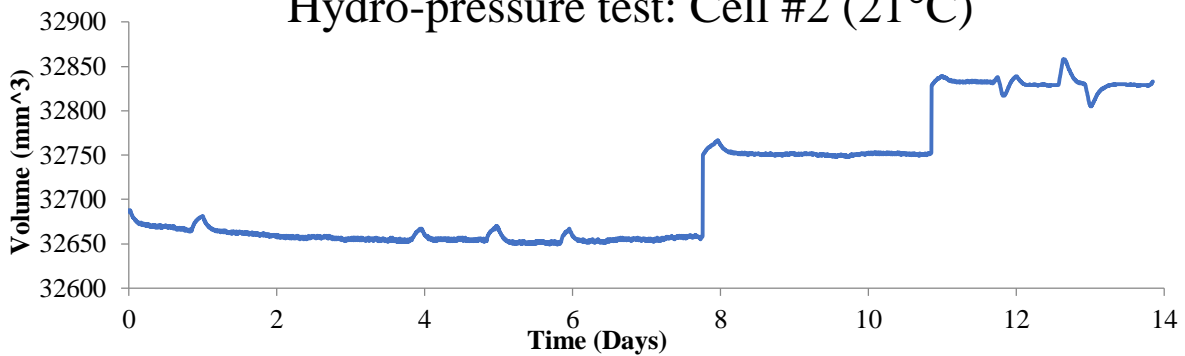


Figure A13: Cell #2 repeated hydrostatic test under ambient conditions

Hydro-pressure test: Cell #3 (21°C)

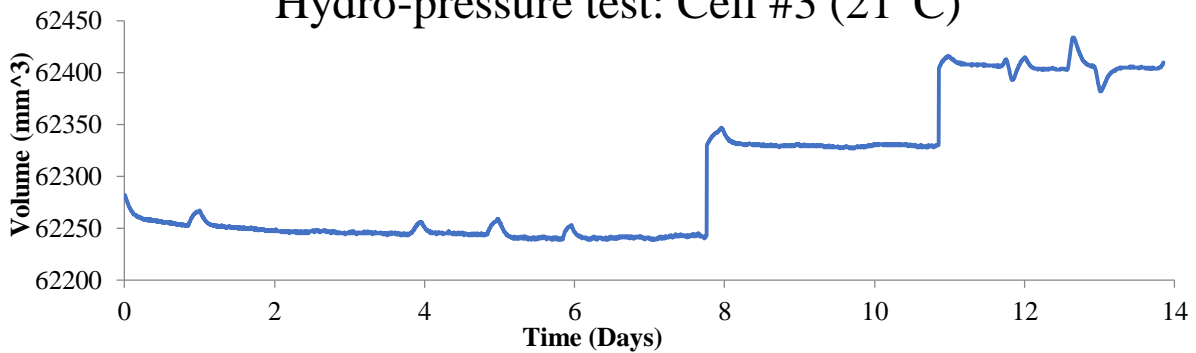


Figure A14: Cell #3 repeated hydrostatic test under ambient conditions

Additionally, the sporadic nature of the data recorded by pressure-volume controller #1 was put down to the resolution/ sensitivity of the system and hardware-software communication settings (This isn't considered an issue). Thermo-hydraulic tests were repeated with all remedial measures in place, figures A15- A18 display the volume graphs for each temperature increment.

Pressure/ Volume test at 35°C with Three-bond sealant

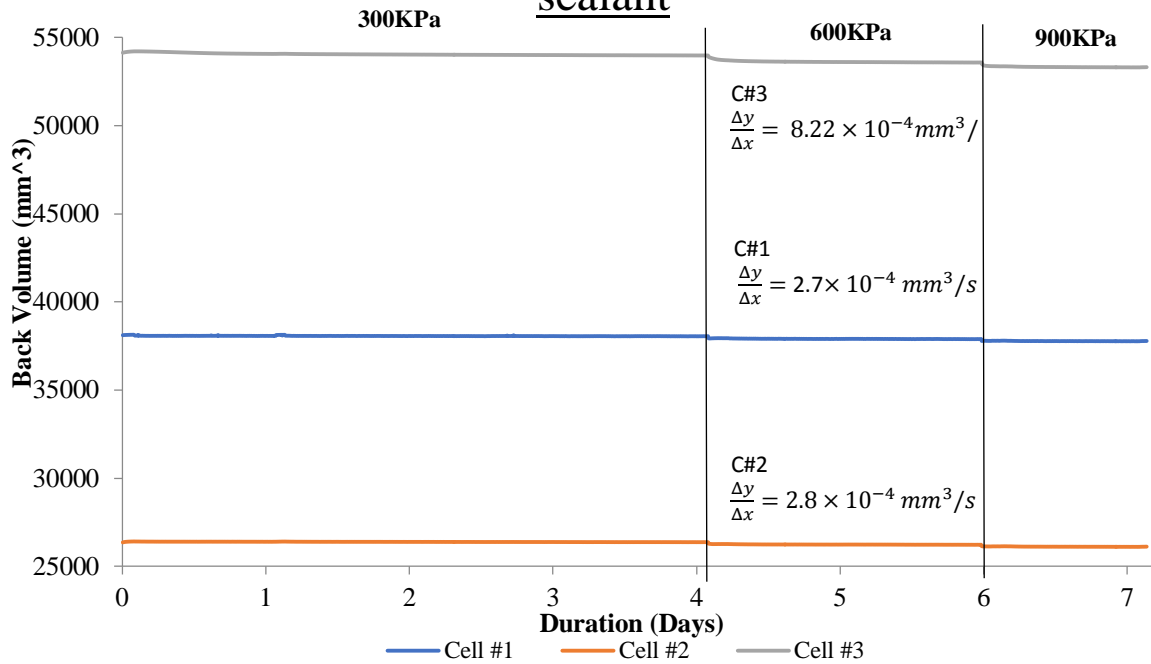


Figure A15: Thermo-pressure calibration run at 35°C

Pressure/ Volume test at 80°C with Three-bond sealant

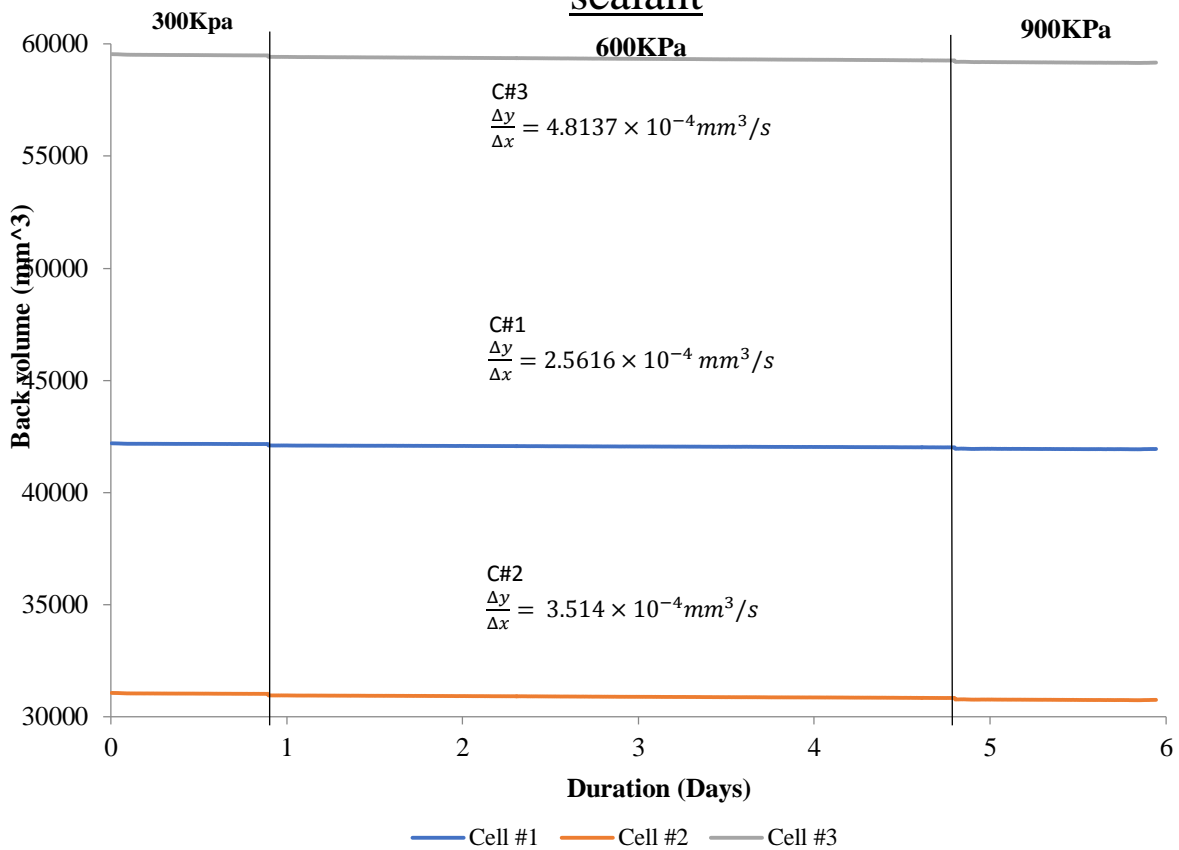


Figure A16: Thermo-pressure calibration run at 80°C

Pressure/ Volume test at 90°C with Three-bond

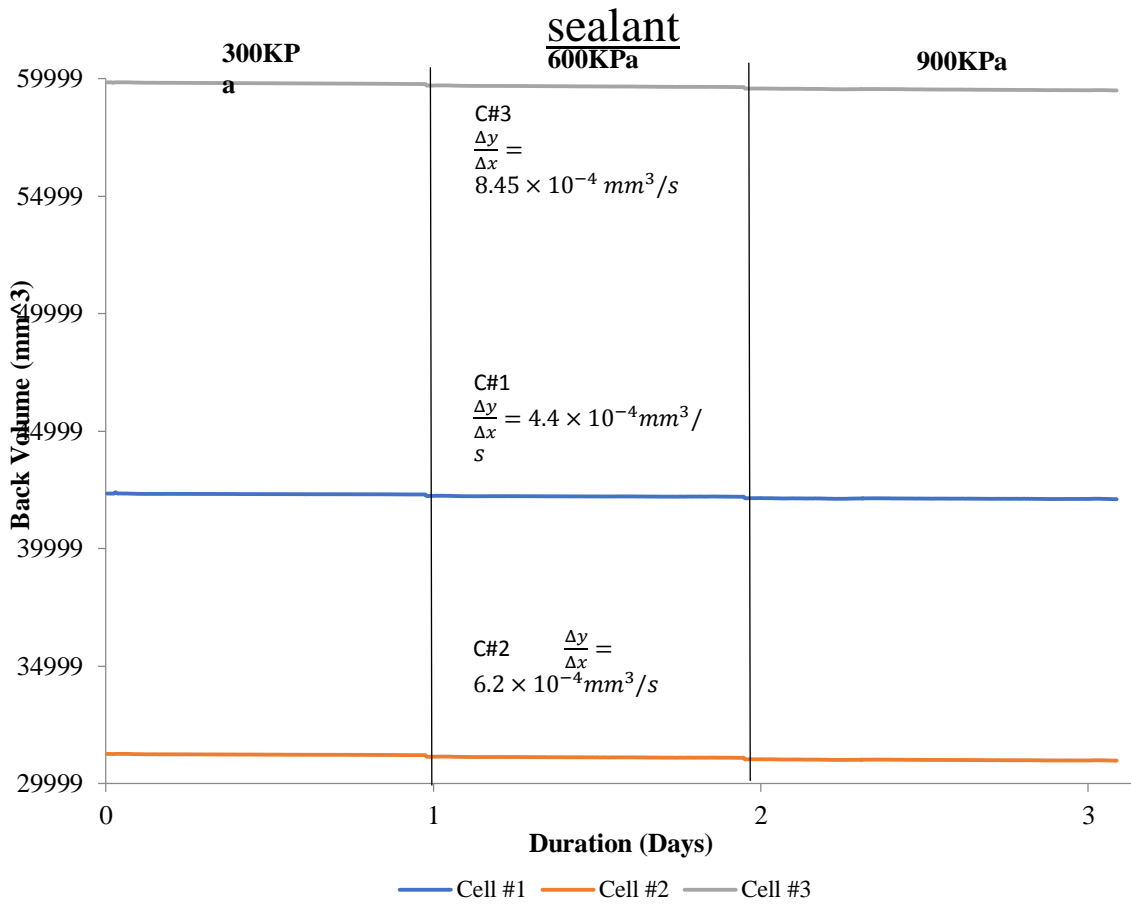


Figure A17: Thermo-pressure calibration run at 90°C

Pressure/ Volume test at 100°C with Three-

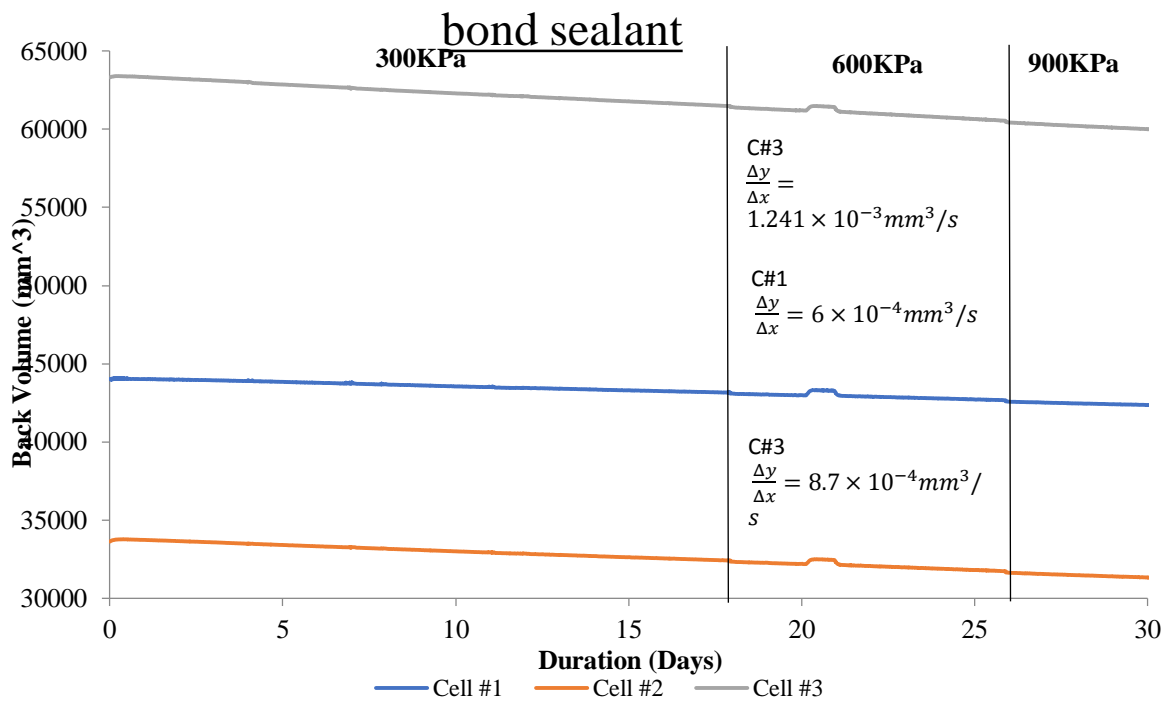


Figure A18: Thermo-pressure calibration run at 100°C

During the 600KPa stage at the 100°C temperature increment, the room temperature control system failed (an issue that was beyond our control), this is observed in figure A18. The slight rise in the volume slope during the aforesaid stage is due to the room temperature spike, during this period the room temperature was recorded at 25°C. This again indicates the sensitivity of these controllers to temperature fluctuations. All graphs display the steepest gradient produced by the controller nearest to the oven (cell #3), which comparatively has the most of the piping exposed to the oven interior. This therefore indicates that the effects of temperature cannot be completely negated as the thermal gradient across the piping from the interior cell to the exterior controller cannot be circumvented; nonetheless the seal issue was resolved as shown on figures A15, A16, A17 and A18 respectively.

